Journal of Heat Transfer

Published Quarterly by The American Society of Mechanical Engineers

VOLUME 118 • NUMBER 4 • NOVEMBER 1996

TECHNICAL PAPERS

(Contents continued)

TECHNICAL NOTES

ANNOUNCEMENTS

Real-Time Physiconeural Solutions for MOCVD

A. S. Kelkar
Department of Chemical Engineering.

R. L. Mahajan[1]
Department of Mechanical Engineering.

R. L. Sani
Department of Chemical Engineering.

University of Colorado at Boulder,
Boulder, CO 80309

This paper presents an integrated physiconeural network approach for the modeling and optimization of a vertical MOCVD reactor. The basic concept is to utilize the solutions obtained from a physical model to build an accurate neural network (NN) model. The resulting model has the attractive features of self-adaptiveness and speed of prediction and is an ideal starting tool for process optimization and control. Following this approach, a first-principles physical model for the reactor was solved numerically using the Fluid Dynamics Analysis Package (FIDAP). This transient model included property variation and thermodiffusion effects. Using software developed in house, neural networks were then trained using FIDAP simulations for combinations of process parameters determined by the statistical Design of Experiments (DOE) methodology. The outputs were the average and local deposition rates. It is shown that the trained NN model predicts the behavior of the reactor accurately. Optimum process conditions to obtain a uniform thickness of the deposited film were determined and tested using the physical model. The results demonstrate the power and robustness of NNs for obtaining fast responses to changing input conditions. A procedure for developing equipment models based on physiconeural network models is also described.

1 Introduction

Semiconductor heterojunctions with very small dimensions such as quantum wells (QWs) and quantum well wires (QWWs) have been attracting considerable attention because they open new ways for manufacturing high performance devices (Naganuma et al., 1990). Examples include single quantum well (SQW) and multi-quantum well (MQW) laser structures that are finding applications in high-speed integrated optics and optical communications because of their significant superiority in performance over conventional double heterostructures (Cockerill et al., 1992; Ando and Fukui, 1989; Seshadri et al., 1992). Device degradation is governed mainly by the abruptness and uniformity of the interfaces between adjacent layers. Therefore, to grow quantum well structures, thin layers with precise thicknesses, abrupt doping profiles, and high quality heterojunctions are required. A commonly used technique for the manufacture of such semiconductor devices is Metal–Organic Chemical Vapor Deposition (MOCVD). This technique is important as a process for growing such compound semiconductors since it allows the fabrication of the multilayer structures by manipulating gas switching manifolds at the inlet of the reactor (Patnaik et al., 1989).

Several researchers have developed mathematical models for different MOCVD reactor configurations in order to understand the flow and temperature patterns. The objective of the various mathematical models employed in numerical computations is to relate performance criteria such as growth rate, uniformity, and interface abruptness to process operating conditions such as pressure, temperature difference, reactant concentrations, rotation rate of susceptor, and reactor geometries (Durst et al., 1992; Dilawari et al., 1990; Fotiadis et al., 1987; Stock and Richter, 1986). Dilawari and Szekely (1989) developed a mathematical description for a MOCVD reactor with a rotating substrate, and observed that uniformity of the deposition in this system can be achieved only by carefully balancing forced and natural convection and the depletion of the reactants. Kleijn (1991) developed two-dimensional and three-dimensional mathematical models for MOCVD of gallium arsenide in a horizontal reactor illustrating the influence of side wall temperatures, buoyancy-driven recirculating flows, and flow instabilities. A comprehensive review of transport phenomena in MOCVD is given by Jensen (1994).

There is a vast body of literature on related thermal CVD. Some earlier studies are from Eversteyn et al. (1970), who developed a stagnation layer model for the epitaxial growth of silicon from silane in a horizontal reactor. Earlier models on silicon CVD (e.g., Berkman et al., 1978; Kusumoto et al., 1985; Ristorcelli and Mahajan, 1987) neglected contributions due to Soret, Dufour, and variable property effects, but it was shown later (Mahajan and Wei, 1991) that the Soret and variable property effects can be significant. In single-wafer Si CVD reactors the ideal hydrodynamic behavior is disturbed by buoyancy-driven mixed convection flows, edge effects, and influence of reactor walls (Evans and Grief, 1987a, b; Houtman et al., 1986; Fotiadis et al., 1990; Weber et al., 1990), necessitating the use of two- or three-dimensional models. For a most recent review on transport phenomena in CVD reactors, see Mahajan (1996).

While these models have increased our understanding of the underlying physics of the process, their utility for real-time performance analysis and control is limited because of the large computational time required to simulate a run. The physical neural network modeling approach presented in this paper is an attractive alternative to mitigate this difficulty. It is shown that real-time predictions of growth rate and uniformity are possible using such models. A methodology for developing equipment models from physiconeural models is also described. These equipment models can then form a basis for process control.

It is to be noted that the main focus of this paper is to demonstrate the attractive features of using physiconeural network models for the MOCVD reactor. Hence certain assumptions have been made in the mathematical model to keep it simple.

2 Mathematical Modeling of MOCVD

A schematic of a vertical MOCVD reactor is shown in Fig. 1. The carrier gas (H$_2$) containing the reactants trimethylgallium

Transactions of the ASME

TMGa + Arsene

Graphite
Susceptor

Quartz
MOCVD
Reactor
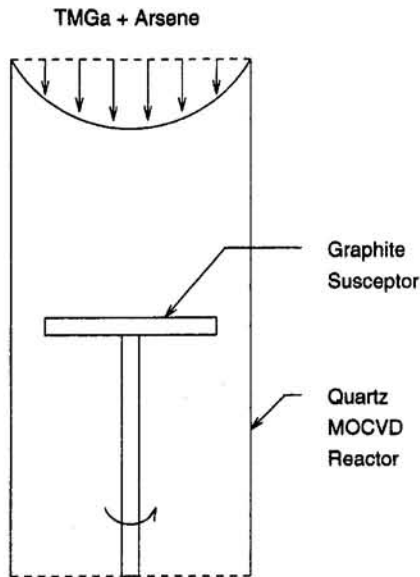
Fig. 1 Schematic of a vertical MOCVD reactor

(TMGa) and arsene (AsH_3) enters through the top of the reactor. A rotating graphite susceptor is placed perpendicular to the flow of the reactants. The reaction takes place at the heated susceptor and GaAs is deposited as a result. A byproduct of the reaction is methane gas that flows out of the reactor along with hydrogen and unused reactants.

For this cylindrical reactor geometry, the equations of continuity, momentum, energy, and mass for an incompressible, Boussinesq flow are as follows:

Continuity:

$$\nabla \cdot \mathbf{v} = 0 \tag{1}$$

Motion:

$$\rho\left(\frac{\partial \mathbf{v}}{\partial t} + \nabla \cdot \mathbf{v}\mathbf{v}\right)$$

$$= -\nabla p - (\nabla \cdot \tau) + \rho_0(1 + \beta(T - T_0))\mathbf{g} \tag{2}$$

where the stress tensor for Newtonian fluids is given by:

$$\tau = -\mu(\nabla \mathbf{v} + (\nabla \mathbf{v})^T) \tag{3}$$

and ρ denotes the gas density, $\mathbf{v}$ the velocity, p the pressure, μ the viscosity, and $\mathbf{g}$ the acceleration due to gravity.

Energy:

$$\rho c_p\left(\frac{\partial T}{\partial t} + \mathbf{v} \cdot \nabla T\right) = \nabla \cdot (k\nabla T) \tag{4}$$

where T denotes the absolute temperature, k the thermal conductivity and c_p the heat capacity at constant pressure.

Dilute Species Transport Equation:

$$\rho \frac{\partial x_A}{\partial t} + \rho(\mathbf{v} \cdot \nabla x_A) = \nabla \cdot [D_{AB}\rho\nabla x_A + D_T\nabla(\ln T)] \tag{5}$$

where D_{AB} is the diffusion coefficient of TMGa in hydrogen and D_T is the Soret coefficient. Thus $D_T\nabla(\ln T)$ is the thermo-diffusion effect term that couples the specie equation with the energy equation. General overviews on thermal diffusion theory are presented by Jones and Furry (1946), Grew and Ibbs (1952) and Hirschfelder et al. (1963). For derivation of the transport equations, the reader is referred to Bird et al. (1960).

Some assumptions have been made that largely reduce the complexity of the problem. They are as follows:

1 The gases are ideal.
2 The gas flow in the reactor is laminar.
3 No heat is consumed or released by the gas phase reactions.
4 The gases are transparent to heat radiation from the susceptor.
5 The Dufour effect is neglected.
6 The surface reaction is instantaneous.
7 Gas phase reactions are neglected.
8 Viscous dissipation is negligible.

Over the range of room to susceptor temperatures, the variation of transport properties of hydrogen is significant. The temperature dependencies of ρ, μ, k, and D_{AB} for the TMGa–hydrogen system are as follows:

$$\rho = pM/RT \tag{6}$$

$$\frac{\mu}{\mu_0} = \left(\frac{T}{T_0}\right)^{0.648} \tag{7}$$

$$\frac{k}{k_0} = \left(\frac{T}{T_0}\right)^{0.691} \tag{8}$$

$$\frac{D_{AB}}{D_{AB,0}} = \left(\frac{T}{T_0}\right)^{1.75} \tag{9}$$

─────── **Nomenclature** ───────

c_p = heat capacity
D_{AB} = diffusion coefficient of TMGa in hydrogen
D_T = Soret coefficient
D = desired output vector
E = error vector of a network
f = activation function
$\mathbf{g}$ = acceleration due to gravity
Gr = Grashof number
J = quadratic performance criterion of a network
k = thermal conductivity
M = molecular weight
m_i = local deposition rate at ith node
$\bar{m}$ = average deposition rate
p = pressure

Pr = Prandtl number
r = radial distance
R = radius of the reactor
Re = Reynolds number
R^2 = correlation coefficient
t = time
t_i = bias vector for NN
T = temperature
v = velocity
w_{ij} = weight matrix for NN
x_j = jth input to a neuron
x_A = mole fraction of TMGa
y_i = ith output from a neuron
z = axial distance
α = momentum coefficient
β = coefficient of thermal expansion

ϵ = mean square error
μ = viscosity
η = learning rate
ρ = gas density
σ^2 = variance
σ_n = standard deviation
τ = shear stress
ω = rotation rate of susceptor

Subscripts

0 = at standard/initial conditions
s = at the susceptor
r = radial component
z = axial component
θ = azimuthal component

The temperature dependences of viscosity and thermal conductivity are obtained from Moffat and Jensen (1988), and that for the diffusion coefficient is obtained from Fuller correlations (Reid et al., 1987). The variation of the thermodiffusion coefficient D_T is obtained from Dilawari and Szekely (1989).

The boundary conditions for solving the equations of continuity, motion, energy, and mass are as follows:
At the reactor inlet:

$$v_z = v_0 \left(1 - \frac{r^2}{R^2} \right), \, T = T_0, \, x_A = x_{A,0}. \qquad (10)$$

At the susceptor:

$$v_z = v_r = 0, \, v_\theta = r\omega, \, T = T_s, \, x_A = 0. \qquad (11)$$

At the reactor walls:

$$\mathbf{v} = 0, \, T = T_0, \, m_i = 0. \qquad (12)$$

At the axis of symmetry:

$$\partial v_z / \partial r = 0, \, \partial T / \partial r = 0, \, m_i = 0. \qquad (13)$$

At time $t = 0$, it was assumed that $x = x_0$ at the reactor inlet and $x = 0$ everywhere else. A parabolic velocity profile is assumed at the reactor inlet, and the walls are kept at the ambient temperature. There is no mass deposition on the reactor walls. The susceptor is heated and rotated at a constant angular velocity. The surface reaction is much faster than the diffusion of reactants to the surface, hence the concentration of the reactant is taken to be zero at the surface.

3 Numerical Simulation

Equations (1), (2), (4), and (5) were solved in a coupled manner using the Fluid Dynamics Analysis Package (FIDAP Version 7.05, Copyright ©1984–1993 Fluid Dynamics International, Inc.). Modifications were made to the existing FIDAP code to predict the growth rate profiles, taking into account the thermodiffusion effect.

Grid-size refinement was performed for the finite element grid using FIDAP as follows. The number of algebraic equations solved was varied from 7000 to 28,000 in steps of 3500, and the results were computed for a typical case of operating conditions. It was observed that the solution did not change within a nodal point tolerance of 10^{-4} for simulations with $\geq 14,000$ algebraic equations. Thus the finite element model with 14,000 equations was used in our analysis. The numerical accuracy of each of the reported simulations is of the order of 10^{-4}.

Simulations were run by choosing the process parameters in the following ranges: temperature difference (500–1000 K), Reynolds number (10–100), inlet mole fraction of GaAs (0.001–0.05), rotation rate (0–100 rpm). For a susceptor temperature of 750 K, Reynolds number of 50, inlet mole fraction of 0.0255, pressure of 0.1 atm, and a rotation rate of zero, the steady-state velocity, temperature, and specie contour plots are shown in Fig. 2. As seen in the figure, the buoyancy-induced flow rises from the center of the susceptor, and forms a cell over the susceptor. The forced flow streams past the cell and out of the reactor. The stagnation cell obstructs the flow of fresh reactants to the surface of the susceptor and is, therefore, undesirable. As expected, the isotherms are not as densely packed near the susceptor as for the forced convection dominated flow (not shown here). This difference is due to the presence of the recirculation cell over the susceptor. The results for the streamlines, isotherms and isoconcentration lines as
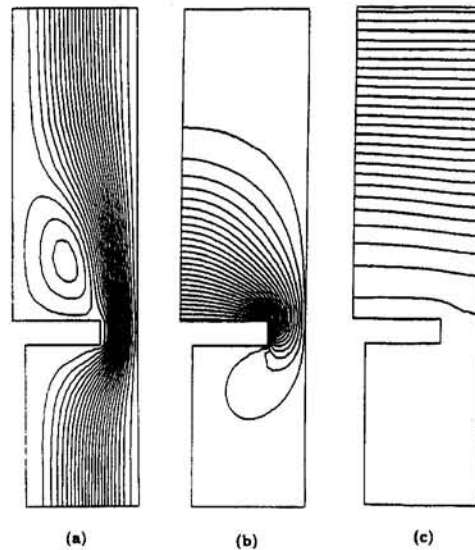
Fig. 2 Typical steady-state velocity, temperature, and concentration profiles for $\Delta T = 750$, Re = 50.0, $x_0 = 0.0255$, $\omega = 0$: (a) streamline contour plot; (b) temperature contour plot; (c) specie contour plot

shown in Fig. 2 are consistent with previous studies (e.g., Patnaik et al., 1989).

The buoyancy-induced cell is generally associated with nonuniform deposition (Kleijn, 1991). To mark the appearance and disappearance of the cell, numerical computations were performed in the following two ways. In the first case, the Gr was held constant at a fixed value (Gr $\approx$ 573) and Re was slowly increased from 10 to 100. With increase in Re, the recirculation cell decreased in size and at a certain value (about 70) the cell disappeared completely. When Re was decreased steadily from a high value, the cell appeared exactly at the same Reynolds number. In the second set of calculations, the Re was held constant (Re = 70) and the Gr was steadily increased from a value of 400 to 900. At some value of Gr (about 573) the cell appeared and then continued to grow. In this case, too, the cell appeared and disappeared at the same Gr when simulations were performed for increasing and decreasing Gr. Thus in both cases, hysteresis was not observed. This is in contrast to the behavior seen in mixed convection systems at atmospheric pressure by Patnaik et al. (1989) and Calmidi and Mahajan (1996), where hysteresis was observed. We conclude that in the range of parameters studied, there is no hysteresis in the MOCVD reactor at 0.1 atm.

4 The Neural Network Model

4.1 Introduction. A neural network (NN) is a computational tool that can be used for the modeling and control of highly nonlinear systems. These networks have the ability to estimate input–output relations from sample data. Unlike statistical estimators, they do not require a mathematical model of the dependence of outputs on inputs. They are, thus, model-free estimators (Kosko, 1992; Simpson, 1992; Freeman and Skapura, 1991). In addition, they are self-adaptive, have generalization capability, and provide quick response. Because of these desirable characteristics, they have been used in identification, control, noise-filtering, optimization, pattern-matching, pattern completion and classification (Simpson, 1992).

Figure 3(a) shows a typical four-layer NN. An input pattern is presented to the leftmost layer of the network (input layer), and the rightmost layer gives the output pattern. Each node of a layer is connected to every node of the adjacent layer(s) by
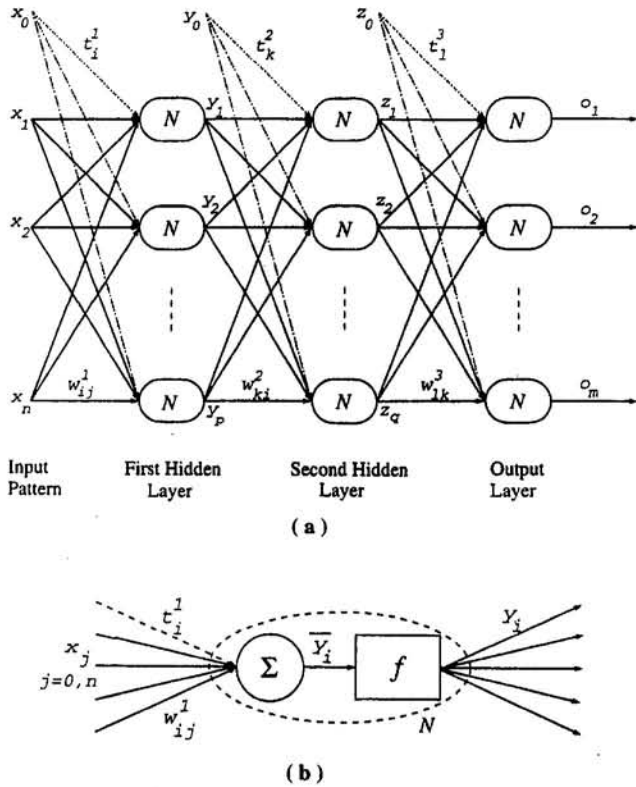
Fig. 3 (a) A typical three-layered NN; (b) one particular node of the second layer of the above NN

synaptic connections. Figure 3(b) shows a schematic of one particular node of the NN. A node performs two functions: summation and nonlinear transformation. The latter is usually a sigmoid function called the activation function. In this work, the activation function used was:

$$f(x) = \tanh(x) \tag{14}$$

Note that when the activation function is defined in this manner, the output of the network lies between -1 and 1. The output of one particular node of the first hidden layer is given by

$$y_i = f(\sum_{j=1}^{n} x_j w_{ij}^1 + t_i^1) \tag{15}$$

where w_{ij} is the weights matrix, t_i is the bias vector, x_j is the input to the neuron, and the superscript 1 denotes the first hidden layer. The objective of NN training is to minimize some performance criterion by updating the weights and the biases. A typical update rule for the weights and biases is given by

$$w_{ij}^{\kappa,new} = w_{ij}^{\kappa,old} - \eta \nabla_{w^\kappa} J + \alpha \Delta w_{ij}^{\kappa,old} \tag{16}$$

$$t_i^{\kappa,new} = t_i^{\kappa,old} - \eta \nabla_{t^\kappa} J + \alpha \Delta t_i^{\kappa,old} \tag{17}$$

where $\kappa = 1, 2, \ldots \tau$, and τ is the number of layers in the network, η is the learning rate and it determines how fast the network will learn, and α is the momentum parameter, which is usually set to a positive value less than unity. J is the quadratic performance criterion of the neural network, and is a function of the error vector E between the desired output of the network (D) and the actual output of the network (O):

$$J(E) = \tfrac{1}{2} E^T E \tag{18}$$

4.2 NN Model Development Technique. Marwah et al. (1996) recently developed a "simple to complex" neural network modeling approach. For selecting the appropriate NN ar-

chitecture, the data points are split into a training set consisting of approximately $\frac{3}{4}$ of the data points and a testing set consisting of approximately $\frac{1}{4}$ of the data points. The inputs and outputs are normalized between -0.8 and $+0.8$ in order to avoid the saturation region of the sigmoid transfer function. The correlation coefficient (R^2) and mean square error (ϵ) are used to evaluate the performance of the network. These are defined as:

$$R^2 = 1 - \left[\frac{\sum_{i=1}^{N} (y_i - y_i^p)^2}{\sum_{i=1}^{N} (y_i - \bar{y})^2} \right] \tag{19}$$

$$\epsilon = \frac{1}{N} (\sum_{i=1}^{N} (y_i - y_i^2)^2)^{1/2} \tag{20}$$

where y_i and y_i^p are the actual and predicted values, respectively, and $\bar{y}$ is the averaged value.

To find the optimum network architecture, we start with one hidden layer with one neuron. The network is trained with the training data and $R^2_{training}$ is monitored to check the performance of the network. If R^2 is below 0.8, then another neuron is added. After this prescribed threshold value of R^2 is reached, testing data is simultaneously introduced to the network. As the network is trained, $\epsilon_{testing}$ and $R^2_{testing}$ are calculated. Training is stopped when the minimum of $\epsilon_{testing}$ is obtained, and no further improvement in performance results with the addition of one more neuron.

Once the number of hidden layers and neurons are fixed, additional parameters such as the learning rate η and momentum α have to be chosen. The optimum values of these parameters are obtained by using the same training/testing technique. This procedure results in a network that is the simplest, requires minimum training time and avoids overdetermination.

4.3 The NN Model Development for MOCVD. For the vertical MOCVD reactor described earlier, the mathematical model predicts the average deposition rate and variance of deposition rate as a function of the following process parameters: temperature difference between the susceptor and reactor walls, inlet Reynolds number, inlet TMGa mole fraction, and rotation rate of susceptor. The average deposition rate ($\bar{m}$) along the susceptor is defined as:

$$\bar{m} = \frac{1}{n} \sum_{i=1}^{n} m_i \tag{21}$$

where the local deposition flux (m_i) (from Eq. (5)) is given by:

$$m_i = -c D_{AB} \frac{\partial x_A}{\partial z} + \frac{D_T}{T} \frac{\partial T}{\partial z} \tag{22}$$

The variance σ^2 of deposition rate is defined as:

$$\sigma^2 = (1/n) \left[\sum_{i=1}^{n} \left(\frac{m_i - \bar{m}}{\bar{m}} \right)^2 \right] \tag{23}$$

where n is the number of grid points along the radius of the susceptor.

Two NN models, one relating the average deposition rate and the other the variance of deposition rate with the four input parameters, were developed. A set of 25 experiments identified by statistical central composite design (Montgomery, 1991) was split into a training set of 19 points and a testing set of 6 points. Six additional data points within the domain of the central composite design were chosen as the validation points.

Table 1   DOE training/testing points from FIDAP model

	ΔT	Re	x_0	ω
1	594.6	10	0.00119	0
2	594.6	10	0.00119	84.09
3	594.6	10	0.042	0
4	594.6	10	0.042	84.09
5	594.6	84.09	0.00119	0
6	594.6	84.09	0.00119	84.09
7	594.6	84.09	0.042	0
8	594.6	84.09	0.042	84.09
9	840.9	10	0.00119	0
10	840.9	10	0.00119	84.09
11	840.9	10	0.042	0
12	840.9	10	0.042	84.09
13	840.9	84.09	0.00119	0
14	840.9	84.09	0.00119	84.09
15	840.9	84.09	0.042	0
16	840.9	84.09	0.042	84.09
17	500.0	50.0	0.0255	50.0
18	1000.0	50.0	0.0255	50.0
19	750.0	10	0.0255	50.0
20	750.0	100.0	0.0255	50.0
21	750.0	50.0	0.001	50.0
22	750.0	50.0	0.05	50.0
23	750.0	50.0	0.0255	0
24	750.0	50.0	0.0255	100.0
25	750.0	50.0	0.0255	50.0

Table 2   Validation points from FIDAP model

	ΔT	Re	x_0	ω
26	850.0	85.0	0.035	85.0
27	600.0	60.0	0.02	40.0
28	650.0	75.0	0.03	25.0
29	550.0	92.0	0.01	92.0
30	900.0	35.0	0.008	18.0
31	950.0	15.0	0.025	65.0

reactor model, a NN with only one hidden layer was sufficient and adding another hidden layer did not improve the predictions of the network significantly. Figure 4 shows the effect of the number of neurons in the hidden layer on the testing error of the NN for the case of a four-input one-output network. Clearly there exists an optimum number of neurons that minimizes the testing error of the NN. This is intuitively reasonable because as we add more neurons to the network the system becomes overdetermined.

To ensure robustness, several neural networks for different combinations of training and testing data were built. For each of these networks, different sets of 19 training points and 6 testing points were chosen. The network that gave the minimum error was used in all further calculations. The best NN configuration was found to be (4–4–1), i.e., 4 neurons in the input layer, 4 in the hidden layer, and 1 in the output layer. A comparison of this NN model with the mathematical model is shown in Fig. 5. The error between the predictions of the two models is small ($\epsilon_{\text{testing}} = 0.01$; $R^2_{\text{testing}} = 0.95$).

4.4   The Local Deposition Rate Network. In order to predict the deposition rate as a function of radial distance along the susceptor, it was necessary to develop a NN that could learn the deposition rate profiles rather than the average deposition rate. For this purpose, a network was trained with an added input, viz., the radial distance, and 43 experimental training points were determined using a central composite design for 5
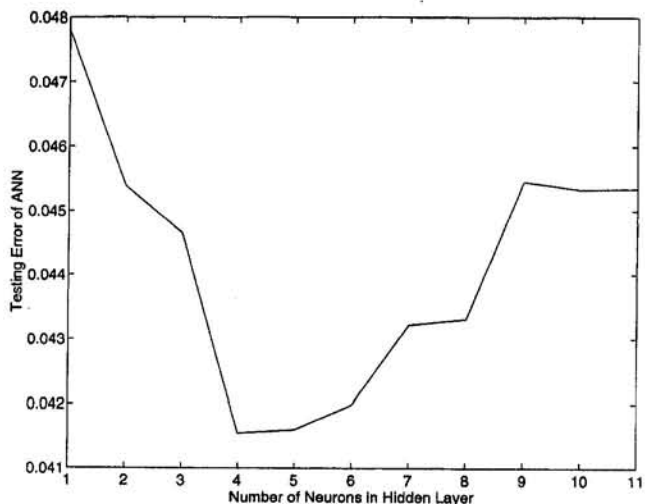
Fig. 4   Effect of number of neurons on testing error of NN

These data points are listed in Tables 1 and 2. The mathematical model was solved for these test conditions to obtain the deposition rate and variance of deposition rate.

The procedure outlined in Section 4.2 was used to develop an optimum NN model. The simulations described above supplied the training and testing data. It was found that for the
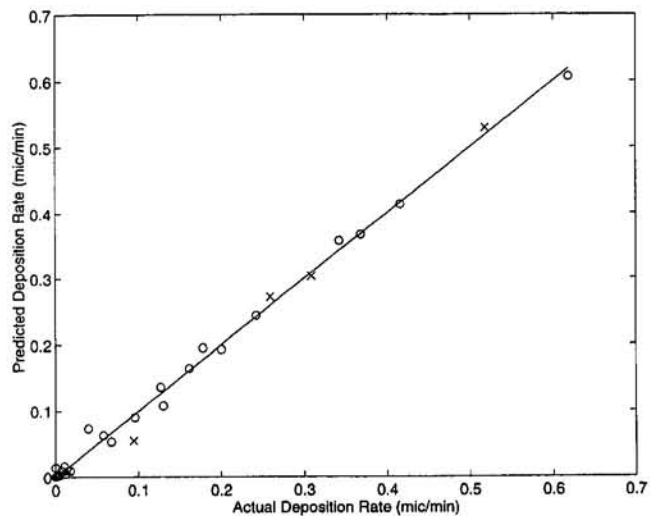
Fig. 5 Comparison between NN model and physical model (o-training and testing points, x-validation points)

Fig. 7 Steady-state velocity, temperature, and concentration profiles for the optimum conditions: $\Delta T = 673.8$, Re $= 28.8$, $x_0 = 0.0122$, $\omega = 3.0$: (a) streamline contour plot; (b) temperature contour plot; (c) specie contour plot

variables. A set of 13 other validation points was chosen for testing. It was found that even though R^2_{testing} was about 0.91 for this local NN, the $\epsilon_{\text{testing}}$ was unacceptably high. Thirty more data points were therefore added to the original 43. The network was retrained till $\epsilon_{\text{testing}}$ reached 0.01. A comparison of the retrained NN model with the mathematical model in Fig. 6 indicates good accuracy.

5 Application of the Physico-NN Model

The physico-NN model (PNM) developed in Section 4 can be used as a fast analysis tool to predict the responses of the MOCVD reactor system to different operating parameters, or to predict the minimum variance (σ^2) of deposition rate over the entire range of process operating parameters. These two capabilities are discussed next.

5.1 PNM as a Real-Time Analysis Tool. The physical models described above are useful for capturing the underlying relationships between the various input and output variables. However, many a time, they tend to be computationally intensive and are not attractive for performing fast analysis of ''what-if scenarios.'' For example, it took us about 80 CPU minutes

Fig. 6 Local deposition rate: comparison between NN model (*) and physical model (−)

to complete one simulation on a DEC 5000 workstation. However, with the physiconeural network model, the computational time was only ≈ 0.09 seconds. The PNM can thus be effectively used to obtain real-time predictions or performance measures for the MOCVD reactor.

5.2 Minimum Variance of Deposition Rate Using PNM. The variance network described in Section 4.3 was used to determine the minimum variance of the deposition rate along the susceptor for different sets of process operating conditions. Following the procedure given in Wang and Mahajan (1996), a steepest descent optimization algorithm was used to obtain the operating point at which the variance of the deposition rate was minimum. It is important in a real process to operate at this point because the deposited film will be uniform.

An iterative procedure was followed to determine the optimum settings. The minimum variance obtained by the PNM was compared to that obtained using FIDAP, for the same operating conditions. If the error between these was greater than the preset exit criterion (10 percent in this case), this new point was added to the training data, and the PNM was retrained. This iterative procedure was terminated when the minimum variance predicted by the PNM was within 10 percent of that obtained by the FIDAP model. Typically about 6–10 iterations were required in this case in order to obtain the desired accuracy.

The optimum process operating conditions predicted by the NN-optimization algorithm for a minimum variance of 0.010 are: $\Delta T = 673.8$ K, Re $= 28.8$, $x_0 = 0.0122$, $\omega = 3.0$. For these parameters, the FIDAP simulations give a variance of 0.011. The streamline, temperature, and concentration contours are shown in Fig. 7. Note that there is no buoyancy-induced cell (Fig. 7(a)) for these optimum conditions. A comparison of the deposition rate at the optimum conditions to that at the conditions shown in Fig. 2 is shown in Fig. 8. Clearly, the deposition rate is more uniform for the optimum settings. This is due to a lack of the buoyancy-induced cell at these settings. An examination of the temperature as well as the concentration gradients for the two cases indicated that these were more uniform along the susceptor for the optimum conditions. According to Eq. (22), this results in more uniform deposition rates.

6 Physiconeural Network Models for Process Control

The two applications of PNMs discussed in the previous section illustrate their use as a design tool for performing "what-if" analyses and arriving at initial process recipe for optimum operation. However, because of the simplifying assumptions made in the physical model, the PNM may not provide an accurate description of the actual process equipment. The equipment model then needs to be built to capture the peculiarities of the equipment involved. Two strategies to update PNMs to equipment models are represented schematically in Fig. 9. As a first step, the predictions of the PNM are compared against the experimental data. In approach 1 (Fig. 9(a)), if the predictions of the PNM do not match with the experimental data to within a prescribed accuracy, part of the experimental data is fed back into the training set and the model is retrained and evaluated for the unseen data. Once the PNM has been sufficiently trained to predict the experimental data accurately, it can be used as the equipment model.

In the second approach (Fig. 9(b)), if the predictions of the PNM do not match with the experimental data to within a prescribed accuracy, the difference between these values is used to train a deviation-NN model. Once this network is trained, the equipment model can be obtained by:

$$\text{Deviation-NN} + \text{PNM} = \text{Equipment Model}$$

The equipment model so developed can be used for process optimization on the lines described in Section 5.2 or for process control in the manner described in Wang and Mahajan (1995).

7 Summary

A mathematical model for a vertical MOCVD reactor was developed that included Soret and variable property effects. A finite element-based computational package (FIDAP) was used numerically to solve the three-dimensional coupled PDEs for the conservation of mass, momentum, and energy to determine the deposition rates of GaAs in the reactor. Using data from simulations based on statistical DOE, neural networks were trained to mimic the behavior of the reactor. The best NN architecture that minimized the testing error was determined. The NN model compared well with the predictions of the mathematical model. Optimum process operating conditions were obtained that minimized the variance in deposition rate. It was shown that the computational time required for the NN model was

(a)

(b)

Fig. 9 Methodology for the development of equipment models using PNMs: (a) updating approach, (b) deviation model approach

orders of magnitude smaller as compared to the mathematical models, thus enabling NN models to be used as tools for real-time process modeling and optimization.

Research is in progress to build an equipment model for a production MOCVD reactor. The physiconeural model will have to be retrained using experimental data points. The expectation is that the number of data points would be much smaller than building an equipment neural network model from scratch. The findings of this research will be reported in an upcoming paper.

References

Ando, S., and Fukui, T., 1989, "Facet Growth of AlGaAs on GaAs With SiO_2 Gratings by MOCVD and Applications to Quantum Well Wires," *J. Crystal Growth*, Vol. 98, p. 646.

Berkman, S., Ban, V. S., and Goldsmith, N., 1978, "An Analysis of the Gas Flow Dynamics in a Horizontal CVD Reactor," *Heteroepitaxial Semiconductors for Electronic Devices*, G. W. Cullen and C. C. Wang, eds., Springer, New York, Ch. 7, p. 264.

Bird, R. B., Stewart, W. E., and Lightfoot, E. N., 1960, *Transport Phenomena*, Wiley, New York.

Calmidi, V., and Mahajan, R. L., 1995, "Mixed Convection on a Horizontal Surface Within a Partial Enclosure: presented at ASME Int. Mech. Eng. Cong. Exp., Nov. 13–18, San Francisco.
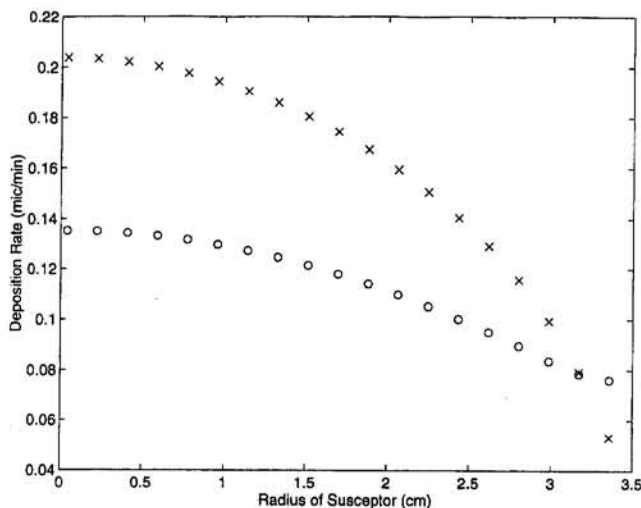
Fig. 8 Deposition rate for minimum variance: (o); $\Delta T = 673.8$, Re = 28.8, $x_0 = 0.0122$, $\omega = 3.0$; and for the conditions in Fig. 2: (x); $\Delta T = 750.0$, Re = 50.0, $x_0 = 0.0255$, $\omega = 0$
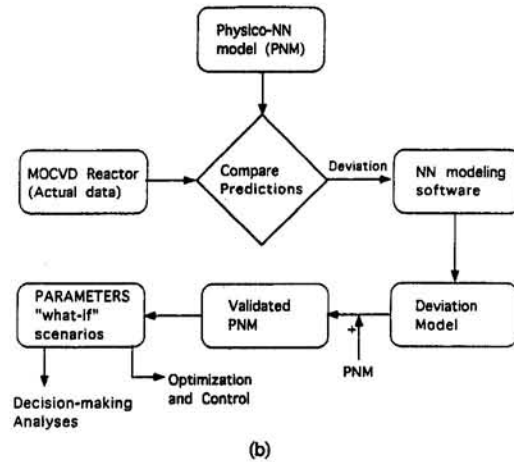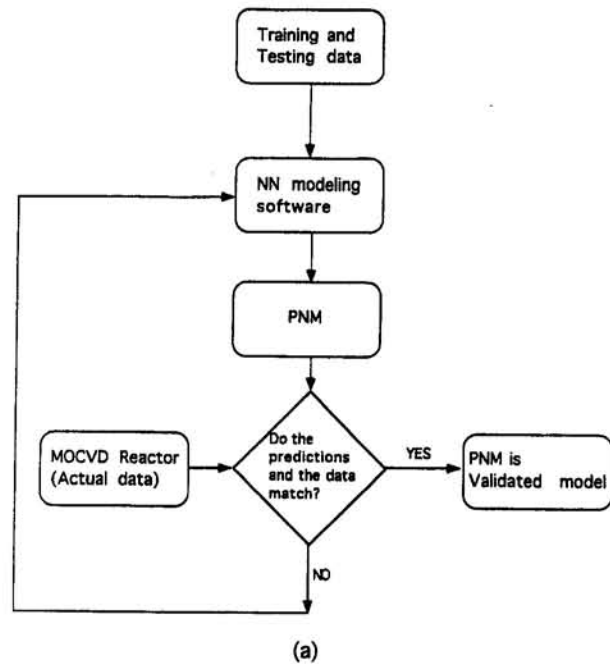
Cockerill, T. M., Honig, J., Forbes, D. V., Beernink, K. J., and Coleman, J. J., 1992, "Characterization of Electrical and Optical Loss of MOCVD Regrowth in Strained Layer InGaAs–GaAs Quantum Well Heterostructure Lasers," *J. Crystal Growth,* Vol. 124, p. 553.

Dilawari, A. H., and Szekely, J., 1989, "Computed Results for Deposition Rates and Transport Phenomena for an MOCVD System With a Conical Rotating Substrate," *J. Crystal Growth,* Vol. 97, p. 777.

Dilawari, A. H., Szekely, J., and Daly, J., 1990, "Experimental Measurements and Theoretical Predictions for the MOCVD of Gallium Arsenide Using a Barrel-Type Reactor," *J. Crystal Growth,* Vol. 102, p. 635.

Durst, F., Kadinskii, L., Peric, M., and Schafer, M., 1992, "Numerical Study of Transport Phenomena in MOCVD Reactors Using a Finite Volume Multigrid Solver," *J. Crystal Growth,* Vol. 125, p. 612.

Evans, G., and Grief, R., 1987a, "Effects of Boundary Conditions on the Flow and Heat Transfer in a Rotating Disk Chemical Vapor Deposition Reactor," *Numer. Heat Transfer,* Vol. 12, p. 243.

Evans, G., and Grief, R., 1987b, "A Numerical Model of the Flow and Heat Transfer in a Rotating Disk Chemical Vapor Deposition Reactor," ASME JOURNAL OF HEAT TRANSFER, Vol. 109, p. 928.

Eversteyn, F. C., Severin, P. I. W., vida Brekel, C. H. J., and Peck, H. L., 1970, "A Stagnation Layer Model for the Epitaxial Growth of Silicon From Silane in a Horizontal Reactor," *J. Electrochem. Soc.,* Vol. 117, No. 7, p. 925.

Fotiadis, D. I., Kremer, A. M., McKenna, D. R., and Jensen, K. F., 1987, "Complex Flow Phenomena in Vertical MOCVD Reactors: Effects on Deposition Uniformity and Interface Abruptness," *J. Crystal Growth,* Vol. 85, p. 154.

Fotiadis, D. I., Kieda, S., and Jensen, K. F., 1990, "Complex Flow Phenomena in Vertical MOCVD Reactors: Effects on Deposition Uniformity and Interface Abruptness," *J. Crystal Growth,* Vol. 102, p. 441.

Freeman, J. A., and Skapura, D. M., 1991, *Neural Networks,* Addison-Wesley.

Grew, K. E., and Ibbs, T. L., 1952, *Thermal Diffusion in Gases,* Cambridge Univ. Press, Cambridge, United Kingdom.

Hirschfelder, J. O., Curtiss, C. F., and Bird, R. B., 1967, *Molecular Theory of Gases and Liquids,* Wiley, New York.

Houtman, C., Graves, D. B., and Jensen, K. F., 1986, "CVD in Stagnation Point Flow. An Evaluation of the Classical 1D Treatment," *J. Electrochem. Soc.,* Vol. 133, No. 5, p. 961.

Jensen, K. F., 1994, "Transport Phenomena in Epitaxy Systems," *Handbook of Crystal Growth,* Vol. 3b, D. Hurle, ed., Elsevier, Amsterdam.

Jones, C. R., and Furry, W. H., 1946, *Rev. of Modern Phys.,* Vol. 18, No. 2, p. 151.

Kelkar, A. S., 1993, "Neural Networks for the Modeling of Diabetes Mellitus," Master's Thesis, Univ. of Colo., Boulder.

Kleijn, C., 1991, "Transport Phenomena in Chemical Vapor Deposition Reactors," Ph.D. Thesis, Netherlands.

Kosko, B., 1992, *Neural Networks and Fuzzy Systems,* Prentice-Hall.

Kusumoto, Y., Hayashi, T., and Komiya, S., 1985, "Numerical Analysis of the Transport Phenomena in MOCVD Process," *Jap. J. App. Physics,* Vol. 24, No. 5, p. 620.

Mahajan, R. L., and Wei, C., 1991, "Buoyancy, Soret, Dufour and Variable Property Effects in Silicon Epitaxy," ASME JOURNAL OF HEAT TRANSFER, Vol. 113, p. 688.

Mahajan, R. L., 1993, "Process Optimization and Control in Semiconductor Manufacturing," invited paper, presented at the ASME Winter Annual Meeting, New Orleans, LA, Nov. 30.

Mahajan, R. L., 1996, "Transport Phenomena in Chemical Vapor Deposition Systems," *Advances in Heat Transfer,* Academic Press, Vol. 28, p. 339.

Marwah, M., Li, Y., and Mahajan, R. L., 1996, "Integrated Neural Network Modeling for Electronic Manufacturing," *J. Electronic Manufacturing,* Vol. 6, No. 2, June.

Moffat, H., and Jensen, K. F., 1988, "Three-Dimensional Flow Effects in Silicon CVD in Horizontal Reactors," *J. Electrochem. Soc.,* Vol. 135, p. 459.

Montgomery, D. C., 1991, *Design and Analysis of Experiments,* Wiley, New York.

Naganuma, M., Notomi, M., Iwamura, H., Okamoto, M., Nishida, T., and Tamamura, T., 1990, "In GaAs/InP Quantum Well Wires Fabricated by GSMBE, MOCVD, and Selective Chemical Etching Techniques," *J. Crystal Growth,* Vol. 105, p. 254.

Patnaik, S., Brown, R. A., and Wang, C. A., 1989, "Hydrodynamic Dispersion in Rotating-Disk OMVPE Reactors: Numerical Simulation and Experimental Results," *J. Crystal Growth,* Vol. 96, p. 153.

Reid, R. C., Prausnitz, J. M., and Poling, B. E., 1987, *The Properties of Gases and Liquids,* 4th ed., McGraw-Hill, New York, p. 587.

Ristorcelli, J. R., Jr., and Mahajan, R. L., 1987, "Silicon Deposition and Dopant Incorporation in Epitaxial Processes," *Proc. 2nd ASME–JSME Thermal Engineering Joint Conference,* HI, Mar. 22–27.

Seshadri, S., Guido, L. J., Moise, T. S., Beggy, J. C., Cunningham, T. J., and Barker, R. C., 1992, "Non-equilibrium Al-Ga Interdiffusion in MOCVD Reactor Annealed AlGaAs Quantum Well Heterostructures," *J. Electronic Materials,* Vol. 21, No. 1, p. 33.

Simpson, P. K., 1992, "Foundations of Neural Networks," *Artificial Neural Networks,* IEEE Press.

Stock, L., and Richter, W., 1986, "Vertical Versus Horizontal Reactor: An Optical Study of the Gas Phase in a MOCVD Reactor," *J. Crystal Growth,* Vol. 77, p. 144.

Wang, X. A., and Mahajan, R. L., 1995, "CVD Epitaxial Deposition in a Vertical Barrel Reactor: Process Modeling and Optimization Using Neural Network Models," *J. Electrochem. Soc.,* Vol. 142, No. 9, p. 3123.

Wang, X. A., and Mahajan, R. L., 1996, "Artificial Neural Network Model-Based Run-to-Run Process Controller," *IEEE Trans. CPMT,* Part C, Vol. 19, No. 1, p. 9.

Weber, C., Opdorp, C. van, and Keijser, M. de, 1990, "Modeling of Gas-Flow Patterns in a Symmetrical Vertical Vapor-Phase-Epitaxy Reactor Allowing Asymmetric Solutions," *J. Appl. Phys.,* Vol. 67, No. 4, p. 2109.

A Kelvin–Clapeyron Adsorption Model for Spreading on a Heated Plate

R. Reyes

P. C. Wayner, Jr.[1]
email: wayner@rpi.edu

The Isermann Department of
Chemical Engineering,
Rensselaer Polytechnic Institute,
Troy, NY 12180-3590

A new adsorption model for the spreading dynamics of completely wetting fluids on a heated solid substrate that emphasizes interfacial phenomena is developed and evaluated. The model is based on the premise that both interfacial intermolecular forces and temperature affect the vapor pressure in change-of-phase heat transfer and (therefore) the spreading velocity. Classical change-of-phase kinetics, and interfacial concepts like the Clapeyron, Kelvin, and the augmented Young–Laplace equations are used to evaluate the effects of stress (change in apparent dynamic contact angle), temperature, and superheat on the rewetting velocity. Explicit equations are obtained for the velocity, heat flux, and superheat in the contact line region as a function of the initial plate temperature. Comparisons with experimental data for substrate superheats below a critical value demonstrate that the resulting interfacial model of evaporation/condensation in the contact line region can describe the effect of the saturation temperature and superheat on the rewetting velocity.

Introduction

Although the spreading dynamics of fluids on heated surfaces are of importance to many change-of-phase heat transfer processes, a comprehensive model that describes movement in the contact line region and includes interfacial phenomena has not been completely developed and evaluated. This is due to both the complex nature of interfacial phenomena near the leading edge of a liquid film on a substrate and the large number of possible externally imposed conditions. For example, we tend to expect that forced spreading on a flat surface with a large superheat is fundamentally different from movement in an oscillating evaporating meniscus with a small superheat located at the exit of a pore. We might also expect that completely wetting fluids behave differently from partially wetting fluids. However, we propose that these processes are similar at superheats below a critical superheat and that these processes can be modeled using mathematical descriptions of intermolecular forces like interfaces, contact lines, and contact angles. Unfortunately, this is complicated by the fact that the contact angle on a molecular scale at the contact line cannot be seen and the tangent to the liquid vapor interface can change rapidly near the unobservable contact line. Further, due to molecular dynamics, concepts like interfaces, contact angles, and contact lines are not mathematically sharp but physically diffuse and irregular on the molecular scale. Therefore, we note that, in the distant future, the molecular details of these concepts will be completely addressed using computer simulation. Nevertheless, we successfully focus now and herein on a relatively simple model of interfacial dynamics to obtain a better understanding of the effects of both intermolecular forces and temperature on the rewetting of a hot surface by a completely wetting fluid.

Previously, the rewetting of a superheated surface was explained using models based on conduction controlled heat transfer. Conduction through the solid is balanced by a heat sink in the contact line *region*, which is the three-phase junction region where the vapor, liquid, and solid substrate (as modified by the vapor) meet. In this region, the removal of excess heat from the solid conditions the surface for rewetting. Previous researchers used one-dimensional and two-dimensional conduction models for rewetting at high temperatures with various evaporative heat transfer coefficients and different values for the contact line temperature to predict the velocity of rewetting (e.g., Yamanouchi, 1968; Thompson, 1972; Duffey and Porthouse, 1973; Blair, 1975; Dua and Tien, 1976; Elias and Yadigaroglu, 1977; Linehan et al., 1979; Olek et al., 1988; Peng et al., 1992). Recently, Anderson and Davis (1993) discussed the details of thermocapillary fluid motion in the contact line region of spreading volatile droplets on a heated surface.

In a series of change-of-phase heat transfer papers emphasizing interfacial phenomena in evaporating thin films and rewetting, Wayner and co-workers (e.g., Potash and Wayner, 1972; Wayner et al., 1976; Wayner, 1982, 1994; and DasGupta et al., 1994) addressed the coupling of interfacial phenomena and temperature near the contact line in a unique way. These studies used several results on adsorption from the Russian School (Derjaguin et al., 1987). The significance of these studies is that they demonstrated that the effects of temperature and interfacial forces on the vapor pressure can be easily combined to obtain useful models. In particular, the local variation of the surface temperature, heat flux, stress, and film shape can be predicted in the contact line region. In essence, a better phenomenological description of the transport processes was obtained using these models. In a related study emphasizing conduction and interfacial phenomena, Stephan and Busse (1992) evaluated the steady-state two-dimensional temperature field associated with an evaporating meniscus in a groove. Stephan and Hammer (1994) used similar models in nucleate boiling. Dhir and co-workers developed a time and area-averaged model for fully developed nucleate boiling. The boiling process is conceptualized into three regions: thermal layer, intermediate region, and vapor flow dynamics dominated region (Dhir and Liaw, 1989). The thermal layer is modeled as an evaporating extended meniscus (or contact line region) that provides most of the evaporation near the nucleation site (Lay and Dhir, 1994). In another closely related study, Unal et al. (1992) have used the hypothesis that connects the critical heat flux (CHF) with the rewetting of hot surfaces. The importance of the liquid staying in contact with the superheated solid was discussed. Although these papers model change-of-phase heat transfer in the wetting front, they do not address the large effects that interfacial phenomena have on the rewetting process.

Copyright © 1996 by ASME

Herein, we extend the use of a model of forced spreading, which was previously used by Wayner (1994) to predict the superheat at CHF and the *isothermal* spreading velocity. This model of the nonequilibrium film thickness profile is based on the Gibbs–Duhem equation, which describes the effects of the normal stress field (Kelvin effect) and the temperature field (Clapeyron effect) on the equilibrium vapor pressure: In a completely wetting system at equilibrium, the vapor pressure decrease due to a change in the normal stress field resulting from positive capillarity (curvature effect) and the close proximity of the solid substrate (thickness effect) is offset/enhanced by a vapor pressure change due to an increase/decrease in the temperature. The intermolecular force effect due to the film profile can be modified by an imposed temperature field that can either increase or decrease the vapor pressure and thereby result in either evaporation/condensation. Briefly, for rewetting, a forced increase in the apparent contact angle leads to condensation because of a curvature increase near the contact line and, thereby, contact line motion. We find that the predicted macroscopic rewetting velocities can be compared successfully with experimental results available in the literature (Simopoulos et al., 1979) for the forced spreading of F113 (CCl_2F–$CClF_2$) on heated stainless steel when the substrate superheat is below a critical value. Previously, Segev and Bankoff (1980) assumed that the minimum film boiling temperature was the temperature at which only a monolayer exists. We find that we can relate the range of applicability of our adsorption model to this minimum film boiling critical temperature.

Three-Region Model

To describe the rewetting process for a completely wetting fluid on a heated surface, we propose the three-region model for the small contact line region presented in Fig. 1. The use of the Kelvin--Clapeyron equation in Region II to model the rewetting of a hot surface by the process of condensation is new to this field. The *average* liquid profile presented in Fig. 1 represents the physically indistinct contact line region, which fluctuates at the molecular level and which can vary spatially in the ''z'' direction; although we do not know the size of these variations, we expect that they are small. The system is modeled as a solid substrate with an ultrathin liquid film with an average
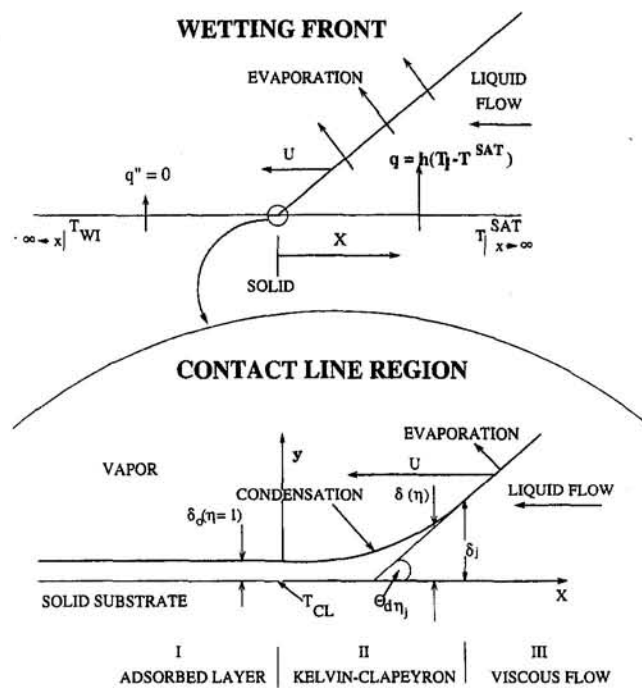
Fig. 1 The rewetting front and schematic of the three region model for a completely wetting fluid rewetting a superheated substrate

(with respect to z, perpendicular to the plane of the page) thickness, $\delta(x)$, which varies in the flow direction. The average temperature, superheat, and interfacial force also vary in the flow direction. The characteristic length in Fig. 1, δ_o, which represents the average adsorbed film thickness at the tri-junction of the vapor, the condensing (and/or evaporating) thin film (Region II), and the equilibrium (for mass transfer) portion of the adsorbed thin film on a solid substrate (Region I) is a function of the local temperature, the local superheat, and the intermolecular force field (as described by Eq. (13) below). In previous papers, δ_o was also called the interline, which is more

Nomenclature

A = Hamaker constant
$\bar{A}$ = modified Hamaker constant = $A/(6\pi)$
a_1 = defined by Eq. (8)
b = defined by Eq. (17)
c = change in stress, defined in Eqs. (15) and (17)
C = specific heat
C_1 = constant (ideal evaporation coefficient)
D = molecular cutoff distance, Eq. (14)
h = heat of vaporization, heat transfer coefficient
IP = intersection points in Fig. (7)
K = curvature
k = thermal conductivity
M = molecular weight
$\dot{m}$ = interfacial mass flux
P = pressure
q'' = heat flux
R = gas constant
r = radius
T = temperature
t = time

U = rewetting velocity
x = parallel to flow direction
y = superheat
β = constant in Eq. (18)
$\Delta\tau$ = dimensionless temperature difference, Eq. (9)
δ = liquid film thickness
λ = wall thickness
ϕ = dimensionless chemical potential, Eq. (7)
$\eta = \delta/\delta_o$ = dimensionless film thickness
$\xi = x/\delta_o$ = dimensionless position
Π = disjoining pressure
σ = surface free energy per unit area
θ = local apparent contact angle
ρ = fluid density
ψ = dimensionless curvature, Eq. (11)
Ω = dimensionless vapor pressure difference, Eq. (5)

Subscripts and Superscripts

c = thermodynamic critical point
CL = contact line

CT = critical transition in the boiling curve
CHF = critical heat flux
d = dynamic
j = junction (see Fig. 1)
i = initial condition, average film
KC = Kelvin–Clapeyron model
l = liquid
M = molar
m = unit mass
max = maximum value
o = contact line
r = reference
s = solid
sat = equilibrium saturation
t = time
v = vapor
$'$ = derivative
η = at thickness η
W = wall

specific than the term "contact line." Herein, both contact line and interline are used for δ_o. The thickness, δ_o, can (but does not have to) be of the order of a monolayer or less and can be discontinuous while filling in "depressions" on a "rough" surface. At the other extreme, for a large volume of a completely wetting liquid under isothermal conditions, δ_o would be the uniform thickness of the liquid.

Although Region I is viewed as being at equilibrium for mass transfer in the model, in reality a small amount of condensation does occur for physical consistency in this region of extremely small slope during rewetting. For a completely wetting fluid, the decrease in vapor pressure due to the adsorption (adhesion) of the liquid on the solid at the interline completely offsets the increase in vapor pressure due to superheat. Below, the temperature and the Hamaker constant, which characterizes the relative effects of cohesion and adhesion, are used to evaluate the thickness of the adsorbed film at δ_o.

In Region II, which is called the Kelvin–Clapeyron (KC) region, the normal stress field is kept constant by a change in both thickness and curvature whereas the temperature decreases with an increase in thickness. Therefore, *condensation* due to the interfacial forces, which produces rewetting of the heated surface, occurs in this extremely short region. This region removes the large resistance to movement normally associated with displacement at the contact line. We can further assume that a recirculating heat flow occurs in an extremely small region: In the immediately adjacent small region, which is the start of Region III, net evaporation removes the heat of condensation from the KC region. The film thickness at the junction of Regions II and III is δ_j. Conceptually, we could say that the usual dynamic equilibrium process at the liquid–vapor interface is replaced by an evaporation–condensation process in which some of the molecules rotate around the junction of Regions II and III. The details of this molecular process are not addressed herein.

In Region III of the liquid, which is not analyzed, *evaporation* occurs over a large area because the superheat is still large but the intermolecular force field is reduced to that of a bulk liquid as a result of an increase in thickness and a decrease in curvature. For the substrate, a one-dimensional conduction model discussed below describes the decrease in the substrate temperature as the fluid rewets the surface.

The relative effects of intermolecular forces (which depend on the film thickness profile) and temperature on the vapor pressure produce this consistent picture of the dynamic transport processes with high heat fluxes in the interline region. The molecular averaging process normally associated with a continuum approach can be viewed as occurring along the interline. We feel that the apparent liberties associated with this quasi-thermodynamic kinetic model are acceptable because the results and equations agree with macroscopic experimental observations and rational extrapolations of these to the microscopic scale. We propose that the numerical results presented below significantly enhance the understanding of the phase change phenomena occurring in the contact line region and thereby allow the detailed evaluation of transport processes.

Theoretical

In the *extremely small* Kelvin–Clapeyron region depicted in Fig. 1, we assume that the curved thin film grows solely by condensation. In this constant stress region, the net relative motion of the *liquid* molecules is assumed negligible. However, due to condensation, there is a uniform velocity of the liquid–vapor interface that preserves the shape of the rewetting fluid in the contact line region. In Region III, which is very large compared to Region II, fluid flows, as a result of an external force, toward the liquid–vapor interface where it evaporates due to conduction from the superheated substrate. This flow also causes an increase in the film thickness at the junction of

Regions II and III, which gives an increase in film curvature in Region II. However, the details of the flow field in Region III, e.g., the transition region from condensation to evaporation, are of secondary importance. Therefore, we assume that steady-state condensation in the translating KC region controls the rewetting velocity. The small heat flow rate (extremely large flux due to dimensions) of condensation in Region II is removed by evaporation in the initial portion of Region III.

Rewetting Velocity. The velocity due to phase change in Region II can be obtained from the condensation rate and thickness profile using the following procedure for a shape-preserving profile (Wayner, 1994). Since the average film profile is a function of time and position, $\delta(x, t)$, the film velocity, U, at a particular film thickness is

$$U = \left(\frac{\partial x}{\partial t}\right)_\delta = \frac{-\left(\frac{\partial \delta}{\partial t}\right)_x}{\left(\frac{\partial \delta}{\partial x}\right)_t} \tag{1}$$

Using Eqs. (1) and (2) for a condensation process that is perpendicular to the liquid–vapor interface gives Eq. (3) for the velocity:

$$\frac{\left(\frac{\partial \delta}{\partial t}\right)_x}{\left(\frac{\partial \delta}{\partial x}\right)_t} = \frac{-\dfrac{\dot{m}}{\rho_l}\cos\theta_{d\eta}}{\tan\theta_{d\eta}} \tag{2}$$

$$U = \frac{q''_{lv}\cos^2\theta_{d\eta}}{\rho_l h_{lvm}\sin\theta_{d\eta}} \tag{3}$$

In Eqs. (2) and (3), the local dynamic angle, which is a function of the dimensionless thickness, $\eta = \delta/\delta_o$, is $\theta_{dh} = \arctan\delta'$, $\dot{m}$ is the interfacial mass flux, and q''_v is the condensation heat flux at the liquid–vapor interface. Since the velocity of the interface is a constant, the heat flux perpendicular to the liquid–vapor interface is a function of the profile (local angle of the tangent, e. g., $q''_{lv} \to 0$ as $\theta_{d\eta} \to 0$) and superheat. The temperature and thickness profiles give the necessary vapor pressure field at the liquid–vapor interface. The variation in liquid superheat is a result of the coupling between the temperature fields in the substrate and liquid.

Kinetic Theory Interfacial Heat Flux. Using kinetic theory, the net interfacial heat flux for a flat surface due to condensation or evaporation can be obtained using (Schrage, 1953)

$$q''_{lv} = C_1 P_v h_{lvm}\left(\frac{M}{2\pi R T_{lv}}\right)^{0.5}\left(\frac{P_{lv} - P_v}{P_v}\right) \tag{4}$$

in which P_{lv} is the vapor pressure of the liquid film at the liquid–vapor interface and P_v is the pressure in the vapor a short distance away. Schrage (1953) and Carey (1992) discussed the limitations associated with Eq. (4). In our case, P_v is the reference equilibrium vapor pressure of the bulk liquid at T_v. For the curved thin film, the vapor pressure difference is a function of the temperature profile and the intermolecular force field which is a function of the thickness profile. Due to various local effects (like microconvection, conduction, etc.) the theoretical ideal limit of Eq. (4), which is extremely large with $C_1 = 2$, has not been attained in boiling (see, e.g., Gambill and Lienhard, 1987, and Carey, 1992). Therefore, we will use in our numerical calculations the following upper limit for the maximum achievable value of the vapor pressure difference at $\eta = \eta_j$:

$$\Omega_{max} = \left(\frac{P_{lv} - P_v}{P_v} \right)_{max} \qquad (5)$$

Based on the results of Gambill and Lienhard (1987), we will assume that $(C_1 \Omega_{max}) = -0.1$. However, we note that the exact value of this upper limit is an unknown.

Kelvin–Clapeyron Model for Vapor Pressure Difference. Using the Gibbs–Duhem, Kelvin, and Clapeyron equations, Wayner (e.g., 1994) obtained the following model for the effects of temperature (Clapeyron effect) and van der Waals intermolecular forces (Kelvin effect) on the change in the dimensionless chemical potential, ϕ, at the liquid–vapor interface:

$$\phi = \Delta \tau + \psi - \frac{1}{b\eta^3} \qquad (6)$$

The dimensionless chemical potential, ϕ, is related to the vapor pressure difference in Eq. (4) by

$$\phi = a_1 \ln \left(1 + \frac{P_{lv} - P_v}{P_v} \right) \qquad (7)$$

$$a_1 = \frac{\rho_{lM} R T_{lv} \delta_o}{\sigma_{lv}} \qquad (8)$$

The dimensionless superheat is

$$\Delta \tau = \frac{h_{lv} \delta_o \rho_{lM}}{\sigma_{lv} T_v} (T_{lv} - T_v) \qquad (9)$$

The dimensionless thickness, η, and dimensionless curvature, ψ, are

$$\eta = \frac{\delta}{\delta_o} \qquad (10)$$

$$\psi = \left(1 + \left(\frac{d\eta}{d\xi} \right)^2 \right)^{-1.5} \frac{d^2\eta}{d\xi^2} \qquad (11)$$

with

$$\xi = x/\delta_o \quad \text{and} \quad b = \sigma_{lv} \delta_o^2 / \bar{A} \qquad (12)$$

Characteristic Thickness, δ_o. The value of the characteristic thickness, which is the thickness of the adsorbed film at the junction of Regions I and II, is obtained from Eq. (6) with $\Delta t = \Delta t_o$, $\phi = 0$ (for equilibrium, $P_{lv} = P_v$), $\psi = \psi_o = 0$ (for a flat completely wetting liquid) and $\eta = 1$:

$$\delta_o = \left(\frac{-\bar{A} T_v}{\rho_{lm} h_{lvm} (T_{lv} - T_v)_o} \right)^{1/3} \qquad (13)$$

In Eq. (13), the intermolecular force field is represented by the modified Hamaker constant, $\bar{A}$. In the numerical calculations presented below, the value of the superheat at the interline (contact line, CL) is $\Delta T_{CL} = (T_{lv} - T_v)_o$. Due to the thinness of the liquid film, the solid surface and liquid temperatures are equal in Regions I and II: $T_s(x, 0) = T_l(x, 0) = T_{lv}(x, \delta)$.

Value of the Modified Hamaker Constant, $\bar{A}$. It is possible to calculate the theoretical value of the modified Hamaker constant for an ideal surface using the frequency-dependent dielectric properties of the liquid and solid (e.g., Truong and Wayner, 1987). However, for real engineering systems, we find it useful (more direct and possibly more accurate) to use the following approximate equation for apolar fluids, which relates the modified Hamaker constant to the interfacial free energies of the solid, σ_{ss}, and liquid, σ_{lv}.

$$\bar{A} = 4D^2(\sigma_{lv} - \sqrt{\sigma_{ss}\sigma_{lv}}) \qquad (14)$$

For completely wetting systems ($\sigma_{ss} > \sigma_{lv}$), this sign convention gives $\bar{A} < 0$. The value of the cutoff separation distance is usually taken to be $D = 0.165$ nm (Israelachvili, 1992).

Thickness Profile in Region II. Following Wayner (1994), we use a constant stress model for the intermolecular force field portion of Eq. (6) in Region II:

$$\psi - \frac{1}{b\eta^3} = c \qquad (15)$$

The constant stress approximation, c, allows Eq. (15) to be easily integrated. Using the contact angle, $\theta_{d\eta} = 0$ at $\eta = 1$ for the boundary condition, Eq. (16) is obtained for the "profile" of the thin film:

$$\cos \theta_{d\eta} = 1 - \frac{1}{2b} \left(1 - \frac{1}{\eta^2} \right) + c(1 - \eta) \qquad (16)$$

The subscript "$d\eta$" refers to the dynamic value of the arctan δ' at η. Using Eqs. (15) and (12) with $\psi = 0$ at $\eta = 1$ gives

$$c = -\frac{1}{b} = \frac{-\bar{A}}{\sigma_{lv}\delta_o^2} \qquad (17)$$

Therefore, knowing the values of σ_{ss}, T_v, and $(T_{lv} - T_v)_o$, the profile of the thin film can be obtained from Eqs. (13), (14), (16), (17). Physically, we find that the change in the intermolecular force field associated with the profile change given by $c > 0$ lowers the vapor pressure in Region II. However, the varying value of the superheat gives a varying rate of condensation and the rewetting velocity described by Eqs. (3), (4), (6), (16), and (17). In a later section, the value of the superheat at the contact line is related to the experimentally measured value of the superheat for the forced spreading of F113 on heated stainless steel. First, we present some theoretical calculations that demonstrate the sensitivity of the equations given above. However, the selected physical values and temperatures are directly related to the experimental system discussed later.

Numerical Values of $\bar{A}$ and δ_o. Using Eqs. (13) and (14), the values of $\bar{A}$ and δ_o can be calculated as a function of $(T_s - T_v)_o$ if T_v, and σ_{ss} are known. Although the value of the interfacial free energy of the experimental substrate is usually not measured in heat transfer studies, we presume that its value for the stainless steel discussed below is approximately $\sigma_{ss} \cong 30$ mJ/m^2 for the following reasons. First, we presume that the stainless steel substrate has a surface composed of a few monolayers of oxide slightly contaminated with bonded water. The surface chemistry of such a stainless steel surface was recently discussed by Mantel and Wightman (1994). Second, in our own laboratory studies of phase-change heat transfer on cleaned silicon substrates, we usually find a surface energy of approximately this magnitude for the same reason (DasGupta et al., 1994). This leads us to presume that most high-energy metal substrates used in heat transfer are at least slightly oxidized with some bonded water and/or covered with adsorbed low-energy organic contaminants. Therefore, these surfaces usually have moderate surface energies. Finally, a higher value of the surface energy would not alter the primary conclusion of this study: that adsorption controls the rewetting of a superheated substrate at superheats below a critical transition value. In Fig. 2 the values of δ_o and $\bar{A}$ obtained using Eqs. (13) and (14) are presented as a function of superheat for two values of the substrate surface energy for the F113/stainless steel system. The lower value, $\sigma_{ss} = 30$ mJ/m^2, reflects the normal condition of a metallic surface with an adsorbed layer of contaminants (Mantel and Wightman, 1994). Therefore, the lower value of σ_{ss} is more appropriate and is used below.
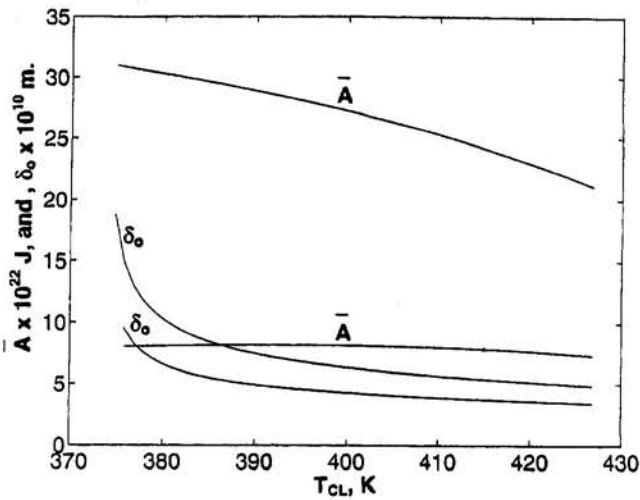
Fig. 2 Variation of modified Hamaker constant, $\bar{A}$, and interline thickness, δ_o, for F113 on stainless steel with σ_{ss} = 150 mJ/m² (higher values of δ_o and $\bar{A}$) and with σ_{ss} = 30 mJ/m² (lower values of δ_o and $\bar{A}$ at P_v^{sat} = 4.46 bar (T_v^{sat} = 374 K)

Fig. 4 Cos (arctan δ') versus η at P_v^{sat} = 4.46 bar for various values of c obtained using Eq. (16)

In Fig. 3, Eq. (13) is presented for various values of $(T_{lv} - T_v)_o$, T_v, $\bar{A} = f(T_{lv})$ for σ_{ss} = 30 mJ/m²; σ_{lv} = 54.114−0.1186 T_{lv} (Perry and Chilton, 1973) gives σ_{lv} = 19.36 mN/m at 293 K. We find that reasonable values for the temperature, intermolecular forces, and superheat give adsorption thicknesses for the thin film that are physically meaningful for describing the rewetting experimental data presented below.

The Extended Meniscus "Profile"

Equation (16) represents the needed "profile" of the extended meniscus in terms of the cos θ_{dh} where $\theta_{dh}(h)$ = arctan δ'. Equation (16) is presented in Fig. 4 for various values of the constant c obtained using Eqs. (13), (14), and (17). In Fig. 5, $\delta(x)$ profiles are presented. We find that significant changes in the profile can occur with reasonable values of c and ΔT, which thereby cause condensation and rewetting to occur.

Effect of P_v^{sat} on Experimental Data

Reyes and Wayner (1995b) used the Kelvin–Clapeyron model to analyze the rewetting data of Simopoulos et al. (1979)

at one saturation pressure: P_v^{sat} = 4.46 bar. Keeping in mind that surface characteristics were not determined in the original experimental study, we now need to develop a consistent method, which includes interfacial concepts, whereby the data for various saturated pressures can be evaluated. The results presented above and those of Reyes and Wayner (1995a) and Wayner (1994) indicate that the superheat at a "critical transition" in the boiling curve, $(\Delta T)_{CT}$, is indicative of the surface characteristics. Whether this critical superheat is the one at the Leidenfrost conditions or DNB conditions is not resolved herein. However, the temperature at the Leidenfrost conditions calculated using Speigler's criterion (Speigler et al., 1963), T_{CT} = (27/32) T_c was used herein to obtain the approximate value for the critical conditions at one pressure. Then the following criterion, which was developed by Reyes and Wayner (1995a) for the superheat at DNB, was used to calculate that superheat at different saturation pressures:

$$\left(\frac{h_{lv}\rho_{lM}(T_{lv} - T_v)_o}{T_v \sigma_{lv}^{1.5}} \right)_{CT} = \left(\frac{c^3}{-\bar{A}} \right)^{0.5} = \beta_{CT} \qquad (18)$$

where the constant β_{CT} is evaluated at one value of P_v^{sat}. To be

Fig. 3 Effect of T_v, $(T_s - T_v)_o$, and $\bar{A}$ on interline thickness δ_o obtained using Eq. (13) and Table 1 for σ_{ss} = 30 mJ/m²

Fig. 5 Meniscus thickness profiles, $\delta(x)$, for various values of c at P_v^{sat} = 4.46 bar: (a) c = 0.520 for ΔT = 20 K; (b) c = 0.780 for ΔT = 30 K; (c) c = 1.114 for ΔT = 40 K

consistent with Speigler's development, the reported data at the lowest value of the saturation pressure were used to characterize the surface conditions. The iterative procedure to obtain the results presented in Table 1 is described in the section on Numerical Results presented below. In essence, the datum at P^{sat} = 1.70 bar (ΔT_{CT} = 77.6 K) was used to obtain the value of β_{CT} and then Eq. (18) was used to obtain the other values in Table 1. Assuming that $(\theta_{d\eta})_{CT} \rightarrow$ 90 deg, the values of η_j at each P_v^{sat} were obtained from Eq. (16).

Substrate Temperature: Regions I and III. The temperature field in the substrate can be divided into three regions: (I) the superheated region ahead of the contact line where the heat flux is relatively small when sputtering in the thicker region is absent or small; (II) the extremely short KC region where the *net* heat flow rate to the substrate is small even though the heat fluxes are large; (III) a relatively long region where a large amount of net evaporation occurs and the substrate temperature decreases to the saturation value. If substantial sputtering occurs in Region III, the heat flux in Region I would be large due to droplets depositing on the 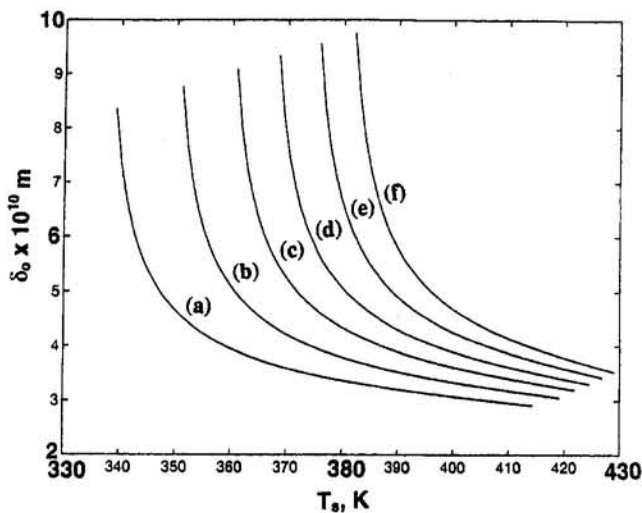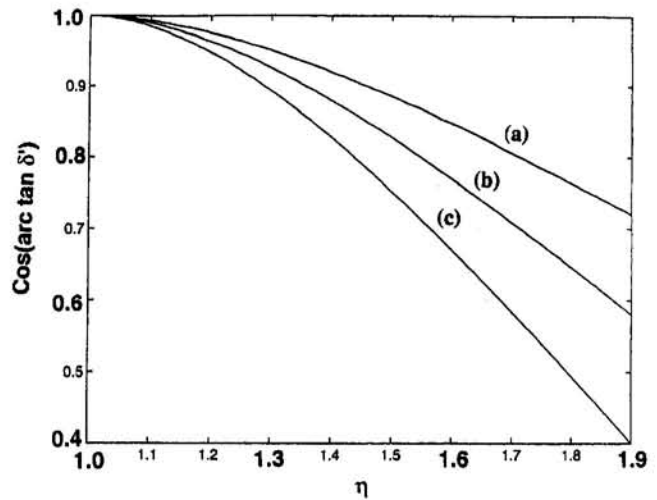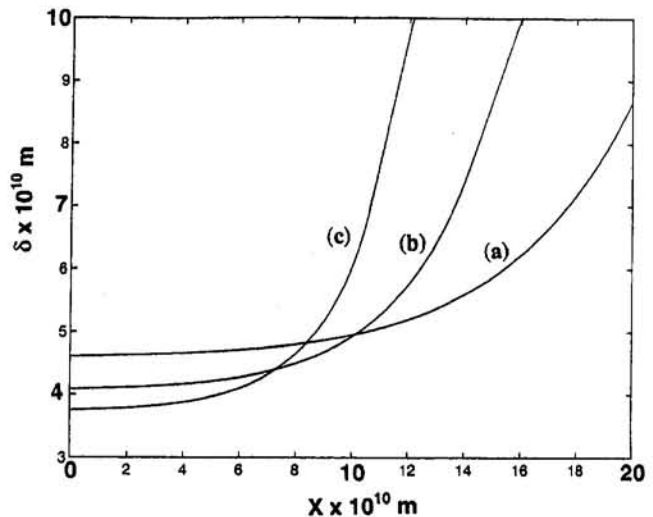substrate. A complete model of the wetting front requires the two-dimensional temperature profile in the substrate and liquid. However, to avoid additional complexities in this analysis and to focus on the KC model, the classical one-dimensional analysis for rewetting of a superheated substrate is adapted to obtain an estimate of the relative size of the temperature changes in Regions I and III. The liquid–vapor interfacial temperature profile in Region II discussed above is not addressed in this portion of the modeling.

We note the following assumptions that satisfy the experimental conditions of the data (Simopoulos et al., 1979), which are used below to evaluate the model:

- The advancing interface moves at a constant velocity, U, as depicted in Fig. 1.
- Liquid and vapor enter the test chamber at saturation conditions. The bulk liquid and the bulk vapor remain at saturated conditions during the experiments.
- The velocity of displacement is independent of the liquid flow for low draining rates (experimental observation).
- The temperature distributions in the solid and in the liquid are invariant with respect to the rewetting front.
- The overall evaporative heat transfer coefficient is approximately constant for the wetted region.
- The dry region ahead of the rewetting front is approximately adiabatic.
- The heat source in the solid is negligible because the power supply was shut down at the beginning of each experiment.

Considering these assumptions, the one-dimensional Fourier heat conduction equation for the solid is (see, e.g., Yamanouchi, 1968; Thompson, 1972)

$$k_w \frac{dY^2}{dx^2} - \rho_w C_w U \frac{dY}{dx} - \frac{h}{\lambda_w} Y = 0 \qquad (19)$$

Table 1 ΔT_{CT} and Adsorption parameters at the contact line for β_{CT} = 9.285×10^{10} $J^{-0.5}$: $\bar{A}$, c, η_j.

P_v^{SAT}, bar	ΔT_{CT}, K	$-\bar{A} \times 10^{22}$, J	c	η_{j}
1.70	77.6	7.882	1.894	1.8876
2.39	70.0	7.734	1.882	1.8916
3.08	63.6	7.587	1.870	1.8955
3.77	58.6	7.455	1.859	1.8992
4.46	53.7	7.313	1.847	1.9033
5.15	49.5	7.179	1.836	1.9072
P_c=34.38	T_c=487.4			
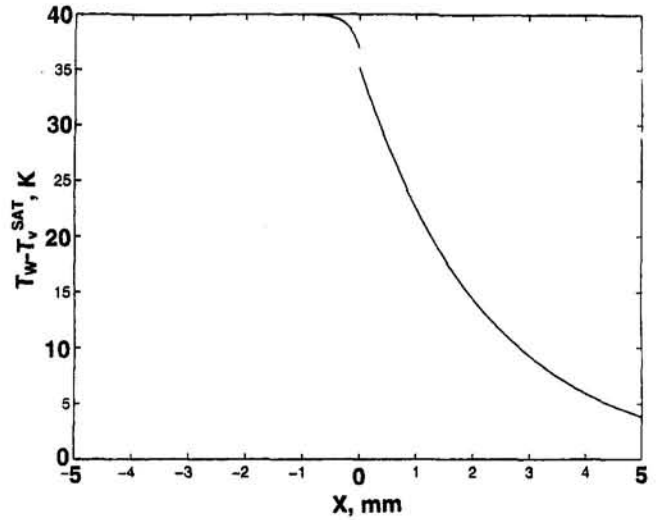
Fig. 6 Substrate temperature profile in Regions I and III based on Eq. (26) for P^{sat} = 4.46 bar , T^{sat} = 374 K, T_{wi} = 414 K , T_{CL} = 410.9

with

$$Y = T_w - T^{sat}$$
h = constant, for the wet side, and
h = 0, for the dry side

and the boundary conditions,

$$Y(\infty) = 0, \quad Y(-\infty) = T_{wi} - T^{sat} = Y_i,$$
$$Y(0^-) = T_{CL} - T^{sat} = Y_{CL},$$
$$Y(0^+) = T_{CL} - T^{sat} - \Delta T_{KC} \qquad (20)$$

The temperature distribution has a relatively small discontinuity, ΔT_{KC}, in Region II at $x = 0$, which is of molecular dimensions. This change in temperature comes from the change in the chemical potential addressed by the KC model in the liquid and does not affect the one-dimensional analysis. If the sum of the last two terms in Eq. (6) is a constant, $\Delta \tau$ varies with Φ, which, in turn, varies because of the constant velocity in Eq. (3) (see, e.g., Wayner, 1994). An additional restriction on the temperature profile is

$$\left. \frac{dY}{dx} \right|_{x=0^+} = \left. \frac{dY}{dx} \right|_{x=0^-} \qquad (21)$$

that describes the continuity in the substrate heat flux since there is no net loss from the substrate at the contact line. The relatively small heat of condensation in Region II is removed in a small adjacent portion of Region III as heat of vaporization.

The resulting temperature distribution in the solid is

$$Y = (Y_{CL} - \Delta T_{KC})$$
$$\times \exp \left(\frac{\rho_w C_w \lambda_w U - \sqrt{(\rho_w C_w \lambda_w U)^2 + 4 k_w \lambda_w h}}{2 k_w \lambda_w} x \right) \qquad (22)$$

for the wet region, $x \geq 0$, and

$$Y = Y_i + (Y_{CL} - Y_i) \exp \left(\frac{\rho_w C_w U x}{k_w} \right), \quad x < 0 \qquad (23)$$

for the dry region. A representative profile in the macroscopic region represented by this model is presented in Fig. 6. As described by the KC model, in a microscopic region near the liquid–solid interface, an average temperature jump, ΔT_{KC} = 1.8 K occurs over a distance of 1.07 nm for this case.
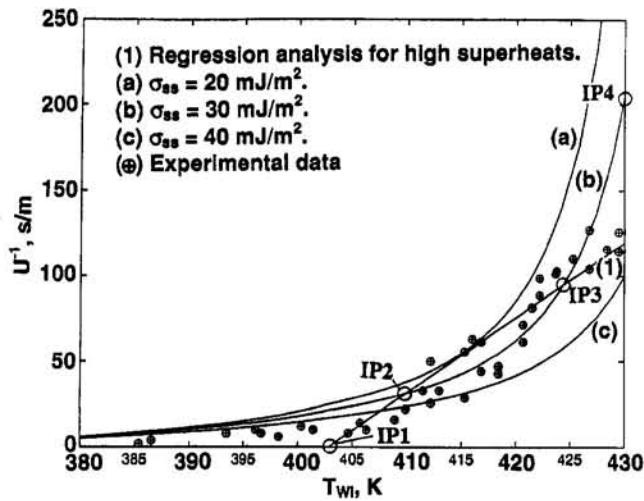
Fig. 7 Comparison of Kelvin–Clapeyron model ($n_j = 1.9033$) with experimental data of Simopoulos et al. (1979): (———) regression analysis for high superheats, (+) experimental data for $P_v^{sat} = 4.46$ bar, $T_v^{sat} = 374$ K; (a) $\sigma_{ss} = 20$ mJ/m², (b) $\sigma_{ss} = 30$ mJ/m², (c) $\sigma_{ss} = 40$ mJ/m²

For one of the experimental system studied ($P_v^{sat} = 4.46$ bar, Biot number ≈ 5), we find that the values of Y_i and Y_{CL} are approximately related by the linear correlation

$$Y_i \cong 1.529Y_{CL} - 17.92 \quad (Y_i \geq 34 \text{ K})$$

$$Y_i \cong Y_{CL} \quad (Y_i < 34 \text{ K}) \tag{24}$$

To discuss this result, we note that Duffey and Porthouse (1973) obtained one-dimensional and two-dimensional analytical solutions for the quenching of a superheated rod. Their analysis, which covers a large range of Biot numbers, demonstrated that at high superheats the rewetting of the solid is represented by the coupled equations of heat diffusion within the surface and boiling heat transfer. Blair (1975) obtained similar results using a two-dimensional model. In order to evaluate Eq. (24), we use the results of their two-dimensional solution, and find that the average Y (experimental) in the range $0 < Y_i < 60$ K is given by

$$Y_i = 1.23Y_{CL} \tag{25}$$

Although Eq. (25) was derived for high superheats, it provides values of Y_{CL} close to those provided by Eq. (24) in the same range of initial solid's superheat.

Numerical Results and Discussion

The following procedures were used to compare the Kelvin–Clapeyron model predictions with experimental data provided by Simopoulos et al. (1979) for the inverse velocities of rewetting, U_{exp}^{-1} of F-113 on stainless steel at various saturation pressures. Using Eqs. (21)–(23), the following equation relates the value of the measured initial wall temperature, T_{wi}, to the value of the contact line temperature, $T_{CL} = T_o$, and other variables:

$$T_{wi} = T_{CL} + \frac{k_w}{\rho_w C_w U_{exp}} (T_{CL} - \Delta T_{KC})$$

$$\times \left(\frac{\sqrt{4k_w\lambda_w h + (\rho_w C_w \lambda_w U_{exp})^2} - \rho_w C_w \lambda_w U_{exp}}{2k_w\lambda_w} \right) \tag{26}$$

The values of the experimental variables in Eq. (26) from Simopoulos et al. (1979) are: $\rho_w = 8027$ kg/m³; $\lambda_w = (r_o^2 - r_i^2)/2r_o$; $C_w = 502.4$ J/kg K; $k_w = 16.3$ W/mK; $r_o = 0.015785$ m; $h = 923500\,P^{0.29}/(T_{wi} - T_{IP1})$; $r_i = 0.012155$ m. In Eq.

(26), we have modified the classical one-dimensional conduction solution by introducing $h(P^{sat}, T_{wi})$, which leads to a better prediction of T_{wi}. The value of $\Delta T_{KC} = [T_{lv}(\eta = 1) - T_{lv}(\eta = \eta_j)]$ and T_{CL} are determined using the KC model. An example of the temperature profile based on Eq. (26) around the contact line region is given in Fig. 6.

Using the KC model, the predicted rewetting velocity was calculated as a function of ($T_{CL} - T_v$) as follows. Initially, an estimated value for ΔT_{CT} was picked for a given datum $P_v = P_v^{sat}$. Then, $\Delta T_{CT}(P_v^{sat})$ for the other saturation pressures were calculated using Eq. (18). The values of δ_o, $\bar{A}$, and c are then obtained from Eqs. (13), (14) and (17). The value η_j was obtained using $\theta_{d\eta} \to 90$ deg in Eq. (16) at $(\Delta T)_{CT}$ and kept constant for each value of P^{sat}. The values of $\theta_{d\eta}$ are then obtained from Eq. (16) at $\eta = \eta_j$ for other values of "c" (which is a function of the superheat) for each value of P^{sat} while keeping $\eta_j = $ const. This allows the rewetting velocity to vary with a change in $\theta_{d\eta}$ at η_j. The heat flux was then calculated using these values in Eqs. (4), (6), and (7), while keeping the restriction on the maximum value of heat flux given by Eq. (5). Using the heat flux and the angle, Eq. (3) gives the value of the rewetting velocity. In order to obtain consistent results for $P^{sat} = 4.46$ bar (presented in Fig. 7) and other values of the saturation pressure (presented in Fig. 8), which we believe successfully model the physical process of rewetting, we found it necessary to iterate on the value of ΔT_{CT} picked for the datum $P_v = P_v^{sat}$ and finally select the values listed in Table 1. The most important criterion used in this selection was fitting the curves to the data at all six values of P_v^{sat}.

In Fig. 7, the experimental data and four lines are presented: the straight line of Simopoulos et al. (1979) and three curves representing the KC model for three different values of the substrate surface free energy. In order to compare the two results, four interception points are designated. We find that the model fits these data fairly well up to approximately interception point IP3. IP4 represents the critical conditions in this model where $\theta_{d\eta} \to 90$ deg and $U \to 0$. The difference between the temperatures at IP3 and IP4 is not large. Therefore, we conclude that this model successfully predicted the effect of substrate superheat on the rewetting velocity below a critical transition superheat. Since Simopoulos et al. were more concerned with the data at superheats higher than IP3, they focused on the linear model represented by IP1 and neglected the curvature in their data below IP3. As discussed by Peng et al. (1992), the time for thermal conditioning increases substantially at low rewetting velocities. This is probably associated with dewetting at the
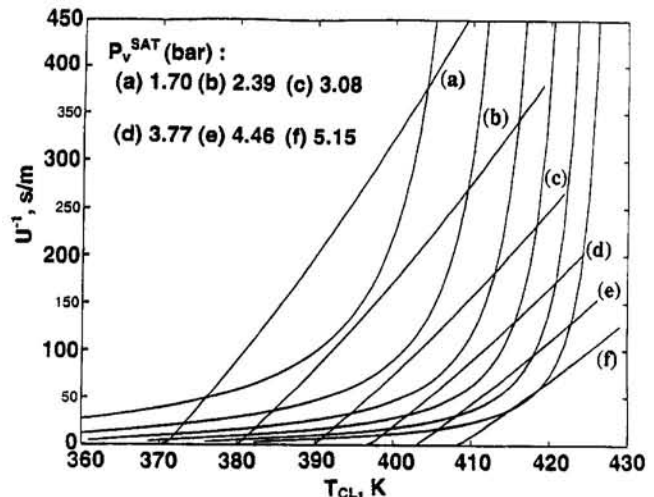

Fig. 8 Comparison of Kelvin–Clapeyron model for various saturation pressures with experimental data represented by straight lines P_v^{sat} (bar): (a) 1.70; (b) 2.39; (c) 3.08; (d) 3.77; (e) 4.46; and (f) 5.15

contact line, which occurs when $\theta_{d\eta} \rightarrow 90$ deg in the model. Therefore, in the region above IP3 or IP4, a different model is needed.

The rewetting velocity was also calculated for the other values of the saturation pressure presented in Table 1. These results are presented in Fig. 8. Except for $P^{sat} = 3.08$ and 4.46 bars, only the presented straight lines without the data points were given in the literature. The lowest saturation pressure experimentally studied was $P^{sat} = 1.70$ bar. At this pressure, the model predicts that the temperature at IP4 is $T_{CT} = 414.8$ K. This compares with Speigler's criterion of $T_{CT} = 411.2$ K. As expected (see e.g., Reyes and Wayner, 1995a), the values of ΔT at IP4 presented in Table 1 decrease with an increase in saturation pressure.

In addition, examples of the heat flux profile and temperature profile in the contact line region obtained using Eqs. (3) and (6) are presented in Fig. 9. The variation of the apparent contact angle, $\theta_{d\eta}$, at η_j with contact line temperature is presented in Fig. 10. We find that an increase in $\theta_{d\eta}$, at the junction of Regions II and III, η_j, is associated with an increase in curvature but a decrease in the rewetting velocity. This counterintuitive result occurs because the effect of the increases in the curvature and thickness on the vapor pressure is more than offset by the superheat effect.

The relative size of the various temperatures changes can be obtained by combining the results presented in Figs. (6) and (9). We find that the results presented in Fig. 6 from the classical one-dimensional modeling of the substrate are consistent with the results obtained from the KC model. The successful coupling of these two results through the use of Eq. (26) to describe experimental data demonstrates at least the efficacy of the KC model. We also find that all aspects of the modeling results are consistent with expectations based on past research.

Conclusions

1 A Kelvin–Clapeyron model for the spreading dynamics of a completely wetting fluid on a heated solid substrate was developed.
2 A critical superheat can be used to characterize the unknown surface conditions.
3 Using reasonable values for the interfacial forces, the model successfully predicted the effect of substrate superheat on the rewetting velocity of R113 on stainless steel at superheats below a critical superheat.
4 Because of adsorption, the velocity of rewetting decreases with an increase in the substrate superheat.
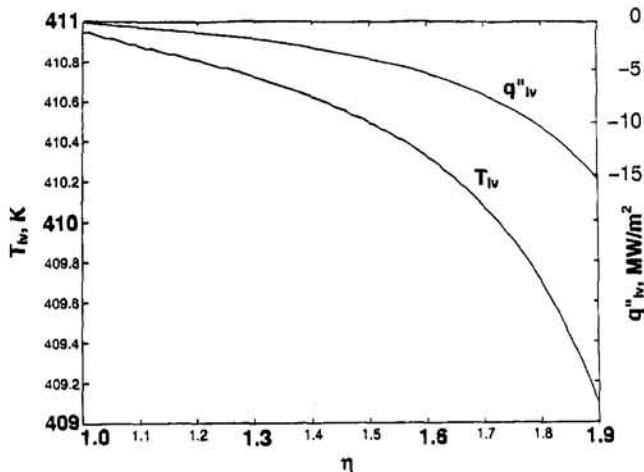
Fig. 9 Temperature distribution and condensation heat flux distribution in the contact line region based on the Kelvin–Clapeyron model: $P_v =$ 4.46 bar, $T_v = 374$ K, $\sigma_{ss} = 30$ mJ/m^2, $\eta_{lj} = 1.9033$, $T_{wl} - T^{sat} = 40$ K, $U = 0.019$ m/s
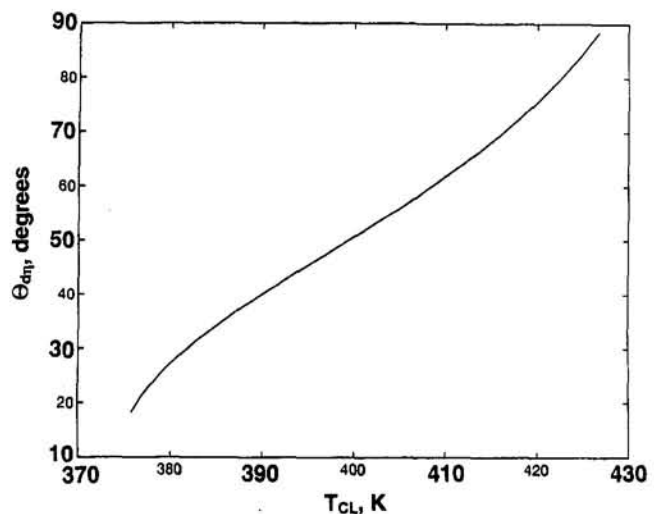
Fig. 10 Variation of apparent contact angle at the junction of Regions II and III, η_j, for $P_v = 4.46$ bar and $\sigma_{ss} = 30$ mJ/m^2

5 Because of adsorption, which is a function of the substrate superheat, the velocity of rewetting decreases with an increase in the apparent contact angle.
6 Both adsorption in the contact line region and conduction in the substrate control the rewetting of a superheated surface by a completely wetting liquid at superheats below a critical heat flux.

Acknowledgments

References

Anderson, D.M., and Davis, S.H., 1993, "The Spreading of Volatile Liquid Droplets on Heat Surfaces," Technical Report No. 9210, Applied Mathematics, Northwestern University, Evanston, IL.

Blair, J.M., 1975, "An Analytical Solution to a Two-Dimensional Model of the Rewetting of a Hot Dry Rod," Nucl. Eng. Des., Vol. 32, pp. 159–170.

Carey, V.P., 1992, Liquid–Vapor Phase Change Phenomena: An Introduction to the Thermophysics of Vaporization and Condensation Processes in Heat Transfer Equipment, Hemisphere Publishing Corp., Washington, DC.

DasGupta, S., Kim, I.Y., and Wayner, P.C., Jr., 1994, "Use of the Kelvin–Clapeyron Equation to Model an Evaporating Curved Microfilm," ASME JOURNAL OF HEAT TRANSFER, Vol. 116, pp. 1007–1015.

Derjaguin, B.V., Churaev, N.V., Muller, V.M., and Kitchener, J.A., 1987, Surface Forces, Plenum Press, New York.

Dhir, V.K., and Liaw, S.P., 1989, "Framework for a Unified Model for Nucleate and Transition Pool Boiling," ASME JOURNAL OF HEAT TRANSFER, Vol. 111, pp. 739–746.

Dua, S.S., and Tien, C.L., 1976, "Two-Dimensional Analysis of Conduction-Controlled Rewetting With Precursory Cooling," ASME JOURNAL OF HEAT TRANSFER, Vol. 98C, pp. 407–413.

Duffey, R.B., and Porthouse, D.T.C., 1973, "The Physics of Rewetting in Water Reactor Emergency Core Cooling," Nucl. Eng. Design, Vol. 25, pp. 379–394.

Elias, E., and Yadigaroglu, G., 1977, "A General One Dimensional Model for Conduction-Controlled Rewetting of a Surface," Nucl. Eng. Design, Vol. 42, pp. 185–194.

Gambill, W. R., and Lienhard, J. H., 1987, "An Upper Bound for the Critical Boiling Heat Flux," Proc. ASME–JSME Thermal Engineering Joint Conf., Vol. 3, pp. 621–626.

Israelachvili, J., 1992, Intermolecular and Surface Forces, 2nd ed., Academic Press Inc., San Diego, CA, p. 203.

Lay, J.H., and Dhir, V.K., 1994, "A Nearly Theoretical Model for Fully Developed Nucleate Boiling of Saturated Liquids," Proc. of the Tenth Int. Heat Transfer Conf., R. J. Berryman, ed., Paper No. 10-PB-17, Brighton, United Kingdom.

Linehan, J.H., Howard, P.A., and Grolmes, M.A., 1979, "The Stationary Boiling Front in Liquid Film Cooling of a Vertical Heated Rod," Nucl. Eng. Design, Vol. 52, pp. 201–218.

Mantel, M., and Wightman, J. P., 1994, "Influence of the Surface Chemistry on the Wettability of Stainless Steel," *Surface and Interfacial Analysis*, Vol. 21, pp. 595–605.

Olek, S., Zvirin, Y., and Elias, E., 1988, "Rewetting of Hot Surfaces by Falling Liquid Films as a Conjugate Heat Transfer Problem," *Int. J. Multiphase Flow*, Vol. 14, pp. 13–33.

Peng, X.F., Peterson, G.P., and Wang, B.X., 1992, "On the Wetting Mechanism of Liquid Flow on Hot Surfaces," *Int. J. Heat MassTRANSFER*, Vol. 35, pp. 1615–1624.

Perry, R.H., and Chilton, C.H., 1973, Chemical Engineers' Handbook, McGraw-Hill, New York, Chap. 3.

Potash, M., Jr., and Wayner, P. C., Jr., 1972, "Evaporation From a Two Dimensional Extended Meniscus," Int. J. Heat Mass Transfer, Vol. 15, pp. 1851–1863.

Reyes, R., and Wayner, P.C., Jr., 1995a, "An Adsorption Model for the Superheat at the Critical Heat Flux," ASME JOURNAL OF HEAT TRANSFER, Vol. 117, pp. 779–781.

Reyes, R., and Wayner, P.C., Jr., 1995b, "A Kelvin–Clapeyron Model for Spreading on a Heated Plate," in: *Basic Aspects of Two Phase Flow and Heat Transfer* V. K. Dhir, ed., ASME HTD-Vol. 308, pp. 47–56.

Schrage, R.W., 1953, "A Theoretical Study of Interphase Mass Transfer," Columbia University Press, NY, Chap. II.

Segev, A., and Bankoff, S. G., 1980, "The Role of Adsorption in Determining the Minimum Film Boiling Temperature," Int. J. Heat Mass Transfer, Vol. 23, pp. 637–642.

Simopoulos, S. E., El-Shirbini, A. A., and Murgatroyd, W.,1979, "Experimental Investigation of the Rewetting Process in a Freon-113 Vapor Environment," *Nuclear Engineering and Design*, Vol. 55, pp. 17–24.

Speigler, P., Hopenfeld, J., Silberberg, M., Bumpus, C. F., Jr., and Dorman, A., 1963, "Onset of Stable Film Boiling and the Foam Limit," *Int. J. Heat Mass Transfer*, Vol. 6, pp. 987–994.

Stephan, P., and Hammer, J., 1994, "A New Model for Nucleate Boiling Heat Transfer," *Wärme- und Stoffübertrangung*, Vol. 30, pp. 119–125.

Stephan, P. C., and Busse, C. A., 1992, "Analysis of the Heat Transfer Coefficient of Grooved Heat Pipe Evaporator Walls," *Int. J. Heat Mass Transfer*, Vol. 35, pp. 383–391.

Thompson, T. S., 1972, "An Analysis of the Wet-Side Heat-Transfer Coefficient During Rewetting of a Hot Dry Patch," *Nucl. Eng. Design*, Vol. 22, pp. 212–214.

Truong, J. G., and Wayner, P. C., Jr., 1987, "Effect of Capillary and van der Waals Dispersion Forces on the Equilibrium Profile of a Wetting Liquid: Theory and Experiment," *J. Chem. Phys.*, Vol. 87(7), pp. 4180–4188.

Unal, C., Daw, V., and Nelson, R., 1992, "Unifying the Controlling Mechanisms for the Critical Heat Flux and Quenching: The Ability of the Liquid to Contact the Hot Surface," ASME JOURNAL OF HEAT TRANSFER, Vol. 114, pp. 972–982.

Yamanouchi, A., 1968, "Effect of Core Spray Cooling in Transient State After Loss of Coolant Accident," *J. Nuclear Science and Technology*, Vol. 5, pp. 547–558.

Wayner, P.C., Jr., Kao, Y.K., and LaCroix, L.V., 1976, "The Interline Heat Transfer Coefficients of an Evaporating Film," *Int. J. Heat Mass Transfer*, Vol. 19, pp. 487–492.

Wayner, P.C., Jr., 1982, "Adsorption and Capillary Condensation at the Contact Line in Change-of-Phase Heat Transfer," *Int. J. Heat Mass Transfer*, Vol. 25, pp. 707–713.

Wayner, P.C., Jr., 1994, "Thermal and Mechanical Effects in the Spreading of a Liquid Due to a Change in the Apparent Finite Contact Angel," ASME JOURNAL OF HEAT TRANSFER, Vol. 116, pp. 938–945.

The Effect of the Thermal Boundary Condition on Transient Method Heat Transfer Measurements on a Flat Plate With a Laminar Boundary Layer

R. J. Butler
Department of Aeronautics,
United States Air Force Academy,
USAFA, CO 80840

J. W. Baughn
Department of Mechanical and
Aeronautical Engineering,
University of California,
Davis, CA 95616

The heat transfer coefficient distribution on a flat plate with a laminar boundary layer is investigated for the case of a transient thermal boundary condition (such as that produced with the transient measurement method). The conjugate problem of boundary layer convection with simultaneous wall conduction is solved numerically, and the predicted transient local heat transfer coefficients at several locations are determined. The numerical solutions for the surface temperature are used to determine the Nusselt number that would be measured in a transient method experiment for a range of (nondimensionalized) surface measurement temperatures (liquid crystal temperatures when they are used as the surface sensor). These predicted transient method results are compared to the well-known results for uniform temperature and uniform heat flux thermal boundary conditions. Measurements are made and compared to the numerical predictions using a shroud (transient) experimental technique for a range of nondimensional surface temperatures. The numerical predictions and measurements compare well and both demonstrate the strong effect of the (nondimensional) surface temperature on transient method measurements. Transient method measurements will give heat transfer coefficients that range from as low as that of the uniform temperature case to higher than that of the uniform heat flux case (a 36 percent difference). These results demonstrate the importance of the temperatures used with the transient method.

Introduction

Many different experimental methods are used to measure local heat transfer. These methods can be categorized by the thermal boundary condition produced during the measurements. There are three commonly used conditions: uniform temperature, uniform heat flux, and transient conditions. The thermal boundary condition influences the measurement and for the same geometry and flow conditions different thermal boundary conditions may give significantly different results for the heat transfer measurement. For a laminar flat plate boundary layer it is known from theory that the local heat transfer for uniform heat flux boundary conditions is 36 percent higher than that for uniform temperature boundary conditions. The extent of the effect of the transient wall temperature associated with transient methods is unknown. Transient heat transfer measurement methods produce unsteady thermal boundary conditions since each location of the surface changes temperature at a different rate (dependent on the local heat transfer coefficient). It would be expected that an unsteady and nonuniform temperature plate (which exists when using the transient method) would yield different results than either the uniform wall temperature case or the uniform heat flux case. The heat transfer during a transient will depend on the temperature gradients along the wall and on the time for the transient to take place.

Sugawara et al. (1988) used a transient technique for measuring flat plate heat transfer. They measured heat transfer levels

44 percent higher than that of other reported measurements or that predicted by theory for the case of a uniform temperature. The results presented in the present work suggest that the results of Sugawara et al. (1988) were influenced by the thermal boundary condition associated with the transient test technique they used.

O'Brien et al. (1986) compared measurements from uniform temperature, uniform heat flux, and transient methods on the leading edge of a cylinder in crossflow. At 80 deg from the stagnation point, they found a significant difference between the results. The transient measurements were only extended to 60 deg. The uniform wall temperature boundary condition was also compared to a uniform heat flux on a cylinder in crossflow by Baughn and Saniei (1991). They found the results to be the same at the stagnation point, followed by an increasing heat transfer rate for the uniform heat flux case relative to the uniform temperature case as the position increases downstream from the stagnation point (becoming nearly twice the heat transfer rate for the uniform heat flux case relative to the uniform temperature case at the separation point). Their results suggest that the greatest difference between measurements that use different thermal boundary conditions will occur in regions where the heat transfer coefficient exhibits large gradients.

Kim et al. (1993) showed, using numerical calculations, that impinging jet local heat transfer is independent of the thermal boundary condition within 2.5 diameters of the jet.

For flat plate turbulent flow, theory predicts that the heat transfer rate for the uniform heat flux conditions is only 4 percent larger than the uniform temperature boundary condition and it has generally been assumed that transient methods will give nearly the same result. Taylor et al. (1989) experimentally investigated the turbulent boundary layer with uniform wall

Contributed by the Heat Transfer Division for publication in the JOURNAL OF HEAT TRANSFER. Manuscript received by the Heat Transfer Division May 29, 1995; revision received May 16, 1996. Keywords: Forced Convection, Measurement Techniques, Transient and Unsteady Heat Transfer. Associate Technical Editor: B. W. Webb.

Journal of Heat Transfer

NOVEMBER 1996, Vol. 118 / **831**

Copyright © 1996 by ASME

Downloaded 11 Dec 2010 to 193.140.21.150. Redistribution subject to ASME license or copyright; see http://www.asme.org/terms/Terms_Use.cfm

temperature, uniform heat flux, and linear wall temperature thermal boundary conditions. They found the uniform heat flux results are on average 4–5 percent higher than the uniform temperature case, but measured 10–15 percent differences near the origin of the boundary layer. Moreover, they found the heat transfer to be as much as 20 percent lower than the uniform temperature plate when larger wall temperature gradients were used (a linear decreasing wall temperature profile). Their results suggest that thermal boundary conditions may even sometimes be important for the turbulent boundary layer.

The present study investigates the effects of the thermal boundary condition for transient method heat transfer measurements on a flat plate with a laminar boundary layer. Numerical solutions were obtained for the laminar flow boundary layer over a flat plate with different thermal boundary conditions (uniform temperature, constant heat flux, and an unsteady wall temperature used to simulate the transient experimental method). Experiments were performed using a shroud technique, which is a transient method. This allowed for a direct comparison of the heat transfer measurements for the different thermal boundary conditions associated with different experimental methods.

Theory

The effect of the thermal boundary condition on steady-state local heat transfer was first understood through analytical solutions. The classical solution for velocity profiles in a laminar boundary layer solution was done by H. Blasius (1908). Pohlhausen (1921) furthered this theory by solving the energy equation for a uniform temperature wall. His result for the local Nusselt number was:

$$\text{Nu}_x = 0.332 \sqrt{\text{Re}_x} \, \text{Pr}^{1/3} \qquad (1)$$

This solution only applies to a uniform temperature plate and a specific (broad) range of Prandtl numbers. Baxter and Reynolds (1958) duplicated this solution and solved the energy equation using other steady-state thermal boundary conditions. They showed that the solution for a plate with uniform heat flux is:

$$\text{Nu}_x = 0.453 \sqrt{\text{Re}_x} \, \text{Pr}^{1/3} \qquad (2)$$

while the solution for a plate with a linear wall temperature rise is:

$$\text{Nu}_x = 0.535 \sqrt{\text{Re}_x} \, \text{Pr}^{1/3} \qquad (3)$$

These solutions show that the heat transfer for laminar flow over a flat plate is dependent on the thermal boundary condition with significant differences for different conditions. The heat transfer for the uniform heat flux is 36 percent greater than the uniform wall temperature solution and the linear temperature boundary condition is 61 percent greater. It is clear that the heat transfer coefficient increases as the wall temperature profile deviates from the uniform temperature condition. The wall temperature distribution is proportional to $x^{1/2}$ for the uniform heat flux boundary condition and is proportional to x (by definition) for the linear wall temperature. Therefore, as the wall temperature deviates further from the uniform temperature condition (lower upstream temperatures), the heat transfer becomes larger than that of the uniform wall temperature case.

The effect of the thermal boundary condition on turbulent boundary layers was first examined by analytical solutions. Kays and Crawford (1980) showed the turbulent uniform temperature plate solution to be:

$$\text{Nu}_x = 0.0296 \, \text{Re}_x^{4/5} \, \text{Pr}^{1/3} \qquad (4)$$

and the solution for a uniform heat flux boundary condition to be:

$$\text{Nu}_x = 0.0308 \, \text{Re}_x^{4/5} \, \text{Pr}^{1/3} \qquad (5)$$

For a turbulent boundary layer, the heat transfer for the uniform heat flux boundary condition is only 4 percent larger than the uniform wall temperature. Although it would appear that turbulent boundary layers are not as dependent on the thermal boundary condition as the laminar case, the effect can still be substantial if pressure gradients produce large heat transfer and wall temperature gradients. For flat plate turbulent boundary layers the wall temperature gradient is more shallow than the laminar case and it more closely matches a uniform wall temperature. The heat transfer coefficient is inversely proportional to $x^{1/5}$ for flat plate turbulent boundary layers. The wall temperature gradients are larger in laminar boundary layers, where the heat transfer coefficient is inversely proportional to $x^{1/2}$. This produces larger wall temperature gradients for the laminar case when using uniform heat flux or transient methods, thus increasing the effect of different thermal boundary conditions.

Transient Method for Heat Transfer Measurements

The transient method determines local heat transfer coefficients by measuring the transient response of a surface temperature to a change in the fluid temperature. The fluid can be changed to either a higher or lower temperature than the surface. Although transient methods for heat transfer measurement have a long history, only a brief review is included here. The transient method was used extensively in shock tunnels with resistance thermometers on ceramic substrates (Schultz and Jones, 1973). Some early measurements using thermal paints are reviewed by Schultz and Jones (1973) and Jones (1977). Clifford et al. (1983) used phase-change paints on acrylic models to study heat transfer within gas turbine blade cooling passages and Metzger and Larson (1986) used melting point coatings to study heat transfer in rectangular ducts with turns. Ireland and Jones (1985, 1986), Jones and Hippensteele (1987), Metzger et al. (1991), and Baughn and Yan (1991a, b) have used liquid crystals for the surface temperature measurement. Liquid crystals are very suitable to measure the surface temperature transient, since their response is repeatable and their colors can be easily recorded with a video system.

The basic principles and further details about the transient method are available from Ireland and Jones (1985, 1986) and Ireland (1987). A one-dimensional approximation for the substrate conduction is often used since the surface temperature

———— Nomenclature ————

C_p = specific heat of substrate
erfc = complementary error function
h = total heat transfer coefficient
h_r = heat transfer coefficient due to radiation
k = thermal conductivity of substrate
Nu_x = local Nusselt number
Nu_{xt} = local Nusselt number determined with the transient method

Nu_{xc} = Nu_{xt} corrected to the uniform temperature boundary condition
Pr = Prandtl number
Re_x = Reynolds number based on distance x
t = time from start of transient
T_{LC} = liquid crystal temperature
T_o = initial temperature
T_∞ = free-stream temperature

T^* = nondimensional liquid crystal temperature
x = distance from leading edge of plate
$\gamma = h(t/\rho C_p k)^{1/2}$
ϵ = surface emissivity
ρ = substrate density
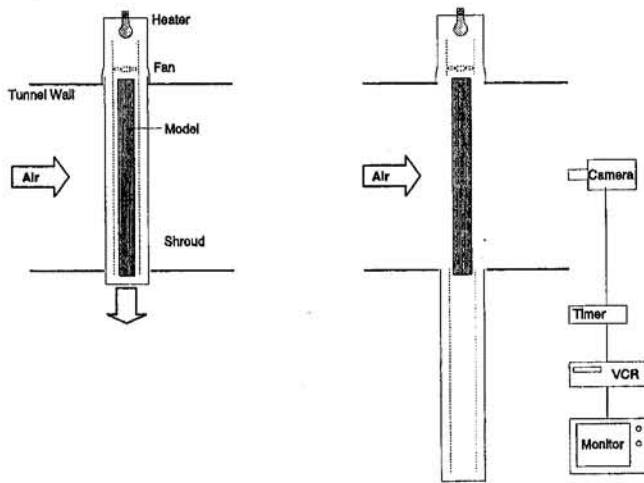σ = Stefan–Boltzmann constant

Fig. 1 Diagram of experimental apparatus used for the shroud (transient) technique

response is limited to a thin layer near the surface and lateral conduction can be shown to be small (Dunne, 1983). The transient method is compared to the heated-coating method by Baughn et al. (1989).

There are a variety of techniques used to accomplish the fluid temperature change relative to the surface. For example, Clifford et al. (1983), Ireland and Jones (1985, 1986), and Metzger et al. (1991) all use an ambient temperature sample and then suddenly raise the temperature of their flow with switching valves. Jones and Hippensteele (1987) used in-situ heating of a wind tunnel wall and then initiated the flow using a diverter door. They also used multiple liquid crystal coatings to reduce the dependence of the results on the initial wall temperature distribution. O'Brien et al. (1986) used a preheated cylinder and suddenly inserted it into place across a channel with an ambient temperature flow field. Baughn and Yan (1991a) developed an insertion technique in which a preheated section of duct is suddenly connected onto another section of duct with developed flow to study internal heat transfer. Baughn and Yan (1991b) also describe a preheated wall method for a study of heat transfer from a surface to an impinging jet.

The technique described in the present study, referred to as the shroud technique, is a new variation on the transient method and was developed by Butler and Baughn (1995). In this technique, a model is preheated inside a removable shroud to a uniform and constant temperature. To produce the transient, the model is suddenly exposed to ambient temperature wind tunnel air by ejecting the shroud. With this technique the model itself does not move while the flow develops around the model. The flow development time is generally short compared to the measured transient. This technique avoids any effects of the motion of the model, which in other techniques may affect the heat transfer for a portion of the transient. This technique also has the flexibility of allowing the models to have complex shapes. The models themselves are simple and are made of Plexiglas without a need for instrumentation or heating in the model.

Shroud Technique (Transient Method) Apparatus

Figure 1 is a diagram of the apparatus used for the shroud technique. The apparatus has three major components: a shroud, a computer-controlled heater assembly, and an ejection mechanism (not shown in Fig. 1). The shroud consists of two concentric tubes with the model inside the center tube. Although these tubes can be of any shape, in the present study they are constructed from a 0.127 m PVC pipe, with a 0.102 m pipe mounted in the center.

The heater assembly has similar concentric tubes, which mate to one end of the shroud. It also contains a small fan and an electrical heater (a 100 W light bulb in the present study). Air is circulated from the heating unit between the two tubes and up through the center of the shroud alongside the model. The air can circulate in either direction, but was circulated past the heater and then between the tubes in the present study in order to mix it thoroughly before it flows by the model.

In order to control the temperature of the air and the model (keep the model temperature uniform and constant with time), the temperatures on the model were measured with four thermocouples along the span using an A/D card in a PC. A program was written to switch the electric power to the heater in accordance with these measured temperatures. The A/D card had low-voltage digital DC outputs, which were used with solid state relays to provide power to the heater and the fan.

The technique involves heating the model for an extended period of time (approximately 3 or more hours) inside the shroud. During this time the Plexiglas model comes to a uniform and constant temperature. The initial temperature of the model is set above the color transition temperature of the liquid crystal on the model surface. The wind tunnel flow is then established and when ready the shroud is ejected exposing the model to the wind tunnel flow. This establishes the surface temperature transient required for the transient method. The liquid crystal color changes are recorded on video tape and the method for data reduction is described below.

The flat plate model used was constructed from Plexiglas and was 0.098 m long in the flow direction and 0.00635 m thick. The measurement side of the model was flat and the backside of the leading edge was machined with a sharp 30 deg angle. The flat surface was mounted 1 deg windward to prevent flow separation off the sharp leading edge. The test portion of the model was air brushed with black paint and a thin layer of liquid crystals. The liquid crystal selected had a yellow-red color change temperature of 36.85°C. The wind tunnel test section was 0.61 m by 1.02 m wide. The model was mounted vertically in the tunnel and was 0.61 m high. The wind tunnel is open loop with a variable speed from 6.5 to 21 m/s. The freestream turbulence was measured with a hot-film anemometer to be approximately 1.0 percent.

Transient Shroud Data Reduction

A typical video record shows the color changing first near the leading edge and the color change moving along the plate in the direction of the flow slowly (the high heat transfer regions cool faster and change color first). A timer in the video record is used to measure the starting time and the elapsed time until color transition for each location. Because the model aspect ratio is high, the data are two dimensional and the video shows vertical isothermal color lines, which are parallel to the leading edge of the model. The liquid crystal color band clearly shows green, yellow, and red. As each location cools, the surface there will first turn green, followed by yellow and red. For each location, the time for the color change for the yellow to red transition is recorded.

In order to determine the temperature for the yellow to red transition, liquid crystal calibrations were performed. A calibration system with a linear temperature gradient was used to establish the color appearance on a video monitor, as described by Baughn and Yan (1991a). In this method, four calibrated thermocouples establish the temperature gradient, and the location of the yellow color band is measured from the video monitor.

The local heat transfer coefficients can be found from the time for each location to cool to the liquid crystal color transition. The time is used in solving for the conduction transient in the Plexiglas substrate. It has been shown that in most cases the conduction is nearly one dimensional. With large heat trans-

fer coefficient gradients on small models this may not be the case. For example, Perera and Baughn (1994) find a two-dimensional solution for the flutes in a spirally fluted tube. In the present study, and for most wind tunnel models, the conduction can be assumed to be one dimensional. For one-dimensional conduction into a semi-infinite medium with a convective boundary condition, the solution for the surface temperature is:

$$T^* = \frac{T_{LC} - T_\infty}{T_o - T_\infty} = e^{\gamma^2} \text{ erfc } (\gamma) \tag{6}$$

where γ is a nondimensional parameter related to the heat transfer coefficient h by:

$$h = \frac{\gamma\sqrt{\rho C_p k}}{\sqrt{t}} \tag{7}$$

The nondimensional liquid crystal temperature (T^*) in Eq. (6) is defined in terms of the liquid crystal transition temperature (T_{lc}), free-stream air temperature (T_∞), and the initial temperature (T_o). In these experiments, these temperatures are all fixed in advance. The value of γ is found for the selected T^* from Eq. (6). Since Eq. (6) is an implicit equation in γ, it requires an iterative solution, which is done using a approximation for the complementary error function from Abramowitz and Stegun (1970). Using the video record, the time (t) for each location's local surface temperature to cool to the yellow–red liquid crystal transition temperature is measured. The local heat transfer coefficients are then calculated using Eq. (7) with the known thermal properties of the Plexiglas model.

These heat transfer coefficients include convection and radiation. The convection component can be determined by subtracting the radiation component, which is found by the following equation:

$$h_r = \epsilon\sigma(T_{LC} + T_\infty)(T_{LC}^2 + T_\infty^2) \tag{8}$$

The radiation component generally cannot be neglected since the model views surroundings at the ambient temperature. The emissivity for the black paint/liquid crystal coating is estimated to be 0.85 ± 0.15. The uncertainty analysis includes uncertainty in the radiation correction.

In the present technique (and other transient techniques) the ambient air, liquid crystal, and model initial temperatures are chosen in advance. These variables show up in the data reduction in the form of the liquid crystal nondimensional temperature T^* (see Eq. (6)). For the limit of T^* equal to 1.0, the model initial temperature and the liquid crystal temperature are the same. This produces a uniform wall temperature during the transient but cannot be used since measurements with transient techniques require the initial wall temperature to be measurably higher (or lower) than the liquid crystal temperature. If uniform temperature boundary conditions are desired, transient tests should be run at T^*s as close as possible to 1.0, but the higher the value of T^*, the higher the uncertainty of the measurement. The effort to approximate a uniform wall temperature boundary condition using transient methods has to be balanced with the desire for keeping the uncertainties low. This tradeoff requires an understanding of the effect of transient boundary conditions on the heat transfer measurement.

Uncertainty Analysis

The results of an uncertainty analysis (using ASME standard uncertainty methods and 95 percent confidence) are summarized in Table 1. The individual contributions of each measurement to the total uncertainty are given for typical conditions. The thermal properties of the model and the initial temperature of the transient contribute to the largest individual uncertainties in the measurement. The total uncertainty of the local heat transfer coefficient is estimated to be approximately 6 percent.

Table 1   Uncertainty analysis for the transient shroud technique

Measured Parameter (x)	Typical Value	δx (+)	Uncertainty (%)*
T_∞	22.7° C	.1	.77
T_o	38.97° C	.1	3.05
T_{LC}	35.85° C	.1	.93
$\sqrt{(\rho C_p k)}$	575	25	4.57
ϵ	.85	.15	.89
t	1.15 sec	.03	1.29
			Total=5.9%

* $(1/h)(\partial h/\partial x)\delta x$

Numerical Scheme

Computer codes were written to solve numerically for laminar flow over a flat plate with different thermal boundary conditions (uniform temperature, uniform heat flux, and an unsteady wall temperature associated with transient methods). The governing equations and numerical techniques are standard. The numerical scheme used is described by Anderson et al. (1984). The uniform temperature and uniform heat flux cases were done as a check on the numerical techniques since results for these cases are well known.

The transient method case is a conjugate problem requiring a simultaneous solution of the boundary layer convection and the wall conduction. (The wall temperatures during the transient are continually changing and are not uniform.) For this case the uniform wall temperature code was modified to allow for the wall temperatures to be variable. The code first calculates the boundary layer velocity and temperature profiles for a uniform wall temperature (i.e., the starting temperature of a transient test) and the corresponding local heat transfer coefficients. Since each location on the plate has a different initial heat transfer coefficient, the initial rates of change of the local wall temperatures are also different. The change in the wall temperatures for the next time step are calculated using the one-dimensional transient wall conduction equation with the local heat transfer coefficients. New values of h are then determined from the new wall temperature distribution using the boundary layer energy equation. For subsequent time steps, a time-averaged heat transfer coefficient is used in the one-dimensional transient wall conduction equation to update the surface temperatures. Since the one-dimensional transient wall conduction equation assumes h is constant with time (which is not the case here), this numerical procedure is approximate. Butler (1995) has shown that (for the time periods of interest in the transient method) this numerical method produces nearly identical results to those obtained with a true conjugate solution of the simultaneous convection and wall conduction.

The energy equation for the boundary layer assumes that at any time step the boundary layer is at steady state. This is a common assumption for boundary layers and is reasonable because the time scale for the wall conduction is much greater than the time scale for convection. For example, Kurkal and Munukutla (1989) showed the time scale for the boundary layer and convection is very short (on the order of x/u), as compared to the transient conduction through the wall (L^2/α).

Numerical Results

The numerical predictions for the uniform temperature and uniform heat flux are compared to theory (given by Eqs. (1) and (2)) in Fig. 2. These test cases were used to validate the codes. As expected, the local Nusselt number for the constant heat flux is 36 percent higher than the uniform temperature solution independent of location. A typical wall temperature distribution for the uniform heat flux condition is shown in Fig. 3. For this case the wall temperature is lower near the beginning of the plate (where there is a higher heat transfer rate) and
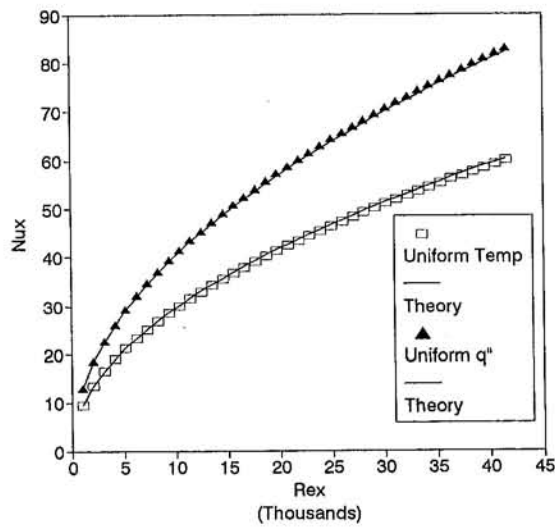
Fig. 2 Comparison of theoretical and numerical prediction of the local Nusselt number distributions for uniform temperature and uniform heat flux boundary conditions
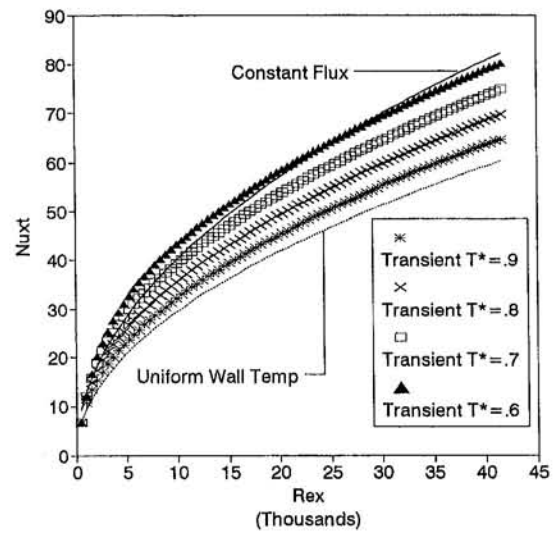
Fig. 4 Local Nusselt number distributions for transient boundary conditions (numerical prediction)

increases at a rate proportional to $x^{1/2}$. The lower upstream wall temperatures results in a higher heat transfer rate downstream than would be the case if the wall temperature were uniform.

The numerical predictions for the conjugate solution provide the time for each location to reach the liquid crystal temperature (depending on T^*). A transient method Nusselt number (Nu_{xt}) is calculated from this time using Eqs. (6) and (7). It should be noted that this Nu_{xt} is not the actual local Nusselt number, which is a function of time. It is the local Nusselt number that the standard transient method would produce using Eqs. (6) and (7) for a selected T^*. The values are shown in Fig. 4 as a function of position for a range of T^*'s. As a reference, the steady-state uniform wall temperature and constant heat flux predictions are also shown on this plot. It is clear that the local Nusselt number as determined by the transient method is highly dependent on the nondimensional liquid crystal temperature (T^*) used in the transient method. As expected, the closer T^* is to 1.0, the more the transient method acts like a uniform wall temperature method (although even at $T^* = 0.9$, the results are quite different). This strong effect of the value for T^* can be understood by examining the sketch in Fig. 5, where the temperature distribution along the wall is shown for different

times. As time increases during the transient, the upstream temperatures are lowered relative to the downstream temperatures due to the higher upstream heat transfer coefficients. Lower T^*s require longer transients during which the downstream heat transfer increases. This has significant ramifications to the interpretation of measurements made using transient methods.

Transient methods assume that the local heat transfer coefficients are constant over time (Eqs. (6) and (7) assume h is constant with time). In fact, this is not actually the case. For example, the variation of the heat transfer coefficient for one location is plotted in Fig. 6 as a function of time. The time used for the calculation of h using the transient method is shown on this graph for a range of T^*'s. The lower the T^*, the greater the change in h. For this laminar layer there is even a significant change for a T^* of 0.9 (more than 10 percent). This is true for the laminar boundary layer because of the large gradients in heat transfer coefficient (which are proportional to $1/x^{1/2}$). The gradients are shallower on a flat plate with turbulent boundary layers because the heat transfer coefficient is proportional to $1/x^{1/5}$; therefore, this transient effect would not be as large. However, Taylor et al. (1989) showed that the thermal boundary condition can have a larger effect in turbulent boundary layers when the heat transfer and wall temperature gradients are larger.
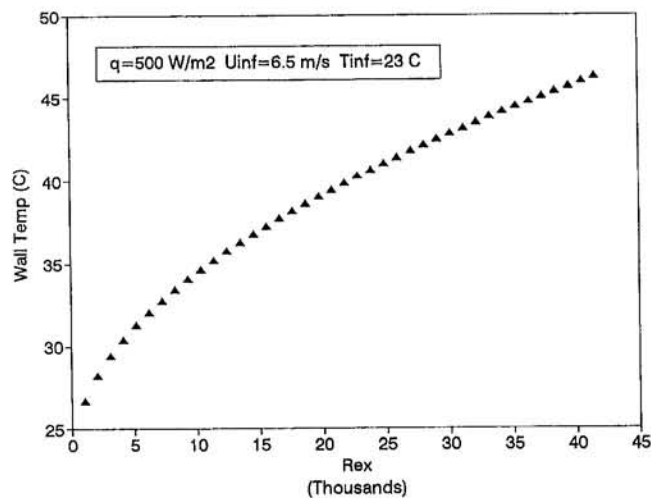
Fig. 3 Typical wall temperature distribution with a uniform heat flux boundary condition (numerical prediction)
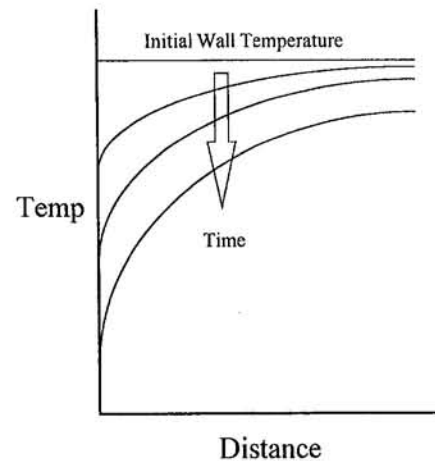
Fig. 5 Sketch of the temperature distribution along the flat plate during a transient
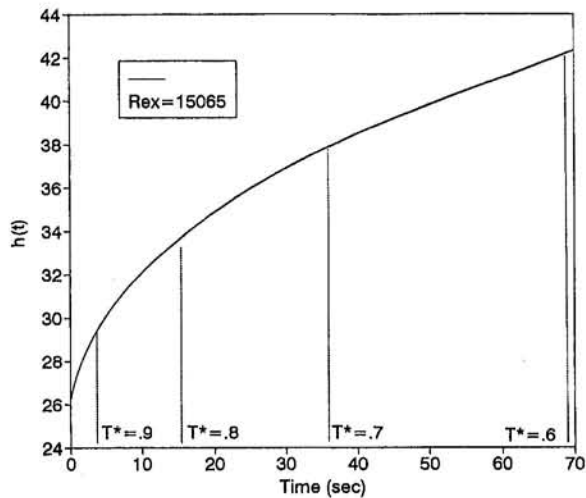
Fig. 6 Time history of the local heat transfer coefficient during a transient (numerical prediction)

Experimental Results Using the Shroud Technique

The flat plate laminar boundary layer heat transfer was measured using the shroud technique (a transient method) using four different nondimensional temperatures ($T^* = 0.6, 0.7, 0.8,$ and 0.9). The transient method Eqs. (6) and (7) were used to calculate local h's, which are shown in Fig. 7. Also shown in this figure are the theoretical heat transfer coefficients for the uniform wall temperature and constant heat flux boundary conditions. As expected, the higher the nondimensional temperature T^*, the closer the measurements are to the uniform wall temperature solution. The graph also shows how strongly dependent the heat transfer is on the transient nondimensional temperature (T^*). It should be noted that the experimental data for $T^* = 0.6$ diverge near the end of the plate. This is due to the longer transients required for $T^* = 0.6$ at these locations. The long duration of the transient allows the semi-infinite substrate assumption to break down and this causes the calculated heat transfer to increase further. The $T^* = 0.6$ data were included to show the overall effect of T^* (in practice, T's this low should not be used).

Comparison of Numerical Predictions and Measurements

The numerical predictions using the transient boundary conditions are compared to the shroud (transient) experimental
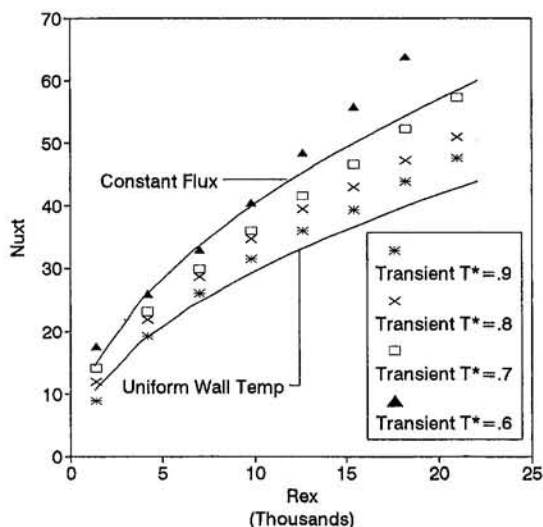
Fig. 7 Measured local Nusselt number distributions for transient boundary conditions using the shroud (transient) method
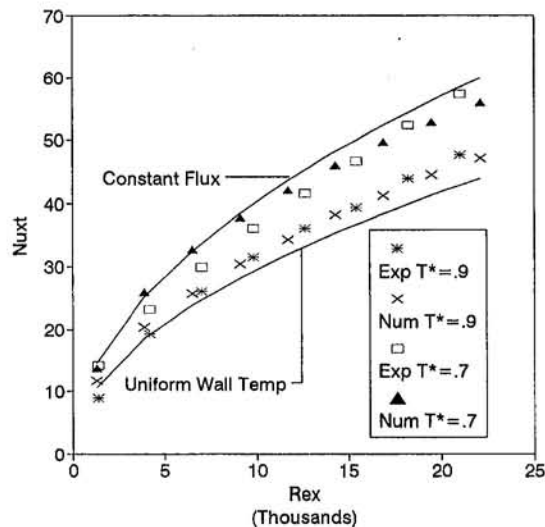
Fig. 8 Comparison of measurements and numerical predictions of the local Nusselt number with transient boundary conditions ($T^* = 0.9$ and 0.7)

measurements in Figs. 8 and 9. For reference, the theoretical solutions for a uniform wall temperature and a constant heat flux are also shown on these plots. Figure 8 compares the $T^* = 0.9$ and $T^* = 0.7$ transients. For clarity, a separate plot (Fig. 9) is used for $T^* = 0.8$ and $T^* = 0.6$. The experimental results compare favorably to the numerical solutions, showing higher heat transfer as the nondimensional temperature decreases.

Correlation for T^* Effect on Transient Method

The transient method produces thermal boundary conditions that are very different from the common thermal boundary conditions used in most experimental heat transfer. Since $T^* = 1.0$ (one limit on the transient method) corresponds to a uniform temperature boundary condition, it is possible to collapse transient method results to the uniform temperature case. A correlation that transforms the Nusselt number determined from the transient method (Nu_{xt}) to a corrected Nusselt number Nu_{xc} for a uniform temperature boundary condition has been determined using the numerical results. This correlation is dependent on T^* and the Reynolds number:
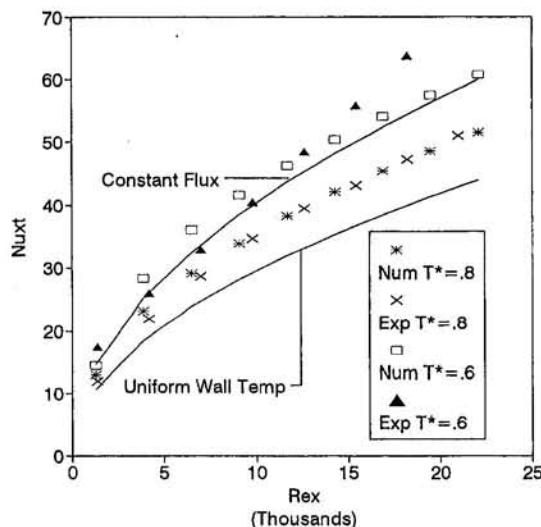
Fig. 9 Comparison of measurements and numerical predictions of the local Nusselt number with transient boundary conditions ($T^* = 0.8$ and 0.6)
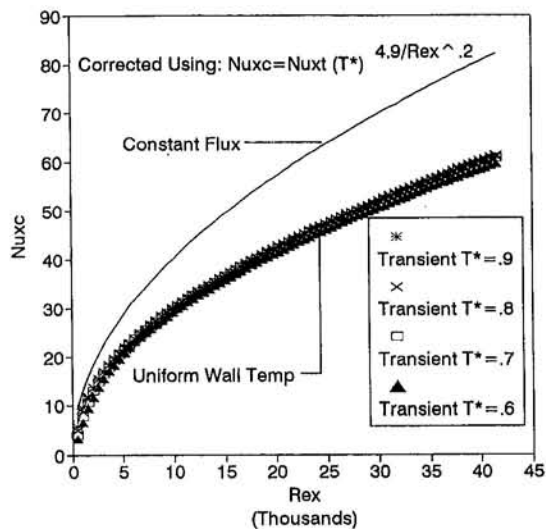
Fig. 10 Transient method Nusselt number corrected to the uniform temperature boundary condition

$$\mathrm{Nu}_{xc} = \mathrm{Nu}_{xt}(T^*)^{(4.9/\mathrm{Re}_x^{0.2})} \qquad (9)$$

The correlation is strongly dependent on the transient nondimensional temperature (T^*) with a weak dependence on Reynolds number. It is plotted in Fig. 10. This correlation collapses the transient numerical results to within 1.5 percent of the theoretical uniform wall temperature solution. The correlation was determined for a T^* range between 0.6 and 1.0 and a Reynolds number between $700/(T^*)^4$ and 40,000. Since it is weak function of Reynolds number, it may be valid over a much broader range of Reynolds numbers.

Conclusions

This study has shown the importance of the thermal boundary condition used by different heat transfer measurement methods. This effect is especially significant for transient methods with laminar boundary layers where it can have a strong effect on the measurements and their interpretation. For example, in the present study, the results that would be obtained using the transient method ranged from those of a uniform temperature boundary condition (for the limiting case of $T^* = 1.0$) to more than 36 percent above that value (for a T^* of 0.6)

A correlation was developed to collapse the transient method data to that of a uniform temperature boundary condition for a limited range of T^*'s and Reynolds numbers.

It is best when using the transient method to select the temperatures to obtain the highest possible value of T^* if the data are to be compared to uniform temperature boundary conditions. In a given application, this requires a tradeoff between the effect of the thermal boundary conditions and the uncertainty in the measurements (which increases with increasing T^*)

This study was limited to the laminar boundary layer. It is expected that in most cases, the effect of the thermal boundary conditions for turbulent boundary layers will be less (and therefore the effect on the transient method also less). However, in cases where there are large heat transfer gradients (for example, near regions of separation), the effects could be significant.

References

Abramowitz, X. X., and Stegun, Y. Y., 1970, *Handbook of Mathematical Functions*, Department of Commerce, National Bureau of Standards, Washington, DC.

Anderson, D. A., Tannehill, J. C., and Pletcher, R. H., 1984, *Computational Fluid Mechanics and Heat Transfer*, Hemisphere Publishing Company, New York, pp. 333–335.

Baughn, J. W., Ireland, P. T., Jones, T. V., and Saniei, N., 1989, "A Comparison of the Transient and Heated-Coating Methods for the Measurements of the Local Heat Transfer Coefficients on a Pin Fin," ASME JOURNAL OF HEAT TRANSFER, Vol. 111, pp. 877–881.

Baughn, J. W., and Saniei, N., 1991, "The Effect of the Thermal Boundary Condition on Heat Transfer From a Cylinder in Crossflow," ASME JOURNAL OF HEAT TRANSFER, Vol. 113, pp. 1020–1022.

Baughn, J. W., and Yan, X., 1991a, "An Insertion Technique Using the Transient Method With Liquid Crystals for Heat Transfer Measurements in Ducts," ASME HTD-Vol. 164, pp. 77–83.

Baughn, J. W., and Yan, X., 1991b, "A Preheated-Wall Transient Method for Measurements of the Heat Transfer From a Surface to an Impinging Jet," *Proc. Eurotherm Seminar No. 25*, pp. 1–7.

Baxter, D. C., and Reynolds, W. C., 1958, "Fundamental Solutions for Heat Transfer From Nonisothermal Flat Plates," *Journal of the Aeronautical Sciences*, Vol. 25, pp. 403–404.

Blasius, H., 1908, *Z. Math. Phys.*, Vol. 56, p. 1; English translation: NACA TM 1256.

Butler, R. J., and Baughn, J. W., 1995, "A Shroud Technique using the Transient Method for Local Heat Transfer Measurements," *Experimental Heat Transfer*, Vol. 8, pp. 161–173.

Butler, R. J., 1995, "The Effects of the Thermal Boundary Condition and Turbulence on Heat Transfer From a Cylinder, Flat Plate, and Turbine Blade Using the Transient Shroud and Heated-Coating Techniques," Ph.D. Dissertation, University of California at Davis.

Clifford, R. J., Jones, T. V., and Dunne, S. T., 1983, "Techniques for Obtaining Detailed Heat Transfer Coefficient Measurements Within Gas Turbine Blade and Vane Cooling Passages," ASME Paper No. 83-GT-58.

Dunne, S. T., 1983, "A Study of Flow and Heat Transfer in Gas Turbine Cooling Passages," D. Phil. Thesis, Oxford University, Oxford, United Kingdom.

Hinze, J. O., 1975, *Turbulence*, McGraw-Hill, New York.

Ireland, P. T., and Jones, T. V., 1985, "The Measurement of Local Heat Transfer Coefficients in Blade Cooling Geometries," *AGARD Conference Proceedings No. 390*, Paper No. 28.

Ireland, P. T., and Jones, T. V., 1986, "Detailed Measurements of Heat Transfer on and Around a Pedestal in Fully Developed Passage Flow," *Proc. 8th International Heat Transfer Conference*, Vol. 3, pp. 975–980.

Ireland, P. T., 1987, "Internal Cooling of Turbine Blades," D. Phil. Thesis, Oxford University, Oxford, United Kingdom.

Jones, T. V., 1977, "Heat Transfer, Skin Friction, Total Temperature and Concentration Measurements," *Measurements of Unsteady Fluid Dynamic Phenomena*, B. E. Richards, ed., McGraw-Hill, pp. 63–102.

Jones, T. V., and Hippensteele, S. A., 1987, "High-Resolution Heat-Transfer-Coefficient Maps Applicable to Compound Surfaces Using Liquid Crystals in a Transient Wind Tunnel," *Developments in Experimental Technique in Heat Transfer and Combustion*, ASME HTD-Vol. 71, pp. 1–9.

Kays, W. M., and Crawford, M. E., 1980, *Convective Heat and Mass Transfer*, McGraw-Hill, New York.

Kim, K., Wiedner, B., and Camci, C., 1993, "Fluid Dynamics and Convective Heat Transfer in Impinging Jets Through Implementation of a High Resolution Liquid Crystal Technique, Part II: Navier–Stokes Computation of Impulsively Starting Heat Transfer Experiments," presented at the International Symposium on Air-Breathing Engines, Tokyo, Japan.

Kurkal, K. R., and Munukutla, S., 1989, "Thermal Boundary Layer Due to Sudden Heating of Fluid," *Journal of Thermophysics*, Vol. 3, No. 4, pp. 470–472.

Metzger, D. E., and Larson, E. E., 1986, "Use of Melting Point Surface Coatings for Local Convective Heat Transfer Measurements in Rectangular Channel Flows With 90-Degree Turns," ASME JOURNAL OF HEAT TRANSFER, Vol. 108, pp. 48–54.

Metzger, D. E., Bunker, R. S., and Bosch, G., 1991, "Transient Liquid Crystal Measurement of Local Heat Transfer on a Rotating Disk With Jet Impingement," ASME *Journal of Turbomachinery*, Vol. 113, pp. 52–59.

O'Brien, J. E., Simoneau, R. J., LaGraff, J. E., and Morehouse, K. A., 1986, "Unsteady Heat Transfer and Direct Comparison for Steady-State Measurements in a Rotor-Wake Experiment," *Proc. 8th International Heat Transfer Conference*, San Francisco, CA, pp. 1243–1248.

Perera, K. K. K., and Baughn, J. W., 1994, "The Effect of Pitch Angle and Reynolds Number on Local Heat Transfer in Spirally Fluted Tubes," ASME HTD-Vol. 279, pp. 99–112.

Pohlhausen, E., 1921, "Der Wärmeaustausch zwischen festen Körpern und Flüssingkeiten mit kleiner Reibung und kleiner Wärmeleitung," *ZAMM*, Vol. 1, p. 115.

Schlichting, H., 1968, *Boundary-Layer Theory*, McGraw-Hill, New York.

Schultz, D. L., and Jones, T. V., 1973, "Heat Transfer Measurements in Short Duration Hypersonic Facilities," AGARDograph No. 165.

Sugawara, S., Sato, T., Komatsu, H., and Osaka, H., 1988, "Effect of Free-Stream Turbulence on Flat Plate Heat Transfer," *Int. Journal of Heat and Mass Transfer*, Vol. 31, pp. 5–12.

Taylor, R. P., Coleman, H. W., Hosni, M. H., and Love, P. H., 1989, "Thermal Boundary Condition Effects on Heat Transfer in the Turbulent Incompressible Flat Plate Boundary Layer," *Int. Journal of Heat and Mass Transfer*, Vol. 32, pp. 1165–1174.

D. D. Hobson

Lincoln Laboratory,
Massachusetts Institute of Technology,
Lexington, MA 02173

Thermocouple Lag in Transient Heat-Shield Measurements Due to Thermal Mass Difference[1]

Introduction

Ballistic missile flight test designers use thermocouples to make in-depth temperature measurements of the missile's heat shield. A cylindrical plug, fashioned of the heat-shield material, is fitted with thermocouple wires at precise depths and mounted into a complementary hole in the heat shield. The plug surface is flush with the heat-shield surface and the thermocouple wires run some distance parallel to the surface before bending to the missile interior, as shown in Fig. 1. A reading of the voltage difference between the two wires joined at the center of the plug is directly correlated with the temperature of the joint. If the isothermal length parallel to the surface is sufficiently long relative to the wire thickness, thermal conduction down the colder vertical segments will have little effect on the joint temperature. In such a case the measured thermocouple temperature is generally thought to be the same as the temperature of the heat-shield material at that depth.

The thermocouple temperature actually lags the heat-shield temperature during transient heating, most notably in atmospheric re-entry. Common thermocouple wires consist of metals with high thermal mass (the product of specific heat and density). Ablating heat-shield materials have significantly lower thermal mass, in some cases an order of magnitude lower. For the same amount of heat, the thermocouple wire experiences a smaller temperature change than the same volume of heat-shield material. This gives rise to a temperature difference between the thermocouple wire and the surrounding heat shield. Conduction of heat from the surrounding heat shield to the thermocouple wire lessens this effect, but a finite difference persists. Similar problems have been considered by previous authors (Beck, 1962, 1968; Pfahl and Dropkin 1966), though not in the context of the plug design of Fig. 1.

This paper shows that the thermocouple and heat-shield temperatures can be related through a time-dependent Volterra integral equation of the second kind involving a heat kernel. An approximate solution of the equation in the presence of exponentially increasing temperature shows that the thermocouple lags the heat shield by a fixed percentage. The lag is expressed quantitatively in terms of the thermal mass mismatch and the thermocouple wire thickness. The analysis ignores variations in thermal properties with respect to temperature, but establishes the relationships between the lag and design parameters. Thus, the analysis enables effective thermocouple design for re-entry heat shields but should not be construed as a tool for post-mission correction of lagging thermocouple data.

Thermocouple Analysis

Figure 2 depicts the cross section of two types of thermocouple wire embedded in heat-shield material. The circular wires

appear more frequently in applications, but the ribbon wires have the advantage of superior strength for the same thickness. Local heating problems concerning circular wires require two-dimensional analysis. The ribbon wires are much wider than they are thick and can be treated as one-dimensional across their thickness. The two-dimensional case demands more careful attention and we treat it first. The one-dimensional case follows using appropriate simplifications.

A number of strict assumptions apply to thermocouples embedded in typical re-entry heat shields. It is assumed that the thermocouple is a much better thermal conductor than the heat-shield material and that all heat transfer within the heat shield and between the heat shield and the thermocouple is conductive. We neglect any thermal contact resistance between the thermocouple surface and the surrounding heat shield, though one may well imagine such resistance exists in practice. The thermocouple is treated as an isothermal body characterized by the single temperature $T_c(t)$. The thermocouple radius a is assumed to be small compared to the length scale of temperature gradients in the heat shield. This allows approximation of the temperature distributions by perturbation series in the thermocouple radius (i.e., truncations of convergent Taylor series expansions in powers of a).

The heat shield is assumed to be of infinite extent and the heat-shield temperature far from the thermocouple is assumed to be unperturbed by the thermocouple. This limits the results to cases in which the thermocouple radius is small compared to its depth beneath the heat-shield surface. The heat-shield thermal properties are assumed to be uniform and independent of temperature. This is a poor approximation for real heat-shield materials. It is necessary because it allows modeling of the conduction by linear equations, which can be treated analytically. The results will allow basic understanding of thermocouple lag and provide approximate answers useful for design purposes, but they will fall short of the quantitative accuracy necessary for post-mission analysis of thermocouple data.

The following equations govern the dependence of the heat-shield temperature distribution $T(r, \theta, t)$ on the thermocouple temperature $T_c(t)$ and the unperturbed (far-field) heat-shield distribution $T^*(r, \theta, t)$:

$$\frac{\partial T}{\partial t} = \alpha \nabla^2 T \quad r \geq a \tag{1a}$$

$$T(r, \theta, t) \to T^*(r, \theta, t) \quad r \to \infty \tag{1b}$$

$$T(a, \theta, t) = T_c(t) \tag{1c}$$

$$T(r, \theta, 0) = T^*(r, \theta, 0) \tag{1d}$$

$$\dot{T}_c(t) = \frac{\alpha}{\epsilon \pi a^2} \oint \nabla T \cdot \hat{n} ds \tag{1e}$$

The line integral is taken over the circumference of the thermocouple wire cross section. The parameter ϵ is the ratio of thermocouple thermal mass to heat-shield thermal mass and a is the thermocouple wire radius. These coupled equations imply a direct relationship between the unperturbed temperature T^* and the thermocouple temperature T_c, as shown below.
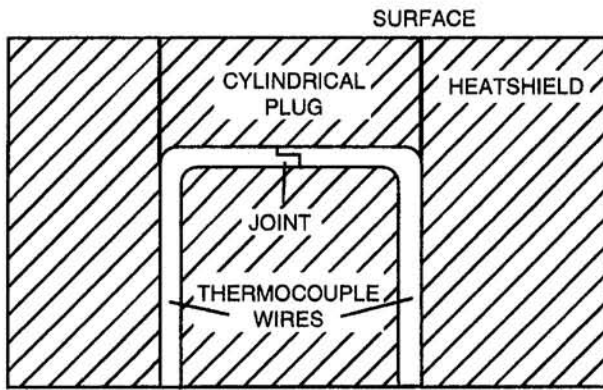
Fig. 1 Heat-shield thermocouple plug

(a) CIRCULAR WIRE   (b) RIBBON WIRE

Fig. 2 Circular and ribbon thermocouple cross sections

It is convenient to express these equations in terms of deviations from the unperturbed temperature distribution. To that end, we make the following definitions:

$$T_1(t) = T^*(0, \theta, t)$$

$$u = T^* - T$$

$$u_c = T_1 - T_c$$

Ideally the thermocouple matches the heat-shield temperature T_1 at its depth. In transient heating the thermocouple error u_c is nonzero. The equations for u and u_c are

$$\frac{\partial u}{\partial t} = \alpha \nabla^2 u \quad r \geq a \qquad (2a)$$

$$u(r, \theta, t) \to 0 \quad r \to \infty \qquad (2b)$$

$$u(a, \theta, t) = u_c(t) + T^*(a, \theta, t) - T_1(t) \qquad (2c)$$

$$u(r, \theta, 0) = 0 \qquad (2d)$$

$$\dot{u}_c(t) = \dot{T}_1 - \frac{\alpha}{\epsilon \pi a^2} \left(\oint \nabla T^* \cdot \hat{n} ds - \oint \nabla u \cdot \hat{n} ds \right). \qquad (2e)$$

Exploiting the assumption that a is small compared to spatial gradients in the temperature distributions, consistent expansions for u and T^* near the thermocouple surface are

$$u(r, \theta, t) = A(r, t) + O(a)$$

$$T^*(r, \theta, t) = T_1(t) + O(a)$$

where $A(r, t)$ is the main component of the distribution $u(r, \theta, t)$. These approximations are a direct consequence of expanding the unperturbed distribution T^* in a Taylor series in

powers of a. Applying the divergence theorum and the conduction equation for T^* gives

$$\oint \nabla T^* \cdot \hat{n} ds = \iint \nabla^2 T^* dA = \pi a^2 \frac{\partial T^*}{\partial t} (0, \theta, t) + O(a^4)$$

$$= \pi a^2 \dot{T}_1(t) + O(a^4).$$

The second integral in Eq. (2e) becomes

$$\oint \nabla u \cdot \hat{n} ds = a \int_0^{2\pi} \frac{\partial u}{\partial r} (a, \theta, t) d\theta$$

$$= 2\pi a \frac{\partial A}{\partial r} (a, t) + O(a^2)$$

The system of equations (2) for $u(r, \theta, t)$ can be expressed in terms of $A(r, t)$:

$$\frac{\partial A}{\partial t} = \alpha \left(\frac{\partial^2 A}{\partial r^2} + \frac{1}{r} \frac{\partial A}{\partial r} \right) \qquad (3a)$$

$$A(r, t) \to 0 \quad r \to \infty \qquad (3b)$$

$$A(a, t) = u_c(t) + O(a) \qquad (3c)$$

$$A(r, 0) = 0 \qquad (3d)$$

$$\dot{u}_c = \left(1 - \frac{1}{\epsilon} \right) \dot{T}_1 + \frac{2\alpha}{a\epsilon} \frac{\partial A}{\partial r} (a, t) + O(a) \qquad (3e)$$

Note that Eq. (3e) can be rewritten as

$$\frac{\partial A}{\partial r} (a, t) = \frac{a\epsilon}{2\alpha} \left(\dot{u}_c - \left(1 - \frac{1}{\epsilon} \right) \dot{T}_1 \right),$$

——————— Nomenclature ———————

a = thermocouple radius
A = radially symmetric component of u
B = Laplace transform of A
c = thermocouple fractional lag
f = boundary value for A
F = Laplace transform of f
g = boundary value for $\partial A/\partial r$
G = Laplace transform of g
k = heat-shield thermal conductivity
c_p = heat-shield specific heat
r = radial distance from thermocouple center
t = time

T = heat-shield temperature distribution
T_1 = heat-shield temperature at thermocouple depth
T^* = unperturbed heat-shield temperature distribution
T_c = thermocouple temperature
$u = T^* - T$ = difference between unperturbed and perturbed temperature distributions
$u_c = T_1 - T_c$ = difference between heat-shield and thermocouple temperatures

$\alpha = k/\rho c_p$ = heat-shield diffusivity
$\delta = a\sqrt{\sigma/\alpha}$ = dimensionless thermocouple radius
$\epsilon = \rho' c_p'/\rho c_p$ = thermal mass ratio
ρ = heat-shield density
ρc_p = heat-shield thermal mass
$\rho' c_p'$ = thermocouple thermal mass
σ = reciprocal of heating e-fold time
Φ = Laplace transform of heat kernel
ϕ = heat kernel

This system overdetermines the distribution $A(r, t)$ in general. To see this, consider the generalized form of the system (3):

$$\frac{\partial A}{\partial t} = \alpha\left(\frac{\partial^2 A}{\partial r^2} + \frac{1}{r}\frac{\partial A}{\partial r}\right)$$

$$A(a, t) = f(t)$$

$$\frac{\partial A}{\partial r}(a, t) = g(t)$$

$$A(r, 0) = 0$$

$$A(r, t) \rightarrow 0 \quad r \rightarrow \infty$$

Letting $B(r, s)$, $F(s)$, and $G(s)$ be the Laplace transforms of $A(r, t)$, $f(t)$, and $g(t)$, respectively, we see that this system yields a solution without knowledge of $g(t)$:

$$B(r, s) = \Psi(r, s)F(s)$$

where

$$\Psi(r, s) = \frac{K_0\left(r\sqrt{\frac{s}{\alpha}}\right)}{K_0\left(a\sqrt{\frac{s}{\alpha}}\right)}$$

and $K_0(z)$ is a modified Bessel function of the second kind. Satisfying the condition $\partial A/\partial r(a, t) = g(t)$ requires

$$G(s) = -\frac{as}{\alpha}\Phi(s)F(s)$$

where

$$\Phi(s) = -\frac{\alpha}{as}\frac{\partial \Psi}{\partial r}(a, s) = \frac{K_1(z)}{zK_0(z)} \quad (4)$$

and $z = a\sqrt{s/\alpha}$. Inverting the Laplace transform we find

$$\frac{\alpha}{a}\int_0^t g(t')dt' = \int_0^t \phi(t - \tau)f(\tau)d\tau \quad (5)$$

where $\phi(t)$ is the inverse Laplace transform of $\Phi(s)$. The boundary values $f(t)$ and $g(t)$ must satisfy Eq. (5) in order that the system not overdetermine $A(r, t)$.

Interpreting Eq. (5) in terms of the thermocouple error u_c and the local heat shield temperature T_1 using Eqs. (3c) and (3e) gives

$$\epsilon u_c(t) + 2\int_0^t \phi(t - \tau)u_c(\tau)d\tau = (\epsilon - 1)T_1(t) \quad (6)$$

in which we have assumed that $T_1(0) = 0$ and $u_c(0) = 0$. The first assumption amounts to setting the temperature scale and imposes no loss in generality. The second assumption requires that the thermocouple initially read the correct heat-shield temperature. Equation (6) is a Volterra integral equation of the second kind for the thermocouple error $u_c(t)$ in terms of the heat-shield temperature $T_1(t)$ and a heat kernel $\phi(t)$. In principle, this equation provides a means of determining the heat-shield temperature from the thermocouple measurement $T_c(t)$ (recall that $u_c(t) = T_1(t) - T_c(t)$). The analysis above assumes the thermal properties, characterized by the diffusivity α, are constant with respect to temperature. Practical heat shields almost always violate this assumption. Equation (6) relates design parameters, a, ϵ, and α, to the thermocouple accuracy, $u_c(t)$, and should not be viewed as a practical means of correcting data collected from poorly designed thermocouples.

Thermocouple accuracy during transient heating is the primary interest of this paper. Heat-shield temperatures increase

Table 1 Thermocouple lag for various heat shields

Heat shield material	1	2	3	4
α (mm²/s)	0.25	0.08	0.02	0.25
ρc_p (J/cm³ K)	2.0	2.5	0.33	0.24
ϵ^*	2.0	1.6	12	17
Lag† (percent)				
Circular: 3 mil	0.28	0.42	22.9	4.4
Circular: 1 mil	0.04	0.07	4.0	0.7
Ribbon: 0.5 mil	0.35	0.37	13.5	5.6
Ribbon: 0.2 mil	0.14	0.15	5.4	2.2

1. Silica-Phenolic 2. Avcoat 2 3. Cork 4. Acusil 2
* Type-K thermocouple, $\rho'c_p' = 4.0$ J/(cm³ K)
† Mach 10 reentry, $\sigma = 0.3$ s^{-1}

exponentially during atmospheric re-entry and one can determine how well thermocouples perform in such an environment using Eq. (6). Assume $T_1(t) = e^{\sigma t}$ and that the thermocouple error is asymptotically proportional, $u_c(t) \rightarrow ce^{\sigma t}$ as $t \rightarrow \infty$. Equation (6) becomes

$$c\left(\epsilon + 2\int_0^\infty \phi(t)e^{-\sigma t}dt\right) = \epsilon - 1$$

The integral is the Laplace transform of $\phi(t)$, fortunate because a closed-form expression for $\phi(t)$ itself is unavailable. So, we have

$$c = \frac{\epsilon - 1}{\epsilon + 2\Phi(\sigma)} \quad (7)$$

For typical parameter values, the dimensionless argument $\delta = a\sqrt{\sigma/\alpha}$ is small and we have from Eq. (4)

$$\Phi(\sigma) = \frac{K_1(\delta)}{\delta K_0(\delta)} \approx \frac{-1}{\delta^2 \ln \delta}$$

as $\delta \rightarrow 0$. Equation (7) becomes

$$c \approx \frac{1}{2}(\epsilon - 1)\delta^2 \ln(1/\delta). \quad (8)$$

The coefficient c is the ratio of the thermocouple error $u_c(t)$ to the heat-shield temperature $T_1(t)$ at the thermocouple depth. Since this is constant in time, the error can be characterized as a lag proportional to the change in heat-shield temperature. The parameter δ is a dimensionless thermocouple wire radius and ϵ is the ratio between thermal masses of the thermocouple wire and the heat-shield material. A thermal mass ratio not equal to 1 will produce a nonzero lag. That is, if the thermocouple is thermally heavier than the heat shield, it will respond more slowly than the heat shield and will thus read low. The lag can be minimized by using sufficiently thin wires, making δ small.

Table 1 shows results for various heat-shield materials used commonly today. A type-K thermocouple wire (Dunlap, 1988) and a nominal heating rate of $\sigma = 0.3s^{-1}$ are assumed. Circular wires of diameter 3 mil (0.003 in.) and 1 mil and ribbon wires of thickness 0.5 mil and 0.2 mil are represented. The larger value for each type corresponds to the thinnest available off-the-shelf wire. The smaller value for each type corresponds to specially manufactured or hand-made wire. The heating rate is typical of Mach 10 re-entry with re-entry angle of roughly 45 deg. The lags in Table 1 were computed using Eqs. (8) and (9). For heavy heat shields, such as silica-phenolic or the epoxy-based materials, the ratio ϵ is greater than 1 but less than 2. Lags for such heat shields are rather small. Light heat shields, such as cork, suffer rather large lags and require superior engineering (circular wires of 1 mil diameter or ribbon wires of 0.2 mil thickness) to yield useful re-entry measurements. Data collected with lags exceeding roughly 10 percent require post-flight correction similar to that modeled by Eq. (6) assuming

constant thermal properties. Ideally, the temperature depen-
dence of the heat-shield thermal properties should be taken into
account, but Eq. (6) can be used to make rough post-flight
corrections.

Thermocouple lag correlates most directly with the thermal
mass ratio ϵ. Low thermal mass materials, such as cork and
Acusil 2, heat much more quickly than the type-K thermocouple
assumed in Table 1, thus causing significant lags. Types G and
R thermocouples have somewhat lower thermal mass and can
mitigate this problem slightly. Unfortunately, both have practi-
cal limitations that render them unfit for use in re-entry heat
shields. Type G wires are composed primarily of tungsten,
which is too brittle to make thin wires (Liptak and Venczel,
1982). Type R thermocouple have poor linearity and low output
below 800 K (Liptak and Venczel, 1982).

The analysis is much the same for the ribbon thermocouples.
Instead of circular geometry around the wire, one assumes a
one-dimensional geometry with the ribbon thickness sand-
wiched between heatshield material on either side as in Fig.
2(b). An equation identical to Eq. (6) holds, with the Laplace
transform $\Phi(s)$ of the heat kernel $\phi(t)$ in Eq. (4) being replaced
by

$$\Phi_{\text{ribbon}} = \frac{1}{a}\sqrt{\frac{\alpha}{s}}$$

The expression for the lag c_{ribbon} corresponding to Eq. (8) is

$$c_{\text{ribbon}} = \tfrac{1}{2}(\epsilon - 1)\delta \qquad (9)$$

Table 1 shows that ribbon thermocouples of commonly used
thickness have lags very close to circular thermocouples of
commonly used diameters. Figure 3 shows the results from Eqs.
(8) and (9) applied to thermocouples in silica-phenolic and
cork using the same parameters as in Table 1. The fractional
lag is plotted versus thermocouple radius for circular wires and
versus half-thickness for ribbon wires. The lags for cork are
significantly higher than those for silica-phenolic since the ther-
mal mass mismatch is much greater for cork. The lags for ribbon
thermocouples exceed those for circular thermocouples of the
same thickness.

Summary

A thermocouple wire embedded in a heat-shield material lags
in responding to temperature changes in the heat shield. The
thermal mass mismatch between thermocouple and heat shield
causes the thermocouple to heat more slowly in response to
transient heating. A Volterra integral equation, derived assum-
ing constant thermal properties and infinite thermocouple con-
ductivity, relates the local heat-shield temperature history to the
thermocouple temperature history. This equation quantifies the
relationship between the thermocouple behavior and design pa-
rameters, enabling effective pre-mission design so that the data
collected will be free of unwanted lags. For exponentially in-
creasing heat loads, typical of atmospheric re-entry, the thermo-
couple lag is a fixed percentage of the change in local heat-
shield temperature. The lag is proportional to the thermal mass
excess of the thermocouple compared to the heat shield, with
the proportionality constant dependent upon the thickness of
the thermocouple wire. The thinnest off-the-shelf thermocouple
wires reduce lags to a few percent or less in heavy heat shields,
such as silica-phenolic. Specially manufactured wires are neces-
sary to achieve similar reductions in lags in light heat shields,
such as cork. Ribbon wires of commonly used thickness have
lags roughly the same as circular wires of commonly used diam-
eter.

Fig. 3 Lag versus thermocouple thickness

Acknowledgments

References

Beck, J. V., 1962, ASME JOURNAL OF HEAT TRANSFER, Vol. 84, pp. 124–132.
Beck, J. V., 1968, *Nuclear Engineering and Design*, Vol. 7, pp. 9–12.
Dunlap, R. A., 1988, *Experimental Physics, Modern Methods*, Oxford Univer-
sity Press.
Liptak, B., and Venczal, K., eds., 1982, *Instrument Engineers Handbook*, Chil-
ton Book Co.
Pfahl, R. C., Jr., and Dropkin, D., 1966, ASME Paper No. 66-WA/HT-8.

Solution of the Inverse Heat Conduction Problem From Thermal Strain Measurements

G. Blanc

M. Raynaud
email: raynaud@cethil.insa-lyon.fr

Centre de Thermique,
INSA de LYON-ESA CNRS 5008,
Bât. 404, 20 av. A. Einstein,
69621 Villeurbanne Cedex, France

Another approach for the solution of the inverse heat conduction problem is presented. The unknown boundary conditions are recovered from thermal strain and temperature measurements instead of temperature measurements only. It is required to calculate both the temperature field and the strains induced by this field. The sensitivity coefficient analysis and the results of two benchmark test cases show that it is possible to recover higher temporal frequencies when the inversion is done from strains instead of temperatures. An experimental setup was specially designed to validate the numerical results. The numerical predictions are verified. Special attention is given to the strain gage measurements.

1 Introduction

The Inverse Heat Conduction Problem (IHCP) is commonly defined as the estimation of a solid's temperature and surface heat flux from remote temperature measurements. This problem was first addressed by Stolz (1960). Since then, many methods have been proposed and several books (Beck et al., 1985; Hensel, 1991; Murio, 1993; Alifanov, 1994; Kurpitz and Nowak, 1995) were entirely devoted to this particular problem. In a recent paper, Scarpa and Milano (1995) showed how the robust technique of Kalman filter could be used to handle the high sensitivity of the IHCP to measurement errors. However, the comparative studies (Raynaud and Bransier, 1986; Raynaud and Beck, 1988; Marquardt and Auracher, 1990; Maillet et al., 1991; Scarpa and Milano, 1995) show that many methods that have a tunable stabilizing parameter give more or less the same results when applied to the same experimental data. As a matter of fact, any efficient technique extracts all the information given by the sensors and it is difficult to recover the high temporal surface frequencies that are damped within the solid. This indicates that the thermocouple may not be the most appropriate sensor to solve an IHCP or the experiment is poorly defined.

This fact led us to try to solve the IHCP from information given by strain gages instead of thermocouples. The literature review shows that such an approach has already been used by Crysa et al. (1981), Noda (1989), and Morilhat et al. (1992). Unfortunately, the proposed methods are based on transfer functions. They are thus limited to linear problems and none of them uses a stabilizing parameter. Consequently, their range of applications is limited. Raynaud et al. (1993) introduced a stabilized technique based on thermal stress variations, but it was revealed not to be completely satisfying. Thus a similar method using thermal strain variations has been developed.

The objective of the paper is to present this new method, to show its efficiency on benchmark test cases, and to validate the method with experimental data. The study is limited to the unidirectional problem shown in Fig. 1: A long tube, initially at a uniform temperature, insulated on its outer surface, is heated uniformly on its inner surface. The inner temperature and flux variations are to be estimated either from external temperature variations or from external thermal strain variations. The goal is to determine the most efficient type of measurement.

2 Method Description

Finite difference space marching techniques, developed for the IHCP, cannot be used because the thermal displacements result from an integral effect. Since sequential methods are computationally efficient for the IHCP, it has been decided to develop a method based on the same principle than the function specification method proposed by Beck (1970).

In the sequential procedure, at the time step "$n + 1$", the following functional is minimized versus the unknown heat flux density q^{n+1}, all parameters being known at the previous time step "n":

$$J(q^{n+1}) = \sum_{j=1}^{nfs} (X_{ll}^{n+j} - \epsilon_{ll}^{n+j})^2 \qquad (1)$$

where X is the measured strain in the direction l and ϵ the strain calculated in the same direction by a model that involves q^{n+1}. The stabilizing parameter "nfs" is the number of future time strains. Minimization of J versus q^{n+1} using Gauss linearization and assuming temporally that the heat flux is constant over "nfs" time steps, leads to:

$$q^{n+1} = q^n + \frac{\displaystyle\sum_{j=1}^{nfs} (X_{ll}^{n+j} - \epsilon_{ll}^{n+j}) S_\epsilon^{n+j}}{\displaystyle\sum_{j=1}^{nfs} (S_\epsilon^{n+j})^2} \qquad (2)$$

This equation is similar to the one obtained when temperature measurements are considered, but the S_ϵ terms are the strain sensitivity coefficients and not the temperature sensitivity coefficients. The thermal strains are calculated from the temperature field with the quasi-static and uncoupled assumptions, i.e., inertial effects are neglected in the equilibrium equation and the effect of thermal expansion due to strains are neglected in the heat diffusion equation. For steel, the quasi-static assumption hold as long as the frequencies of the thermal or mechanical loading are less than several kHz. Based on the criterion given by Boley and Weiner (1996, p. 42) the uncoupling is justified for steel tube in most practical cases, the error induced by this assumption being less than 1 percent. For the one-dimensional problem shown in Fig. 1 and with the following dimensionless variables:

$$r^* = \frac{r}{e} \quad D^* = D/e \quad t^* = \frac{at}{e^2} \quad T^* = \lambda \frac{T - T_o}{q^{ref} e} \quad q^* = \frac{q}{q^{ref}}$$
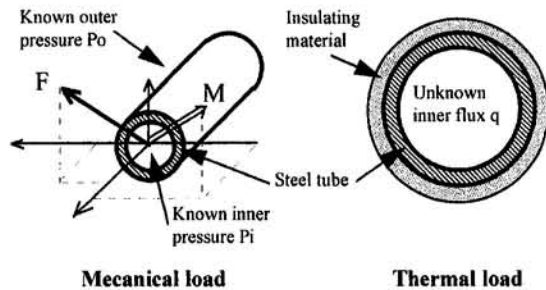
Fig. 1 Geometry and boundary conditions of the problem

$$P^* = \frac{P}{E\epsilon^{\text{ref}}} \quad \epsilon^{\text{ref}} = \alpha \frac{q^{\text{ref}} e}{\lambda} \quad \epsilon^* = \frac{\epsilon}{\epsilon^{\text{ref}}} \quad \sigma^* = \frac{\sigma}{E\epsilon^{\text{ref}}}$$

$$u^* = \frac{u^*}{e\epsilon^{\text{ref}}} \quad F^* = \frac{F}{E\epsilon^{\text{ref}} e^2} \quad M^* = \frac{M}{E\epsilon^{\text{ref}} e^3}$$

the dimensionless governing equations are:

Heat diffusion equation:

$$\frac{1}{r^*} \frac{\partial}{\partial r^*} \left(r^* \frac{\partial T^*}{\partial r^*} \right) = \frac{\partial T^*}{\partial t^*} \tag{3}$$

Thermal boundary conditions and initial condition:

$$r^* = D^*/2 \quad \frac{\partial T^*}{\partial r^*} = q^*(t^*) \tag{4a}$$

$$r^* = D^*/2 + 1 \quad \frac{\partial T^*}{\partial r^*} = 0 \tag{4b}$$

$$t^* = 0 \quad T^* = 0 \tag{4c}$$

Relations between displacement and strain (where the symmetry imposes $u_\theta^* = 0$):

$$\epsilon_{rr}^* = \frac{\partial u_r^*}{\partial r^*} \tag{5a}$$

$$\epsilon_{zz}^* = \frac{\partial u_z^*}{\partial z^*} \tag{5b}$$

$$\epsilon_{\theta\theta}^* = \frac{u_r^*}{r^*} \tag{5c}$$

$$\epsilon_{zr}^* = \frac{1}{2} \frac{\partial u_r^*}{\partial z^*} + \frac{\partial u_z^*}{\partial r^*} \tag{5d}$$

Equilibrium equation:

$$\frac{\partial \sigma_{rr}^*}{\partial r^*} + \frac{\sigma_{rr}^* - \sigma_{\theta\theta}^*}{r^*} = 0 \tag{6a}$$

$$\frac{\partial \sigma_{rz}^*}{\partial r^*} + \frac{\sigma_{rz}^*}{r^*} = 0 \tag{6b}$$

Relations between strain and stress:

$$\epsilon_{\theta\theta}^* = [\sigma_{\theta\theta}^* - \nu(\sigma_{rr}^* + \sigma_{zz}^*)] + T^* \tag{7a}$$

$$\epsilon_{rr}^* = [\sigma_{rr}^* - \nu(\sigma_{\theta\theta}^* + \sigma_{zz}^*)] + T^* \tag{7b}$$

$$\epsilon_{zr}^* = (1 + \nu)\sigma_{zr}^* \tag{7c}$$

$$\epsilon_{zz}^* = [\sigma_{zz}^* - \nu(\sigma_{\theta\theta}^* + \sigma_{rr}^*)] + T^* \tag{7d}$$

Mechanical boundary conditions:

$$r^* = D^*/2 \quad \sigma_{rr}^* = P_i^*(t^*) \tag{8a}$$

$$r^* = D^*/2 + 1 \quad \sigma_{rr}^* = P_o^*(t^*) \tag{8b}$$

$$\sigma_{zz}^* = \frac{1}{(1 + \nu)(1 - 2\nu)} (\nu(\epsilon_{\theta\theta}^* + \epsilon_{rr}^*) + (1 - \nu)\epsilon_{zz}^*$$
$$- (1 + \nu)T^*) + g(F^*(t^*), M^*(t^*)) \tag{8c}$$

These equations involve six parameters, namely, D^*, P_i^*, P_o^*, F^*, M^*, and ν. The following paragraph will show that it is possible to eliminate the terms related to pressure.

For convenience, the star symbol $*$ is now omitted; all variables are considered dimensionless. The total strain is the sum of the strain due to the temperature field ϵ^T, the inner pressure ϵ^P, and the mechanical load ϵ^M. Equation (2) can be rewritten as:

a = thermal diffusivity, m²/s
e = tube wall thickness
g = function of mechanical effects
nfs = number of future time strains
nft = number of future time temperatures
q = exact surface heat flux, W/m²
$\hat{q}$ = estimated surface heat flux, W/m²
(r, θ, z) = cylindrical coordinates
t = time
C_g = gage factor
D = inner diameter
E = Young modulus
Ec = measured temperature standard deviation
Ec_q = estimated flux standard deviation

F = mechanical force
M = mechanical moment
P_i = inner pressure
P_o = outer pressure
$S_T = \partial T/\partial q$ = temperature sensitivity coefficient
$S_\epsilon = \partial\epsilon/\partial q$ = strain sensitivity coefficient
T_m = mean temperature
T_o = reference temperature
u = displacement
V = voltage across Wheatstone's bridge
X = measured thermal strain
Y = measured temperature
α = thermal coefficient of dilatation
β = thermal coefficient of the strain gage
$\Delta T = (T - T_o)$ = temperature variation
ΔV = Wheatstone's bridge voltage variation

Δt = time step
ϵ = calculated strain
ϵ_i = inversion strain
$\epsilon_{\text{ref}} = \alpha q e/\lambda$ reference strain
ν = Poisson ratio
λ = thermal conductivity, W/m·K
σ = stress

Superscripts

j = refer to time
P = due to pressure
T = thermal
M = mechanical
$*$ = dimensionless

Subscripts

g = refer to strain gage
s = refer to the solid
e = refer to the calibration specimen
ll = refer to direction l

$$q^{n+1} = q^n + \frac{\sum\limits_{j=1}^{nfs} \{[X_{ll}^{Tn+j} - \epsilon_{ll}^{Tn+j}(q^n)] + [X_{ll}^{Pn+j} - \epsilon_{ll}^{Pn+j}(P_i^{n+j}, P_o^{n+j})] + [X_{ll}^{Mn+j} - \epsilon_{ll}^{Mn+j}]\} S_\epsilon^{n+j}}{\sum\limits_{j=1}^{nfs} (S_\epsilon^{n+j})^2} \quad (9)$$

Note that ϵ^T is calculated assuming that the flux is constant over the ''nfs'' time steps. On the other hand, if the inner and outer pressure histories are measured, then

$$X_{ll}^{Pn+j} - \epsilon_{ll}^{Pn+j}(P_i^{n+j}, P_o^{n+j}) \approx 0 \quad (10)$$

which allows us to neglect the pressure influence compared to the other two influences.

The sensitivity coefficients of the strain to the heat flux are:

$$S_\epsilon = \frac{\partial \epsilon}{\partial q} \quad (11)$$

They can be calculated by solving the sensitivity system, which is obtained by differentiating Eq. (3) to Eq. (8) with respect to the heat flux q:

$$\frac{1}{r} \frac{\partial}{\partial r} \left(r \frac{\partial S_T}{\partial r} \right) = \frac{\partial S_T}{\partial t} \quad (12)$$

$$r = D/2 \quad \frac{\partial S_T}{\partial r} = 1 \quad (13a)$$

$$r = D/2 + 1 \quad \frac{\partial S_T}{\partial r} = 0 \quad (13b)$$

$$t = 0 \quad S_T = 0 \quad (13c)$$

$$S_{\epsilon_{rr}} = \frac{\partial S_{u_r}}{\partial r} \quad (14a)$$

$$S_{\epsilon_{zz}} = \frac{\partial S_{u_z}}{\partial z} \quad (14b)$$

$$S_{\epsilon_{\theta\theta}} = \frac{S_{u_r}}{r} \quad (14c)$$

$$S_{\epsilon_{zr}} = \frac{1}{2} \frac{\partial S_{u_r}}{\partial z} + \frac{\partial S_{u_z}}{\partial r} \quad (14d)$$

$$\frac{\partial S_{\sigma_{rr}}}{\partial r} + \frac{S_{\sigma_{rr}} - S_{\sigma_{\theta\theta}}}{r} = 0 \quad (15a)$$

$$\frac{\partial S_{\sigma_{rz}}}{\partial r} + \frac{S_{\sigma_{rz}}}{r} = 0 \quad (15b)$$

$$S_{\epsilon_{\theta\theta}} = [S_{\sigma_{\theta\theta}} - \nu(S_{\sigma_{rr}} + S_{\sigma_{zz}})] + S_T \quad (16a)$$

$$S_{\epsilon_{rr}} = [S_{\sigma_{rr}} - \nu(S_{\sigma_{\theta\theta}} + S_{\sigma_{zz}})] + S_T \quad (16b)$$

$$S_{\epsilon_{zr}} = (1 + \nu) S_{\sigma_{zr}} \quad (16c)$$

$$S_{\epsilon_{zz}} = [S_{\sigma_{zz}} - \nu(S_{\sigma_{\theta\theta}} + S_{\sigma_{rr}})] + S_T \quad (16d)$$

$$r = D/2 \quad S_{\sigma_{rr}} = 0 \quad (17a)$$

$$r = D/2 + 1 \quad S_{\sigma_{rr}} = 0 \quad (17b)$$

$$S_{\sigma_{zz}} = \frac{1}{(1 + \nu)(1 - 2\nu)} [\nu(S_{\epsilon_{\theta\theta}} + S_{\epsilon_{rr}}) + (1 - \nu)S_{\epsilon_{zz}} - (1 + \nu)S_T] \quad (17c)$$

This set of equations does not involve the pressure terms,

i.e., the thermal strain sensitivity coefficients do not depend on the inner or outer pressure. Thus using Eq. (10), Eq. (9) becomes:

$$q^{n+1} = q^n + \frac{\sum\limits_{j=1}^{nfs} ((X_{ll}^{Tn+j} + X_{ll}^{Mn+j}) - (\epsilon_{ll}^{Tn+j}(q^n) + \epsilon_{ll}^{Mn+j}))S_\epsilon^{n+j}}{\sum\limits_{j=1}^{nfs} (S_\epsilon^{n+j})^2} \quad (18)$$

Equation (18) shows that the estimation of q^{n+1}, as long as the pressure variations are known, does not depend on the actual pressure values. Consequently, in the remainder of the paper, the inner and outer pressures are set to zero.

The mechanical boundary conditions (F and M) are now discussed. In practice forces and moments are exerted on each extremity of the tube (Fig. 1). Since the total strain depends on the mechanical load, the estimation of q^{n+1} requires that the applied mechanical load be known. Unfortunately, for a large real system, the load varies over time and is often difficult to evaluate. In order to get rid of the mechanical load influences, the following linear combination of the strain is studied:

$$\epsilon_i = \epsilon_{\theta\theta} + \nu\epsilon_{zz} \quad (19)$$

The substitutions of Eqs. (7a) and (7d) into Eq. (19) lead to:

$$\epsilon_i = \left(\frac{1 - \nu^2}{E} \right)(\sigma_{\theta\theta}^T + \sigma_{\theta\theta}^M) + \alpha(1 - \nu)\Delta T \quad (20)$$

For a beam, the stress $\sigma_{\theta\theta}^M$ is equal to zero regardless of the mechanical load, thus ϵ_i varies only with the temperature field, which in turn is only influenced by the heat flux we try to determine. Therefore, this particular combination of strains will be used for the inversion and is called, from now on, ''inversion strain.'' Consequently, the inversion strain does not depend on P, F, and M, but only on the temperature T and the two parameters D and ν.

For simple geometries, such as the one considered here, it is possible to get an analytical solution for the strain calculation. For a tube with a radial temperature distribution, the displacement in direction θ is equal to zero. Since the inversion strain does not depend on the mechanical loads, the state of plane strain is used and the displacement in the z direction is also equal to zero. Thus the displacement components are:

$$u_r = f(r), \quad u_\theta = 0, \quad u_z = o \quad (21)$$

In order to write the equilibrium equation, Eq. (6a), in term of displacements, the substitution of σ is first made by using the strain–stress relations, Eqs. (7a, 7b). Then the substitution of ϵ is made from the strain-displacement relations, Eqs. (5a, 5b, 5c). Thus u_r must satisfy:

$$\frac{\partial}{\partial r} \left(\frac{1}{r} \frac{\partial(ru_r)}{\partial r} \right) = \frac{1 + \nu}{1 - \nu} \alpha \frac{\partial T}{\partial r} \quad (22)$$

The general solution of this equation is obtained by integration between $D/2$ and r:

$$u_r(r) = \frac{1 + \nu}{1 - \nu} \frac{\alpha}{r} \int_{D/2}^{r} rTdr + \frac{C1}{2} r + \frac{C2}{r} \quad (23)$$

The substitution of this equation in Eqs. (5a, 5b, 5c) and Eqs. (7a, 7b) successively gives the value of σ_{rr}. The two constants of integration $C1$ and $C2$ are determined from the known inner and outer pressures:

$$r = D/2 \quad \sigma_{rr} = 0 \tag{24a}$$

$$r = D/2 + 1 \quad \sigma_{rr} = 0 \tag{24b}$$

Thus, for this particular case, the inversion strain at the outer surface, $r = D/2 + 1$, is related to the temperature field by the simple relation:

$$\epsilon_i = (1 + \nu)T_m \tag{25a}$$

$$T_m = \frac{2}{(D/2 + 1)^2 - (D/2)^2} \int_{D/2}^{D/2+1} rT dr \tag{25b}$$

Equation ($25a$) indicates that the inversion strain depends only on the mean temperature defined by Eq. ($25b$). Thus, during the inversion, an infinite number of inner surface heat fluxes, which would all lead to the same mean temperature, can be estimated. Consequently, the temperature measured on the outer radius, which will be needed to correct the strain gage response, is used instead of Eq. ($4b$), as a boundary condition of the thermal problem. With such a procedure, the absolute temperature is imposed on the outer surface by the temperature measurements and the unknown inner heat flux is estimated from strain measurements:

$$q^{n+1} = q^n + \frac{\sum_{j=1}^{nfs} (X_i^{n+j} - \epsilon_i^{n+j})S_\epsilon^{n+j}}{\sum_{j=1}^{nfs} (S_\epsilon^{n+j})^2}$$

$$T^{n+j} (r = D/2 + 1) = Y^{n+j} \quad \forall j \in [1, nfs] \tag{26}$$

Note that it is possible to use other procedures to solve this IHCP. For example, the following functional could be minimized:

$$J(q^{n+1}) = \sum_{j=1}^{nfs} (X_i^{n+j} - \epsilon_i^{n+j})^2 + W \sum_{j=1}^{nft} (T^{n+j} - Y^{n+j})^2 \tag{27}$$

where Y and T are the measured and calculated temperatures at the outer surface, respectively, and W a weighting coefficient that is used to balance the two terms of the functionnal. It must be introduced to account for the different units and the different level of sensitivity coefficients of the two terms. In this case, the outer thermal boundary condition is given by Eq. ($4b$) and the temperature measurements are used simultaneously with the strain measurements to estimate the unknown flux. It has been found that such a procedure is less efficient than the one proposed herein (Raynaud et al., 1993). Particularly, it is difficult to determine the optimal values of W, nfs, and nft.

3 Sensitivity Coefficient Analysis

The sensitivity coefficient analysis allows us to compare immediately the advantages/disadvantages of the inversion based either on strain or on temperature measurements. The case depicted in Fig. 1 is considered. The sensitivity coefficients are calculated from the sensitivity system. The time variations of these coefficients, for a strain gage and for a thermocouple, located on the outer radius are shown in Fig. 2 for various values of the dimensionless parameter $D*$. Since the Poisson ratio is the same for most steels (around 0.3), this parameter is kept constant in this study.

The same trend is noted for both sensitivity coefficients: They increase with future times and when $D*$ increases, i.e., for a fixed tube diameter when the tube thickness decreases. This figure shows that the strain sensitivity coefficients, S_ϵ, are always larger than the temperature sensitivity coefficients, S_T.
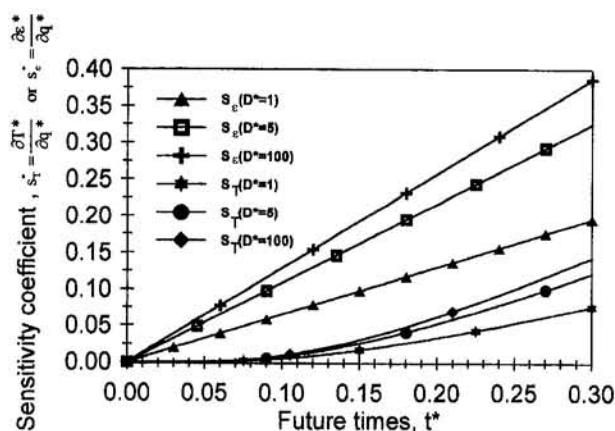
Fig. 2 Comparison of the sensitivity coefficients

The most interesting point is the fact that the S_ϵ increases immediately; there is no time lag as for the S_T. These preliminary results indicate that it is potentially more accurate to estimate the inner surface heat flux from thermal strain measurements than from temperature measurements. However, the accuracy of the inversion also depends on the noise-to-signal ratio. This particular point will be addressed in paragraph 5.3.

4 Benchmark Test Cases

The methodology proposed in 1986 by Raynaud and Beck to compare Inverse Heat Conduction Methods has been, since then, used by several authors (Scarpa and Milano, 1995; Ruperti et al., 1996). It is very simple, can be used for any methods, and allows us to compare performances of methods quantitatively and visually. This methodology, which is based on two test cases, is used to compare the efficiencies of the inversion based either on strain or on temperature variations. In both cases, the function specification method is used.

The first test case allows us to quantify the deterministic bias: It is desired to reconstruct a heat flux that is constant just over one time step and zero otherwise. The bias is calculated from the difference between the true heat flux q and the estimated heat flux $\hat{q}$:

$$B = \sqrt{\sum_{n=1}^{\infty} (q^n - \hat{q}^n)^2} \tag{28}$$

The second test case is even more simple: the surface heat flux, which arose from a single change of unity in the measurements, is calculated and compared to the true heat flux, which is equal to zero. It has been shown by Hills et al. (1986) that, for a linear problem with a constant heat flux, this test case gives the standard deviation of the estimated surface heat flux:

$$Ec_q = Ec \sqrt{\sum_{n=1}^{\infty} (q^n)^2} \tag{29}$$

Figures 3 and 4 show results of these test cases with $\Delta t* = a\Delta t/e^2 = 0.01$ and $D* = 5$ for several values of the stabilizing parameters "nfs". Figure 3 shows that the accuracy of step heat flux estimation degrades with the number of future times while Fig. 4 shows that the sensitivity to measurement errors decreases with the number of future times. This is the classical trade-off that exists between accuracy and resolving power (Hills and Mulholland, 1979). This trade-off is shown in Fig. 5 for the inversion made with the two measurement types and for several time steps and $D* = 5$. It indicates that the thermal strains inversion allows a much smaller sensitivity to measurements errors for the same bias. Thus the resolving power can be increased. For example, the strain inversion curve for $\Delta t*$

Fig. 3 Estimation of the bias: inversion with $\Delta t^* = 0.01$ and $D^* = 5$

Fig. 5 Trade-off between bias and sensitivity to measurement errors; influence of the time steps and type of measurement

$= 0.001$ is similar to the temperature inversion with $\Delta t^* = 0.01$. It can also be noted that the standard deviation for the temperature inversion decreases exponentially with the bias, whereas for the strain inversion, the decrease is almost linear.

The benchmark test cases have shown the potential superiority of the inversion based on thermal strains. The last step is to validate these numerical results with an experimental apparatus.

5 Experimental Validation

5.1 Experimental Setup. The experimental setup represented in Fig. 6 was designed to satisfy the following requirements:

- radial unidirectional temperature field in the tube thickness, $T = T(r, t)$.
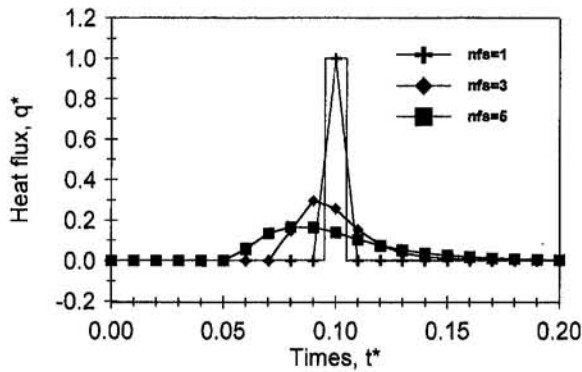- thermocouples and strain gages on the outer surface.
- thermocouples on the inner surface for validation.
- variable mechanical load on the tube to check that the inversion strains do not depend on the mechanical stresses.

Thus a 0.75-m-long, 0.048-m i.d., and 0.006-m-thick steel tube has been embedded in a concrete block, Fig. 6. The inner surface is uniformly heated with a 3000 W, 0.8-m-long infrared tube. The outer surface is insulated with a 0.02-m-thick ceramic fiber to prevent a natural convection effect, which could create a circumferential heat transfer in the tube. The small ratio $e/L = 0.003$ prevents any end effects that would disturb the heat flux lines around the tube midlength. In this region, five 0.01-mm-dia type K thermocouples were soldered with a capacitance discharge apparatus. Two were mounted on the inner surface for validation, three on the outer surface for inversion and to check that circonferential effects are indeed negligible. Two

strain gages were glued on the outer surface to measure the two strains ϵ_{zz} and $\epsilon_{\theta\theta}$. The thermal and mechanical properties of the steel were measured separately: $a = 9.8 \ 10^{-6} \ m^2/s$, $\nu = 0.3$, $\alpha_s = 12.0 \ 10^{-6} \ m/K$, $\lambda = 36 \ W/(m \cdot K)$.

5.2 Strain Gage Measurements. The strain gage measurement requires special attention since the gages are usually designed to suppress thermal effects. The quality of the measurements is obviously an essential point of the inversion. This paragraph briefly describes the procedure that must be used to account for temperature variations.

A strain gage is a sensor whose resistance varies when its length changes. If the gage is glued on a solid, a local strain, ϵ, and a local temperature variation, ΔT, give rise to the following relative length variation of the gage: $\epsilon - \alpha_g \Delta T$, where $\alpha_g \Delta T$ represents the gage dilatation. But the temperature change also creates a relative resistance variation of the gage $\beta \Delta T$. Thus the total relative resistance variation is:

$$\frac{\Delta R}{R} = \beta \Delta T + C_g (\epsilon - \alpha_g \Delta T) \tag{30}$$

In order to take the temperature-dependent term into account, the gage is calibrated on a specimen, kept at uniform temperatures, on which there is no mechanical force. The manufacturer gives the dilatation coefficient of the specimen α_e, and the calibration law in the form of the apparent strain:

$$\epsilon_{app}(T) = \frac{1}{C_g} \frac{\Delta R}{R} = \left(\frac{\beta}{C_g} + (\alpha_e - \alpha_g) \right) \Delta T \tag{31}$$

The combination of Eqs. (30) and (31) allows us to calculate the total gage relative resistance variation:

$$\frac{\Delta R}{R} = C_g (\epsilon + \epsilon_{app} - \alpha_e \Delta T) \tag{32}$$

Fig. 4 Estimation of the sensitivity to measurement errors ($\Delta t^* = 0.01$ and $D^* = 5$)

Fig. 6 Sketch of the experimental setup
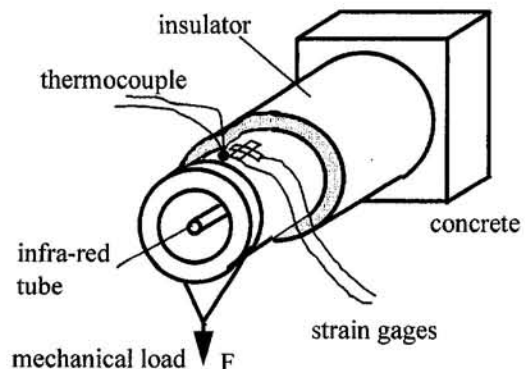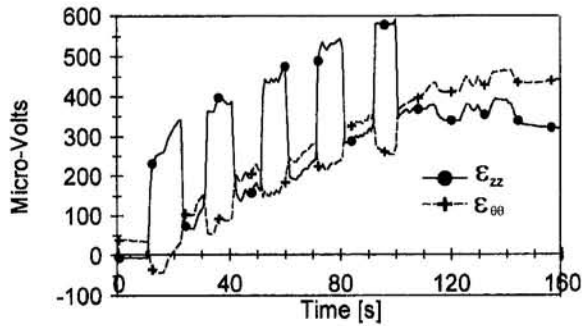
Fig. 7 Voltage variations across the Wheatstone bridge

Fig. 9 Measured and estimated temperatures over the whole time domain

Practically, the resistance variation is determined from the voltage variation across a Wheatstone's bridge (ΔV). Finally the total strain measured by a gage at temperature T, mounted on a solid initially at T_0, is:

$$\epsilon = \frac{4\Delta V}{C_g(T)V} - \epsilon_{app} + \alpha_e(T - T_0) \qquad (33)$$

If the temperature is constant and equal to the calibration temperature of the gage, then the two last terms cancel, otherwise they must be absolutely accounted for. This explains why a thermocouple must be mounted near to the strain gage.

The characteristics of the strain gages mounted on the experimental setup are: $C_g = 2.04$ at 24°C with a -0.01 percent variation when T changes, $\epsilon_{app}(T) = -62.1 + 2.75T - 1.45 \, 10^{-2}T^2 + 1.56 \, 10^{-5}T^3$, $\alpha_e = 12.1 \times 10^{-6}$ m/°C. The voltage across the Wheatstone bridge is 10.0 V.

5.3 Experimental Results. The data acquisition rate is 25 Hz, i.e., the time step is 0.04 s. The dimensionless time step $\Delta t^* = 9.47 \, 10^{-3}$ is very close to 0.01, which was used for the comparison of methods. The experiment starts at steady state when the tube temperature is uniform. The infrared tube voltage is changed manually, small and quick variations are introduced on purpose, to check the capability of the inverse method to detect abrupt variations.

Figure 7 shows the measured values of the gage voltage variations induced by the strains in the z and θ directions. The microstrains are given in Fig. 8, where the combination $\epsilon_{\theta\theta} + \nu\epsilon_{zz}$ is also shown. The square pulse variations for $\epsilon_{\theta\theta}$ and ϵ_{zz} come from the mechanical load (Fig. 6) due to a weight suspended periodically during heating. These pulses disappear when the inversion strain ϵ_i is calculated, showing that this particular strain combination does not depend on the mechanical load. Temperatures measured on the inner and outer surface as well as the temperature estimated from the strain variations,
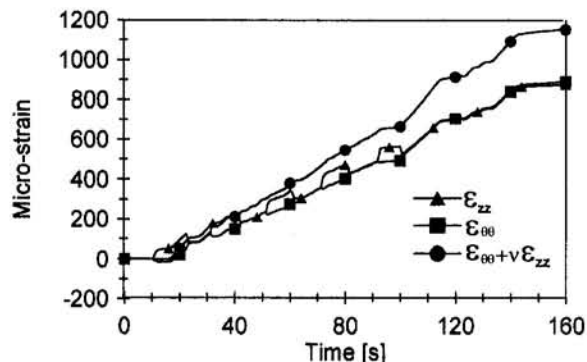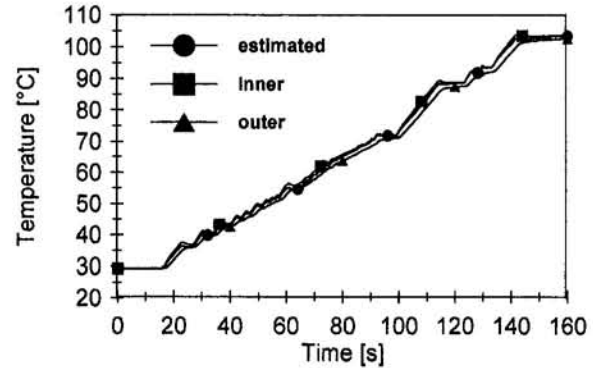
with $nfs = 4$, are presented in Fig. 9. The zoom of Fig. 10 shows that the agreement is quite good; in particular, the square temperature variations are well recovered. For comparison, the surface temperature estimated from the outer temperature measurements, with $ntf = 15$, is also shown in Fig. 10. The values of nfs and ntf given above have been optimized. As shown in Fig. 11, lower values lead to oscillations of the surface temperature, i.e., very large oscillations of the surface flux. On the other hand, larger ones increase the smoothing unnecessarily. The inversion from temperature does not allow us to estimate as well the quick fluctuations that contain high frequencies. Since it is not obvious in Fig. 10, the time derivative of the inner surface temperature has been calculated for several cases. Figure 12 shows the inner surface temperature time rate of variation calculated from the measured and estimated inner temperature for two values of nfs. Clearly, it oscillates for $nfs = 2$ and becomes acceptable for $nfs = 4$. For comparison, the results for $nft = 10$ and $nft = 15$ are given in Fig. 13. Contrary to the inversion from the strain, which can be stabilized without too much smoothing, the stabilization of the inversion from the temperature introduces a larger filter. The results for $nft = 13$ or 14 are not better. The flux entering into the tube is shown in Fig. 14. The reference flux is obtained from the solution of the direct problem in which the inner and outer measured temperatures are used as boundary conditions. The heat flux shape is better recovered from the strain than from the temperature measurements.

These results are in agreement with the sensitivity analysis. For the IHCP, apart from the sensitivity coefficient, the noise to temporal temperature rate of variation ratio is an important parameter. If the ratio is too large, one can imagine that it will be difficult to discriminate the variations of the surface estimates due to the noise from the ones due to the inner flux fluctuations.

Fig. 8 Measured strains and "inversion" strain
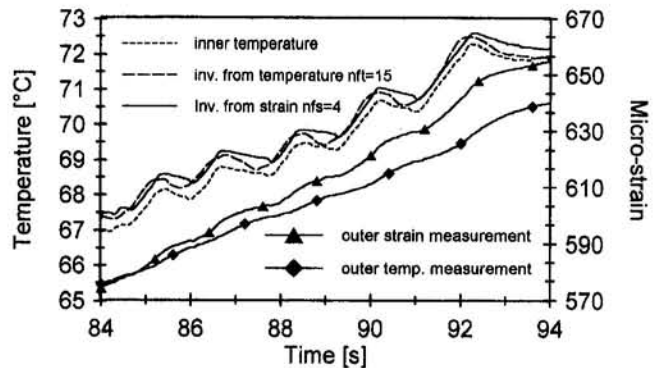
Fig. 10 Time zoom, comparison between the measured inner surface temperature and the temperature estimated from the two types of outer surface measurement: nfs = 4 and nft = 15
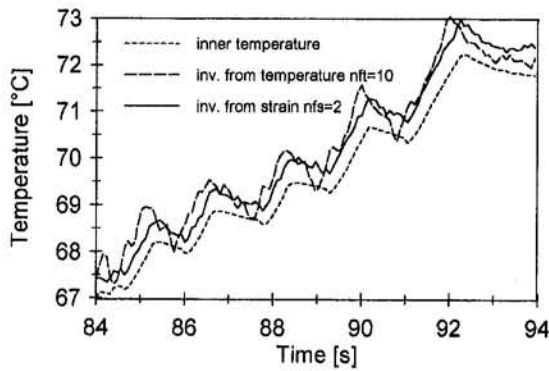
Fig. 11 Time zoom, comparison between the measured inner surface temperature and the temperature estimated from the two types of outer surface measurements: *nfs* = 2 and *nft* = 10

Fig. 13 Inversion from temperature, influence of the number of future temperature on the time rate of variation of the estimated surface temperature: *nft* = 10 and 15

The standard deviations of the microstrain and temperature measurements are 0.27 μstrain and 0.02°C, respectively. As shown by Figs. 8 and 9, the outer strain and temperature vary almost linearly; the slopes are 8 μstrain/s and 0.7°C/s. Thus, for these two measurement types, the ratios for the strain and temperature are 0.034 and 0.029, respectively. On the one hand, this indicates that the quality of the information given by the two types of measurement is similar with a little advantage to the temperature measurements. But for the particular time step, *nfs* and *nft* used for this inversion, the benchmark test cases indicate that the sensitivity to measurement errors is 2.4 times larger for the temperature-based inversion than for the strain-based inversion, the bias being also 11 percent larger. Thus, on the second hand, the inversion from the strain should be better, which is agreement with the results shown Figs. 10 to 14.

For the strain-based IHCP, a sensitivity analysis to the thermomechanical properties was carried out. This showed that the thermal diffusivity has almost no influence on results, while the coefficient of thermal linear expansion is the most important parameter. This is logical since the thermal strains are based on this coefficient.

6 Conclusions

An original approach for the solution of the inverse heat conduction problem has been presented. The unknown boundary condition is recovered from thermal strain and temperature measurements instead of temperature measurements only. The solution method is similar to the well known function specification method (Beck, 1970). In this sense, it is not particularly original.

However, it has been shown through the sensitivity coefficient analysis and from results of two benchmark test cases that the integral effect of the thermal strains allows the use of a smaller time step than the classical temperature measurements does. For the same bias, the sensitivity to measurement error is alway smaller for the strain-based inversion than for the temperature-based inversion. This is then a real improvement for the IHCP.

An experimental setup was made to validate the numerical results. It has been shown that special care must be taken to measure the thermal strains. It is a little more difficult to place a strain gage on a surface than a thermocouple. This is one drawback to the method since the computational time is similar or even smaller (less future times are needed). It was also shown that the mechanical properties must be well known. On the other hand, it was possible to recover higher frequencies by using the strain measurements. The conclusions drawn from this experimental study may not be applied directly to other problems. In particular, the noise-to-signal ratio is an important parameter, which can vary significantly from one experiment to another.

The proposed method is based on an inversion strain that is only defined for beams. The inversion strain is independent of the mechanical load variations and thus allow us to recover the thermal load. For other geometries, another procedure should be found to distinguish the thermal strain from the mechanical strain. Presently, this method has been used by Electricité de France to recover the fluctuations of the inner temperature of nuclear power plant tubes. Work is now under way to apply this approach to solve multidirectional IHCP.

Fig. 12 Inversion from stain, influence of the number of future strain on the time rate of variation of the estimated surface temperature: *nfs* = 2 and 4
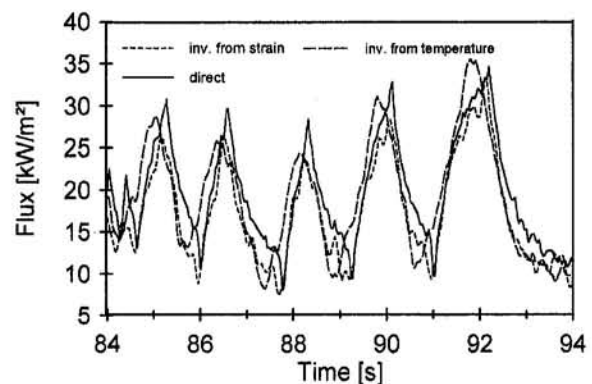
Fig. 14 Comparison of the flux entering into the tube calculated from the direct problem and estimated from the two types of outer surface measurements: *nfs* = 4 and *nft* = 15

Acknowledgments

References

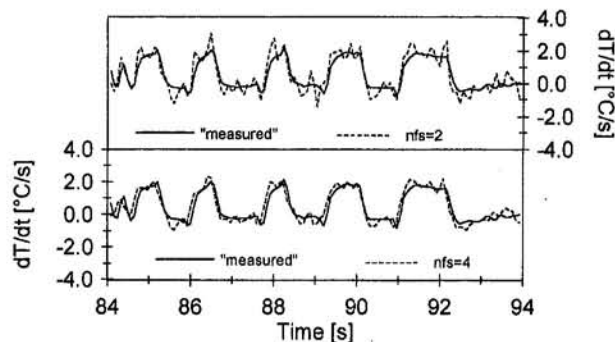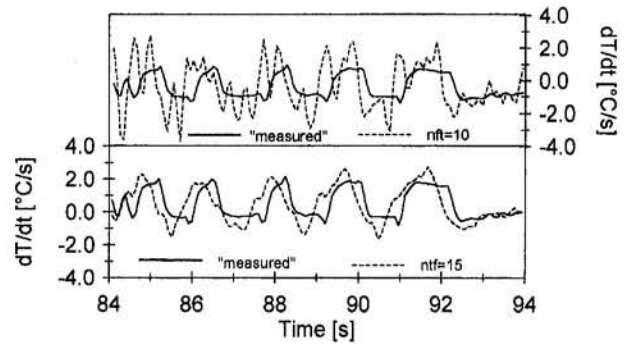Alifanov, O. M., 1994, *Inverse Heat Transfer Problems*, Springer-Verlag Publishers, Berlin.

Beck, J. V., 1970, "Nonlinear Estimation Applied to the Nonlinear Inverse Heat Conduction Problem," *Int. J. Heat Mass Transfer*, Vol. 13, pp. 703–716.

Beck, J. V., Blackwell, B., and St. Clair, C. R., 1985, *Inverse Heat Conduction, Ill-Posed Problems*, Wiley Intersciences Publishers, New York.

Boley, B. A., and Weiner, J. H., 1966, *Theory of Thermal Stresses*, 3rd ed., Wiley, New York.

Crysa, K., Cialkowski, M. J., and Kaminski, H., 1981, "Inverse Temperature Field Problem of the Theory of the Thermal Stresses," *Nucl. Eng. Design*, Vol. 64, pp. 169–184.

Hensel, E., 1991, *Inverse Theory and Applications for Engineers*, Prentice Hall Publishers, Englewood Cliffs, NJ.

Hills, R., and Mulholland, G. P., 1979, "The Accuracy and Resolving Power on One Dimensional Transient Inverse Heat Conduction Theory as Applied to Discrete and Inaccurate Measurements," *Int. J. Heat Mass Transfer*, Vol. 22, pp. 1221–1229.

Hills, R., Raynaud, M., and Hensel, E., 1986, "Surface Variance Estimates Using an Adjoint Formulation for a One Dimensional Nonlinear Inverse Heat Conduction Technique," *Numerical Heat Transfer*, Vol. 10, pp. 441–461.

Kurpisz, K., and Nowak, A. J., 1995, *Inverse Thermal Problems*, Computational Mechanics Publications, Southampton, United Kingdom.

Maillet, D., Degiovanni, A., and Pasquetti, R., 1991, "Inverse Heat Conduction Applied to the Measurement of Heat Transfer Coefficient on a Cylinder. Comparison Between an Analytical and a Boundary Element Technique," ASME JOURNAL OF HEAT TRANSFER, Vol. 113, pp. 549–557.

Marquardt, W., and Auracher, H., 1990, "An Observer-Based Solution of Inverse Heat Conduction Problems," *Int. J. Heat Mass Transfer*, Vol. 33, pp. 1545–1562.

Morilhat, P., Maye, J. P., Brendle, E., and Hay, B., 1992, "Résolution d'un problème thermique inverse par la méthode analytique et impulsionnelle," *Int. J. Heat Mass Transfer*, Vol. 35, No. 6, pp. 1377–1382.

Murio, D., 1993, *The Mollification Method and the Numerical Solution of Ill-Posed Problems*, Wiley Interscience Publishers, New York.

Noda, N., 1989, "On Certain Problem of Coupled Thermal Stress Fields in a Long Circular Cylinder," *JSME International Journal*, Series 1, Vol. 32, No. 3, pp. 348–354.

Raynaud, M., and Bransier, J., 1986, "A New Finite Difference Method for the Nonlinear Inverse Heat Conduction Problem," *Numerical Heat Transfer*, Vol. 9, No. 1, pp. 27–42.

Raynaud, M., and Beck, J. V., 1988, "Methodology for Comparison of Inverse Heat Conduction Methods," ASME JOURNAL OF HEAT TRANSFER, Vol. 110, pp. 30–37.

Raynaud, M., Blanc, G., and Chau, T. H., 1993, "Solution of an Inverse Heat Conduction Problem Using Strain Gage Measurements," *Proc. 1st Int. Conf. Inverse Problems* in *Engineering: Theory and Practice*, Palm Coast, FL, ASME Publications, New York, pp. 47–52.

Ruperti, N., Raynaud, M., and Sacadura, J. F., 1996, "A Method for the Solution of the Coupled Inverse Heat Conduction-Radiation Problem," ASME JOURNAL OF HEAT TRANSFER, Vol. 118, 10–17.

Scarpa, F., and Milano, G., 1995, "Kalman Smoothing Technique Applied to the Inverse Heat Conduction Problem," *Numerical Heat Transfer*, Part B, Vol. 28, pp. 79–96.

Stolz, G., 1960, "Numerical Solution to an Inverse Problem of Heat Conduction for Simple Shapes," ASME JOURNAL OF HEAT TRANSFER, Vol. 82, pp. 20–27.

Determination of Convective Heat Flux on Steady-State Heat Transfer Surfaces With Arbitrarily Specified Boundaries

B. G. Wiedner[1]

C. Camci
email: c-camci@psu.edu.

Department of Aerospace Engineering,
The Pennsylvania State University,
153-E Hammond Building
University Park, PA 16802-1400

The present study focuses on the high-resolution determination of local heat flux distributions encountered in forced convection heat transfer studies. The specific method results in an uncertainty level less than 4 percent of the heat transfer coefficient on surfaces with arbitrarily defined geometric boundaries. Heat transfer surfaces constructed for use in steady-state techniques typically use rectangular thin foil electric heaters to generate a constant heat flux boundary condition. There are also past studies dealing with geometrically complex heating elements. Past studies have either omitted the nonuniform heat flux regions or applied correctional techniques that are approximate. The current study combines electric field theory and a finite element method to solve directly for a nonuniform surface heat flux distribution due to the specific shape of the heater boundary. Heat generation per unit volume of the surface heater element in the form of local Joule heating is accurately calculated using a finite element technique. The technique is shown to be applicable to many complex convective heat transfer configurations. These configurations often have complex geometric boundaries such as turbine endwall platforms, surfaces disturbed by film cooling holes, blade tip sections, etc. A complete high-resolution steady-state heat transfer technique using liquid crystal thermography is presented for the endwall surface of a 90 deg turning duct. The inlet flow is fully turbulent with an inlet Re number of 360,000. The solution of the surface heat flux distribution is also demonstrated for a heat transfer surface that contains an array of discrete film cooling holes. The current method can easily be extended to any heat transfer surface that has arbitrarily prescribed boundaries.

Introduction

The desire to extend the cycle efficiency or to improve specific power of gas turbine engines has produced a large collection of component specific convective heat transfer research areas. Most of the emphasis in heat transfer research of gas turbine engines is directed toward the first-stage guide vanes and rotor blade passages that are exposed to the hot free-stream gases that originate from the combustor. In addition to the external blade passages, the internal cooling schemes of these turbine blades have also received much attention. The geometric complexity of the turbine passage configurations requires detailed, high-resolution heat transfer studies.

Convective heat transfer studies can be divided into two major experimental groups as steady state and transient. Transient experiments usually rely on a means of impulsively initiating the flow past the test surface. Steady-state techniques rely on the construction of an instrumented heat transfer surface and are typically restricted to geometrically simple test surfaces such as rectangular flat plates and two-dimensional curved rectangular surfaces. The heat transfer surface usually includes an electrically heated foil at the fluid/solid interface. A prior knowledge of the electrically generated local heat flux is required. Both techniques have been widely used with considerable success. MacMullin et al. (1989) used a simple constant heat flux surface having a perfect rectangular shape in a convective heat

transfer study performed on a flat plate. The steady-state experiments of Boyle and Russell (1989), Hippensteele et al. (1985), Blair (1974), and Blair et al. (1989, 1991) all employed steady-state techniques to investigate the convective heat transfer process in turbine blade passages. Simonich and Moffat (1984) and Wang and Simon (1987) used the steady-state heat transfer technique to study the effects of concave curvature on turbulent boundary layers and convex curvature on transitional boundary layers, respectively. The heat transfer surfaces in each of these experiments were geometrically simple and the resultant surface heat flux was uniform.

Film cooling studies by Eriksen and Goldstein (1974), Mick and Mayle (1988), Ou et al. (1992), Ou and Han (1992) and Mehendale and Han (1992) were also performed using the steady state heat transfer technique. Film cooling studies represent a geometric configuration that introduce a complication to steady-state experiments. Significant variations in both the film cooling effectiveness and the local heat transfer coefficient may occur within the near cooling hole regions. To resolve the heat transfer characteristics experimentally in this area, the generated local surface heat flux levels must be accurately determined. Due to the geometric complexity of the heat flux surface boundaries, the current density field and the electric field will be distorted to a condition where a uniform heat flux assumption becomes weak. Several studies including Mick and Mayle (1988) and Mehendale and Han (1992) have used correctional techniques to determine the surface heat flux variations near the film cooling holes. Discrete point thermocouples were used to map the surface temperature distributions of the local regions where the heat flux distributions significantly deviated from a constant value.

Copyright © 1996 by ASME

An alternative method to the correctional technique is a direct calculation of the generated surface heat flux at each point of the heater surface using electrostatic theory. In addition to film cooling studies, the direct calculation approach presented in this study can be adapted to many other complex, two-dimensional heater surface geometries that have arbitrarily specified external and internal boundaries. The endwall surface of a turbine passage, the tip surface of a rotor blade, and local surfaces of an internal cooling arrangement in a turbine blade are a few examples of arbitrarily specified component surfaces.

The objective of the current study is to present a complete procedure for determining local convective heat transfer coefficients in steady-state experiments when the heater shape is not rectangular. The procedure can also take into account arbitrarily specified cooling holes and slots on the heat transfer surface. Local generation of Joule heating through internal electrical heat generation can be accurately determined by solving the partial differential equation governing the electrical potential distribution on the heater element even with arbitrarily specified internal and external boundaries. The complete method is demonstrated for the endwall surface of a 90 deg turning duct in which a fully turbulent flow exists at the inlet section. The influence of film cooling holes on the local Joule heating distribution of a heat transfer surface is also demonstrated. The method uses second-order accurate quadrilateral finite elements to discretize the heat flux surface and a variational principle known as Euler's theorem to determine the heat flux distribution accurately. High-resolution surface temperature distributions were resolved using Chiral-nematic liquid crystals, a high-sensitivity CCD sensor, and an HSI domain image processor. Radiative and conductive losses from the composite heat transfer surface were also taken into account. Deviations from the one-dimensional conduction loss model have been incorporated into the uncertainty analysis.

Determination of the Nonuniform Surface Heat Flux

Analytical Model of Electrical Heat Generation. Determination of the steady heat flux field on an arbitrarily specified heat transfer surface requires the solution of an electrostatic boundary value problem. For a two-dimensional, linear, isotropic, homogeneous conducting medium with zero free charge, the electric potential must satisfy

$$\vec{\nabla}^2 V(x, y) = 0. \quad (1)$$

For thin foil heaters, such as Inconel foil ($\delta = 0.025$ mm), the thickness of the foil relative to the surface area is such that negligible current conducts in the direction normal to the surface plane. Therefore, the current and potential fields are two dimensional. The electrical boundary conditions for the heater surface are a uniform potential at the busbar/Inconel foil junctions and
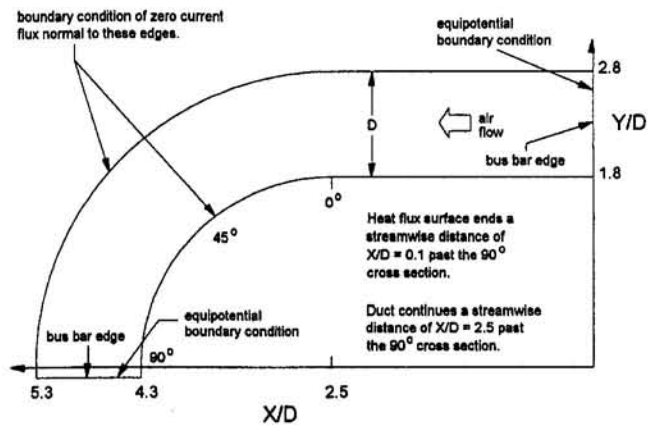
Fig. 1 Endwall heat transfer surface geometry

zero current flow normal to the two unbounded streamwise edges, Fig. 1. An electric field vector $\mathbf{E}$ can be defined as the gradient of the scalar potential field, $V(x, y)$:

$$\vec{E} = -\vec{\nabla}V \quad (\text{V/m}) \quad (2)$$

The negative sign is introduced to account for the conventional coordinate system used. Once the electric potential and field are resolved, the current density field, $\mathbf{J}$, can be determined by a scalar multiplication of the electric field and the electrical conductivity of the medium, σ.

$$\vec{J} = \sigma\vec{E} \quad (\text{A/m}^2) \quad (3)$$

The conductivity of a medium is a material property equivalent to the inverse of the resistivity ρ. The power density within a medium under steady current conditions is a point function determined from the dot product of the electric field and current density, $\mathbf{E} \cdot \mathbf{J}$ (W/m^3). Therefore, the electric power converted into heat per unit surface area is

$$\dot{q}_{\text{gen}} = \delta\vec{E}\cdot\vec{J} \quad (\text{W/m}^2) \quad (4)$$

where δ is the thickness of the conducting medium. The solution of the electrostatic boundary value problem is analogous to conduction heat transfer solution. In the electrostatic solution, the current density field is analogous to the thermal conduction heat flux field. A prescribed temperature boundary condition of the thermal conduction problem is analogous to a specified electric potential condition. A zero electric current flux condition normal to a boundary or edge corresponds to an adiabatic condition in the thermal problem. This analogy conveniently lends itself to the application of any existing solution technique

Nomenclature

CCD = charged coupled device for visual imaging
d = film cooling hole diameter, mm; resistance element length, mm
D = duct width, cm
E = electric field, V/m
h = heat transfer coefficient = $\dot{q}/(T_w - T_{o\infty})$, $\text{W/m}^2\,\text{K}$
J = current density, A/m^2
k = thermal conductivity, W/m K
$\dot{q}$ = heat flux, W/m^2
R = total resistance = $(\rho \cdot d/\delta \cdot w)$, Ω
rms = root mean square

R35C1W = liquid crystal starting to respond (red) at about 35°C with an approximate color bandwidth of 1°C
R_r = radius ratio = $(R_i + R_o)/2D$
Re = Reynolds number = UD/ν
T = mean temperature, °C
U = mean velocity, m/s
V = electric potential, V
w = width, mm
X, Y, Z = local coordinate system, cm
δ = Inconel foil thickness, mm
ρ = resistivity, Ωm; density, kg/m^3

σ = electrical conductivity = $1/\rho$, $(\Omega\text{m})^{-1}$
ν = viscosity, m^2/s

Subscripts

cond = conductive
conv = convective
gen = generated
i = inner
o = outer
rad = radiative
w = wall quantity
$o\infty$ = free stream total quantity
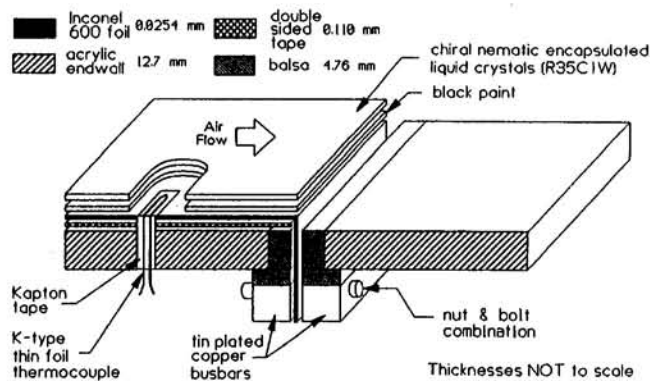
Fig. 2 Composite heat transfer surface

of a two-dimensional conduction heat transfer problem to the electrostatic domain.

Numerical, Computation of the Local Heat Generation. In the current study, the electric potential and current density distributions of the endwall heat transfer surface were determined using the thermal/electrical analogy described in the previous paragraph. The heat transfer surface was discretized with eight-noded, isoparametric, quadrilateral finite elements. The computational domain contained a total of 402 nodes and 104 elements. A finite element technique based on Euler's theorem of variational calculus was used to solve for the potential and current density distributions. The essence of the technique is the direct minimization of an integral relation for each element in the domain with prescribed boundary conditions:

$$I_f = \iint_s \frac{1}{2} \sigma \left[\left(\frac{\partial V}{\partial x} \right)^2 + \left(\frac{\partial V}{\partial y} \right)^2 \right] dx \cdot dy \quad (5)$$

The minimization technique is analogous to satisfying the Laplace equation, Eq. (1), over the entire domain. The procedure results in a set of linear algebraic equations that are then solved simultaneously to provide the electric potential field with prescribed boundary conditions. Further details of the numerical technique are given in Zienkiewicz (1971) and Camci (1989).

Experimental Method and Apparatus

Facility and Test Section. The surface under consideration was the endwall of a square cross-sectional, 90 deg turning duct. The test section was constructed of 1.27-cm-thick flat endwalls and 0.476-cm-thick curved side walls of clear acrylic. The test section was located on the downstream side of an open-loop wind tunnel. The facility consisted of an axial blower, diffuser with multiple screens, plenum chamber, high area ratio nozzle, circular to rectangular transition nozzle, a section of constant cross-sectional duct, and the test section. The constant cross-sectional duct that preceded the test section housed several additional screens. Further details of the tunnel are provided by Wiedner and Camci (1992, 1993). An illustration of the endwall test section geometry and coordinate system is shown in Fig. 1. The 90 deg bend has a radius ratio, R_r, of 2.3 and cross-sectional width of 20.3 cm. The heat transfer measurements were performed at an inlet free-stream velocity of 28.3 m/s corresponding to Re = 360,000 with inlet air at ambient temperature.

Composite Heat Transfer Surface. The heat transfer surface consists of several layers that include double-sided tape, Inconel 600 foil, black paint, and Chiral-nematic encapsulated (R35C1W) liquid crystals, Fig. 2. A low-resistivity steel foil, Inconel 600, was used as the heater material. The material has a low temperature coefficient of resistivity ($0.112 \times 10^{-3}°C^{-1}$)

that restrains a change in the resistance of the foil within the experimental temperature range (less than 0.23 percent). The heat transfer surface begins 50.8 cm upstream of the 0 deg position and ends 2 cm past the 90 deg position as shown in Fig. 1. At the upstream end of the test surface, the foil exited the test section at a flange interface. The downstream end passed through a transverse slot cut in the endwall acrylic. To minimize conduction to the endwall surface at the foil entry and exit planes, the foil was fitted between two 0.476 cm balsa sections. On the ambient side of the endwall, copper busbars were connected to the foil by compression contact. To minimize contact resistance and prohibit oxidation, the contact faces of the copper busbars were machined smooth, chemically cleaned in an acid bath, and electroplated with a 0.5-μm-thick tin film. To ensure an equipotential boundary condition existed at the busbar and foil junction, 1.27 cm square cross-sectioned busbars were used. An experimental verification indicated less than 0.1 percent potential variation existed across the busbar length. A 1000 W, variable current DC power supply was used to heat the heat transfer surface. Two K-type thin foil thermocouples were located on the foil surface for calibration of the liquid crystals. They were fastened with double-sided Kapton tape (0.1 mm thick). The physical properties of the Kapton tape (resistivity, 3×10^{14} Ωcm and thermal conductivity, 0.37 W/m K) provided excellent electrical isolation and thermal contact of the thermocouple junction and leads with the heat flux surface. The surface was then covered with flat black background paint and a layer of Chiral-nematic encapsulated liquid crystal (R35C1W) using an air brush.

Liquid Crystal and Image Processing Techniques. The liquid crystal image capturing and processing techniques adapted in the present study are described fully by Camci et al. (1992) and Kim (1991). A 24-bit color image processing system was used to convert color information from a (red, green, blue) coordinate system to (hue, saturation, intensity) system. The color attributes of an image were captured with a high-sensitivity CCD sensor that acquired complete images at a rate of 30 Hz. A linear hue versus temperature relation was determined through calibration for the specific camera and illumination configuration used in the study. All surface temperature information was obtained from the hue attributes contained in a given image frame. Further details on the specific liquid crystal data reduction process are given by Kim (1991).

The endwall heat transfer surface temperatures were mapped using a Chiral-nematic encapsulated liquid crystal with an event temperature of approximately 35°C. All visible liquid crystal generated colors from red to blue were approximately contained in a 1°C temperature band. To minimize the deviation of the viewing angle from normal, three camera positions were used to capture the complete endwall surface. The illumination sources for each of the views were two 500 W, 3200 K incandescent lamps. For all experiments, the camera configuration and illumination setup were identical between calibration runs and heat transfer tests. The calibration of the crystals was performed in slow transients using the heater surface and the variable power supply to cycle the surface through the liquid crystal color range. Each cycle of the slow transient experiment took about 20 seconds between the appearance of the first red and first blue colors. Two thin foil thermocouples were imbedded on the endwall surface in view of the video camera. The thermocouple output was also displayed in the calibration images. The response time of the thermocouples was approximately 3–5 ms. The thin film thermocouple and associated amplifier circuitry were calibrated against an approximately zero bias mercury thermometer prior to the liquid crystal calibration. Hue information and the corresponding surface temperature could then be extracted from successive images at the precise pixel location of the thermocouple junction. Typical calibration results from three individual heating cycles are shown in Fig. 3. In addition,
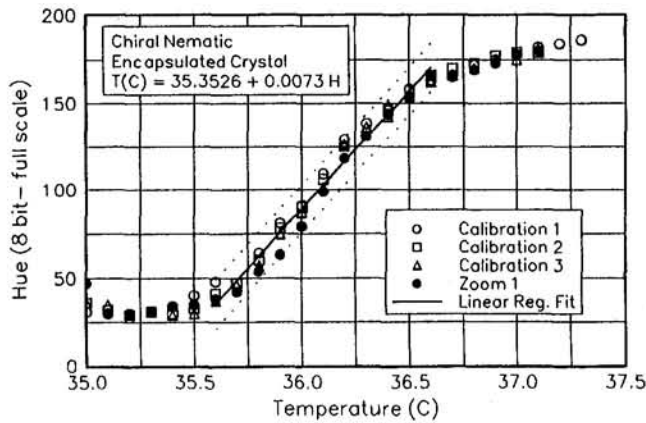
Fig. 3 Liquid crystal calibration with temporal averaging

the effects of altering the zoom position of the camera lens are also shown. The change in the zoom position of the camera resulted in a pixel resolution twice that of the other positions. The surface temperatures that were extracted in each of the heat transfer tests were restricted to a hue range of 40 to 160. A linear regression analysis was performed on the calibration data in this range and the results including a 95 percent confidence interval have been superimposed on the raw calibration data, Fig. 3. The pixels with intensity values less than 25 and greater than 200 were also eliminated to avoid possible unstable hue conversion. All of the hue and intensity values described were in 8-bit scale with a maximum value of 255. Further details of the current hue capturing process are presented in detail by Camci et al. (1992, 1993), Kim (1991), and Wiedner (1993).

Experimental Results and Discussion

Test Conditions and Data Analysis. All heat transfer tests were conducted at a Reynolds number of approximately 360,000 based on the inlet centerline velocity, duct width, and ambient free-stream conditions. The results from a single sensor hot wire located at a distance of 5 cm upstream of the heat transfer surface and at $Y/D = 2.30$ are shown in Fig. 4. The mean velocity profile indicates a boundary layer thickness of 2.54 cm ($Z/D = 0.125$), and uniform free-stream conditions. The streamwise velocity fluctuations had a rms level of 0.7 percent of the mean velocity in the free stream and a peak of 6.8 percent of the free-stream mean velocity within the endwall boundary layer. The details of the duct aerodynamics are included in Wiedner (1993) and Wiedner and Camci (1992, 1993). Steady-state conditions for heat transfer experiments required approximately two hours to achieve. The thermal conditions on the convective heat transfer side of the endwall, ambient side of the endwall, and the tunnel free stream were used to monitor steady-state conditions. The primary focus of the heat transfer tests was to map the convective heat transfer coefficient quantitatively on the endwall surface. The heat transfer coefficient was determined according to

$$h = \frac{\dot{q}_{conv}}{(T_w - T_{o\infty})} = \frac{\dot{q}_{gen} - \dot{q}_{cond} - \dot{q}_{rad}}{(T_w - T_{o\infty})} \quad (6)$$

To count for conduction losses through the acrylic endwall, temperature measurements were recorded at multiple locations on the ambient side surface. The measurement locations were clustered near the corresponding area of the liquid crystal color band that existed on the convective side of the surface. The temperature measurements on the ambient side of the endwall surface were recorded with an infrared thermometer. The same mercury thermometer used to calibrate (in an oil bath) the thin foil thermocouples on the heat transfer side of the test section

was used to calibrate the infrared thermometer. To calibrate the infrared thermometer, a known surface temperature was first recorded. The calibration constant of the infrared thermometer (emissivity of the surface) was then adjusted until the infrared thermometer indicated the true temperature of the surface. A uniform surface emissivity is required for a local surface calibration to be valid over the entire surface. This was obtained by air brush spraying the acrylic surface with flat black paint. The uniform emissivity criterion was then experimentally verified with the thermometer. During a typical steady-state heat transfer experiment, the ambient side of the endwall exhibited a temperature variation of approximately ±0.5°C and a distribution similar to the temperature distribution depicted by the liquid crystals on the inner side of the endwall exposed to the flow. The conduction losses were calculated locally at each pixel coordinate in which hue/temperature information was available. The corresponding ambient side temperature of the endwall was determined from a high-density grid of the infrared thermometer measurements. A two-dimensional interpolation scheme was used to calculate the temperature grid. The conduction losses through the endwall surface were estimated including the effects of lateral conduction on the back surface (ambient side) of the endwall. The significance of lateral conduction on the total conduction loss was documented in several areas on the endwall surface. The maximum local lateral conduction component found on the back surface had a magnitude of 19.2 percent of the respective normal component of heat flux loss vector. This resulted in an increased conduction heat flux loss of less than 0.25 percent of the local generated heat flux. The conduction losses typically accounted for approximately 5–8 percent of electrically generated heat flux. Local radiation losses from the heat transfer surface were approximated using an enclosure model and considering each surface as black. The unheated duct walls were assumed to be in thermal equilibrium with the free stream. The heat flux lost to radiation from the heater surface accounted for approximately 8–10 percent of the generated heat flux. The free-stream temperature upstream of the test section was measured using a fine wire K-type thermocouple probe. A recovery factor of unity was assumed due to the low-speed character of the inlet flow. When the endwall images were obtained, a short duration "light pulse" from the illumination lamps was used to minimize the accumulative effects of thermal radiation from the lamps. A test was also performed in which the hue attribute of several discrete pixels in a series of images from a test with continuous illumination were extracted. Over the duration of the illumination period, the hue value at each pixel evaluated was constant. This test showed that the radiation heat flux contribution to the surface temperature measurement was minimal.
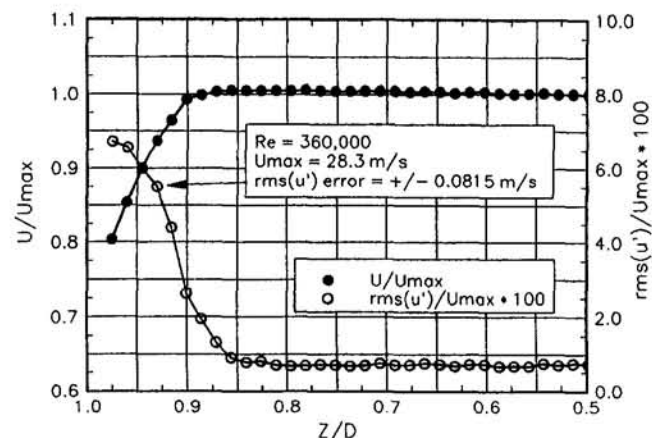
Fig. 4 Mean and fluctuating velocity profiles 5 cm upstream of the duct inlet plane, at the endwall centerline, $Y/D = 2.3$
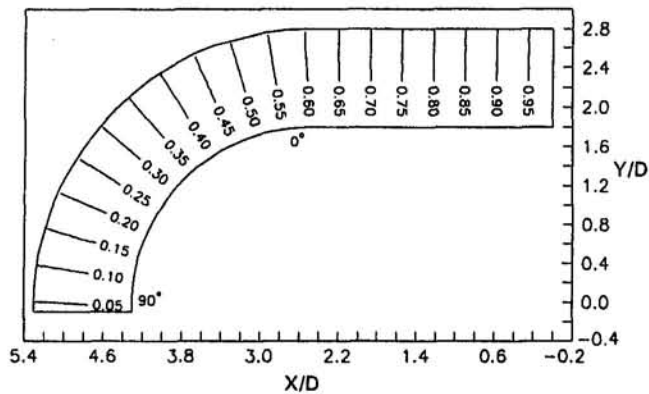
Fig. 5 Numerically determined electric potential distribution (V) on the endwall heat transfer surface for a 1 VDC potential drop across the busbars

Fig. 7 Vector representation of the current density field (A/m²) of the endwall heat transfer surface for a 1 VDC potential drop across the busbars

The temperature information from an image was mapped from pixel to duct coordinates using several previously marked reference points on the test section surface. The white reference points allowed easy identification by the image processor due to the high intensity attribute. For a given heat transfer test, the coordinates of an endwall region that contained the hue attributes between 40 and 160 could be extracted. These pixels provided accurate wall temperature measurements at high resolution after the hue to temperature conversion, Fig. 3. To match the spatial resolution of the surface temperature distribution, a high-density grid of the generated surface heat flux was produced using the same interpolation scheme as used for the ambient side temperature distribution. After locally correcting the surface heat flux distribution for conduction and radiation losses, the convective heat transfer coefficient was calculated based on the wall to free-stream temperature difference, Eq. (6).

Application to Endwall Heat Transfer Problem. Results of the numerical procedure described for the solution of the electrostatic boundary value problem are shown in Figs. 5–8. The calculations were performed for a unit drop in electrical potential across the busbars. A 1 VDC equipotential line at the leading edge of the foil, $X/D = 0.0$, and a 0 VDC equipotential line at the trailing edge of the foil, $Y/D = -0.1$, were used as the prescribed potential boundary conditions. The numerically predicted potential field for the endwall heat flux surface is shown in Fig. 5 and an experimentally measured potential field is shown in Fig. 6. Several predicted equipotential contours are compared with the experimental measurements. The comparison indicates that the numerical results sufficiently predict the
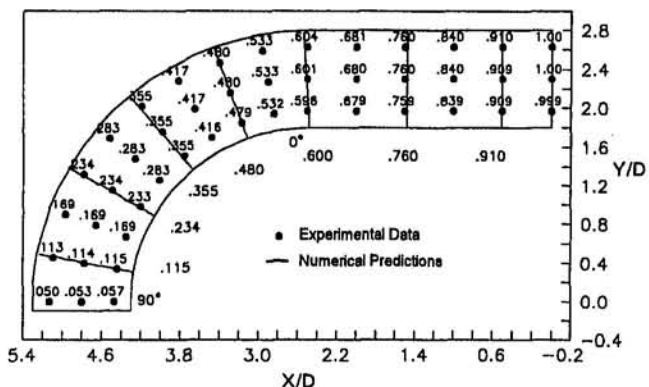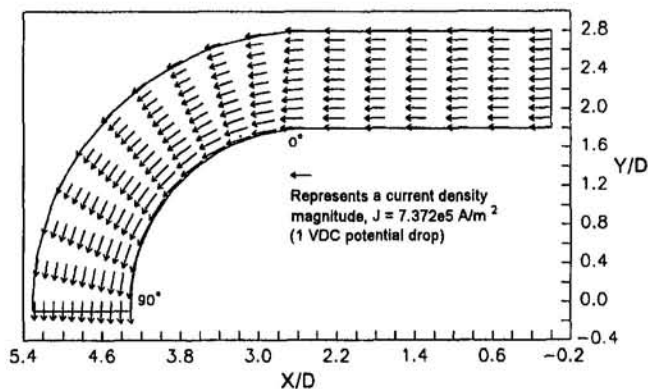
measured potential distribution on the endwall within ±0.0005 V. The initiation of the geometric complexity in the form of endwall/duct curvature occurs at a distance of $X/D = 2.5$. Initially vertical equipotential lines start turning toward the horizontal direction because of the specific current flow pattern imposed by the external boundaries of the heater foil. The influence of the heater boundary geometry is shown in current density field, Fig. 7. At $X/D = 2.5$ (0 deg), the current density vectors start displaying a gradient in magnitude from inner radius to outer radius. Also, as the 0 deg plane is approached, the direction of the current density field is seen to shift downward from horizontal. This observation is consistent with the turning pattern of the heater foil. Physically, the uniform current density field that enters the foil at the leading edge busbar, $X/D = 0.0$, is searching for the path of the least resistance. The path of the least resistance is related to a condition of the shortest path and largest cross-sectional area between busbars. The transverse gradient in the current density field through the curve, as well as upstream of the curve, represents the current density field's interpretation of this condition. The combination of the potential field and the current density field, as modeled by Eq. (4), is shown in Fig. 8 as the distribution of the generated surface heat flux. A strong variation of local heat flux exists throughout the curved portion of the endwall, whereas a weaker variation is evident in the straight inlet section. Only a 0.4 percent variation in the surface heat flux exists along the endwall centerline between the foil leading edge ($X/D = 0.0$) and $X/D = 0.5$.

The results of 23 steady-state heat transfer experiments are shown as a complete map of the endwall convective heat trans-

Fig. 6 Comparison of computed electric potential distribution (V) and measured values on the endwall surface for a 1 VDC potential drop across the busbars
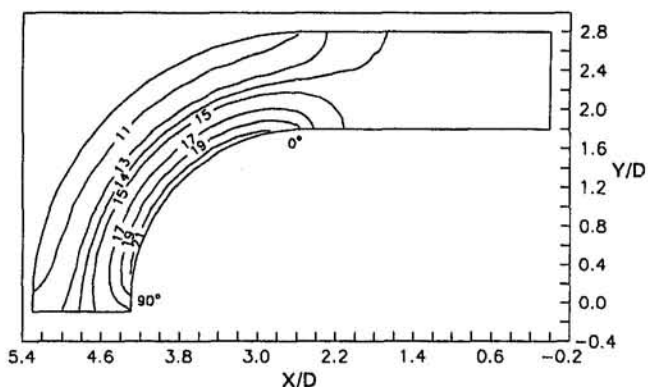
Fig. 8 Distribution of electrically generated heat flux (W/m²) on the endwall heat transfer surface for a 1 VDC drop in potential across the busbars

fer coefficient distribution in Figs. 9(a, b). The map was obtained from a series of experiments performed at different surface heat flux levels (potential drops across the busbars). For each experiment, the liquid crystal color play region was located in a different region of the endwall surface. The 23 experiments required to achieve a high-resolution heat transfer coefficient map were due in part to the large test section and narrow band width of the liquid crystals used in this study.

Further Application to Film-Cooled Heat Transfer Surfaces. To demonstrate the capability of the present method in another area of convective heat transfer, a square heat flux surface with an array of film cooling holes has been selected for the computation of local heat generation. The geometry of the heat flux surface and the hole pattern are shown in Fig. 10. The computational domain contained 144 eight-noded, isoparametric, quadrilateral elements and 490 nodes. The film cooling hole pattern is a 1 × 3 array of 3-mm-dia holes that are inclined 30 deg to the foil surface and spaced three diameters apart. The conducting medium is Inconel foil ($\delta = 0.025$ mm) and a 1 mVDC potential drop was prescribed across busbars located on the left and right edges. A zero current flux condition normal to the top and bottom surfaces was also prescribed. The generated surface heat flux distribution is shown in Fig. 10 with strong variations near the cooling hole locations. For a simple square heat flux surface without film cooling holes, a uniform heat flux of 190 W/m² would exist. Introducing the holes in the surface increases the total resistance of the foil, thus for the same 1 mVDC potential drop across the busbars, the heat flux far from the holes decreases to approximately 175 W/m². More importantly, the local surface heat flux levels in the near field of the cooling holes indicate severe enhancements. A maximum generated heat flux of 656 W/m² exists on each of the upper and lower edges of the cooling holes. The minimum heat flux
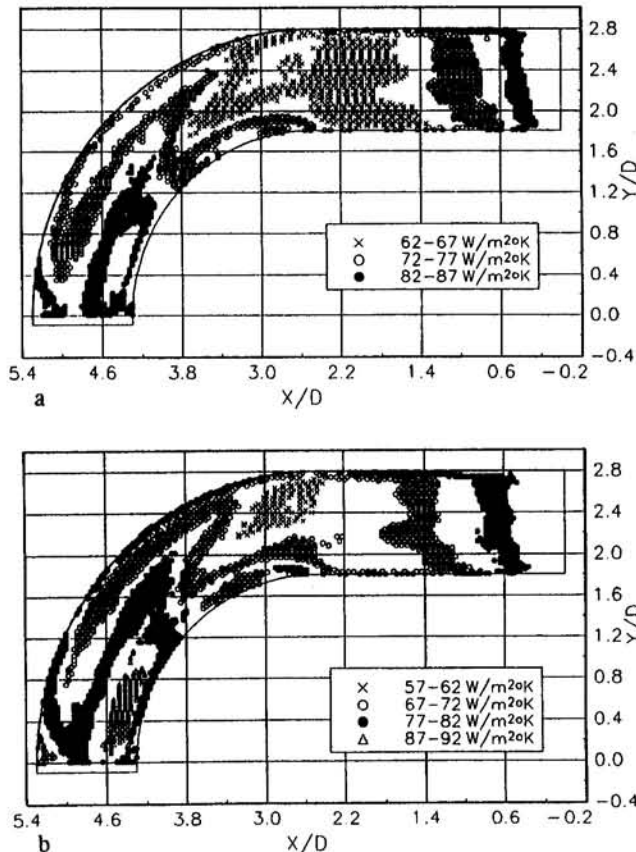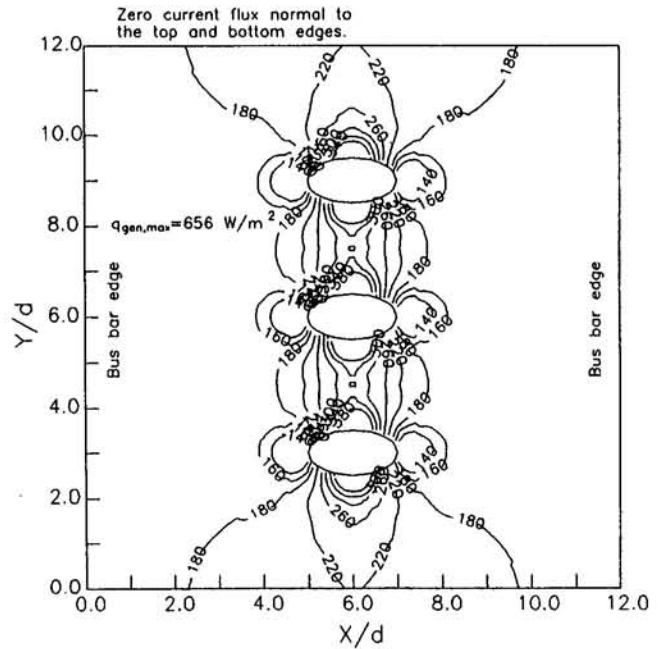
Fig. 10 Electrically generated heat flux (W/m²) for a square heater surface that contains three film cooling holes in a row, hole spacing $Y/d = 3$; potential drop of 1 mVDC across the busbars

regions occur near the stagnation regions of the current field located at the left-most and right-most edges of the holes.

Experimental Uncertainty. The experimental uncertainty in the convective heat transfer coefficient was estimated according to the procedures detailed by Abernethy et al. (1985). The following list summarizes the initial sources of error and the propagation of the source precision and bias errors to the final uncertainty in the heat transfer coefficient. The uncertainty level quoted is analogous to 95 percent coverage. The quantitative nature of the finite element numerical procedure and careful quantification of the conductive and radiative heat flux losses results in a relatively low measurement uncertainty of the generated heat flux and consequently a low uncertainty level for the convective heat transfer coefficient.

	Precision index, percent	Bias error, percent	Uncertainty, percent
$\dot{q}_{gen}$	1.0	0.3	1.0
$\dot{q}_{cond}$	5.5	5.9	8.1
$\dot{q}_{ad}$	1.6	1.9	2.5
$T_{o\infty}$	1.0	0.8	1.3
$T_w - T_{o\infty}$	2.7	2.6	3.4
h	2.8	2.7	3.8

The heat loss to conduction through the endwall was considered one-dimensional in the error and uncertainty values provided. An analysis that considered multidimensional conductive heat loss indicated a maximum variation in the heat transfer coefficient to be less than 0.25 percent of the reported value. The variation in resistivity of the heater material due to temperature changes was found to be less than 0.23 percent within the experimental temperature range. This effect has been included in the uncertainty levels provided. A complete discussion of the error analysis is given by Wiedner (1993).

Conclusions

A generalized steady-state heat transfer technique has been presented for arbitrarily specified heat transfer surface boundaries. A numerical technique based on electric field theory was

Fig. 9 Convective heat transfer coefficient (W/m² K) distribution on the endwall surface

used directly to solve a nonuniform surface heat flux distribution for two different geometries common in aeropropulsion heat transfer studies. A finite element method was implemented into a heat transfer technique to improve accuracy and spatial resolution. Details of the numerical and experimental approach were first demonstrated for the endwall surface of a strongly curved 90 deg duct flow. The solution of the nonuniform surface heat flux distribution was also shown for a heat transfer surface that contained a single row of three film cooling holes. Significant variations in the locally generated heat flux were evident in both configurations. Strong electrical potential gradients are imposed by the specific shape of the heater boundaries and electrical boundary conditions. Liquid crystal thermography and correctional techniques for conductive and radiative heat losses were combined with the numerical solution of the generated surface heat flux to provide convective heat transfer coefficients on the endwall surface of the 90 deg turbulent duct flow. The hue, saturation, and intensity attributes of 30 consecutive frames were temporally averaged for the first time to reduce the uncertainties in the hue/temperature conversion. This process successfully eliminated some of the inherent noise that exists in high sensitivity imaging sensors. The method resulted in an estimated uncertainty of ±3.8 percent for the convective heat transfer coefficient. The current finite element based method can also take the local variation of heater foil thickness into account. Although the resistivity of the current heater element (Inconel 600) did not vary within the experimental surface temperature range, the specific approach can successfully model local variations in heater resistivity due to temperature dependency. The present method is valid on any heat transfer surface with arbitrarily defined external boundaries including void sections such as the ones created by film cooling holes. The methodology described is also an excellent candidate for future tip clearance heat transfer research near high-pressure turbine blade tip sections.

Acknowledgments

References

Abernethy, R. B., Benedict, R. P., and Dowdell, R. B., 1985, "ASME Measurement Uncertainty," ASME *Journal of Fluids Engineering*, Vol. 107, pp. 161–164.

Arts, T. A., Lambert de Rouvroit, M., Rau, G., and Acton, P., 1992, "Aerothermal Investigation of the Flow Developing in a 180 Degree Turn Channel," *Proc. 1992 International Symposium on Heat Transfer in Turbomachinery*, Marathon, Greece, Aug. 24–28.

Blair, M. F., 1974, "An Experimental Study of Heat Transfer and Film Cooling on Large Scale Turbine Endwalls," ASME JOURNAL OF HEAT TRANSFER, Vol. 96, pp. 524–529.

Blair, M. F., Dring, R. P., and Joslyn, H. D., 1989, "The Effects of Turbulence and Stator/Rotor Interactions on Turbine Heat Transfer: Part I Design Operating Conditions," ASME *Journal of Turbomachinery*, Vol. 111, pp. 87–95.

Blair, M. F., Wagner, J. H., and Steuber, G. D., 1991, "New Applications of Liquid-Crystal Thermography in Rotating Turbomachinery Heat Transfer Research," ASME paper 91-GT-354.

Blair, M. F., 1983, "Influence of Free Stream Turbulence on Turbulent Boundary Layer Heat Transfer and Mean Profile Development: Part I—Experimental Data," ASME JOURNAL OF HEAT TRANSFER, Vol. 105, pp. 33–40.

Boyle, R. J., and Russell, L. M., 1989, "Experimental Determination of Stator Endwall Heat Transfer," ASME *Journal of Turbomachinery*, Vol. 112, pp. 547–558.

Camci, C., 1989, "An Experimental and Numerical Investigation of Near Cooling Hole Heat Fluxes on a Film Cooled Turbine Blade," ASME *Journal of Turbomachinery*, Vol. 111, pp. 63–70.

Camci, C., Kim, K., and Hippensteele, S. A., 1992, "A New Hue Capturing Technique for the Quantitative Interpretation of Liquid Crystal Images Used in Convective Heat Transfer Studies," ASME *Journal of Turbomachinery*, Vol. 114, pp. 765–775.

Camci, C., Kim, K., Hippensteele, S. A., and Poinsatte, P. E., 1993, "Evaluation of a Hue Capturing Based Transient Liquid Crystal Method for High Resolution Mapping of Convective Heat Transfer on Curved Surfaces," ASME JOURNAL OF HEAT TRANSFER, Vol. 115, pp. 311–318.

Eriksen, V. L., and Goldstein, R. J., 1974, "Heat Transfer and Film Cooling Following Injection Through Inclined Circular Tubes," ASME JOURNAL OF HEAT TRANSFER, Vol. 96, pp. 239–245.

Hippensteele, S. A., Russell, L. M., and Torres, F. J., 1985, "Local Heat Transfer Measurements on a Large Scale Model Turbine Blade Airfoil Using a Composite of Heater Element and Liquid-Crystals," ASME *Journal of Engineering for Gas Turbines and Power*, Vol. 107, pp. 953–960.

Kim, K., 1991, "A New Hue Capturing Technique for the Quantitative Interpretation of Liquid Crystal Images Used in Convective Heat Transfer Studies," Ph.D. Thesis, Aerospace Engineering Department, The Pennsylvania State University.

MacMullin, R., Elrod, W., and Rivir, R., 1989, "Free-Stream Turbulence From a Circular Wall Jet on a Flat Plate Heat Transfer and Boundary Layer Flow," ASME *Journal of Turbomachinery*, Vol. 111, pp. 78–86.

Mehendale, A. B., and Han, J. C., 1992, "Influence of High Mainstream Turbulence on Leading Edge Film Cooling Heat Transfer," ASME *Journal of Turbomachinery*, Vol. 114, pp. 707–715.

Mick, W. J., and Mayle, R. E., 1988, "Stagnation Film Cooling and Heat Transfer, Including Its Effect Within the Hole Pattern," ASME *Journal of Turbomachinery*, Vol. 110, pp. 66–72.

Ou, S., Mehendale, A. B., and Han, J. C., 1992, "Influence of High Mainstream Turbulence on Leading Edge Film Cooling Heat Transfer: Effect of Film Hole Row Location," ASME *Journal of Turbomachinery*, Vol. 114, pp. 716–723.

Ou, S., and Han, J. C., 1992, "Influence of Mainstream Turbulence on Leading Edge Film Cooling Heat Transfer Through Two Rows of Inclined Film Slots," ASME *Journal of Turbomachinery*, Vol. 114, pp. 724–733.

Simonich, J. C., and Moffat, R. J., 1984, "Liquid Crystal Visualization of Surface Heat Transfer on a Concavely Curved Turbulent Boundary Layer," ASME *Journal of Engineering for Gas Turbines and Power*, Vol. 106, pp. 619–627.

Wang, T., and Simon, T. W., 1987, "Heat Transfer and Fluid Mechanics Measurements in Transitional Boundary Layers on Convex-Curved Surfaces," ASME *Journal of Turbomachinery*, Vol. 109, pp. 443–450.

Wiedner, B., and Camci, C., 1992, "A Low Speed, Transient Facility for Propulsion Heat Transfer Studies," *Proc. 1992 International Symposium on Heat Transfer in Turbomachinery*, Marathon, Greece, Aug. 24–28.

Wiedner, B. G., 1993, "Passage Flow Structure and Its Influence on Endwall Heat Transfer in a 90° Turning Duct," Ph.D. Thesis, Aerospace Engineering Department, The Pennsylvania State University.

Wiedner, B., and Camci, C., 1993, "Passage Flow Structure and Its Influence on Endwall Heat Transfer in a 90° Turning Duct: Mean Flow and High Resolution Heat Transfer Experiments," ASME Paper No. 93-WA/HT-52, accepted for publication in ASME *Journal of Turbomachinery*.

Zienkiewicz, O. C., 1971, *The Finite Element Method in Engineering Science*, McGraw-Hill, London.

O. Kwon

F. E. Ames

Heat Transfer Department,
Allison Engine Company,
P.O. Box 420,
Indianapolis, IN 46206

A Velocity and Length Scale Approach to $k-\epsilon$ Modeling

This paper describes a velocity and length scale approach to low-Reynolds-number $k-\epsilon$ modeling, which formulates the eddy viscosity on the normal component of turbulence and a length scale. The normal component of turbulence is modeled based on the dissipation and distance from the wall and is bounded by the isotropic condition. The model accounts for the anisotropy of the dissipation and the reduced length of mixing in the near wall region. The kinetic energy and dissipation rate were computed from the k and ϵ transport equations of Durbin (1993). The model was tested for a wide range of turbulent flows and proved to be superior to other $k-\epsilon$ based models.

Introduction

Two-equation $k-\epsilon$ (base) models are most popular in predicting fluid flow and heat transfer because of their capability of predicting a wide range of flows with minimal adjustment of the coefficients and their relative simplicity in formulation. However, they suffer from deficiencies for wall bounded flows that require wall functions, while low-Reynolds-number $k-\epsilon$ models need empirical damping functions to take account of the wall blocking on the turbulence mixing. These functions were derived to be consistent with experimental or numerical data for constant pressure boundary layers. Consequently, they are often blamed for the inaccurate solutions of complex flows. A detailed discussion on the deficiencies of $k-\epsilon$ models can be found elsewhere (Wilcox, 1988).

Lately, the turbulence modeling community has directed a significant effort to developing more physically sound $k-\epsilon$ models. The approaches of a renormalization group (RNG) method (Yakhot and Orszag, 1986), the Kolmogorov time scale introduction (Yang and Shih, 1993), and an elliptic relaxation method for the near-wall turbulence blocking effect (Durbin, 1993) are among the most significant developments. The RNG $k-\epsilon$ model was first derived by Yakhot and Orszag (1986) by means of the RNG method, which uses dynamic scaling and invariance together with iterated perturbation methods. This theory provided an elimination of experimentally adjustable parameters in the model. A high-Reynolds-number version of the RNG $k-\epsilon$ model was successfully tested for separated flows downstream of a rearward-facing step by Speziale and Thangam (1992).

Yang and Shih (1993) reformulated a low-Reynolds-number version of a $k-\epsilon$ model by introducing the Kolmogorov time scale into the transport equation for the turbulence dissipation rate. With the new time scale, they were able to eliminate the wall singularity of the equation and to keep the same model constants as those used in the standard high-Reynolds-number model. The model, however, still employs a damping function in the eddy viscosity formulation to account for kinematic blocking by the wall.

The elliptic relaxation model proposed by Durbin (1993) was devised for the strongly nonhomogeneous region near the wall. In this model, the wall blocking effect, which suppresses the normal component of turbulent intensity, was modeled by an elliptic relaxation equation for the redistribution terms in the Reynolds stress equations. Durbin also introduced the "local

anisotropy" term in the dissipation rate equation of this model. The introduction of these two features into the model eliminated the "ad hoc" damping functions from the model equations, however, at the cost of an increase in the size of the system by two model transport equations: one for the variance of the normal component of turbulent velocity, v'^2, and another for the velocity-pressure-gradient correlation, p_{22}.

These new approaches show improved modeling physics and appear to offer the prospect of improved predictions for anisotropic flows. However, they still need to be tested and verified for various practical flows. Recent studies (Ames and Moffat, 1990) indicate that the normal component of turbulence, v', is a key variable in the prediction of surface heat transfer and skin friction, and the magnitude of v' can be tied to the dissipation rate. Durbin (1993) also found that the normal fluctuation is a better velocity scale for characterizing the turbulent motion than the turbulent kinetic energy in the near wall shear layer. It is, therefore, logical to formulate the turbulent eddy diffusivity in terms of the local velocity v', which is modeled as a function of the local dissipation rate and the local length scale.

Analysis

Boundary Layer Equations. This study focused on the thin viscous region near a solid wall, called the boundary layer. In the steady two-dimensional boundary layer approximation, with the Reynolds shear stress and heat flux replaced by an "eddy" (or "turbulent") viscosity and a turbulent Prandtl number, the conservation of mass, momentum, and energy can be written in the following form:

$$\frac{\partial}{\partial x}(\rho U) + \frac{\partial}{\partial y}(\rho V) = 0 \tag{1}$$

$$\rho U \frac{\partial U}{\partial x} + \rho V \frac{\partial U}{\partial y} = -\frac{\partial P}{\partial x} + \frac{\partial}{\partial y}\left[(\mu + \mu_t)\frac{\partial U}{\partial y}\right] \tag{2}$$

$$\rho U \frac{\partial H}{\partial x} + \rho V \frac{\partial H}{\partial y} = \frac{\partial}{\partial y}\left[\left(\frac{\mu}{\text{Pr}} + \frac{\mu_t}{\text{Pr}_t}\right)\frac{\partial H}{\partial y}\right]$$
$$+ \frac{\partial}{\partial y}\left\{\left[(\mu + \mu_t) - \left(\frac{\mu}{\text{Pr}} + \frac{\mu_t}{\text{Pr}_t}\right)\right]U\frac{\partial U}{\partial y}\right\} \tag{3}$$

where U and V are the time-averaged mean velocities; μ, the molecular viscosity; Pr, the Prandtl number; H, the total enthalpy; and x and y, the streamwise and normal coordinates. The subscript "t" denotes the turbulent quantity. For the turbulent Prandtl number, Pr_t, a constant value of approximately 1.0 is

often used in heat transfer analyses. This analysis, however, incorporates Kays' correlation [Kays and Crawford, 1980, Eqs. $(12)-(41)$] using his recommendations for the free-stream turbulent Prandtl number ($Pr_{t\infty} = 0.86$) and an experimental constant ($C_{Pr} = 0.2$).

The system of equations, Eqs. $(1)-(3)$, is subject to the following boundary conditions:

at y = 0,

$$U = 0, \quad \text{and} \quad H = H_w \quad \text{or} \quad \frac{\partial H}{\partial y} = -\left(\frac{C_p}{k_m}\right) \dot{q}_w'' \quad (4)$$

as y → ∞,

$$U = U_e, \quad \text{and} \quad H = H_e \quad (5)$$

where c_P denotes the specific heat; k_m, the thermal conductivity; and $q_{w''}$, the rate of the wall heat flux. The subscripts 'w' and 'e' imply the wall and free-stream conditions, respectively.

k–ε Transport Equations. Conventional low-Reynolds-number $k-\epsilon$ turbulence models suffer from the wall singularity caused by the vanishing time scale of k/ϵ at the wall. Recently, Yang and Shih (1993) and Durbin (1993) showed that the wall singularity could be eliminated by introducing the Kolmogorov time scale into their $k-\epsilon$ base models as the lower bound of the usual time scale in the near-wall region. Furthermore, Durbin was able to integrate the standard high-Reynolds-number form of his k and ϵ transport equations directly down to the wall. The k and ϵ transport equations implemented a local anisotropy term but no "ad hoc" damping function or additional source terms. Durbin solved the k and ϵ equations in a coupled manner with the wall characteristics of the kinetic energy ($k = \partial k/\partial y = 0$) as the wall boundary conditions to the coupled

system of equations. Although the Durbin model formulates the k and ϵ transport equations in a simple and singularity-free form, it is more sophisticated as the additional v'^2-p_{22} system of equations is introduced to model the variance of the normal component of velocity, v'^2.

The transport equations for the turbulent kinetic energy and the dissipation rate proposed by Durbin (1993) were employed in this study because of their aforementioned attractive features of the simple and wall singularity-free formulation. The equations can be written as

$$\rho U \frac{\partial k}{\partial x} + \rho V \frac{\partial k}{\partial y}$$
$$= \mu_t \left(\frac{\partial U}{\partial y}\right)^2 - \rho\epsilon + \frac{\partial}{\partial y}\left[\left(\mu + \frac{\mu_t}{\sigma_k}\right)\frac{\partial k}{\partial y}\right] \quad (6)$$

$$\rho U \frac{\partial \epsilon}{\partial x} + \rho V \frac{\partial \epsilon}{\partial y}$$
$$= \frac{1}{T}\left[C_{\epsilon 1}^* \mu_t \left(\frac{\partial U}{\partial y}\right)^2 - C_{\epsilon 2}\rho\epsilon\right] + \frac{\partial}{\partial y}\left[\left(\mu + \frac{\mu_t}{\sigma_\epsilon}\right)\frac{\partial \epsilon}{\partial y}\right] \quad (7)$$

where σ_k, σ_ϵ, and $C_{\epsilon 2}$ are empirical constants. $C_{\epsilon 1}^*$ is a function of the ratio of the energy production to the energy dissipation, representing the production by local anisotropy. Durbin suggested the following linearized equation for $C_{\epsilon 1}^*$:

$$C_{\epsilon 1}^* = C_{\epsilon 1}\left(1 + a_1 \mu_t \left(\frac{\partial U}{\partial y}\right)^2 \Big/ \rho\epsilon\right) \quad (8)$$

where $C_{\epsilon 1}$ and a_1 are constants. The time scale is defined by the

------

Nomenclature

a_1, C, C_T, C_{vl} = constants
c_p = specific heat
C_f = friction coefficient
C_{f0} = reference velocity friction coefficient
C_{Pr} = constant in the turbulent Prandtl number correlation
$C_{\epsilon 1}, C_{\epsilon 2}, C_\mu$ = constants in the turbulence model
$E_2(k)$ = one-dimensional energy spectrum of v'
f_μ = damping function
H = total enthalpy
H = boundary layer shape parameter = δ^*/θ
k = kinetic energy or wavenumber
k^+ = nondimensional kinetic energy = k/u_τ^2
k_m = thermal conductivity
Lu = energy scale = $\sqrt{(2/3)}k^{3/2}/\epsilon$
l = length scale
l^+ = nondimensional mixing length = lu_τ/ν
p = pressure
Pr = Prandtl number
p_{22} = velocity–pressure gradient correlation + term related to dissipation tensor

$\dot{q}_w''$ = wall heat flux rate
$Re_{L=1}$ = Reynolds number based on the unit length
Re_x = Reynolds number
Re_θ = momentum thickness Reynolds number
St = Stanton number
T = temperature or time scale
T^+ = Nondimensional temperature = $(T - T_w)u_\tau/[U_e St(T_e - T_w)]$
Tu = free-stream turbulence intensity
U, V = streamwise and cross-stream mean velocities, respectively
U^+ = nondimensional mean velocity = U/u_τ
u_τ = friction velocity
u', v', w' = rms streamwise, normal, and spanwise fluctuation velocities, respectively
x, y = horizontal and vertical coordinates, respectively
x_0 = unheated starting length
y^+ = nondimensional vertical coordinate = yu_τ/ν
$\Delta x, \Delta y$ = grid sizes in the streamwise and vertical directions, respectively
β = equilibrium parameter = $(\delta^*/\tau_w)dp/dx$

β_K = nondimensional strain rate
δ = boundary layer thickness
δ^* = displacement thickness
ϵ = dissipation rate
ϵ^+ = nondimensional dissipation rate = $\epsilon\nu/u_\tau^4$
η_K = Kolmogorov length scale
θ = momentum thickness
κ = von Karman constant
μ = molecular viscosity
ν = kinematic viscosity
ρ = density
$\sigma_k, \sigma_\epsilon$ = empirical constants in the turbulent kinetic energy and dissipation rate model equations, respectively
τ = shear stress
τ_K = Kolmogorov time scale

Subscripts

e = boundary layer edge
i, j = grid indices in the horizontal and vertical directions, respectively
t = turbulent flow
w = wall
∞ = upstream infinity

Table 1 The closure coefficients employed in the k and ϵ transport equations

C_T	a_1	$C_{\epsilon 1}$	$C_{\epsilon 2}$	σ_k	σ_ϵ
6.0	0.09	1.44	1.9	1.0	1.3

usual scale, k/ϵ, with the lower bound given by the Kolmogorov scale, $(\nu/\epsilon)^{1/2}$, as suggested by Durbin (1993):

$$T = \max\left[\frac{k}{\epsilon}, \quad C_T\left(\frac{\nu}{\epsilon}\right)^{1/2}\right] \qquad (9)$$

where C_T is a constant. The values of the closure coefficients used in this study for wall-bounded flow predictions are similar to those suggested by Durbin (1993). They are given in Table 1.

In this study, a conventional low-Reynolds-number k–ϵ model designated "base model" is formed by combining the k and ϵ transport equations of Durbin (1993) and the eddy viscosity closure of Yang and Shih (1993). This "base" model is fully described by Kwon and Ames (1995).

In order to solve the governing k and ϵ transport equations, appropriate boundary conditions should be imposed on the wall and free-stream boundaries along with the initial profiles of k and ϵ upstream of the flow field. At the wall there exists no correct explicit condition of ϵ. As discussed by Durbin (1993), the limiting behavior of k and ϵ is $k \rightarrow \epsilon(0)y^2/2\nu$ as $y \rightarrow 0$, which implies $\partial k/\partial y = 0$ at the wall. Therefore, the coupled system of transport equations should be solved in a coupled manner with the wall boundary conditions $k = \partial k/\partial y = 0$ or with the limiting behavior relationship between k and ϵ and the no-slip condition $k = 0$. For the present study, the latter set of the conditions is used, since it is slightly less cumbersome to implement with the coupled numerical algorithm. In the free-stream, the vanishing normal gradient condition was imposed.

$v'l$ Formulation. Eddy diffusivity, ν_t, has the dimensional units of a fluctuating velocity scale times a length scale. From the simplest physical model, an eddy with a normal fluctuation velocity, v', takes a mass of fluid from one location in a flow to another a distance l away. If a gradient in a property exists, its diffusion across the flow will be proportional to the gradient times the product of this velocity scale and length scale. Tennekes and Lumley (1972) suggested the local eddy diffusivity is roughly equal to the normal variance, v'^2, times the Lagrangian integral time scale, τ_{22}. Durbin (1991) formulated his eddy diffusivity in this manner observing that k–ϵ damping functions are approximately proportional to v'^2/k. Since the Lagrangian integral time scale times the magnitude of v' is the Lagrangian integral scale, this $v'^2\tau_{22}$ formulation of eddy viscosity is equivalently $v'l$. The eddy viscosity, therefore, can be written as

$$\mu_t = \rho v'l \qquad (10)$$

where ρ denotes the density; v', the magnitude of the normal component turbulent velocity; and l, the turbulent length scale.

Near the wall, the lateral Eulerian integral scale is proportional to the normal distance, y, from the wall. Hunt and Graham (1978) found this proportionality in their analysis of a shear free turbulent flow. This proportionality provides a simple yet sound way to model the mixing length through the boundary layer and near the wall.

The turbulent boundary layer statistics provided by the direct numerical simulation (DNS) calculation of Spalart (1988) offers an opportunity to test the validity of these modeling assumptions. First, the turbulent scale of mixing, l, determined from the DNS data indicates that the distance to the wall con-

strains the near wall mixing. Figure 1 shows a comparison between the mixing length l estimated from the data, by dividing $[-u'v']^+$ by v'^+ and dU^+/dy^+, and a line represented by 0.38 $(y^+ - 5)$ for y^+ greater than 5. From $y^+ = 10$ through the logarithmic law region, this mixing length is well represented by the linear relationship of 0.38 $(y^+ - 5)$. The offset in this representation in the sublayer region, where $y^+ < 10$, indicates that the turbulent mixing is less effective. The inviscid damping of the wall, viscous dissipation of small eddies, and high near-wall strain rates contribute to the fall off of the near wall dependence of mixing length l^+ on y^+.

In the $v'l$ formulation of eddy viscosity, the length scale was correlated based on the DNS data as

$$l^+ = \kappa(y^+ - \eta_K/4)/(1 + 0.4\beta_K) \quad \text{for} \quad y^+ \geq \eta_K/4$$
$$l^+ = 0 \quad \text{for} \quad y^+ < \eta_K/4 \qquad (11)$$

where η_K denotes the Kolmogorov length scale defined by $\eta_K = (\nu^3/\epsilon)^{1/4}$; and β_K, a nondimensional strain rate defined by

$$\beta_K = \tau_K(dU/dy) \qquad (12)$$

in which the Kolmogorov time scale, τ_K, is defined by $\tau_K = (\nu/\epsilon)^{1/2}$; and the von Karman constant, κ, is set equal to 0.38. Figure 1 shows a comparison between l^+ determined from the DNS data, Eq. (11), and the conventional k–ϵ model length scale of $(3/2)^{1/2}C_\mu k^{3/2}/\epsilon$ (or 0.116 $k^{3/2}/\epsilon$ for $C_\mu = 0.0945$ as used for the base k–ϵ model). The conventional length scale can be obtained from the definition of the eddy diffusivity that $\nu_t = v'l = C_\mu k^2/\epsilon$. Since $v' = \sqrt{(2k/3)}$ for isotropic turbulence, the length scale becomes $l = (3/2)^{1/2}C_\mu k^{3/2}/\epsilon$. The dependence of mixing length with y^+ begins to drop off beyond the logarithmic law region or past a y^+ of about 90 to 100. This slowed growth of l is probably due to the intermittency of turbulent and free-stream fluid in this region. Modeling l in this region can be readily accomplished by using the minimum of l and the k–ϵ formulation of mixing length, 0.116 $k^{3/2}/\epsilon$.

Based on both the experimental study of Thomas and Hancock (1977) and analytical studies of Hunt and Graham (1978) and Spalart (1988), v' is strongly attenuated by the wall. Modeling v' can be accomplished by developing a model spectrum based on the dissipation rate. In the inertial subrange of the spectrum, the v' spectra can be represented by

$$E_2(k) = C\epsilon^{2/3}k^{-5/3} \qquad (13)$$

where $E_2(k)$ denotes the one-dimensional energy spectrum of v'; ϵ, the dissipation rate; k, the wavenumber; and C, a constant. This model is expected to be valid in the regions of the boundary layer where the turbulent Reynolds number is high enough to support an inertial subrange. Very close to the wall, the validity of an inertial subrange for the v' spectra becomes questionable, yet this model has been found to work quite well. Based on Hunt and Graham (1978), v'^2 scales on $(y/Lx)^{2/3}$ near the wall
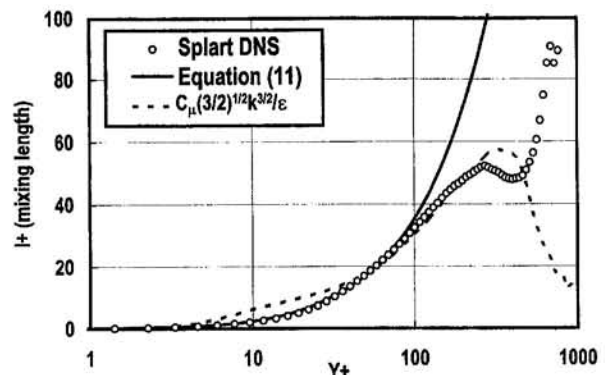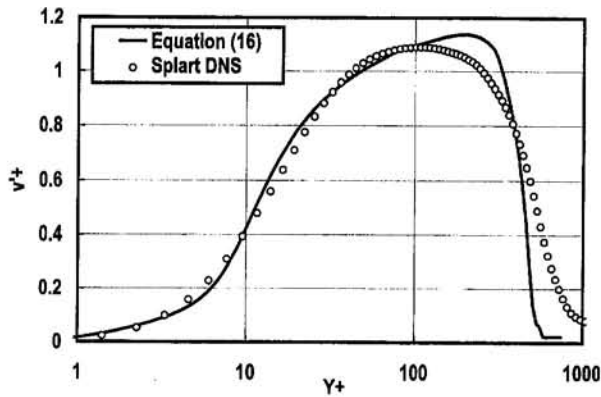
Fig. 1 Mixing length comparison

Fig. 2 Comparison of $v'+$

of their shear free turbulence layer. This implies that the energy from the attenuation of larger scale eddies due to wall blocking can be modeled by scaling a large-scale cutoff wavenumber on $1/y$. Hinze (1975) reports that according to Pao the spectrum is determined only by ϵ and k (wavenumber) in the dissipation range so the natural length scale for the high wavenumber cutoff is the reciprocal of the Kolmogorov length scale, $1/\eta_K$. Near the wall in a turbulent boundary layer, the dissipation is known to be anisotropic, and according to Durbin (1993), scales approximately on v'^2/k, so an anisotropic form of ϵ (ϵ_v) is needed in this region. Away from the wall, in the log layer and beyond, the dissipation becomes more and more isotropic with respect to spectral scaling. Using the concept of the low wavenumber ($1/y$) and high wavenumber ($1/\eta_K$) cutoffs, Eq. (13) can be integrated to provide an estimate for the local value of v'^2. The simple spectrum model for v' becomes

$$v'^2 = C\epsilon_v^{2/3}(2.5y^{2/3} - 1.5\eta_K^{2/3}) \qquad (14)$$

In the region where the expression in the parentheses is less than zero, v'^2 is taken as 0. This condition only arises around a y^+ less than 2 or 3 in a region where the turbulent viscosity is negligible. The anisotropy of ϵ can be modeled using an empirical damping function. The damping function uses a nondimensionalized strain rate, β_K, to provide the majority of the damping and an exponential term to give the proper near-wall dependence:

$$\epsilon_v = \epsilon[1 - \exp(-y/1.2\eta_K)]^5/(1 + 2\beta_K + 5\beta_K^2 + \beta_K^4) \quad (15)$$

The exponential term in Eq. (15) is introduced to achieve a correct near-wall limiting behavior of v' and its effect on the analysis is generally small. The variable β_K nondimensionalizes the strain rate using the Kolmogorov time scale, τ_K. This is an attempt to correlate the influence of strain empirically on the attenuation of v' in the sublayer. The strain rate also correlates with the anisotropy of ϵ, which is due to the near-wall dissipation of the highly anisotropic fluctuating components u' and w'.

The final representation for v' is the following function of dissipation, strain rate, and relative position from the surface:

$$v' = C_{vl}[\epsilon_v^{2/3}(2.5y^{2/3} - 1.5\eta_K^{2/3})]^{1/2} \qquad (16)$$

where the constant C_{vl} is set equal to 0.584. The DNS data of Spalart were used to develop these formulas and Fig. 2 shows a comparison between Spalart's v'^+ statistics and the equation for v' given above. The computed v' profile compares well with the DNS data.

The turbulent viscosity, μ_t, can be calculated from Eq. (10) along with Eqs. (11) and (16). However, in order to bound v' and l in y, a check is made to ensure that μ_t obtained from Eq. (10) is less than that from the formulation given below for the $k-\epsilon$ model:

Table 2 The closure coefficients employed in the $v'l$ model

C_{vl}	C_μ	κ
0.584	0.0945	0.38

$$\mu_t = C_\mu \rho k^2/\epsilon \qquad (17)$$

Furthermore, v' is also bounded by $(2k/3)^{1/2}$. The closure coefficients of the $v'l$ model are summarized in Table 2.

Computation Results and Discussions

The $v'l$ closure model was applied to analyzing various turbulent flows for model verification. For these analyses, the governing conservation equations for mass, momentum, and energy, Eqs. (1)–(3), were solved using an implicit finite difference scheme in an uncoupled manner. The turbulent kinetic energy and dissipation rate transport equations, Eqs. (6) and (7), were also solved using an implicit finite difference scheme, but in a coupled manner. For the turbulent transport equations, the convective terms were discretized by using a second-order accurate scheme. A detailed solution procedure for a coupled system of equations can be found elsewhere (Anderson et al., 1984). All calculations were performed using double precision arithmetic on an IBM RS6000 work station.

A Flat Plate Boundary Layer. The first test case for the proposed $v'l$ model along with the base $k-\epsilon$ model was a flat plate turbulent boundary layer. The boundary layer form of the mass and momentum conservation equations, Eqs. (1) and (2), were solved with the proposed turbulence models. The upstream starting profiles were generated based on the one-seventh power law assumption. The computation was performed from near the leading edge of a flat plate until Re_θ became approximately 15,000. The assumed upstream free-stream turbulence intensity was 1 percent. The grid in the normal direction was stretched at the rate of $\Delta y_{j+1}/\Delta y_j = 1.05$, where Δy and j denote the grid spacing and index, respectively. The first grid point from the wall was located at $y^+ \approx 0.05$. The grid was also stretched in the streamwise direction at the rate of $\Delta x_i/\Delta x_{i-1} = 1.03$ but not exceeding 0.2δ, where δ is the boundary layer thickness. The first streamwise grid spacing was only a fraction of the boundary layer thickness ($\sim 0.001\delta$) in order to keep the influence of the initial profile on the flow solution within a short distance near the leading edge.

Figure 3 presents the computed skin friction coefficients using the $v'l$ and base models along with the data measured by Wieghardt and Tillmann (1969) and Purtell et al. (1981). The computed data agreed well with the measured data. In detail, the $v'l$ model provided the higher value than the base model.
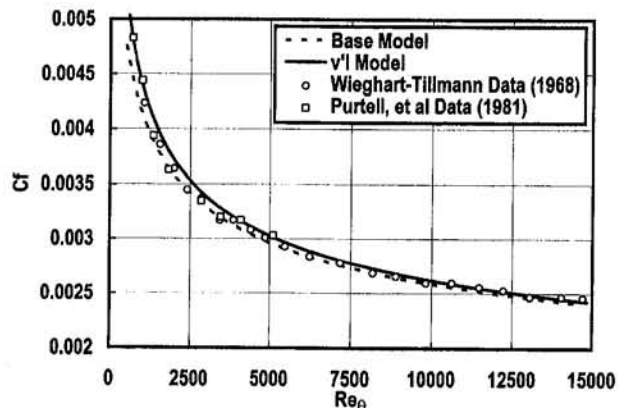

Fig. 3 Comparison of skin friction coefficients

Table 3 Flat plate turbulent boundary layer integral parameters

	$Re_\theta = 670$		$Re_\theta = 1410$	
	$C_f \times 10^3$	H	$C_f \times 10^3$	H
Wieghardt-Tillmann Data	4.96	—	3.98	—
Purtell et al. Data	4.91	1.53	3.99	1.46
Spalart DNS Data	4.86	1.50	4.14	1.43
Base k-ϵ Model	4.72	1.53	3.85	1.45
$v'l$ Model	4.86	1.56	4.05	1.47

Table 3 compares the computed friction coefficient, C_f, and shape parameter, H, with measured data and DNS data at two streamwise locations. The momentum thickness Reynolds numbers Re_θ at these locations were 670 and 1410, respectively. The DNS data were obtained by Spalart (1988). At both locations, the $v'l$ and base k-ϵ models gave a fair to good agreement with the data. The agreement between the computed and measured data was in general better at the higher Re_θ. At $Re_\theta = 670$, the $v'l$ predicted a similar friction coefficient to the DNS data. However, both of the computed values were lower than the measured data by 1–2 percent. At higher Re_θ, the $v'l$ model predicted a C_f between the measured data and the DNS data.

Figure 4 shows the predicted mean velocity profiles at $Re_\theta = 1410$ compared with the DNS data of Spalart (1988) and the predictions of the Durbin and Yang–Shih models. The proposed $v'l$ model and the base k-ϵ model gave a good agreement with the DNS data, which is natural since the model coefficients were set based on the DNS data. In Figs. 5 and 6, the predicted kinetic energy and dissipation rate profiles at $Re_\theta = 1410$, using the $v'l$ and base k-ϵ models are compared to DNS data (Spalart, 1988). The predictions from the Durbin model and Yang and Shih model are also shown in comparison. Overall, the proposed models gave good agreement with the data. The most significant difference between the model predictions and the data was observed in the near wall dissipation rates as shown in Fig. 6. The $v'l$ model provided the best agreement with the DNS data in that region. The second peak of the dissipation rate occurring at $y^+ \approx 10$ was well predicted by both $v'l$ and base k-ϵ models as compared with the DNS data.

A Turbulent Boundary Layer With an Increasingly Adverse Pressure Gradient. Samuel and Joubert (1974) measured a nonequilibrium turbulent boundary layer developed under an increasingly adverse pressure gradient and later under a brief decreasingly adverse pressure gradient near the end of the test section. Such a nonequilibrium flow is difficult to predict with conventional k-ϵ models and, therefore, has been often used as a test case for turbulence models.
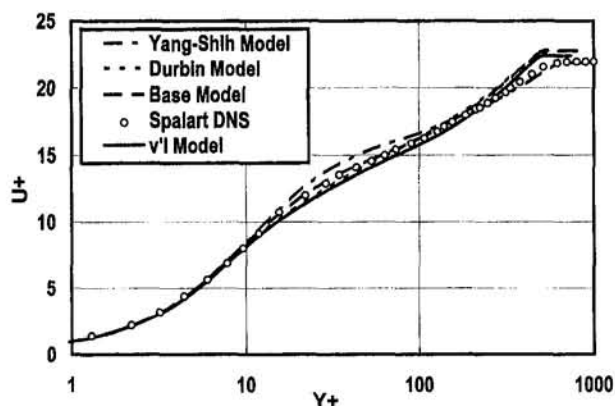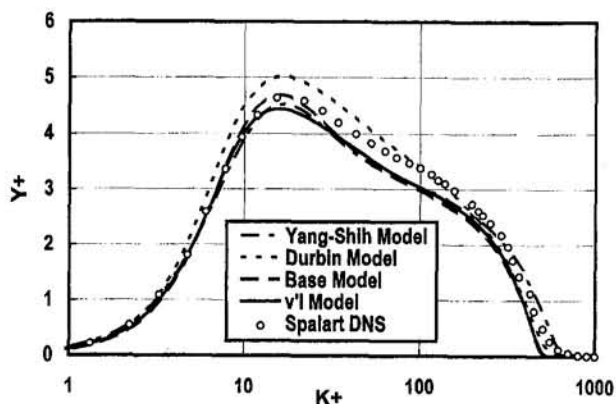
Fig. 5 Comparison of turbulent kinetic energy

The proposed $v'l$ and base k-ϵ models were tested to verify their prediction capabilities for this nonequilibrium flow. For comparison purposes, the flow was also analyzed by using the models developed by Launder and Sharma (1974) and Durbin (1993). The calculation started with a zero pressure gradient boundary layer at $x = 0$ m. The computed momentum thickness Reynolds numbers at the first measurement location where $x_1 = 0.855$ m were matched iteratively to the measured data of $Re_\theta \cong 4830$ based on the inlet reference velocity. The measured Reynolds number based on the inlet reference velocity per unit length was approximately 1.7×10^6 m^{-1}. The free-stream velocity distribution was estimated from the measured streamwise gradient of the pressure coefficient. The computational grid arrangement was similar to the previous flat plate boundary layer case except the streamwise stretching was limited to 0.05δ.

In Fig. 7, the computed friction coefficients, normalized on the upstream reference velocity, were compared with measured data. The friction coefficient, C_{f0}, at the first measurement location ($x - x_1 = 0$ m) was overpredicted by all the models. Downstream, the $v'l$ model as well as the Durbin model provided good comparisons with the data, although the $v'l$ model gave a slight underprediction in the relatively strong pressure gradient region. The base k-ϵ model prediction was slightly higher than the data in the entire region. Meanwhile, the prediction of the Launder and Sharma model initially compared well with the data but deviated gradually as the pressure gradient built up.

Turbulent Boundary Layer With Heat Transfer. The proposed $v'l$ model as well as the base k-ϵ model were evaluated for their heat transfer prediction capabilities. For a relatively clean flow with low free-stream turbulence intensity ($Tu_\infty < 0.5$ percent), these two models predicted surface heat transfer

Fig. 4 Comparison of mean velocity profiles with DNS
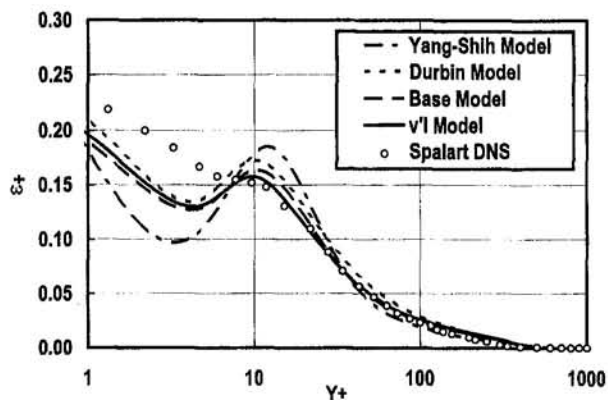
Fig. 6 Comparison of dissipation rate
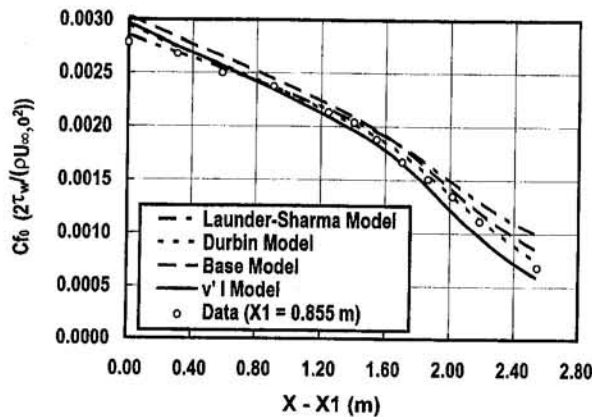
Fig. 7 Comparison of Samuel–Joubert flow
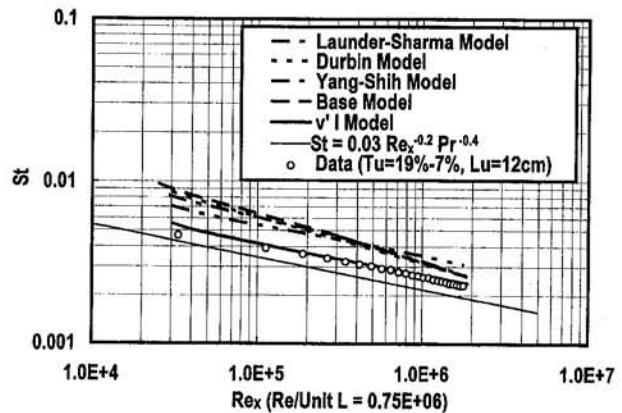
Fig. 9 Heat transfer with high level turbulence

in good agreement with measured data and the turbulent boundary layer correlation given by Kays and Crawford (1980) as shown in Fig. 8. The data shown in Fig. 8 were measured by Ames and Moffat (1990) for a zero pressure gradient boundary layer, which developed on a uniformly heated flat plate with an upstream unheated length of 0.19 m. The measured upstream Reynolds numbers per unit length were approximately 1×10^6 m^{-1} and 2×10^6 m^{-1}. The turbulent Prandtl number was obtained from the Kays correlation [Kays and Crawford, 1980, Eqs. (12)–(41)].

The $v'l$ and base $k-\epsilon$ models were also assessed for predicting heat transfer from flat plate boundary layers with high-intensity, large-scale turbulence. Ames and Moffat (1990) generated high-intensity, large-scale turbulence in a simulated combustor, which produced turbulence levels up to 19 percent with a length scale ranging from about 11 to 14 cm. Such high-intensity, large-scale free-stream turbulence can cause high anisotropies in the wall boundary layer. Ames and Moffat observed from their experiment that the normal component turbulence was strongly attenuated by the wall, which resulted in a significant reduction of the influence of free-stream turbulence on boundary layer development. Such phenomena cannot be predicted by conventional $k-\epsilon$ models since the models have no mechanism to deal with the anisotropic behavior of external turbulence.

Heat transfer analyses were performed for three turbulent boundary layers measured by Ames and Moffat (1990) with their turbulence generator #5. The measured upstream Reynolds numbers per unit length of these flows were approximately 0.38 $\times 10^6$ m^{-1}, 0.75×106 m^{-1}, and 1.4×10 m^{-1}. The upstream turbulence was $Tu_\infty \approx 19$ percent and $Lu_\infty \approx 12$ cm. At the end of the test section, the turbulence intensity level decreased to approximately 7 percent. The calculations started near the lead-

ing edge of the uniformly heated test plate. The computed Re_θ at the first profile measurement location ($x = 0.2032$ m) was matched to the data with the $v'l$ model. However, for other $k-\epsilon$ models such as the Launder and Sharma, Durbin, Yang and Shih, and base $k-\epsilon$ models, some difficulties were experienced in the trial-and-error matching of Re_θ. Such problems were caused by the prediction of unrealistically high mixing, which resulted in rapid boundary layer growth. For these models, an arbitrarily thin boundary layer thickness was specified upstream such that it provided the closest Re_θ at the first measurement location compared to the data. The energy equation was solved with measured surface heat flux as the wall boundary condition.

The computed results for the three Reynolds numbers were similar and, therefore, the results of Reynolds number per unit length of 0.75×10^6 m^{-1} are presented in this paper. Figure 9 shows the computed wall Stanton numbers along with measured data. The agreement between the computed heat transfer using the $v'l$ model and the data was excellent, while other models overpredicted significantly. Compared with unaugmented heat transfer represented by the Kays and Crawford correlation (Kays and Crawford, 1980), the conventional $k-\epsilon$ models' prediction of heat transfer augmentation was approximately 50–150 percent higher than the measured augmentation level. The Durbin relaxation model, which provided reasonable predictions for the nonequilibrium flow under increasingly adverse pressure gradient, performed equally poorly as the conventional $k-\epsilon$ models. Figure 10 shows calculated velocity and temperature profiles at the near exit plane ($x = 2.13$ m) using the proposed $v'l$ model. Computed profiles agreed reasonably well with the measured data.

The relatively good performance of the $v'l$ model for nonequilibrium flows such as the Samuel–Joubert flow (Samuel
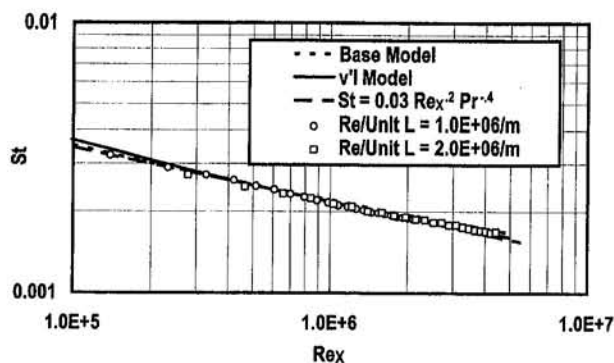
Fig. 8 Comparison of surface heat transfer distributions for uniformly heated plate
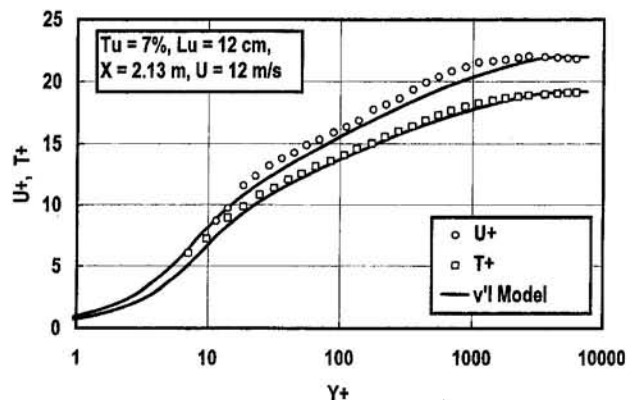
Fig. 10 Comparison of velocity and temperature profiles

and Joubert, 1974) and flat plate boundary layers with high-intensity, large-scale turbulence measured by Ames and Moffat (1990) might be attributed to the formulation of the eddy diffusivity in terms of the velocity and length scales, which were modeled based on the dissipation rate and the local coordinate. With such formulations, the proposed $v'l$ model was able to account for the anisotropy of the turbulence and the reduced length of mixing in the near wall region more adequately. Additionally, the $v'l$ model has performed better in correlating the high turbulence heat transfer data than Durbin's relaxation model. For flows like those of Ames and Moffat (1990) the turbulence is highly anisotropic near the wall, including the outer portion of the boundary layer, and Durbin's time scale (k/ϵ) is too large. The second important factor in the $v'l$ model performance was the use of Durbin's (1993) more adequate nonsingular ϵ equation augmented with the local anisotropy term. This argument was based on the observation that the base $k-\epsilon$ model, which employed the conventional eddy viscosity formulation with a damping function, provided often comparable solutions to the Durbin relaxation model and significantly better than conventional $k-\epsilon$ models.

Summary

In this study, a $k-\epsilon$ based velocity and length-scale closure model was successfully developed. In the model, the velocity scale of the eddy viscosity formulation was evaluated by integrating the normal component energy spectrum; and the length scale from the local distance from the wall. The energy spectrum was based on the local dissipation rate. The kinetic energy and dissipation rate were obtained from the modeled form of k and ϵ transport equations proposed by Durbin (1993). The model was tested in various turbulent flows including nonequilibrium, anisotropic flows. The results showed that the proposed velocity and length scale approach provided substantial improvements in flow and heat transfer predictions, especially for the nonequilibrium, anisotropic flows tested. Existing $k-\epsilon$ models including the Durbin's relaxation model failed to predict such nonequilibrium, anisotropic flows. The good performance of the proposed model resulted from the velocity scale and mixing length scale formulations, which constrained the eddy diffusivity to physically realizable levels, and accounted for the reduced mixing more adequately.

Acknowledgments

References

Ames, F. E., and Moffat, R. J., 1990, "Heat Transfer With High Intensity, Large Scale Turbulence: The Flat Plate Turbulent Boundary Layer and the Cylindrical Stagnation Point," Report No. HMT-44, Thermosciences Division of Mechanical Engineering, Stanford University.

Ames, F. E., 1994, "Experimental Study of Vane Heat Transfer and Aerodynamics at Elevated Levels of Turbulence," NASA CR-4633, Nov.

Anderson, D. A., Tannehill, J. C., and Pletcher, R. H., 1984, Computation Fluid Mechanics and Heat Transfer, Hemisphere Publishing Corporation, Washington, DC.

Durbin, P. A., 1991, "Near-Wall Turbulence Closure Modeling Without Damping Functions," Theoretical and Computational Dynamics, Vol. 3, p. 1.

Durbin, P. A., 1993, "Application of a Near-Wall Turbulence Model to Boundary Layers and Heat Transfer," Int. J. Heat Fluid Flow, Vol. 14, No. 4, pp. 316–323.

Herring, H., and Norbury, J., 1969, "Equilibrium Boundary Layer in Mild Negative Pressure Gradient," Computation of Turbulent Boundary Layers-1968 AFOSR-IFP-Stanford Conference, D. E. Coles and E. A. Hirst, eds., Vol. 2, Stanford Univ., Stanford, CA, p. 249.

Hinze, J., 1975, Turbulence, 2nd ed., McGraw-Hill, New York.

Hunt, J. C. R., and Graham, J. M. R., 1978, "Free-Stream Turbulence Near Plane Boundaries," J. Fluid Mech., Vol. 84, p. 209.

Kays, W. M., and Crawford, M. E., 1980, Convective Heat and Mass Transfer, McGraw-Hill, New York.

Kwon, O., and Ames, F. E., 1995, "Advanced $k-\epsilon$ Modeling of Heat Transfer," NASA CR-4679, July.

Launder, B. E., and Sharma, B. I., 1974, "Application of the Energy-Dissipation Model of Turbulence to the Calculation of Flow near a Spinning Disc," Letters in Heat and Mass Transfer, Vol. 1, p. 131.

Purtell, L. P., Klebanoff, S., and Buckley, F. T., 1981, "Turbulent Boundary Layer at Low Reynolds Number," Physics of Fluids, Vol. 24, p. 802.

Samuel, A. E., and Joubert, P. N., 1974, "A Boundary Layer Developing in an Increasingly Adverse Pressure Gradient," J. Fluid Mech, Vol. 66, Pt. 3, p. 481.

Spalart, P. R., 1988, "Direct Simulation of a Turbulent Boundary Layer up to $Re_\theta = 1410$," J. Fluid Mech, Vol. 187, p. 61.

Speziale, C. G., and Thangam, S., 1992, "Analysis of an RNG Based Turbulence Model for Separated Flows," NASA CR-189600, Jan.

Tennekes, H., and Lumley, J. L., 1972, A First Course in Turbulence, MIT Press, Cambridge, MA.

Thomas, N. H., and Hancock, P. E., 1977, "Grid Turbulence Near a Moving Wall," J. Fluid Mech, Vol. 82, Part 3, p. 481.

Wieghardt, K., and Tillmann, W., 1969, "Equilibrium Boundary Layer of Constant Pressure," Computation of Turbulent Boundary Layers-1968 AFOSR-IFP-Stanford Conference, D. E. Coles and E. A. Hirst, eds., Vol. 2, Stanford Univ., Stanford, CA, p. 98.

Wilcox, D. C., 1988, "Reassessment of the Scale Determining Equation for Advanced Turbulence Models," AIAA Journal, Vol. 26, No. 11, pp. 1299–1310.

Yakhot, V., and Orszag, S. A., 1986, "Renormalization Group Analysis of Turbulence. I. Basic Theory," J. Scientific Computing, Vol. 1, No. 1, p. 1.

Yang, Z., and Shih, T. H., 1993, "New Time Scale Based $k-\epsilon$ Model for Near-Wall Turbulence," AIAA Journal, Vol. 31, No. 7, p. 1191.

Uneven Wall Heat Flux Effect on Local Heat Transfer in Rotating Two-Pass Channels With Two Opposite Ribbed Walls

Shou-Shing Hsieh
Professor
email: sshsieh@mail.nsysu.edu.tw.
Fellow ASME

Wei-Jen Liu
Graduate Student.

Department of Mechanical Engineering,
National Sun Yat-Sen University,
Kaohsiung, Taiwan 80424

The influence of rotation and uneven heating condition on the local heat transfer coefficient in rotating, two-pass rib-roughened (rib height $e/D_H \approx 0.17 - 0.20$; rib pitch $p/e = 5$) rectangular channels with cross-sectional aspect ratios of 1 and 1.5 were studied for Reynolds numbers from 5000 to 25,000 and rotation numbers from 0 to 0.6152. Regionally averaged Nusselt number variations along the duct have been determined over the trailing and leading surfaces for two pass channels. In general, Coriolis-induced secondary flows are shown to enhance local heat transfer over the trailing (leading) surface in the first (second) pass compared to a duct without rotation. Centrifugal buoyancy is shown to influence the heat transfer response with heat transfer being imposed on both leading and trailing surfaces as the wall-to-bulk fluid temperature difference is increased with other controlling parameters fixed. Results also indicate a slight decrease in heat transfer coefficient for an increase in passage aspect ratio. Results are compared with previous studies. It is found that the results agree quite well with those reported by other works for two-pass flow channels.

1 Introduction

Owing to the increase in the turbine inlet temperature of gas turbine engines, there is an urgent need today to obtain a higher efficiency in the engines of aircraft, ships, and many other industrial applications. Parallel with the evolution of metal working at high temperatures, several methods of cooling rotor blades have been tried and developed. Cooled blades are widely used in modern engines. Radial channel cooling is a commonly used method. These channels are often designed with two artificially roughened and two smooth walls, and the designer must know the heat transfer coefficient on each of the walls in order to predict the turbine airfoil's life correctly. Naturally, it is also necessary to know the pressure loss for such a channel. Highly sophisticated cooling techniques such as augmented internal convective cooling have been employed for turbine blades in order to maintain acceptable safety requirements under extreme operating conditions. However, it is important to understand the effect of blade rotation on local heat transfer coefficient distribution inside the serpentine coolant passages and the surface heating conditions.

As the increase in heat transfer rate is accompanied by a friction factor increase, the preferred roughness geometry will yield the desired heat transfer augmentation with a minimum friction factor. The internal passages can be approximately modeled as square or rectangular channels with two opposite rib-roughened walls. The heat transfer and friction characteristics in these channels are different from those of circular tubes, parallel plates, or annuli.

Rotation of turbine blade cooling passages gives rise to Coriolis and buoyancy forces that can significantly alter the local heat transfer in the inward coolant passage from the development of cross-stream (Coriolis), as well as radial (buoyant) secondary flows.

Buoyancy forces in gas turbine blades are substantial because of high rotational speeds and coolant temperature gradients. Therefore, a better understanding of Coriolis and buoyancy effects and the capability to predict the heat transfer response to these effects will allow the turbine blade designer to achieve optimum cooling configurations that utilize less flow and, consequently, reduce the compressor power as well as thermal stresses in the airfoil. In addition, under realistic conditions, the blade surface is subjected to different or uneven heat flux or temperature on the leading or trailing surface of the serpentine square channels. Furthermore, it is shown (Parsons et al., 1994) that the uneven wall heat flux/temperature creates local buoyancy forces that would change the effect of the rotation, which results in changes in the local heat transfer coefficients on the leading/trailing surface due to the uneven heat flux especially for multipass flow channels. The results presented in this paper are aimed at studying the uneven heating load effects of rotation on a two-pass square and rectangular channels with two oppositely ribbed walls from heat transfer measurements.

1.1 Summary of Previous Studies. Results of several investigations have been extensively discussed for rotating passages with smooth walls. Heat transfer enhancement was studied with the use of rib turbulators in the stationary case, but it had not been treated in the rotating system before 1990. In recent years, Taslim et al. (1991a, b) has begun to study the roughened surfaces. A number of investigators have studied the phenomena of the Coriolis force induced secondary flow. These include the analytical works by Hart (1971), Moore (1967), and Rothe and Johnston (1979), and the experimental works by Wagner and Velkoff (1972) and Johnston et al. (1972). They all came to the same conclusion that, when a channel is being rotated, there would be strong secondary flows, and they have identified aspects of flow stability that produce streamwise-oriented vortexlike structures in the flow of a rotating radial passage. However, the effect of centrifugal buoyancy force seems not to be mentioned until the report from Morris and Ayhan (1979). Based on their results, the buoyancy force would make the

Table 1 Relevant data for experimental investigations on rotating cooling channels

Investigators	Physical Geometry	Boundary Condition	Rotation Number	Reynold Number	Smooth/Roughened Channel	Developing/ Fully Developed	Parameters Investigated	Flow Direction	Local/Mean Nu
Wanger et al. (1991a)	Square Duct	UWT	$0 \leq Ro \leq 0.48$	12,500 50,000	Smooth Channel(single pass/orthogonally rotating)	FD	$Re,Ro,\Delta\rho/\rho$ $R/D,Gr/Re^2$	Radially Outward Flow	Local
Wanger et al. (1991b)	Square Duct	UWT	$0 \leq Ro \leq 0.48$	25,000	Smooth Serpentine Channel(three pass/ orthogonally rotating)	D/FD	$Re,Ro,\Delta\rho/\rho$ $R/D,Gr/Re^2$	Radially Inward/ Outward Flow	Local
Yang et al. (1992)	Square Duct	UHF	$0 \leq Ro \leq 0.042$	44,000 110,000	Smooth Serpentine Channel(four pass/ orthogonally rotating)	D/FD	Re,Ro,Ra_Ω	Radially Inward/ Outward Flow	Local
Wanger et al. (1992)	Square Duct	UWT	$0 \leq Ro \leq 0.35$	25,000	Roughened Channel (three pass/orthogonally rotating)	D/FD	$Re,Ro,\Delta\rho/\rho$ $R/D,Gr/Re^2$	Radially Inward/ Outward Flow	Local
Han et al. (1992)	Square Duct	UWT (uneven)	$0 \leq Ro \leq 0.352$	2,500 25,000	Smooth Channel(single pass/horizontally rotating)	FD	$Re,Ro,\Delta\rho/\rho$	Radially Outward Flow	Local
Han et al. (1993)	Square Duct	UWT (uneven)	$0 \leq Ro \leq 0.352$	2,500 25,000	Smooth Channel (two pass/horizontally rotating)	D/FD	$Re,Ro,\Delta\rho/\rho$	Radially Inward/ Outward Flow	Local
Parsons et al. (1994)	Square Duct	UWT (uneven) /UHF	$0 \leq Ro \leq 0.352$	2,500 25,000	Roughened Channel(two pass/horizontally rotating)	D/FD	$Re,Ro,\Delta\rho/\rho$	Radially Inward/ Outward Flow	Local
Johnson et al. (1994)	Square Duct	UWT	$0 \leq Ro \leq 0.35$	25,000	Smooth(skew) Serpentine Channel (orthogonally rotating)	D/FD	$Re,Ro,\Delta\rho/\rho$ $R/D,Gr/Re^2$	Radially Inward/ Outward Flow	Local
Hsieh and Hong (1995)	Square Duct	UHF	$0 \leq Ro \leq 0.50$	5,000 25,000	Roughened Channel (single pass/orthogonally rotating)	D/FD	Re,Ro,Re_Ω Ra_Ω	Radially Outward Flow	Local
Parsons et al. (1995)	Square Duct	UWT/UHF	$0 \leq Ro \leq 0.352$	2,500 25,000	Roughened Channel(two pass/horizontally rotating)	D/FD	$Re,Ro,\Delta\rho/\rho$	Radially Inward/ Outward Flow	Local
Zhang et al. (1995)	Square Duct	UWT (uneven) /UHF	$0 \leq Ro \leq 0.352$	2,500 25,000	Roughened Channel(two pass/horizontally rotating)	D/FD	$Re,Ro,\Delta\rho/\rho$	Radially Inward/ Outward Flow	Local
Present Study	Rectangular and Square Duct	UHF (uneven)	$0 \leq Ro \leq 0.615$	5,000 25,000	Roughened Channel (two pass/orthogonally rotating)	D/FD	$Re,Ro,\Delta\rho/\rho$	Radially Inward/ Outward Flow	Local (regionally averaged)

significant change of heat transfer and depends strongly on the flow direction (radially inward or radially outward flow).

Meanwhile, studies on the combined effects of Coriolis and buoyancy forces in smooth rotating channels start to emerge, such as Mori et al. (1971), Morris and Ayhan (1982), Lokai and Gunchenko (1979), Clifford et al. (1984), Iskakov and Trushin (1983) Guidez (1989), etc. Several of them found that the combined effects would increase the heat transfer coefficient, but others found the opposite results. This may be caused by different experimental techniques used and different test conditions. These differences have been further confirmed by Wagner et al. (1992). They experimentally determined the influences of heat transfer in rotating multipass on the buoyancy and Coriolis effects. It was found that, for radially outward flow,

the heat transfer coefficient on the trailing side is increasing with the rotating speed. On the other hand, it decreases with rotating speed increase on the leading surface. During their experiments, the angle of attack of the ribs was 90 deg. Later, they did the same experiments but with the angle of attack of 45 deg. The same results were found except that for smaller buoyancy effects.

Recently, Yang et al. (1992) experimentally studied the heat transfer characteristics in a four-passage smooth duct and, more recently, Zhang et al. (1995) and Han et al. (1993) conducted several experiments for two passages in roughened channels. Despite the differences of the number of flow passages and surface geometry, they all reached the same results as Wagner and Johnson, which is different from that of Hsieh and Hong

———— Nomenclature ————

A = projected area
AR = channel aspect ratio = H/W
C_0 = discharge coefficient
C_p = specific heat at constant pressure
D_H = hydraulic diameter = $2WH/(W + H)$
e = rib height
G = mass flow rate
H = height of channel
h = heat transfer coefficient
k_f = thermal conductivity of air at film temperature
L = test channel length
Nu = regionally averaged Nusselt number = hD_H/k_f
Nu_0 = fully developed Nusselt number
$Nu_{r,r}$, $Nu_{r,s}$ = regionally averaged Nu on ribbed wall with/without rotation, respectively

p = pitch
$q_{l,t}$ = local heating boundary conditions
Q_t = the total power input to the test section
$\bar{R}$ = midspan eccentricity (300 mm)
Ra_Ω = rotational Rayleigh number = $\beta\Delta T_m\bar{R}(Re\ Ro)^2\ Pr/k_f$
Re_H = Reynolds number = UD_H/ν
Re_Ω = rotational Reynolds number = $\Omega D_H^2/\nu$
Ro = rotation number = Re_Ω/Re_H $(= \Omega D_H/U)$
T = local temperature
T_{bi} = bulk temperature at inlet
T_{bx} = local bulk temperature
T_f = film temperature = $(T_w + T_{bx})/2$
T_w = local wall temperature
T_0 = free-stream temperature
U = mean channel velocity/ throughflow velocity

W = width of channel
x = downstream distance
β = coefficient of thermal expansion and model orientation
$\Delta T = T_w - T_{bi}$
ΔT_m = used in calculation of Ra, which was chosen at an average of inlet and exit fluid bulk temperature differences for all the rotational speeds under study
$(\Delta\rho/\rho)_i$ = density ratio based on the inlet bulk temperature
ν = kinematic viscosity of air
Ω = rotational speed

Subscripts

0 = free stream/discharge
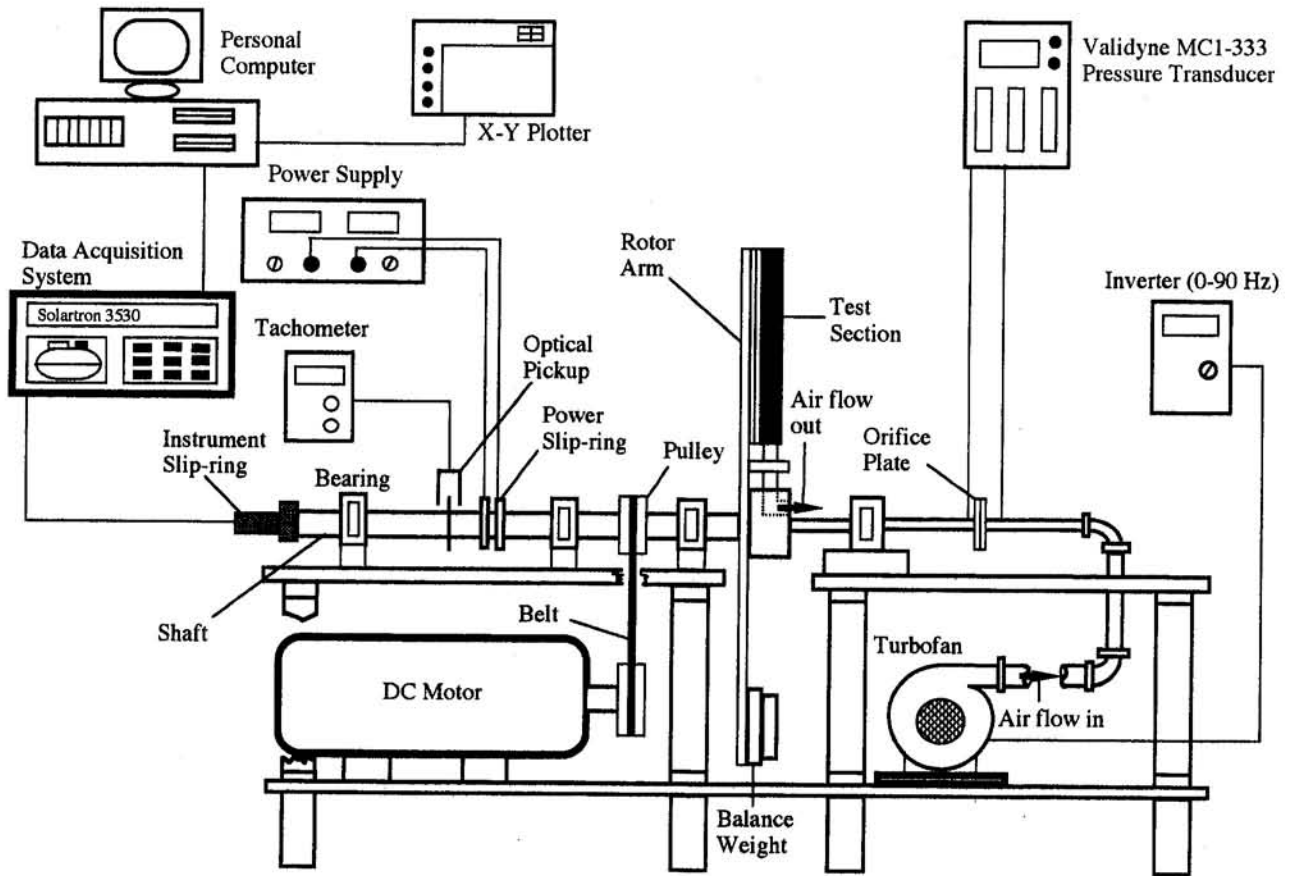t = total
w = wall
Ω = rotational

Fig. 1 Experimental setup and instrumentation details (side view)
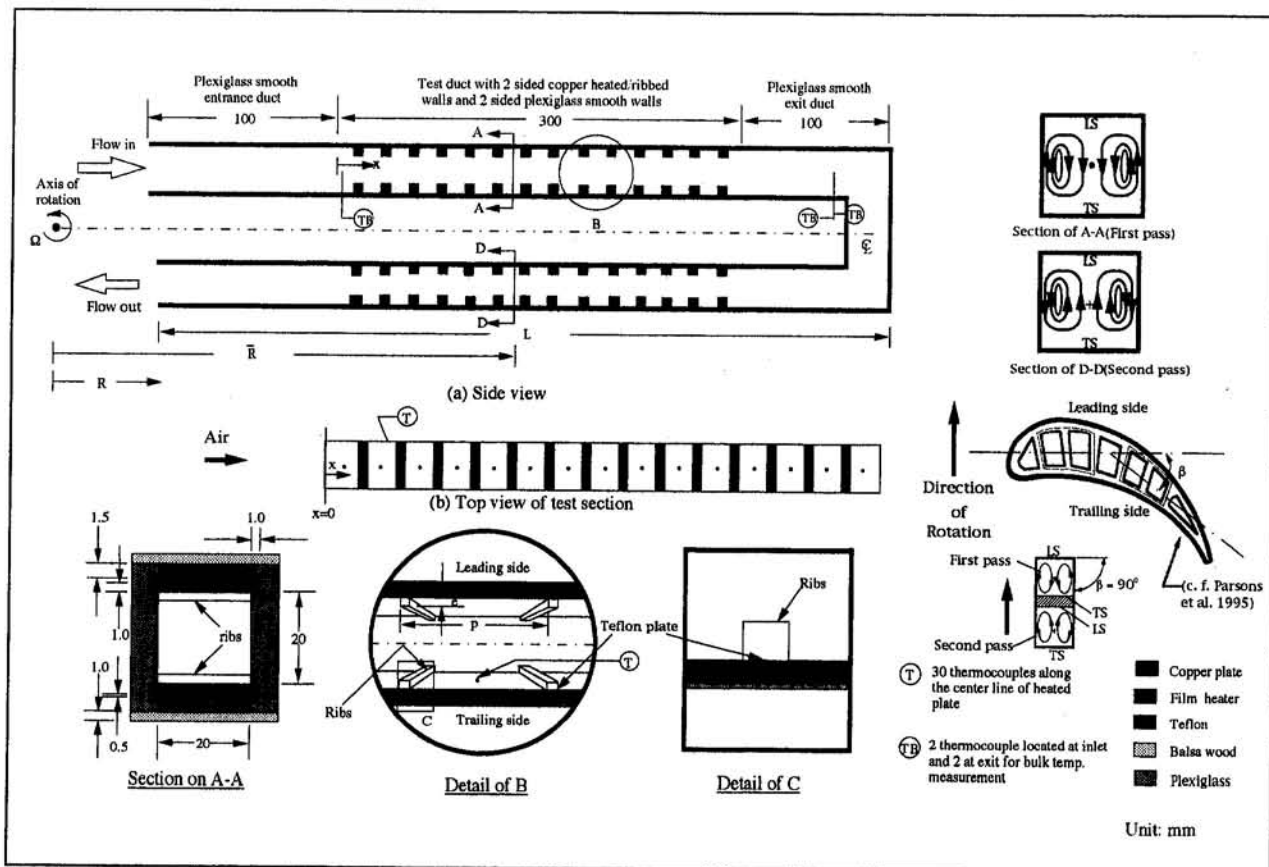

Fig. 2 Detailed thermocouple measurement position and dimensions of the test section ($AR = 1$)

Table 2 Rib geometries and operating conditions in the channel under study*

geometries	p/e	W (mm)	H (mm)	AR	D_H (mm)	e/D_H
	5	20	20	1	20	0.20
			30	1.5	24	0.17

relavent parameters	Re_H	Re_Ω	Ra_Ω	Ro
	5000 -25000	0 -3076	$0 - 1.1 \times 10^9$	0 -0.6152

boundary conditions	First pass		Second pass	
	q_ℓ (leading)	q_t (trailing)	q_ℓ (leading)	q_t (trailing)
	1860W/m² (case 1) 7440W/m² (case 2)	7440W/m² (case 1) 1860W/m² (case 2)	1860W/m² (case 1) 7440W/m² (case 2)	7440W/m² (case 1) 1860W/m² (case 2)

* corresponding dimensions shown in Figure 2

(1995) for a single passage. Both trailing and leading surfaces heat transfer coefficients were found to be increased. This may be caused by different geometric configurations of the test channels (e.g., rectangular and square ducts) which needs further confirmation. Later, Parsons et al. (1994) experimentally studied the uneven wall temperature effect on heat transfer in a rotating two pass ducts. Most recently, Parsons et al. (1995) experimentally studied the effect of model orientation ($\beta = 0$ and 45 deg) and wall heating condition on local heat transfer in a rotating two-pass square channel with rib turbulators. Table 1 lists the relevant previous experimental investigations on heat transfer in rotating channels.

1.2 Scope and Objectives. This paper is a continuation of work by Hsieh and Hong (1995) on a single passage with isoflux heating. The test section is expanded to two passages with uneven heat flux effect on heat transfer characteristics. The objectives for the study are further examination of the different buoyancy effects induced by inward and outward flows, and the complicated mixing effect with Coriolis force on heat transfer during the rotation. Besides, the present two-pass model is more realistic compared to that of a single passage reported by Hsieh and Hong (1995).

Moreover, the change of boundary conditions from constant heat flux to uneven heat flux is to meet practical needs (more realistic) and to further verify the phenomena of heat transfer

Table 3 Typical nondimensional interval for the relevant variables

Variables		Uncertainty
Specific heat of air	C_p	± 3%
Hydraulic diameter of flow pass	D_H	±0.5%
Air flow rate	G	±5.2%
Thermal conductivity of air	k	± 3%
Temperature	T	±0.5°C
Rotational speed	Ω	±1%
Reynolds number	Re_H	±6.9%
Rotational Reynolds number	Re_Ω	±2.5%
Local Nusselt number	Nu	±13.6%

in the first passage of the previous study, which resulted in different results with other investigators due to different geometric configurations of the test channels.

With different boundary conditions on leading/trailing surfaces in the present study, one may get a clearer picture regarding the heat transfer behavior and flow phenomena than before. The main controlled parameters are wall heat flux, rotation number, Reynolds numbers, and cross-sectional aspect ratios.

2 Experimental Apparatus and Procedure

The present test facility is similar to that used by Hsieh and Hong (1995) with a slight modification in heating element design and flow passage, which is schematically shown in Fig. 1. The facility comprised a heat section, a blower, a motor, a heat source, two slip ring assemblies, and a datalogger. The test section consisted of a ribbed two-pass serpentine flow channel with 2.0 × 2.0 cm square and 2.0 × 3.0 cm rectangular cross-sectional channels, respectively, mounted on a shaft supported by two bearings. The rotating shaft speed is measured by a digital photo tachometer. The air used for the test fluid was blown through the test section via a rotating seal assembly in the radially outward direction with a 2 kW centrifugal blower. A 34.0-mm-dia pipe, equipped with a 17.0-mm-dia orifice plate ($C_0 = 0.66$), was used to measure mass flow rate. After passing through the orifice plate, the air enters the plenum cylinder in the hollow shaft and it flows through the straightener fixed in the interior of the shaft to eliminate the initial swirl before entering the square duct. The Reynolds numbers based on the channel hydraulic diameter (D_H) ranged from 5000 to 25,000.

To determine the locally averaged streamwise heat transfer coefficients in the channel along the flow direction, the two-pass test flow channel is divided into 15 sheet copper sections (Zhang et al., 1995) (see Fig. 2 for details). Each copper section is composed of two copper plates (23 × 19 × 3 mm each) with two other sides made of plexiglass, with has an inner cross section of 20 mm by 20 mm. The Teflon strips are machined along the periphery contact surface between copper section for insulation to prevent possible heat conduction. The ratio of channel length to hydraulic diameter (L/D_H) is 34, which gives that ratio for each pass of 17. The ratio of the mean rotating arm radius to the channel hydraulic diameter is 30. The rib is oppositely positioned on two walls of the square test channel. The rib height-to-hydraulic diameter ratio (e/D_H) is 0.2. The rib pitch-to-height ratio (p/e) is 5 and the angle between the rib and coolant flow direction equals 90 deg. The aspect ratios

Table 4 Values of relevant parameters performed in the study

Re_H (Ra_Ω)	\\ Ro \\ AR \\ Re_H (Ra_Ω) — Ro AR=1				AR=1.5			
	534 (3.3×10⁷)	1068 (1.3×10⁸)	1602 (2.9×10⁸)	2136 (5.1×10⁸)	769 (7.0×10⁷)	1538 (2.8×10⁸)	2307 (6.2×10⁸)	3076 (1.1×10⁹)
5000	0.1068	0.2136	0.3204	<u>0.4272</u>	0.1538	0.3076	0.4614	<u>0.6152</u>
10000	0.0534	0.1068	0.1602	0.2136	0.0769	0.1538	0.2307	0.3076
15000	0.0356	0.0712	0.1068	0.1424	0.0513	0.1025	0.1538	0.2051
20000	0.0267	0.0534	0.0801	0.1068	0.0385	0.0769	0.11535	0.1538
25000	<u>0.0214</u>	0.04272	0.06408	0.0854	<u>0.0308</u>	0.06152	0.09228	0.1230

$q_{\ell}/q_t = 0.25$(case 1) and $q_{\ell}/q_t = 4$(case 2)
Underlined values indicate the maximums / minimums

are 1 and 1.5. The ribbed leading and trailing surface were made by gluing plexiglass ribs (each $20 \times 4 \times 4$ mm), which are different from those in real engines with low thermoconductivity, in between two copper plates to the plexiglass square channel on opposite walls in a required manner. Each wall has its own thin film (1 mm) resistance heater powered by a variac

transformer for controlled heat fluxes. The power to each element was adjust to obtain an uneven heating condition on each leading/and trailing wall. The smooth side walls are insulated from the leading and trailing walls to minimize heat looses to the environment. The entire heated section is insulated by 2-mm-thick styrofoam. The local wall temperature of the test
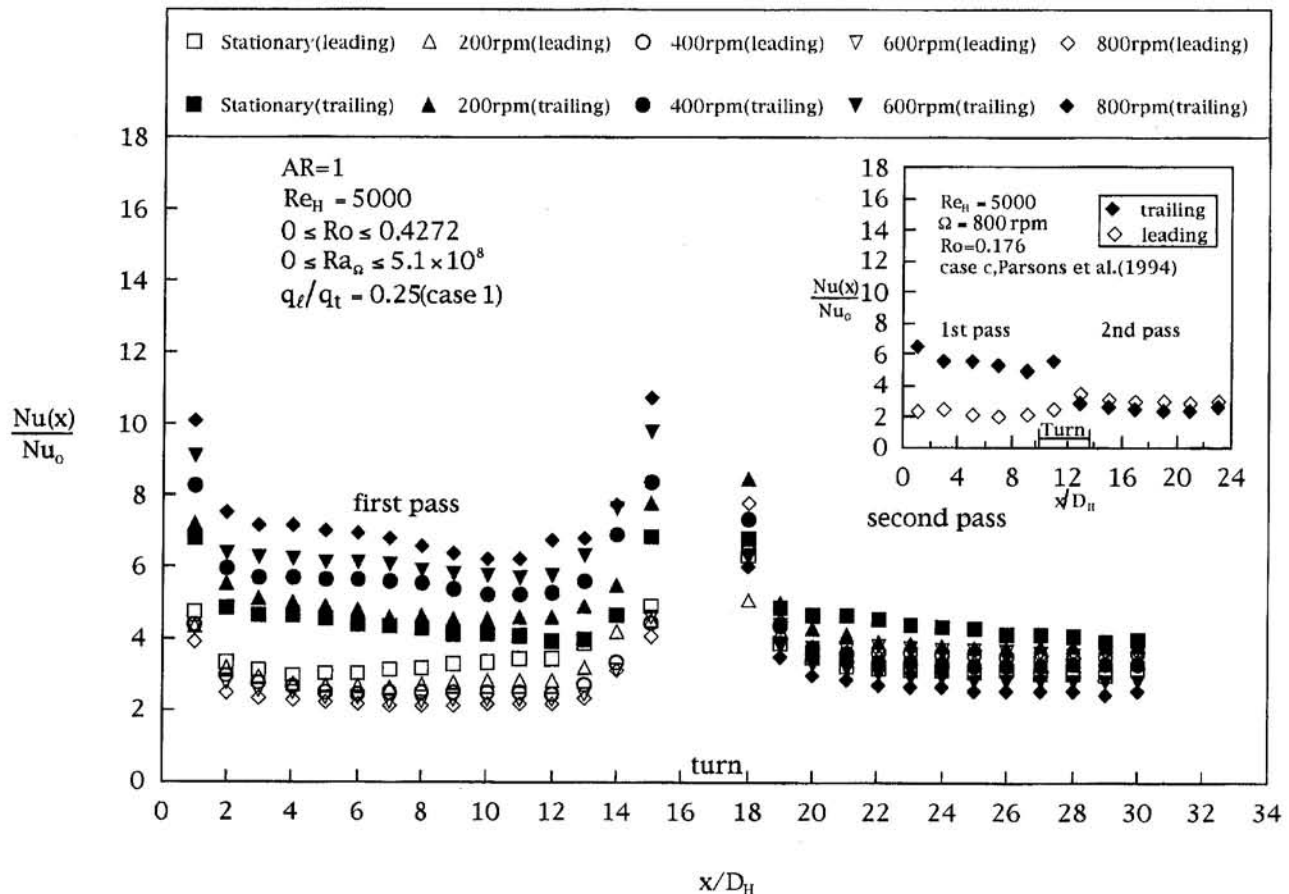
Fig. 3 Effect of rotation on Nusselt number ratio ($q_l/q_t = 0.25$)

section is measured by 30 AWG40 copper-constantan thermocouples distributed along the downstream flow direction and around the perimeter of copper test section. Two more thermocouples measure the inlet and outlet bulk air temperature. There is an unheated plexiglass entrance duct that has the same cross section and length ($x/D_H \approx 5$) shorter than that of the test duct. A Schlumberger Solartron 3530 datalogger was interfaced with an IBM PC/AT for data acquisition.

Experimental data were taken on the leading and trailing surfaces of the test section in both rotating and stationary channels. Rotational speeds of 200, 400, 600, and 800 rpm were set in either the counterclockwise or clockwise direction. The test channel geometry and operating conditions are listed in Table 2.

3 Data Reduction and Uncertainty Analysis

One of the main goals is to analyze the local (regionally averaged) heat transfer phenomenon on both leading and trailing surfaces. The heat transfer quantitative analysis is done by Nusselt number. In order to determine the local (regionally averaged) Nusselt number, it is necessary to obtain the axial variation of heat flux from the passage wall and the difference between the wall temperature and the bulk mean temperature of the coolant. To get the local Nusselt number, one uses the equation $h(x) = Q_{net}/[A(T_w - T_{bx})]$, where $h(x)$ is the local heat transfer coefficient, (Q_{net}/A) is the local heat transfer rate per unit area from the wall to the cooling air, (T_w) is the local wall temperature of the plate, and (T_{bx}) is the bulk mean air temperature. The surface area is the projection area not including the surface of the rib. The electrical power generated from the heater is determined from the measured heater resistance and voltage on each wall of the test duct. The effect of axial wall conduction between copper sections on the local net heat transfer rate is less than 3.2 percent, which is also included in the data analysis.

The value of (T_{bx}) is obtained by energy balance, and defined as $T_{bx} = T_0 + \Sigma Q_{net}/(GC_p)$, where ΣQ_{net} is the summation of net heat given to the air from the entrance (about 26°C) to a specified position along the downstream distance. Heat loss measurements were obtained with no coolant flow and constant electrical power supplied under steady-state conditions with rotation, identical to the heat transfer Q_{net} experiments, but without coolant flow. The heat loss to the outside of the test channel ranged from 13 to 24 percent of the total heat supplied for stationary heat transfer levels. The local Nusselt number was calculated by $Nu = h(x)D_H/k_f$ where k_f is the thermal conductivity of air. The local Nusselt number, normalized by the Nusselt number for a stationary fully developed turbulent flow in a smooth circular tube, is correlated by Dittus-Boelter/McAdams (Rohsenow and Choi, 1961) as:

$$Nu/Nu_0 = (hD_H/k)/[0.023\ Re^{0.8}\ Pr^{0.4}] \tag{1}$$

with $Pr = 0.7$. The uncertainty in temperature measurement is estimated to be $\pm 0.5°C$. The maximum nondimensional uncertainty intervals for the variables concerned in this study are estimated and given in Table 3.

4 Results and Discussion

The convective heat transfer performance inside of a rotating two-pass roughened channel is governed by the ratio of the rotating mean radius to channel hydraulic diameter, Reynolds number, Prandtl number, rotation number, rotational Rayleigh number, channel aspect ratio, wall to fluid density difference ratio, flow direction (radial outward flow/or radial inward flow), and rib geometry and size. In other words,

Fig. 4 Effect of rotation on Nusselt number ratio ($q_l/q_t = 0.25$)
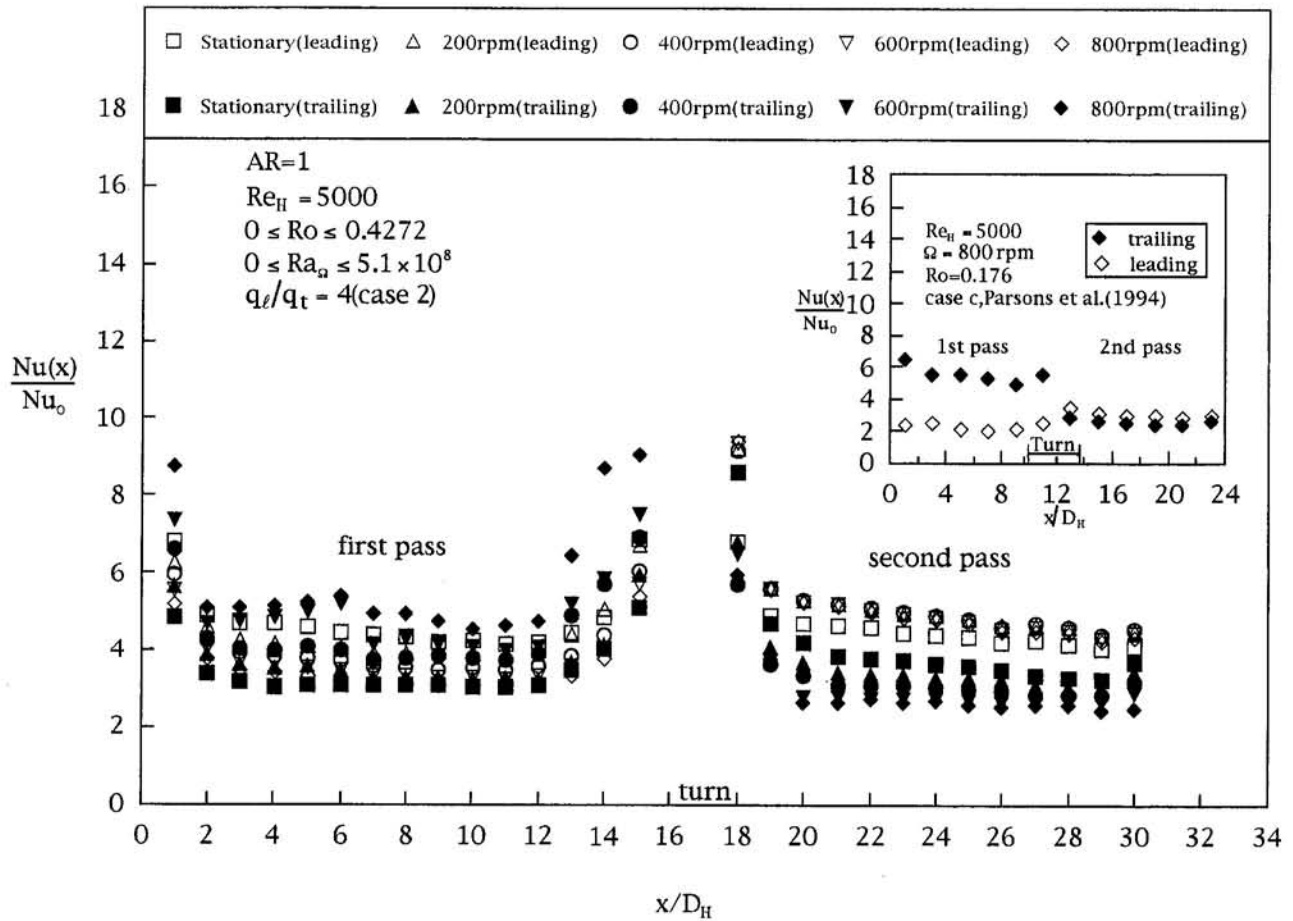
Fig. 5 Effect of rotation on Nusselt number ratio ($q_l/q_t = 4$)
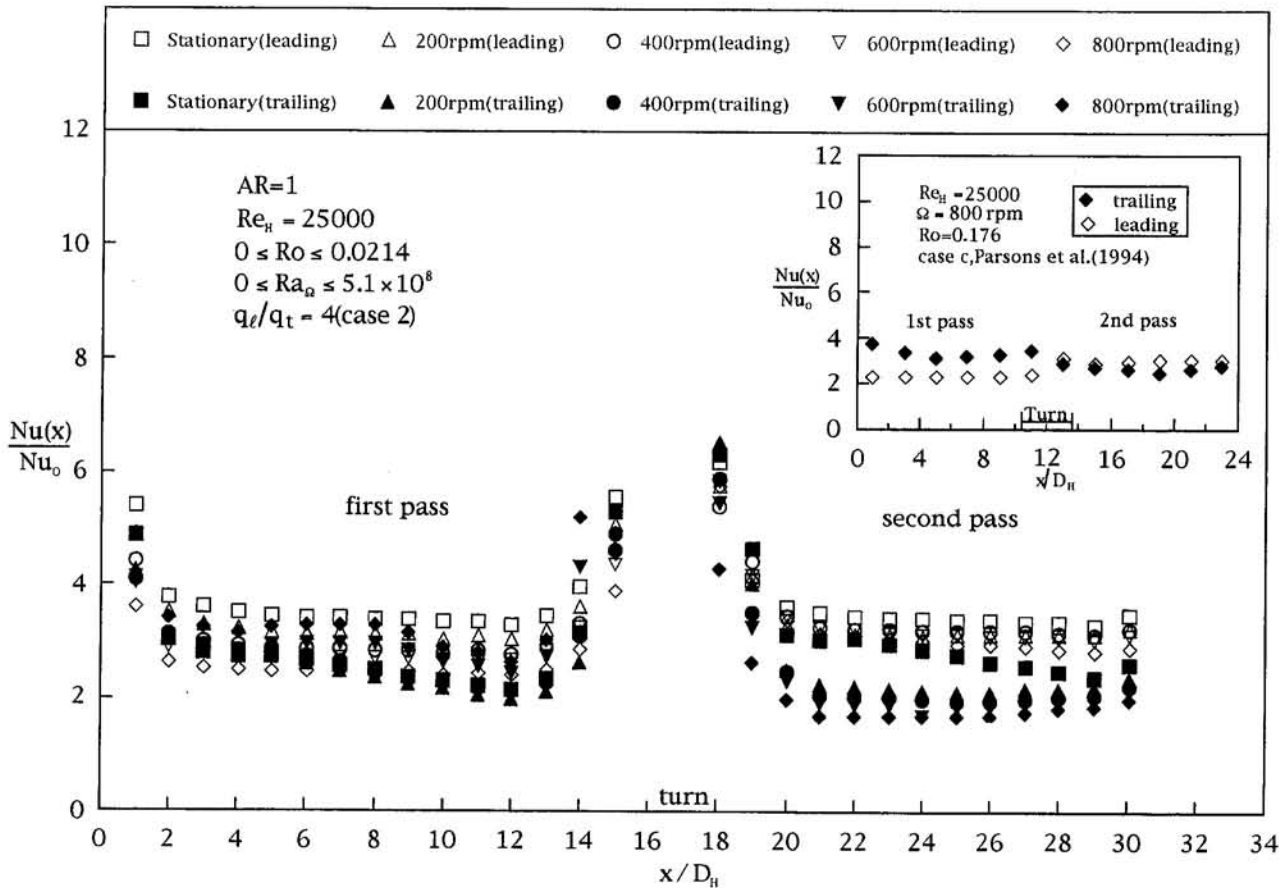
Fig. 6 Effect of rotation on Nusselt number ratio ($q_l/q_t = 4$)
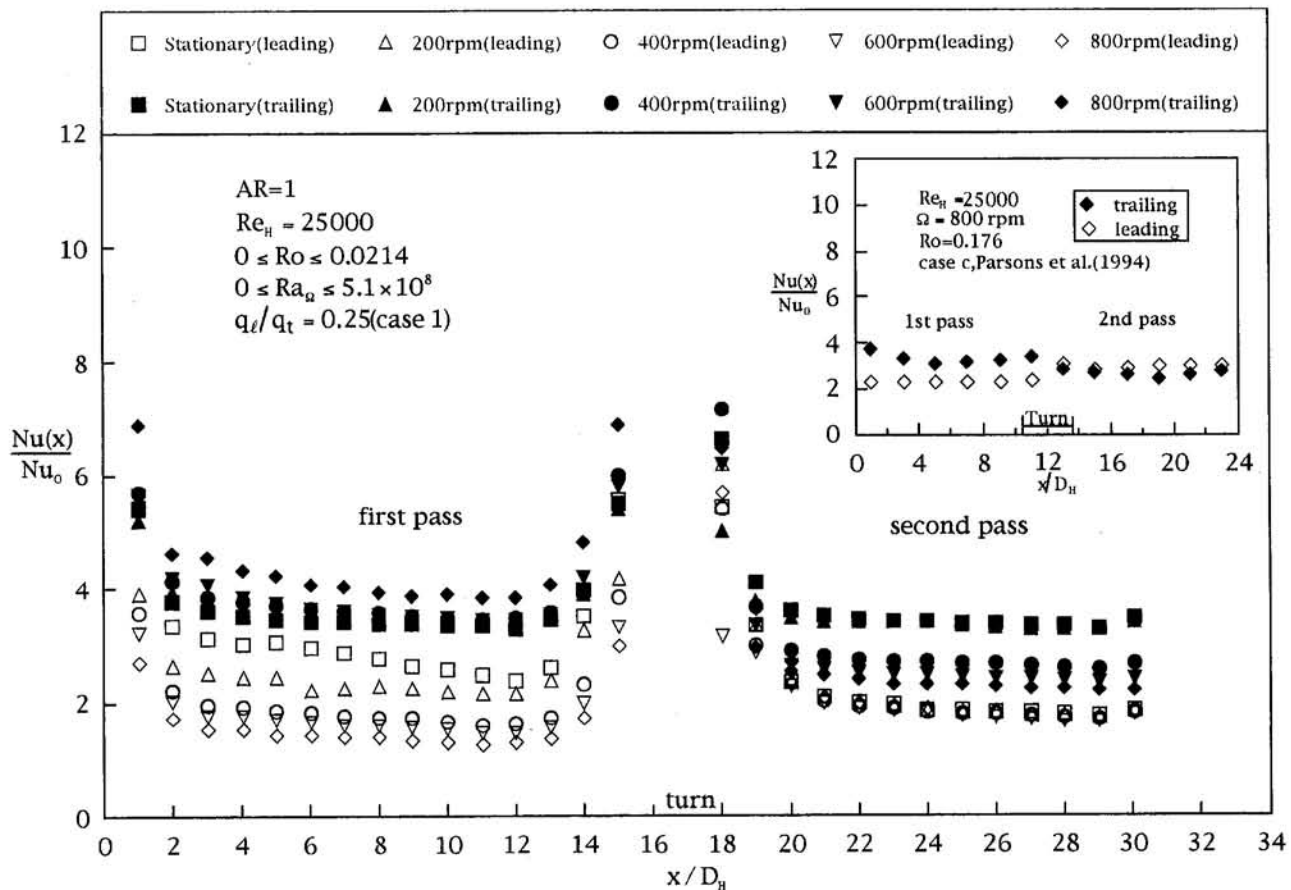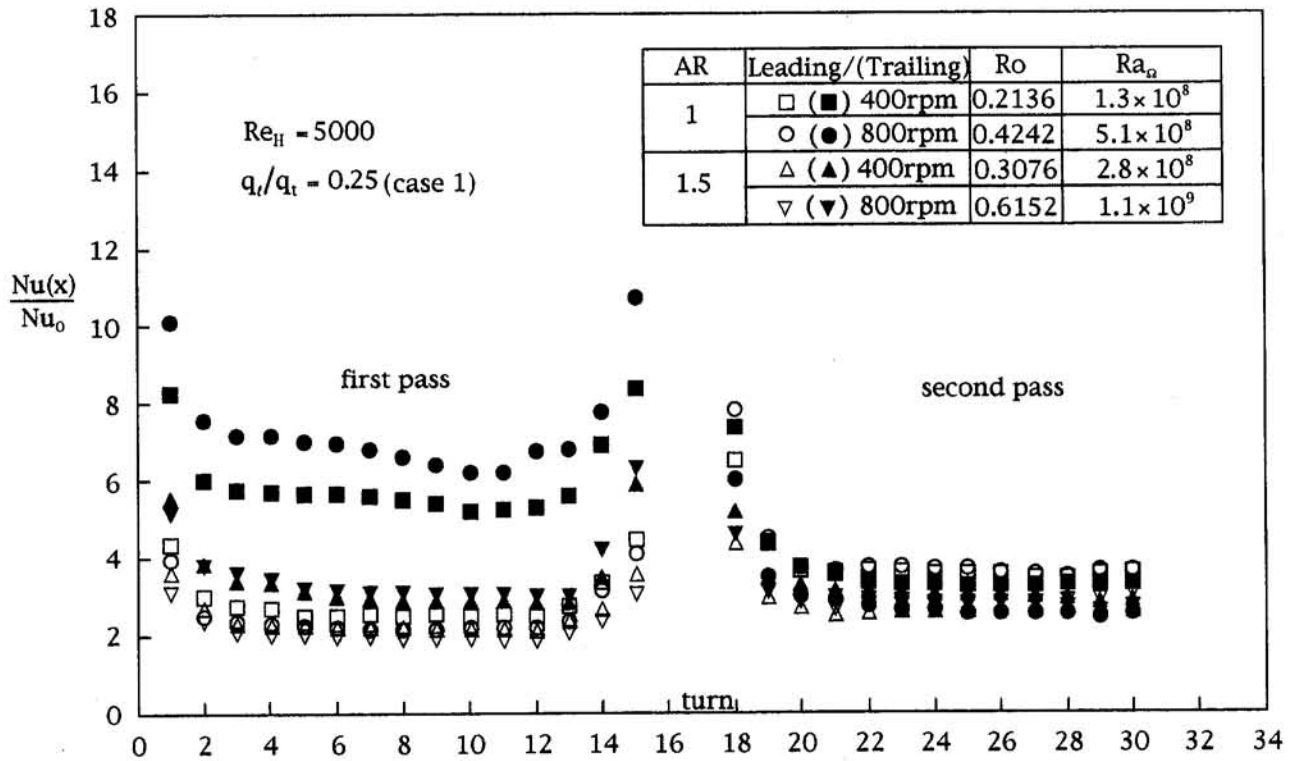
Fig. 7   Effect of aspect ratio on Nusselt number ratio
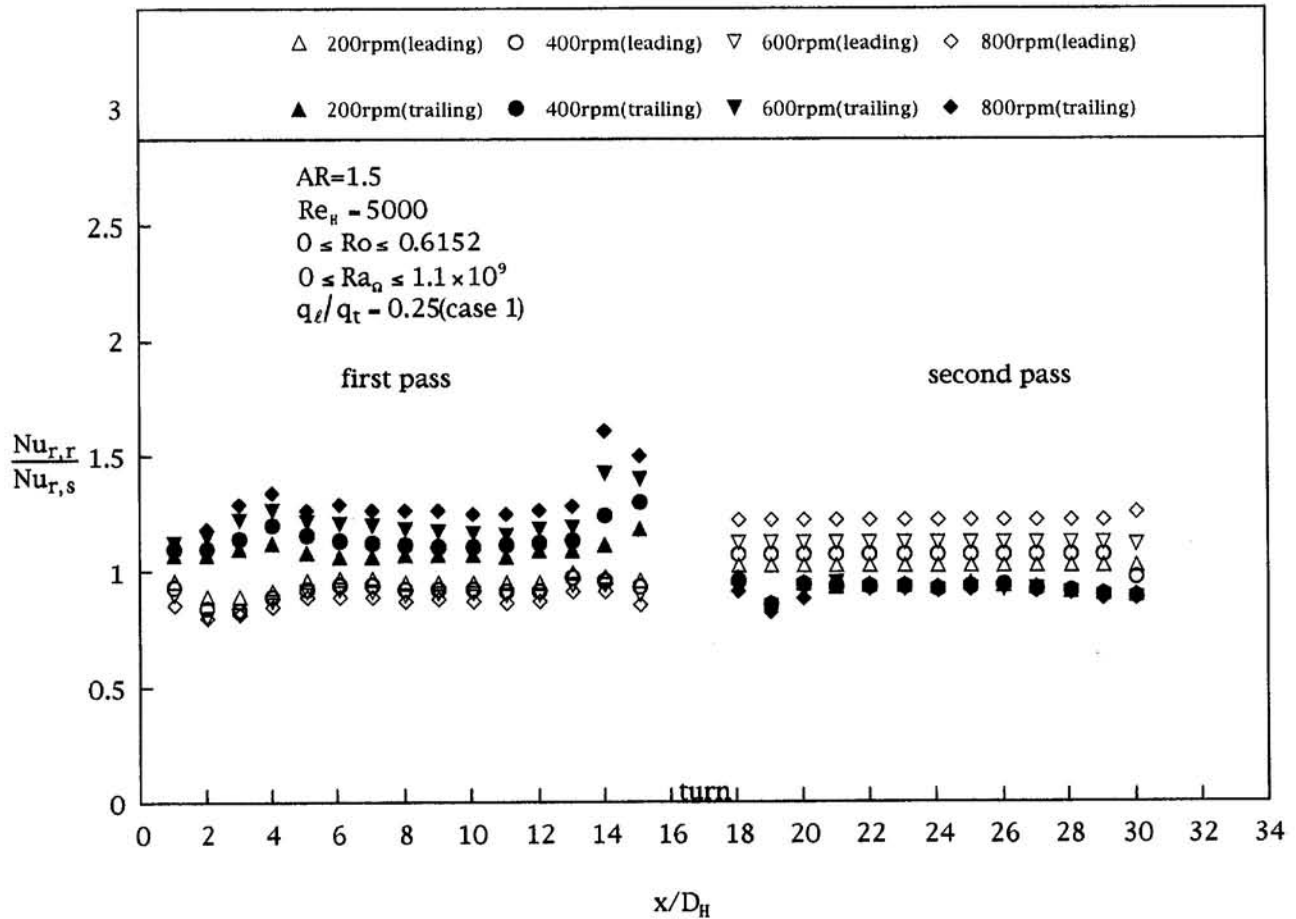
Fig. 8 $Nu_{r,r}/Nu_{r,s}$ versus x/D_H for $Re_H = 5000$ ($q_l/q_t = 0.25$, $AR = 1.5$)
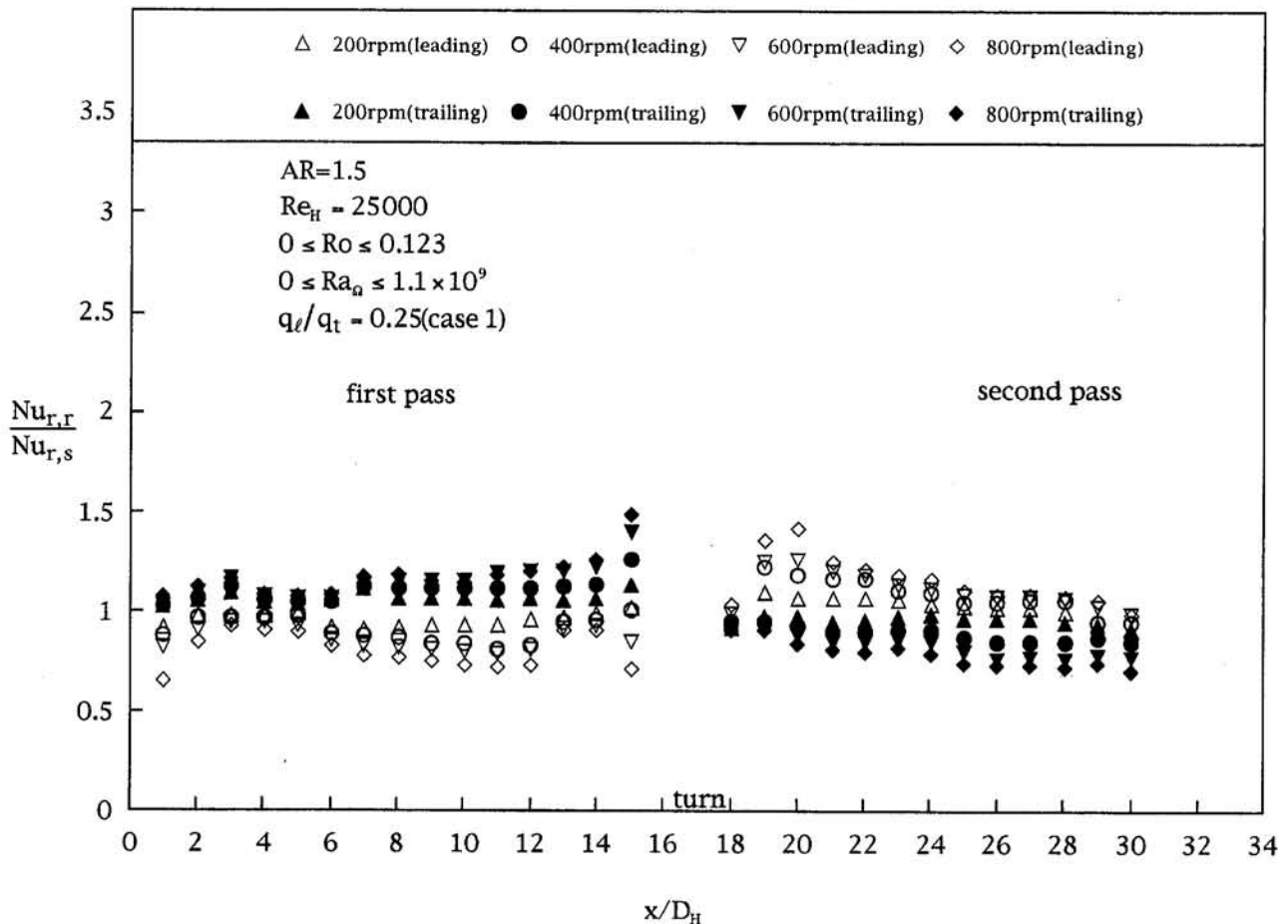
Fig. 9 $Nu_{r,r}/Nu_{r,s}$ versus x/D_H for $Re_H = 25{,}000$ ($q_l/q_t = 0.25$, $AR = 1.5$)

$$Nu = f\left(\frac{\bar{R}}{D_H}, \frac{x}{D_H}, Re_H, Pr, \Delta\rho/\rho, AR,\right.$$

$$\left. \text{flow direction, rib geometry}\right) \quad (2)$$

where, for the present study, both $\bar{R}/D_H = 13.5$ (40–80 in real engines) and $Pr = 0.7$ are fixed and rib geometry and size are specified. The fluid flow rate, heating rate, rotational speed of the rotor, and cross-sectional aspect ratio were varied to produce various values of Re_H, Ro, AR, and $(\Delta\rho/\rho)_i$. Table 4 lists detailed values of these parameters tested. The results for minimum/maximum values of Ro are presented and discussed.

4.1 Effect of Rotation and Uneven Heating Condition. Since the duct is short, and fully developed flow is not attained, the local (regionally averaged) heat transfer results are presented as the axial distributions of a normalized Nusselt number ratio. Figures 3 and 4 show the effect of rotation for case 1 wall heating condition on the local Nusselt number ratio (Nu/Nu_0) on the leading and trailing walls. In Fig. 3 for $Ro = 0$ and 0.4272 at $Re_H = 5000$, local Nusselt number ratios for the ribbed leading and trailing walls are fairly uniform similar to those of Parsons et al. (1994) for nonrotation (approximately 3–6) throughout the two-pass test channel ($AR = 1$) except for the sharp entrances near the inlet of the first/second pass. Generally, the stationary heat transfer ratio for the present ribs is about 2.5–3, which is a little bit higher than the value of 2 reported in earlier works. This may be due to heat losses from two unheated sides. This part was not corrected for the calculations of Nu values. In the first outflow pass ($0 < x/D_H < 15$),

the local Nusselt number ratios for the trailing wall increase while the Nusselt number ratios for the leading wall decrease relative to their corresponding nonrotating values as Ro increases from 0 to 0.4272. The reverse holds in the second inflow pass ($18 < x/D_H < 30$). This is because rotation induces the Coriolis forces that produce secondary cross-stream flows and it makes the first outflow pass trailing and second inflow pass leading boundary layer become thinner. Simultaneously, it also thickens the first pass leading and the second pass trailing boundary layers. Due to such thinning or thickening of the boundary layers, the heat transfer coefficients for the first pass trailing and second pass leading walls are higher with rotation than those without. This increase is also attributed to the following three reasons based on Prakash and Zerke (1992):

(i) The Coriolis-induced secondary flow transports cooler (heavier) fluid from the core to the trailing surface, which increases the temperature gradient at the wall.

(ii) The secondary flow also transports the higher momentum fluid from the core to the trailing surface, whereby the through velocity, and hence the convective effects, are enhanced.

(iii) The increase in the throughflow velocity near the trailing surface leads to a higher velocity gradient and, thereby, a higher level of turbulent kinetic energy.

On the other hand, the heat transfer coefficients for the first pass leading and second pass trailing walls are lower with rotation than those without. The decrease in heat transfer at the leading (first pass)/trailing (second pass) surfaces due to rotation can be explained by the reverse of the reasons listed earlier. This phenomenon is reduced as Ro decreases. The findings above coincided

well with those reported by Parsons et al. (1994) also shown in Figs. 3 and 4 for the corresponding cases. However, the present results exhibit local peak values of $Nu(x)/Nu_0$ at $x/D_H \approx 1$ and 15 in first pass and $x/D_H \approx 18$ in second pass, respectively, which is different from Parsons et al. (1994). This is perhaps partly due to the present uneven boundary conditions (case 1) and is perhaps partly due to the combination of buoyancy forces and the stabilization of the near-wall flow for low Ro as well as the developing, Coriolis-driven secondary flow for higher Ro. Besides, the effect of the present uneven wall heating condition seems not noted. Moreover, the enhanced effect in the present study is a little bit higher than those in Parsons et al. due to the present higher Ro (0.0214 to 0.4272) and a higher e/D_H (≈ 0.20), which is also shown in Figs. 3 and 4.

The magnitude of local Nusselt number ratio differences on the leading/trailing walls are further found to be smaller in the second pass. This is, following Parsons et al. (1994), because the rotation-induced centrifugal buoyancy force assists the inertia force in the first pass and opposes the inertia force in the second pass, with the result that throughflow velocity and Coriolis force effect are both reduced in the second pass as compared to the first pass. This situation can be clearly noted in Fig. 3 for the second pass for the data points being closely packed together relative to those correspondings in the first pass. This again confirms the findings reported in Parsons et al. (1994).

A comparison of Figs. 3 and 4 reveals the effect of flow rate on local heat transfer performance. It is found that decrease in Re_H raises but preserves the shape of the Nu/Nu_0 versus x/D_H curve without rotation as one would expect. In Fig. 3, at Ro = 0.4272, the local Nusselt number ratios for the first pass trailing wall are higher than those at Ro = 0.0214 in Fig. 4. However, for the leading wall, the opposite trends hold. All these findings are reversed in the second pass. In brevity, the magnitude of difference between the leading and trailing Nusselt number ratios in both passes increases with Ro from 0.0214 to 0.4272. Similar behavior is shown in Figs. 5 and 6, but the order of magnitude of Nu/Nu_0 is a little lower than the corresponding values in Figs. 3 and 4, because $q_l/q_t = 4$ in Figs. 5 and 6, while $q_l/q_t = 0.25$ in Figs. 3 and 4. This strongly indicates that the larger uneven heat flux ratio is the lower heat transfer enhancement exhibits. For case 2, in Figs. 5 and 6, the trailing surface temperature, being lower than the leading surface, can result in cooler fluid near the trailing surface. It is speculated that the cooler fluid is accelerated due to centrifugal buoyancy and so a thinner boundary layer is created near the trailing surface. Meanwhile, the secondary cross-stream flow carries the cooler fluid from trailing back to the leading surface due to the Coriolis force. This cooler fluid causes a sharp temperature distribution near the leading surface due to the centrifugal buoyancy force. Therefore, the difference in local Nu between the trailing and leading surface becomes smaller compared to those shown in Figs. 3 and 4. It is noted that the Nusselt numbers are different for the leading and the trailing walls, even for the stationary case, mainly due to the uneven heat flux imposed on these two walls, and the rest of the reasons may be due to the conduction between two heaters used in the present study.

The general trend in Figs. 3–6 is followed by an entrance decrease: decreasing Nu/Nu_0 with increasing x/D_H until a 180 deg turn is nearly reached. At this stage Nu/Nu_0 increases and peaks at the entrance of the turn with greatest Nu/Nu_0 at the trailing surface in the first pass. This significant enhancement in heat transfer is due to the presence of second flow due to rotation, resulting in a stronger centrifugal buoyancy in the 180 deg return bend. Again, the reverse is true in the second inflow pass.

4.2 Effect of Rotation, Aspect Ratio, and Uneven Heating Conditions. Figure 7 presents the results of the aspect ratio effect on Nusselt number ratio at $Re_H = 5000$ and $q_l/q_t = 0.25$ with Ro from 0.2136 to 0.6152. Generally speaking, the

general trend still holds as compared to those of Figs. 3 and 4. A comparison between the present data for an aspect ratio of unity and 1.5, both for $e/D_H \approx 0.2$, indicates a slight decrease in heat transfer coefficient for an increase in passage aspect ratio. Unlike the results shown in Figs. 3 and 4, an aspect ratio of 1 shows less sensitivity to the Ro in general, and the variation of local Nusselt number with Ro is not as pronounced. This behavior may be due to the relative space between turbulated/roughened walls, especially for $AR = 1.5$ with a lower e/D_H, inadequate for the flow to separate from the leading surface and push against the trailing surface. Consequently, it reduces the throughflow velocity, the velocity gradients, turbulent kinetic energy, and hence, convection is weaker. Moreover, buoyancy also reduces the throughflow velocity of the warmer (lighter) fluid near the leading surface where the decrease in heat transfer is greater for a higher Ra_Ω, especially in first pass. This can be seen from Fig. 7 as compared to the corresponding Fig. 3. Unlike Fig. 3, the results of leading/trailing surfaces in the second pass become closer with rotation. The reasons remain unknown at this stage. Further study in this aspect may be needed. Detailed and extensive results of the rotation effect can be clearly found by taking a close-up examination of Figs. 8 and 9 for $AR = 1.5$ at $Re_H = 5000$ and $25,000$ and $q_l/q_t = 0.25$, in which the effects of enhancement due to ribs and that due to rotation are separated.

As discussed above, the convective heat transfer coefficients on the leading and trailing surfaces of a rotating channel with radial outward/inward flow can be affected by the Coriolis force
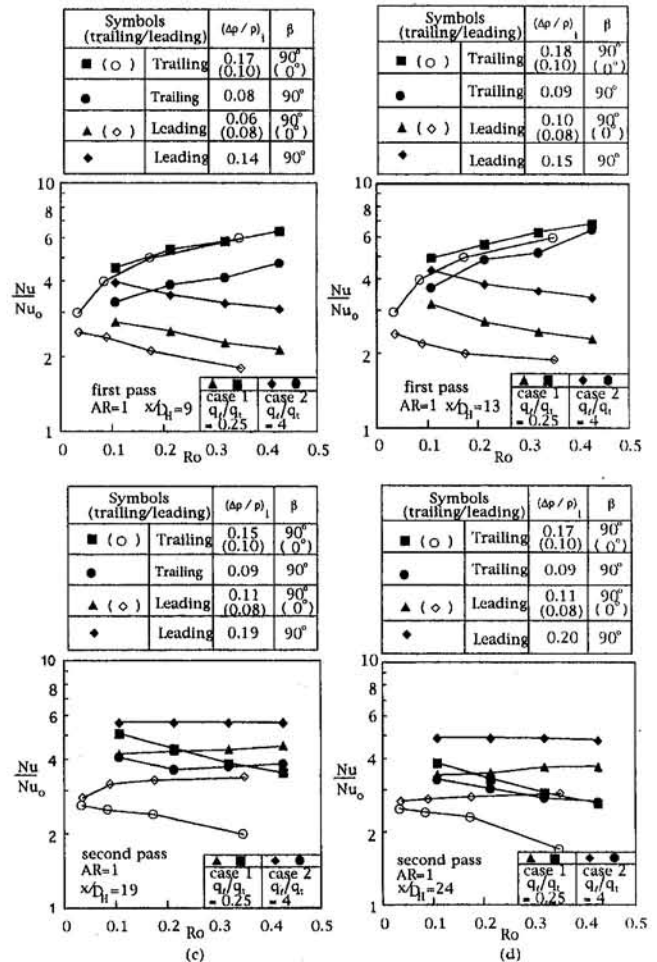

Fig. 10 Effect of rotation number on Nusselt number ratio (the values inside the parentheses are from Parsons et al. (1994); closed symbols: present study; open symbols: Parsons et al. (1994))
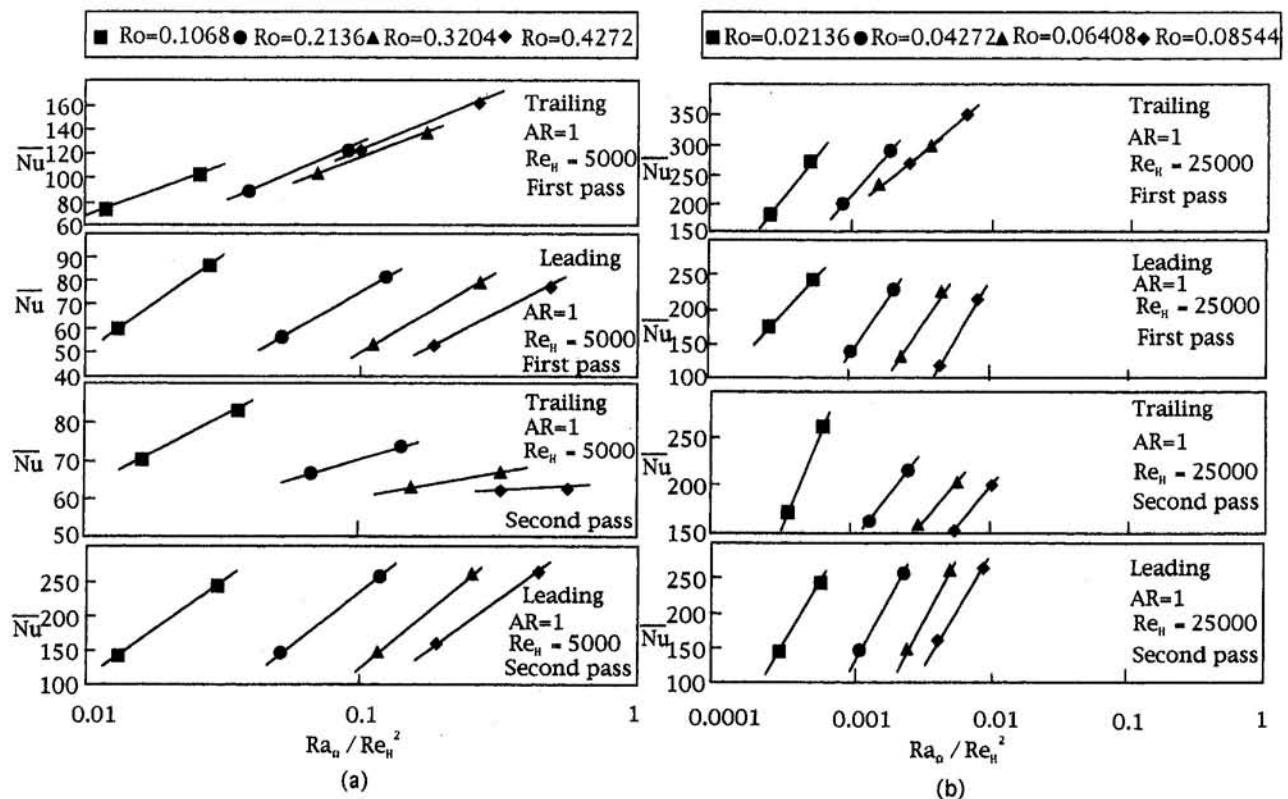
Fig. 11 Centrifugal buoyancy effect on Nusselt number (AR = 1)

(rotation number) and the surface heating condition (centrifugal force). At two values of downstream location ($x/D_H = 9$ and 13), Fig. 10 shows the variation of local Nusselt number with Ro. The effect of the Coriolis force on the increases (decreases) of the Nusselt number ratios for the first pass trailing and second pass leading/first pass leading and second pass trailing walls from nonrotating channels is clearly noted. The reasons have been explained previously in detail. The experimental results from Parsons et al. (1994) at $q_l/q_t = 4$ for the case of $(\Delta\rho/\rho)_i = 0.10$ and 0.08 at $x/D_H = 9$ and 13 are also included for comparison. The results show that the present Nusselt number ratio on the trailing and leading surface agrees with those of Parsons et al. except that the magnitude of the present study is a little bit higher than that of Parsons et al. This confirms that the trailing (leading) surface Nusselt number ratio increases (decreases) in first (second) pass with an increasing Ro. This is shown in Figs. 10(a) and 10(b), respectively. The difference may be caused by the following four reasons: (i) the orientation of the channel of the present study according to Parsons et al. (1995) is $\beta = 90$ deg (see Fig. 2 for details), (ii) a fully developed flow entrance for Parsons et al. versus a sharply developing flow of the present study, (iii) the present blockage ratio $e/D_H \approx 0.2$ is much higher than that of Parsons et al. ($e/D_H = 0.125$), and the pitch is also different ($p/e = 10$ for Parsons et al.), (iv) air density ratios of $(\Delta\rho/\rho)_i$ in Figs. 10(a) and 10(b) are different from Parsons et al. Figures 10(c) and (d) show the results in the second pass in which a lower local Nu was found, but the trend is similar to the corresponding Figs. 10(a) and 10(b) and even milder.

As previously discussed, the uneven surface heat flux on both the leading and trailing surfaces in the first pass creates a local imbalance of the force that alters the heat transfer coefficients. This unequal force serves to transport cooler (heavier) fluid from the core to the trailing surface. In comparison, the fluid near the leading surface is warmer (lighter) since it reached there after exchanging heat with the remaining walls. As a result

of such density variation, the centrifugal buoyancy is greater on the fluid near the trailing surface and smaller on the fluid near the leading surface. Consequently, due to an unequal force, the throughflow velocity of the fluid is increased near the trailing surface and decreased near the leading surface. The reverse trend is true in the second pass. For small air density ratios (e.g., 0.06) and small Ro, the centrifugal buoyancy effect is small. However, for high density ratios (e.g., 0.18) and high Ro, the centrifugal buoyancy can be significant. This was further verified in Fig. 10.

4.3 Effect of Centrifugal Buoyancy and Uneven Heating Condition. When tests were conducted at a fixed Reynolds number (Re_H) and rotational speed, but with varying levels of wall-to-fluid bulk temperature difference, evidence of a buoyant interaction was noted. Figures 11 and 12 plotted the average Nusselt number against the quotient Ra_Ω/Re_H^2 for both $AR = 1$ and 1.5, respectively. The average Nusselt number ($\overline{Nu}$) on the leading/trailing surfaces is the average value of the entire leading/trailing surface local Nusselt number from $x/D_H \approx 1$ to $x/D_H \approx 15$ in the first pass and from $x/D_H \approx 18$ to $x/D_H \approx 30$ in the second pass. The quotient Ra_Ω/Re_H^2 is the local level of wall-to-fluid bulk temperature difference, representing the driving potential. It is found, generally, that an increase in average Nusselt number with increases in Ra_Ω/Re_H^2 occurred on both leading and trailing surfaces, which quite coincided with those from Morris and Ghavami-Nasr (1991) and Wagner et al. (1992), except for $Re_H = 5000$ and $Re_H = 25,000$ on trailing surfaces for $AR = 1.5$. A possible explanation is that as buoyancy increases the leading side heat transfer, Coriolis-induced secondary flow entrains this "hotter" fluid and deposits it on the trailing edge bringing about an accompanied reduction in heat transfer due to a mild temperature gradient; this situation did not occur for $AR = 1$. This effect is only noticeable for $AR = 1.5$ at $Re_H = 5000$ and 25,000. It was not found possible, because of data limitations for Ra_Ω/Re_H^2, to incorporate the
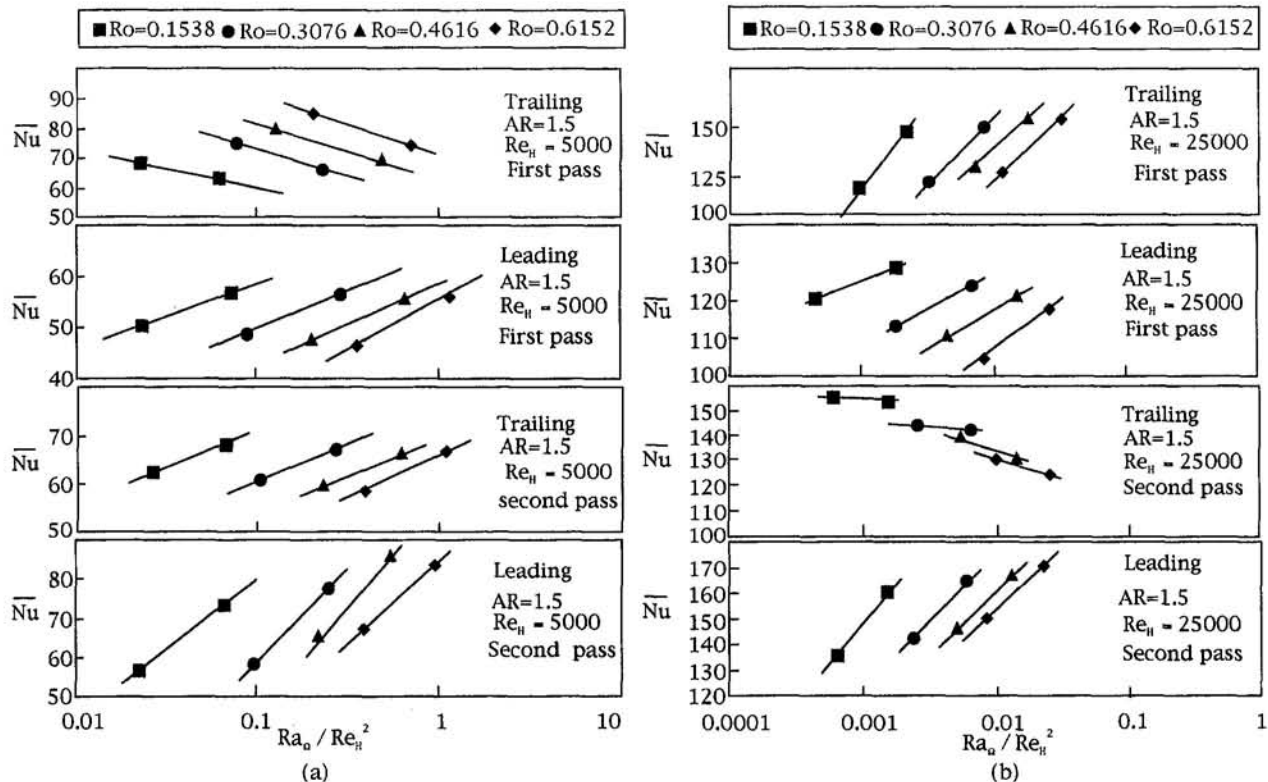
Fig. 12 Centrifugal buoyancy effect on Nusselt number ($AR = 1.5$)

buoyancy effect into the conventional correlating equations. Further data obtained with more values of Rayleigh number for centrifugal buoyancy are needed to quantify the effect of rotational buoyancy. Nevertheless, the present wall heating condition has a significant effect on centrifugal buoyancy, as indicated in Figs. 11 and 12.

5 Conclusions

The paper presents an extensive study of experimental data from heat transfer experiments in rotating two-pass rectangular oppositely rib-roughened channels with uneven heating walls. The analysis of these experimental results to determine the separate effects of forced convection, Coriolis, and buoyancy on the heat transfer has produced the following observations and conclusions:

1 The streamwise distribution of heat transfer in the first pass with rotation is similar to that of developing flow in the entrance region of a passage without rotation and is in good agreement with previous study result.

2 Local Nusselt number increases (decreases) with increases in density ratio over most of the passage surface area in radially outward (inward) flow.

3 For the first pass, increasing buoyancy causes an increase in heat transfer. Trailing surface heat transfer is usually higher than that on the leading surface due to the secondary flows. Increase in Ro causes an increase in the averaged Nusselt number, again due to a strengthening of the secondary flows.

4 For the second pass, increasing centrifugal buoyancy generally tends to increase the heat transfer further on the leading surface while reducing it on the trailing surface for $AR = 1.5$. This is attributed to a coupling between Coriolis-induced secondary flow and centrifugal buoyancy. An increase in Ro has a significant effect on heat transfer to the leading wall, which results in the Nu values of leading and trailing surfaces getting closer as the flow gets farther downstream.

5 Reconfirmation of the previous study of Hsieh and Hong (1995) for a single pass was made. It has been shown that the heat transfer characteristics in a two-pass channel are apparently different from those for a single pass.

References

Clifford, R. J., Morris, W. D., and Harasgama, S. P., 1984, "An Experimental Study of Local and Mean Heat Transfer in a Triangular-Sectioned Duct Rotating in the Orthogonal Mode," ASME *Journal of Engineering for Gas Turbines and Power*, Vol. 106, pp. 661–667.

Guidez, J., 1989, "Study of the Convective Heat Transfer in Rotating Coolant Channels," ASME *Journal of Turbomachinery*, Vol. 111, pp. 43–50.

Hart, J. E., 1971, "Instability and Secondary Motion in a Rotating Channel Flow," *J. Fluid Mech.*, Vol. 45, part 2, pp. 341–351.

Han, J. C., Zhang, Y. M., and Kalkuehler, K., 1993, "Uneven Wall Temperature Effect on Local Heat Transfer in a Rotating Two-Pass Square Channel With Smooth Walls," ASME JOURNAL OF HEAT TRANSFER, Vol. 115, pp. 912–920.

Hsieh, S. S., and Hong, Y. J., 1995, "Heat Transfer Coefficients in an Orthogonally Rotating Duct With Turbulators," ASME JOURNAL OF HEAT TRANSFER, Vol. 117, pp. 69–78.

Iskakov, K. M., and Trushin, V. A., 1983, "Influence of Rotation on Heat Transfer in a Turbine-Blade Radial Salt Channel," *Izvestiya VUZ. Aviatsionnaya Tekhnika*, Vol. 26, No. 1, pp. 97–99.

Johnson, B. V., Wagner, J. H., Steuber, G. D., and Yeh, F. C., 1994, "Heat Transfer in Rotating Serpentine Passages With Trips Skewed to the Flow," ASME *Journal of Turbomachinery*, Vol. 116, pp. 112–123; NASA TM 105581.

Johnston, J. P., Halleen, R. M., and Lezius, D. K., 1972, "Effects of Spanwise Rotation on the Structure of Two-Dimensional Fully Developed Turbulent Channel Flow," *J. Fluid Mech.*, Vol. 56, Part 3, pp. 533–557.

Lokai, V. I., and Gunchenko, E. I., 1979, "Heat Transfer Over the Initial Section of Turbine Blade Cooling Channels Under Conditions of Rotation," *Therm. Enging.*, Vol. 26, pp. 93–95.

Moore, J., 1967, "Effects of Coriolis on Turbulent Flow in Rotating Rectangular Channels," MIT Gas Turbine Laboratory Report No. 89.

Mori, Y., Fukada, T., and Nakayama, W., 1971, "Convective Heat Transfer in a Rotating Radial Circular Pipe (2nd Report)," *Int. J. Heat Mass Transfer*, Vol. 14, pp. 1807–1824.

Morris, W. D., and Ayhan, T., 1979, "Observations on the Influence of Rotation on Heat Transfer in the Coolant Channels of Gas Turbine Rotor Blades," *Proc. Inst. Mech. Engrs.*, Vol. 193, pp. 303–311.

Morris, W. D., and Ayhan, T., 1982, "An Experimental Study of Turbulent Heat Transfer in the Tube Which Rotates About an Orthogonal Axis," *Proc. XIV*

ICHMT Symposium on Heat and Mass Transfer in Rotating Machinery, Dubrovnik, Yugoslavia, Aug. 30–Sept. 3.

Morris, W. D., and Ghavami-Nasr, G., 1991, "Heat Transfer Measurements in Rectangular Channels With Orthogonal Mode Rotation," ASME *Journal of Turbomachinery,* Vol. 113, pp. 339–345.

Parsons, J. A., Han, J-. C., and Zhang, Y. M., 1994, "Wall Heating Effect on Local Heat Transfer in a Rotating Two-Pass Square Channel With 90° Rib Turbulators," *Int. J. Heat Mass Transfer,* Vol. 37, pp. 1411–1420.

Parsons, J. A., Han, J-. C., and Zhang, Y. M., 1995, "Effect of Model Orientation and Wall Heating Condition on Local Heat Transfer in a Rotating Two-Pass Square Channel With Rib Turbulators," *Int. J. Heat Mass Transfer,* Vol. 38, pp. 1151–1159.

Prakash, C., and Zerlke, R., 1992, "Prediction of Turbulent Flow and Heat Transfer in a Radially Rotating Square Duct," ASME *Journal of Turbomachinery,* Vol. 114, pp. 835–846.

Rohsenow, W. M., and Choi, H., 1961, *Heat, Mass and Momentum Transfer,* Prentice-Hall, Englewood Cliffs, NJ, pp. 192–193.

Rothe, P. H., and Johnston, J. P., 1979, "Free Shear Layer Behavior in Rotating Systems," ASME *Journal of Fluids Engineering,* Vol. 101, pp. 117–120.

Taslim, M. E., Rahman, A., and Spring, S. D., 1991a, "An Experimental Investigation of Heat Transfer Coefficients in a Spanwise Rotating Channel With Two Opposite Rib-Roughened Walls," ASME *Journal of Turbomachinery,* Vol. 113, pp. 75–82.

Taslim, M. E., Bondi, L. A., and Kercher, D. M., 1991b, "An Experimental Investigation of Heat Transfer in an Orthogonally Rotating Channel Roughened With 45 deg Criss-Cross Ribs on Two Opposite Walls," ASME *Journal of Turbomachinery,* Vol. 113, pp. 346–353.

Wagner, R. E., and Velkoff, H. R., 1972, "Measurements of Secondary Flows in a Rotating Duct," ASME *Journal of Engineering Power,* Vol. 94, pp. 261–270.

Wagner, J. H., Johnson, B. V., Graziani, R. A., and Yeh, F. C., 1992, "Heat Transfer in Rotating Serpentine Passages With Trips Normal to the Flow," ASME *Journal of Turbomachinery,* Vol. 114, pp. 847–857.

Yang, W. J., Zhang, N., and Chiou, J., 1992, "Local Heat Transfer in a Rotating Serpentine Flow Passage," ASME JOURNAL OF HEAT TRANSFER, Vol. 114, pp. 354–361.

Zhang, Y. M., Han, J. C., Parsons, J. A., and Lee, C. P., 1995, "Surface Heating Effect on Local Heat Transfer in a Rotating Two-Pass Square Channel With 60 deg Angled Rib Turbulators," ASME *Journal of Turbomachinery,* Vol. 117, pp. 272–280.

F. Takahashi

M. D. Vangsness

M. D. Durbin

W. J. Schmoll

University of Dayton,
Research Institute,
300 College Park,
Dayton, OH 45469

Structure of Turbulent Hydrogen Jet Diffusion Flames With or Without Swirl

The near-field turbulent structure of double-concentric hydrogen–air jet diffusion flames, with or without swirl, has been investigated using conditionally sampled, three-component laser-Doppler velocimetry and coherent anti-Stokes Raman spectroscopy. The turbulent flame zone became thinner and shifted inward as the mean jet velocity was increased, whereas swirl created a radial velocity even at the jet-exit plane, thereby broadening and shifting the flame zone outward. The probability-density functions of velocity components, their 21 moments (up to fourth order), mean temperature, and root-mean-square temperature fluctuation were determined in the near field. The data can be used to validate advanced turbulent combustion models.

Introduction

In practical combustion systems such as gas turbines and industrial furnaces, turbulence and swirl play an essential role in enhancing fuel–air mixing, flame stabilization, and combustion intensity. Previous studies of turbulent jet diffusion flames (Bilger, 1976; Eickhoff, 1982; Faeth and Samuelsen, 1986; Dibble et al., 1987; Tangirala et al., 1987; Stårner, 1985; Stårner and Bilger, 1988; Drake, 1988; Pitz et al., 1991; Nandula et al., 1994; Barlow and Carter, 1994) have focused primarily on nonswirling flames and have not included detailed velocity and temperature data in the developing region of the flame. The majority of the existing velocity data in turbulent jet diffusion flames were obtained using single- or two-component laser-Doppler velocimetry (LDV). Thermocouples and, more recently, Raman scattering spectroscopy were used for temperature measurements. Reports on high-order moments, particularly triple correlations, of the probability-density functions (pdf) of velocity components are rare; they are available for nonreacting flows (Hinze, 1975; Wygnanski and Fiedler, 1969). Accurate measurement of high-order moments is a challenge especially in reacting flows.

In addition, the conventional turbulence models such as a $k–\epsilon$ model use gradient diffusion models for turbulent transport (Launder and Spalding, 1972; Eickhoff, 1982) and cannot predict high-order moments; thus, a demand for such data for model validation has been minimal. Unlike these models, recent turbulence models such as pdf methods do not need to model the turbulent transport terms because they appear in closed form (Pope, 1990). The joint velocity-scalar pdf method, capable of calculating high-order moments, has recently been applied to a number of reacting and nonreacting flows (Anand et al., 1993, 1996). Such advanced turbulent combustion models must be validated in detail in laboratory flames incorporating the essential features of practical flows. Therefore, the demand for the detailed experimental data, including high-order moments (in swirling or nonswirling flows), has been growing rapidly in recent years.

A major challenge in accurate LDV measurements is how to avoid inherent particle statistical bias problems (Edwards, 1987). Conditional sampling techniques (Libby et al., 1982)

have been applied to LDV measurements (Dibble et al., 1987; Tangirala et al., 1987; Stårner, 1985; Takahashi et al., 1992) to avoid velocity bias originated in different flow channels with different initial velocities. However, the conditionally sampled velocity data obtained specifically for model validation are unavailable. The developing region of the jet flame is particularly important because various physical and chemical processes occur rapidly in the near-nozzle region, and the flame structure downstream depends significantly on the early development. Moreover, substantial errors due to an elongated (ellipsoidal) measuring volume of a two-component LDV system (Durbin et al., 1993) were observed by comparisons with the results obtained by a three-component system with a small probe volume (Takahashi et al., 1995). Furthermore, the use of a thermocouple exerts serious limitations on the maximum measurable temperature, delayed time responses, radiation heat losses, flow and catalytic disturbances on the flame, and so forth.

This work is an attempt to provide a reliable data base in response to the above-mentioned demands and requirements for accurate velocity and temperature measurements. The contributions of the current results relative to previous work are as follows: (1) This study provides the first detailed velocity and temperature data in swirling and nonswirling turbulent hydrogen jet diffusion flames, specifically designed for the validation of advanced turbulent combustion models capable of predicting high-order moments. (2) A unique contribution of this study stems from the nonintrusive laser diagnostic techniques. The conditionally sampled, three-component LDV measurements with a small probe volume were made, for the first time, to obtain the unbiased velocity data, including high-order cross-correlations. The coherent anti-Stokes Raman spectroscopy (CARS) thermometry generated the temperature data without causing disturbances on the flame. (3) All data obtained are tabulated (in ASCII file format) and plotted in five technical reports (Takahashi et al., 1993, 1994a, b). Therefore, selected results are presented in this paper to extract physical insights into the near-field turbulent structure of hydrogen jet diffusion flames.

Experimental Techniques

The combustor (Fig. 1) consists of a central fuel tube (9.45-mm inner diameter [d], 0.2-mm lip thickness, 806-mm length) and a concentric annulus-air tube (26.92-mm inner diameter), centered in a vertical test section (150 × 150-mm square cross section with rounded corners [quasi-octagonal], 486-mm length), through which external air is supplied. The test section

Downloaded 11 Dec 2010 to 193.140.21.150. Redistribution subject to ASME license or copyright; see http://www.asme.org/terms/Terms_Use.cfm
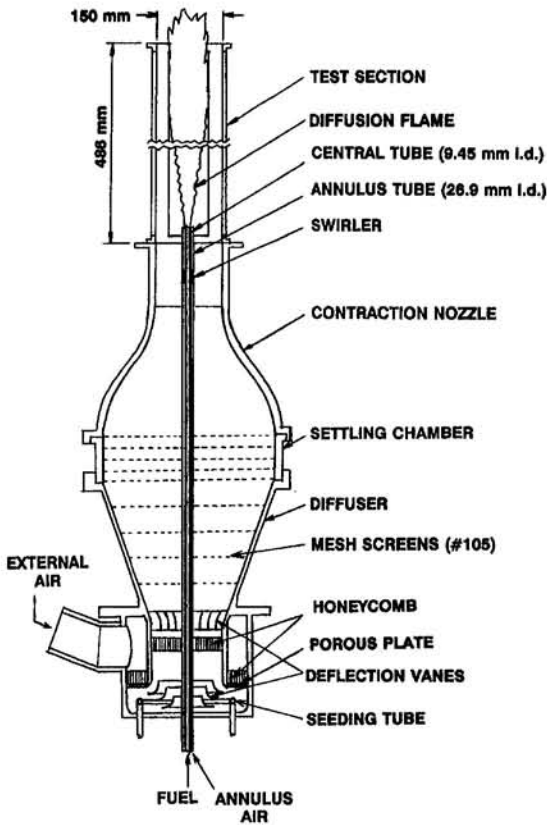
Fig. 1 Schematic of the combustor used

is sided with four quartz windows for optical observations and diagnostics. A helical vane swirler unit is placed in the annulus channel 96 mm upstream from the jet exit. Table 1 shows the experimental conditions (θ: helical vane angle, U_j: mean jet velocity, U_a: mean annulus air velocity, and U_e: mean external air velocity). Hydrogen (purity: 99.3 percent) is the fuel. The jet Reynolds number ($\mathrm{Re}_j = U_j d / \nu_j$ where ν_j is the kinematic viscosity of hydrogen) is 2208 for Case 1 and 8830 for the others. Case 1 is in the pipe-flow transition region, in which breakpoint to the turbulent flame rapidly approaches the jet exit (Takahashi et al., 1982). Thus, Case 1 is a transitional (or weakly turbulent) flame, and Cases 2 through 4 are fully developed turbulent flames. Both LDV and CARS measurements were made at numerous radial locations at seven axial locations ($x = 1.5, 10, 25, 50, 75, 150,$ and 225 mm).

The three-component LDV system, described in detail elsewhere (Takahashi et al., 1993, 1994a), consists of two segments: (1) three-beam two-channel optics and (2) two-beam one-channel optics. The former uses a 514.5-nm line of an argon-ion laser (15 W) and measures the velocity components in the directions of ± 45 deg off the jet axis. The latter uses a 488.0-nm line and measures the tangential velocity component. The coincident measuring volume is minimized to a 100-μm-dia sphere by aligning the axes of the two segments perpendicularly. The calculated fringe spacing is approximately 3.6 μm. Submicron-size zirconia particles (<1 μm, 97 percent) are the tracer. LDV measurements are made by seeding one stream at a time. Thus, all LDV data reported are conditional upon the fluid originating from either the jet, annulus, or external flow channel. A portion of the data is filtered out by the so-called $n\sigma$ method (i.e., velocities whose deviation from the mean exceeded n times the standard deviation [σ] are eliminated). Because the conventional 3σ method occasionally cuts off some valid data and alters high-order moments significantly, $n = 4$ is used in this study. The 21 independent flow variables determined are U, V, W, $\sqrt{\overline{u'^2}}$, $\sqrt{\overline{v'^2}}$, $\sqrt{\overline{w'^2}}$, $\overline{u'v'}$, $\overline{v'w'}$, $\overline{w'u'}$, $\overline{u'^3}$,

$\overline{v'^3}$, $\overline{w'^3}$, $\overline{u'^2 v'}$, $\overline{v'^2 u'}$, $\overline{v'^2 w'}$, $\overline{w'^2 v'}$, $\overline{w'^2 u'}$, $\overline{u'^2 w'}$, $\overline{u'^4}$, $\overline{v'^4}$, and $\overline{w'^4}$. Hence, u, v, and w represent the axial, radial, and tangential velocity components, respectively; a capital letter indicates the mean value and a lowercase letter with a prime indicates the velocity fluctuation from the mean. The kinetic energy of turbulence, skewnesses, and kurtoses are derived from these quantities. The accuracy of the velocity measurements is estimated as ~ 2 percent for the means and 5 to 10 percent for the higher moments.

The CARS system, described in detail elsewhere (Takahashi and Vangsness, 1993; Takahashi et al., 1994b), consists of a pulsed Nd:YAG laser, dye laser optics, incident and collection optics, and a spectrometer with an intensified charge-coupled device camera. A broadband Stokes beam (~ 607 nm) and the two pump beams (532 nm) are then focused together in a folded BOXCARS configuration using a lens (250-mm f.1.). The ellipsoidal probe volume size, estimated by assuming Gaussian beams with a 7-mm diameter and a 5-deg crossing angle, is approximately 25 μm in diameter and 250 μm in length. Typically, 500 CARS signals from nitrogen are acquired at each location. The accuracy of the temperature measurements is estimated to range between 10 percent near room temperature and 5 percent near the flame temperature, with the largest contribution to uncertainty from shot-to-shot variation in the Stokes-laser spectral distribution. The reproducibility of both LDV and CARS measurements is checked prior to final runs.

Results and Discussion

Thermal Structure. Figures 2 and 3 show the radial profiles of the mean gas temperatures and root-mean-square (rms) values of temperature fluctuations at five selected heights in swirling and nonswirling turbulent hydrogen jet diffusion flames. The outermost data point is bounded by the location where the temperature is nearly room temperature (or the outer edge of the test section's window). The innermost data point is the location where the intermittency of the jet fluid (defined as the fraction of CARS realizations for which nonresonant background interference from the fuel occur in the total number of data [Takahashi and Vangsness, 1993]) is very high, and accurate temperature determination is prevented beyond this point.

In all cases (Cases 1–4), the flame base anchored near the fuel tube exit on the air side of the dividing streamline (whose radial distance from the axis: $y \approx 4.7$ mm) as the sharp temperature peaks (~ 1900 K at $x = 1.5$ mm, $y = 5$ to 5.5 mm in Fig. 2(e)) indicate. The temperature peak shifted outward and broadened downstream, as expected. The rms temperature fluctuation reached a maximum (up to 900 K) in the outer thermal layer where the mean temperature gradient was large. As the jet velocity was increased in nonswirling flames (from Case 1 to Case 2), the flame zone (temperature peak) shifted inward and both mean and rms temperature peaks became narrower and slightly lower. Furthermore, the innermost data points shifted slightly outside from Case 1 to Case 2 as a result of faster

Table 1 Experimental conditions

Case No.	θ (°)	U_j (m/s)	U_a (m/s)	U_e (m/s)
1	0	25	4	1
2	0	100	20	4
3	30	100	20	4
4	45	100	20	4
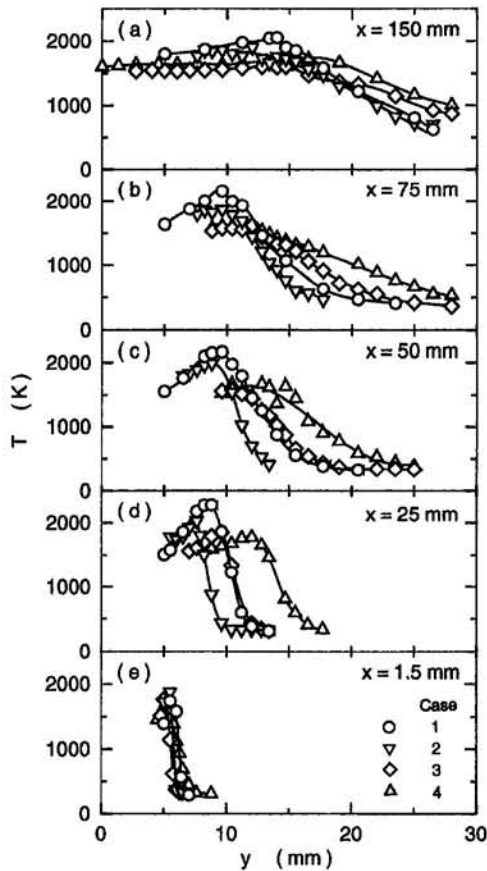
Fig. 2 Mean-temperature distribution across the hydrogen jet flame at five different heights

Fig. 3 Temperature fluctuation distribution across the hydrogen jet flame at five different heights

spread of the fuel jet. Consequently, the layer between the innermost data point and the temperature peak, where hydrogen was transported by both turbulent and molecular diffusion, became thinner. As swirl was added to the annulus airflow (see Cases 2–4), the innermost data points and the temperature peak locations shifted outward substantially, the mean temperature profiles became flatter, and both mean and rms temperature peak values decreased. Swirl-induced radial velocity, and thus, the hydrogen jet spread outward with a larger angle (as will be explained in detail in the next section).

Although the mean and rms temperature profiles show global features of the thermal structure of the flame, more precise information can be retrieved from temperature pdf's. Only few examples at selected locations for three conditions (Cases 1–3) are shown here, but the general trend peculiar to the radial location relative to the flame zone is illustrated well. In fact, qualitative trends are similar to that for methane jet diffusion flames (Takahashi and Vangsness, 1993) in which the jet velocities were much lower (<17 m/s). Figure 4 shows the pdf's in nonswirling (Figs. 4(a)–4(e), Cases 1; Figs. 4(f)–4(j); Case 2) and swirling (Figs. 4(k)–4(o), Case 3) hydrogen flames at $x = 25$ mm. At the edge of the outer thermal layer (Figs. 4(e), 4(j), and 4(o)), the pdf showed a sharp single peak with near room temperature. In the outer thermal layer outside the flame zone (Figs. 4(d), 4(i), and 4(n)), the pdf showed a bimodal distribution over a wide range from room temperature to flame temperature as a result of the radial movement of the flame zone. Thus, the rms value peaked in this layer. Occasional entrainment of cold air is seen still at the temperature peak location (Figs. 4(c), 4(h), and 4(m)). Inside the flame zone (Figs. 4(b), 4(g), and 4(l)), the pdf showed a single peak in a high-temperature range; thus, the rms value decreased. Further inside the innermost data point (Figs. 4(a),
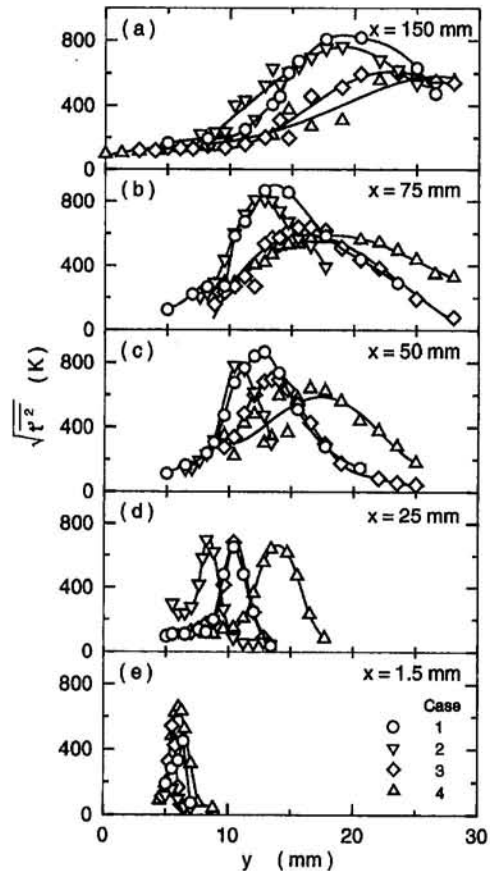
4(f), and 4(k)) where the intermittency began to increase, the mean temperature might be biased somewhat toward higher values than the time-average because the CARS measurement is based on nitrogen in hot combustion products.
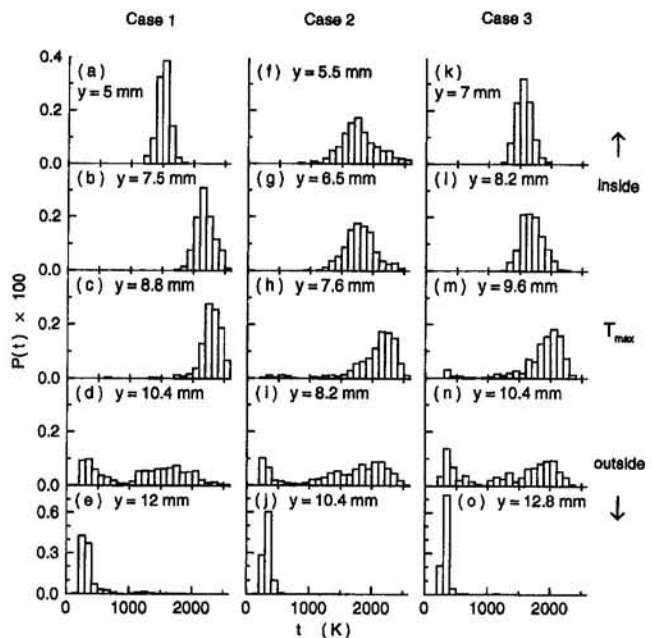
Fig. 4 Probability-density functions of temperature in the hydrogen flame (Cases 1–3) at five different radial locations at $x = 25$ mm

Mean and Turbulent Velocity Fields. In addition to the quantitative LDV measurements, the conditional sampling based on the origin of seed particles provided qualitative characteristics of the turbulent structure of swirling and nonswirling hydrogen jet diffusion flames. Figure 5 shows the radial profiles of the mean axial velocity component at selected heights in the near field. Only the data points conditioned on the jet and annulus fluids are presented in the figure. The radial location of the apparent flame zone determined by the temperature peak is also included in the figure. Near the jet exit ($x = 1.5$ mm; Fig. 5(c)), the data points for jet and annulus fluids do not overlap, and the shear layers originating from the boundary layers on both sides of the tube walls were observed in a wake region. The flame base is anchored in the low-velocity region of the annulus fluid stream. It is notable (in Figs. 5(a) and 5(b)) that the flame zone resides in the annulus fluid where the mean axial velocity profile is nearly constant; thus, not in the shear layer. As the jet velocity was increased for the non-swirling flow (from Case 1 to Case 2), the jet fluid spread with a larger angle because of enhanced turbulent stirring, whereas the flame zone shifted inward as mentioned earlier (Fig. 2). Swirl lowered the mean axial velocity of both jet fluid and annulus fluid (cf. Cases 2–4).

The impact of swirl appeared more evidently in the mean radial velocity profiles (Fig. 6); swirl induced the radial velocity component of the annulus fluid even at the near-exit plane. At $x = 1.5$ mm (Fig. 6(c)), the mean radial velocity of the annulus fluid was small (<1 m/s) for nonswirling flows (Cases 1 and 2), whereas for swirling flows (Cases 3 and 4), it increased up to ~2.5 m/s and ~5 m/s, respectively. Since the mean axial velocity of the annulus fluid was ~20 m/s for Cases 3 and 4 (Fig. 5(c)), these values of radial velocity translate to the streamline off-axis angle of 7 and 14 deg, respectively. This peculiar behavior was not observed for cold air jets with swirl under the same jetting velocities (Takahashi et al., 1992). Since the effect of centrifugal forces on submicron-size tracer particles
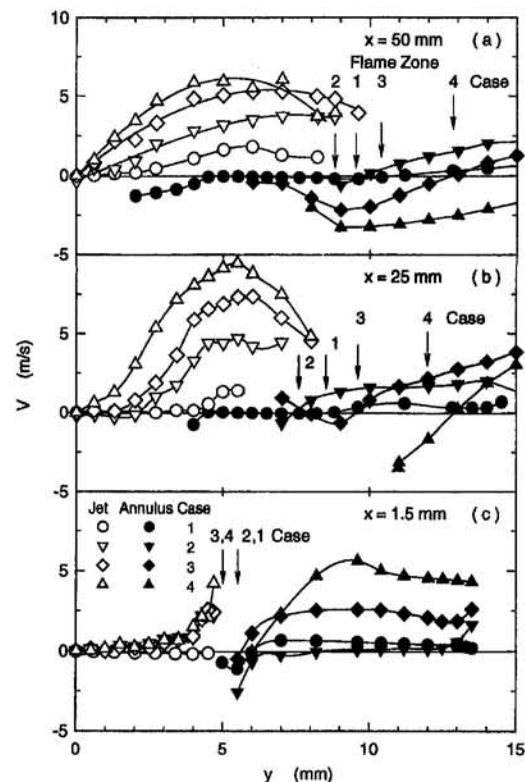
Fig. 6 Mean radial-velocity distribution across the hydrogen jet flame at three different heights

is small, the deflection of the streamlines was likely to be induced by the pressure field, which was distorted by swirl in a combusting flow with the density several times smaller than that of air. Although the geometric swirling number (based on the annulus flow) for $\theta = 45$ deg was larger (0.78) than a critical value (~0.6 [Chigier and Beer, 1972]) for the formation of recirculation, no recirculation zone was formed because of a large jet velocity. However, the outward deflection of the annulus fluid apparently induced the radial velocity of the jet fluid downstream (Figs. 6(a) and 6(b)) to satisfy continuity of the fluid. Moreover, the differences in the mean velocities between jet fluid and annulus fluid at a same location were significant, particularly swirling flows. If conditional samplings were not made in the LDV measurement, the measured mean velocities would have been biased toward those of jet fluid, which had a higher axial velocity (and data rate), thus degrading the accuracy of measurements and covering the structure of the turbulent flow field.

Figure 7 shows the radial profiles of the mean tangential velocity component for swirling flows (Cases 3 and 4). The swirling motion, initially given only in the annulus fluid, spread into the jet fluid downstream. For $\theta = 45$ deg, the tangential momentum penetrated into the jet fluid even near the axis at $x = 25$ mm, whereas for $\theta = 30$ deg, it did not reach the near-axis location even at $x = 50$ mm.

Figure 8 shows the radial profiles of (absolute) turbulence intensities of axial, radial, and tangential velocity components at $x = 25$ mm. The rms values of fluctuations (or the square root of second central moments) indicate the directional components of the absolute turbulence intensity (or twice turbulent kinetic energy [TKE]). For Case 1 ($Re_j = 2208$), the turbulence intensities were relatively small (<5 m/s) and nearly constant except for the region where the jet and annulus fluids overlap (the turbulent stirring layer). By contrast, for Cases 2–4 ($Re_j = 8830$), all components of turbulence intensities showed a peak in the shear layer of the jet where the radial
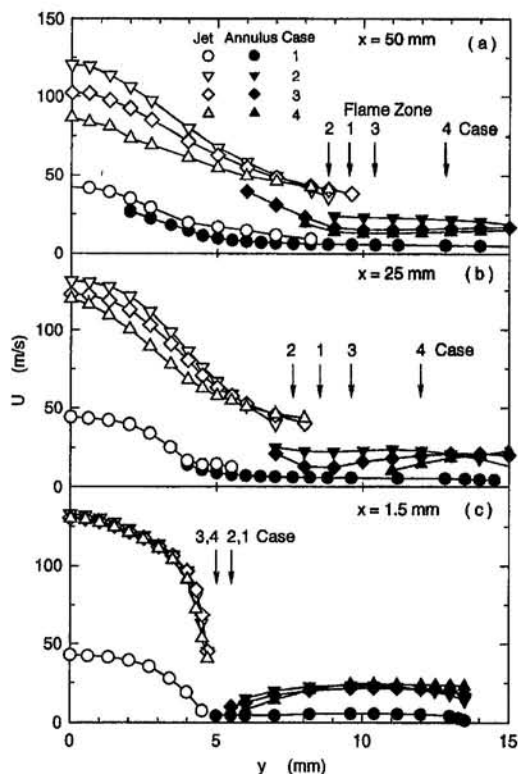

Fig. 5 Mean axial-velocity distribution across the hydrogen jet flame at three different heights
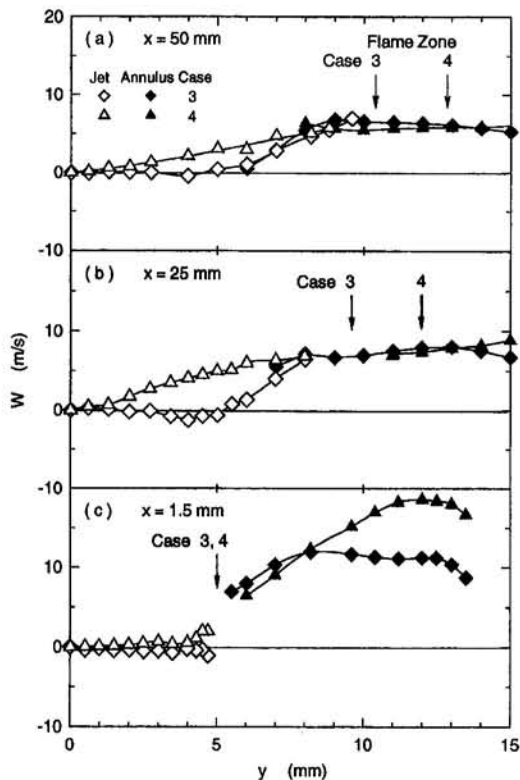
Fig. 7 Mean tangential-velocity distribution across the hydrogen jet flame at three different heights

gradient of mean axial velocity component was large, and the turbulence level of annulus fluid inside the flame zone increased rapidly in the turbulent stirring layer. The turbulence was aniso-

tropic (i.e., the rms of the axial component was larger than those of radial and tangential components), typical of turbulent jets. As swirl became stronger (cf. Cases 2–4), the turbulence intensities increased, particularly in the central region ($y < 4$ mm), where the mean axial velocity component decreased while the mean radial and tangential velocity components increased. It is noticed that for Case 4, the flame zone was subjected to high-intensity turbulence at $x = 25$ mm; radial rms fluctuation reached ~4 m/s in the near flame region where the mean radial velocity was −3 m/s.

Figure 9 shows the pdf's (histograms) of axial, radial, and tangential velocity components for both jet fluid (top three rows) and annulus fluid (bottom row) for Case 3 at selected radial locations at $x = 25$ mm. Although these pdf's are selected samples, they represent typical characteristics of the mean and turbulent velocity fields in turbulent hydrogen jet diffusion flames shown as the mean velocity components (first central moments of the pdf's) in Figs. 5–7 and the turbulent intensities (second central moments) in Fig. 8. The characteristics related to shape of the pdf's (skewness and kurtosis) will be discussed in the next section.

Figure 10 shows the axial variations in the mean axial velocity component and turbulence intensities. As the jet velocity was increased for the nonswirling flames (from Cases 1 to 2), the mean axial velocity decayed more rapidly, and the turbulence intensities peaked at a location closer to the jet exit as a result of enhanced turbulent stirring, promoting transverse diffusion of turbulence. As swirl became stronger (cf. Cases 2–4), the velocity decay was accelerated further because of the faster spreading of the jet and enhanced turbulent mixing. The turbulence intensity peak shifted upstream further and became larger because of more intense turbulent stirring. Compared to nonreacting air jets studied previously (Takahashi et al., 1992), the axial velocity decayed more rapidly and turbulence intensity peak locations approached to the jet exit in current combusting flows (Cases 2–4).

Turbulence Structure. The detailed structure of the turbulence field in hydrogen jet diffusion flames is presented next for selected locations and conditions. Figure 11 shows the radial profiles of the Reynolds shear stress and gradient of the mean axial velocity. The most significant component of Reynolds shear stress tensor (or a cross central moment), $\overline{u'v'}$, indicates

Fig. 8 Turbulence intensity distribution across the hydrogen jet flame at $x = 25$ mm: (a) axial, (b) radial, and (c) tangential velocity components
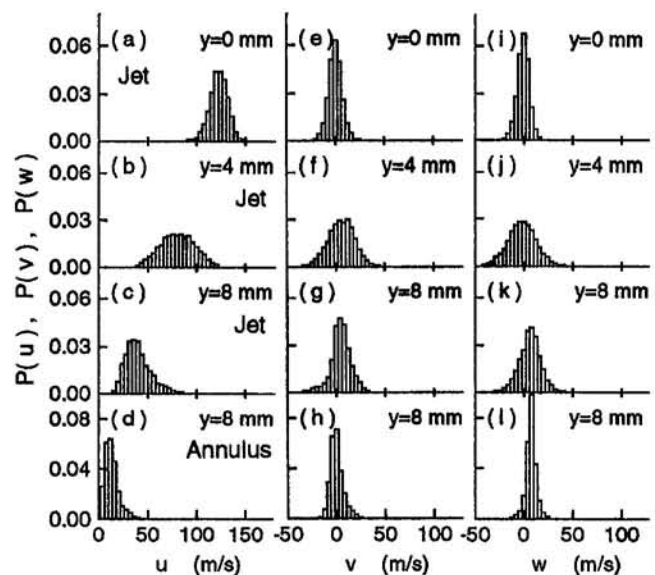
Fig. 9 Probability-density functions of velocity in the hydrogen jet flame (Case 3) at $x = 25$ mm: (a–d) axial, (e–h) radial, and (i–l) tangential velocity components
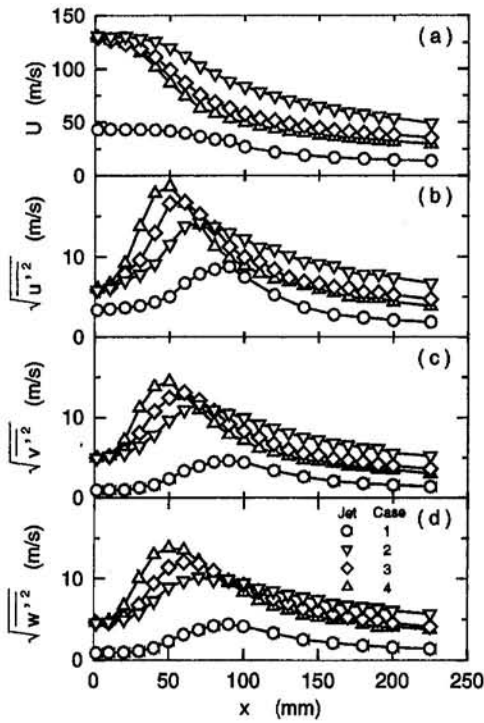
Fig. 10 (a) Mean axial velocity, (b) axial, (c) radial, and (d) tangential velocity fluctuations along the center-line of the hydrogen jet flame

the radial diffusion of axial momentum by turbulent transport. For all cases, the peak locations of the turbulence intensity of axial fluctuations (Fig. 8(a)) approximately coincide with those of the Reynolds shear stress (Fig. 11(a)) and the velocity gradient (Fig. 11(b)). The result is consistent with a most significant production term of the conservation equation for TKE: shear stress multiplied by strain. Thus, the production of TKE is primarily in the shear layer in the developing region in the near field, similar to self-preserving air jets (Hinze, 1975; Wygnanski and Fiedler, 1969). The production of TKE decays downstream as the shear stress and velocity gradient decrease (Takahashi et al., 1994a). For the low-velocity condition without swirl (Case 1), the peak values of the Reynolds shear stress are an order of magnitude smaller than that for the high-velocity
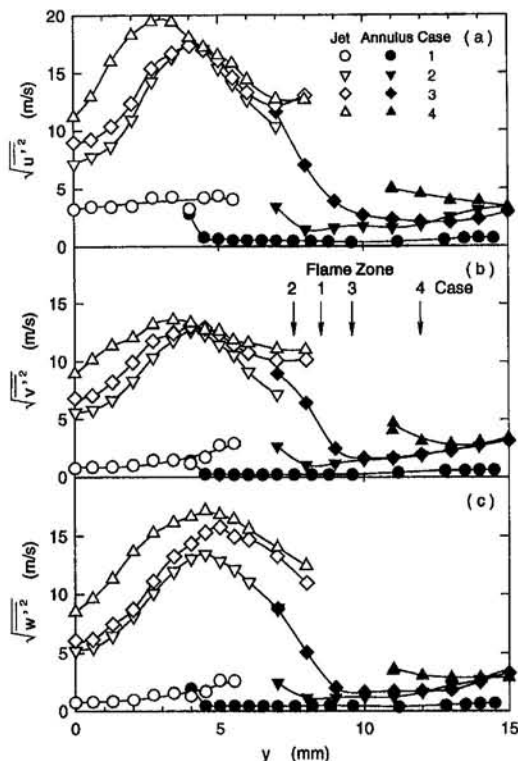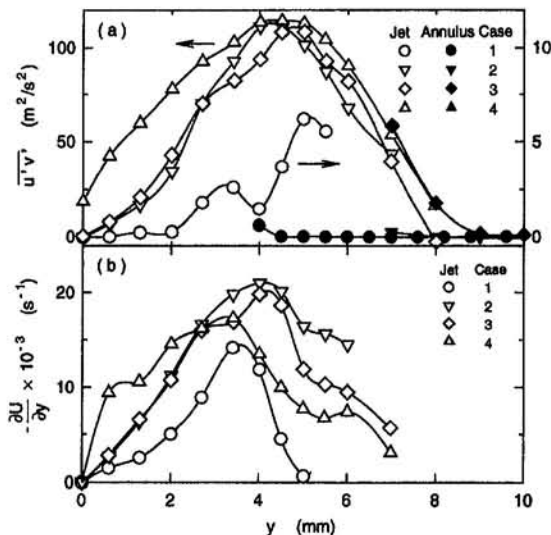
flame (Cases 2–4) and increased toward the outermost data point despite the vanished velocity gradient. This result might be caused by large-scale vortices that evolved near the boundary of the low-turbulence jet flame. The effect of swirl on the Reynolds shear stress is weak except for the central region (<4 mm) for Case 4, where turbulence intensities increased. The other components of Reynolds shear stress tensor (not shown) are much smaller than $\overline{u'v'}$.

Third-order central moments (triple correlations) provide characteristics of the diffusion term of the TKE equation. Figure 12 shows (a) the axial, (b) radial, and (c) tangential transport of the three components of TKE for Case 3 at $x = 25$ mm. The axial diffusion of the axial and radial TKE components ($\overline{u'^3}$, $\overline{v'^2u'}$) and the radial diffusion of the axial and radial TKE components ($\overline{u'^2v'}$, and $\overline{v'^3}$) show a common trend: They are negative in the inner region ($y < 4$ mm) and positive in the outer region ($y > 4$ mm) with a zero value at $y = 0$ and 4 mm. The zero crossing point ($y \approx 4$ mm) approximately coincides with the location where the second-order moments peaked (Figs. 8 and 11), as mentioned earlier. Therefore, the change in sign indicates that TKE was produced in the shear layer near $y \approx 4$ mm and diffused both inward and outward. The radial gradients of these quantities appearing in the TKE balance equation indicate a gain or loss of each term. In the axial direction, TKE was transported upstream in $y < 4$ mm and downstream in $y > 4$ mm. The other moments are relatively small except for $\overline{w'^3}$, which had a peak at $y \approx 5$ mm.

Figure 13 shows the skewness and kurtosis (i.e., the third and fourth central moments, respectively, normalized by variance) of each velocity component for Case 3 at $x = 25$ mm. Skewness is a measure of asymmetry of the pdf, with positive values implying a more gradual tailing off toward the higher-velocity side than the lower-velocity side. Kurtosis is a measure

Fig. 11 Distribution of (a) Reynolds shear stress and (b) axial-velocity gradient across the hydrogen jet flame at $x = 25$ mm

Fig. 12 Triple-correlation distribution across the hydrogen jet flame (Case 3) at $x = 25$ mm
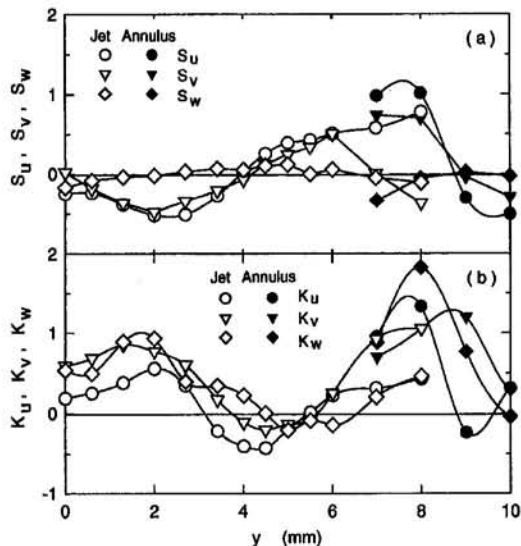
Fig. 13 Distribution of (a) skewness and (b) kurtosis across the hydrogen jet flame (Case 3) at $x = 25$ mm

of the flatness of the pdf, with larger values corresponding to a top-hat shape rather than a gently curved hill. Both skewness and kurtosis for the Gaussian distribution are zero (kurtosis is defined here as the normalized forth moment minus three). The skewness for the axial velocity component (S_u) at $x = 1.5$ mm and $y = 0$ mm (not shown) was approximately -0.4, consistent with the value observed in fully developed turbulent pipe flows, implying upward TKE transport. Thus, the distributions of skewnesses and kurtoses in the developing region of jet flame are strongly affected by pipe-flow turbulence; they are different from self-preserving jets (Wygnanski and Fiedler, 1969). The variations in skewness and kurtosis are consistent with the shape of the pdf's shown earlier (Fig. 9). The pdf's of the axial velocity component at $y = 0$ and 4 mm (Figs. 9(a) and 9(b), respectively) show symmetric distributions ($S_u \approx 0$), while at $y = 8$ mm for both jet and annulus fluids (Figs. 9(c) and 9(d), respectively) the dist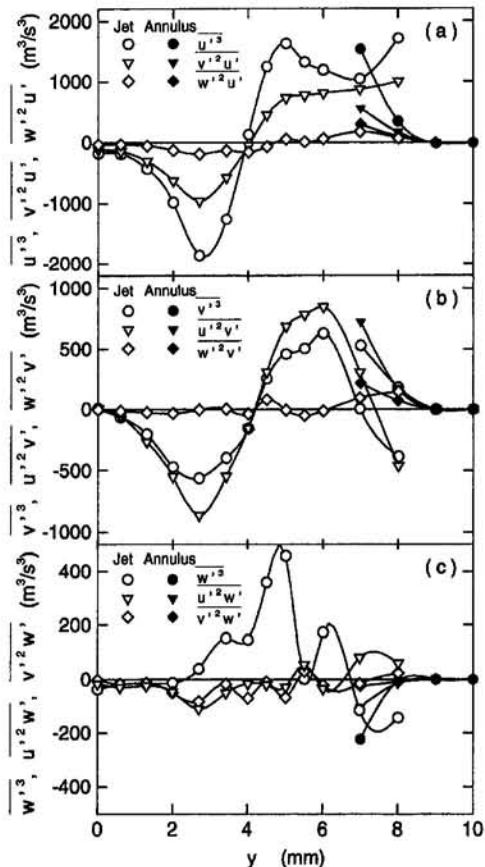ribution was skewed toward the high-velocity side ($S_u \approx 1$). Compared to the axial velocity component, the pdf's of radial and tangential components (Figs. 9(e)–9(l)) are fairly symmetric, except for the radial component for annulus fluid (Fig. 9(h)). Unlike self-preserving jets (Wygnanski and Fiedler, 1969), in which both skewness and kurtosis increased monotonously toward the edge of the jet, their variations in the developing region of jet flames are more complicated due to the presence of the high-temperature region near the outermost data point for jet fluid.

Conclusions

Detailed nonintrusive measurements of the velocity and temperature fields with the statistical treatment of the data revealed some characteristics of the developing region of turbulent hydrogen jet diffusion flames with or without swirl. Increasing the jet velocity shifts the apparent turbulent flame zone inward, makes the thermal layer thinner, and thus, strains the flame zone in the near field. On the other hand, swirl generally promotes turbulence and creates a positive radial velocity component even at the jet-exit plane (which, in turn, induces the radial velocity of the jet fluid), thereby shifting the flame zone outward and broadening the thermal layer. (The outward flow deflection was not observed in nonreacting air jets studied previously.) The peculiar result for the swirling flame is particularly important when applying the boundary conditions in computations; the upstream boundary may need to be taken well below the jet exit outside the pressure field variation due to swirl if the experimental results are not used as the boundary condition.

The distributions of second and third-order velocity moments provide a physical insight into the generation and diffusion of TKE. TKE is generated in the shear layer, where velocity gradient and Reynolds shear stress reach their peaks. TKE diffuses inward and outward from the shear layer and then downstream in the outer region and upstream in the inner region. Both skewnesses and kurtoses of velocity components in the near field were largely affected by the pipe-flow turbulence. The presence of swirl in the flame promoted early jet spread and turbulent stirring, thus accelerating the decay of the mean axial velocity and shifting the turbulence intensity peaks upstream. Bimodal temperature pdf's and, in turn, large rms values were observed on the air-side of the flame zone. The conditionally sampled velocity data and the nonintrusively measured temperature data presented in this paper can be used to validate advanced computational models capable of predicting the high-order moments (triple correlations) for each fluid.

Acknowledgments

References

Anand, M. S., Pope, S. B., and Mongia, H. C., 1993, "PDF Calculations for Swirling Flows," AIAA Paper No. 93-0106.

Anand, M. S., Takahashi, F., Vangsness, M. D., Durbin, M. D., and Schmoll, W. J., 1996, "An Experimental and Computational Study of Swirling Hydrogen Jet Diffusion Flames," ASME *Journal of Engineering for Gas Turbines and Power*, in press.

Barlow, R. S., and Carter, C. D., 1994, *Combustion and Flame*, Vol. 97, p. 261.

Bilger, R. W., 1976, "Turbulent Jet Diffusion Flames," *Progress in Energy and Combustion Science*, Vol. 1, pp. 87–109.

Chigier, N. A., and Beer, J. M., 1972, *Combustion Aerodynamics*, Applied Science Publishing, London.

Dibble, R. W., Hartmann, V., and Schefer, R. W., 1987, "Conditional Sampling of Velocity and Scalars in Turbulent Flames Using Simultaneous LDV-Raman Scattering," *Experiments in Fluids*, Vol. 5, pp. 103–113.

Drake, M. C., 1988, "Stretched Laminar Flamelet Analysis of Turbulent H_2 and $CO/H_2/N_2$ Diffusion Flames," *Twenty-First Symposium (International) on Combustion*, The Combustion Institute, pp. 1579–1589.

Durbin, M. D., Vangsness, M. D., and Takahashi, F., 1993, "Stability of Hydrogen/Air Double-Concentric Jet Diffusion Flames With and Without Swirl," Eastern States Section/The Combustion Institute Meeting, Princeton, NJ, Oct.

Edwards, R. V., 1987, "Report of the Special Panel on Statistical Particle Bias Problems in Laser Anemometry," ASME *Journal of Fluids Engineering*, Vol. 109, pp. 89–93.

Eickhoff, H., 1982, "Turbulent Hydrocarbon Jet Flames," *Progress in Energy and Combustion Science*, Vol. 8, pp. 159–168.

Faeth, G. M., and Samuelsen, G. S., 1986, "Fast Reaction Nonpremixed Combustion," *Progress in Energy and Combustion Science*, Vol. 12, pp. 305–372.

Gollahalli, S. R., Savas, Ö., Huang, R. F., and Rodoriquez Azara, J. L., 1988, "Structure of Attached and Lifted Gas Jet Flames, in Hysteresis Region," *Twenty-First Symposium (International) on Combustion*, The Combustion Institute, pp. 1463–1471.

Harsha, P. T., 1971, "Free Turbulent Mixing: A Critical Evaluation of Theory and Experiment," AEDC-TR-71-36, Arnold Engineering Development Center, Arnold Air Station, TN.

Hinze, J. O., 1975, *Turbulence*, 2nd ed., McGraw-Hill, New York.

Launder, B. E., and Spalding, D. B., 1972, *Lectures in Mathematical Models of Turbulence*, Academic Press, London.

Libby, P. A., Chigier, N., and LaRue, J. C., 1982, "Conditional Sampling in Turbulent Combustion," *Progress in Energy and Combustion Science*, Vol. 8, pp. 203–231.

Nandula, S. P., Brown, T. M., and Pitz, R. W., 1994, "Measurements of Scalar Dissipation in the Reaction Zones of H_2–Air Turbulent Diffusion Flames," *Combustion and Flame*, Vol. 99, p. 775.

Pitz, R. W., Cheng, T. S., March, S. R., and Wehrmeyer, J. A., 1991, "Effects of Swirl on Finite-Rate Chemistry in Lifted Jet Diffusion Flames," AIAA Paper No. 91-2139.

Pope, S. B., 1990, "Computations of Turbulent Combustion: Progress and Challenges," *Twenty-Third Symposium (International) on Combustion*, The Combustion Institute, pp. 591–612.

Stårner, S. H., 1985, "Conditional Sampling in a Turbulent Diffusion Flame," *Combustion Science and Technology*, Vol. 42, pp. 283–299.

Stårner, S. H., and Bilger, R. W., 1988, "Joint Measurements of Velocity and Scalars in a Turbulent Diffusion Flame With Moderate Swirl," *Twenty-First Symposium (International) on Combustion,* The Combustion Institute, pp. 1569–1577.

Takahashi, F., Mizomoto, M., and Ikai, S., 1982, "Transition From Laminar to Turbulent Free Jet Diffusion Flames," *Combustion and Flame,* Vol. 48, pp. 85–95.

Takahashi, F., and Goss, L. P., 1992, "Near-Field Turbulent Structures and the Local Extinction of Jet Diffusion Flames," *Twenty-Fourth Symposium (International) on Combustion,* The Combustion Institute, pp. 351–359.

Takahashi, F., Vangsness, M. D., and Belovich, V. M., 1992, "Conditional LDV Measurements in Swirling and Nonswirling Coaxial Turbulent Air Jets for Model Validation," AIAA Paper No. 92-0580.

Takahashi, F., and Vangsness, M. D., 1993, "Near-Field CARS Measurements and the Local Extinction of Turbulent Jet Diffusion Flames," *Dynamics of Heterogeneous Combustion and Reacting Systems,* A. L. Kuhl, J.-C. Leyer, A. A. Borisov, and W. A. Sirignano, eds., *Progress in Aeronautics and Astronautics,* Vol. 152, pp. 37–55.

Takahashi, F., Durbin, M. D., Vangsness, M. D., and Schmoll, W. J., 1993, "LDV Measurements in Swirling and Nonswirling Coaxial Turbulent Hydrogen Jet Diffusion Flames—No. 1: No Swirl, 25 m/s," UDR-TR-93-88; "No. 2: No Swirl, 100 m/s," UDR-TR-94-116, University of Dayton, Dayton, OH.

Takahashi, F., Durbin, M. D., Vangsness, M. D., and Schmoll, W. J., 1994a, "LDV Measurements in Swirling and Nonswirling Coaxial Turbulent Hydrogen Jet Diffusion Flames—No. 3: 30-degree Swirl, 100 m/s," UDR-TR-94-116; "No. 4: 45-degree Swirl, 100 m/s," UDR-TR-94-117, University of Dayton, Dayton, OH.

Takahashi, F., Vangsness, M. D., Schmoll, W. J., and Durbin, M. D., 1994b, "CARS Temperature Measurements in Swirling and Nonswirling Coaxial Turbulent Hydrogen Jet Diffusion Flames," UDR-TR-94-89, University of Dayton, Dayton, OH.

Takahashi, F., Durbin, M. D., and Vangsness, M. D., 1996, "Stabilization of Hydrogen Jet Diffusion Flames With or Without Swirl," *Transport Phenomena in Combustion,* S. H. Chan, ed., Taylor & Francis, Washington, DC, in press.

Tangirala, V., Chen, R. H., and Driscoll, J. F., 1987, "Effect of Heat Release and Swirl on the Recirculation Within Swirl-Stabilized Flames," *Combustion Science and Technology,* Vol. 51, pp. 75–95.

Wygnanski, I., and Fiedler, H., 1969, "Some Measurements in the Self-Preserving Jet," *Journal of Fluid Mechanics,* Vol. 38, pp. 577–612.

Observations of Spanwise Symmetry Breaking for Unsteady Mixed Convection in Horizontal Ducts

R. E. Spall[1]

Assistant Professor,
Department of Mechanical Engineering,
University of South Alabama,
Mobile, AL 36688
Mem. ASME

Three-dimensional mixed convection in a horizontal rectangular duct heated from below was studied numerically for a non-Boussinesq fluid. The duct was of aspect ratio four, with cold side-wall boundary conditions. Results were obtained at a reduced temperature of 2.33, Rayleigh number of 130,700, and Reynolds numbers of 5 and 20. Using the Re = 20 solution as initial conditions, the Re = 5 solution developed asymmetries about the duct centerline plane, with a streamwise periodic generation and dissolution of the inner pair of vortices. The consequence of these coherent vortical structures was a complex time-dependent distribution of the Nusselt number on the lower wall, with implications in the area of chemical vapor deposition. Specifically, when compared with the steady flow case occurring at Re = 20, an increased spatial uniformity of the time-averaged Nusselt number along the lower duct surface resulted.

Introduction

The interaction of forced and buoyancy-driven convection in horizontal ducts plays an important role in many areas of technological interest. Of particular concern in the present work is the role of unsteady mixed convection in horizontal chemical vapor deposition (CVD) reactors. CVD involves the deposition of molecules from a fluid phase onto a substrate, with the deposition rate being governed by the rate of diffusion from the fluid to the surface, and by chemical kinetics. CVD films range in thickness from a few nanometers to tens of microns, depending upon the specific application. Tolerances on the quality of the film vary with application, although tolerances for thin-film deposition on electronic and optical materials are very stringent. The quality of the deposition is driven, to a large degree, by the access of (dilute) film precursors to the substrate. Hence, for other than very-low-pressure reactors where operation is in the transition regime and multicomponent diffusion and reaction are the crucial elements, an understanding of the fluid flow within the reactor is essential (cf. Jensen et al., 1991).

The primary parameters governing the flow in horizontal reactors are the Reynolds (Re) and Rayleigh (Ra) (or Grashof (Gr)) numbers, and a reduced temperature defined as $\epsilon = (T_1 - T_0)/T_0$, where T_0 is a mean inlet temperature and T_1 is the heated susceptor temperature. For CVD applications, these parameters usually fall within the ranges $1 \leq \text{Re} \leq 100$, $\text{Gr} < 10^6$, and $\epsilon \approx 2$ (cf. Jensen et al., 1991).

The results from the stability analysis of the classical Rayleigh–Bénard problem of a two-dimensional fluid between infinite plates heated from below indicates that for Rayleigh numbers above a critical value $\text{Ra}_{cr} = 1708$, longitudinal convection (roll) cells develop (independent of the Reynolds number; cf. Gage and Reid, 1968). The imposition of sidewall boundaries increases the value of Ra_{cr} for adiabatic sidewalls. For cold sidewalls the critical Rayleigh number approaches zero (for further discussion, see Platten and Legros, 1984). The presence of sidewalls does not, however, alter the Reynolds number independence of the critical Rayleigh number (Chiu et al., 1987).

For high values of the Rayleigh number and at low Reynolds numbers, transverse recirculation cells may occur. Ingle and Mountziaris (1994) have identified numerically limits below which transverse recirculations do not exist. Their numerically predicted limits were given as $(\text{Gr}/\text{Re}) < 100$ over the range $10^{-3} < \text{Re} \leq 4$, and $(\text{Gr}/\text{Re}^2) < 25$ over the range $4 \leq \text{Re} < 100$. These recirculations are primarily stationary, but traveling wave instabilities have been observed experimentally (Luijkx et al., 1981) and numerically for flows with relatively small temperature differences (cf. Evans and Greif, 1991, 1993) and also in the non-Boussinesq regime (Spall, 1996).

Based upon the experimental results of several investigators, Busse (1978) indicated that transition to unsteady flow patterns may occur for Rayleigh numbers greater than about 5000. Unsteady flows in the form of a "snaking" motion in the low Reynolds number/high Rayleigh number regimes have been observed experimentally (Chiu and Rosenberger, 1987). Experimental observations of Nyce et al. (1992) revealed spatially and temporally oscillating flows at low Reynolds numbers in a horizontal rectangular channel heated from below. This (unsteady) flow regime has been investigated numerically by Evans and Greif (1991, 1993) for a low aspect ratio ($W/H = 2$) reactor at supercritical Rayleigh numbers with adiabatic side walls. Huang and Lin (1995) have also numerically investigated the unsteady flow characteristics of a horizontal rectangular insulated duct for values of $15 \leq (\text{Gr}/\text{Re}^2) \leq 90$. They reported unsteady flows with a "merging and splitting" of the longitudinal roll cells, although the details of this process were difficult to discern. In the numerical and experimental works described above (with the exception of Spall (1996)) the primary emphasis was on low temperature differences, and hence (essentially) constant property fluids.

Both longitudinal and transverse roll cells may adversely affect the uniformity of the CVD deposition process (cf. Jensen et al., 1991; Moffat and Jensen, 1988; Ouazzani and Rosenberger, 1990). Thus, in the present work, the unsteady thermal

and fluid dynamics of horizontal CVD reactors (modeled as a rectangular duct) in the low Reynolds number/high Rayleigh number regime, and at high values of the reduced temperature (where variations in fluid properties cannot be neglected) is investigated numerically.

Numerical Approach and Boundary Conditions

By assuming the concentration of film precursors is low and film growth rates are small, the solution of the fluid and temperature fields may be decoupled from the equations for mass transfer and chemical reaction. In addition, the thickness of the deposited film is much less than the characteristic length scales of the flow, so that no effect of the growth on the fluid dynamics is incurred. The governing equations, then, are those of conservation of mass, momentum, and energy, along with appropriate boundary conditions. In the low Re/high Ra regime, parabolic and two-dimensional approximations are not valid, and thus the fully three-dimensional time-dependent form of the equations must be solved. The governing equations are well known (cf. Jensen et al., 1991); hence, for purposes of brevity they are not shown.

For large temperature differences the Boussinesq approximation, which specifies that the fluid density varies linearly with the temperature, is inappropriate. Hence, in the work presented herein the density of the carrier gas, which was taken as helium, was computed using the ideal gas law. The temperature dependence of viscosity was computed using Sutherland's law in the form $\mu = AT^{3/2}/(B + T)$ where the constants were given as $A = 1.46 \times 10^{-6}$ N s m^{-2} K$^{-1/2}$ and $B = 80.1$ K. The Prandtl number was assumed constant (Pr = 0.7) and thus the conductivity was computed based upon the local viscosity and a constant specific heat ($k = \mu C_p/$Pr), where $C_p = 5200$ J/(kg K). The relevant dimensionless parameters are then the reduced temperature, the Rayleigh number, and the Reynolds number. The Rayleigh number is defined as Ra = $\rho_0 g \epsilon h^3/\mu_0 \alpha_0$, where the characteristic length h was taken as the duct height, μ is the dynamic viscosity, ρ is the density, and α is the thermal diffusivity. The Reynolds number is defined as Re = $\rho_0 u_0 h/\mu_0$ where u_0 represents a characteristic axial inlet velocity. (The reduced temperature, which arises due to the ideal gas law dependence of density on temperature, was defined in the Introduction.) All properties appearing within the dimensionless parameters were evaluated at the duct inlet (denoted by subscript 0).

The computations were performed utilizing the pressure-based finite-volume code CFD-ACE (CFD Research Corporation, Huntsville, AL). Convective terms were discretized using a second-order upwind interpolation scheme, while the viscous terms were represented by second-order central differences. The temporal discretization utilized an implicit Crank–Nicolson-type time differencing scheme with a blending factor of $\phi = 0.6$ to ensure numerical stability ($\phi = 0.5$ results in Crank–Nicolson, $\phi = 1.0$ results in first-order implicit). Convergence within a time step was assumed when the sum of the normalized residuals for each conservation equation was reduced to 10^{-6}, which required approximately 40 iterations. Pressure-velocity coupling was implemented using the SIMPLEC algorithm. A general discussion of pressure-based incompressible flow algorithms is provided in Patankar (1982).

The geometry considered was that of a three-dimensional rectangular channel of length, height, and width 1.0, 0.05, and 0.2 m, respectively. The geometry was discretized using 100 points in the streamwise (x) direction, 30 points in the vertical (y) direction, and 46 points in the spanwise (z) direction. For 0 s $\leq t \leq 38$ s, the gravity vector was oriented in the negative y direction. At $t = 38$ s, and over a time span of 1 s, the gravity vector was rotated 2 deg about the x axis. The purpose of this rotation was to introduce a small perturbation into the flow field. For $t > 39$ s, the vector was again oriented in the negative y

(a)

(b)
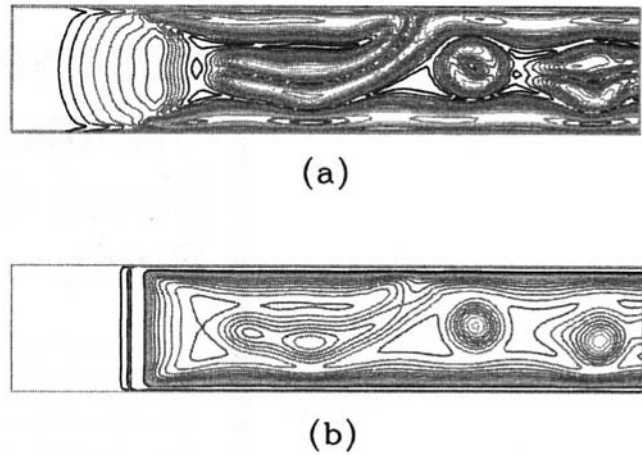
Fig. 1 (a) Contours of constant total vorticity on an x–z plane at $y = 0.05$; 42.25 s after initiation of perturbation; (b) contours of constant Nusselt number on the duct lower surface

direction. (The effects of the perturbation on the flow field are discussed in the results section.) Cold (300 K) side and upper wall boundary conditions were employed. (Cold wall conditions may be employed in CVD applications to minimize side wall deposition.) Zero gradient conditions were enforced at the outlet boundary. A uniform inlet axial (u_0) velocity profile was specified, the inlet fluid temperature was specified as 300 K, and the reference pressure was chosen as atmospheric. The lower duct wall temperatures were chosen as 300 K over 0.0 m $\leq x \leq 0.2$ m and 1000 K over 0.2 m $< x \leq 1.0$ m. The heated lower surface was initiated at $x = 0.2$ m in order to ensure that the initial transverse roll cell did not appear too close to, and hence interfere with, the inlet boundary. Calculations were made for Reynolds numbers of 5 and 20. A numerical time step of 0.1 s was used. Evaluations of the adequacy of the numerical time step and grid spacing were performed, and will be described later.

Results and Discussion

The flow field for the case Re = 20, $\epsilon = 2.33$ and Ra = 130, 700 (or Gr/Re^2 = 467) was computed to provide the initial conditions for the lower Reynolds number calculation. The dominant features at Re = 20 included a leading transverse roll cell, and four steady counterrotating longitudinal vortices, with a clear symmetry about the duct centerline. Since the duct walls were cooled, the rotation of the outer vortices was such that the fluid rotates downward at the wall. The inner two vortices then rotate in a direction opposite to that of their outer neighbors. In CVD and other technological applications, one is interested in the heat transfer from the substrate, toward which these vortical structures exert considerable influence. For instance, along the duct centerline, relatively cold fluid is transported downward, greatly increasing the local Nusselt numbers (and deposition rates) along the midplane of the lower wall. The effect of grid resolution on the initial conditions was investigated through a comparison between Nusselt numbers at nine points along the lower surface computed using the aforementioned 100 $\times$ 30 $\times$ 46 grid, and a 100 $\times$ 20 $\times$ 30 grid. Results revealed differences of less than 2 percent.

Results for which the buoyancy effects take on increased importance are the primary concern of this paper. Toward that end, the dynamics of the flow at Re = 5 (or Gr/Re^2 = 7469) were investigated. To help clarify the structure of this lower Reynolds number flow, contours of constant vorticity magnitude (on an x–z plane at $y = 0.025$ m) are shown in Fig. 1(a) at time level $t = 80.25$ s. Note that this flow is highly unsteady and that this time level is subsequent to the introduction of the

perturbation into the flow field at $t = 38$ s (as discussed in the previous section). For $t < 38$ s, the flow field is unsteady (containing streamwise traveling waves) but appears symmetric about the duct centerline. The effect of the perturbation then is to introduce self-sustaining spanwise asymmetries into the flow field. These asymmetries are clearly observed in Fig. 1(a) for $x > 0.3$ m. The inner two vortices "meander" in the spanwise direction as a function of time and spatial location. At $x \approx 0.6$ m, the inner vortices terminate, either upon themselves, or by merging with one of the outer longitudinal vortices (as shown in the figure). The outer vortex pair then immediately induces the formation of a new inner pair, which subsequently forms a ring vortex and is convected downstream. (The formation of the new inner vortex pair is difficult to discern from contours at a single time level. However, the author has constructed a time-accurate videotape of the flow, which provides insight not available from the contour plot. A copy of the tape may be borrowed from the author.) The ring vortex may then merge with one of the outer vortices, or convect out the end of the computational domain. The formation and termination of the inner vortex pair appears to be a stream-wise periodic process, related to the stability of the longitudinal vortices in the low Re/high Ra regime. We also note that the instability affects the leading transverse roll cell, via a temporal variation in its strength (not apparent from the figure).

As expected, the vortical motions have a dramatic effect on the local Nusselt number distribution along the lower wall, contours of which are plotted in Fig. 1(b). (Here, the Nusselt number is defined as $Nu = -(\bar{T}_{yy})$, where temperature has been made dimensionless with respect to $(T_1 - T_0)$, and lengths with respect to the duct height h.) A comparison between Figs. 1(a) and 1(b) clearly reveals the effect of the longitudinal and ring vortices on the heat transfer rates. Rates are high along the outer regions of the lower wall, due to the presence of the stable outer longitudinal vortices and associated downward transport of relatively cold fluid. The streamwise dissolution and generation of the inner vortex pair causes considerable variation in the heat transfer rates over the inner regions of the lower surface. The highest heat transfer rates over the inner portion of the duct occur beneath the centers of the ring vortices where fluid is convected downward. In regions in which the inner vortex pair is weak or absent, local Nusselt numbers are relatively low. The effect of these asymmetries on mean heat transfer rates is of interest in CVD applications, and is addressed next.

The heat transfer to the lower surface is strongly affected by the presence of the longitudinal and ring vortices. Under steady conditions, the longitudinal vortices affect strong spanwise variations in chemical vapor deposition rates (which are proportional to the heat transfer rates, cf. Jensen et al., 1991). However, at very low Reynolds numbers, which are desirable from the point of view of increased film precursor residence time, the flow may be unsteady. Under these conditions, the temporal development of the Nusselt number along the lower surface, as revealed in a time series plotted in Figs. 2(a-c) (at nine selected points), is of interest. The results at $t = 0$ s indicate the value of the local Nusselt numbers for the steady Re = 20 case. As the solution evolves in time, the influence of the developing streamwise traveling waves becomes apparent. A power spectral analysis reveals the fundamental frequency of these traveling waves (for $t < 38$ s) to be approximately 0.19 cycles/s. Along the duct centerline, at streamwise points $x = 0.675$ m and 0.91 m, a first harmonic of this frequency is also observed. Subsequent to the perturbation of the flow field, the spanwise symmetry is broken. The resulting sharp peaks in the local Nusselt number shown in Figs. 2(a-c) are coincident with the passage of longitudinal and ring vortex structures. Most importantly, the figures suggest that, with the onset of the asymmetric motion, mean Nusselt numbers along the duct centerline abruptly decrease while mean Nusselt numbers at the outer locations increase.
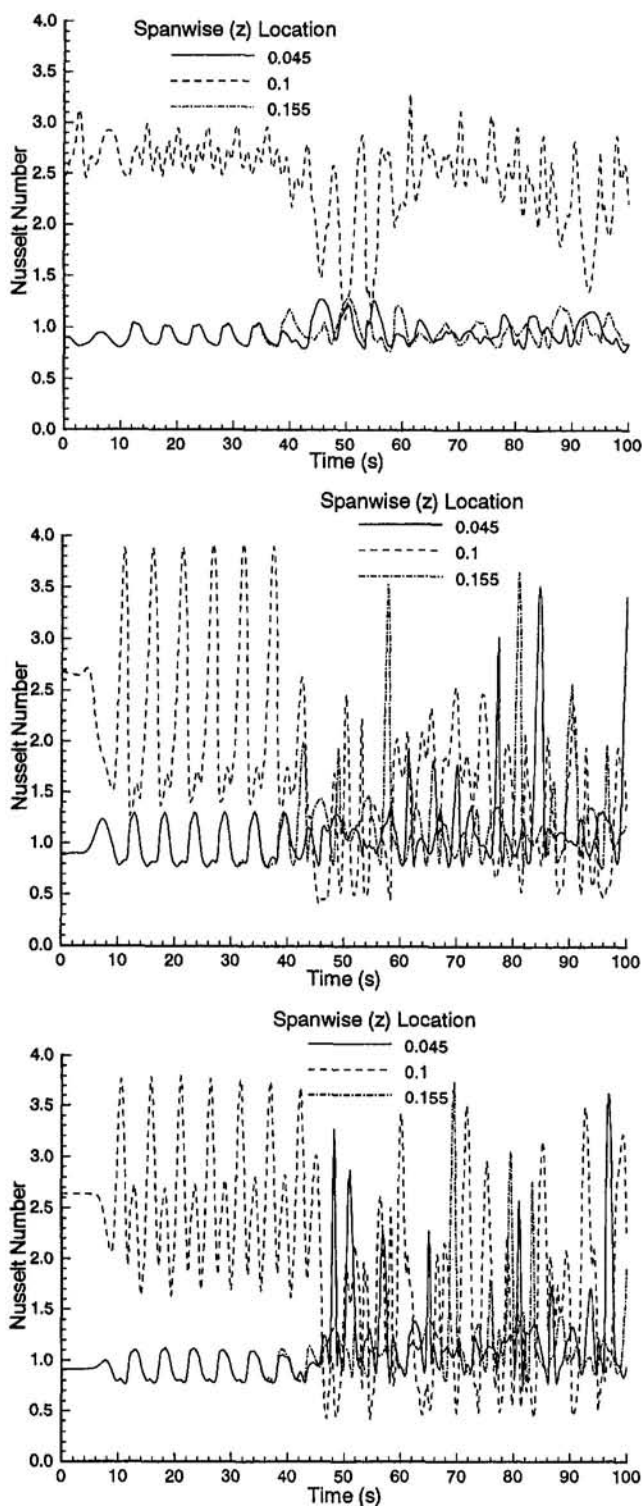
Fig. 2 Nusselt number as a function of time for various locations along the lower surface: (a) $x = 0.44$ m; (b) $x = 0.675$ m; (c) $x = 0.91$ m

This trend is quantified in Figs. 3(a-b) in which mean values of local Nusselt numbers are plotted (following the transition to the spanwise asymmetric flow, and averaged over a sufficiently long time period of 60 s). In addition, the figure provides an indication of the sensitivity of these calculations to the numerical time step and grid resolution. Toward that end, in addition to the "baseline" $100 \times 30 \times 46$ grid calculations with $\Delta t = 0.1$ s (denoted as case 1), results employing a decreased time step $\Delta t = 0.05$ s (on the $100 \times 30 \times 46$ grid; case 2),
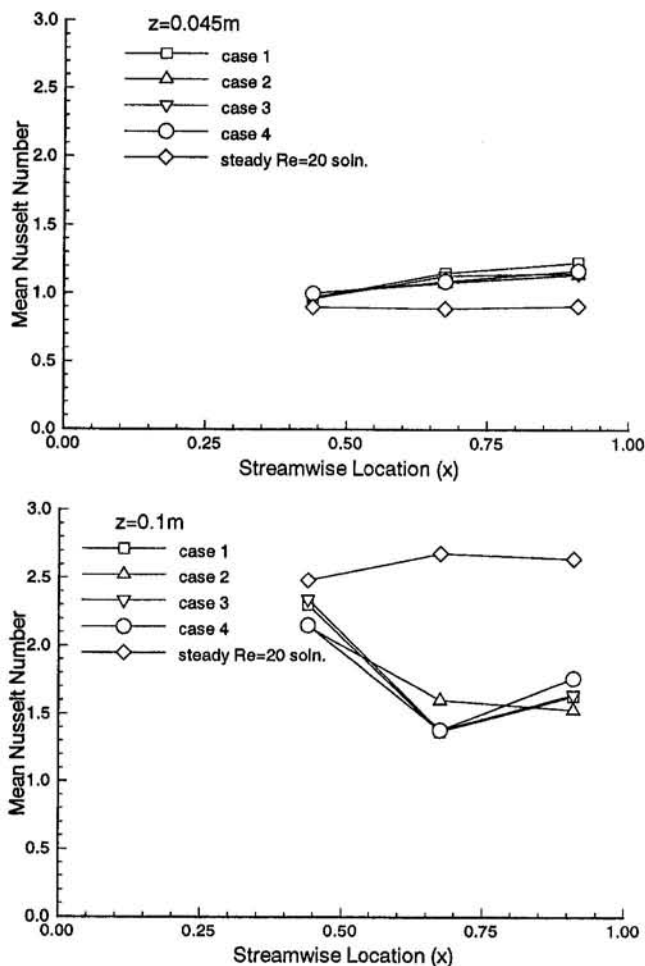
Fig. 3 Mean Nusselt number at selected points along lower surface; case 1: 100 × 30 × 46 grid, Δt = 0.1 s; case 2: same as case 1, except first-order upwinding; case 3: same as case 1, except Δt = 0.05 s; case 4: same as case 1, except 100 × 20 × 30 grid; (a) spanwise location z = 0.045 m; (b) along duct centerline

decreased grid resolution (100 × 20 × 30) (with Δt = 0.1 s; case 3), and first-order upwinding (100 × 30 × 46 grid, Δt = 0.1 s; case 4) are included in the figures. In terms of the baseline calculations, the results reveal that at the streamwise locations x = 0.675 m and x = 0.91 m, and with respect to the steady Re = 20 solution, mean values along the centerline have decreased by approximately 40 percent, while the mean values at the outer locations have increased by approximately 25 percent. The net result is that spanwise variations of the Nusselt number have been considerably reduced. Qualitatively similar results, although not nearly so distinct, occur at x = 0.44 m (where the spanwise asymmetries are less pronounced).

The figure also reveals that the numerical time step of 0.1 s is sufficient; halving the time step reveals no significant change in the mean Nusselt numbers. The effect of spatial resolution is less clear with the largest differences occurring when the first-order upwinding is applied. There is no doubt that additional refinement of the grid would be desirable. However, the calculations are CPU intensive—on the order of 30 h of Cray C94 time was required to advanced the baseline case to 100 s—and thus computational costs prohibited further refinement of the grid. However, the purpose of the study was not to provide precise quantitative values for mean surface heat transfer rates, but to describe qualitatively the spatial smoothing of the heat transfer due to the behavior of the inner vortex pair. In that

sense, spanwise asymmetries, which are key in the smoothing of the mean heat transfer rates, were not significantly diminished under time step and/or grid refinement.

Concluding Remarks

Numerical results indicating time-dependent flows in rectangular geometries heated from below (although with adiabatic side walls) have also been presented in Chiu et al. (1987) and Evans and Greif (1993). However, in those works the results were for constant-property fluids, and the time dependence was found to ensue at values of Gr/Re^2 below 100. (We note that one case in Evans and Greif was computed for variable properties; however, at the relatively low value Gr/Re^2 = 12, the resulting flow was steady.) Additionally, in the works of Chiu et al. (1987), and Evans and Greif (1993), there was no indication of spanwise symmetry breaking.

The observed symmetry breaking, reminiscent of the experimentally observed "snaking" motion described in Chiu and Rosenberger (1987), results in a considerable increase in the spatial uniformity of the mean Nusselt number along the lower surface (when compared with the higher Re steady flow). This uniformity may be expected to result in a more uniform deposition rate for CVD reactors, where time scales are much longer than the period of oscillation of the local Nusselt number as observed in this study.

Acknowledgments

References

Busse, F. H., 1978, "Non-linear Properties of Thermal Convection," *Rep. Prog. Phys.,* Vol. 41, pp. 1930–1967.

Chiu, K. C., and Rosenberger, F., 1987, "Mixed Convection Between Horizontal Plates—I. Entrance Effects," *Int. J. Heat Mass Transfer,* Vol. 30, pp. 1645–1654.

Chiu, K. C., Ouazzani, J., and Rosenberger, F., 1987, "Mixed Convection Between Horizontal Plates—II. Fully Developed Flow," *Int. J. Heat Mass Transfer,* Vol. 30, pp. 1655–1662.

Evans, G., and Greif, R., 1993, "Thermally Unstable Convection With Applications to Chemical Vapor Deposition Channel Reactors," *Int. J. Heat Mass Transfer,* Vol. 36, pp. 2769–2781.

Evans, G., and Greif, R., 1991, "Unsteady Three-Dimensional Mixed Convection in a Heated Horizontal Channel Flow With Applications to Chemical Vapor Deposition," *Int. J. Heat Mass Transfer,* Vol. 34, pp. 2039–2051.

Gage, K. S., and Reid, W. H., 1968, "The Stability of Thermally Stratified Plane Poiseuelle Flow," *J. Fluid Mech.,* Vol. 33, pp. 21–32.

Huang, C. C., and Lin, T. F., 1995, "Vortex Flow and Thermal Characteristics in Mixed Convection of Air in a Horizontal Rectangular Duct: Effects of the Reynolds and Grashof Numbers," *Int. J. Heat Mass Transfer,* Vol. 38, pp. 1661–1674.

Ingle, N. K., and Mountziaris, T. J., 1994, "The Onset of Transverse Recirculations During Flow of Gases in Horizontal Ducts With Differentially Heated Lower Walls," *J. Fluid Mech.,* Vol. 277, pp. 249–269.

Jensen, K. F., Einset, E. O., and Fotiadis, D. I., 1991, "Flow Phenomena in Chemical Vapor Deposition of Thin Films," *Ann. Rev. Fluid Mech.,* Vol. 23, pp. 197–232.

Luijkx, J.-M., Platten, J. K., and Legros, J. C., 1981, "On the Existence of Thermoconvective Rolls, Transverse to a Superimposed Mean Poiseuille Flow," *Int. J. Heat Mass Transfer,* Vol. 24, pp. 1287–1291.

Moffat, H. K., and Jensen, K. F., 1988, "Three-Dimensional Flow Effects in Silicon CVD Horizontal Reactors," *J. Cryst. Growth,* Vol. 135, pp. 459–471.

Nyce, T. A., Ouazzani, J., Arnaud, D,-D., and Rosenberger, F., 1992, "Mixed Convection in a Horizontal Rectangular Channel—Experimental and Numerical Velocity Distributions," *Int. J. Heat Mass Transfer,* Vol. 35, pp. 1481–1494.

Ouazzani, J., and Rosenberger, F., 1990, "Three-Dimensional Modeling of Horizontal Chemical Vapor Deposition. I. MOCVD at Atmospheric Pressure," *J. Crystal Growth,* Vol. 100, pp. 577–599.

Patankar, S. V., 1982, *Numerical Heat Transfer and Fluid Flow,* Hemisphere Publishing Corporation, New York.

Platten, J. K., and Legros, J. C., 1984, *Convection in Liquids,* Chap. 8, Springer, Berlin.

Spall, R. E., 1996, "Unsteady Mixed Convection in Horizontal Ducts With Applications in Chemical Vapor Deposition Processes," *Int. Comm. Heat Mass Transfer,* Vol. 23, pp. 115–122.

Experimental Investigation on Pulsating Horizontal Heating of a Water-Filled Enclosure

B. V. Antohe[1]
Assoc. Mem. ASME

J. L. Lage
J. Lindsey Embrey Associate Professor.
Assoc. Mem. ASME
email: jll@seas.smu.edu

Mechanical Engineering Department,
Southern Methodist University,
Dallas, TX 75275-0337

Experimental results of the natural convection generated by the time periodic horizontal heating of a square cross-section enclosure filled with water are reported. A pulsating (on/off) heat flux is delivered to the heating wall of the enclosure, with the opposite wall cooled by a high thermal capacitance system. All other surfaces are insulated. Heating periods from 32 to 1600 seconds and cycle-averaged heat-flux based Rayleigh numbers from 2.5×10^8 to 1.0×10^9 are considered. Results presented in terms of time series, phase-plane portraits, and cyclic evolution of surface-averaged cooling and heating wall temperatures illustrate the main characteristics of the evolution to periodic regime. Also presented are the cycle-averaged heat transfer coefficient versus heating period, and the corresponding average Nusselt number versus Rayleigh number for various heating frequencies. These results, which support published theoretical and numerical analysis, indicate that by tuning the heating period properly, the heat transfer across an enclosure can be enhanced. The results also reveal that short heating periods hinder the convection within the enclosure, in general (e.g., for $Ra = 7.5 \times 10^8$ and a period of 32 s the heat transfer coefficient is 13 percent smaller than the steady heating value). The sensitivity of the transport phenomenon to pulsating heat is shown to depend strongly on Ra. Finally, a correlation for estimating the maximum heat transfer coefficient, derived from the experimental results, is presented.

Introduction

Natural convection is an important phenomenon with multiple practical applications, such as cooling of electronic equipment, crystal growth, energy storage, mixing, and casting. The periodic reviews of the subject offered by Catton (1978), Hoogendoorn (1986), Yang (1987), and Ostrach (1988) show the diversity of problems related to natural convection. New theories, numerical simulations, and experimental studies are often combined to explain different aspects of natural convection, e.g., flow intensity, temperature distribution, heat transfer, bifurcation, and the influence of geometry, boundary conditions, and fluid properties.

Most studies of natural convection within rectangular enclosures have considered steady processes. Some have considered the unsteady transition from a conduction regime to a steady convection regime. For instance, Patterson and Armfield (1990) presented a thorough experimental, theoretical, and numerical study of transient natural convection initiated by instantaneously heating and cooling the walls of a square cross section cavity filled with water. A similar experimental study was reported more recently by Jeevaraj and Patterson (1992). In their work, an enclosure containing a glycerol–water mixture was heated and cooled at opposing walls. The transient response of the local temperatures allowed the identification of various natural convection regimes depending on the Rayleigh and Prandtl numbers.

Poujol et al. (1993) presented a numerical study of the transition to steady-state natural convection within a square cavity heated uniformly (and steadily) from one side and cooled isothermally from the opposite side. The heat flux based Rayleigh

number and the fluid Prandtl number were equal to 3.9×10^9 and 224, respectively. This same configuration was studied numerically by Lee and Lin (1993) with water filling a tall cavity (aspect ratio equal to six). They showed that the heat capacity of the heating wall has a significant effect on the transport phenomena. Janssen et al. (1993) numerically investigated the transition to time-periodicity of the natural convection in a three-dimensional enclosure filled with air and steadily heated from the sides.

A feature that might promote or hinder the natural convection within an enclosure is to change in time the thermal boundary condition imposed to the system. An example would be the periodic boundary condition that occurs, for instance, in solar-based heating of water reservoirs and residences, on–off operation of electronics, thermally cycled polymerase chain reaction, etc. This feature might trigger the mechanisms responsible for increasing the heat transfer or prevent the same mechanisms from occurring. The increase or decrease in heat transfer can be accessed better by comparing it to the heat transferred by the same system operating at steady state with the same total energy input.

Natural convection within enclosures induced by time-periodic thermal boundary conditions has been investigated in some detail during the last five years. The vast majority of these investigations are numerical and theoretical. The lack of experimental studies has been stressed in a review paper presented recently by Fusegi and Hyun (1994).

The influence of sinusoidal wall temperature on the flow inside a rectangular enclosure of aspect ratio three was studied numerically by Yang et al. (1989). They found, for Pr = 7 (water) and fixed frequency of $50\alpha/L^2$, that the heat transfer amplitude was insensitive to the temperature fluctuation up to a temperature-based Rayleigh number of 5×10^4. From that point on, the heat transfer amplitude increases monotonously until a Rayleigh number of 10^6 is reached. The heat transfer amplitude is estimated to increase by about 15 percent within the Rayleigh number range investigated.

Kazmierczak and Chinoda (1992) simulated the natural convection induced in a square cavity by varying the hot wall temperature in time. The temperature-based Rayleigh number was fixed at 1.4×10^5 and the Prandtl number at 7. Temperature amplitude varied from 20 to 80 percent of the temperature difference between the cycle-averaged hot wall temperature and the cold wall (steady) temperature. Pulsation frequency varied from $50\alpha/H^2$ to $500\alpha/H^2$. Their results indicated that the cycle-averaged heat transfer across the enclosure is insensitive to the wall temperature period and amplitude of oscillation, only changing by approximately 4 percent.

The theoretical and numerical works of Lage and Bejan (1993) and Antohe and Lage (1994) focused on the influence of periodic horizontal heating on the natural convection within a square enclosure. Recently, Antohe and Lage (1996) investigated the amplitude effect on the convective transport within a fluid-filled enclosure and a fully saturated porous enclosure under periodic horizontal heating. Also relevant is the work by Xia et al. (1995) on the natural convection flow stability under wall temperature oscillations.

Obviously, the instantaneous thermal response depends on the frequency and amplitude of the boundary condition (oscillating temperature or heat flux). Less obvious are the frequency and amplitude effects, if any, on the cycle-averaged heat transfer coefficient.

The main motivation of our effort is to provide experimental evidence of a system's response to periodic thermal (heat flux) boundary conditions. We examine the frequency effect of horizontally heating a water-filled enclosure with square cross section. A periodic heat flux is delivered to one wall of the enclosure. The opposite wall is cooled by a high thermal capacitance system designed to reduce the temporal and spatial (three dimensional) effects by minimizing the cooling wall temperature variation. The cycle-averaged heat flux varies from 355 to 1420 W/m² (equivalent heat flux based Rayleigh number from 2.5×10^8 to 1.0×10^9) and the heating period from 32 s to 1600 s (equivalent nondimensional period from 9.2×10^{-4} to 4.6×10^{-2}). The corresponding cycle-averaged temperature-based Rayleigh number range, from 4.76×10^7 to 1.19×10^8, goes beyond the ranges considered by Yang et al. (1989) and by Kazmierczak and Chinoda (1992).

Experimental Setup

Figure 1 outlines the experimental apparatus designed to estimate the influence of periodic heating on the heat transfer process within a 305-mm-deep, 70-mm-high, and 70-mm-wide fluid filled enclosure. The experimental test section is the square cross section at middepth of the enclosure. Notice that the depth is over four times the height of the enclosure minimizing end-side effects as the maximum boundary layer thickness is esti-
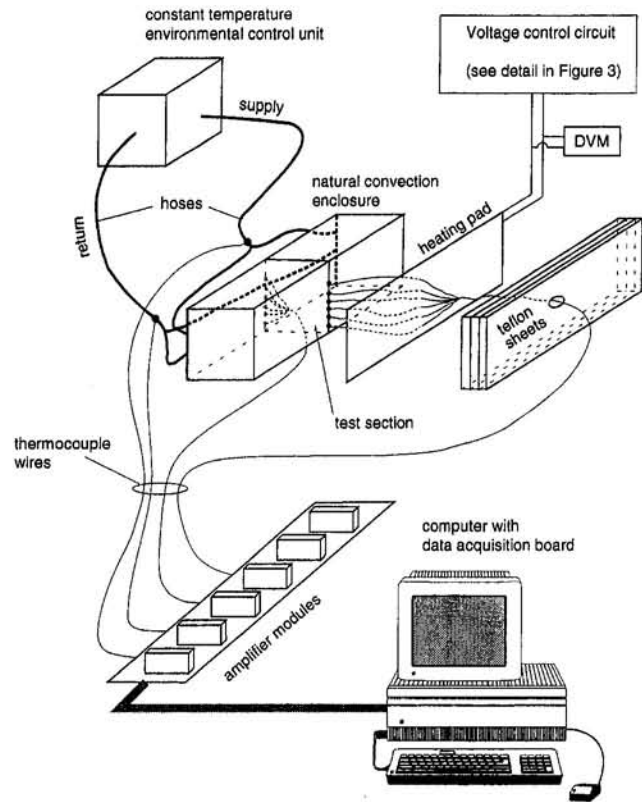
Fig. 1 Experimental setup and data acquisition system

mated to be 1.4 mm (see Eq. (69) of Bejan (1984), p. 132). We note that Lee and Kim (1994) used a rectangular enclosure with a 4:1 depth to height aspect ratio also to minimize end side effects when studying the heat-up of a contained fluid.

The enclosure is built of 25.4-mm-thick Plexiglas surfaces, except for the heating and cooling walls, which are made of 1.5-mm-thick aluminum plates, and sealed with silicon rubber. All Plexiglas surfaces are insulated with 50-mm-thick styrofoam.

A uniform heat flux, dissipated by a flexible heating pad with peak power of 9 kW/m² at 120 V, is delivered to the enclosure through the heating wall. The back side of the electric heater is insulated with 20 sheets of 1.5-mm-thick Teflon insulation pressed against the heating pad (Fig. 1). The surface-averaged heating wall temperature is monitored with five thermocouples placed along the height of the enclosure. Care is taken to obtain a realistic hot wall temperature with minimum disruption of the

--- Nomenclature ---

B = bias limit
g = acceleration of gravity, m/s²
h = instantaneous heat transfer coefficient = $q''/\Delta T$, W/m²K
$\bar{h}$ = cycle-averaged heat transfer coefficient = $\overline{q''}/\overline{\Delta T}$, W/m²K
H = enclosure height, m
k = thermal conductivity, W/mK
L = enclosure width, m
Nu = Nusselt number = $\overline{q''}L/(k\overline{\Delta T})$
P = precision
Pr = Prandtl number = ν/α
$\dot{Q}$ = electric power, W
q'' = heat flux, W/m²

R = electric resistance, ohm
Ra = heat flux based Rayleigh number = $g\beta\overline{q''}H^4/(\nu k\alpha)$
Ra_T = temperature based Rayleigh number = $(H/L)g\beta\overline{\Delta T}H^3/(\nu\alpha)$
S = surface area, m²
t = time, s
T = surface-averaged temperature, K
V = voltage, V
U = uncertainty
α = thermal diffusivity, m²/s
β = isobaric coefficient of volumetric thermal expansion, 1/K
Δ = difference
ν = kinematic viscosity, m²/s

ω = dimensionless period of heat pulsation = $\Omega\alpha/H^2$
Ω = period of heat pulsation, s

Subscripts
h = high (on) heating interval
l = low (off) heating interval
rep = representative
s = steady (constant) heat flux regime
T = temperature based
0 = initial

Superscripts
$(\bar{\ })$ = cycle-averaged

thermal contact between the electric heater and the aluminum wall. To this end, the thermocouple wires are passed through small holes drilled through the Teflon sheets and the electric heating pad. A good thermal contact between the heating pad and the aluminum wall is guaranteed by the slight compression applied to the Teflon sheets during the experiments.

The effectiveness of the heating wall insulation arrangement is checked by calculating the heat loss through the back of the Teflon sheets with the heating pad dissipating 75 W continuously and 0.32 kg/s of water at 17.5°C flowing through the heat exchanger attached to the cooling wall. This is an extreme case because the maximum power used in the experiments is only 60 W. Moreover, this maximum power was never dissipated continuously during the experiments but intermittently, with the maximum cycle-averaged power smaller than 30 W.

A conservative estimate of the heat loss is obtained by assuming the thermal conductivity of the assembled Teflon sheets to be equal to that of a solid Teflon piece ($k_{\text{Teflon}} = 0.23$ W/mK, from Bejan, 1993, p. 629) of same thickness (35 mm). In reality the effective thermal conductivity of the assembly would be smaller than that of a solid Teflon piece due to the thermal contact resistance between the successive sheets. After measuring the average temperature of the heating wall and of the furthermost Teflon sheet, the estimated heat loss was calculated to be less than 6 percent of the total energy dissipated by the electric pad. This result is confirmed indirectly by reducing the coolant flow rate through the cooling wall, and comparing the energy transported by the coolant with the energy dissipated by the heating pad.

It is worth mentioning that a guard-heater, as used by Kazmierczak and Muley (1994), is an option to reduce the heat loss. However, a complex and costly control mechanism would be necessary to adjust the guard-heater power over time to mimic the variation of the heat flowing through the insulation.

An environmental control unit (HX-75 NESLAB), capable of maintaining a constant coolant temperature between zero and 65°C within 0.1°C, extracts heat from the cooling wall by circulating water through a heat exchanger, built specially for this experiment. The water coming from the constant-temperature bath (Fig. 1) to the heat exchanger is distributed to two inlet plena and collected at two outlet plena. Each pair of inlet and outlet plena is linked by eight 6.4 mm diameter copper tubes, forming a counter current heat exchanger. Design details are presented in Fig. 2.

To guarantee superior thermal contact between the copper tubes of the heat exchanger and the cooling aluminum wall, a high-conductivity alloy (70Sn 18Pb 12In, $k_{\text{alloy}} = 46$ W/mK, melting point equal to 162°C) is molded over the tubes. The final contact surface is machined flat. Difficulties in molding the alloy, mainly because of the low adherence of the molten metal to the copper tube surfaces, were overcome by removing the exterior copper oxide layer with an appropriate flux, and by preheating the mold and tubes before pouring the molten alloy.
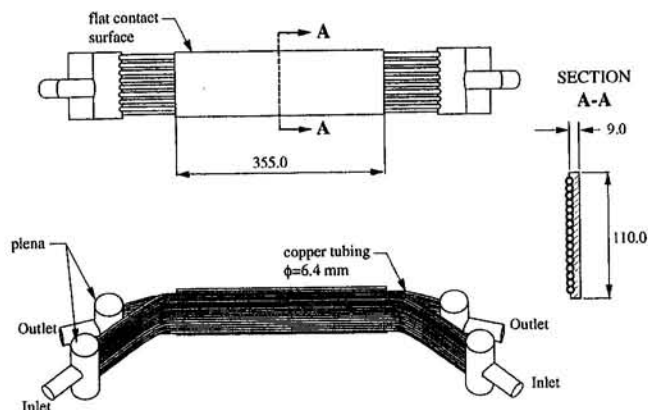
The surface-averaged cooling wall temperature is monitored with five thermocouples distributed along its height. A thin layer of high conductivity thermal paste (OMEGATHERM 201) is used between the molded metal contact surface and the aluminum wall surface to provide the space necessary for the thermocouple wires passing between the two flat surfaces. Extra thermocouples, distributed along the depth of the surface, are used to verify the temperature uniformity of the cooling wall. In the worst case, a heating flux of 60 W and a heating period of 1600 s, the temperature variation along the depth of the enclosure is less than 10 percent (2°C).

The water flow rate through the heat exchanger is measured with a calibrated rotameter and maintained at 0.32 kg/s. This flow rate leads to a uniform cooling temperature in the heat exchanger since the maximum recorded inlet–outlet temperature difference is less than 1°C. The rear of the cooling wall heat exchanger is insulated with approximately 50 mm of expanding insulating foam (Foam Plus™, $k_{\text{Foam}} = 0.032$ W/mK).

A special electronic circuit was designed to control the voltage signal fed to the heating pad. The main circuitry is sketched in Fig. 3(a). The control system, depicted in Fig. 3(b), is built with three relays, three resistance potentiometers, and a recycle timer. All relay switches are drawn in the nonactive position.

The control system is sufficiently flexible to deliver a constant or a pulsating voltage signal with independent high and low amplitudes to the heating pad (see Fig. 3(c)). In the constant voltage regime, the switch S is closed and the electric current flows through the rheostat VR1 that controls the constant (steady) voltage level V_s. In the pulsating regime, the switch S is open and the main circuit is closed alternatively through rheostats VR2 and VR3 following the timer command. In this case, the voltage delivered to the heating pad switches from a high voltage V_h to a low voltage V_l, respectively. Note that all the voltages V_s, V_l, and V_h, can be set independently from zero to 120 V.

High heating (Ω_h) and low heating (Ω_l) periods are also set independently by adjusting the on and off intervals of the timer, from one to 1023 seconds. The voltage applied to the electric pad is continuously monitored by a digital voltmeter. Small fluctuations (less than 0.5 V) are observed during the experiments due to electric load variation. We assume that the heat flux across the heating aluminum wall (into the enclosed fluid) mimics the time evolution of the electric power dissipated by the heating pad due to Joule effect, $\dot{Q} = V^2/R$. Therefore, the instantaneous heating wall heat flux, in W/m², is

$$q'' = \frac{\dot{Q}}{S} \tag{1}$$

where S is the heating wall surface area in square meters. Equation (1) neglects the thermal capacitance of the heating wall, a reasonable assumption because the time constant of the aluminum wall is of the order of 0.01 s (wall thickness of 1.5×10^{-3} m, and thermal diffusivity of 8.5×10^{-5} m²/s), that is, three orders of magnitude smaller than the shortest heating interval (16 s) investigated here.

Teflon insulated type-K thermocouple wire (40 AWG, 380 μm diameter), with an operational temperature range from 0°C to 1000°C, is used to measure the surface temperatures. The response time of this thermocouple is 0.04 s for 63.2 percent response to a temperature increase from 37°C to 93°C in still water. Electronic modules (GWI-5B47K-05, 0.05 percent accurate) amplify and transmit the low voltage output signal from each thermocouple to the computer data acquisition board (Fig. 1). These amplifiers linearize the output voltage, provide a cold junction compensation, and reduce noise by continuous transformer isolation.

Fig. 2 Cooling system design
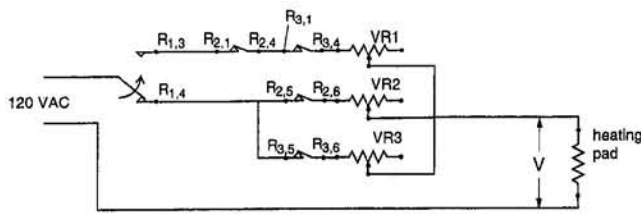
(a) Main circuit
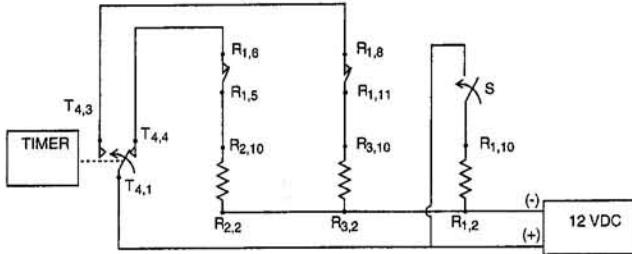
(b) Control circuit
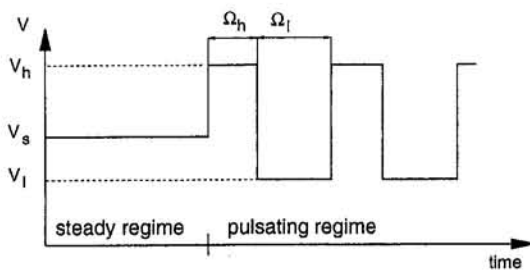
(c) Ouput voltage

Fig. 3 Voltage control circuits and output voltage

A data acquisition hardware, consisting of a MacADIOS II/16 A/D nubus board manufactured by GW Instruments installed on a Macintosh IIci computer, provides a high-speed, real-time interface capable of acquiring and converting data at 15 μs per channel operating at 16 bit resolution. The data acquisition process is controlled by setting the sampling rate (from 0.25 s to 1.0 s) and the number of points to be collected.

Procedure

Each experiment starts by filling up the enclosure with previously boiled distilled water. The environmental control system is turned on and set at the cooling temperature of $T_0 = 17.5°C$. This temperature is maintained constant for all experiments. After the water inside the enclosure achieves thermal equilibrium with the cooling wall, the electric circuit is activated in the steady heating regime with an average heat flux obtained by setting the voltage to the heating pad at V_s,

$$V_s^2 = \frac{V_l^2 + V_h^2}{2} \quad (2)$$

The heater is kept on until the system reaches a steady state (when the temporal variations of the heating wall and the cooling wall temperatures are less than 0.5°C within two hours). At this point, the pulsating regime between pre-established high and low voltages (V_l and V_h) is started. The experimental results reported here are obtained with zero low voltage, $V_l = 0$, in an on/off heating configuration. Therefore, the steady heat flux q_s'' is half of the high heat flux q_h''.

The heating and nonheating intervals are equal, $\Omega_h = \Omega_l = \Omega/2$, during each experiment. After an initial transient, a periodic convection regime is observed to set in for all cases. The initial transient is relatively short, taking from 5 to 15 cycles depending on the heat flux and heating period, as illustrated in Fig. 4 (top). In it, a time series of the surface-averaged heating and cooling wall temperatures for a heating period of 320 s and an average heat flux of 1420 W/m^2 is presented. The corresponding phase-plane portrait of the surface-averaged heating and cooling wall temperatures, shown in Fig. 4 (bottom), indicates the periodic regime.

Uncertainty Analysis

A cycle-averaged global heat transfer coefficient across the enclosure is defined as

$$\bar{h} = \frac{\overline{q''}}{\overline{\Delta T}} = \frac{q_s''}{\overline{\Delta T}} \quad (3)$$

where $\overline{\Delta T}$ and $\overline{q''}$ are the surface-averaged hot and cold wall temperature difference and the heat flux crossing the heating wall, respectively, both averaged during one cycle. Notice that in the present study $\overline{q''}$ equals the steady heat flux q_s''.

In order to estimate the uncertainty of the computed heat transfer coefficient, an analysis is performed following the general guidelines provided by Kim et al. (1993). Accounting for the bias B and the precision P limits of the measured variables, the uncertainty of the average heat transfer coefficient is calculated as

$$U_{\bar{h}} = [P_{\bar{h}}^2 + B_{\bar{h}}^2]^{1/2} \quad (4)$$
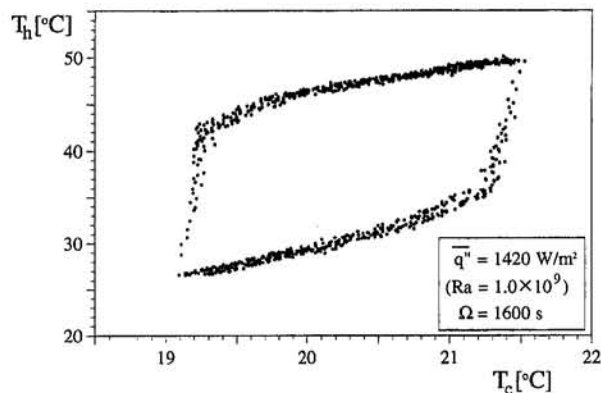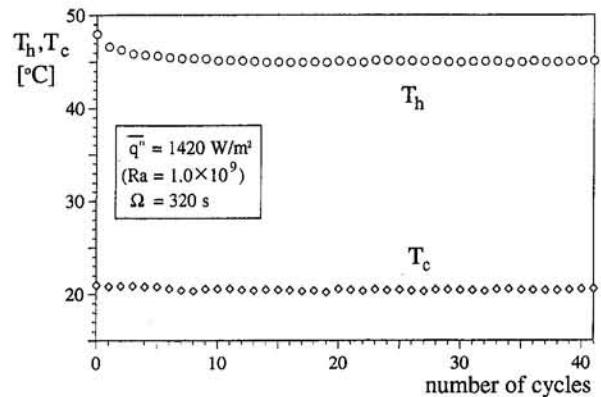
Fig. 4 Time series of hot and cold wall temperatures: evolution to periodic regime, $q_s'' = 1420$ W/m^2 (Ra = 1.0 × 10^9); top: temperatures at midcycle for $\Omega = 320$ s; bottom: phase portrait for $\Omega = 1600$ s

Applying the error propagation equation (Kline and McClintock, 1953) to Eq. (3), the bias and precision limits of the heat transfer coefficient are, respectively:

$$\left(\frac{B_{\bar{h}}}{\bar{h}}\right)^2 = \left(\frac{B_{\overline{q''}}}{\overline{q''}}\right)^2 + \left(\frac{B_{\overline{T_h}}}{\overline{\Delta T}}\right)^2 + \left(\frac{B_{\overline{T_c}}}{\overline{\Delta T}}\right)^2 - 2\frac{B_{\overline{T_h}}^{\bar{L}} B_{\overline{T_c}}^{\bar{L}}}{(\overline{\Delta T})^2} \quad (5)$$

$$\left(\frac{P_{\bar{h}}}{\bar{h}}\right)^2 = \left(\frac{P_{\overline{q''}}}{\overline{q''}}\right)^2 + \left(\frac{P_{\overline{T_h}}}{\overline{\Delta T}}\right)^2 + \left(\frac{P_{\overline{T_c}}}{\overline{\Delta T}}\right)^2 \quad (6)$$

Because all the thermocouples are calibrated by the manufacturer, using the same equipment and procedure, the bias limits for hot and cold temperatures cancel out in Eq. (5).

The bias of the cycle-averaged heat flux can be derived from Eq. (1), written as $\overline{q''} = V_h^2/(2RS)$, using the error propagation equation. The bias of the surface and resistance measurements as well as the bias of the averaging time (equal to one period) are negligible in comparison with the voltage measurement bias obtained from calibrating the multimeter, equal to 0.5 percent for AC voltage. Therefore,

$$\frac{B_{\bar{h}}}{\bar{h}} = 2\frac{B_{V_h}}{V_h} \quad (7)$$

The precision limit of the cycle-averaged heat flux is determined by the heat lost to the ambient. This really represents a precision limit, because in the computation of this heat transfer coefficient, the energy dissipated by the heating pad is used instead of the heat delivered to the enclosure. As mentioned before, a conservative upper bound estimate for the heat flux precision, $P_{\overline{q''}}/\overline{q''}$, is 6 percent.

Several runs with the same steady heat flux q'' were performed, and the results used to estimate the precision limit of the cycle-averaged cold and hot wall temperatures. A final formula for computing the uncertainty of the heat transfer coefficient is obtained as:

$$\frac{U_{\bar{h}}}{\bar{h}} = \left[\left(2\frac{B_{V_h}}{V_h}\right)^2 + \left(\frac{P_{\overline{q''}}}{\overline{q''}}\right)^2 + \left(\frac{P_{\overline{T_h}}}{\overline{\Delta T}}\right)^2 + \left(\frac{P_{\overline{T_c}}}{\overline{\Delta T}}\right)^2\right]^{1/2} \quad (8)$$

A summary of the values used to calculate the uncertainty of $\bar{h}$ is presented in Table 1. A representative hot/cold wall temperature difference is considered for each average heat flux $\overline{q''}$. Also included is the corresponding heat flux based Rayleigh number (all properties at the reference temperature of 23°C). As can be seen, the $\bar{h}$ uncertainty decreases as $\overline{q''}$ increases, which corresponds to an increase in $\overline{\Delta T}_{\text{rep}}$. It is worth mentioning that the predominant source of experimental uncertainty is the precision of the heat flux value, conservatively estimated to be 6 percent.

Table 1 Representative uncertainty values of heat transfer coefficients at different cycle-averaged heat fluxes

$\overline{q''}$ [W/m²]	Ra	B_{V_h}/V_h [%]	$P_{\overline{q''}}/\overline{q''}$ [%]	$P_{\overline{T_h}}$ [°C]	$P_{\overline{T_c}}$ [°C]	$\overline{\Delta T}_{\text{rep}}$ [°C]	$U_{\bar{h}}/\bar{h}$ [%]
355	2.5×10⁸	0.5	6	0.4	0.2	8	8.3
710	5.0×10⁸	0.5	6	0.5	0.2	12	7.6
1065	7.5×10⁸	0.5	6	0.7	0.3	18	7.4
1420	1.0×10⁹	0.5	6	0.8	0.4	20	7.6
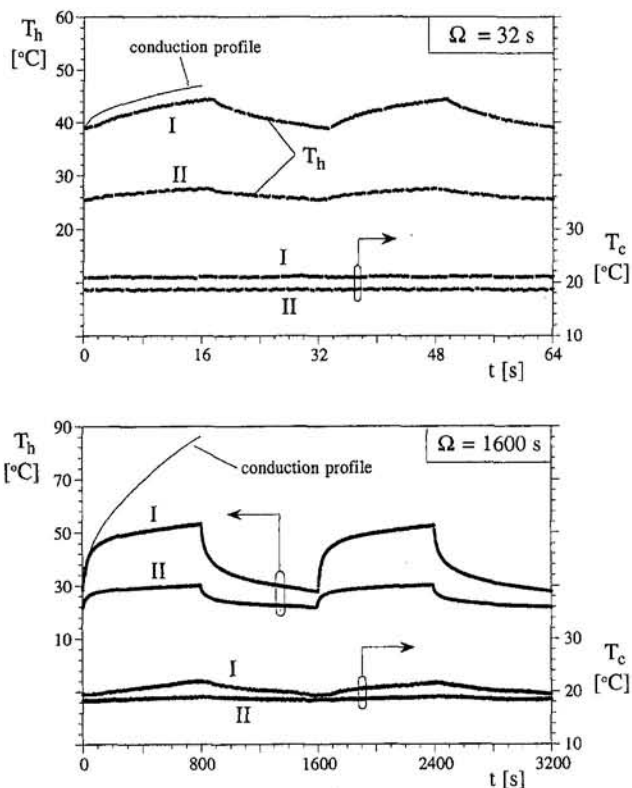
Fig. 5 Time evolution of hot and cold wall temperatures: (I) $q_s'' = 1420$ W/m² (Ra = 1.0 × 10⁹); (II) $q_s'' = 355$ W/m² (Ra = 2.5 × 10⁸)

Results and Discussion

The cycle-averaged global heat transfer coefficient, defined in Eq. (3), is computed from the instantaneous hot and cold wall temperatures. These temperatures were recorded using at least 128 points per cycle after the steady periodic regime is achieved.

Typical time evolutions of hot and cold surface temperatures are presented in Fig. 5, where, for convenience, the temperatures corresponding to the smallest (curves II: for $\overline{q''} = 355$ W/m², Ra = 2.5 × 10⁸) and largest (curves I: for $\overline{q''} = 1420$ W/m², Ra = 1.0 × 10⁹) heat fluxes are plotted in the same graph. The heating period is 32 s (Fig. 5, top) and 1600 s (Fig. 5, bottom).

For the configuration shown in the top graph, the temperature of the hot wall T_h increases smoothly during the heating interval. The hot wall temperature when $q'' = 1420$ W/m² (Ra = 1.0 × 10⁹) is approximately 50 percent higher than the temperature when $q'' = 355$ W/m² (Ra = 2.5 × 10⁸), and the temperature amplitudes are around 5°C and 2°C, respectively. The cold wall temperature variation is within the uncertainty of the temperature measurement.

Figure 5 (bottom), corresponding to $\Omega = 1600$ s, shows similar characteristics. A distinct feature is the higher cold wall temperature amplitude, around 2°C for the largest heat flux case. Also, the hot wall temperature amplitudes are increased to around 25°C for $q'' = 1420$ W/m² (Ra = 1.0 × 10⁹) and 8°C for $q'' = 355$ W/m² (Ra = 2.5 × 10⁸).

We included in both graphs the hot wall temperature evolution during a high heating interval obtained from the solution given by Carslaw and Jaeger (1959), for an infinitely long solid wall with constant heat flux and constant temperature boundary conditions. These pure conduction results are obtained numerically by setting the isothermal wall at a temperature equal to the cooling wall temperature value of our experiment, and using the temperature profile of constant heating at cycle-averaged
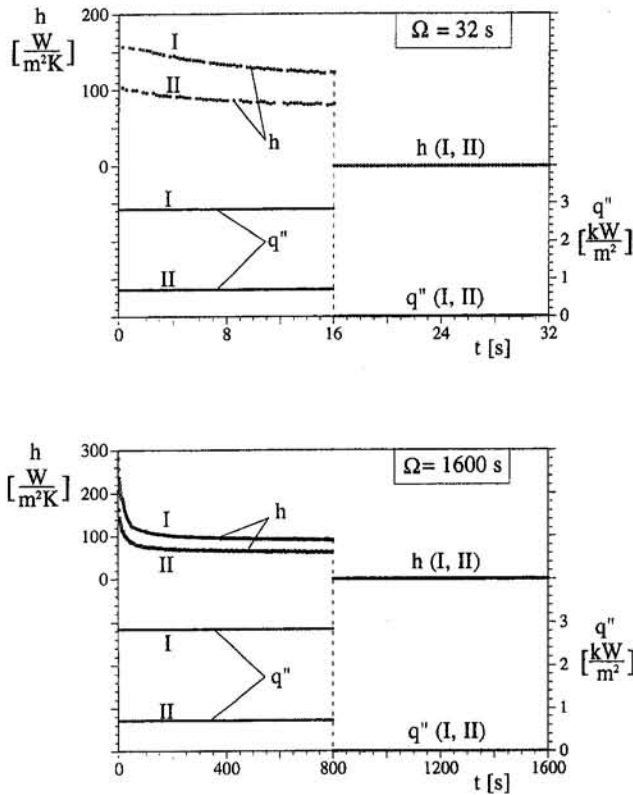
Fig. 6 Time evolution of instantaneous heat transfer coefficient and hot wall heat flux: (I) $q''_h = 1420$ W/m² (Ra = 1.0 × 10⁹); (II) $q''_h = 355$ W/m² (Ra = 2.5 × 10⁸)

evolution of h during the high heating interval is essentially the same as the inverse of the hot wall temperature because the variation in time of the cold wall temperature is negligible compared to the variation of the hot wall temperature, and because the heat flux is constant. For long heating periods, Fig. 6 (bottom) h evolves asymptotically toward a steady value (corresponding to heating with high heat flux—values presented in Figs. 7 and 8) following a sharp decrease at the beginning of the high heating interval. It is worth mentioning that h is zero during the low heating interval by definition (q'' is zero).

Using Eq. (3) and the temperature difference $\overline{\Delta T}$, the cycle-averaged heat transfer coefficient, $\overline{h}$, is computed and presented in Figs. 7 and 8 as function of the pulsation period, Ω. Reference error bars display the uncertainties of the experimental results (summarized in Table 1). Two configurations are chosen for comparison, namely: (1) steady heating with the average heat flux, $\overline{q''}$, and (2) steady heating with the high heat flux used in the pulsating experiment, q''_h. The dashed lines in Figs. 7 and 8 indicate the corresponding heat transfer coefficients obtained experimentally with these configurations. Configuration (1) is important because it uses the same energy input of the pulsating case for heating the enclosure. Configuration (2) provides an important upper bound reference of steady heating.

A general feature of all the graphs is the increase of $\overline{h}$ with the pulsation period. This is not obvious in the top graph of Fig. 7 ($\overline{q''} = 355$ W/m², Ra = 2.5 × 10⁸). In this case, all of the points are in the uncertainty band due to the small temperature differences, $\overline{\Delta T}$. Although the results for $\overline{q''} = 710$ W/m² (Ra = 5.0 × 10⁸) are still within the estimated uncertainty band, the increasing tendency can be clearly observed. Cases of higher cycle-averaged heat flux, depicted in Fig. 8, show an increase in the heat transfer coefficient beyond the uncertainty band. For $\overline{q''} = 1420$ W/m² and $\Omega = 426$ s for instance, the maximum $\overline{h}$ is approximately 20 percent higher than the heat

heat flux as the initial temperature distribution of the wall. The temperature distribution at the end of the high heating interval is used as the initial condition for the computation during the low heating interval. Calculations proceed until a steady periodic regime is reached. The solution for high heat flux (case I) is scaled down (for comparison) to the experimental temperature value at the beginning of the heating interval.

Notice that the experimental hot wall temperature evolution of case I and $\Omega = 1600$ s (Fig. 5, bottom) presents two distinct phases. An initial short phase shows the same time rate of increase as the pure conduction profile. The following phase indicates a much slower rate of increase as compared to the conduction profile (at the same time). This behavior indicates the predominance of convection, enhancing the heat transfer across the enclosure and lowering the hot wall temperature. The flattening of the hot wall temperature evolution indicates the asymptotic tendency of the system toward a steady state. A shorter transient regime is noticed when decreasing the heat flux (note how the hot temperature curve II, in the bottom graph, gets to steady regime faster than curve I).

Figure 5 (top), for period $\Omega = 32$ s, indicates that the experimental temperature evolution is similar (in shape) to the conduction profile. In this case, a convection-dominated phase is not achieved because the shorter heating interval does not provide enough time for a strong convection regime to occur.

Figure 6 presents the instantaneous heat transfer coefficient defined as

$$h = \frac{q''}{\Delta T} \qquad (9)$$

where ΔT is the instantaneous temperature difference between heating and cooling walls and q'' is the instantaneous heat flux crossing the heating wall, for the same heating configurations of Fig. 5. Note, for short periods (Fig. 6, top), that the time
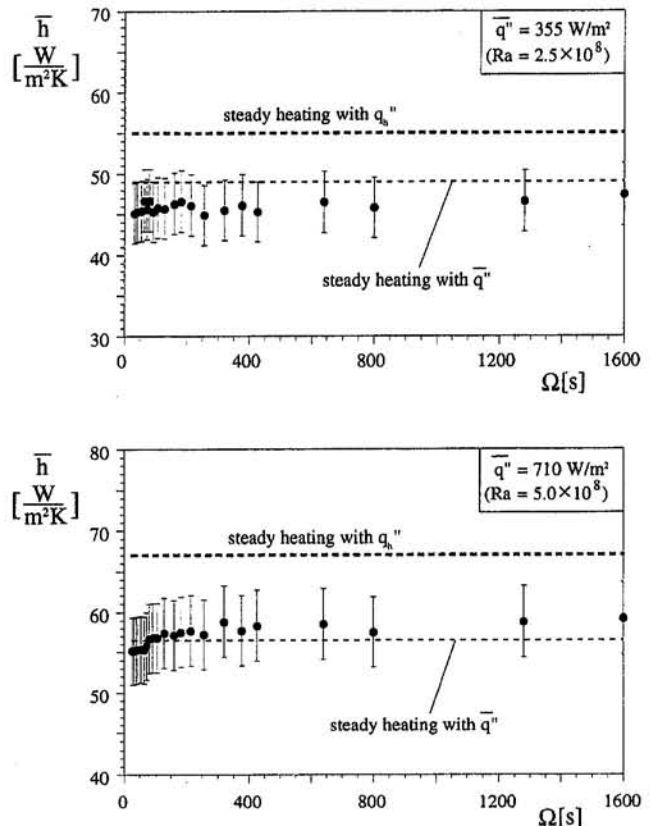

Fig. 7 Cycle-averaged heat transfer coefficient as a function of pulsation period for small (top) and intermediate (bottom) heat fluxes
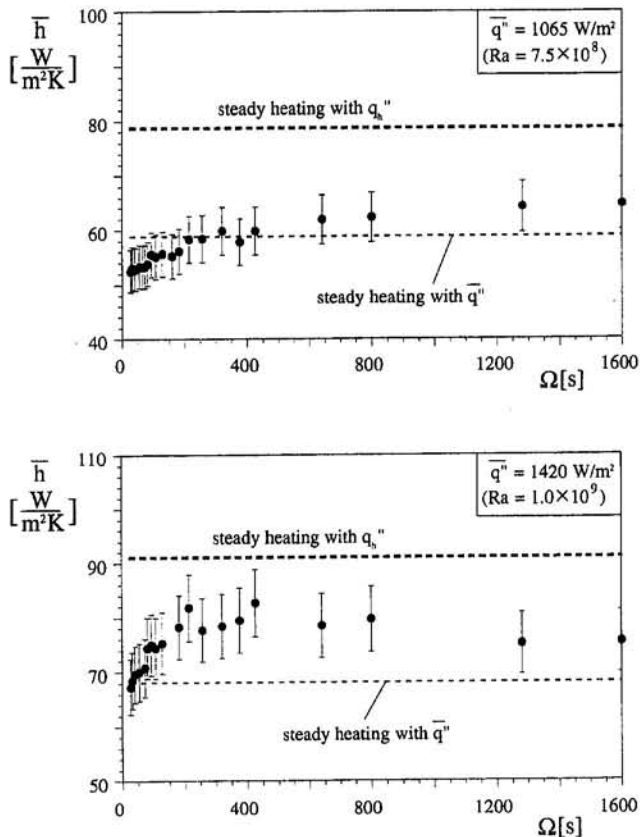
Fig. 8 Cycle-averaged heat transfer coefficient as a function of pulsation period for intermediate (top) and large (bottom) heat fluxes

transfer coefficient obtained when heating the enclosure steadily with $\overline{q}''$. This agrees qualitatively with the findings of Yang et al. (1974) that an increase in the pulsation period leads to an increase of about 15 to 20 percent in the cycle-averaged heat transfer coefficient when heating a vertical plate with oscillatory surface temperature (Rayleigh number from 7×10^5 to 7×10^8).

Notice also that the period range investigated by Kazmierczak and Chinoda (1992), from 70 to 700 seconds, is within the range presented in Figs. 7 and 8. The fact that in their analysis the cycle-averaged heat transfer coefficient seems insensitive to the pulsating thermal condition might be associated with the relatively low Rayleigh number they investigated, equal to 1.4 $\times 10^5$, compared to the equivalent temperature based Rayleigh number range studied here, from 4.76×10^7 to 1.19×10^8, and the different boundary condition (temperature instead of heat flux).

It is worth noting the position of the thin dashed lines relative to the pulsating heat results (black circles). For $\overline{q}'' = 355$ W/m^2 (Ra $= 2.5 \times 10^8$), in Fig. 7, the line is above all the experimental results, indicating that for this particular configuration pulsating heat hinders the heat transfer across the enclosure. In fact, all the graphs of Figs. 7 and 8 indicate that at short pulsation periods, the cycle-averaged heat transfer coefficient is smaller than the one obtained by heating the enclosure steadily with the corresponding average heat flux, $\overline{q}''$.

We offer the following explanation for this apparent anomaly. As the high heating interval is shortened, the fluid acceleration (negative buoyancy effect) along the heating wall is reduced because the adjacent fluid has less time to have its temperature increased. Therefore, a fluid pack adjacent to the heating wall travels a shorter distance. Now, consider a situation in which this heated fluid pack reaches the top section of the enclosure at the end of the high heating interval, where its movement is con-strained by slower fluid ahead and by the top surface of the enclosure. During the following low (off) heating interval, this heated fluid pack continues to move by inertia, sinking toward the center of the enclosure and bringing with it its internal energy. The fluid pack, now stable at the center of the enclosure, has to transfer its energy to the cooling wall by diffusion (increased thermal resistance), deteriorating the global heat transfer process across the enclosure. Consequently, the temperature difference between the heating and the cooling walls increases, thus reducing the heat transfer coefficient (Eq. (3)) compared with the value obtained with steady $\overline{q}''$ heating. We note in passing that this explanation is qualitatively supported by the numerical visualization of streamlines and isotherms presented by Antohe and Lage (1994).

For the same $\overline{q}''$ value, the increase in heat pulsation period should cause an enhancement of the heat transfer process because the longer heating interval allows the fluid pack to reach the cold wall, improving the heat transfer mechanism. One would expect the cycle-averaged heat transfer coefficient to at least approach that of steady heating (thin dashed lines in Figs. 7 and 8). However, the generation of intermittent flow eddies that sweep across the center of the enclosure (as shown numerically by Antohe and Lage, 1996) supports the expectation of higher cycle-averaged heat transfer coefficient, clearly detected in the bottom graph of Fig. 8. These flow eddies provide a better heat transport inside the enclosure. Evidently, further increase in pulsation period should lead to a decrease in heat transfer coefficient toward the value obtained by heating the enclosure steadily with $\overline{q}''$, as in Fig. 8 (bottom), because the unsteady flow (eddies) decays rapidly within each heating interval. Therefore, the majority of the heating interval becomes dominated by a flow resembling the steady flow (this conclusion is supported by the long heating period results of Fig. 6, bottom).

Notice that the equivalent cycle-averaged temperature based Rayleigh number, Ra$_T$, obtained here as (notice that $H/L = 1$)

$$\mathrm{Ra}_T = \frac{\mathrm{Ra}}{\mathrm{Nu}} \tag{11}$$

ranges from 4.76×10^7 to 1.19×10^8. Therefore, the largest Rayleigh number is of the same order of magnitude as that in the experiments performed by Patterson and Armfield (1990), 3.26×10^8. Their results showed an oscillatory approach to steady-state regime under steady heating and cooling. The heat transfer oscillation presents an initial cycle of 87 seconds. Therefore, at the high Ra limit, our system may be prone to natural instability that would justify the heat transfer coefficient increase for periods of the order of 100 s (Fig. 8, bottom).

The matching between the natural frequency of the system and the forcing frequency of the pulsating heat increases the cycle-averaged heat transfer coefficient. Lage and Bejan (1993) presented a theory for estimating the natural frequency of our system under pulsating horizontal heating. Antohe and Lage (1996) offered a refined method for estimating this frequency. They showed that the heat transfer enhancement is proportional to Ra and that the natural frequency is inversely proportional to Ra, predictions that agree well with the experimental results of Figs. 7 and 8. The well-defined heat transfer enhancement for the period 200–400 s, shown in Fig. 8 (Ra $= 1.0 \times 10^9$), compares well with the predicted resonance period of 90 s.

In Fig. 9 the dimensionless cycle-averaged global heat transfer coefficient, Nu, is presented versus the heat flux based Rayleigh number for several nondimensional pulsating periods, defined as $\omega = \Omega \alpha / H^2$. The nondimensional pulsation periods show that the dimensional period is much smaller than the characteristic diffusion time.

For low Rayleigh numbers (Ra $< 5 \times 10^8$) the pulsation period has a negligible effect on Nu. For Ra $> 5 \times 10^8$, Nu becomes highly dependent on ω. The variation from the mean
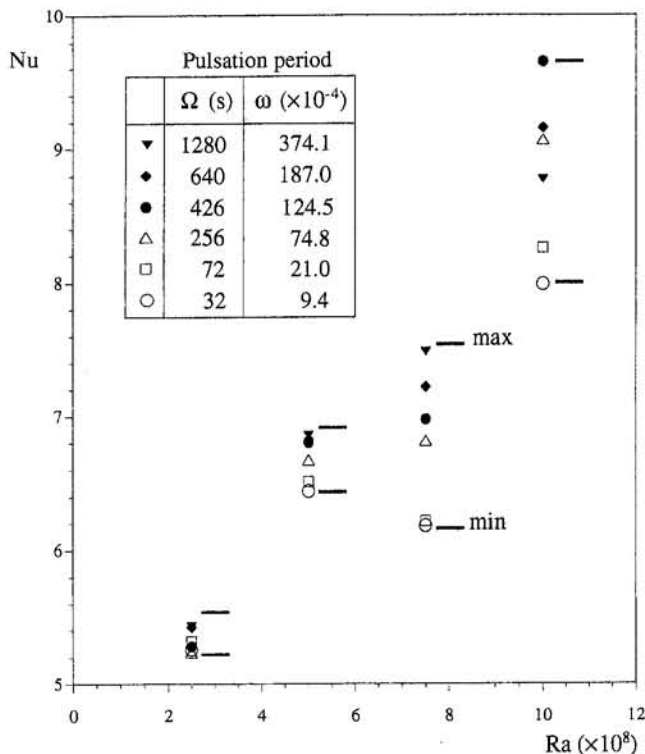
Fig. 9 Cycle-averaged Nusselt number as a function of Rayleigh number and pulsation period

Pulsation period		
	Ω (s)	ω ($\times 10^{-4}$)
▼	1280	374.1
◆	640	187.0
●	426	124.5
△	256	74.8
□	72	21.0
○	32	9.4

Nu value is about ±14 percent for Ra = 7.5×10^8 and about ±16 percent for Ra = 10^9. For a fixed pulsation period, the Nu variation is not uniform as Ra increases. For instance, from Ra = 7.5×10^8 to 10^9, Nu varies by 38 percent if the pulsation period is equal to 1.08×10^{-2} ($\Omega = 376$ s), and by just 17 percent if $\omega = 3.7 \times 10^{-2}$ ($\Omega = 1280$ s). This is a consequence of combining buoyancy (represented by Ra) and pulsation (represented by ω) effects.

From the experimental results, the maximum Nusselt number at each Rayleigh number can be approximated by

$$\text{Nu} = 5.16 \times 10^{-3}\,\text{Ra}^{0.36} \qquad (12)$$

with a maximum error of ±5.6 percent. Note that the Rayleigh number exponent is greater than the exponent for the isothermal–isothermal and the isoflux–isoflux configurations, i.e., about 0.22 (Bejan, 1993, pp. 369–371). This result suggests a stronger buoyancy influence on the convection heat transfer under optimum pulsating heating.

Conclusions

Our experimental results indicate that pulsating heat can enhance or hinder the heat transfer across a water-filled enclosure, depending on the pulsation frequency, when compared to heating the same enclosure steadily with the cycle-averaged heat flux. For short pulsation periods the heat transfer across the enclosure is hindered, decreasing the average global heat transfer coefficient by as much as 13 percent in the case of Ra = 7.5×10^8 and $\Omega = 32$ s. Generally, the heat transfer coefficient increases with the pulsation period. For Ra $\geq 7.5 \times 10^8$ the coefficient increases beyond the steady heating value and then decreases asymptotically toward it. We observed a heat transfer enhancement of 20 percent for Ra = 1.0×10^9 and $\Omega = 426$ s. This increase seems to occur when the frequency of pulsating heat approaches the natural frequency of the flow inside the

enclosure, a quantity that can be estimated theoretically, inducing a form of thermal resonance.

For low Rayleigh numbers (Ra $< 5 \times 10^8$), the results indicate a negligible pulsation period effect on Nu. For Ra $> 5 \times 10^8$, Nu becomes highly dependent on ω. An equation obtained by interpolating the experimental results estimates the maximum cycle-averaged global heat transfer coefficient within the pulsation period and Ra ranges considered here.

References

Antohe, B. V., and Lage, J. L., 1994, "A Dynamic Thermal Insulator: Inducing Resonance Within a Fluid Saturated Porous Medium Enclosure Heated Periodically From the Side," *Int. J. Heat Mass Transfer*, Vol. 37, pp. 771–782.

Antohe, B. V., and Lage, J. L., 1996, "Amplitude Effect on Convection Induced by Time-Periodic Horizontal Heating," *Int. J. Heat Mass Transfer*, Vol. 39, pp. 1121–1133.

Bejan, A., 1984, *Convection Heat Transfer*, Wiley, New York.

Bejan, A., 1993, *Heat Transfer*, Wiley, New York.

Carslaw, H. S., and Jaeger, J. C., 1959, *Conduction of Heat in Solids*, Oxford University Press.

Catton, I., 1978, "Natural Convection in Enclosures," *Sixth Int. Heat Transfer Conference*, Vol. 6, pp. 13–30.

Fusegi, T., and Hyun, J. M., 1994, "Laminar and Transitional Natural Convection in an Enclosure With Complex and Realistic Conditions," *Int. J. Heat Fluid Flow*, Vol. 15, pp. 258–268.

Hoogendoorn, C. J., 1986, "Natural Convection in Enclosures," *Eighth Int. Heat Transfer Conference*, Vol. 1, pp. 111–120.

Janssen, R. J. A., Henkes, R. A. W. M., and Hoogendoorn, C. J., 1993, "Transition to Time-Periodicity of a Natural-Convection Flow in a 3D Differentially Heated Cavity," *Int. J. Heat Mass Transfer*, Vol. 36, pp. 2927–2940.

Jeevaraj, C. G., and Patterson, J. C., 1992, "Experimental Study of Transient Natural Convection of Glycerol–Water Mixtures in a Side Heated Cavity," *Int. J. Heat Mass Transfer*, Vol. 35, pp. 1573–1587.

Kazmierczak, M., and Chinoda, Z., 1992, "Buoyancy-Driven Flow in an Enclosure With Time Periodic Boundary Conditions," *Int. J. Heat Mass Transfer*, Vol. 35, pp. 1507–1518.

Kazmierczak, M., and Muley, A., 1994, "Steady and Transient Natural Convection Experiments in a Horizontal Porous Layer: The Effects of a Thin Top Fluid Layer and Oscillating Bottom Wall Temperature," *Int. J. Heat Fluid Flow*, Vol. 15, pp. 30–41.

Kim, J. H., Simon, T. W., and Viskanta, R., 1993, "Journal of Heat Transfer Policy on Reporting Uncertainties in Experimental Measurements and Results," ASME JOURNAL OF HEAT TRANSFER, Vol. 115, pp. 5–6.

Kline, S. J., and McClintock, F. A., 1953, "Describing Uncertainties in Single-Sample Experiments," *Mechanical Engineering*, Vol. 75, Jan., pp. 3–8.

Lage, J. L., and Bejan, A., 1993, "The Resonance of Natural Convection in an Enclosure Heated Periodically from the Side," *Int. J. Heat Mass Transfer*, Vol. 36, pp. 2027–2038.

Lee, T. L., and Lin, T. E., 1993, "Transient Oscillatory Conjugate Natural Convection in a Tall Water Cavity," *Wärme-und Stoffübertragung*, Vol. 29, pp. 95–105.

Lee, S. L., and Kim, J. H., 1994, "Temperature Measurements During Heat-up of a Contained Homogeneous Fluid," *Int. J. Heat Fluid Flow*, Vol. 15, pp. 111–115.

Ostrach, S., 1988, "Natural Convection in Enclosures," ASME JOURNAL OF HEAT TRANSFER, Vol. 110, pp. 1175–1190.

Patterson, J. C., and Armfield, S. W., 1990, "Transient Features of Natural Convection in a Cavity," *J. Fluid Mechanics*, Vol. 219, pp. 469–497.

Poujol, F., Rojas, J., and Ramos, E., 1993, "Transient Natural Convection in a Cavity With Heat Input and a Constant Temperature Wall on Opposite Sides," *Int. J. Heat Fluid Flow*, Vol. 14, pp. 357–365.

Xia, Q., Yang, K. T., and Mukutmoni, D., 1995, "Effect of Imposed Wall Temperature Oscillations on the Stability of Natural Convection in a Square Enclosure," ASME JOURNAL OF HEAT TRANSFER, Vol. 117, pp. 113–122.

Yang, H. Q., Yang, K. T., and Xia, Q., 1989, "Periodic Laminar Convection in a Tall Vertical Cavity," *Int. J. Heat Mass Transfer*, Vol. 32, pp. 2199–2207.

Yang, J. W., Scaccia, C., and Goodman, J., 1974, "Laminar Natural Convection About Vertical Plates With Oscillatory Surface Temperature," ASME JOURNAL OF HEAT TRANSFER, Vol. 96, pp. 9–14.

Yang, K. T., 1987, "Natural Convection in Enclosures," in: *Handbook of Single Phase Convective Heat Transfer*, K. Kakac, R. K. Shah, and W. Aung, eds., Chap. 13, Wiley, New York.

Comparison of Several Heat Transfer Enhancement Technologies for Gas Heat Exchangers

M. J. Andrews

Assistant Professor.
Mem. ASME

L. S. Fletcher

Thomas A. Dietz Professor.
Fellow ASME

Department of Mechanical Engineering,
Texas A&M University,
College Station, TX 77843-3123

A comparative study about the performance of several enhanced heat transfer technologies for gas heat exchangers is presented. A Reynolds number range from 100 to 50,000 is considered for plate heat exchangers and the tube side of shell-and-tube heat exchangers. A volumetric performance measure has been adopted to evaluate the comparative performance of widely different technologies. The performance parameter, based on the heat transfer rate per unit pumping power, is suitable for different geometries, Reynolds numbers, and fluid properties. Modern technologies can achieve significant heat transfer enhancement, but comparison reveals that recent advances offer only marginal improvements that are often associated with more complex technology. Care must be exercised in choosing a technology because the best performing one is not necessarily the preferred choice since construction, retrofit, and maintenance costs may significantly alter the economic viability. However, there is an intrinsic interest in the comparative performance of very different technologies. Our performance evaluation indicates an upper limit may exist for single-mode convective heat transfer enhancement and compound enhancement may exceed this limit.

Introduction

Rapid growth of heat exchanger research and development for gas-fired applications has resulted in a large array of alternative heat exchanger technologies (Webb, 1994). A recent extensive review of previous publications about heat exchanger technologies for gas-fired applications (Bergles et al., 1991) presented a classification with the following "highly applicable" and "possibly applicable" categories: rough surfaces; extended surfaces; displaced enhancement devices; swirl-flow devices; jet impingement; compound enhancement; additives for gases; fluid vibration; and electric fields. Many technologies have been developed and reported. However, performing a detailed comparison is hard because technologies are often developed under widely varying conditions and geometries.

Here we compare several newly developed heat transfer enhancement technologies and several well-known, and practically important, enhancement technologies for gas-to-gas, gas-to-solid, and gas-to-liquid heat exchangers in gas-fired applications. The enhancement technologies cover low-Reynolds-number flows (nominally laminar) to high-Reynolds-number flows (turbulent). A low Reynolds number is typical of compact heat exchangers such as plate exchangers, and a high Reynolds number usually occurs on the tube side in shell-and-tube exchangers.

This division of enhancement technology by Reynolds number is a useful means of separating different enhancement strategies. Typical enhancement methods for low Reynolds numbers seek to reduce the critical Reynolds number that separates laminar flow from transitional flow. In the technologies investigated here this is done by deliberately driving secondary motions (finned tubes, wire coil inserts) or by stimulating the growth of unstable waves (grooved or wavy channels). It is well known that such methods can produce significant heat transfer enhancement, but there is also an increased pressure drop penalty (Bergles et al., 1991).

Enhancement for high-Reynolds-number flows becomes progressively more difficult with increasing Reynolds number because turbulent eddies become more vigorous, giving high turbulent diffusivity and more isotropic heat transfer. In fact, at sufficiently high Reynolds numbers, the enhanced heat transfer may be comparable with that of a smooth tube. The new technologies reviewed here for high-Reynolds-number flows seek to take advantage of mechanisms that either enhance the turbulence transport using buoyancy (tangential flow injection), or use particulate matter suspended in the gas flow to provide higher heat transfer rates (fluidized bed enhancement). The twisted-tape, wire coil insert and finned tube technologies are also included for comparative purposes.

An alternative classification is to divide the enhancement techniques into "passive" and "active." A passive technique endeavors to enhance heat transfer without additional power, whereas active enhancement makes use of an external source of power. The technologies considered in this work, tangential flow injection, grooved or wavy channel, twisted-tape, wire coil, finned tube, and fluidized bed enhancement, may be viewed as passive.

During this work we developed computer programs that use published correlations to evaluate performance criteria. These computer programs could be used in a parametric analysis of each technology, similar to that of Webb and Scott (1980) for finned tubes. However, we choose to present a comparative performance evaluation in which we have selected the reported best performance arrangement for each technology as described below.

Next the technologies and their relation to the classes identified by Bergles et al. (1991) are described. As a base reference, the heat transfer in a smooth tube is included. Several performance evaluation criteria are then reviewed. The selection of a performance parameter and its use for a comparative study is explained. This is followed by a comparative study based on

performance plots of the technologies considered. The paper closes with conclusions and some recommendations for others seeking to compare enhanced heat transfer technologies.

Background

A recent assessment by Andrews and Fletcher (1994) examined a wide variety of advanced heat transfer technologies suitable for gas-fired applications. A list of the technologies considered in the assessment with the Bergles et al. (1991) classification and a recent reference are shown in Table 1. A more extensive set of references for the new technologies may be found in Andrews and Fletcher (1994). As Bergles suggests, the classification scheme is not clear cut and some technologies such as finned and enhanced plates could be classified as "displaced enhancement" or "rough surface."

Table 2 summarizes the scope of various experimental studies for the new technologies (Table 1, items 1–3). Some of these studies are continuing, which may improve the performance of the technologies considered here. Table 2 shows the experimental studies were conducted with air over a wide range of Reynolds numbers, tube or hydraulic diameters, and temperatures. This extensive range of parameters is from independently performed research projects. Consequently, the variety of conditions and fluids complicates our efforts to compare these wide ranging technologies. However, they are typical of what a heat exchanger engineer might encounter when trying to select an optimum technology. Each technology in Table 1 is briefly reviewed.

Tangential Flow Injection. A series of reports, papers, and a recent patent invention disclosure (Tung et al., 1989; Dhir et al., 1990; Dhir and Chang, 1992; Son and Dhir, 1993) describe this technology. The purpose of this technology is to enhance heat transfer on the tube side in shell-and-tube heat exchangers. The idea is to introduce a tangential flow and thereby induce a swirling fluid motion down the tube. The swirling motion creates a pressure gradient that drives hot fluid (from a heated outer wall) into the center of the tube and thus establishes an enhanced mixing process. Furthermore, movement of cold fluid outward to the hot outer tube carries with it momentum that accelerates the tangential velocity, thus thinning the boundary layer and further enhancing heat transfer. These mechanisms were first speculatively described by Razgaitis and Holman (1976).

The specific tangential injection technology investigated here involves the attachment of an end-cap to the inflow of the tube. The cap integrates an injector that tangentially injects fluid into the tube. Fluid enters the tube through the tangential injectors so that no fluid enters the tube along its axis. Many alternative designs were investigated and evaluated. However, we have selected the best performing design of a six-hole injector cap for this assessment.

Fluidized Beds. This technology takes a radically different approach to enhancing heat transfer in tubes. The method involves using a two-phase flow of gas (air or combustion prod-

ucts) and particulate matter in a vertical tube. Fluidizing the bed of particles can generate various flow regimes. The particles can be used to enhance tube-side heat transfer by several mechanisms: the presence of particles causes the gas flow to be more turbulent and irregular; the suspended particles transport heat from the gas to the heat transfer surface or other colder particles; and, by thermal radiation of gas and particles at high temperatures. So compound (conduction, convection, and radiation) heat transfer enhancement is used. However, it is likely that this fluidized bed technology will find a wider application for shell-side heat transfer where the technology will be easier to implement and offer significant opportunities for the reduction of fouling; however, problems with removal and injection of particles need to be carefully considered.

The work by Tuzla and Chen (1993, 1994) concentrated on the fast fluidization regime, or "circulating fluidized bed" (CFB), or "entrained particulate flow" (EPF). The EPF regime is particularly attractive for enhanced heat transfer because it exhibits cross-sectional temperature uniformity and enhanced heat transfer coefficients, while allowing a higher gas throughput and a lower pressure drop. Fast fluidization is characterized by strands or clusters of particles descending the outer wall while other particles are conveyed upward in dilute flow in the core of the vessel.

For this assessment the best operating conditions (highest h) were selected, which were at high operating temperatures and low particle velocities.

Finned and Enhanced Plates. Classical convective heat transfer enhancement involves modifying the heat exchanger geometry by adding fins to extend the surface, or louvers to interrupt thermal boundary layers. In the work by Wirtz et al. (1990), attention was focused on passive techniques that excite hydrodynamic instabilities to promote heat transfer to or from surfaces. The work has significant application to compact heat exchanger applications. The gas side passage Reynolds numbers are relatively low, about 2000 or less, due to small hydraulic diameters and low face velocities. This gives laminar or transitional flows. The methods investigated aim to promote transitional flows by introducing surface geometry induced disturbances. The penalty is an increased pressure drop and therefore unwanted increases in pumping power.

Two types of enhancement technology were investigated: a grooved surface (saw-tooth) that lowered the critical Reynolds number; and a wavy (serpentine) wall geometry to induce secondary flows. The grooved surface comprises transverse (to flow) grooves that produce early transition (super critical Reynolds number) to unstable free shear layers, with traveling waves that augment heat transfer. In the serpentine technology the channel walls are made wavy. This waviness introduces streamline curvature that produces swirling Goertler vortices. These swirling vortices transport fluid normal to the heat transfer surface, thus augmenting convection. Care was taken in the research to avoid flow separation (which would significantly increase pumping power). We chose the serpentine channel for

─────── **Nomenclature** ───────

A = area over which heat transfer takes place, m^2

c_p = specific heat capacity, J/kg K

D = hydraulic diameter, m

d_i = tube inside diameter, m

f_D = Moody friction factor

H = axial distance for a 180 deg twist, m

h = heat transfer coefficient, W/m^2 K

j = Colburn j factor = Nu_D Pr$^{2/3}$/(Re$_D$ Pr)

k = thermal conductivity, W/m K

L = tube length, m

Nu_D = Nusselt number = hD/k

P = pumping power, W

Pr = Prandtl number

Δp = pressure drop over length L, Δp = Ldp/dx = $Lf_D\rho U^2/(2D)$, N/m^2

Re$_D$ = Reynolds number = $\rho UD/\mu$

t = tape thickness, m

U = mean velocity of fluid, m/s

V = heat exchange volume, m^3

α = nondimensional scaling factor for pumping power

β = nondimensional scaling factor for heat transfer rate

η = friction factor enhancement factor (=1 for a smooth tube)

μ = fluid viscosity, Ns/m^2

ξ = heat transfer coefficient enhancement factor (=1 for a smooth tube)

Table 1 Technologies considered for comparison

	Technology	Classification	Recent reference
1	Tangential flow injection	Swirl flow device (Bergles classifies it as a jet impingement technique, but the jets are tangential to impart swirl).	Son and Dhir (1993)
2	Fluidized bed enhancement	Compound enhancement (convective, particulate, and radiation heat transfer)	Tuzla and Chen (1993)
3	Finned and enhanced plates	Displaced enhancement (serpentine and wavy channels displace the flow causing enhancement)	Wirtz et al. (1990)
4	Smooth tube	Reference technology	Incropera and DeWitt (1990)
5	Continuous twisted-tape	Swirl flow device	Manglik and Bergles (1992)
6	Wire coil inserts	Rough surface	Sethumadhavan and Rao (1983)
7	Internally finned tubes	Extended surface	Carnavos (1980)

the present comparison because Wirtz et al. (1990) suggests that it has a superior performance to the grooved channel.

Twisted-Tape Inserts. According to Manglik and Bergles (1992), twisted-tape inserts have been used for almost a century, have extensive applications, and are a relatively simple retrofit technology. Manglik and Bergles (1992) and Webb (1994) give further details and additional references about the technology. Twisted-tape heat transfer enhancement may be attributed to: a reduction in the hydraulic diameter causing increased heat transfer coefficients; the tape twist imparting a swirl component, thus increasing the flow velocity and curvature, which in turn increases the shear stress at the wall and drives secondary motions; and heat transfer from the tape through thermal contact. Thorsen and Lundis (1968) showed that centrifugal acceleration, acting like gravity, causes destabilizing radial buoyancy forces when the tube fluid is being heated. The resulting enhanced mixing process is the same one that occurs in tangential injection, and moves higher density (colder) fluid from the tube core toward the hot tube wall. When the tube fluid is being cooled, the buoyancy forces are stabilizing and act to maintain radial thermal stratification. Such stabilizing phenomena are well known in the ocean thermocline, and Snider and Andrews (1994) studied the destabilizing phenomena as Rayleigh–Taylor mixing.

In the present comparison continuous twisted tapes have been considered and laminar flow data have not been used because the complex flows and corresponding performance variations make comparisons difficult. However, various correlations have been developed for turbulent flow, and we used the most recent by Manglik and Bergles (1992). Their correlation is valid for a constant wall temperature, $Re_D > 10,000$, and for liquids and gases, and is appropriate for comparison with the other technologies considered here. The present comparison uses reference tube conditions described in the next section. For the twisted tape, the twist ratio, H/d_i, and tape thickness ratio, t/d_i, were chosen as 2.5 and 0.05, respectively, since these values represent the more severe twist ratio and tape thickness used in practical applications.

Wire Coil Inserts. This technology is in the class of rough surfaces and involves fitting a tube with a tightly fitted helical-wire-coil of fixed helix angle and wire diameter. Our primary reference for wire coil inserts is Sethumadhavan and Rao (1983), and they report correlations of a Nusselt number and friction factor for a Prandtl number range $5.2 \leq Pr \leq 32$. We agree with Webb (1994) and expect that the correlations should be valid for air ($Pr = 0.7$). Sethumadhavan and Rao also provided a performance evaluation based on maximizing heat transfer rate, minimizing pumping power, and minimizing exchanger size. The present work concentrates on maximizing heat transfer

and minimizing pumping power for the same exchanger size. Therefore, the performance results of Sethumadhavan and Rao are appropriate so we have used a helix angle of 60 deg and a wire to tube diameter ratio of 0.08 in our performance comparison.

Internally Finned Tubes. This technology augments tube side heat transfer by placing fins around the periphery of the tube inner surface, in which pitch, elevation, and thickness can vary (Carnavos, 1980). Empirical correlations for heat transfer and pressure drop have been reported by Carnavos (1980) and a parametric analysis by Webb and Scott (1980). As with wire coil inserts, the fins disrupt the tube wall boundary layer, causing secondary fluid motions and higher heat transport to or from the walls. Furthermore, the fins can be angled so they wind in a helix down the tube to impart a swirl component to the flow with effects similar to those that occur for twisted tapes.

For our comparison we considered the performance analysis of Webb and Scott (1980), and have taken the fin height as 10 percent of the tube diameter, with a helix angle of 30 deg, and a pitch of 16 fins equally spaced around the circumference of the tube. As Webb and Scott show, an optimal design for this technology depends on the evaluation criteria. Our choice is motivated by Webb and Scott's results for increased heat duty for equal pumping power and total length of heat exchanger tubing, specifically their Figs. 5–7.

Performance Parameters

Selecting Appropriate Evaluation Criteria. Our primary goal is to compare heat exchanger technologies, but on what basis should the comparison be made? Webb (1994) suggests that alternative comparative choices might include: heat transfer enhancement versus pumping power; size reduction for fixed heat duty and pumping power; absolute heat transfer based on maximum Nusselt number; or improved thermodynamic efficiency by reduced LMTD for fixed heat duty and surface area. However, practical considerations may dictate the ultimate choice. For example, an increased pumping power at the same duty may be used if there are size constraints or specialized operating conditions. Other considerations might include capital costs, maintenance and installation costs, and life expectancy of the equipment.

Table 2 Summary of test conditions for technologies considered

Technology	Configuration	Primary application	Re Range	Flow type and working fluids	Temperature Range	Pr
Tangential Flow Injection	1). Single tube staged injection.	Shell-and-Tube Heat Exchangers; tube-side only	1) 10,000 - 30,000	1) Turbulent (air)	50° C	0.7
Primary reference: Son and Dhir (1993).	2) Multi-tube.		2) 5426 & 8800	2) Turbulent (air)		
	3) Single-tube multi-injectors		3) 10,130 - 52,850	3) Turbulent (air)		
	4) Single tube low Re		4) 1060	4) Laminar (air)		
	5) Annulus.		5) 10,130 - 18,200	5) Turbulent (air)		
Fluidized Bed Enhancement	1) Single tube - room temperature.	Shell-and-Tube Heat Exchangers; tube-side only	1) 17,370 - 69,470	1) Turbulent (air)	1) 50° C	0.7
Primary reference: Tuzla and Chen (1993)	2) Single tube high temperature.		2) 1300 - 8457 (using properties of air at 500°C)	2) Laminar/ Turbulent (combustion gases)	2) 200 - 600° C	0.7
Finned and Enhanced Plates	1) Wavy channel.	Plate Heat Exchangers	1) 400 - 10,000	Laminar, Re < 1000 (air)		0.7
Primary reference: Wirtz et al. (1990)	2) Grooved channel.		2) 300 - 5,000	Laminar, Re < 1000 (air).		0.7
	3) Intermittent grooved.		3) 300 - 5,000	Laminar, Re < 1000 (air)		0.7

The present analysis is restricted to performance issues, and following Soland et al. (1977), the following two parameters are considered:

$$\frac{P}{V} = \text{pumping power per unit volume.}$$

$$\frac{Ah}{V} = \begin{array}{l} \text{heat transfer rate per unit volume} \\ \text{per unit temperature difference.} \end{array} \quad (1)$$

The objective of using these two parameters is to seek technologies that provide a high Ah/V for a low P/V. Soland et al. (1977) took these parameters from previous work by Smith (1966), and compared the plate-fin heat exchanger surfaces of Kays and London (1964). Fortunately, Kays and London collected data for the same fluid at the same temperature levels. As a result, the fluid properties were constant and permitted Soland et al. to rewrite the parameters of Eq. (1) into the following forms:

$$\frac{P}{V} = \frac{\dot{m}\Delta p}{\rho V} = \frac{1}{2}\frac{\mu^3}{\rho^2}\frac{f_D \, \text{Re}_D^3}{D^4} \propto \frac{f_D \, \text{Re}_D^3}{D^4} \quad (2)$$

$$\frac{Ah}{V} = \frac{4c_p\mu}{\text{Pr}^{2/3}}\frac{j \, \text{Re}_D}{D^2} \propto \frac{j \, \text{Re}_D}{D^2} \quad (3)$$

The second term in Eq. (2) expresses the pumping power in terms of volumetric flow rate × pressure drop divided by the exchange volume. The third term in Eq. (2) is obtained using the expressions for Δp and V given in the nomenclature. Similarly, the second term in Eq. (3) uses the expression for the Colburn j factor in the nomenclature. The proportionality on the right of Eqs. (2) and (3) is appropriate when fluid properties are constant. If the diameter D is also constant, then the right-hand side expressions can be readily reduced to nondimensional forms appropriate for experiments that vary the Reynolds number using a fixed apparatus over a limited temperature range. The third term of Eq. (2) and the second term of Eq. (3) are of interest since they contain physical property effects and flow conditions (laminar and turbulent).

The test conditions (geometry and temperatures) given in Table 2 show that the nondimensional forms on the right of Eqs. (2) and (3) cannot be used, but instead the following dimensional forms are used in subsequent analysis:

$$\frac{P}{V} = \frac{1}{2}\frac{\mu^3}{\rho^2}\frac{f_D \, \text{Re}_D^3}{D^4} \quad \text{and} \quad \frac{Ah}{V} = \frac{4c_p\mu}{\text{Pr}^{2/3}}\frac{j \, \text{Re}_D}{D^2} \quad (4)$$

An immediate consequence is that fluid properties and exchanger geometry can significantly affect the comparison of Ah/V with P/V, which is undesirable because it could lead to erroneous conclusions. An alternative view of Eq. (4) is that at a given Re_D, Eq. (4) determines the effect of properties and diameter on measured Ah/V and P/V. Thus, Eq. (4) can be used to rescale measured Ah/V and P/V back to a reference fluid, temperature, and diameter and then performance comparisons can be made. The present work's chosen reference is a smooth tube of 25.4 mm (1 in.) o.d. and thickness 1.24 mm (0.049 in.) with air at 30°C. This is a convenient choice that matches the conditions used to investigate tangential flow injection, and so data for this item require no rescaling. The rescaling relationships are:

$$\left(\frac{P}{V}\right)_{\text{scaled}} = \alpha\left(\frac{P}{V}\right)_{\text{experiment}} \quad \text{with}$$

$$\alpha = \left(\frac{\mu^3}{\rho^2 D^4}\right)_{\text{reference}}\bigg/\left(\frac{\mu^3}{\rho^2 D^4}\right)_{\text{experiment}} \quad (5)$$

$$\left(\frac{Ah}{V}\right)_{\text{scaled}} = \beta\left(\frac{Ah}{V}\right)_{\text{experiment}} \quad \text{with}$$

$$\beta = \left(\frac{c_p\mu}{D^2 \, \text{Pr}^{2/3}}\right)_{\text{reference}}\bigg/\left(\frac{c_p\mu}{D^2 \, \text{Pr}^{2/3}}\right)_{\text{experiment}} \quad (6)$$

As an example of the rescaling procedure, the hydraulic diameter used in the EPF Transport tests (Table 1, item 2) was combined with the property variation suggested in Eq. (5) to adjust the P/V while maintaining the same Reynolds number and friction factor. Similarly, since for air the Colburn j factor is approximately constant for a fixed Reynolds number, the hA/V result was rescaled using Eq. (6). Table 3 gives the scaling factors α and β used for the wavy channel (needed for geometrical scaling) and for EPF transport (needed for high temperatures). There is no factor for the tangential injection data because it is the reference case, and the correlations for other technologies are evaluated at the reference conditions.

Expected Performance. Most of the technologies described above involved convective heat transfer. Typically a Dittus and Boelter (1930) correlation is then appropriate, which we express as:

$$\text{Nu}_D = 0.023\xi \, \text{Re}_D^{0.8} \, \text{Pr}^n \quad (7)$$

where ξ is a heat transfer coefficient enhancement factor ($=1$ for a smooth tube) that might depend on geometry, temperature differences, and swirl; with $n = 0.4$ for heating and 0.3 for cooling. Since we are interested in air, the variation of n with heating and cooling has only a minor effect and we take a value of $\frac{1}{3}$ for convenience. Similarly, a Blasius correlation is appropriate for the friction factor, which we express as:

$$f_D = 0.316\eta \, \text{Re}_D^{-0.25} \quad (8)$$

where η is a friction factor enhancement factor ($=1$ for a smooth tube) that might depend on geometry, temperature differences, swirl, Reynolds number. Substituting Eqs. (7) and (8) into Eqs. (2) and (3), and using the relationship for the j factor given in the nomenclature, the performance parameters may be rewritten as:

$$\frac{P}{V} = \eta \frac{0.0316\mu^3}{2\rho^2 D^4} \, \text{Re}_D^{2.75} \quad \text{and}$$

$$\frac{Ah}{V} = \xi \frac{0.023 \times 4c_p\mu}{D^2 \, \text{Pr}^{2/3}} \, \text{Re}_D^{0.8} \quad (9)$$

Since our results are later plotted with $\log_{10}$ axes, we now take the logarithm of Eq. (9) and eliminate $\log_{10}(\text{Re}_D)$ to obtain:

$$\log_{10}\left(\frac{Ah}{V}\right) = 0.29 \log_{10}\left(\frac{P}{V}\right) + \log_{10}\left(\frac{\xi}{\eta^{0.29}}\right)$$

$$+ \log_{10}\left(\frac{0.023 \times 4c_p\mu}{D^2 \, \text{Pr}^{2/3}}\bigg/\left(\frac{0.316\mu^3}{2\rho^2 D^4}\right)^{0.29}\right) \quad (10)$$

Our scaling procedure ensures the last term on the right of Eq. (10) is a constant, so we can expect the technologies consid-

Table 3 Multiplication factors for rescaling

Technology	α	β
Serpentine channel (air): geometrical scaling	0.556	0.746
EPF transport (air): temperature (property) scaling	1.63	3.05

ered to have different displacements and thus comparative enhancements according to the performance ratio $\xi/\eta^{0.29}$. If this performance ratio is independent of Re_D, then for a plot of $\log_{10}(P/V)$ versus $\log_{10}(Ah/V)$ we should expect a straight line of gradient 0.29 for most of the enhancement technologies. The Reynolds–Colburn analogy, $j = f_D/2$, implies the existence of such a constant gradient. However, the gradient of 0.29 will no longer be appropriate if compound heat transfer is involved. For example, radiation can significantly increase Nu_D but would not effect f_D. The performance ratio $\xi/\eta^{0.29}$ is interesting since it implies a performance improvement when Eq. (10) is a straight line even if the friction factor increases much more rapidly than the heat transfer coefficient. This fact is well known to heat transfer enhancement practitioners.

Performance Comparison

The different technologies are compared using Eqs. (4)–(6). The computation of P/V and Ah/V for the different experimental and reference technologies was performed using correlations for friction factor and Nusselt number reported by the various researchers or from data supplied directly. Details of the calculations can be found from Andrews and Fletcher (1994). In the following figures the ''best'' results as described above have been taken to give a best performance analysis.

Figure 1 presents P/V as a function of Ah/V without property scaling. The plot may be usefully read by taking a fixed P/V and reading off the associated heat transfer performance with a higher Ah/V implying better overall performance. The flow Reynolds numbers are shown on the figure but play no role in the performance comparison; however, higher Reynolds numbers correspond to higher Ah/V and P/V as expected. The plots for twisted-tape and tangential injection show significant performance improvement over the reference smooth tube conditions. The serpentine and tangential injection technologies perform with a similar enhancement. The EPF transport seems comparable with a smooth tube, but care must be exercised because the EPF data are at a high temperature so the air properties can significantly affect the results, which shows the need for rescaling.

Figure 2 presents the same plot as Fig. 1 but the data have been rescaled to the reference conditions. Comparing Fig. 1 with Fig. 2 reveals a shift for the EPF Transport data caused by the scaling properties from a high temperature. This is re-
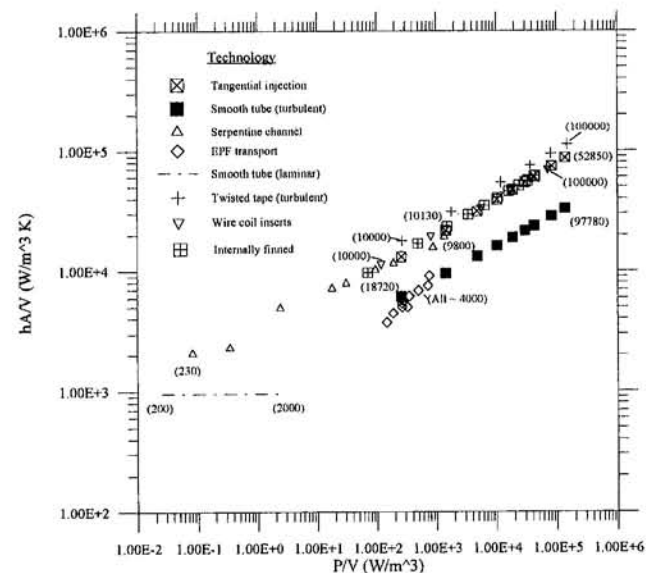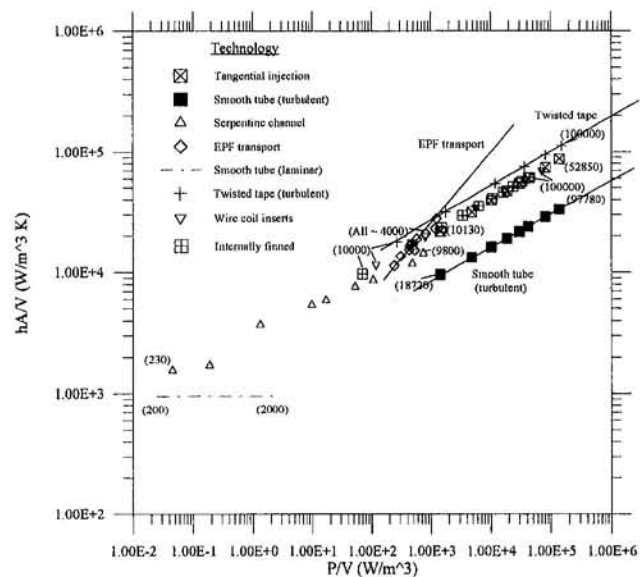

Fig. 2 Comparative performance of enhancement technologies scaled to reference conditions of air at 300 K and a tube of diameter 23 mm; Reynolds numbers are in parentheses

flected in the scaling multipliers of Table 3. Inspection of Fig. 2 shows that the serpentine channel, EPF transport, and tangential injection technologies offer a similar enhanced performance over the smooth tube. The best performing technology, lowest P/V for highest Ah/V, is the twisted tape, closely followed by tangential injection, wire coil inserts, and finned tubes. Similar enhancement for twisted-tape, tangential injection, and wire coil inserts is to be expected since they all take advantage of the same swirl flow enhancement processes. For fin tubes at higher velocities (Reynolds numbers), it is to be expected that the flow would skip over the fins and only show a weak, if any, swirl enhancement.

Solid lines have been added to Fig. 2 to help identify technologies and show that all the single mode convective heat transfer technologies have the same performance gradient of 0.29, which agrees with the expected result. Moreover, the plots show as straight lines and so the performance ratio $\xi/\eta^{0.29}$ is independent of Re_D. Thus, this plot demonstrates that fundamentally all these technologies operate in the same way, with their performance differences arising from the best use of geometry and swirl-induced secondary flow patterns that are perhaps independent of Reynolds number. The exception is the EPF result shown in Fig. 2. The EPF line has a distinctly steeper gradient. This may be attributed to multiple heat transfer modes and suggests that EPF multiphase enhancement, and more generally, compound enhancement, presents an opportunity to exceed an upper performance limit reached by many convective heat transfer technologies.

However, a word of caution: Fig. 2 demonstrates performance based only on heat transfer and pumping power and does not include manufacturing, maintenance, and installation costs. Nevertheless, Fig. 2 shows that in turbulent flow, at our reference conditions, the technologies typically provide a threefold enhancement compared with a smooth tube based on a constant pumping power per unit volume, and up to a sixfold enhancement in laminar flow.

Existence of a Performance Limit

The results in Fig. 2 suggest the existence of a performance upper limit. It is interesting to consider whether such a limit might exist for our performance comparison. The temperature gradient in the laminar boundary sublayer at the wall determines

Fig. 1 Comparative performance of enhancement technologies; Reynolds numbers are in parentheses

the heat transfer rate for a fluid moving in a tube. Similarly, the wall shear stress and pumping power are determined by the velocity gradient in the laminar sublayer next to the wall. Therefore we might expect to increase the heat transfer rate if the thermal boundary layer is thinned. However, the thermal and momentum boundary layer thicknesses are related by the Prandtl number and so the momentum boundary layer also thins thus increasing the wall stress. Our choice of performance parameters and the rescaling procedure includes this complementary effect, and is shown by the constant performance gradient of the convective heat transfer technologies. However, turbulent transport mechanisms can affect the shape of the velocity and thermal boundary layers and wall gradients. In particular, Fig. 2 shows that swirling flow acts to promote performance when cold fluid flows through heated tubes. Under such circumstances buoyancy-driven secondary motions preferentially transport cold fluid away from the center of the tube toward the hot tube wall, and warmer fluid adjacent to the tube wall toward the tube center. Such preferential transport enhances performance by lowering the temperature in the outer regions of the thermal boundary layer and so effectively increases the temperature gradient at the wall. However, Fig. 2 also shows that at the same Reynolds number, the smooth tube turbulent pumping power is close to that of all the swirl technologies. So it appears that adding swirl does not significantly affect pressure drop. Perhaps this is because, unlike heat, there is no preferential mechanism for momentum transport.

The constant gradient for the convective heat transfer technologies emphasizes the fundamental similarity of boundary layer structure for all the convective technologies. Swirl takes advantage of the density gradients associated with temperature gradients. Since the swirl flow technologies were optimized and since they perform similarly in Fig. 2, they do present an upper limit. However, as shown by EPF transport, the gradient and upper limit can be increased with compound heat transfer. Moreover, other fluid properties also vary with fluid temperature, notably fluid viscosity, so using non-Newtonian property fluids to modify the transport mechanisms preferentially might be possible. Indeed, EPF transport might be considered an example. Thus, the performance limit indicated in Fig. 2 for gas heat exchange exists in the context of convective heat transport with swirl but is not necessarily a limit for compound heat transfer.

Conclusions

A comparative performance study of seven different heat transfer enhancement technologies and a reference smooth tube has been performed. The technologies differed by geometry, flow conditions, and operating temperatures. The performance comparison used a heat transfer rate as a function of the pumping power parameter. The chosen performance parameters made sense but by necessity are dimensional, so a rescaling procedure was used to compare technologies.

The performance comparison revealed that the advanced technologies provided a similar threefold enhancement over a smooth tube for turbulent flow at reference conditions and a sixfold enhancement for laminar flow. This similar performance for a wide range of technologies suggests an inherent performance limit for convective enhancement techniques. The analysis has been successful in collapsing the performance of a wide range of technologies and operating conditions onto a single performance plot. However, care must be taken to rescale data to a standard reference before comparing performance.

All the technologies, except EPF transport, showed the same heat transfer performance increase with an associated increase in power. This result was attributed to their use of the same fundamental convective heat transfer mechanism. However, EPF transport showed a steeper performance line due to com-

pound heat transfer, which suggests future development possibilities.

Our work suggests that many enhancement technologies have a similar performance. However, other factors such as capital costs, retrograde fit costs, reliability, fouling, and ease of maintenance were not considered here but are also important in the practical selection of a heat exchanger technology.

References

Andrews, M. J., and Fletcher, L. S., 1994, "Technical Assessment of Heat Exchanger Enhancement Technologies," GRI Topical Technical Report 94/0247, Gas Research Institute/Heat Transfer Research, Inc., College Station, TX, Apr.

Bergles, A. E., Jensen, M. K., Somerscales, E. F. C., and Manglik, R. M., 1991, "Literature Review of Heat Transfer Enhancement Technology for Heat Exchangers in Gas-Fired Applications," GRI Topical Technical Report, GRI 91-0146.

Carnavos, T. C., 1980, "Heat Transfer Performance of Internally Finned Tubes," Heat Transfer Engineering, Vol. 4, No. 1, pp. 32–37.

Dittus, F. W., and Boelter, L. M. K., 1930, University of California at Berkley, Publications on Engineering, Vol. 2, p. 443.

Dhir, V. K., Chang, F., and Yu, J., 1990, "Enhancement of Single Phase Forced Convection Heat Transfer in Tubes Using Staged Tangential Flow Injection," Final Report, June 1987–Dec. 1989, GRI report No. GRI-90/0134.

Dhir, V. K., and Chang, F., 1992, "Heat Transfer Enhancement Using Tangential Injection," ASHRAE Transactions, Vol. 98, BA-92-4-1.

Incropera, F. P., and Dewitt, D. P., Fundamentals of Heat and Mass Transfer, 3rd ed., Wiley, New York.

Kays, W. M., and London, A. L., 1964, Compact Heat Exchangers, 2nd ed., McGraw-Hill, New York.

Manglik, R. M., and Bergles, A. E., 1992, "Heat Transfer and Pressure Drop Correlations for Twisted-Tape Inserts in Isothermal Tubes: Part II—Transition and Turbulent Flows," in: Enhanced Heat Transfer, M. B. Pate and M. K. Jensen, eds., ASME HTD-Vol. 202, pp. 99–106.

Razgaitis, R., and Holman, J. P., 1976, "A Survey of Heat Transfer in Confined Swirl Flow," Heat and Mass Transfer Processes, Vol. 2, pp. 831–866.

Sethumadhavan, R., and Rao, M. R., 1983, "Turbulent Flow Heat Transfer and Fluid Friction in Helical-Wire-Coil-Inserted Tubes," Int. J. Heat Mass Transfer, Vol. 26, No. 12, pp. 1833–1845.

Smith, J. L., 1966, "Prediction of Heat Transfer and Friction Data for Heat Exchanger Design," ASME Paper No. 66-WA/HT-59.

Snider, D. M., and Andrews, M. J., 1994, "Rayleigh–Taylor and Shear Driven Mixing With an Unstable Thermal Stratification," Physics of Fluids, Vol. 6 (10), October, pp. 3324–3334.

Soland, J. G., Mack, W. M., Jr., and Rohensow, W. M., 1977, "Performance Ranking of Plate-Fin Heat Exchanger Surfaces," ASME, Paper No. 76-WA/HT-31.

Son, D., and Dhir, V. K., 1993, "Enhancement of Heat Transfer in an Annulus Using Tangential Flow Injection," in: Heat Transfer in Turbulent Flows, ASME HTD-Vol. 246.

Thorsen, R., and Landis, F., 1968, "Friction and Heat Transfer Characteristics in Turbulent Swirl Flow Subject to Large Transverse Temperature Gradients," JOURNAL OF HEAT TRANSFER, Vol. 90, pp. 87–89.

Tung, V. X., Dhir, V. K., Chang, F., Karagozian, A. R., and Zhou, F., 1989, "Enhancement of Forced Convection Heat Transfer in Tubes Using Staged Tangential Flow Injection," Annual Report, June 1987–Sept. 1988, GRI report No. GRI-89/020.

Tuzla, K., and Chen, J. C., 1993, "Enhanced Heat Transfer for Gas Convective Exchangers," Final Report, Oct. 1988–Dec. 1991, GRI report No. GRI-93/0305.

Tuzla, K., and Chen, J. C., 1994, Personal Communication Containing Experimental Measurements of Pressure Drop and Heat Transfer Coefficient; the Data are Reported in Andrews and Fletcher (1994).

Webb, R. L., and Scott, M. J., 1980, "A Parametric Analysis of the Performance of Internally Finned Tubes for Heat Exchanger Application," JOURNAL OF HEAT TRANSFER, Vol. 102, pp. 38–43.

Webb, R. L., 1994, Principles of Enhanced Heat Transfer, Wiley, New York.

Wirtz, R. A., Greiner, M., and Snyder, B., 1990, "Free Shear Layer and Swirl Flow Heat Transfer Enhancement," Final Report, Sept. 1987–Dec. 1989, GRI report No. GRI-90/0088.

Trajectories and Deposition of Silica Particles on Cylinders in Crossflow With and Without a Magnetic Field

S. H. Chan
Wisconsin Distinguished Professor.
email: shc@csd.uwm.edu
Fellow ASME

B. Moussa
Graduate Student.

Department of Mechanical Engineering,
University of Wisconsin—Milwaukee,
P.O. Box 784,
Milwaukee, WI 53201

To investigate magnetic effects on silica scale deposition, two cylindrical probes with and without magnet insert were placed in a crossflow fluid solution containing dissolved silica, iron ion, and NaCl salt. The differences in silica deposition are reported. To explain the differences on the basis of first principles, a Lagrangian analysis is presented to predict the silica colloidal particle trajectories and deposition onto the probes under the influence of nonuniform magnetic field force and other relevant surface forces including London–van der Waals forces, viscous force, and added mass force. The results of the predication show that the particles made of pure silica can be deflected away from the magnetic probe. However, the particles made of silica–iron can be attracted toward the probe, more so at the magnetic poles than at the midsection of the magnetic probe. These and other results presented can explain all the qualitative differences of scale deposit found experimentally on magnetic and nonmagnetic probes.

Introduction

Most of the energy conversion systems are plagued by scale deposition on their heat exchanger surfaces. The scale, once formed, reduces the heat transfer rate and increases the pressure drop across heat exchangers, often resulting in a dramatic reduction in the energy conversion efficiency. Thus effective scale prevention and removal techniques are needed. Among the removal techniques, chemical treatments and mechanical scrubbing devices have been used by industries. However, they can be lengthy and costly, with long down times and possible damage to existing equipment.

A nondestructive and noninterfering technique that has attracted interest in the last few decades is magnetic water treatment, which claims to prevent further scale buildup and the removal of existing scale by the use of a strong magnetic field operating perpendicular to the direction of fluid flow. Raisen (1984) investigated actual water magnetic systems installed in air conditioning and boiler systems and found positive antiscaling results. Conflicting results relating to the effectiveness of magnetic water treatment devices have been obtained by many researchers and businesses alike. Clyburn (1983) compared many different hypotheses of magnetic water treatment offered by various researchers. Soviet scientist (Boichenko and Sapogin, 1977; Kochmarskii et al., 1982; Martynova et al., 1969, 1979) favor the magnetic technique highly and offer different mechanisms responsible for the scale control. A vast majority of researchers such as Hasson and Bramson (1981) found experimentally that magnetic treatment had no effect on the scaling process. Similarly they found no effect on the adhesive capability of the scale as a result of magnetic exposure.

The hypotheses developed to explain the phenomenon are varied. One popular belief is that the magnetic field causes minerals with magnetic properties to form a suspended layer in the magnetic field (Martynova et al., 1979), thus decreasing the solubility of the supersaturated component, causing it to precipitate immediately in solution rather than on the pipe walls. Still others (Clyburn, 1983) believe that the magnetic field somehow lowers the zeta potential of suspended particles, which makes it easier for two particles to collide and form a nucleation site in solution. Duffy (1977) has shown that ferric hydroxides retard formation of calcium carbonate under the allotropic form of calcite and claims that magnetic water treatment devices simply accelerate corrosion of piping, thereby introducing higher levels of ferric hydroxide in solution. Some researchers argue that since charged particles passing through the magnetic field are subjected to a force perpendicular to the direction of flow, these particles will experience movement perpendicular to the flow where they are bombarded with particles traveling with the fluid. This in effect is much like the suspended layer hypothesis in that the collisions result in the creation of nucleation sites in solution, rather than on pipe walls. Presently, however, no sound theory has been developed because of the complexities and variabilities that exist in the scaling process.

The primary objective of this study is to develop a theory based on first principles to predict effects of the magnetic and other associated surface forces on the Lagrangian motion of colloidal silica particles in a solution containing supersaturated silica and $FeCl_3$. Two cylindrical probes with and without a magnet insert were placed simultaneously in a crossflow position in a fouling heat transfer loop so that they were subjected to the same thermal, physical, and chemical conditions (see Fig. 1). The trajectories and deposition of the particles on magnetic and nonmagnetic probes were predicted and used to explain all the qualitative differences of the scale formation found on the probes.

Experimental Investigation

An existing fouling heat transfer facility as described previously (Chan et al., 1988) was used in the present study. Briefly, this test facility was made up of two loops (see Fig. 2). A heated solution saturated with a high-grade silica was circulated in the primary loop where the solution passed through the tube side of a titanium tube and shell heat exchanger. The secondary loop was used to circulate the coolant distilled deionized water in the shell side of the heat exchanger. The whole

system was designed to run under many flow, thermal, and chemical conditions. The different flow, thermal, and chemical conditions were achieved by varying the inlet flow rates and temperatures in both loops, by varying the chemical addition to the primary loop of a number of salts (NaCl, KCl, $FeCl_3$, etc.) and by varying the super-saturation of silica with respect to the cooler surface temperature of the tube. The thermal and hydraulic behaviors of the heat exchanger are then recorded. To investigate the effect of magnetic field on silica scale deposition, another test section was considered in which two cylindrical probes were installed in a tube at the exit of the heat exchanger of the main loop (view P-P of Fig. 2). One of these probes was imbedded with a Samarium Cobalt permanent magnet, the other was just solid titanium. A schematic of the magnetic probe is also shown in Fig. 1(a). After passing through the tube and shell heat exchanger, a supersaturated silica solution is produced due to lower tube surface temperature and therefore suspended colloid particles appeared in the solution, which could then be deposited farther downstream on the inserted probes. Prior to the probe test section, a mixing cup was installed to homogenize the temperature profile. Since the downstream pipe and probes are insulated, the temperature difference between them is expected to be small, such that the thermal effect is in essence decoupled from magnetic effects to allow for a better focus on magnetic effects of silica deposition on the probes. The thermal effects were investigated separately in the upstream heat exchanger section as reported earlier (Chan et al., 1995).

The present study was based on the same test conditions found in run T5-Fe2 of Chan et al. (1995). A silica-saturated solution containing dissolved salts of NaCl and $FeCl_3$ was prepared in the saturation tank of the primary loop and the relevant test parameters are listed in Table 1 for later use in the theoretical prediction. Due to the high temperature and high pressure nature of the loop, the probes were removed only at the end of the experiment and the scales formed on the surfaces of both probes were compared and shown qualitatively in Fig. 1(b).

Several distinct features were found. First, for the magnetic probe, more deposition was found at the north and south pole regions than in the midsection. Second, in comparison of scale deposition on both probes, the scale in the midsection of the magnetic probe was found thinner than that of the nonmagnetic probe. Finally, by an electron microscope analysis, the scale deposit on the magnetic probe at the midsection of the magnet was found to be mainly made of silica (85 percent SiO_2, 15 percent Fe) while the pole regions were mostly iron.

Since only qualitative features of the scale formation are reported in Fig. 1(b), no error analysis is needed for scale formation. The error of the measurement values of the magnetic flux densities to be seen in Fig. 4 is about ±15 percent. Other errors associated with the loop measurement were given previously (Chan et al., 1988).

Theory

To explain these findings on a theoretical basis, it is necessary to develop a proper theory to predict magnetic effects on trajectories and deposition of colloidal silica particles on a cylindrical surface in a crossflow. Since the scale deposit was found to be composed of silica and iron on various proportion depending on the location of the probe surface, the suspended colloidal particle in the fluid can be considered to be made of either pure silica or a silica–iron composite.

As these suspended particles approach the cylindrical probes, the particles in the solution are subjected to many external forces, contributed to by various physical and chemical phenomena. Besides the magnetic force $\vec{F}_m$, they include the thermophoretic force $\vec{F}_{th}$, London–van der Waals attraction force $\vec{F}_l$, fluid drag force $\vec{F}_d$, and added mass force $\vec{F}_a$. Other minor forces including the gravitational, basset, lift and electric double layer forces have been evaluated and found to be negligible in the present work. Then the trajectory of a particle of radius of

Nomenclature

a = cylindrical probe radius, m
a_p = particle radius, m
A = ratio of particle to cylinder radii
  = a_p/a
b = length of magnet, m
b_+ = cylinder length to radius ratio = b/a
$\vec{B}$ = magnetic field induction, Gauss
B_r = radial magnetic field, Gauss
B_z = axial magnetic field induction
h = separation between particle and cylinder, m
$\vec{H}$ = magnetic field vector, A/m
H_r = radial magnetic field, A/m
H_z = axial magnetic field, A/m
$\mathcal{H}_{132}$ = Hamaker constant, J
I = ionic mobility, mole/L
κ = reciprocal double layer thickness, m^{-1}
M = magnetization of permanent magnet, A/m
M_p = magnetization of particle, A/m
π_p = particle magnetic moment, A/m^2
N_h = hydrodynamics force number, N
N_i = inertia force number, N
N_l = London–van der Waals force number, N
N_m = magnetic force number, N
N_{hi} = ratio of hydrodynamic to inertia forces

N_{mi} = ratio of magnetic to inertia forces
N_{li} = ratio of London attraction to inertia forces
N_{e1} = electric double layer number 1, N
N_{e2} = electric double layer number 2, N
N_{ei} = ratio of electric double layer to inertia forces
η = fluid dynamic viscosity, kg/m/s
ν = fluid kinematic viscosity = η/ρ, m^2/s
ρ = fluid density, kg/m^3
ρ_p = particle density, kg/m^3
Re = Reynolds number
Re_p = particle Reynolds number
t = time, s
t_+ = dimensionless time
T = temperature, K
r = radial distance, m
r_+ = dimensionless radius, r/a
θ = angle, rad
z = axial distance (from center of probe), m
x = coordinate shown in Fig. 3, m
$\vec{U}$ = fluid velocity vector, m/s
$\vec{V}$ = particle velocity vector, m/s
z_i = ionic charge of ion i

U_∞ = upstream velocity, m/s
v_p = particle volume, m^3
μ = magnetic permeability, Henry/m
χ = magnetic susceptibility
ζ_p = particle zeta potential, mV
ζ_c = cylinder zeta potential, mV
k = fluid thermal conductivity, W/mK
k_p = particle thermal conductivity, W/mk
χ_p = composed particle magnetic susceptibility
Δ = ratio of particle to fluid densities = ρ/ρ_p
$\vec{F}$ = force, N
$\vec{H}_d$ = magnetic field induced by dipole, A/m
pH = acidity of solution

Subscripts

a = added mass (acceleration) term
c = cylinder
e = equivalent
d = fluid drag term
l = London–van der Waals term
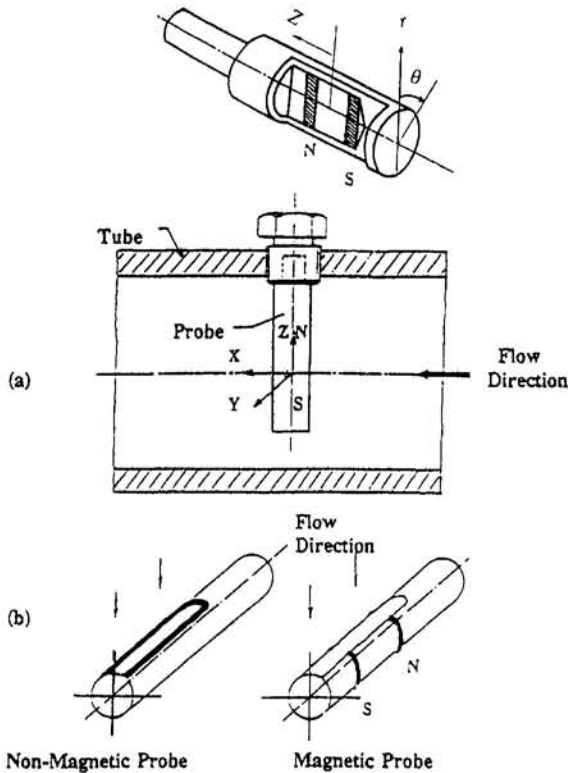m = magnetic term
o = free space
p = particle

Fig. 1 (a) Probe in tube and (b) scale profiles for the magnetic and nonmagnetic probes

		Dimensionless Number
$a = 3.175 \times 10^{-3}$ m	(.125 in)	
$a_p = 10^{-5}$ m	(10 μm)	$A = a_p/a = 0.00315$
$b = 9.652 \times 10^{-3}$ m	(.38 in.)	$b_+ = b/a = 3.04$
$\rho = 937.2$ Kg/m³	(H₂O@400K)	$\Delta = \rho_p/\rho = 2.347$
$\rho_p = 2200.0$ Kg/m³	(SiO₂)	$Re = 2a\rho U_\infty/\eta = 37500$
$U_\infty = 0.523$ m/sec	(Q = 4.2 gpm)	$N_i = 4\pi \rho_p (U_\infty)^2 A^3/3 = 7.94 \times 10^{-10}$ N
$T = 400$ K		$N_h = 6\pi\eta (U_\infty a) A = 2.139 \times 10^{-11}$ N
$\eta = 2.17 \times 10^{-7}$ Nsec/m²	(H₂O@400K)	$N_m = \pi (Mb)^2 \mu_0\chi_e A^3 = 9.1 \times 10^{-6}$ N
$M = 5 \times 10^5$ A/m	(SmCo₅ magnet)	$N_l = (2\mathcal{H}_{132}/3a) A^3 = 6.865 \times 10^{-29}$ N
χ (Fe) = 5000	$(\mu = \mu_0 (1 + \chi))$	$\kappa = 0.0451\sqrt{I} = 9.2 \times 10^7$ m⁻¹
χ (Ti) = 18×10^{-5}, χ (SiO₂) = $-.493 \times 10^{-6}$		$\tau = \kappa a A = 920$
$\chi_p = 0.15\chi$ (SiO₂) + 0.85χ (Fe) = 745¹		$N_{e1} = \varepsilon\varepsilon_0\kappa a\zeta_p\zeta_e A = 2.466 \times 10^{-13}$ N
$\mu_{H2O} = \mu_0 = 4\pi \times 10^{-7}$ H/m, H = Vsec/A		$N_{e2} = (\zeta_p^2 + \zeta_e^2)/(2\zeta_p\zeta_e) = 1.97$
$\mathcal{H}_{123} = 3.0 \times 10^{-20}$ J		$N_{hi} = N_h/N_i = 1/N_{St} = 2.221 \times 10^{-2}$
pH = 7.0, I = .1 mol/L²		$N_{mi} = N_m/N_i = 1.146 \times 10^4$
$\zeta_p = -55$ mV	(at pH = 7)	$N_{li} = N_l/N_i = 1.044 \times 10^{-16}$
$\zeta_e = -15$ mV	(at pH = 7)	$N_{ei} = N_{el}/N_i = 3.11 \times 10^{-4}$

1: determined from electron microscope scale composition
2: the ionic strength is based on 0.1 M NaCl, 20 ppm Fe³⁺

a_p and density ρ_p is governed by the Lagrangian equation of motion of the particle along its path,

$$\frac{4\pi}{3} a_p^3 \rho_p \frac{d\vec{V}}{dt} = \vec{F}_m + \vec{F}_l + \vec{F}_d + \vec{F}_a \quad (1)$$

The thermophoretic force is ignored in Eq. (1) and will be shown next not to be a factor in the tube section of the primary loop in the vicinity of the probes.

Thermophoretic Force. The thermophoretic force exerted on the suspended particle is due to the thermal gradient of the carrying fluid and tends to move the particle toward a cooled surface and away from a heated one. This force exerted on a particle (with radius a_p and thermal conductivity k_p) suspended
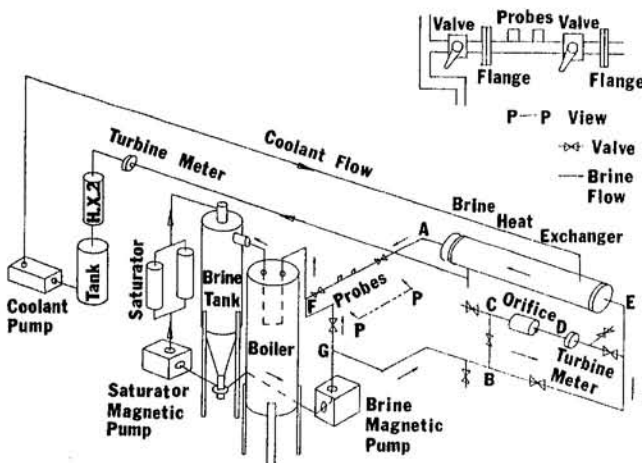

Fig. 2 Fouling heat transfer loop and location of probes

in a flowing fluid with density ρ, viscosity η, and thermal conductivity k is given (Brock, 1962) by:

$$\vec{F} = -9\pi a_p^2 \frac{\eta^2}{\rho T} \left(\frac{k}{2k + k_p} \right) \nabla T$$

The particle material of the present work was determined from the Electron Microscope analysis of the scales formed on the probe. At the middle section of the probe their mean composition was found to be composed of 85 percent SiO₂ and 15 percent Fe by weight. The thermal conductivity of the composed silica–iron particle is then given by the weight average according to the results of the scale analysis, i.e.,

$$k_p = .85 \, k_{SiO_2} + 0.15 \, k_{Fe}$$

Since a mixing cup was installed after the end of the heat exchanger tube and far ahead of the probes, and since the whole pipe connecting the tube and enclosing the probes was well insulated, the parabolic temperature profile of the hot fluid exiting the tube was flattened out and reached the far downstream probes in a uniform fashion. Hence the thermal gradients near the probes were insignificant and the thermophoretic forces can therefore be neglected in the present study.

Since the magnetic effect on particle deposition is of primary interest here, a careful formulation of the magnetic force exerted on the silica–iron composed particle is presented next, followed by other required forces.

Magnetic Force. Consider the magnetic force acting on a particle of volume v_p and magnetic susceptibility χ_p, surrounded by a solution with the same magnetic susceptibility as water, χ_{H2O}, and subject to a nonhomogeneous magnetic field $\vec{H}$. If the particle is assumed to be small enough to be represented magnetically as a point dipole of moment $\vec{\pi}_p = v_p\vec{M}_p$, where $\vec{M}_p$ is the particle magnetization, then from the fundamental equation for the force on a point dipole (Jackson, 1975), the force on the spherical particle can be expressed as:

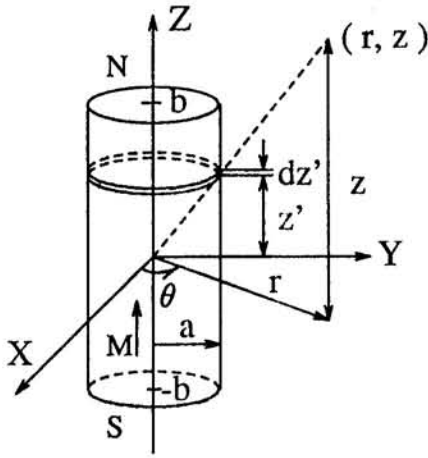$$\vec{F}_m = \mu_0(\vec{\pi}_p \cdot \nabla)\vec{H} = \mu_0 v_p(\vec{M}_p \cdot \nabla)\vec{H} \quad (2)$$

Fig. 3 Magnetic dipole approximation

	$z = -b$	$z = 0$	$z = b$
H_r^*	$\dfrac{r}{(r^2 + 4b^2)^{3/2}} - \dfrac{1}{r^2}$	0	$\dfrac{1}{r^2} - \dfrac{r}{(r^2 + 4b^2)^{3/2}}$
H_z^*	$\dfrac{-2b}{(r^2 + 4b^2)^{3/2}}$	$\dfrac{-2b}{(r^2 + b^2)^{3/2}}$	$\dfrac{-2b}{(r^2 + 4b^2)^{3/2}}$

A summary of the expressions of the magnetic fields

$$(H_{r,z}^* \equiv 4H_{r,z}/Ma^2)$$

on three radial planes at three axial probe locations (i.e., at both north and south poles and center) is given in Table 2.

Magnetic Force Derivation. If we define

$$\bar{F}_m = \mu_o \chi_e v_p \bar{F}_m^*, \tag{8}$$

the r component of the magnetic force given by Eq. (5) is written as

$$F_{m_r}^* = H_r \frac{\partial H_r}{\partial r} + H_z \frac{\partial H_r}{\partial z} \tag{9}$$

Substituting Eqs. (6) and (7) into Eq. (9) yields

$$F_{m_r}^* = 2r \left(\frac{Ma^2}{4} \right)^2 \left(\frac{r^2 + (z + b)(z - 2b)}{D_1^{5/2} D_2^{3/2}} \right.$$
$$\left. + \frac{r^2 + (z - b)(z + 2b)}{D_1^{3/2} D_2^{5/2}} - \frac{1}{D_1^3} - \frac{1}{D_2^3} \right) \tag{10}$$

where $D_1 = r^2 + (z + b)^2$ and $D_2 = r^2 + (z - b)^2$.

Similarly, the axial component of the force is

$$F_{m_z}^* = H_r \frac{\partial H_z}{\partial r} + H_z \frac{\partial H_z}{\partial z} \tag{11}$$

and after the substitutions

$$F_{m_z}^* = -2 \left(\frac{Ma^2}{4} \right)^2 \left(\frac{z + b}{D_1^3} + \frac{z - b}{D_2^3} + \frac{z - b}{(D_1 D_2)^{3/2}} \right.$$
$$\left. - \frac{3}{2} \frac{r^2 + z^2 - b^2}{(D_1 D_2)^{3/2}} \right) \left(\frac{z + b}{D_1} + \frac{z - b}{D_2} \right) \tag{12}$$

A summary of the two components of the magnetic force $F_{m_{r,z}}^+ \equiv F_{m_{r,z}} (4/Ma^2)^2/2$ for the three position (middle, north, and south poles) are given in Table 3.

Thus, by Eq. (8) and Table 3, the magnetic force on the particle in the radial plane at $z = 0$ is

$$\bar{F}_m = -N_m [r_+ / (r_+^2 + b_+^2)^4] \hat{e}_r \tag{13}$$

in which $r_+ = r/a$, $b_+ = b/a$. N_m is a magnetic number defined by

$$N_m = \pi \mu_o \chi_e (Mb)^2 A^3, \quad A \equiv a_p/a \tag{14}$$

with units of force (Newton). For the case when the particle is made up of both silica and iron (i.e., the susceptibility is positive), this number is positive, giving rise to an attractive force.

Calculation of the Magnetization M. Finally, the magnetization M of the Samarium Cobalt magnet, for the evaluation of the magnetic force from Eqs. (10) and (12), is determined from the measurement values of the magnetic induction B at the water side of the magnetic probe surface. The measured values of the three components, B_r, B_θ, and B_z on the cylindrical

The particle magnetization, or the response of the particle material to the applied external field $\bar{H}$ is given for a paramagnetic material by (Jackson, 1975):

$$\bar{M}_p = [\chi/(1 + \chi/3)]\bar{H} = \chi_e \bar{H} \tag{3}$$

where the equivalent susceptibility is $\chi_e \equiv \chi/(1 + \chi/3)$ and χ is the difference between the equivalent magnetic susceptibilities of the particle and that of the water surrounding it,

$$\chi = \chi_p - \chi_{H_2O} \tag{4}$$

with $\chi_p = (\mu_p/\mu_o) - 1$ and $\chi_{H_2O} = (\mu_{H_2O}/\mu_o) - 1$ where μ_p, μ_o, and μ_{H_2O} are the magnetic permeabilities of the particle free space and water, respectively (Henry/M). Using the results of the scale analysis as listed in Table 1, $\chi_p = 0.85 \, \chi_{SiO_2} + 0.15 \, \chi_{Fe}$. Substituting Eq. (3) into Eq. (2) yields the magnetic force induced by the magnetic field $\bar{H}$,

$$\bar{F}_m = \mu_o \chi_e v_p (\bar{H} \cdot \nabla) \bar{H} \tag{5}$$

Derivation of the Magnetic Field H Around the Probe. The magnetic field at the particle location (r, z) induced by the cylindrical magnet probe (see Fig. 3) is needed to evaluate the magnetic force. However, for the present cylindrical magnet of finite length, the magnetic field formula needed is unavailable and is therefore derived next.

The magnetic field vector induced by an infinitesimal volume $dV = (\pi/4)a^2 dz$ of a magnetic dipole with a saturation flux density (i.e., the magnetization of Samarium Cobalt magnet) M at $(r = 0, z = z')$ is given by:

$$\bar{H}_d = \frac{MdV}{4\pi(r^2 + (z - z')^2)^{5/2}}$$
$$\times (3r(z - z')\hat{e}_r + (2(z - z')^2 - r^2)\hat{e}_z)$$

The present cylindrical probe is considered as a series of magnetic dipoles (see Fig. 3) and the field around it is obtained by integrating the equation given above along the length of the probe,

$$\bar{H} = H_r \hat{e}_r + H_z \hat{e}_z = \int_{-b}^{b} \bar{H}_{d_r} dz' \hat{e}_r + \int_{-b}^{b} \bar{H}_{d_z} dz' \hat{e}_z$$

in which $\bar{H}$ is only dependent on radial and axial directions due to symmetry. The r and z components can be evaluated analytically to yield,

$$H_r = -\frac{Ma^2}{4} r \left(\frac{1}{(r^2 + (z + b)^2)^{3/2}} - \frac{1}{(r^2 + (z - b)^2)^{3/2}} \right)$$
$$\tag{6}$$

$$H_z = \frac{Ma^2}{4} \left(\frac{z - b}{(r^2 + (z - b)^2)^{3/2}} - \frac{z + b}{(r^2 + (z + b)^2)^{3/2}} \right) \tag{7}$$

Table 3 Magnetic forces for different axial position

z	$F_{m_r}^+$	$F_{m_z}^+$
$-b$	$\dfrac{2/(r^2+b^2)}{r^2(r^2+4b^2)^{5/2}} - \dfrac{r}{(r^2+4b^2)^3} - \dfrac{1}{r^5}$	$2b\left(\dfrac{1}{(r^2+4b^2)^3} - \dfrac{r^2-2b^2}{r^3(r^2+4b^2)^{5/2}}\right)$
0	$-6\,b^2\,\dfrac{r}{(r^2+b^2)^4}$	0
b	$\dfrac{2(r^2+b^2)}{r^2(r^2+4b^2)^{5/2}} - \dfrac{r}{(r^2+4b^2)^3} - \dfrac{1}{r^5}$	$2b\left(\dfrac{-1}{(r^2+4b^2)^3} + \dfrac{r^2-2b^2}{r^3(r^2+4b^2)^{5/2}}\right)$

probe surface, $r = a$, along the axial distance, z, are given in Fig. 4. From the electromagnetic theory, the boundary condition of the magnetic field at the interface between two media of different susceptibilities is such that the tangential components of the magnetic field inside the magnet, H_{1_z}, is equal to that of the water side, H_{2_z}.

$$H_{1_z} = H_{2_z} \qquad (15)$$

In terms of the magnetic flux density, H_{1_z} can be written as

$$H_{1_z} = B_{1_z}^{(m)}/\mu_o\mu_{r_1} \qquad (16)$$

where $\mu_{r_1} = 1.05$ for a Samarium Cobalt magnet, dimensionless. $B_{1_z}^{(m)}$ is the experimental value of the magnetic flux density measured at $z = 0$ and $r = a$, namely, 300 Gauss for the present magnetic probe. Also using Eq. (7) to evaluate H_{2_z} at $r = a$ and $z = 0$,

$$H_{2_z|_{(r_+=1, z_+=0)}} = \frac{M}{4}\frac{b_+}{(1+b_+^2)^{3/2}} \qquad (17)$$

where $b_+ = b/a = 3.04$. Therefore, the boundary condition, Eq. (15), becomes

$$\left(\frac{1}{2}\frac{b_+}{(1+b_+^2)^{3/2}}\right)M = \frac{B_{1_z}}{\mu_o\mu_{r_1}} \qquad (18)$$

from which M is calculated to yield $M \simeq 5 \times 10^5$ A/m as listed in Table 1, which is to be used in later computations and is close to the values of $0.6 \sim 0.7 \times 10^5$ A/m reported in the literature.

Other Forces. The London–van der Waals force is an important part of the surface forces, also known as adhesion forces. Depending on many factors, these adhesion forces are responsible for the short-range attraction or repulsion of particles onto surfaces and the London–van der Waals force constitute the attraction part of these surface phenomena. In the present work, because the particles are very small compared to the cylindrical probe, we can approximate the London–van der Waals attractive force between the particle and the magnetic cylindrical probe as that between a small particle of radius a_p and a flat surface (Spielman, 1977),

$$\vec{F}_l(h) = -\frac{2}{3}\frac{\mathcal{H}_{132}a_p^3}{h^2(h+2a_p)^2}\,\hat{n}$$

where $\mathcal{H}_{132}$ is the Hamaker constant, $\hat{n}$ is a unit vector outward and normal to the magnetic surface (i.e., $\check{e}_r$). For the particle located at a radial distance r from the center of the probe with a radius a, the separation distance between the particle and probe surfaces is $h = r - a - a_p$. Thus the equation given above becomes

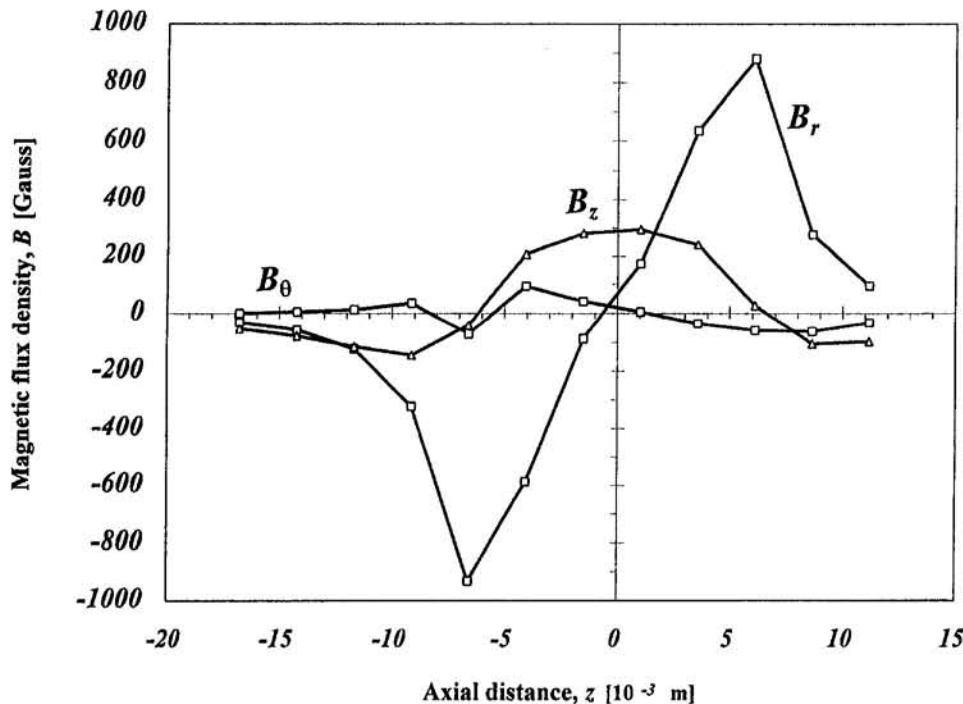$$\vec{F}_l(r_+) = -N_1\check{e}_r/[(r_+ - 1 - A)^2(r_+ - 1 + A)^2] \qquad (19)$$

Fig. 4 Experimental values of the magnetic flux densities on the cylindrical probe surface, $r = a$, along the axial distance, z

in which again $r_+ = r/a$, $A = a_p/a$, and the London–van der Waals force number $N_1 = 2\mathcal{H}_{132}A^3/(3a)$. For a tertiary system made up of composed silica–iron particles (denoted 1) and titanium cylindrical probe (2) submerged in liquid water (3), the Hamaker constant is given by Lifshitz (1956), $\mathcal{H}_{132} = (\sqrt{\mathcal{H}_{11}} - \sqrt{\mathcal{H}_{33}})(\sqrt{\mathcal{H}_{22}} - \sqrt{\mathcal{H}_{33}})$. H_{ii} for many materials are available (Visser, 1972). In evaluating H_{11}, we assume the silica–iron composite particle to be made of silica only since $\mathcal{H}_{\text{iron}} \simeq \mathcal{H}_{\text{SiO}_2}$. The calculated $\mathcal{H}_{132}$ value is shown in Table 1.

Since the difference in particle velocity $(\bar{V})$ and the carrier fluid velocity $(\bar{U})$ is small, the drag force can be approximated by the Stokes law (Kladas and Georgiou, 1993)

$$\bar{F}_d = 6\pi a_p \eta(\bar{U} - \bar{V}) \qquad (20)$$

where η is the fluid viscosity. As to the added mass force, which is the additional force the particle experiences when it accelerates with respect to the carrier fluid, it is generally given as

$$\bar{F}_a = (2\pi a_p^3 \rho/3)\frac{d}{dt}(\bar{U} - \bar{V}).$$

The carrier fluid velocity is approximated, for simplicity, by a steady potential flow, thus

$$\bar{F}_a \simeq -(2\pi a_p^3 \rho/3)\frac{d}{dt}\bar{V}. \qquad (21)$$

Two-Dimensional Predictions and Comparisons

Upon the substitution of all forces, Eqs. (13), (19)–(21), into Eq. (1) yields

$$\frac{4\pi}{3}a_p^3 \rho_e \frac{d\bar{V}}{dt} = 6\pi\eta a_p(\bar{U} - \bar{V}) - N_m \frac{r_+}{(r_+^2 + b_+^2)^4}\hat{e}_r$$
$$- N_1(r_+ - 1 - A)^{-2}(r_+ - 1 + A)^{-2}\hat{e}_r \quad (22)$$

where, due to the added mass term in the left-hand side of this equation, the effective density is $\rho_e \equiv \rho_p + \rho/2$.

For two-dimensional solutions, a particle once originating from an upstream point in a two-dimensional (r, θ) plane perpendicular to the probes' axis is assumed to travel only in that plane. The angular and the radial components of Eq. (22) on the center plane at $z = 0$ for example are

$$\frac{4\pi}{3}a_p^3 \rho_e\left(\frac{dV_\theta}{dt} + \frac{V_\theta V_r}{r}\right) = 6\pi\eta a_p(U_\theta - V_\theta) \qquad (23)$$

$$\frac{4\pi}{3}a_p^3 \rho_e\left(\frac{dV_r}{dt} - \frac{V_\theta^2}{r}\right) = 6\pi\eta a_p(U_r - V_r) - N_m \frac{r_+}{(r_+^2 + b_+^2)^4}$$
$$- N_1(r_+ - 1 - A)^{-2}(r_+ - 1 + A)^{-2} \quad (24)$$

To evaluate the drag force term in Eqs. (23)–(24), the carrier fluid velocity components, U_θ and U_r, are needed. Since no exact solutions of U_θ and U_r are currently available for a flow in a pipe over an inserted cylindrical probe, they are approximated by that of the potential flow solution

$$U_r = U_\infty(1 - a^2/r^2)\cos\theta \qquad (25)$$

$$U_\theta = -U_\infty(1 + a^2/r^2)\sin\theta \qquad (26)$$

It should be noted that the viscous drag force around the particle is still included in the analysis and that this approximation is merely used to approximate $\bar{U}$ in the evaluation of the drag force. The approximation is made without loss of generality since the present study is mainly interested in magnetic effects. Besides, it approximates the fluid flow very closely in front of probes where deposition is mainly occurring. Using the nondimensional quantities, $V_{\theta+} = V_\theta/U_\infty$, $V_{r+} = V_r/U_\infty$, $r_+ = r/a$,
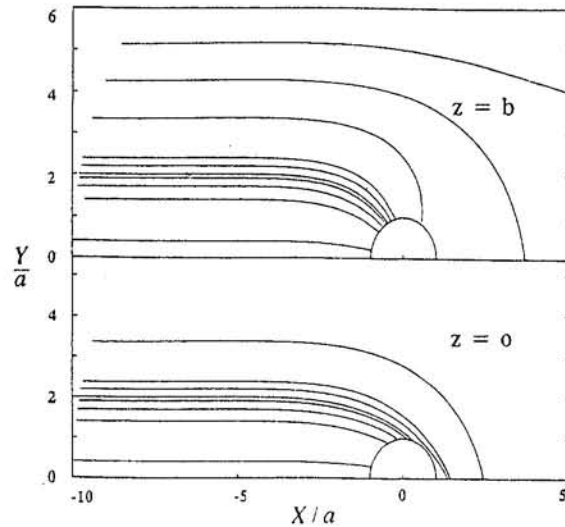

Fig. 5   Composed silica particle trajectories around the magnetic probe at the middle plane, $z = 0$, and at the magnetic pole plane, $z = b$

and $t_+ = U_\infty t/a$ and the definitions of the velocity components V_r and V_θ in terms of r and θ,

$$\frac{d\theta}{dt_+} = \frac{V_{\theta+}}{r_+}, \qquad \frac{dr_+}{dt_+} = V_{r+} \qquad (27)$$

Similarly, Eqs. (23)–(26) can be combined and written as

$$\left(\frac{dV_{\theta+}}{dt_+} + \frac{V_{\theta+}V_{r+}}{r_+}\right) = N_{hi}\left(-\left(1 + \frac{1}{r_+^2}\right)\sin\theta - V_{\theta+}\right) \quad (28)$$

$$\left(\frac{dV_{r+}}{dt_+} - \frac{V_{\theta+}^2}{r_+}\right)$$

$$= N_{hi}\left(\left(1 - \frac{1}{r_+^2}\right)\cos\theta - V_{r+}\right) - N_{mi}r_+(r_+^2 + b_+^2)^{-4}$$

$$- N_{1i}(r_+ - 1 - A)^{-2}(r_+ - 1 + A)^{-2} \quad (29)$$

in which $N_{hi} \equiv N_h/N_i$, $N_{mi} \equiv N_m/N_i$, $N_{1i} \equiv N_1/N_i$. N_m is the magnetic number given by Eq. (14), the inertial number $N_i = 4\pi a_p^3 \rho_e U_\infty/3a$, the hydrodynamic number $N_h = 6\pi\eta a_p U_\infty$, and the London–van der Waals attraction number $N_1 = 2\mathcal{H}_{132}/3a_p$. Their values and the constants used for their derivations are given in Table 1. These constants were based on experimental parameters and conditions in our fouling heat transfer loop.

The particle trajectories around the nonmagnetic probe are modeled by applying a zero magnetic number in the trajectory Eqs. (27)–(29) and using different initial conditions $r = 10.0$ and an angular span from 3.14 to 2.6 rad. These trajectories are found to be almost straight lines. This is due to the appreciable size and inertia of the particles that take over the hydrodynamics force in the absence of magnetic field and prevent the particles from following the potential flow streamlines, hence retaining their original velocity directions acquired at the release positions.

The results of the magnetic probe are given by Fig. 5. The trajectories in the midplane at $z = 0$, shown in Fig. 5, are obtained using the dimensionless parameters derived earlier and as given in Table 1, that is for a magnetic number $N_{mi} = 11460.0$. In the computations, the long-range magnetic and inertia forces were found dominant over other surface or adhesion forces. Particles released at far distances will travel mostly under the influence of inertia and drag in almost straight lines until the magnetic attraction takes over at the surrounding of the probe

and the particles start deviating toward the probe. Once they reach the surface of the cylindrical probe, these particles will be deposited there (an assumption used for qualitative description in light of the fact that the adhesion forces, being very strong near the surface, will retain the particles and prevent them from rebounding). Figure 5 also shows the trajectories in the magnetic probe case at the north pole plane $z = b$. These trajectories show the same trend as in the previous case with much sharper deviations toward the magnetic probe. Thus the particles in the midplane will travel by the probe and escape, while they will be captured at the pole plane. These results agree with experimental findings as shown in Fig. 1, namely more deposit is collected at the north and south poles than in the middle position of the magnetic probe. Also found experimentally in the comparison of the scale formation on magnetic and nonmagnetic probes was the presence of thinner scale at the midsection of the magnetic probe. This can be explained by the fact that in the flowing liquid there also exists particles made of just silica (no iron) and these have negative magnetic susceptibilities and their behavior under the same magnetic field is opposite to the one by the iron–silica composed particles presented in the previous figures. These silica-only particles will tend to be rejected away from the magnetic probe, as can be seen by examining the magnetic forces on the particles at the mid and pole planes. From Eq. (8) and Table 3 and taking for simplicity $b \sim a$, they are

$$(F_{m_r})_o \sim -\frac{3}{8}\frac{1}{b^5}\chi_e \quad \text{at} \quad z = 0,$$

$$(F_{mr})_b \sim -\left(1 + \frac{1}{5^3} - \frac{4}{5^{5/2}}\right)\frac{1}{b^5}\chi_e \quad \text{at} \quad z = b$$

For pure silica particles, $\chi_e < 0$, they yield positive values, namely, acting in the r direction. Thus the silica particles experience a repulsive force as they approach the magnetic probe, and less deposition is to be expected on the magnetic probe than on the nonmagnetic probe. For the composite particles containing iron, $\chi_e > 0$, and the particles should experience an attractive force. Since $(F_{mr})_b$ is larger than $(F_{mr})_o$, more iron particles should be deposited at the north or south poles than in the midsection of the magnetic probe. By the same token, more silica-only particles are expelled at the poles than in the middle. Thus composition of the scale, formed as a result of a combination of iron–silica particle deposition and silica-only particle deposition, should contain more iron at the poles than in the middle of the magnetic probe. This is also in agreement with the experimental finding described in the earlier section.

Figure 6(a) shows the effect of increasing the magnetic number $N_{mi} = 0$, 2.06, 20.67, 206.7, 2066.7 at the pole plane on the trajectory of a particle of size $A = a_p/a = 0.00315$ released from $r_o = 10.0$ and $\theta_o = 2.8$ rad. As the magnetic number is increased, the particles are progressively deflected toward the cylindrical probe until a threshold magnetic number for which the particle will bend enough to reach the surface and deposit there. The trajectories of the composed particles with increasing dimensionless sizes $A = 3.15 \times 10^{-5}$, 3.15×10^{-3}, and 3.15×10^{-2} (i.e., $a_p = 0.1, 10.0, 100.0$ μm) at the middle plane ($z = 0$) are shown in Fig. 6(b). This figure shows that for a given magnetic number ($N_{mi} = 114650.0$) as the size decreases, the particles tend to be attracted toward the cylindrical probe and eventually are deposited. Therefore capture of composed particles away from the probe is only possible when the size is small. This observation and the fact that composed particles are large in general due to the fact that they are the result of coagulation of silica particles with iron, should also explain that there is an optimum condition of size and magnetic field for which deposition occurs.
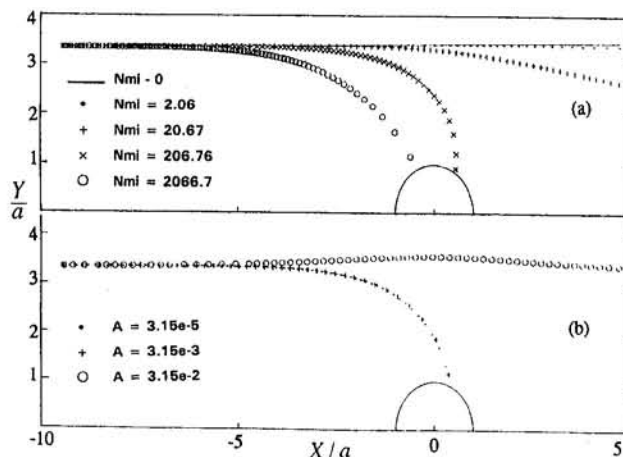

Fig. 6 (a) Magnetic field effect on composed silica particle trajectories ($z = b$); (b) particle size effect on composed silica particle trajectories in the midplane ($z = 0$) with $N_{ml} = 11,460$

Conclusion

The deposition of silica colloidal particle in suspension in a supersaturated silica–iron solution onto magnetic and nonmagnetic probes has been investigated experimentally and theoretically. The following conclusions are reached: (1) The long-range magnetic and inertia forces were found dominant over surface and adhesion forces; (2) in the absence of a magnetic field, inertia is more important than fluid drag and the silica particles tend to travel in almost straight paths; (3) with a magnetic field, the trajectory of a silica-only particle can be deflected away from the magnetic probe at a threshold magnetic number. But the silica–iron particles can be attracted toward the magnetic probe, more so at the poles than in the midsection; (4) the predictions explained and were in qualitative agreement with experimental results, namely, more deposit at the pole regions than in the midsection, less scale in the midsection of the magnetic probe than on the nonmagnetic probe, and more iron element in the composition of scale deposit at the poles than in the midregion of the magnetic probe.

Acknowledgments

References

Boichenko, V. A., and Sapogin, L. G., 1977, "Theory of Magnetic Water Treatment," *Inzhenerno-Fizicheskii Zhurnal* (translated), Vol. 33, No. 2, pp. 350–355.

Brock, J. R., 1962, "On the Theory of Thermal Forces Acting on Aerosol Particles," *J. Colloid Science*, Vol. 17, p. 768.

Chan, S. H., Rau, H., DeBellis, C., and Neusen, K. F., 1988, "Silica Fouling of Heat Transfer Equipment Experiments and Model," ASME JOURNAL OF HEAT TRANSFER, Vol. 110, pp. 841–849.

Chan, S. H., Chen, Z. J., and He, P., 1995 "Effect of Ferric Chloride on Silica Fouling," ASME JOURNAL OF HEAT TRANSFER, Vol. 117, pp. 323–328.

Clyburn, R. M., 1983, "Non-chemical Water Treating: Comparing the Theories," Research Report, CIVE 6398, University of Houston, Jan.

Duffy, A. E., 1977, "Investigation of Magnetic Water Treatment Devices," Ph.D. Dissertation, Clemson University, Clemson, SC.

Hasson, D., and Bramson, D., 1981, "The Performance of a Magnetic Water Conditioner Under Accelerated Scaling Conditions," *Proc. Progress in the Prevention of Fouling in Industrial Plant*, Nottingham University, United Kingdom, Apr.

Jackson, J. D., 1975, *Classical Electrodynamics*, Wiley, New York.

Kladas, D. D., and Georgiou, D. P., 1993, "A Relative Examination of C_D–Re Relationships Used in Particle Trajectory Calculations," ASME *Journal of Fluids Engineering*, Vol. 115, pp. 162–165.

Kochmarskii, V. Z., Kul'skii, L. A., and Krivtsov, V. V., 1982, "After Effects of Magnetic Anti-Scale Treatment," *Khimiya i Tekhonologiva Vody* (translated), Vol. 4, No. 3, pp. 217–222.

Lifshitz, E. M., 1956, "Soviet Physics," *JETP*, Vol. 2.

Martynova, O. I., Gusev, B. T., and Leontev, E. A., 1969, "Concerning the Mechanism of the Influence of a Magnetic Field of Aqueous Solutions of Salts," *Soviet Physic Uspekhi*, Vol. 12, pp. 440–443.

Martynova, O. I., Kopylov, A. S., Tebenikhin, E. F., and Ochkov, V. F., 1979, "The Mechanism of the Influence of Magnetic Treatment of Water on the Process of Scale Formation and Corrosion," *Teploenergetika* (translated), Vol. 26, No. 6, pp. 67–69.

Raisen, E., 1984, "The Control of Scale and Corrosion in Water Systems Using Magnetic Fields," *Corrosion/84*, Paper No. 117, New Orleans, LA, Apr.

Spielman, L. A., 1977, "Particle Capture," *Annual Review of Fluid Mechanics*, Vol. 9, pp. 297–317.

Visser, J., 1972, "On Hamaker Constants," *Advances in Colloid Interface Science*, Vol. 3, pp. 331–363.

New Radiative Analysis Approach for Reticulated Porous Ceramics Using Discrete Ordinates Method

T. J. Hendricks

Advanced Modular Power Systems, Inc.
System Design Department
4667 Freedom Drive
Ann Arbor, MI 48108
email: thendricks@ampsys.com
Mem. ASME

J. R. Howell

Department of Mechanical Engineering,
University of Texas at Austin,
Austin, TX 78712
Fellow ASME

A novel radiative modeling technique using discrete ordinates has been developed for reticulated porous ceramics (RPCs) from experimental measurements of transmittance and reflectance on small samples of partially stabilized zirconium oxide (PS ZrO₂) and oxide-bonded silicon carbide (OB SiC). The new technique defines and quantifies the direct transmittance fraction, f_{dt}, of a reticulated porous ceramic, demonstrates how it redefines the extinction process, and creates a new effective extinction coefficient, $K_{\lambda, eff}$. This ultimately produces a modified form of the radiative transfer equation (RTE) and an innovative discrete ordinates formulation to solve the RTE unique to RPCs. The direct transmittance modeling approach has been compared to a more conventional homogeneous modeling approach, in which the direct transmittance effects are essentially ignored and the RPC is treated as a homogeneous lump of material. The two modeling approaches yield identical results in predicting small test sample reflectances and transmittances. The direct transmittance technique does demonstrate explicitly, through a unique relationship between absorption coefficients in the two modeling approaches, the importance of scattering processes in enhancing the absorption mechanism in RPCs. It can also be an important secondary modeling technique that imposes additional parameter constraints in an inverse analysis to help refine derived radiative coefficients.

Introduction

Reticulated porous ceramics (RPCs) are highly porous ceramics (i.e., porosity ≈ 80 percent) with an open, weblike, dodecahedral internal structure with continuous void volume connecting adjacent pores. RPCs are typically characterized by their manufacturer in terms of ppi-rating (ppi is pores per linear inch) and pore diameter, which is generally inversely related to ppi-rating within an RPC material category. RPCs are being developed rapidly for advanced energy systems, such as advanced porous combustion burners (Howell et al., 1995) and volumetric absorbers in solar thermal receivers and reactors (Skocypec et al., 1991). Knowledge of radiative modeling techniques for RPCs is critical to accurate modeling of radiative transport in anticipated high-temperature applications of future advanced energy systems. Very little past work has been done to date to develop or update radiative modeling techniques in RPCs. Skocypec et al. (1991) did some radiative modeling with alumina/mullite reticulated porous ceramics in solar energy applications.

The highly porous and open structure of RPCs creates complex electromagnetic scattering and interference patterns within the structure, which tremendously complicates radiative modeling in these materials. In addition, the highly porous structure allows a certain fraction of incident radiative energy to transmit directly through the structure without any interaction with the structure. A novel radiative modeling technique has been developed that effectively treats this complex radiative interaction by quantifying the direct transmittance fraction and incorporating it into a discrete ordinates formulation to predict experimental

reflectance and transmittance behavior in small RPC test samples. In particular, this technique has been used to predict experimental transmittance and reflectance measurements on small samples of partially stabilized zirconium oxide (PS ZrO₂) and oxide-bonded silicon carbide (OB SiC) (Hendricks, 1993).

Direct Transmittance

This new radiative modeling technique postulates an experimentally determined radiative property in RPCs called the direct transmittance fraction, f_{dt} (Hendricks, 1993). The direct transmittance fraction essentially defines the fraction of incident radiative intensity that penetrates a depth, s, without any interaction with the RPC internal structure. This property is assumed to be isotropic because a given RPC sample has a homogeneous structure on a macroscale defined by a typical pore diameter in all directions. The quantity $(1 - f_{dt})$ is then the fraction of radiative intensity that interacts with the RPC structure through normal absorption and scattering processes. Radiative experiments on PS ZrO₂ and OB SiC have found that f_{dt} obeys an exponential relationship:

$$f_{dt}(s) \equiv \frac{i'_{dt}(s)}{i'(0)} = T_o \exp(-\beta \cdot s) \qquad (1)$$

where T_o and β are experimentally derived direct transmittance coefficients for the particular RPC (Hendricks, 1993).

Figures 1 and 2 illustrate recent experimental data for f_{dt} from transmittance tests on 10 ppi, 20 ppi, and 65 ppi PS ZrO₂ and OB SiC. Hendricks (1993) describes in detail the experimental radiative technique for determining f_{dt}, and specifically the use of polarized films to eliminate forward-scattering contributions from f_{dt}. Figures 1 and 2 show that f_{dt} decreases significantly as ppi rating increases (i.e., pore size decreases) and both materials become much more opaque. In addition, a given ppi-rating of PS ZrO₂ has smaller direct transmittance fractions than a compa-

Note: Symbols are Experimental Data

Lines Are Exponential Curve Fits
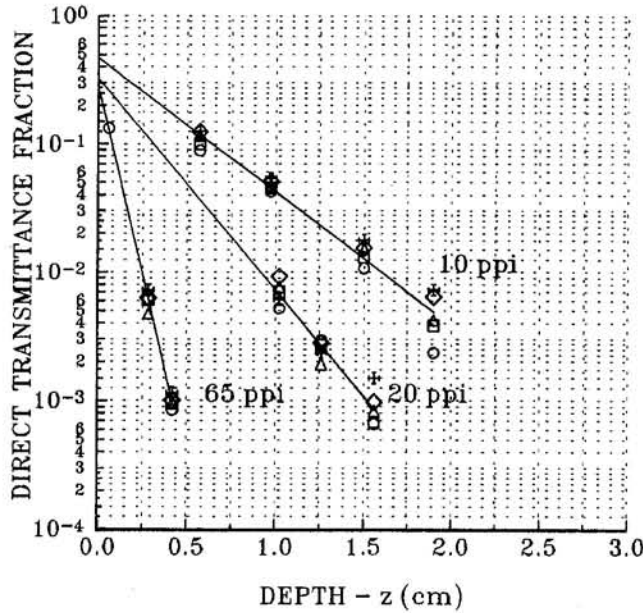
Fig. 1 Direct transmittance fraction versus depth in 10 ppi/20 ppi/65 ppi porous PS ZrO$_2$

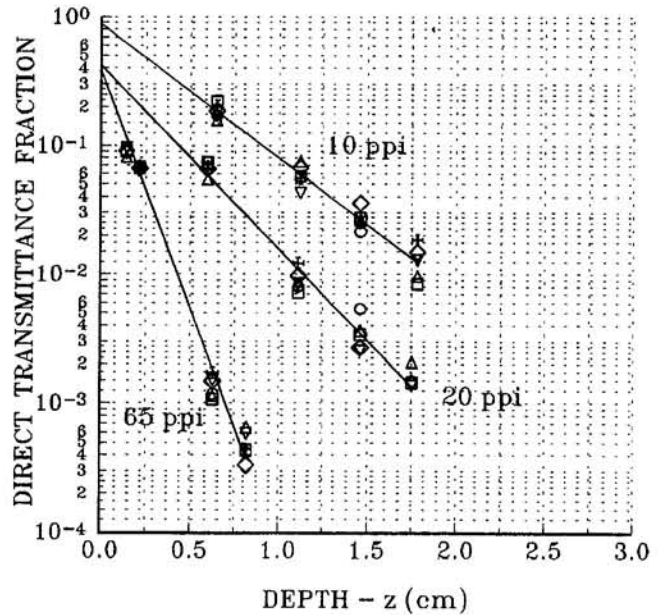**Fig. 2 Direct transmittance fraction versus depth in 10 ppi/20 ppi/65 ppi porous OB SiC**

rable ppi-rating of OB SiC. Visual inspection of the two materials clearly shows that a given ppi-rating of OB SiC has larger pore diameters and a more open structure than a comparable ppi-rating of PS ZrO$_2$; thus, incident radiation experiences less structural blockage. This characteristic is determined by the manufacturing processes and material details unique to the RPCs used in this investigation [RPCs supplied by Hi-Tech Ceramics, Alfred, New York]. Figures 1 and 2 also show that f_{dt} does not necessarily go to 1 as sample thickness goes to zero. This is indeed the case because there is a finite amount of

structure at the front surface of a reticulated porous ceramic that interacts with the incident radiation immediately at $z = 0$.

Figures 1 and 2 also display several experimental data points at each depth because typically multiple f_{dt} measurements were taken for each depth in a given sample (Hendricks, 1993). The data variation at each depth is then an indication of typical measurement error in f_{dt} in this work.

Values for T_o and β in Eq. (1) were derived from exponential curve fits to the experimental data in Figs. 1 and 2. Tables 1 and 2 show the experimentally derived values of T_o and β for

Nomenclature

a_λ = spectral absorption coefficient, cm^{-1} or m^{-1}

f_{dt} = direct transmittance fraction

$I_{m,p}$ = specific intensity in discrete ordinate direction m at point p, W/ m^2-μm-sr

I_b = blackbody intensity in discrete ordinate direction m, W/m^2-μm-sr

I_i = incident radiative beam intensity, W/m^2-sr

I_c = collimated beam intensity, W/ m^2-sr

$I_{c,max}$ = maximum collimated beam intensity, W/m^2-sr

$i'_{dt}(s)$ = directional radiative intensity that is directly transmitted at s, W/m^2-sr

i'_λ = spectral directional radiative intensity, W/m^2-μm-sr

$i'_{\lambda,sc}$ = spectral directional scattered intensity in Eq. (9), W/m^2-μm-sr

$i_{\lambda b}$ = blackbody radiative intensity

p = porosity

r = radial direction, cm or m

s = path length, cm or m

T_o = direct transmittance coefficient

ds = incremental path length, cm or m

V_p = volume of radiative element, m^3

w_m = discrete ordinate quadrature point weight for m direction

z = depth dimension, cm or m

α_1 = angular differencing coefficients defined in Carlson and Lathrop (1968)

β = direct transmittance exponential attenuation coefficient, cm^{-1} or m^{-1}

$\Delta r, \Delta z$ = radial and in-depth node increments, cm or m

δ = Dirac delta function

δ_w = interpolation weighting factor

η_m = direction cosine of discrete ordinates direction m

K_λ = spectral extinction coefficient $(a_\lambda + \sigma_\lambda)$, m^{-1}

$K_{\lambda,eff}$ = spectral effective extinction coefficient, m^{-1}

κ_λ = spectral optical depth

λ = wavelength, μm

μ_m = direction cosine of discrete ordinates direction m

ξ_m = direction cosine of discrete ordinates direction m

σ_λ = spectral scattering coefficient, cm^{-1} or m^{-1}

Φ = scattering phase function

ϕ = angle of revolution around the ξ axis

Ω_λ = scattering albedo = σ_λ/K_λ

ω = direction of a given radiative intensity

ω_c = incident direction of collimated radiative intensity

ω_i = incident direction of given radiative intensity

$d\omega$ = solid angle of a given direction ω, steradians or sr

Table 1 Least-squares exponential curve-fit coefficients for PS ZrO₂

Material Category	T_o	β (meter⁻¹)	Correlation Coefficient
10 ppi	0.4629	239.7	0.9602
20 ppi	0.3209	380.0	0.9313
65 ppi	0.2628	1336.0	0.9931

Table 2 Least-squares exponential curve-fit coefficients for OB SiC

Material Category	T_o	β (meter⁻¹)	Correlation Coefficient
10 ppi	0.8686	239.3	0.9655
20 ppi	0.4111	327.3	0.9722
65 ppi	0.3706	842.2	0.9823

PS ZrO₂ and OB SiC, respectively. As expected, values of T_o decrease and values of β increase significantly as ppi rating increases and the material becomes more opaque.

Equation (1) generally describes how radiative intensity attenuates simply due to the structural blockage by the complex structure of pores and webs in an RPC. The direct transmittance fraction can be thought of as a two-dimensional attribute of the porous material that is different from the material porosity, which is a three-dimensional property. The two-dimensional alignment of the RPC structure determines f_{dt}, and materials of similar porosity can have many different two-dimensional alignments. Direct transmittance results in Figs. 1 and 2 demonstrate that 10 ppi, 20 ppi, and 65 ppi PS ZrO₂ and OB SiC can have dramatically different direct transmittance factors, while they all have approximately the same material porosity (i.e., $p \approx 80-85$ percent). Of course, one could also argue that Eq. (1) indicates that f_{dt} is a one-dimensional attribute in the sense that it is only a function of distance along a path, s, and is assumed to be isotropic. In any event, the direct transmittance coefficients represent additional radiative properties, which must be independently quantified (i.e., measured) for a given RPC material and ppi-rating when analyzing radiative transfer within RPCs. Fortunately, the structure of each given RPC is homogeneous enough that direct transmittance coefficients do not vary appreciably for a given ppi-rating or pore diameter, and the material is isotropic within a given specimen so that properties are independent of incident radiation direction.

Modification of Radiative Transfer Equation

The impact of Eq. (1) on radiative transfer in porous ceramics is to modify the attenuation of a radiative intensity in any given direction compared to normal radiative transfer in participating media. Siegel and Howell (1992) present the fundamental mathematical development of the radiative transfer equation for homogeneous, nonporous materials. This section will present the detailed mathematical arguments leading to modifications in the basic radiative transfer equation from direct transmittance effects of RPCs and the subsequent definition of $K_{\lambda,\text{eff}}$. The basic assumptions are those associated with the radiative transfer equation plus the assumption of an isotropic, homogeneous structure in RPCs.

Direct transmittance effects in RPCs are essentially a result of the RPC porous structure creating a relatively predictable amount of structural blockage as a given intensity travels through it. The radiative transfer analysis begins by considering a specific spectral intensity, $i'_\lambda(s)$, traveling in a given direction along a path length, Δs, within the RPC structure. Figure 3 illustrates the geometry and radiative intensities in this analysis. The direct transmittance fraction, $f_{dt}(\Delta s)$, is that fraction of energy (or intensity) that is directly transmitted through the RPC structure without any interaction or blockage from the structure. The direct transmittance fraction for Δs is:

$$f_{dt}(\Delta s) = T_o \exp(-\beta \Delta s) \qquad (2)$$

where T_o and β are experimentally determined direct transmittance coefficients for a given RPC.

As the specific spectral intensity travels along its path, Δs, the amount of change in intensity *just due to the porous structure blockage and no other attenuation* is given by:

$$di'_{\lambda,ps}(\Delta s) = -f_{dt}(0)i'_\lambda(s)[1 - \exp(-\beta \Delta s)] \qquad (3)$$

where β and $f_{dt}(0) = T_o$ are experimentally determined direct transmittance coefficients. This expression explicitly accounts for the fraction of energy undergoing structural blockage and not the fraction subject to emission, absorption, or scattering processes during intensity interaction with the structure. The fraction of energy subject to absorption and scattering processes during interaction with the structure is given by $(1 - T_o)i'_\lambda(s)$. Figure 3 shows these two components explicitly broken out at path point s.
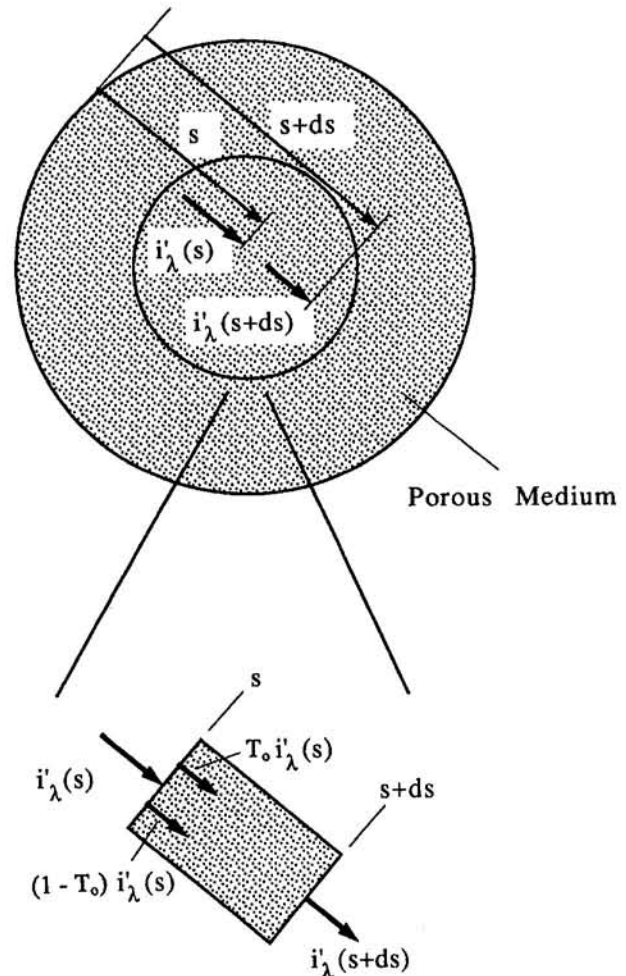

Fig. 3 Radiative transfer analysis in one direction in absorbing, emitting, and scattering porous medium

The change in intensity, $di'_{\lambda,ps}(\Delta s)$, due to porous structure blockage as $\Delta s \to 0$ then becomes:

$$di'_{\lambda,ps}(ds) = -T_o\beta i'_\lambda(s)ds \qquad (4)$$

This same expression applies to that portion of an incident collimated beam subject to porous structure blockage as it enters the RPC front surface.

The total change in intensity, $di'_\lambda(ds)$, from all radiative processes in incremental distance, ds, is then due to absorption, scattering out of the given direction, porous structure blockage, blackbody emission into the given direction, and scattering into the given direction from all other directions. Using Eq. (4) and the mathematical formulation of terms given in Siegel and Howell (1992), Chap. 14, this is mathematically expressed as:

$$\frac{di'_\lambda}{ds} = -[(a_\lambda + \sigma_\lambda)(1 - T_o) + T_o\beta]i'_\lambda(s)$$

$$+ a_\lambda i_{\lambda b}(s) + \frac{\sigma_\lambda}{4\pi}\int_{\omega_i} i'_\lambda(s, \omega_i)\Phi(\lambda, \omega_i, \omega)d\omega_i \qquad (5)$$

Equation (5) now allows easy identification of the effective extinction coefficient, $K_{\lambda,\text{eff}}$, resulting from absorption effects, scattering effects, and porous structure blockage (i.e., direct transmittance) effects. $K_{\lambda,\text{eff}}$ is found to be a function of absorption and scattering coefficients, and direct transmittance coefficients in Eq. (1), through the relation:

$$K_{\lambda,\text{eff}} = (\alpha_\lambda + \sigma_\lambda)(1 - T_o) + T_o\beta \qquad (6)$$

Equation (6) defines how the sources of attenuation in RPCs are distributed in the overall effective extinction coefficient for these materials. The combination of both T_o and β in the second term determines how strong a role porous structure blockage and direct transmittance effects play in the overall extinction process and corresponding extinction coefficient. Of course, smaller values of T_o, for a given value of β, dictate that normal absorption and scattering coefficients will more adequately describe the overall extinction process.

Some special cases are evident by considering Eq. (6). If there are no direct transmittance effects and $T_o = 0$, then $K_{\lambda,\text{eff}}$ reverts back to the normal definition of $K_\lambda = a_\lambda + \sigma_\lambda$. This is one way to analyze reticulated porous ceramics as a normal, homogeneous material. This effectively lumps all the radiative processes into the normal definition of extinction coefficient. The absorption and scattering coefficients in this type of homogeneous model are then effective coefficients, accounting for both ceramic structure and pore effects in the RPC.

One additional interesting situation occurs when $\beta = 0$ and $T_o > 0$. This combination describes the extinction process in a material that possesses a uniform structure in depth such that there is no additional structural blockage after the initial blockage at the surface. The value of T_o describes the initial structural blockage at the surface. This initial blockage and the fraction of intensity involved with the blockage would not change with depth.

The modified Radiative Transfer Equation (RTE) applicable for porous ceramics is then developed by replacing K_λ with $K_{\lambda,\text{eff}}$ in the basic RTE equation, since $K_{\lambda,\text{eff}}$ applies to each direction of interest:

$$\ddot{\omega} \cdot \nabla i'_\lambda(\kappa_\lambda) + K_{\lambda,\text{eff}} i'_\lambda(\kappa_\lambda)$$

$$= a_\lambda i_{\lambda b}(\kappa_\lambda) + \frac{\sigma_\lambda}{4\pi}\int_{4\pi} i'_\lambda(\kappa_\lambda, \omega_i)\Phi(\lambda, \omega, \omega_i)d\omega_i \qquad (7)$$

A collimated incident beam, being a unidirectional intensity, can also be effectively analyzed and modeled as discussed above as it penetrates the porous structure. Equation (6) then also applies as the effective extinction coefficient for attenuation of any incident collimated beam intensity, $I_i(r, z)$. Incident

collimated beam models are then modified by replacing K_λ with $K_{\lambda,\text{eff}}$:

$$I_i(r, z) = I_c(r) \exp[-K_{\lambda,\text{eff}}z] \qquad (8)$$

The actual intensity in the RTE can then be expressed as a sum of the scattered intensity and the incident collimated intensity appropriately attenuated with depth (Jendoubi et al., 1993; Modest, 1993; Kim and Lee, 1989):

$$i'_\lambda(r, z)$$

$$= i'_{\lambda,sc}(r, z) + [I_{\lambda,c}(r) \exp(-K_{\lambda,\text{eff}}z)]\delta(\omega_c - \omega). \qquad (9)$$

Equation (9) is then substituted into Eq. (7) to yield:

$$[\ddot{\omega} \cdot \nabla + K_{\lambda,\text{eff}}][i'_{\lambda,sc}(\kappa_\lambda) + [I_{\lambda,c} \exp(-K_{\lambda,\text{eff}}z)]\delta(\omega_c - \omega)]$$

$$= a_\lambda i_{\lambda b}(\kappa_\lambda) + \frac{\sigma_\lambda}{4\pi}\int_{4\pi} [i'_{\lambda,sc}(\kappa_\lambda, \omega_i) +$$

$$[I_{\lambda,c} \exp(-K_{\lambda,\text{eff}}z)]\delta(\omega_c - \omega_i)]\Phi(\lambda, \omega, \omega_i)d\omega_i \qquad (10)$$

Equation (10) can now be manipulated and modified for any user-specific application and serves as the starting point for developing any discrete ordinates methodology. This work focused on collimated radiative beams incident on cylindrical samples so cylindrical coordinates were used. Manipulating Eq. (10) for reticulated porous ceramics in cylindrical coordinates with circumferential symmetry creates one form of the modified RTE for discrete ordinates formulation:

$$\left[\mu\frac{\partial}{\partial r} - \frac{\eta}{r}\frac{\partial}{\partial\phi} + \xi\frac{\partial}{\partial z} + K_{\lambda,\text{eff}}\right]i'_{\lambda,sc}(\kappa_\lambda)$$

$$+ \mu\frac{\partial}{\partial r}[I_{\lambda,c}(r) \exp(-K_{\lambda,\text{eff}}z)]\delta(\omega_c - \omega)$$

$$= S(r, z, \omega) \qquad (11)$$

with:

$$S(r, z, \omega)$$

$$= a_\lambda i_{\lambda b}(\kappa_\lambda) + \frac{\sigma_\lambda}{4\pi}\left[I_{\lambda,c}(r) \exp(-K_{\lambda,\text{eff}}z)\Phi(\lambda, \omega, \omega_c)\right.$$

$$\left.+ \int_{4\pi} i'_{\lambda,sc}(\kappa_\lambda, \omega_i)\Phi(\lambda, \omega, \omega_i)d\omega_i\right] \qquad (12)$$

The second term on the left-hand side of Eq. (11), involving the derivative with respect to r of the collimated intensity contribution, typically does not show up in a discrete ordinates formulation to solve the RTE. This is because there is usually not a specific discrete ordinates direction associated with the ω_c direction, so the Dirac delta function cancels this term in the discrete ordinates implementation.

Discrete Ordinates Methodology

Equation (11) can now be manipulated as described in Fiveland (1987, 1988) and Jendoubi et al. (1993) to produce the discrete ordinates approximation of the RTE applicable to reticulated porous ceramics. At each control volume for each radiative intensity direction m in discrete ordinates radiative models, Eq. (11) is multiplied by $2\pi rdrdz$ and integrated over a typical cylindrical control volume. The resulting finite control volume form of the RTE is:

$$\mu_m(A_E I_{m,E} - A_W I_{m,W}) + \xi_m(A_N I_{m,N} - A_S I_{m,S})$$

$$+ (A_E - A_W) \frac{\alpha_{m+1/2} I_{m+1/2,p} - \alpha_{m-1/2} I_{m-1/2,p}}{w_m}$$

$$= -K_{\lambda,\text{eff}} V_p I_{m,p} + a_\lambda V_p I_{b,p} + V_p \sigma_\lambda \int_{4\pi} I_{m',p} \Phi(\omega_i, \omega) d\omega_i$$

$$(13)$$

where $I_{m,p}$ is the intensity in the m direction at point p. $I_{m,N}$, $I_{m,S}$, $I_{m,E}$, and $I_{m,W}$ are the radiative intensities at the corresponding north, south, east, and west boundaries of the control volume, respectively. A_N, A_S, A_E, and A_W are corresponding boundary surface areas of the control volume. In the typical discrete ordinate formulation, the integral over solid angles ω_i in Eq. (13) is replaced by a numerical quadrature sum with an appropriate discrete ordinate quadrature weight, $w_{m'}$, assigned to the m' discrete ordinate direction. In order to solve for the set of discrete ordinate intensities explicitly, $I_{m,p}$ is related to I_{mE}, I_{mW}, I_{mN}, and I_{mS} by a spatially weighted interpolation scheme as described in Fiveland (1987, 1988) and Jendoubi et al. (1993); this is typically the "diamond difference" interpolation scheme of Carlson and Lathrop (1968). The resulting expression is explicitly solved for $I_{m,p}$, yielding:

$$I_{m,p} = \frac{\mu_m A I_{mW} + \xi_m B I_{mS} + \Gamma I_{m-1/2,p} + K V_p S_m}{\frac{\mu_m A_E}{\delta_w} + \frac{\xi_m A_N}{\delta_w} + \frac{(A_E - A_W)\alpha_{m+1/2}}{w_m \delta_w} + K_{\text{eff}} V_p} \quad (14)$$

where:

$$A = \frac{(1 - \delta_w)}{\delta_w} A_E + A_W$$

$$B = \frac{(1 - \delta_w)}{\delta_w} A_N + A_S$$

$$\Gamma = \frac{(A_E - A_W)}{w_m} \left[\frac{(1 - \delta_w)}{\delta_w} \alpha_{m+1/2} + \alpha_{m-1/2} \right]$$

$$S_m = (1 - \Omega) I_b(T_p) + \frac{\Omega}{4\pi} [I_{\lambda,c}(r) \exp(-K_{\lambda,\text{eff}} z)]$$

$$\times \Phi(\lambda, \omega_m, \omega_c) + \sum_{m'=1}^{M} I_{m,p} \Phi(m', m) w_{m'}] \quad (15)$$

All quantities in Eqs. (14) and (15) are on a spectral basis.

The role and importance of $K_{\lambda,\text{eff}}$ in the discrete ordinates formulation for RPCs is clearly apparent in Eqs. (11) and (14). It plays the same role as a normal extinction coefficient defining the total attenuation of a given intensity along a path length, and mathematically occupies the same position in the RTE. However, the sources of attenuation in a RPC are explicitly delineated according to Eq. (6) and inherently connected to the porous structure direct transmittance, f_{dt}.

Radiative Modeling Approaches

The definition of $K_{\lambda,\text{eff}}$ suggests two different radiative modeling approaches in reticulated porous ceramics. The first approach would simply set $T_o = 0$ in Eq. (6), ignore the RPC direct transmittance, and consider the RPC as a homogeneous lump of material. Absorption and scattering coefficients in this approach would then be considered effective coefficients implicitly accounting for RPC direct transmittance effects. This homogeneous (HM) modeling approach was used in the inverse radiative analysis work of Hendricks (1993) and Hendricks and Howell (1994, 1996) to recover absorption and scattering coefficients and phase function behavior from experimental reflectance and transmittance data on small test samples. Hendricks and Howell (1994, 1996) present the inverse analysis

methodology and results and give the uncertainties in the recovered coefficients of: (a) ±18 percent in absorption coefficients and ±20 percent in scattering coefficients for PS ZrO₂ RPCs, (b) ±11 percent in absorption coefficients and ±7 percent in scattering coefficients for OB SiC RPCs.

The second approach is to use the T_o and β values in Tables 1 and 2, and account explicitly for the RPC direct transmittance effects in the radiative attenuation process. Direct transmittance effects are separated explicitly from the absorption and scattering coefficients in this approach. Absorption and scattering coefficients then represent coefficients more directly associated with the RPC materials and internal structure, since the effect of the medium within a pore (i.e., room temperature air) was generally negligible in this investigation.

The direct transmittance (DT) modeling approach was investigated and compared with the homogeneous (HM) modeling approach in the inverse radiative analysis work of Hendricks (1993) in retrieving absorption and scattering coefficients and phase function behavior from experimental reflectance and transmittance data. Tables 3 and 4, for example, show a comparison of absorption and scattering coefficients retrieved using both approaches in 10 ppi PS ZrO₂ and OB SiC porous ceramics. This work discovered a consistent relationship at all wavelengths between absorption and scattering coefficients derived from the two modeling approaches. By inspection of Eq. (14), if K_{eff} in direct transmittance modeling and K in homogeneous modeling are equal, and furthermore if the two modeling approaches have the same $(K\Omega)$ product, then both modeling approaches will calculate the exact same intensity. Therefore, the absorption and scattering coefficient relationship resulted from satisfying the following radiative property conditions between the two models:

$$(a_\lambda' + \sigma_\lambda')(1 - T_o) + T_o \beta = a_\lambda + \sigma_\lambda$$

$$(a_\lambda' + \sigma_\lambda')\Omega_\lambda' = (a_\lambda + \sigma_\lambda)\Omega_\lambda \Rightarrow \sigma_\lambda' = \sigma_\lambda \quad (16)$$

where the primed variables are those in the direct transmittance modeling, and unprimed variables are the corresponding quantities in the homogeneous modeling. The equality between the scattering coefficients produced a relationship between absorption coefficients in the two modeling approaches:

$$a_\lambda' = \frac{a_\lambda + T_o(\sigma_\lambda - \beta)}{(1 - T_o)} \quad (17)$$

The reader is referred to Hendricks (1993) and Hendricks and Howell (1996) for the actual radiative properties $(a_\lambda, \sigma_\lambda)$ determined using the homogeneous modeling approach. Equation (17) exhibits consistency between the modeling approaches such that as $T_o \rightarrow 0$ and direct transmittance effects are either ignored or do not exist, then $a_\lambda' \rightarrow a_\lambda$ and the modeling reverts back to the homogeneous description. It should also be noted that generally Ω_λ' and Ω_λ in Eq. (16) are not equal.

These coefficient relationships were determined to hold invariably at all wavelengths for both PS ZrO₂ and OB SiC (See Tables 3 and 4 as examples) when both radiative modeling approaches produced equivalent results in predicting experimental reflectances and transmittances. Absorption coefficients in direct transmittance (DT) modeling were therefore larger than those from homogeneous (HM) modeling, and had an absorption-enhancing contribution from scattering effects represented by the second term in the numerator of Eq. (17). One reason for this is that direct transmittance absorption coefficients, unlike homogeneous absorption coefficients, did not include the effect of physically nonexistent absorption in the void volumes inside the porous ceramic structure. In addition, the second term in the numerator of Eq. (17) shows explicitly the otherwise hidden importance of scattering processes in augmenting the absorption mechanism within a RPC. Scattering processes in the RPC provide multiple additional opportunities

Table 3 Absorption and scattering coefficients for homogeneous (HM) modeling and direct transmittance (DT) modeling in PS ZrO$_2$ (T_o = 0.4629, β = 239.7)

Wavelength (μm)	a_λ HM [m^{-1}]	a_λ' DT [m^{-1}]	σ_λ HM [m^{-1}]	σ_λ' DT [m^{-1}]	a_λ' * (Eq.17) [m^{-1}]
0.4	60.9	266.	408.	403.	256.
0.6	13.5	401.	681.	677.	404.
0.8	5.9	392.	689.	682.	395.
1.2	1.1	384.	685.	690.	388.
1.6	1.6	361.	660.	658.	364.
2.0	8.0	343.	623.	617.	343.
2.4	23.9	308.	551.	546.	311.
2.8	68.4	331.	480.	474.	332.
3.2	93.1	416.	523.	518.	415.
3.6	80.9	356.	483.	477.	358.
4.0	70.5	327.	471.	465.	328.
4.5	68.5	323.	463.	467.	322.
5.0	68.8	322.	464.	464.	321.

* Note: Calculated Values of a_λ' Use Average Value of σ_λ' and σ_λ

Table 4 Absorption and scattering coefficients for homogeneous (HM) modeling and direct transmittance (DT) modeling in OB SiC (T_o = 0.8686, β = 239.3)

Wavelength (μm)	a_λ HM [m^{-1}]	a_λ' DT [m^{-1}]	σ_λ HM [m^{-1}]	σ_λ' DT [m^{-1}]	a_λ' * (Eq.17) [m^{-1}]
0.4	66.9	2087.	479.	478.	2090.
0.6	59.8	2087.	482.	487.	2076.
0.8	68.6	2096.	473.	478.	2083.
1.2	72.9	2120.	472.	476.	2106.
1.6	77.1	2117.	467.	471.	2105.
2.0	79.3	2143.	467.	472.	2125.
2.4	85.1	2180.	477.	471.	2199.
2.8	95.7	2502.	508.	508.	2505.
3.2	94.0	2520.	509.	508.	2495.
3.6	98.9	2512.	512.	505.	2532.
4.0	102.	2564.	512.	510.	2572.
4.5	105.	2584.	510.	509.	2585.
4.9	97.8	2581.	524.	517.	2603.

* Note: Calculated Values of a_λ' Use Average Value of σ_λ' and σ_λ

for more radiative absorption and effectively shorten the mean free path before absorption.

One important utility of direct transmittance modeling was actually during the inverse analysis process. Inversion results for both homogeneous modeling and direct transmittance modeling could be directly compared to determine how closely Eqs. (16) and (17) were satisfied. In a sense, Eqs. (16) and (17) were additional conditions to establish how well the inverse analysis did in recovering absorption and scattering coefficients which produced acceptable predicted results for the experimental reflectances and transmittances. If the comparison was unsatisfactory, additional inverse analyses adjusted and refined the coefficient combinations to produce more consistent results and better predictions for the experimental data.

It was anticipated beforehand that using the direct transmittance approach would alter phase function behavior, in addition to producing different radiative coefficients, in the inverse analysis modeling work of Hendricks (1993). Because this approach at least partially accounted for direct transmittance effects in the effective extinction coefficient, $K_{\lambda,\text{eff}}$, it was thought initially the phase function should adjust accordingly. Results of the inverse analysis, however, did not support this viewpoint. Instead, it was found consistently, at all wavelengths and for both 10 ppi PS ZrO$_2$ and 10 ppi OB SiC, that optimum inverse analysis solutions had phase functions that remained the same between direct transmittance modeling and homogeneous modeling. This occurred because $K_{\lambda,\text{eff}}$ really represented a method of allocating, or distributing, the different sources of radiative attenuation on a given intensity in a specific direction, and did not necessarily dictate how radiation is directionally scattered throughout the hemisphere via the phase function.

One caution that must be recognized is that thin samples (e.g., 0.6 cm) of 10 ppi materials (in Figs. 1 and 2) do tend to stretch the continuum assumption implicit in the RTE because there are so few pores contained in the short distance. 10 ppi reticulated porous ceramics therefore must be considered as a limiting case for direct transmittance modeling using 0.6 cm

thick samples, and one might consider alternative modeling (e.g., homogeneous modeling) for 5 ppi materials or other materials with larger effective pore diameters. However, as evidenced by properties in Tables 3 and 4 and those presented in Hendricks and Howell (1996), consistent results were obtained with 10 ppi materials relative to smaller pore diameter materials (i.e., 20 ppi and 65 ppi materials), which better satisfy the RTE continuum assumption. Therefore, as with other physical mechanisms and processes, the basic assumptions can be extended somewhat to achieve workable solutions and insights to previously vague and little understood problems.

Conclusions

This work has shown the direct transmittance fraction, f_{dt}, is a measurable and quantifiable attribute in RPCs. It follows predictable exponential attenuation and is characterized by direct transmittance coefficients, which represent additional radiative properties for a particular RPC. Direct transmittance effects modify the definition of the normal extinction coefficient in RPCs, resulting in an effective extinction coefficient, $K_{\lambda,\text{eff}}$. $K_{\lambda,\text{eff}}$ explicitly redefines how the different sources of attenuation are distributed in the extinction process within RPCs. By redefining the extinction process, the new $K_{\lambda,\text{eff}}$ ultimately modifies the basic Radiative Transfer Equation. This creates an innovative discrete ordinates formulation for solving the RTE unique to RPCs.

The relationship for $K_{\lambda,\text{eff}}$ suggests that two radiative modeling approaches are possible with RPCs. One approach is homogeneous (HM) modeling in which RPC direct transmittance effects are ignored ($T_o = 0$) and the RPC treated as a homogeneous lump of material. The second approach, direct transmittance (DT) modeling, explicitly accounts for direct transmittance effects in $K_{\lambda,\text{eff}}$. These two modeling approaches give equivalent results for reflectance and transmittance predictions as long as specific relationships between absorption and scattering coefficients in the two approaches are satisfied. A major

benefit of direct transmittance modeling is that it explicitly demonstrates the important role scattering processes tacitly play in enhancing absorption mechanisms within RPCs. It uncovers the fact that scattering processes within RPCs provide multiple additional opportunities for more absorption and effectively shorten the mean free path for absorption. Another important utility of direct transmittance modeling is that when DT inverse analysis results are compared with HM inverse analysis results, additional conditions are created on the inversion results that can be used to further refine coefficient combinations to produce better predicted results for the experimental data.

Acknowledgments

References

Carlson, B. G., and Lathrop, K. D., 1968, "Transport Theory—The Method of Discrete Ordinates," *Computing Methods in Reactor Physics*, H. Greenspan, C. N. Kelber, and D. Okrent, eds., Gordon & Breach, New York.

Fiveland, W. A., 1987, "Discrete Ordinate Methods for Radiative Heat Transfer in Isotropically and Anisotropically Scattering Media," ASME JOURNAL OF HEAT TRANSFER, Vol. 109, pp. 809–812.

Fiveland, W. A., 1988, "Three-Dimensional Radiative Heat-Transfer Solutions By Discrete-Ordinates Method," *Journal of Thermophysics*, Vol. 2, No. 4, pp. 309–316.

Hendricks, T. J., 1993, "Thermal Radiative Properties and Modelling of Reticulated Porous Ceramics," Ph.D. Dissertation, Mechanical Engineering Department, University of Texas at Austin.

Hendricks, T. J., and Howell, J. R., 1994, "Inverse Radiative Analysis to Determine Spectral Radiative Properties Using Discrete Ordinates Techniques," *Proc. 10th International Heat Transfer Conference*, Vol. 2, Paper #1-RC-14, pp. 75–80, Brighton, United Kingdom.

Hendricks, T. J., and Howell, J. R., 1996, "Absorption/Scattering Coefficients and Scattering Phase Functions in Reticulated Porous Ceramics," ASME JOURNAL OF HEAT TRANSFER, Vol. 118, pp. 79–87.

Howell, J. R., Hall, M. J., and Ellzey, J., 1995, "Combustion in Highly Porous Media," *Proc. 1995 Energy Sources Technology Conference*, Houston, TX.

Jendoubi, S., Lee, H. S., and Kim, T. K., 1993, "Discrete Ordinates Solutions for Radiatively Participating Media in a Cylindrical Enclosure," *Journal of Thermophysics and Heat Transfer*, Vol. 7, No. 2, pp. 213–219.

Kim, T. K., and Lee, H. S., 1989, "Radiative Transfer in Two-Dimensional Anisotropic Scattering Media With Collimated Incidence," *Journal of Quantitative Spectroscopy and Radiative Transfer*, Vol. 42, pp. 225–238.

Modest, M. F., 1993, *Radiative Heat Transfer*, McGraw-Hill, New York, Chap. 16.

Siegel, R., and Howell, J. R., 1992, *Thermal Radiative Heat Transfer*, 3rd ed., Hemisphere Publishing, Washington, D.C.

Skocypec, R. D., Hogan, R. E., Jr., and Muir, J. F., 1991, "Solar Reforming of Methane in a Direct Absorption Catalytic Reactor on a Parabolic Dish: II—Modeling and Analysis," *Proc. 1991 ASME–JSME 2nd International Solar Energy Conf.*, T. R. Mancini et al., eds., pp. 303–310, ASME Solar Energy Div., New York.

The Absorptance of Infrared Radiation by Methane at Elevated Temperatures

S. P. Fuss

O. A. Ezekoye

M. J. Hall

Center for Energy Studies,
Department of Mechanical Engineering,
The University of Texas at Austin,
Austin, TX 78712

In large-scale fires and flames, radiative transport can be an important factor determining the rate of fuel volatilization and flame spread in condensed fuels, and in general can affect the amount of soot that is produced by the flame. The radiant flux can be significantly attenuated by core hydrocarbon gases that have absorption features in the infrared. The spectral absorptance of the v_3 (centered at approximately 3020 cm^{-1}) and v_4 (centered at approximately 1306 cm^{-1}) fundamental bands of methane were measured at elevated temperatures. The measurements were made using a FTIR spectrometer coupled to a gas cell that was maintained at a constant temperature in a furnace. The partial pressure of the methane was varied between 5 and 95 percent, yielding pressure path lengths between 1.14 and 21.72 atm-cm. The total pressure was maintained at 1 atm. Measurements were made at temperatures between 296 and 900 K. The effect of spectral resolution on the measurements and derived parameters was examined. Spectral resolutions between 4 and 32 cm^{-1} were used. The spectral mean parameters of line strength and line shape were determined for the Elsasser narrow band radiation model using the data taken at a resolution of 4 cm^{-1}. The band model parameters were incorporated into RADCAL, a narrow band model used to predict spectral intensity and transmittance. The results are compared with lower resolution predictions and experimental spectral transmittance data. Tabulated narrow band parameters are available on the Internet (WWW) at URL http://www.me.utexas.edu/~combust/students/paul/research.

Introduction

In large-scale fires, heat feedback from the flame to the fuel surface is dominated by radiation and is therefore the primary mechanism determining fuel burning rates. Heat feedback to the fuel surface volatilizes the condensed fuel, which in turn forms a cool, hydrocarbon-rich core between the flame and the fuel surface. As these core gases react, heat is released, and the self-sustaining cycle of the fire continues. The core gases are an important part of the heat transfer process controlling the fire spread rate in that they absorb radiant energy from the flame. Therefore, if accurate predictions of flame spread rates are to be made, the radiative properties of these gases must be known over a wide range of thermodynamic conditions. Before exploring the radiative properties of more complex hydrocarbons formed in condensed fuel combustion, it is worthwhile to characterize more common hydrocarbon species.

Methane is a common hydrocarbon species found in combustion environments, and is the focus of this work. It has three primary regions of absorption in the infrared: the v_3 fundamental centered at approximately 3020 cm^{-1}, the v_4 fundamental centered at 1306 cm^{-1}, and the $v_1 + v_4$ combination centered at approximately 4220 cm^{-1}. As the temperature increases, the v_3 and v_4 fundamentals become the most significant absorption regions (Lee and Happel, 1964), while several other weak bands begin to appear.

Methane is found in combustion environments, and is also important in atmospheric studies and its spectral nature has therefore received a considerable amount of attention. Varanasi (1971) investigated the line structure of the v_3 band under moderately high resolution (0.1-0.5 cm^{-1}) to identify individual line

shapes and positions at room temperature, under self-broadening conditions, in addition to broadening by He, H_2, N_2, O_2, and air. Those results revealed that collision-broadened lines in the v_3 fundamental can be accurately represented by a Lorentz profile. Finkman et al. (1967) calculated the integrated band intensity of the v_3 fundamental using low-resolution spectral transmittance data and the Goody statistical narrow band model. Ko and Varanasi (1977) used moderately high resolution (0.2 cm^{-1}) spectral transmittance measurements to study individual line characteristics within the v_4 fundamental. They measured the (apparent) absorption coefficient of individual multiplets and summed them across the band to obtain the integrated intensity. Lee and Happel (1964) presented correlations for total band absorption in several important IR bands as functions of temperature and pressure path-length based on low-resolution spectral absorptance measurements. Brosmer and Tien (1985) applied the Elsasser narrow band model to their low-resolution spectral absorptance measurements and presented narrow band correlations for the v_3 and v_4 fundamentals. Brosmer and Tien (1987) studied horizontal PMMA (plastic) pool fires by dividing the fire into two zones: a hot reaction zone and a cool fuel-rich core. In their analysis of the fuel core, which assumes a uniform temperature of 900 K and gray gas properties, they estimated that this region is responsible for attenuating 25–35 percent of the incident radiant flux.

Grosshandler (1977, 1979, 1993) presented a narrow band model (RADCAL) that predicts the spectral intensity and transmittance along a nonhomogeneous line of sight, based on both modeled and tabulated spectral absorption data for several gases commonly found in combustion environments. Previously, the parameters for methane that were used in RADCAL were based on spectral absorptance measurements taken at a resolution of approximately 150 cm^{-1}.

In the present study, measurements of the v_3 and v_4 fundamental bands were made using higher resolution data than were previously specified in RADCAL. The effect of instrument reso-

lution and gas temperature on the measured and correlated spectral parameters of the v_3 and v_4 fundamental bands was investigated for a wide range of pressure path lengths. The higher resolution data are correlated in terms of the Elsasser narrow band model based on the analysis of Brosmer and Tien (1985), and incorporated into RADCAL. The use of the present data in RADCAL is validated through comparison with experimental spectral transmittance data. Comparisons are made, over a wide range of conditions, between predictions of spectral transmittance based on higher and lower resolution data.

The measurements taken in this study are not at as high a resolution as measurements by Varanasi (1971) and Ko and Varanasi (1977). However, measurements at 4 cm^{-1} are at sufficient resolution to identify individual lines in the P and R branches of the v_3 fundamental. In addition, the use of 4 cm^{-1} resolution measurements for the correlation of narrow band parameters in RADCAL shows an improvement over the measurements that were used previously. In some respect, the narrow band parameters specified in this study are not rigorously narrow band parameters. As it will be shown, the spectral resolution is finer than the line spacing for the bands, and the correlations are effectively line resolved. Even for these line resolved measurements, the Elsasser correlation is shown to provide a very good correlation. When coupled with the RADCAL program, these measurements provide a means of predicting the line-by-line properties of a gaseous combustion mixture over a range of pressures and temperatures. This represents a novel tool for both heat transfer radiative transfer calculations and combustion diagnostics development.

Experimental Apparatus and Measurements

In the present study, the spectral absorptance of methane was measured at various temperatures and pressure path lengths using a Nicolet model 550 FTIR spectrometer coupled to an external gas cell that was enclosed in a furnace. Figure 1 shows the experimental setup. The gas cell was constructed of stainless steel tubing. BaF$_2$ windows placed on each end defined a fixed optical pathlength of 22.9 cm. Portions of the optical path were purged to minimize the presence of H$_2$O and CO$_2$. The absorption by these gases was small enough to be effectively normalized out of the CH$_4$ measurements. The methane was diluted with nitrogen so that different concentrations could be examined while the total pressure was maintained at approximately 1 atm. The gases were mixed inside a manifold and flowed through the cell at a constant rate; the relative concentration of each gas was maintained by a series of rotameters located in the manifold upstream of the cell. Two rotameters were used to control the methane stream so that the partial pressure could be varied between 0.05 and 0.95 atm, providing a range of pressure path lengths between 1.14 and 21.72 atm-cm. The temperature of the gas mixture was monitored with thermocouples that were placed in inlet and outlet streams of the cell. The two thermocouples were used to ensure that a uniform temperature profile was maintained along the length of the cell. Measurements were made at temperatures of 296, 600, and 900 K and spectral resolutions of 4 cm^{-1} and 32 cm^{-1}.

Uncertainties in the experimental parameters were considered, and the results of a sequential perturbation uncertainty analysis are presented in the Results and Discussions section to clarify the effects of the experimental uncertainties on the narrow band parameters. The temperature variation in the channel
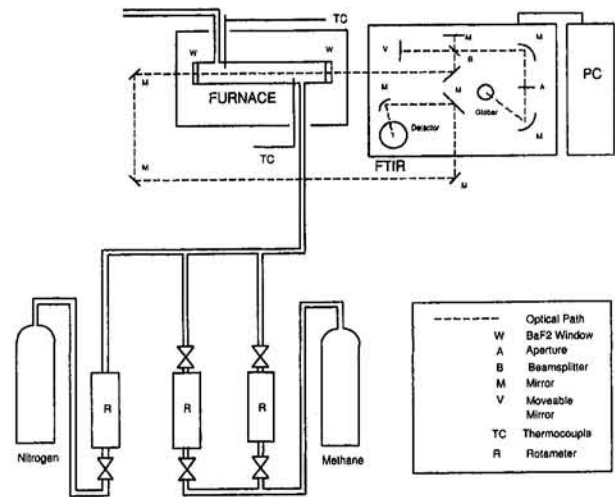

Fig. 1 Experimental configuration

was minimized through the use of a radiation shield and by controlling the total gas flow rate. All temperature inhomogeneities within the channel were kept below the experimental uncertainty associated with the thermocouple measurements (± 2 percent). C.P. grade methane, which specifies a purity of 99.1 percent, and prepurified grade nitrogen, which specifies a purity of 99.998 percent, were used.

Experimental Analysis

Figure 2 shows the effect of instrument resolution on spectral absorptance. The figure compares the spectral absorptance of the v_3 band measured at 4 and 32 cm^{-1} resolution at a temperature of 296 K. Absorptance is defined as: $a_\omega = 1 - I/I_o$. The absorption of the ith band, A_i, defined as the area under each curve can be used as a measure of the net energy absorbed by the gas. The difference in resolution between 4 cm^{-1} and 32 cm^{-1} does not affect this value. If one is interested only in calculating total gas parameters, then the low-resolution measurements are adequate, and may be preferable from a computational standpoint. The band absorption for the v_3 and v_4 fundamentals at a resolution of 4 cm^{-1} and pressure path length of 8.0 atm-cm is given over a range in temperatures in Table 1. These data are in good agreement with the results of Lee and Happel (1964) who used lower resolution measurements than those in the present study. In combustion situations, more than one participating species is typically present, and detailed spectral data are necessary to account for the regions where absorption bands from different gases overlap. For this reason, data collected at higher resolutions are desirable for the narrow band model correlations.

Narrow band radiation models correlate spectral data in terms of two band average parameters: the line strength (S_ω/δ_ω) and line shape ($\gamma_\omega/\delta_\omega$), where S_ω is defined as the line intensity, γ_ω is the line half-width and δ_ω is the line spacing. Previous researchers (Lee and Happel, 1964; Brosmer and Tien, 1985) have determined that the v_3 and v_4 fundamentals are best correlated by the Elsasser model, which assumes a uniform spacing, intensity, and width of individual rotational lines within each

---

Nomenclature

$a_\omega = 1 - T_\omega$ absorptance
$T_\omega = I/I_0 = $ transmittance

$X = P_m L = $ pressure path length, atm-cm
$\alpha(T) = \int_\omega S_\omega/\delta_\omega d\omega = $ integrated intensity

$S_\omega/\delta_\omega = $ line strength parameter, atm^{-1} cm^{-1}
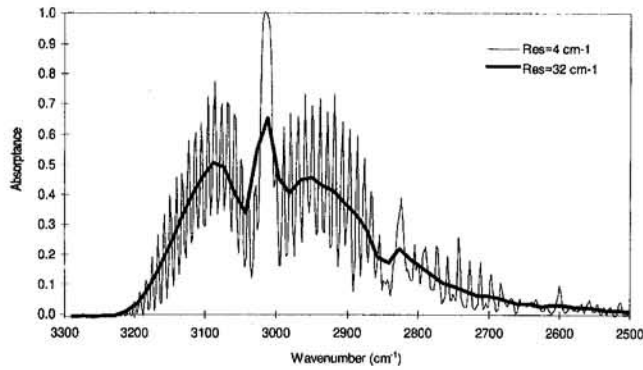$\gamma_\omega/\delta_\omega = $ line shape parameter

---

Fig. 2 Spectral absorptance at $T = 296$ K, $P_{TOT} = 1$ atm; Path length = 22.9 cm, methane partial pressure = 0.25 atm

vibrational absorption band (Elsasser, 1938). In addition to the v_3 band, centered at approximately 3020 cm^{-1}, Fig. 2 shows two weak bands that overlap the P-branch. Examining the higher resolution data, with the exception of the somewhat varying line intensity, the spectral characteristics of the v_3 band are well approximated by the assumptions of the Elsasser model, and it was found to adequately correlate the present results.

Brosmer and Tien (1985) have shown that for the Elsasser model, the line strength parameter can be expressed as:

$$S_\omega/\delta_\omega = \frac{(\mathrm{erf}^{-1} a_\omega)^2}{2\pi X (\gamma_\omega/\delta_\omega)}$$

$$\times \left\{ 1 + \left[1 + \left(\frac{\gamma_\omega}{\delta_\omega}\right)^2 \frac{16\pi}{(\mathrm{erf}^{-1} a_\omega)^2} \right]^{1/2} \right\} \quad (1)$$

where a_ω is the experimentally determined spectral absorptance and X is the pressure path length.

The integrated band intensity, α (atm^{-1} cm^{-2}), is defined as the spectral integral of the line strength parameter:

$$\alpha(T) = \int_\omega S_\omega/\delta_\omega d\omega \quad (2)$$

The integrated intensity must be known before the band parameters can be derived. Once it is known, the line shape parameter is determined iteratively through Eqs. (1) and (2). One method of determining the band intensity (Finkman et al., 1967) is to integrate the measured spectral absorption coefficient:

$$\alpha(T) = \lim_{X \to 0} \int_\omega \frac{-\ln (T_\omega)}{X} d\omega \quad (3)$$

in the limit as the pressure path length, X, approaches zero, where the spectral transmittance, $T_\omega = I/I_o$, is the fraction of transmitted radiation at each wavenumber. One of the goals of this investigation was to provide a set of narrow band parameters compatible with the formulation of RADCAL. In doing so, the basic methodology of Brosmer and Tien was followed. Thus, while the dependence of the integrated band intensity on temperature was available from the present experimental measurements, the requirement of compatibility with the previous work in RADCAL required the assumption that the integrated band absorption varies inversely with the temperature:

$$\alpha(T) = \alpha_0 T_0/T \quad (4)$$

The integrated intensity has been experimentally measured at room temperature in previous studies (Finkman et al., 1967; Ko and Varanasi, 1977), and is in fact independent of any band model. In this analysis, the integrated intensity of the v_3 and v_4 fundamentals were assumed to be 290 atm^{-1} cm^{-2} and 145 atm^{-1} cm^{-2} at STP, again based on their use in the development of RADCAL.

The line shape parameter was assumed to be of the form:

$$\frac{\gamma}{\delta} = \left(\frac{\gamma}{\delta}\right)_0 \left(\frac{P_{e_0}}{P_e}\right)^a \left(\frac{T}{T_0}\right)^b \quad (5)$$

where $P_e = P_T + (B - 1)P_m$ is the effective pressure, P_T is the total pressure, and P_m refers to the partial pressure of methane. The parameter B is the self-broadening coefficient for which a value of 1.3 was used in this study based on the results of Brosmer and Tien (1985) and Burch et al. (1962). The subscript 0 denotes the reference state at which $T_0 = 296$ K. The line shape parameter for each band was determined to be:

$$\gamma/\delta = 0.0256(1.075/P_e)^{1.9}(T/296)^{1.48} \quad v_3 \text{ fundamental} \quad (6)$$

$$\gamma/\delta = 0.0363(1.135/P_e)^{1.7}(T/296)^{1.08} \quad v_4 \text{ fundamental} \quad (7)$$

The constants a and b were evaluated by specifying a best-fit curve, which satisfied both the experimental absorptance data and the integrated intensity values.

Results and Discussion

It was shown in Fig. 2 how instrument resolution can affect the measured spectral absorptance. In addition to affecting measured parameters, the resolution of the data plays a significant role in the narrow band model parameters. Figure 3 shows the line strength parameter calculated from data taken at a resolution of 4 cm^{-1} and compares it with the same parameter as it is currently used in RADCAL, which was calculated from data taken at a resolution of approximately 150 cm^{-1}. This figure demonstrates the ability of the Elsasser model to represent the v_3 fundamental. The manner with which the line strength parameters coincide over a wide range of pressure path lengths is an indication of its applicability. This result was to be expected; by examining Eq. (1) the pressure path length is normalized out of the expression for (S_ω/δ_ω). As was the case with the band absorption A_i, spectral resolution does not affect the integrated band intensity. Spectral resolution differences lie in the spectral variation of the line strength parameter. The highly resolved spectral features become especially significant in non-homogeneous environments where considerable overlapping between bands of different gases can occur.

In the limiting weak line approximation, the line strength parameter is equivalent to the spectral absorption coefficient (Tien, 1968) and is therefore a significant radiative heat transfer parameter in specifying the burning rates of many condensed fuels (DeRis, 1979). The advantage of representing the spectral data in terms of the narrow band model is that data collected at any temperature and concentration can be correlated in terms of two parameters. By normalizing the line strength parameter by the pressure path length, (S_ω/δ_ω) becomes solely a function of temperature. Therefore, only one set of spectral data is required for each temperature once the correlations are known. However, one disadvantage is that each correlation is valid at a single resolution. This follows from the fact that the narrow band parameters are a function of spectral data, which will vary with resolution.

The narrow band parameters derived in this study are available through the Internet at the URL http://www.me.utexas

Table 1 Comparison between current band absorption data and the results of Lee and Happel (1964)

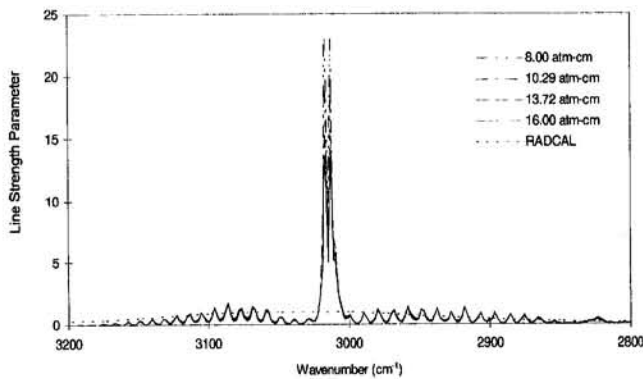| Temperature (K)	Band Absorption A (cm⁻¹) v_3 fundamental		Band Absorption A (cm⁻¹) v_4 fundamental	
	Present Study X = 8.0 atm · cm	Lee and Happel X = 7.72 atm · cm	Present Study X = 8.0 atm · cm	Lee and Happel X = 7.72 atm · cm
296	177.3	193.2	115.7	124.0
569		192.3		139.5
600	205.6		139.8	
668		214.0		146.0
873		242.3		151.7
900	254.0		156.3	
974	265.0			

Fig. 3 Comparison of the spectral line strength parameter at $T = 296$ K, $P_{TOT} = 1$ atm; path length = 22.9 cm

Fig. 5 Measured and predicted spectral transmittance of the v_3 CH$_4$ fundamental at 900 K, $P_{TOT} = 1$ atm, methane partial pressure = 0.25 atm, path length = 22.9 cm

.edu/~combust/students/paul/research. Using a sequential perturbation method where uncertainties in the experimental input parameters (i.e., P_T, P_m, L, T, a_ω, B) are identified, the resulting uncertainties in the line strength parameter were evaluated. A representative case where the nominal values are $T = 296$ K, $P_T = 1$ atm, $P_m = 0.35$ atm, $L = 22.9$ cm yields a line strength parameter with uncertainties as high as 40 percent in the Q branch and values ranging between 6–8 percent in the P and R branches. The major contributor to this uncertainty is the uncertainty in the spectral absorptance, a_ω, which was approximately 1 percent of the measurement value. This value is based on fluctuations in the background that occurred over the time that the measurements were taken. Interestingly, this relatively small uncertainty produces a relatively larger uncertainty in the line strength parameter values in the Q branch primarily as a result of the error function dependence of a_ω in Eq. (1). Due to the asymptotic nature of the error function, this term is extremely sensitive to small perturbations in the absorptance as its value approaches unity.

Applications

An immediate application for the narrow-band model parameters derived in this study is the incorporation of these parameters into RADCAL, replacing those that are based on data taken at a much lower resolution. To verify the validity of the results obtained using these parameters, a comparison was made with experimental spectral transmittance data taken at two temperatures. Figures 4 and 5 compare the experimentally measured spectral transmittance of the v_3 fundamental with the spectral transmittance calculated in RADCAL from both higher and lower resolution data, at temperatures of 296 K and 900 K. The solid line, representing predictions based on high-resolution parameters, nearly coincides with the experimental data, which
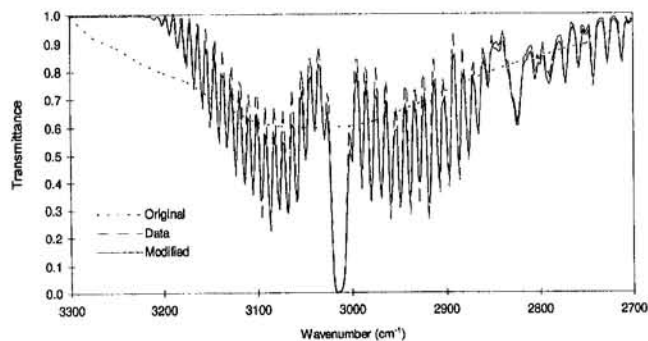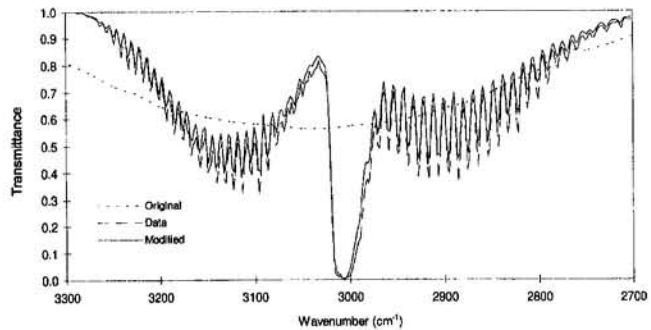
is denoted by the long dashed line. These figures show that the narrow band parameters specified in RADCAL are capable of correlating the line structure in the v_3 fundamental. As a cautionary note, it is unclear how extrapolating beyond the range of experimental conditions will affect the accuracy of the predictions. Within the range of experimental conditions, however, the narrow band parameters perform well. Figures 4 and 5 also show that the use of narrow band model parameters derived from low-resolution data, represented by short dashed lines, does not allow the prediction of the irregular spectral features of the v_3 fundamental, in particular the central Q-branch. In contrast to the v_3 results, it is shown in Figs. 6 and 7 that due to the spectral nature of the v_4 fundamental, the use of lower resolution data does not cause significant discrepancies between measured and predicted spectral transmittance values throughout this band. Unlike the v_3 fundamental, the individual lines within the v_4 CH$_4$ fundamental are broadened to the extent that no fine structure is apparent at a resolution of 4 cm^{-1}. This is consistent with the values of the line shape parameter calculated for each methane band in Eqs. (6) and (7); the line width to spacing ratio is higher in the v_4 fundamental. A comparison of Fig. 7 with Fig. 5 indicates that the temperature dependence of the narrow band parameters in the v_4 band is less accurate than that for the v_3 band. While there was little degradation in the transmittance predictions (when compared with the experimental results) for the v_3 band at 900 K as compared to 300 K, there was significantly more error in the v_4 band. Even with the differences between RADCAL results and experimental data at 900 K, it is evident from examination of Fig. 7 that the newly derived band parameters still more closely match the experimental results than the lower resolution RADCAL results.

By incorporating higher resolution data into the model for the v_3 and v_4 CH$_4$ fundamentals, it was necessary to reduce the data spacing for every gas absorption band in the range 1100–

Fig. 4 Measured and predicted spectral transmittance of the v_3 CH$_4$ fundamental at 296 K, $P_{TOT} = 1$ atm, methane partial pressure = 0.25 atm, path length = 22.9 cm
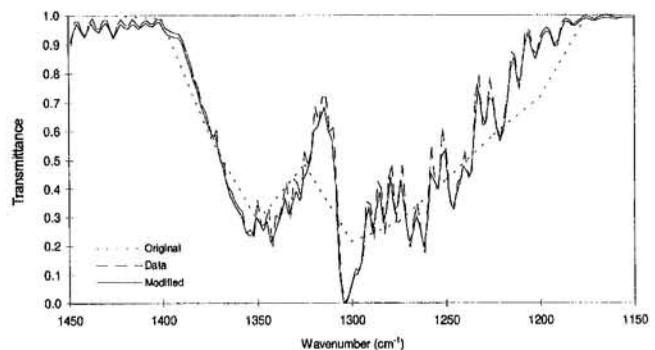

Fig. 6 Measured and predicted spectral transmittance of the v_4 CH$_4$ fundamental at 296 K, $P_{TOT} = 1$ atm, methane partial pressure = 0.25 atm, path length = 22.9 cm
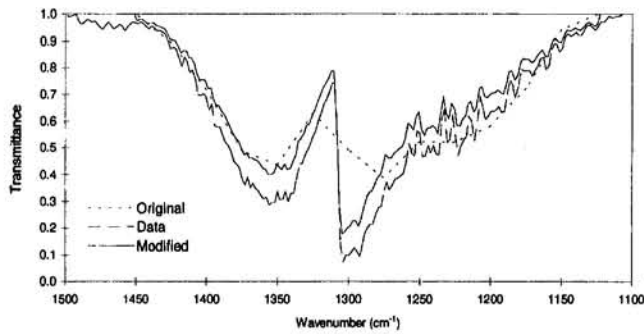
Fig. 7 Measured and predicted spectral transmittance of the v_4 CH$_4$ fundamental at 900 K, P_{TOT} = 1 atm, methane partial pressure = 0.25 atm, path length = 22.9 cm

Fig. 9 Spectral transmittance through a mixture of 0.8 atm N$_2$/0.1 atm CH$_4$/0.1 atm H$_2$O, at a temperature of 900 K along a path length of 22.9 cm

5000 cm^{-1}. Therefore, in addition to investigating the effect of the increased spectral resolution of the methane bands in this range, the effect of varying the data spacing will be examined in the other bands as well.

In addition to enhancing the spectral features of the v_3 fundamental in a pure CH$_4$/N$_2$ mixture, the use of higher resolution parameters has a significant effect on the prediction of spectral transmittance in conditions where more than one absorbing gas is present. N$_2$, like all homonuclear diatomic molecules, does not have a dipole moment and therefore does not absorb infrared radiation. The presence of N$_2$ has the effect of broadening the absorption lines of the other gases present in the mixture. Figure 8 shows the predicted spectral transmittance along a 22.9 cm path length through a mixture of 0.8 atm N$_2$/0.1 atm CH$_4$/0.1 atm H$_2$O, at a temperature of 500 K. In this case overlap occurs between the v_4 CH$_4$ (at 1306 cm^{-1}) and 1587 cm^{-1} H$_2$O bands, and between the v_3 CH$_4$ (at 3020 cm^{-1}) and 3700 cm^{-1} H$_2$O bands. From this figure, it can be concluded that the change in resolution does not affect the predicted overlap between the 1306 cm^{-1} CH$_4$ band and the 1587 cm^{-1} H$_2$O band. This result can be attributed in part to the agreement, shown in Fig. 6, between the predicted spectral transmittance in the v_4 fundamental of methane. In addition, there is no change in the predicted spectral transmittance in the H$_2$O band at 1587 cm^{-1}. This is to be expected, as the features of the 3700 cm^{-1} and 1587 cm^{-1} H$_2$O bands are calculated within RADCAL from tabulated values of the spectral line strength parameter. Therefore, changing the data spacing has no effect on the predicted spectral transmittance. In the region where the 3700 cm^{-1} H$_2$O band overlaps the v_3 CH$_4$ fundamental, there is a significant difference between the predictions of the high and low-resolution data. The model, using low-resolution data, cannot predict the highly varying line intensity in the v_3 CH$_4$ fundamental. Because the band intensity, A_i, must be the same for both high and low-
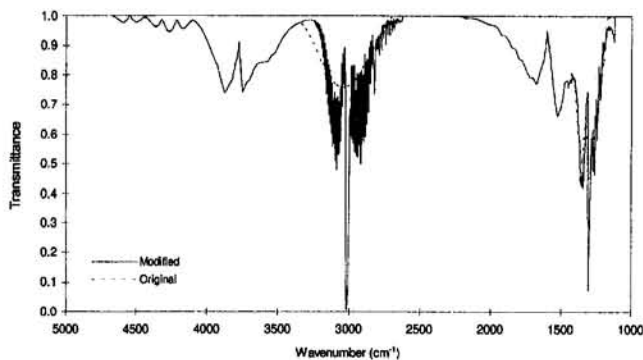
resolution measurements, the low-resolution measurements result in a wider bandwidth near the base. This results in an underprediction of the spectral transmittance in the area of overlap.

It can be inferred from Eqs. (2), (3), (6), and (7) that increasing temperature has the effect of reducing the intensity, and increasing the width, of the individual lines within the v_3 and v_4 CH$_4$ fundamentals. This is seen in Fig. 9, which plots the predicted spectral transmittance of the same mixture of gases as seen in Fig. 8, raised to a temperature of 900 K. The bands tend to become wider, and the combined spectral transmittance in both overlap regions decreases.

Once again, there is good agreement in the predicted region of overlap between the v_4 CH$_4$ fundamental and the 1587 cm^{-1} H$_2$O band. However, the discrepancy between the high and low-resolution predictions of spectral transmittance in the v_3 CH$_4$ fundamental, and in the overlap of its R branch with the 3700 cm^{-1} H$_2$O band, increases with temperature.

In addition to H$_2$O, several other gases have absorption bands in the IR that lie near the v_3 and v_4 CH$_4$ fundamentals, CO$_2$ being one of them. Figure 10 shows the predicted spectral transmittance along a 22.9 cm pathlength through a gaseous mixture of 0.8 atm N$_2$/0.1 atm CH$_4$/0.1 atm CO$_2$ at a temperature of 800 K. Under these conditions there is no significant overlap between CH$_4$ and CO$_2$ bands in the wavenumber range of interest. However, as seen in the case with water present, increasing the temperature of the gases can cause the absorption bands to become broader, which will lead to increased overlapping between bands. It is noteworthy that the predicted transmittance of the 5000 cm^{-1}, 3700 cm^{-1}, and 2350 cm^{-1} CO$_2$ bands is based on spectral models, as opposed to tabulated values of the line strength parameter. The increased number of data points throughout this range, however, has little effect on the predicted

Fig. 8 Spectral transmittance through a mixture of 0.8 atm N$_2$/0.1 atm CH$_4$/0.1 atm H$_2$O, at a temperature of 500 K along a path length of 22.9 cm

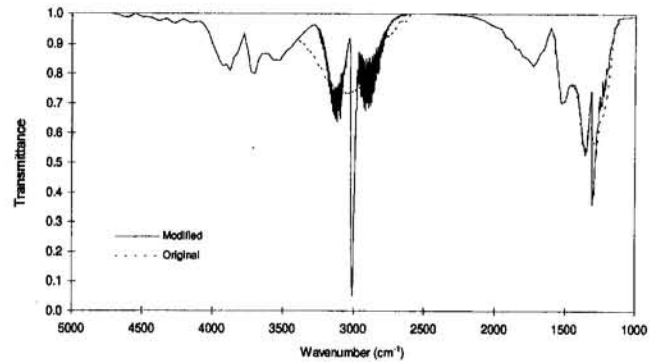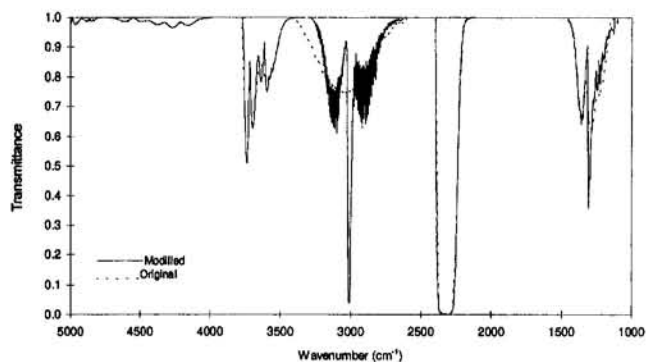Fig. 10 Spectral transmittance through a mixture of 0.8 atm N$_2$/0.1 atm CH$_4$/0.1 atm CO$_2$ at a temperature of 800 K along a path length of 22.9 cm

spectral transmittance. This can be seen through close examination of Fig. 10, where there is only a small deviation between the high and low-resolution predictions in the CO_2 bands. This change is of little significance when compared with the discrepancies between the predictions in the v_3 and v_4 CH_4 fundamentals. Measurements of the spectral transmittance of the 2350 cm^{-1} CO_2 band at a resolution of 0.125 cm^{-1} show that this band has distinct rotational lines similar to the v_3 CH_4 band. Decreasing the data spacing in RADCAL to values as low as 0.01 cm^{-1} did not show evidence of this line structure.

Concluding Remarks

This investigation has demonstrated the benefits of using data collected at higher resolution in situations where the spectral features of methane are important. While total band parameters, such as absorption A_i and intensity α, are not affected by the resolution of the data, the measurements of spectral parameters are significantly affected by instrument resolution. Figures 2 and 3 show that the spectral absorptance and line strength parameter at a resolution of 4 cm^{-1} can change by a factor of 2–5 over a spectral range of only 5 cm^{-1} while the variations at lower resolutions are much smaller. This is important when the effects of band overlap between multiple gases must be accounted for. Due to the high temperatures found in combustion environments, the thermal dependence and range of applicability of spectral gas parameters are important factors. It has been shown here that the application of the Elsasser model to the infrared spectra of methane is valid for temperatures that are typical of the fuel-rich core region above the fuel surface in large pool fires. The validity of the data is demonstrated by the agreement shown with previous studies for both the integrated band intensity and band absorption. Further, while the Elsasser model has been derived for application over several spectral lines, it was shown in this study that it may be applied to data taken at a resolution below the true line spacing. It has also been shown that the use of higher resolution narrow band model parameters within RADCAL can more accurately reproduce experimental spectral transmittance measurements over a wider range of conditions than previous lower resolution results.

References

Brosmer, M. A., and Tien, C. L., 1985, "Infrared Radiation Properties of Methane at Elevated Temperatures," *J. Quant. Spectrosc. Radiat. Tech.*, Vol. 33, pp. 521–532.

Brosmer, M. A., and Tien, C. L., 1987, "Radiative Energy Blockage in Large Pool Fires," *Combust. Sci. Tech.*, Vol. 51, pp. 21–37.

Burch, D. E., Singleton, E. B., and Williams, D., 1962, "Absorption Line Broadening in the Infrared," *Applied Optics*, Vol. 1, pp. 359–363.

De Ris, J., 1979, "Fire Radiation—A Review," *Seventeenth Symposium (International) on Combustion*, The Combustion Institute, pp. 1003–1015.

Elsasser, W. M., 1938, "Mean Absorption and Equivalent Absorption Coefficient of a Band Spectrum," *Phys. Rev.*, Vol. 54, pp. 126–129.

Finkman, E., Goldman, A., and Oppenheim, U. P., 1967, "Integrated Intensity of 3.3 μ Band of Methane," *J. Opt. Soc. Am.*, Vol. 57, pp. 1130–1131.

Grosshandler, W. L., 1977, "A Study of a Model Furnace Burning Methanol and a Methanol/Coal Slurry," Ph.D. Dissertation, University of California, Berkeley.

Grosshandler, W. L., 1979, "Radiation in Nonhomogeneous Fires," *FMRC J.I. OAOE6 BU-4, RC 79-BT-9*, Factory Mutual Research, Norwood, MA.

Grosshandler, W. L., 1993, "RADCAL: A Narrow Band Model for Radiation Calculations in a Combustion Environment," NIST Technical Note 1402.

Ko, F. K., and Varanasi, P., 1977, "Intensity Measurements in the v_4 Fundamental of Methane," *J. Quant. Spectrosc. Radiat. Tech.*, Vol. 18, pp. 145–150.

Lee, C., and Happel, J., 1964, "Thermal Radiation of Methane Gas," *I & EC Fundamentals*, Vol. 3, pp. 167–176.

Tien, C. L., 1968, "Thermal Radiation Properties of Gases," *Advances in Heat Transfer*, T. F. Irvine and J. P. Hartnett, eds., Academic Press, New York, Vol. 5, pp. 253–324.

Varanasi, P., 1971, "Collision-Broadened Half-Widths and Shapes of Methane Lines," *J. Quant. Spectrosc. Radiat. Tech.*, Vol. 11, pp. 1711–1723.

Saturable Absorption During High-Intensity Laser Heating of Liquids

J. P. Longtin

Assistant Professor,
Department of Mechanical Engineering,
State University of New York
at Stony Brook,
Stony Brook, NY 11794-2300

C.-L. Tien

A. Martin Berlin Professor of
Mechanical Engineering,
Department of Mechanical Engineering,
University of California at Berkeley,
Berkeley, CA 94720
Honorary Mem. ASME

The interaction of high-intensity, short-pulse laser radiation with liquids is fundamental to many contemporary technologies. At low laser intensities, the classical model of absorption and heating applies, which assumes a constant absorption coefficient and no dependence on intensity. As the intensity increases, however, many molecules are promoted to excited states, whose absorption properties differ from those of the ground state, and the absorption of the bulk liquid is altered. This phenomenon, called saturable absorption, results in intensity-dependent absorption, heating, and temperature distributions that can deviate significantly from classical absorption. This work investigates the thermal aspects of saturable absorption during laser heating of liquids. A microscopically based model of the radiation absorption and heating processes is presented. Model solutions are discussed and compared with experiment for a contemporary saturable absorbing liquid. Simple engineering criteria and relevant applications are then discussed.

Introduction

Many important technologies involve the interaction of high-intensity, pulsed laser radiation with liquids. Examples include laser pulse generation and modification (Band and Scharf, 1986; Stuke, 1992), laser-induced desorption of thin liquid films (Allen et al., 1984), laser particle removal (Park et al., 1994), and microstructure repair (Fushinobu et al., 1995). Recent research in thermal aspects of high-intensity, short-pulse laser−material interactions, however, has focused almost exclusively on the solid phase (Qiu and Tien, 1992). In liquids at high intensities, the absorption and heating of the laser pulse can deviate significantly from classical, low-intensity predictions, resulting in a markedly different temperature distribution. Such effects must be quantitatively characterized to assess their impact on technologies that employ high-intensity laser−liquid interactions.

Classical models of absorption and heating assume a constant absorption coefficient, independent of the incident intensity, which results in the familiar exponential decrease of intensity with distance into the liquid, i.e., Beer's Law (Brewster, 1992). At high laser intensities, however, the intense laser pulse can significantly alter the population of molecular states of the liquid molecules from their thermal equilibrium distribution. The absorption then becomes an intensity-dependent function of position and time; this phenomenon is called saturable absorption (Penzkofer, 1988).

Most dielectric liquids are capable of saturable absorption. To do so (1) the liquid must absorb at the wavelength of interest, and (2) the light intensity must be high enough to initiate intensity-dependent absorption. Many organic dyes exhibit saturable absorption, as well as common liquids, e.g., water and alcohols at a wavelength of 2.9 μm (Vodop'yanov et al., 1982).

The thermal aspects of saturable absorption have not been addressed. The purposes of this work are thus to develop a thermal model to predict the temperature in liquids during saturable absorption, and to provide simple, quantitative criteria to determine when such effects are important. Heating associated with saturable absorption is herein termed *saturable heating*. The model is used to characterize saturable heating as a function of pulse intensity, duration, wavelength, and liquid properties. Temperature profiles are presented for a common dye used for its saturable absorption properties, and compared to experimental results. It is shown that during saturable heating the temperature distribution becomes much more uniform, with a lower peak value and longer thermal penetration depth than the classical heating model predicts.

Saturable Absorption and Heating

In liquids the nature of the radiation interaction is determined primarily by the structure of the individual molecule. At room temperature, most molecules are in the lowest electronic state; thus nearly all the thermal energy associated with a liquid is present in rotational, vibrational, and translational systems. When a molecule absorbs a photon at optical frequencies (near-IR, visible, UV), the outermost electron is excited into a new orbit, raising the energy of the molecule (Duarte and Hillman, 1990). The diagram in Fig. 1 illustrates the possible electronic transitions a molecule can undergo upon absorbing a photon from a monochromatic laser pulse. Different electronic states are denoted by thick horizontal lines, and are labeled S_0, S_1, S_2, T_1, T_2, etc. More energetic states appear higher on the figure. The states S_0, S_1, S_2, etc., are called *singlet* states, and T_1, T_2, etc. are called *triplet* states (Duarte and Hillman, 1990). State S_0, called the ground state, has the lowest possible energy, and is the electronic state occupied by nearly all the liquid molecules at room temperature. Within each electronic state is a series of unique vibrational states denoted by thin horizontal lines in the figure. The thick horizontal gray arrows represent absorption and emission of photons, solid vertical arrows represent radiative transitions, i.e., a photon is absorbed or emitted, and dashed vertical arrows represent radiationless transitions, which transfer energy from the electronic system to the vibrational, rotational, and translational systems. Radiationless transitions are responsible for heating of the molecule.

The absorption of a photon by the molecule raises it from the ground state S_0 to a combined excited electronic and vibrational state. Within a few femtoseconds, the molecule relaxes nonradiatively to the ground vibrational state in S_1. There are five possible options for the molecule at this point: (1) It can absorb a second photon and be promoted to the S_2 state; (2) it

Fig. 1 Electronic transitions during laser–liquid interactions

Legend:
- ⟶ (thick) Photon absorption/emission
- ⟶ Radiative transition involving a photon
- ⤏ (dashed) Radiationless transition

Increasing Energy

S_2, S_1, S_0, T_2, T_1

Rate Equations. To model the interaction of a laser pulse with the liquid, the so-called *rate equations* are used to account for the number of molecules in different electronic states as a result of excitation by the incident laser pulse and subsequent relaxation back to the ground state. The rate equations are (Duarte and Hillman, 1990):

$$\frac{\partial N_0}{\partial t} = (\sigma_s N_1 - \sigma_g N_0)\frac{I}{h\nu} + (k_f + k_n)N_1 + k_t' N_t \quad (1)$$

$$\frac{\partial N_1}{\partial t} = -(\sigma_s N_1 - \sigma_g N_0)\frac{I}{h\nu} - (k_f + k_n + k_i)N_1 \quad (2)$$

$$\frac{\partial N_t}{\partial t} = k_i N_1 - k_t' N_t, \quad (3)$$

with the conservation equation

$$C_o = N_0 + N_1 + N_t, \quad (4)$$

and the equation for a monochromatic light pulse propagating through the liquid,

$$\frac{1}{c}\frac{\partial I}{\partial t} + \frac{\partial I}{\partial x} = (\sigma_s N_1 - \sigma_g N_0 - \sigma_e N_1 - \sigma_t N_t)I. \quad (5)$$

Here $\{N_0, N_1, N_t\}$ and $\{\sigma_g, \sigma_e, \sigma_t\}$ represent the number of molecules per unit volume (molecules/cm^3) and the effective absorption cross sections (cm^2/molecule) in the S_0, S_1, and T_1 states, respectively. The term σ_s is the cross section for stimulated emission, and the k_j are transition rates (s^{-1}). The reciprocal of k is the transition lifetime $\tau_j = k_j^{-1}$ (k_i and k_t' are transition rates into and out of the triplet state, respectively). The total concentration of absorbing molecules per unit volume is C_o (cm^{-3}), and is constant.

The intensity I in Eqs. (1) and (2) is divided by $h\nu$ to convert the energy flux (W/cm^2) into a photon flux (photons/cm^2). Note that both the pulse intensity and population numbers depend on time and position, i.e., $I = I(x, t)$, $N_j = N_j(x, t)$. The absorption cross sections are a strong function of incident wavelength: $\sigma = \sigma(\lambda)$.

The left-hand side of Eq. (5) represents the hyperbolic propagation of the laser pulse of arbitrary shape and duration through the medium at speed $c = c_0/n$. The first term on the right-hand side of Eq. (5) accounts for stimulated emission into the beam; it adds to the intensity, and hence is positive. The second, third, and fourth terms account for photon absorption by ground, excited singlet, and excited triplet states, respectively. The small

can relax nonradiatively back to the ground state S_0; it can emit a photon of slightly lower frequency either (3) incoherently, called fluorescence, or (4) coherently, called stimulated emission; and (5) it can relax nonradiatively to the ground triplet state, T_1, and then relax from T_1 to S_0. A characteristic rate is associated with each of these transitions, often with one rate dominating.

In practice, excitations to electronic states higher than S_1 or T_1, e.g., S_2 or T_2, result in a very fast ($\sim 10^{-15} - 10^{-13}$ s) nonradiative relaxation back to S_1 and T_1, respectively, hence the number of molecules in these states is usually negligible. Also, transitions to triplet states are unfavorable; however, once in the T_1 state, it takes a long time ($\sim 10^{-8} - 10^{-7}$ s) for the molecule to relax back to S_0.

The absorption properties of a molecule in an excited state often differ considerably from those of the ground state. As the laser intensity increases, a larger fraction of molecules will be promoted to excited states, and the absorption properties of the liquid as a whole will change. If the excited states have a smaller absorption coefficient than the ground state, the liquid becomes more transparent at higher intensities; this is called *saturable absorption*. If the excited state has a larger absorption coefficient, the process is called *reverse saturable absorption* (Band and Scharf, 1986).

Nomenclature

c = speed of light in liquid, cm/s
C_o = number density of absorbing molecules, cm^{-3}
C_p = specific heat, J/g·K
E = energy flux, J/cm^2; energy between transitions, J
f = laser pulse repetition frequency, s^{-1}
h = Planck's constant, J·s
I = laser intensity, W/cm^2
I_s = saturation intensity, W/cm^2
k = transition rate, s^{-1}
l = thermal diffusion distance, cm
n = index of refraction
N = state number density, cm^{-3}
Q = volumetric energy deposition, J/cm^3
q = volumetric heating rate, W/cm^3

R = liquid surface reflectivity
S = singlet state
T = triplet state, temperature, K
ΔT = temperature rise, K
t = time, s
Δt = time step in finite-difference solution, s
x = distance into liquid from surface, cm
Δx = gridpoint spacing in finite-difference solution, cm
α = thermal diffusivity, cm^2/s
δ = classical radiation skin depth, cm
λ = wavelength, nm
ν = radiation frequency, Hz
ρ = density, g/cm^3
σ = effective cross section for absorption, cm^2

τ = excited state lifetime, s; pulse duration, s

Subscripts

e = excited state, stimulated emission
f = fluorescing
g = ground state
i = incident, intersystem crossing
j = dummy index
l = low-level
n = nonradiative
o = free space
p = incident laser pulse, peak
r = repetition rate
s = stimulated emission, stokes shift
t = triplet

contribution to the total intensity from fluorescence, which is isotropic, into the beam has been neglected.

For a Gaussian laser pulse, with full-width-at-half-maximum (FWHM) pulse duration τ_p, incident on the liquid surface $x = 0$ with surface reflection R, the intensity boundary condition becomes

$$I(x = 0, t) = (1 - R)I_p \exp(-4 \ln 2 \, (t/\tau_p)^2), \quad (6)$$

where I_p is the peak intensity of the laser pulse in free space. Since nearly all molecules are in the electronic ground state at room temperature, the initial conditions on the population numbers are $N_0 = C_o$, $N_1 = N_t = 0$.

Simplifications. Transitions both to and from triplet states occur slowly compared to transitions within the singlet states, leading to long triplet state lifetimes. Typical triplet lifetimes, $\tau_t = 1/k_t$, can be on the order of $10^{-8} - 10^{-7}$ s (Duarte and Hillman, 1990). For short, single laser pulse irradiation with a pulse duration much shorter than the triplet decay time, i.e., $\tau_p/\tau_t \ll 1$, the triplet state population can be neglected. For longer pulse durations or CW operation, the triplet states must be considered. Also, if the liquid is exposed to repetitive pulses of sufficient frequency, accumulated triplet populations can become significant, even if the pulse duration is much shorter than the triplet relaxation time. In addition to τ_p/τ_t, then, the time between successive pulses $\tau_r = 1/f$ must be much greater than the triplet state lifetime to neglect triplet formation, i.e., $\tau_r/\tau_t \gg 1$, where f is the repetition rate of the laser pulse train.

Neglecting triplet formation and stimulated emission, the *saturation intensity* is the intensity that makes the first and second terms in Eq. (1) of comparable magnitude:

$$I_s = h\nu(k_f + k_n)/\sigma_g = h\nu/\tau\sigma_g, \quad (7)$$

where the total relaxation time $\tau = (k_f + k_n)^{-1}$ is used.

For laser intensities $I_p \ll I_s$, saturable absorption can be neglected and $N_0 \approx C_o$, $N_1 = N_t \approx 0$. In this case, Eqs. (1)–(5) reduce to the classical absorption model, i.e., Beer's law (Brewster, 1992):

$$T = E(x)/E(0) = \exp(-\sigma_g C_o x). \quad (8)$$

Here the transmission T is the fraction of incident energy that reaches x, and $E(x)$ is the time-integrated intensity, or pulse fluence (J/cm^2), at x:

$$E(x) = \int_{-\infty}^{\infty} I(x, t)dt. \quad (9)$$

The classical volumetric thermal energy deposition $Q_l(x)$ (J/cm^3) is then

$$Q_l(x) = -dE/dx = \sigma_g C_o E(0) \exp(-\sigma_g C_o x). \quad (10)$$

Note that the classical radiation penetration depth, δ, in Eq. (8) is equal to $(\sigma_g C_0)^{-1}$.

Heat Generation. The rate equations, Eqs. (1)–(5), are combined with a microscopic heat generation model to determine the thermal response of the liquid to the incident laser pulse. Expressions for heat generation from molecular transitions have been proposed in the past, primarily for diagnostics purposes (Tam, 1986); however, saturable absorption effects and their effect on the temperature rise and distribution have not been considered.

The nonradiative transitions in Fig. 1 are responsible for heating in the liquid. A nonradiative transition between electronic states transfers the electronic energy to vibrational, rotational, and translational modes of the molecule, temporarily imparting a very high effective temperature to the molecule that can exceed 1000 K (Seilmeier and Kaiser, 1993). The molecule then quickly thermalizes with neighboring molecules via collisions, with typical cooling times on the order of a few picoseconds.

In this work, the thermalizing process is neglected; when a molecule undergoes a nonradiative transition, the molecule is assumed to thermalize immediately, transferring its excess energy to surrounding molecules.

Radiative transitions, i.e., fluorescence and stimulated emission, can also contribute to molecular heating due to *Stokes shifting*. Stokes shifting refers to the increase, or shift, in the wavelength of emitted photons during radiative relaxations. Immediately after absorbing or emitting a photon, the liquid molecule undergoes a small nonradiative relaxation among vibrational states (the small dashed arrows in Fig. 1). These small relaxations result in heating and must be accounted for. The emitted photon has a longer wavelength, and hence less energy, thus a fraction of the absorbed photon energy is converted to heat. Taking the wavelength of the incident and fluorescence photon emissions as λ_i and λ_f, respectively, the thermal energy E_s transferred to the molecule is $h(\nu_i - \nu_f)$, and the fraction η of the incident pulse energy converted nonradiatively to heat is

$$\eta \equiv \frac{E_s}{E_i} = \frac{h(\nu_i - \nu_f)}{h\nu_i} = 1 - \frac{\nu_f}{\nu_i} = 1 - \frac{\lambda_i}{\lambda_f}. \quad (11)$$

Stokes-shift heating can be significant in highly fluorescing liquids, e.g., laser dyes (Longtin, 1995).

The expression for the position- and time-dependent heating rate, $q(x, t)$, is the sum of all possible heating mechanisms:

$$q(x, t) = \overbrace{\sigma_e N_1 I}^{1} + \overbrace{\sigma_t N_t I}^{2} + \overbrace{\sigma_s N_1 I \eta}^{3} + \overbrace{k_f N_1 \eta h\nu_i}^{4}$$

$$+ \underbrace{k_n N_1 h\nu_i}_{5} + \underbrace{k_i N_1 E(S_1 \to T_1)}_{6} + \underbrace{k_t' N_t E(T_1 \to S_0)}_{7}. \quad (12)$$

The contribution from each term is discussed below (see also Fig. 1):

1. *Singlet Excited-State Absorption.* Molecules in the excited state S_1 can absorb a second photon. Since these transitions are nearly 100 percent nonradiative, all of the absorbed radiant energy, i.e., $\sigma_e N_1 I$, is converted to thermal energy. The product $\sigma_e N_1$ represents to total cross-sectional area of the molecules available to absorb the intensity I.

2. *Triplet Excited-State Absorption.* Molecules in the triplet state T_1 can also absorb a second photon. These transitions are nearly 100 percent nonradiative; thus, the heating is expressed as $\sigma_t N_t I$.

3. *Stimulated Emission from $S_1 \to S_0$.* Stimulated emission, though radiative, still results in a small amount of heating due to the Stokes shift, as discussed above. The quantity $\sigma_s N_1 I$ represents the total absorbed energy by molecules that subsequently undergo stimulated emission, and, when multiplied by η, represents the fraction of this energy converted to thermal energy.

4. *Fluorescence from $S_1 \to S_0$.* Fluorescence is also a radiative transition, and thus contributes the Stokes-shift energy to heating; however, the rate of fluorescence is governed by the relaxation rate rather than the intensity. The number of molecules that relax per second is $k_f N_1$, and the thermal energy gained from each relaxation is $\eta h\nu_i$.

5. *$S_1 \to S_0$ Nonradiative Decay.* This is the normal nonradiative decay route. The number of molecules that relax per second is $k_n N_1$ and the thermal energy gained from each relaxation is $h\nu_i$.

6. *$S_1 \to T_1$ Transitions.* This nonradiative transition imparts an amount of energy $E(S_1 \to T_1)$ to the molecule, where $E(S_1 \to T_1) < h\nu_i$. The value of $E(S_1 \to T_1)$ depends on the particular liquid, and must be determined experimentally. For this transition $k_i N_1$ molecules relax per second.

7 $T_1 \rightarrow S_0$ *Nonradiative Transitions.* Similar to the previous term, energy $E(T_1 \rightarrow S_0)$ is acquired by the molecule nonradiatively when the molecule relaxes back to S_0 from T_1. The number of molecules relaxing per second is $k_i' N_i$. Note from Fig. 1 that $E(S_1 \rightarrow T_1) + E(T_1 \rightarrow S_0) = h\nu_i$.

The total heat deposition after the laser pulse has passed is

$$Q(x) = \int_{-\infty}^{\infty} q(x, t)dt \qquad (13)$$

Note that the heating process will not necessarily cease when the laser pulse passes; rather, it will continue for a time comparable to the longest relaxation time in the system. The heating time can be several orders of magnitude greater than the duration of the laser pulse, particularly if triplet excitations are significant (Stuke, 1992). This effect must be considered when the time scale of the heating process is important, e.g., nucleation and phase change, fast-time-scale thermal-based diagnostics, and temperature-dependent chemical reactions.

Often only one or two heating mechanisms will dominate, simplifying Eq. (12) considerably. Also, if the time scale of interest is longer than the triplet relaxation times, terms 6 and 7 can be replaced by $k_i N_1 h\nu_i$, because all triplet transitions will eventually return to the ground state, increasing the thermal energy of the molecule by $h\nu_i$.

Lasers having intensities high enough to effect saturation typically have pulse durations of nanoseconds or less. Also, the heating process is completed quickly, typically in less than 10^{-6} s, which is much faster than the time scales for conduction and convection. To illustrate this point, consider the thermal diffusion distance l:

$$l = (\alpha t)^{1/2}, \qquad (14)$$

where α is the thermal diffusivity (cm^2/s). For the dichloroethane solvent used in this study, and a heating time of 10^{-6} s, $l \sim 0.7$ μm. This distance is much smaller than the radius of the laser beam, even if focused, thus radial conduction can be neglected. Also, unless the liquid has an extremely strong absorption coefficient, e.g., $\delta = (\sigma_g C_0)^{-1} \sim l^{-1} \approx 14{,}000$ cm^{-1}, axial conduction can be neglected as well. The temperature rise at a location x just after the pulse has passed and the liquid molecules have relaxed, i.e., $t \sim O(1 \mu s)$ is

$$\Delta T(x) \cong Q(x)/\rho C_p, \qquad (15)$$

where ΔT is the temperature rise (K), ρ the density (g/cm^3) and C_p the specific heat (J/g·K). Note that Eq. (15) is valid only for the *initial* temperature rise, i.e., several microseconds after the laser pulse arrives. At longer times conduction and convection will occur.

Results and Discussion

The model developed in the preceding sections is valid for a wide range of liquids. To demonstrate the effects of saturable heating, the model is used to compute the temperature rise in a common liquid organic dye solution. The temperature profiles generated in the liquid can deviate significantly from those predicted by the classical model. The model results are compared with experimental data, and the engineering significance and applications capable of exhibiting saturable heating are then discussed.

Saturable Heating Results. The liquid used for the model calculations is a commercial saturable absorber called *Q-Switch I*, also known as Eastman #9740. This dye was specifically chosen because of its excellent properties as a saturable absorbing medium. Accordingly, the dye has a small fluorescence transition rate, $k_f / k_n < 10^{-3}$; hence the dominant relaxation mechanism is non-radiative. Due to a slow pulse repetition rate of 10 Hz, transitions to and from triplet states can be neglected,

as *all* relaxations, triplet and otherwise, will occur orders of magnitude faster than the pulse repetition rate. Also, as an effective saturable absorber, stimulated emission and excited state absorption are insignificant, i.e., σ_s and σ_e are small. The dye has a relaxation time of 11 ps, and a saturation intensity of 2.8 $\times$ 10^7 W/cm^2.

The dye is dissolved in 1,2-dichloroethane (DCE) as a solvent, at a concentration of 2.2 $\times$ 10^{16} cm^{-3} (3.6 $\times$ 10^{-5} M). This concentration was chosen to ensure that the dye solution absorbed strongly at low intensities to illustrate the saturable heating effect. From Eq. (8) and Table 1 the transmission through 1 cm of the liquid is only about 1.5 $\times$ 10^{-6} at $\lambda =$ 1064 nm, i.e., $\delta = 13.4$ cm^{-1}. Table 1 lists the relevant model parameters.

Equations (1)–(3) and (5) constitute a set of linear, first-order, differential equations, and are solved numerically for the time- and space-dependent pulse intensity $I(x, t)$ and population numbers $N(x, t)$. Due to the hyperbolic nature of the pulse propagation equation in Eq. (5), a finite-difference Fromm scheme that is second-order accurate, $O(\Delta x^2)$, in space and first-order accurate, $O(\Delta t)$, in time is used. The laser pulse crosses the liquid surface at $x = 0$. Gridpoints are separated spatially by a distance Δx and temporally by a time Δt. A predictor step advances the solution from t to $t + \Delta t/2$, followed by a corrector step from $t + \Delta t/2$ to $t + \Delta t$. The temperature increase in the liquid is obtained from Eq. (15), using Eq. (10) for the classical temperature rise, and Eqs. (12) and (13) for the temperature rise during saturable heating.

At intensities well below the saturation intensity, the results from both the classical and microscopic models are essentially identical. In Fig. 2 the temperature as a function of distance into the liquid is shown. The laser pulse is incident from the left. For an incident intensity $I_p = 0.1 I_s = 2.8 \times 10^6$ W/cm^2, the difference between the two models is insignificant, i.e., the microscopic model reduces to the classical model, as expected. The temperature in the classical model, Eqs. (10) and (15), has an exponential dependence, hence on a log scale it appears as a straight line.

Also shown in Fig. 2 are results for the intensity equal to the saturation intensity $I_p = I_s = 2.8 \times 10^7$ W/cm^2. The temperature increase from classical predictions is an order of magnitude higher, due to the tenfold intensity increase. The temperature rise at the front region near $x = 0$ is less than that predicted by the classical model, as a result of saturable heating. When the liquid saturates, less energy is absorbed, and the heating decreases. As the laser pulse is absorbed, however, its intensity eventually decreases below I_s, and classical heating resumes.

Table 1 Model parameters for Q-Switch I

Parameter	Value
λ	1064 nm
τ_p	35 ps
C_o	2.2×10^{16} cm^{-3} (3.6×10^{-5} M)
k_n	9.1×10^{10} s^{-1} [a]
k_f	~9×10^7 s^{-1} [a]
σ_g	6.1×10^{-16} cm^2 (at 1064 nm)[b]
σ_e	~ 0
σ_s	~ 0
L	1.0 cm
T	300 K
Δx	0.01 cm
Δt	2×10^{-14} s
ρ (DCE)	1.246 g/cm^3 [b]
C_p(DCE)	1.148 J/g·K [b]
n (DCE)	1.442 [b]

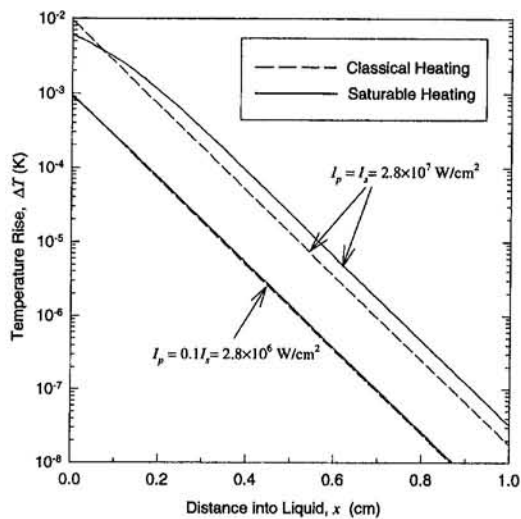[a]Seilmeier et al., 1980; [b]Brackmann, 1994

Fig. 2 Intensity-dependent temperature profiles (Q-Switch I)

This occurs for $x > \sim 0.3$ cm, as evident by the microscopic model results approaching a straight line on the graph.

In Fig. 3 the intensity is $10I_s = 2.8 \times 10^8$ W/cm². For this case, the temperature rise during saturable heating shows several traits. First, the temperature at the front of the liquid is far less than that predicted by the classical model, by nearly an order of magnitude. Likewise, the temperature at the rear of the liquid is much higher than that from the classical model because the laser pulse is not attenuated significantly in passing through the front region of liquid. Around $x \sim 0.8$ cm enough absorption of the pulse has occurred for classical heating to begin to dominate.

Also shown in Fig. 3 are results for an intensity $I_p = 100I_s = 2.8 \times 10^9$ W/cm². The temperature is nearly flat for the entire path of the laser pulse, as the intensity remains high enough to saturate the entire irradiated region of the liquid. The maximum temperature increase from classical heating, which occurs at $x = 0$, exceeds that for saturable heating by a factor of nearly 50. The large difference between the classical and microscopic temperature profiles also has an impact on the nature of the heat conduction in the liquid. The classical heating model results in a large axial temperature gradient in the direction of the beam path, hence significant heat conduction in the axial direction is expected. For the microscopic profile, however, the temperature is much more uniform in the axial direction, 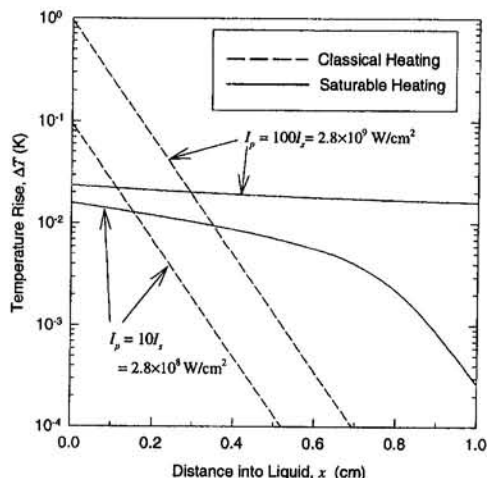and thermal gradient is not nearly as large. In general the temperature predicted from the microscopic model is much more uniform than the classical model when the saturation intensity is exceeded.

Note that an important distinction between pulse energy and pulse intensity exists. The saturable absorption effect depends on the *intensity* of the incident laser pulse; the maximum temperature increase in the liquid depends on the total pulse *energy*. In these results, the temperature rise is relatively small, which is a consequence of the picosecond laser available for the experiment discussed below. For laser pulses of comparable intensity but higher pulse energy, e.g., a nanosecond Nd:YAG, the liquid temperature rise will be 10–100 times larger or more.

The microscopic model for the *Q-Switch I* dye is compared with the temperature rise measured using a noncontact photothermal deflection technique (PTD). A focused Nd:YAG laser at 1064 nm with a pulse duration of 35 ps and ~50 mJ per pulse served as the heating laser, and was passed through a quartz cuvette holding the liquid dye solution. A HeNe probe laser beam was directed into the liquid perpendicular to the Nd:YAG beam about 0.5 mm outside of the heating beam cross section. Liquid in the path of the Nd:YAG beam is heated, generating a radial temperature gradient in the liquid. This temperature gradient, in turn, results in a gradient in the liquid index of refraction, which causes the HeNe probe beam to deflect slightly from its nominal position. The HeNe beam deflection as a function of time is recorded and, through a thermal conduction model, is correlated to the initial, maximum temperature rise in the liquid. Details of the experimental setup and procedure are documented elsewhere (Longtin, 1995; Longtin et al., 1995).

The saturation intensity of the dye was $I_s = 2.8 \times 10^7$ W/cm². The beam intensity after focusing was $I_p \cong 80I_s = 2.2 \times 10^9$ W/cm², which is well in excess of the saturation intensity. The experimental parameters are identical to those listed in Table 1. Measurements were taken at positions of 1, 3, 5, 7, and 9 mm into the liquid. The reported experimental values represent the peak temperature rise in the liquid.

The temperature rise from classical heating, saturable heating, and the experiment is shown on a linear scale in Fig. 4. As can be seen, the disparity between classical and saturable heating is large at the front of the liquid. The experimental measurements are seen to agree in magnitude with the microscopic model, especially near the front. In Fig. 5 a close-up of the microscopic model and experimental data is shown. The error bars on the experimental results reflect the large pulse-to-pulse variation in the laser pulse train. Although the measured values are consistently low, they are of the correct order of magnitude and trend as the microscopic results.
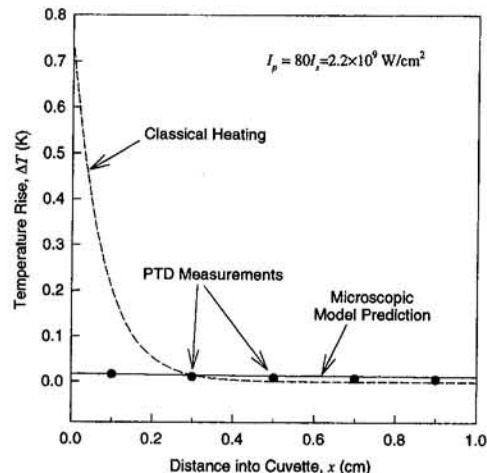

Fig. 3 Intensity-dependent temperature profiles (Q-Switch I)

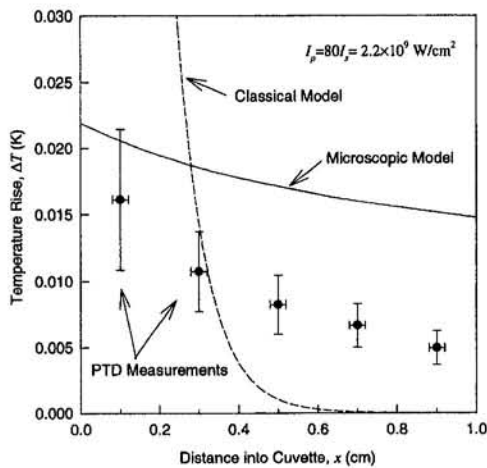Fig. 4 Microscopic model versus experiment (Q-Switch I)

Fig. 5 Microscopic model versus experiment (*Q-Switch I*)

Engineering Impact and Applications. This section discusses the engineering significance of saturable heating, as well as applications where saturable heating can become important. All dielectric liquids are capable of exhibiting saturable heating at the appropriate intensity. The important parameters for determining when saturable absorption will occur are the cross section for absorption, σ_g, at the wavelength of interest, the relaxation time, τ, and the dominant relaxation mechanism(s). All of these parameters can be determined experimentally. Both σ_g and τ, which are intrinsic liquid parameters, uniquely determine the saturation intensity, I_s in Eq. (7), which will then determine whether saturable heating is important at the intensity of interest. The ratio of the classical radiation skin depth, $\delta = (\sigma_g C_o)^{-1}$, to the spatial extent of the liquid, L, is also important. For $\delta/L \gg 1$, most of the laser pulse passes through the liquid, even at low intensities. For $\delta/L \ll 1$, however, most of the pulse is absorbed at low intensities, and significant deviation from classical heating is expected at high intensities (cf. Fig. 3).

For $\delta/L \ll 1$, the important differences between saturable heating and classical heating include (1) a much more uniform temperature profile, (2) a reduced maximum temperature rise, and (3) an increase in the thermal penetration depth. The importance of these parameters is underscored by the fact that they can change by orders of magnitude during saturable heating. A more uniform temperature profile coupled with a longer thermal penetration depth is a potential advantage for situations where a strong axial thermal gradient is undesirable.

Since the temperature rise of the liquid is a function of the pulse *energy,* and the temperature distribution is a function of the pulse *intensity,* the laser parameters can be adjusted to ensure either the presence or absence of saturable heating. The intensity scales as $E_p/A_p\tau_p$, where E_p is the pulse energy (J) and A_p the beam diameter (cm^2). The same energy E_p can be delivered at a higher intensity with a shorter pulse duration, or at a lower intensity with a longer pulse duration. In this way, saturable heating can selectively be used to generate the optimum temperature profile in the liquid; the pulse duration and area can then be adjusted to deliver the necessary energy, E_p, at the required intensity.

One immediate application area of this work is in laser–liquid diagnostics. In liquid-based photothermal techniques (PTD), for example, the laser–liquid heating is usually treated classically (Spear et al., 1990). Since the PTD technique is based on the temperature rise in the liquid, the deviations in temperature by saturable heating can introduce significant errors into the measurement. The thermal model developed herein can be used in the PTD measurement when high laser intensities are involved. In fact, the experimental results in Figs. 4 and 5

represent the disparity that can occur in such PTD measurements if the classical heating model is assumed.

Another area is the use of photochromic dyes. Photochromic dyes change color when exposed to intense laser radiation, and are used for flow visualization and velocity measurements (Durr and Bouas-Laurent, 1990). These dyes absorb strongly, and as such can contribute to significant heating in the liquid. Saturable absorption by the dye will alter the magnitude and distribution of heating, and must be accounted for, particularly if thermal heating by the dye is important.

A potentially broad application area is the laser processing of dielectric solids where a liquid layer melts and remains on top of the solid substrate, e.g., polymers, photoresist, etc. The temperature profile in the film is important as it will influence the liquid–solid interface temperature, cooling through the liquid film, convection, etc. Additionally, if the liquid normally absorbs strongly, the increased transmission at high intensities would allow more of the laser energy to reach the solid substrate for heating.

Laser particle removal (Park et al., 1994) and laser adhesion reduction in microstructures (Fushinobu et al., 1995) both involve laser–liquid interactions. The incident radiation can either interact directly with the liquid, or pass through the liquid to the substrate. Particularly for strong absorption in the liquid, the thermal penetration depth and temperature rise are important. Saturable absorption by the liquid will alter both of these parameters.

Saturable heating may also affect nucleation and vaporization processes. During classical heating of strongly absorbing liquids, the peak temperature rise occurs at the surface and decreases rapidly with distance into the liquid. During saturable heating, however, the more uniform temperature profile may alter the nucleation process, particularly if the thermal energy reaches the solid surface underneath the liquid.

Conclusions

This work investigates thermal aspects of saturable absorption, termed *saturable heating,* during high-intensity laser–liquid interactions. A microscopic model for dielectric liquids is presented that combines the rate equations with a heating model to determine the temperature distribution in the liquid. Model results are presented and compared to experimental data for a commercially available organic dye used for its saturable absorption properties. Several unique aspects of laser–liquid interactions have been quantitatively characterized by the model, including the reduced peak temperature rise in the liquid, highly uniform temperature profiles, and an increased thermal penetration depth. Comparisons with experiments agree in magnitude and trend. Simple criteria are established to determine when saturable heating is important, including intrinsic liquid properties and the heating laser parameters. The significance of saturable heating for engineering applications is discussed.

Acknowledgments

References

Allen, S. D., Porteus, J. O., Faith, W. N., and Franck, J. B., 1984, "Contaminant and Defect Analysis of Optical Surfaces by Infrared Laser Induced Desorption," *Applied Physics Letters,* Vol. 45, pp. 997–999.

Band, Y. B., and Scharf, B., 1986, "Engineering Reverse Saturable Absorbers for Desired Wavelengths," *Chemical Physics Letters,* Vol. 127, pp. 381–386.

Brackmann, U., 1994, *Lambdachrome Laser Dyes,* 2nd ed., Lambda Physik, Göttingen, Germany, pp. 250–251.

Brewster, M. Q., 1992, *Thermal Radiative Transfer and Properties,* Wiley, New York, Chaps. 4 and 7.

Duarte, F. J., and Hillman, L. W., 1990, *Dye Laser Principles*, Academic Press, San Diego.

Durr, H., and Bouas-Laurent, H., 1990, *Photochromism: Molecules and Systems*, Elsevier, New York, pp. 483–509.

Fushinobu, K., Phinney, L. M., and Tien, N. C., 1995, "Ultrashort-Pulse Laser Heating of Silicon to Reduce Microstructure Adhesion," *Int. J. Heat Mass Transfer*, in press.

Longtin, J. P., 1995, "Thermal Aspects of High-Intensity, Short-Pulse Laser-Liquid Interactions," Ph.D. Thesis, University of California at Berkeley, Berkeley, CA.

Longtin, J. P., Tien, C. L., Kilgo, M. M., and Russo, R. E., 1995, "Temperature Measurement During High-Intensity Laser-Liquid Interactions," *Experimental Heat Transfer*, Vol. 8, pp. 241–255.

Park, H. K., Grigoropoulos, C. P., Leung, W. P., and Tam, A. C., 1994, "A Practical Excimer Laser-Based Cleaning Tool for Removal of Surface Contaminants," *IEEE Transactions on Components Packaging and Manufacturing Technology, Part A*, Vol. 17, pp. 631–643.

Penzkofer, A., 1988, "Passive Q-Switching and Mode-Locking for the Generation of Nanosecond to Femtosecond Pulses," *Applied Physics B*, Vol. 46, pp. 43–60.

Qiu, T. Q., and Tien, C. L., 1992, "Short Pulse Laser Heating on Metals," *Int. J. Heat Mass Transfer*, Vol. 35, pp. 719–726.

Seilmeier, A., Kopainsky, B., and Kaiser, W., 1980, "Infrared Fluorescence and Laser Action of Fast Mode-Locking Dyes," *Applied Physics*, Vol. 22, pp. 355–359.

Seilmeier, A., and Kaiser, W., 1993, "Ultrashort Intramolecular and Intermolecular Vibrational Energy Transfer of Polyatomic Molecules in Liquids," *Ultrashort Laser Pulses: Generation and Applications*, 2nd ed., W. Kaiser, ed., Springer-Verlag, Berlin, Chap. 7, pp. 279–317.

Spear, J. D., Russo, R. E., and Silva, R. J., 1990, "Collinear Photothermal Deflection Spectroscopy With Light-Scattering Samples," *Applied Optics*, Vol. 29, pp. 4225–4234.

Stuke, M., 1992, *Dye Lasers: 25 Years*, Springer-Verlag, Berlin.

Tam, A. C., 1986, "Applications of Photoacoustic Sensing Techniques," *Reviews of Modern Physics*, Vol. 58, pp. 381–431.

Vodop'yanov, K. L., Kulevskii, L. A., Pashinin, P. P., and Prokhorov, A. M., 1982, "Water and Ethanol as Bleachable Radiation Absorbers in an Yttrium–Erbium–Aluminum Garnet Laser ($\lambda = 2.94$ μm)," *Soviet Physics, JETP*, Vol. 55, pp. 1049–1051.

Angle of Incidence and Size Effects on Dependent Scattering in Fibrous Media

S.-C. Lee

Vice President,
Applied Sciences Laboratory, Inc.,
Hacienda Heights, CA 91745

The influence of fiber size and angle of incidence on the radiative behavior of fibrous media containing closely spaced, aligned fibers is investigated by utilizing the dependent scattering theory. Numerical analyses are performed to calculate the coherent and incoherent scattering properties of dense fibrous media for several fiber sizes and angles of incidence. Results indicate that as the fiber concentration increases, the radiative properties deviate from their independent scattering values due to dependent scattering interactions. Dependent scattering becomes dominant at a lower volume fraction at normal than at oblique incidence. Increasing the fiber concentration causes the apparent refractive index of the fibrous medium to deviate from unity, thus giving rise to specular reflection due to Fresnel reflection.

Introduction

Radiative transfer through fibrous media has been a subject of considerable interest due to the widespread application of fibrous thermal insulations in many engineering systems over a broad temperature range. High-porosity fibrous media such as building insulation and space shuttle tile materials contain randomly oriented fibers. Refractory liners, filament wound fabric heat shields, and thermal-structural fibrous composites are high-density media, which contain closely spaced, aligned fibers. Radiative energy transfer through fibrous media is strongly influenced by the fiber properties and, in particular, the fiber concentration. As the fiber concentration increases, the average spacing between fibers decreases, thus giving rise to multiple scattering in the near-field and wave interference in the far-field. These dependent scattering effects cause the radiative properties of closely spaced fibers to depart from those of the independently scattering fibers.

The pertinent parameters affecting scattering in a fibrous medium are the fiber spacing, fiber diameter, and wavelength of the incident radiation. A high-porosity fibrous medium is one in which the fiber separation is much greater than the fiber diameter and the incident wavelength, whereas these parameters are comparable to each other in a high-density medium. In a high-porosity medium, each fiber acts as an isolated scatterer. The extinction and scattering coefficients of the medium are simply equal to the sum of the respective cross sections of all the fibers. The radiative transfer equation utilizing the independent scattering radiative properties is applied. In a high-density fibrous medium, both far-field wave interference and near-field multiple scattering occur. The latter arises because the scattered wave from a fiber would not traverse a large enough distance to recover to a plane wave before encountering another fiber. A rigorous solution of Maxwell's equations accounting for these dependent scattering effects is required for the analysis of radiative transfer through a dense fibrous medium.

Earlier analyses on scattering by closely spaced fibers considered only normal incidence on finite configurations of homogeneous fibers (Twersky, 1952a, b; Oloafe, 1970). The general multiple scattering formalisms for oblique incidence on homogeneous and radially stratified fibers were later developed by Lee (1990, 1992a). Radiative analysis of dense fibrous media is usually treated by a statistical approach, which assumes a random distribution of fibers of identical properties. This approach involves the averaging of the multiple-scattering wave equations for a random distribution of fibers. Lax's (1955) quasi-crystalline approximation (QCA) is applied to truncate the hierarchy of multiple scattering terms. This method has been applied to develop the governing equation for the effective propagation constant, which is commonly known as the dispersion relation, of dense fibrous media at normal incidence (Bose and Mal, 1973; Twersky, 1979; Varadan et al., 1978, 1986). The general dispersion relations for oblique incidence on fibrous media containing homogeneous and coated fibers were developed by Lee (1992b, 1993). For dense fibrous media containing a distribution of fiber sizes and different fiber materials, the method as suggested by Lee and Kurtz (1994) can be used. These formulations are applicable to arbitrary fiber size, refractive index, concentration, and wavelength.

The dispersion relations are generally valid for fibers contained in a dielectric medium with nonunity refractive index, because their derivation applies to the interior region of the medium. The wavelength and fiber refractive index in the dispersion relations are implicitly taken as those relative to the refractive index of the medium. Although it is tempting to apply the same parameter shift to the formulas for the scattering amplitudes derived by Lee and Grzesik (1995), this will, however, lead to erroneous results. This is because the refractive index of the medium containing the incident wave is assumed to be identical to that containing the fibers. Interactions due to secondary incident waves arising from Fresnel reflection of the primary incident wave at the interface are therefore absent. Lee (1994) applied the dispersion relations to demarcate the dependent and independent scattering regimes. Chern et al. (1995) utilized Lee's formulations to examine the variation of extinction efficiency with fiber volume fraction at normal incidence for several refractive indices of the fibers and the medium.

The demarcation of scattering regimes by Lee (1994) was based on the consideration of the extinction efficiency at normal incidence. Since infinite fibers behave as two-dimensional scatterers, the effect of oblique angle of incidence must also be examined. The objective of this paper is to investigate the effect of fiber size and angle of incidence on the coherent and incoherent scattering properties of dense fibrous media. In the following sections, the dependent scattering theory is summarized first, followed by the presentation of numerical
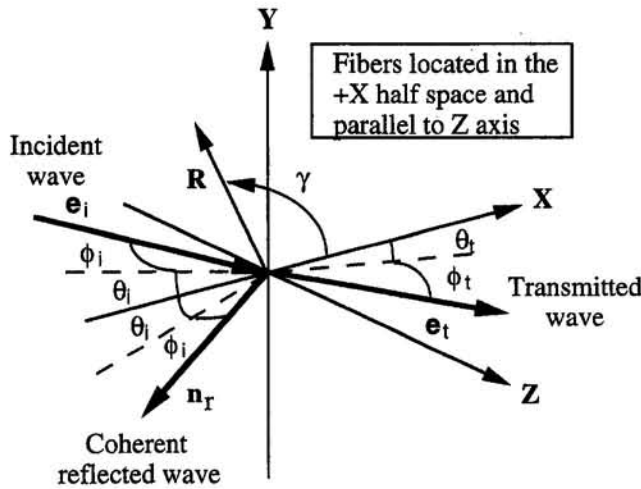
Fig. 1 A schematic diagram depicting scattering by a high-density fibrous medium

results. The significance of these numerical results is then discussed.

Theory

Pertinent aspects of the dependent scattering theory for high-density fibrous media are summarized in this section. Figure 1 depicts a semi-infinite medium containing closely spaced fibers aligned parallel to the Z axis. The medium is irradiated by a plane electromagnetic wave propagating in an arbitrary direction specified by the angles ϕ_i and θ_i. The transverse magnetic (TM) and transverse electric (TE) mode Hertz potentials of the scattered waves including the contributions from all the fibers are given by Lee (1990, 1992a):

$$\{u^{\sigma s}, v^{\sigma s}\} = \exp(-ihz) \sum_{j=1}^{N_o} \sum_{n=-\infty}^{\infty} (-i)^n$$
$$\times \exp(in\gamma_{jp}) H_n(l_o R_{jp}) \{-\tau b_{jn}^\sigma, \tau a_{jn}^\sigma\} \quad (1)$$

respectively, where $\sigma = I$ and $\tau = 1$ for a TM mode incident wave, $\sigma = II$ and $\tau = -1$ for a TE mode incident wave, and the time-dependent term $\exp(i\omega t)$ has been omitted for brevity.

The scattering characteristics of a dense fibrous medium are obtained by first taking the conditional average of the Hertz potentials, then utilizing the effective wave approach and the QCA. This procedure yields the governing equations for the effective propagation constant K^σ and amplitudes X_s^σ and Y_s^σ of the average wave traversing the medium (Lee, 1992b; Lee and Grzesik, 1995):

$$\begin{bmatrix} (\delta_{ns} + {}^o b_n^I F_{sn}) & {}^o b_n^{II} F_{sn} \\ {}^o a_n^I F_{sn} & (\delta_{ns} + {}^o a_n^{II} F_{sn}) \end{bmatrix} \begin{bmatrix} X_n^\sigma \\ Y_n^\sigma \end{bmatrix} = 0 \quad (2)$$

$$\sum_{s=-\infty}^{\infty} \exp(-is\theta_i)\{X_s^\sigma, Y_s^\sigma\} = (i/\beta^\sigma)\{\delta_{\sigma I}, \delta_{\sigma II}\} \quad (3)$$

where ${}^o a_n^\sigma$ and ${}^o b_n^\sigma$ are the independent scattering wave coefficients. The parameters in these equations are:

$$F_{sn} = \frac{2f_v}{r_o^2} \frac{\exp[i(n-s)\theta_t]}{k_o^2 - K^{\sigma 2}} \{[2l_o r_o J_{s-n}(2Lr_o) H'_{s-n}(2l_o r_o)$$
$$- 2Lr_o H_{s-n}(2l_o r_o) J'_{s-n}(2Lr_o)]$$
$$+ (k_o^2 - K^{\sigma 2}) \int_{2r_o}^{\infty} J_{s-n}(LR) H_{s-n}(l_o R)$$
$$\times [g(R) - 1]R dR\} \quad (4)$$

$$\beta^\sigma = \frac{2f_v}{\pi r_o^2} \frac{1}{k_x(K_x^\sigma - k_x)} \quad (5)$$

where the prime denotes differentiation, and $g(R)$ is the two-dimensional statistical radial distribution function. For a non-trivial solution of the amplitudes to exist, the determinant of the coefficients of Eq. (2) must vanish. This yields a transcendental equation containing K^σ, which is commonly known as the dispersion relation. At normal incidence the dispersion relation decomposes into two expressions for the TM and TE modes, respectively (Lee, 1992b). The extinction efficiency accounting for dependent scattering is related to K^σ by

$$Q_e^\sigma = -\frac{\pi\alpha}{f_v} \text{Im}\left(\frac{K^\sigma}{k_o}\right) \quad (6)$$

where Im denotes the imaginary part. Because the dispersion relation is derived for the interior region of the medium, it
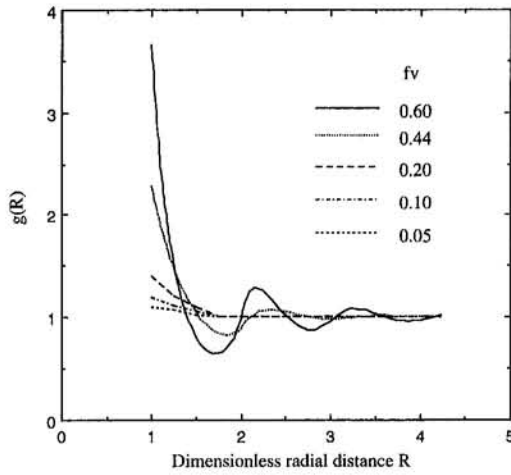

Nomenclature

$a_{jn}^\sigma, b_{jn}^\sigma$ = dependent scattering wave coefficients
$\mathbf{E}$ = electric field
f_v = fiber volume fraction = $\pi r_o^2 n_o L_o$
$g(R)$ = radial distribution function
$h = k_o \sin \phi_i$
$\mathbf{H}$ = magnetic field
H_n = Hankel function of the second kind
$\mathbf{I}_c^\sigma$ = coherent scattering intensity function
$\mathbf{I}_{ic}^\sigma$ = incoherent scattering intensity distribution
J_n = integral order Bessel function
k_o = propagation constant of medium containing the fibers
k_x = x-component of k_o, $= k_o \cos \phi_i \cos \theta_i$

$\mathbf{K}^\sigma$ = effective propagation constant of the fibrous medium
$\mathbf{K}_x^\sigma$ = x-component of $\mathbf{K}^\sigma$, $= K^\sigma \cos \phi_t \cos \theta_t$
$l_o = k_o \cos \phi_i$
$L = K^\sigma \cos \phi_t$
L_o = average fiber length
n_o = number of fibers per unit volume
N_o = total number of fibers
Q_e = extinction efficiency
Q_{sb} = backscattering efficiency
r_o = fiber radius
$\mathbf{R}$ = radial vector
t = time
u^σ = TM mode Hertz potential
v^σ = TE mode Hertz potential
X_n^σ, Y_n^σ = amplitudes of the effective wave

W_o = width of medium along Y axis under observation
α = size parameter = $2\pi r_o/\lambda$
δ_{jk} = Kronecker delta function
γ = polar angle measured from the X axis
λ = wavelength
ω = circular frequency

Superscripts

s = refers to scattering
σ = mode of incident radiation, I (TM) or II (TE)

Subscripts

i = incident wave
j, k = index, refers to the fiber
n, s = index, $-\infty$ to ∞
t = transmitted wave
σ = mode of the incident radiation, I (TM) or II (TE)

Fig. 2 Two-dimensional radial distribution functions (Chae et al., 1969; Wood, 1970)

is generally valid for both finite and semi-infinite media. The scattering amplitudes X_n^σ and Y_n^σ are obtained by solving Eqs. (2) and (3).

The effective propagation constant and amplitudes provide all the information for formulating the coherent and incoherent scattering characteristics of the fibrous medium. The time-averaged coherent scattered intensity function is given by (Lee and Grzesik, 1995):

$$\mathbf{I}_c^\sigma = \frac{1}{2S_o} \operatorname{Re}\left\{\sum_{j=1}^{N_o} \mathbf{E}_j^{\sigma s} \rangle x \langle \sum_{k=1}^{N_o} \mathbf{H}_k^{\sigma s} \rangle^*\right\}$$

$$= |\beta^\sigma \rho^\sigma|^2 \{|\sum_{n=-\infty}^{\infty} (-1)^n X_n^\sigma \exp(in\theta_i)|^2$$

$$+ |\sum_{n=-\infty}^{\infty} (-1)^n Y_n^\sigma \exp(in\theta_i)|^2\}\mathbf{n}_r \quad (7)$$

where S_o is the incident flux, $\mathbf{n}_r = -\cos\phi_i \cos\theta_i\mathbf{e}_x - \cos\phi_i \times \sin\theta_i\mathbf{e}_y + \sin\phi_i\mathbf{e}_z$, and

$$\rho^\sigma = \frac{K_x^\sigma - k_x}{K_x^\sigma + k_x} \quad (8)$$

is the reflection coefficient, which measures the deviation of the effective propagation constant of the medium containing fibers from that without fibers. Derivation of Eq. (7) requires
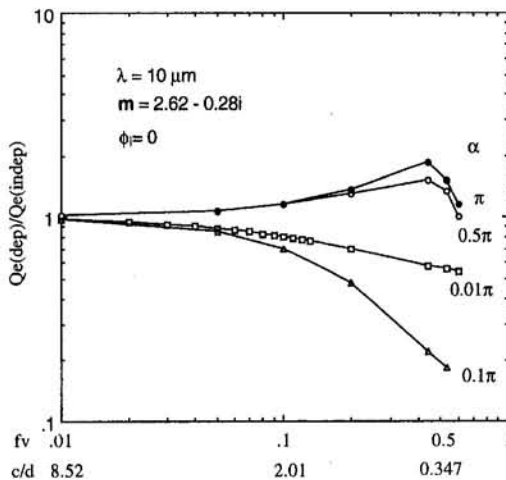
the relations between the electric ($\mathbf{E}_j^{\sigma s}$) and magnetic ($\mathbf{H}_j^{\sigma s}$) fields and the Hertz potentials:

$$\mathbf{E}_j^{\sigma s} = -\nabla x(\mathbf{e}_z v_j^{\sigma s}) + \frac{i}{k_o} \nabla x \nabla x(\mathbf{e}_z u_j^{\sigma s}) \quad (9)$$

$$Z_o\mathbf{H}_j^{\sigma s} = -\nabla x(\mathbf{e}_z u_j^{\sigma s}) - \frac{i}{k_o} \nabla x \nabla x(\mathbf{e}_z v_j^{\sigma s}) \quad (10)$$

where Z_o is the impedance of the medium. Note that $\mathbf{I}_c^\sigma$ corresponds to the specular component of the reflected radiation, which occurs only if the refractive index changes across the interface of the fibrous medium. The apparent refractive index of the fibrous medium is given by K_o^σ/k_o, which is complex and different from unity due to the presence of fibers. Lee (1992) showed that $K_x^\sigma/k_x \to 1$ as $f_v \to 0$, so that the coherent scattered component vanishes in a high-porosity fibrous medium.

The time-averaged incoherent, i.e., diffuse, scattered intensity is equal to the difference between the total and the coherent scattered radiation. The incoherent scattered intensity function is given by (Lee and Grzesik, 1995)

$$\mathbf{I}_{ic}^\sigma(\gamma) = \frac{R_p}{2S_o W_o \cos\phi_i \cos\theta_i}$$

$$\times \operatorname{Re}\{\langle\mathbf{E}^{\sigma s} x\mathbf{H}^{\sigma s}*\rangle - \langle\mathbf{E}^{\sigma s}\rangle x\langle\mathbf{H}^{\sigma s}\rangle^*\}$$

$$= \mathbf{e}_s \frac{f_v}{\pi^2\alpha^2} \frac{1 + \operatorname{Re}\Psi^\sigma(\gamma)}{\cos^2\phi_i \cos\theta_i K_{ix}^\sigma/k_o}$$

$$\times \{|\sum_{n=-\infty}^{\infty} X_n^\sigma \exp(in\gamma)|^2$$

$$+ |\sum_{n=-\infty}^{\infty} Y_n^\sigma \exp(in\gamma)|^2\} \quad (11)$$

where $\mathbf{e}_s = \cos\phi_i\mathbf{e}_r + \sin\phi_i\mathbf{e}_z$, K_{ix}^σ is the imaginary part of K_x^σ, and $\pi/2 \le \gamma \le 3\pi/2$ is the range of the back-scattering angle. Derivation of Eq. (11) requires taking the cross product of Eqs. (9) and (10) prior to performing the conditional averaging. The function Ψ^σ is given by

$$\Psi^\sigma(\gamma) = \frac{2f_v}{r_o^2}\{\psi_o^\sigma + 2\sum_{n=1}^{\infty} \psi_n^\sigma \cos n[\gamma + \tan^{-1}$$

$$\times (k_o \cos\phi_i \sin\theta_i/\operatorname{Re}K_x^\sigma)]\} \quad (12)$$

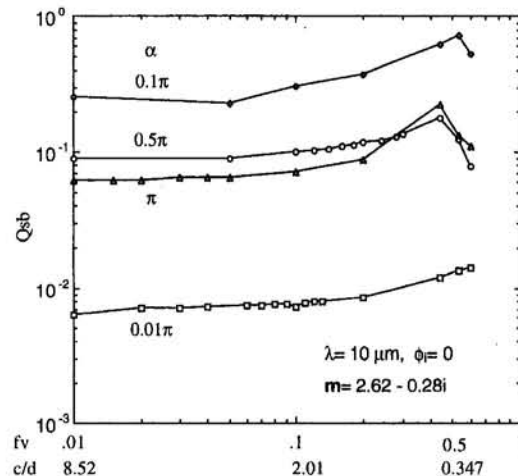**Fig. 3 Extinction efficiency for several fiber sizes**

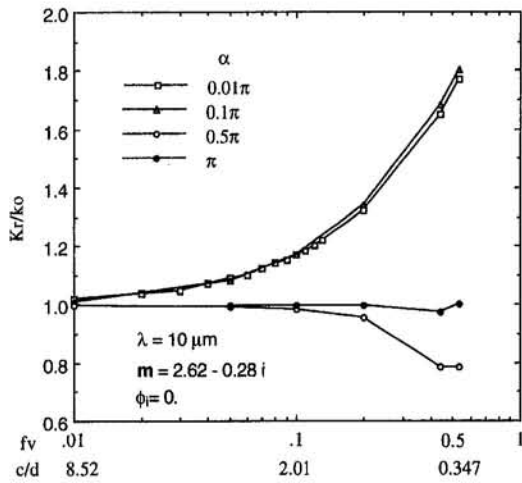**Fig. 4 Back-scattering efficiency for normal incidence**

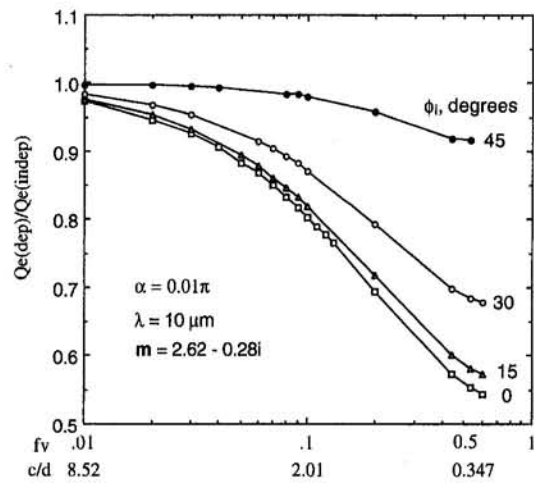Fig. 5 Apparent refractive index for normal incidence

Fig. 7 Extinction efficiency at oblique incidence

where

$$\psi_n^\sigma = \int_{2r_o}^{\infty} J_n\{[(\mathrm{Re}K_x^\sigma)^2 + (k_o \cos \phi_i \sin \theta_i)^2]^{1/2}R\}$$

$$\times J_n(l_o R)[g(R) - 1]R dR \quad (13)$$

Integrating Eq. (11) over the back-scattering direction yields the dependent backscattering efficiency as

$$Q_{sb} = \int_{\pi/2}^{3\pi/2} \mathbf{I}_{ic}^\sigma(\gamma) \cdot \mathbf{e}_r d\gamma. \quad (14)$$

The scattering properties given by Eqs. (2), (3), (6), (7), (11), and (14) are used to analyze the effect of incident angle and fiber size on dependent scattering in dense fibrous media.

Results and Discussion

The objective of the present study is to examine the effects of incident angle and fiber size on dependent scattering in dense fibrous media. The particular emphasis is to determine whether dependent scattering effects are more pronounced at normal or at oblique incidence. Numerical data are presented for silica fibers at the incident wavelength of 10 μm, at which the complex refractive index of silica is $\mathbf{m} = 2.62 - 0.28i$ (Malitson, 1965). Although analyses are performed only for one set of wavelength and refractive index, the trends of results for other wavelengths and refractive indices are expected to be similar. This is because

the scattering properties are governed by the multiple scattering interactions between the fibers, which are described by the formulations presented herein based on a rigorous solution of Maxwell's relations. A different set of wavelength and refractive index would change the magnitude but not the trend of the numerical data. While a specific set of parameters has been used in the present numerical analyses, the conclusions are generally applicable to all parameter values.

The effective propagation constant is solved from the dispersion relation resulting from Eq. (2) by utilizing the double precision complex root finding subroutine DZANLY (IMSL, 1989). The refractive index of the medium containing the incident radiation is assumed to be identical to that containing the fibers, which is taken as unity for convenience. Silica fibers of radius 0.05, 0.5, 2.5, and 5 μm, which correspond to the size parameter $\alpha = 0.01\pi$, 0.1π, 0.5π, and π, and incident angle ranging from 0 to 60 deg are assumed. The two-dimensional radial distribution functions $g(R)$ reported by Chae et al. (1969) and Wood (1970), as shown in Fig. 2, are employed in the present analyses. The relative and absolute tolerances for the complex roots are specified at 0.001.

The influence of dependent scattering is being examined by computing the scattering properties as a function of fiber volume fraction f_v, which is related to the clearance-to-diameter ratio c/d by $c/d = \sqrt{\pi/(2\sqrt{3}f_v)} - 1$. This relationship is based on the geometric consideration of parallel fibers arranged in a hex-
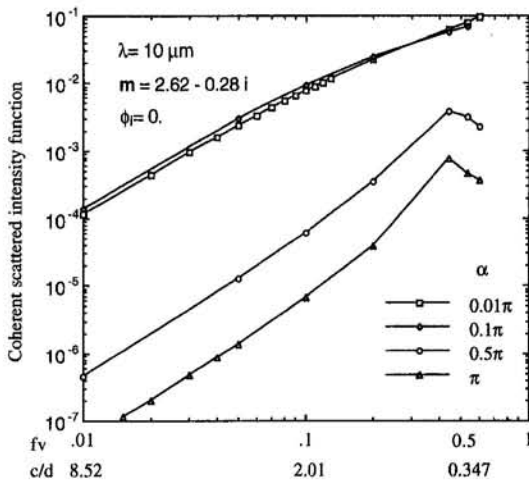

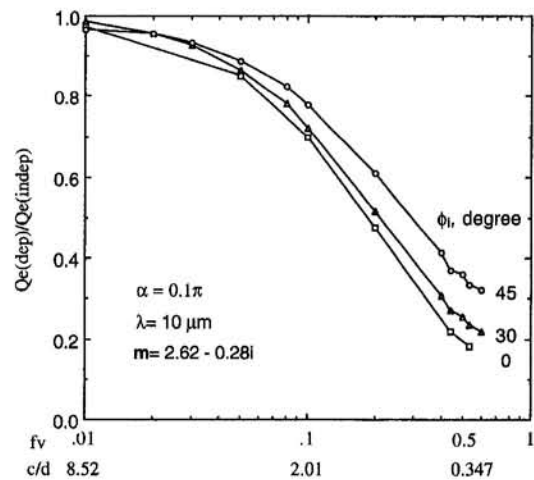Fig. 6 Coherent scattering at normal incidence

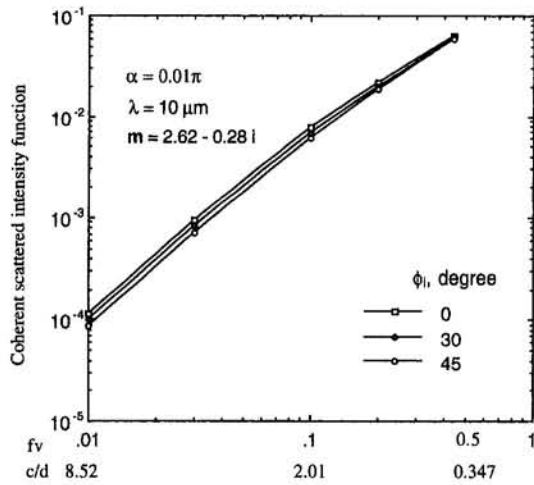Fig. 8 Extinction efficiency for various incident angles
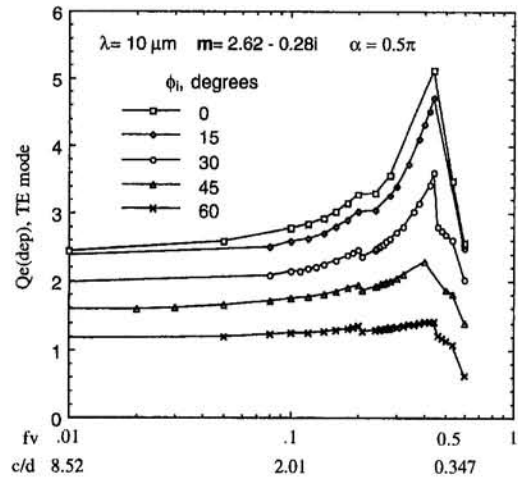
Fig. 9 Coherent scattering for small fibers

Fig. 11 TE mode extinction efficiency for various angles of incidence

agonal pattern, which yields the highest packing density. The effect of fiber size on dependent scattering is first examined by evaluating the radiative properties of the fibrous medium at normal incidence. Figure 3 shows the dependent extinction efficiency (Q_{ed}) normalized by the independent scattering efficiency (Q_{eo}) for several size parameters α. The ratio Q_{ed}/Q_{eo} deviates from unity as f_v increases, which corresponds to decreasing c/d and c/λ for a given α. Dependent scattering is accordingly more pronounced when the clearance between fibers is small compared to the fiber diameter and incident wavelength. For small fibers Q_{ed}/Q_{eo} decreases monotonically with f_v, whereas larger fibers show a different trend due to the higher values of c/d. Figure 4 shows the variation of the backscattering efficiency Q_{sb} with f_v and c/d. The scattering efficiency decreases with larger size parameter due to multiple scattering. These curves suggest that Q_{sb} peaks at $0.01\pi < \alpha < 0.5\pi$. The real part of the effective propagation constant K_r/k_o is shown in Fig. 5, which corresponds to the apparent refractive index of the medium. For a sparse medium K_r/k_o is close to unity. However, a high f_v gives rise to an apparent electrical conductivity, which causes K/k_o to depart from unity and a nonzero reflection coefficient. The coherent scattered radiation due to Fresnel reflection then results, as shown in Fig. 6. Note that the coherent scattered radiation corresponds to the specular reflected component, which is negligible at low f_v but becomes increasingly significant as f_v increases. The magnitude of the coherent scat-

tered component therefore provides a direct measure of the effect of dependent scattering.

The angle of incidence effect on dependent scattering is next examined. Figures 7 and 8 show the variation of Q_{ed}/Q_{eo} with f_v for several incident angles for $\alpha = 0.01\pi$ and 0.1π, respectively. For a given Q_{ed}/Q_{eo}, the f_v or c/d at the onset of dependent scattering is always smaller for normal than for oblique incidence. These results indicate that the demarcation of scattering regimes by Lee (1994) based on normal incidence is conservative. The coherent scattered intensity for oblique incidence is shown in Fig. 9 for $\alpha = 0.01\pi$, which reveals that the magnitude of coherent scattering is higher at normal incidence. These results show the increasingly pronounced effect of dependent scattering as the fiber concentration increases.

Lastly, the influence of fiber size and incident angle on the polarization components of K/k_o is examined. Figures 10 and 11 show the TM and TE mode extinction efficiencies for $\alpha = 0.5\pi$ at several incident angles, respectively. The extinction efficiencies deviate negligibly from their independent scattering values at low f_v, which are less sensitive to f_v at larger angle of incidence. The variation of the TM and TE mode K_r/k_o with f_v is shown in Figs. 12 and 13, respectively. The substantial deviation of K_r/k_o from unity at high f_v indicates that Fresnel reflection is significant. The presence of coherent scattered radiation highlights the major difference between the scattering behavior of high-density and low-density fibrous media.
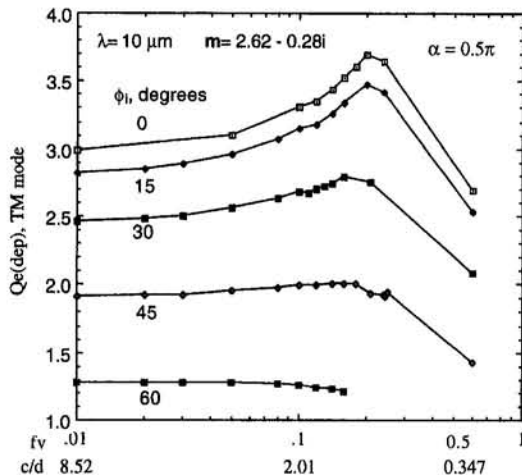

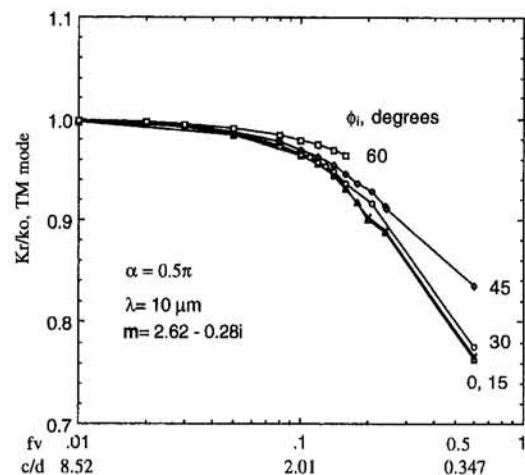Fig. 10 TM mode extinction efficiency for various angles of incidence

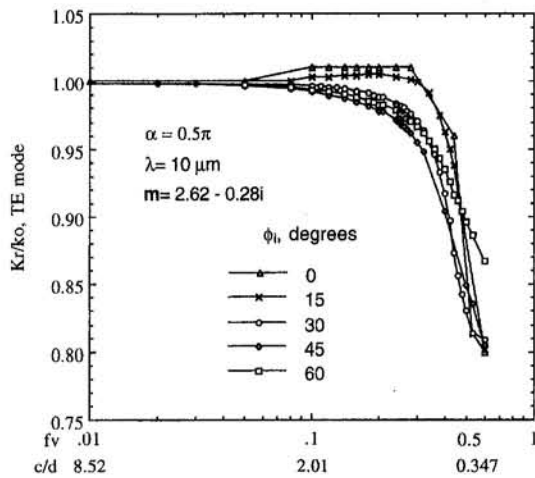Fig. 12 TM mode apparent refractive index of medium

Fig. 13 TE mode apparent refractive index of medium

Conclusion

The influence of fiber size and oblique angle of incidence on the scattering behavior of high-density fibrous media has been examined by utilizing the dependent scattering theory. Dependent scattering is shown to be more pronounced at normal than at oblique incidence. This can be attributed to the shorter distance that the scattered waves would traverse in successive scattering events. High fiber volume fraction causes the apparent refractive index of the medium to deviate from unity, thus giving rise to coherent scattered radiation. The extinction efficiency, apparent refractive index of the medium, coherent scattered radiation, and back-scattering efficiency provide the necessary information for assessing the adequacy of the independent scattering assumption for a given fibrous medium.

References

Bose, S. K., and Mal, A. K., 1973, "Longitudinal Shear Waves in a Fiber-Reinforced Composite," *International Journal of Solid Structure*, Vol. 9, No. 9, pp. 1075–1085.

Chae, D. G., Ree, F. H., and Ree, T., 1969, "Radial Distribution Functions and Equation of State of the Hard-Disk Fluid," *The Journal of Chemical Physics*, Vol. 50, No. 4, pp. 1581–1589.

Chern, B.-C., Howell, J. R., and Moon, T. J., 1994, "Dependent Scattering Effects on Wave Propagation Through Filament-Wound Composites," *6th AIAA/ASME Thermophysics and Heat Transfer Conference*, ASME HTD-Vol. 276, pp. 15–20.

IMSL, 1989, IMSL Math/Library User's Manual, Fortran Subroutines for Mathematical Applications.

Lax, M., 1952, "Multiple Scattering of Waves. II. The Effective Field in Dense Systems," *Physics Review*, Vol. 85, No. 4, pp. 621–629.

Lee, S. C., 1990, "Dependent Scattering of an Obliquely Incident Plane Wave by a Collection of Parallel Cylinders," *Journal of Applied Physics*, Vol. 68, No. 10, pp. 4952–4957.

Lee, S. C., 1992a, "Scattering by Closely-Spaced Radially-Stratified Parallel Cylinders," *Journal of Quantitative Spectroscopy & Radiative Transfer*, Vol. 48, No. 2, pp. 119–130.

Lee, S. C., 1992b, "Effective Propagation Constants of Fibrous Media Containing Parallel Fibers in the Dependent Scattering Regime," ASME JOURNAL OF HEAT TRANSFER, Vol. 114, No. 2, pp. 473–478.

Lee, S. C., 1993, "Propagation of Radiation in High-Density Fibrous Composites Containing Coated Fibers," *Journal of Thermophysics and Heat Transfer*, Vol. 7, No. 4, pp. 637–643.

Lee, S. C., and Kurtz, J., 1994, "Optical Extinction Properties of Space Suite Fabrics: Theory vs. Experiment," AIAA Paper No. Paper 94-1967.

Lee, S. C., 1994, "Dependent Versus Independent Scattering in Fibrous Composites Containing Parallel Fibers," *Journal of Thermophysics and Heat Transfer*, Vol. 8, No. 4, pp. 641–646.

Lee, S. C., and Grzesik, J. A., 1995, "Scattering Characteristics of High-Density Fibrous Media," *Journal of Thermophysics and Heat Transfer*, Vol. 9, No. 3, pp. 403–409.

Malitson, I. H., 1965, "Interspecimen Comparison of Refractive Index of Fused Silica," *Journal of Optical Society of America*, Vol. 55, No. 9, pp. 1206–1210.

Oloafe, G. O., 1970, "Scattering by an Arbitrary Configuration of Parallel Circular Cylinders," *Journal of Optical Society of America*, Vol. 60, No. 9, pp. 1233–1236.

Twersky, V., 1952a, "Multiple Scattering of Radiation by an Arbitrary Configuration of Parallel Cylinders," *Journal of Optical Society of America*, Vol. 24, No. 1, pp. 42–46.

Twersky, V., 1952b, "Multiple Scattering of Radiation by an Arbitrary Planar Configuration of Parallel Cylinders and by Two Parallel Cylinders," *Journal of Applied Physics*, Vol. 23, No. 4, pp. 407–414.

Twersky, V., 1979, "Propagation in Pair-Correlated Distributions of Small-Spaced Lossy Scatters," *Journal of Optical Society of America*, Vol. 69, No. 11, pp. 1567–1572.

Varadan, V. K., Varadan, V. V., and Y.-H. Pao, 1978, "Multiple Scattering of Elastic Waves by Cylinders of Arbitrary Cross Section. I. SH Waves," *Journal of Acoustical Society of America*, Vol. 63, No. 5, pp. 1310–1319.

Varadan, V. K., Ma, Y., and Varadan, V. V., 1986, "Multiple Scattering of Compressional and Shear Waves by Fiber-Reinforced Composite Materials," *Journal of Acoustical Society of America*, Vol. 80, No. 1, pp. 333–339.

Wood, W. W., 1970, "NpT-Ensemble Monte Carlo Calculations for the Hard Disk Fluid," *The Journal of Chemical Physics*, Vol. 52, No. 2, pp. 729–741.

Heater Orientation Effects on Pool Boiling of Micro-Porous-Enhanced Surfaces in Saturated FC-72

J. Y. Chang
Research Assistant
Student Mem. ASME

S. M. You
Associate Professor

Department of Mechanical and
Aerospace Engineering,
The University of Texas at Arlington,
Arlington, TX 76019-0023
Associate Professor
Mem. ASME

Experiments are performed to understand the effects of surface orientation on the pool boiling characteristics of a highly wetting fluid from a flush-mounted, micro-porous-enhanced square heater. Micro-porous enhancement was achieved by applying copper and aluminum particle coatings to the heater surfaces. Effects of heater orientation on CHF and nucleate boiling heat transfer for uncoated and coated surfaces are compared. A correlation is developed to predict the heater orientation effect on CHF for those surfaces.

Introduction

The effects of the surface inclination angle on pool boiling heat transfer have been reported by different authors. Ishigai et al. (1961) investigated boiling from downward-facing copper disks (25 mm and 50 mm in diameter) in saturated water. Githinji and Sabersky (1963) recognized that inclined surfaces display different nucleate boiling curves. Marcus and Dropkin (1963) reported that the vapor bubble agitation motions contributed to a higher heat transfer coefficient when the heater was in the vertical position. Nishikawa et al. (1984) presented experimental data for nucleate boiling of water from a copper surface at various orientations ($\theta = 0$ to 175 deg). Their results showed enhancement of nucleate boiling performance due to increased angle at lower heat fluxes. The enhancement disappeared at heat fluxes higher than ≈ 17 W/cm². Lienhard (1985), using Moissis and Berenson's (1963) model, explained this behavior as the transition from the isolated bubble regime to that of slugs and columns. He explained that bubble frequency and size are controlled by gravity in the isolated bubble regime, and hence surface orientation effects on heat transfer coefficients are significant. The influence of gravity on different orientations appeared to vanish above the transition heat flux. The enhancement of nucleate boiling due to increased angle at lower heat fluxes was also observed by Chen (1978) with saturated R-11, Vishnev et al. (1976), Nishio and Chandratilleke (1989) with saturated helium, and Beduz et al. (1988) with saturated nitrogen.

More recently, El-Genk and Guo (1993) performed quenching experiments investigating transient pool boiling from a copper disk (50.8 mm in diameter and 12.8 mm thick) in saturated water. With the quenching method, compared with the steady-state heating method, the surface heat flux was determined from the rate of change of the energy stored in the disk with time. Their nucleate boiling curves for the inclined, downward-facing disk ($\theta = 90$ to 180 deg) showed a slight decrease of superheat due to increased angle. They also collected available CHF data from other investigators for saturated nitrogen, water, and helium. The collected steady-state CHF data, along with their transient CHF data, were correlated as a function of inclination angle for each of the boiling liquids.

Surface orientation effects on pool boiling heat transfer with enhanced surfaces have also been investigated experimentally.

Fujii et al. (1979) conducted a test with a porous-surface disk (40 mm diameter) in saturated R-113. Their surface was made by electroplating copper particles (0.115 mm mean diameter) to the surface with a thickness of two to three particle diameters. They compared the performance of the porous surface against that of a smooth surface for three angular positions ($\theta = 0$, 45, and 90 deg). For the porous surface, a small decrease in performance versus orientation angle was observed, while the performance of the smooth surface increased with increasing angle. Bubbles trapped within the porous layer were thought to produce an added thermal resistance, resulting in a decrease in the nucleate boiling heat transfer coefficient. Czikk et al. (1981) noted that surface orientation had a small effect on the pool boiling heat transfer coefficient of the porous High-Flux surfaces. Jung et al. (1987) investigated the pool boiling curves of 80 mm diameter circular surfaces enhanced with a flame-sprayed metal coating. Their experimental data in saturated R-11 showed nearly identical nucleate boiling curves for different θ values. They also observed negligible CHF enhancement over unsprayed surfaces, indicating that metal spraying is not effective for augmenting CHF. Beduz et al. (1988) found an angular dependence of CHF for saturated liquid nitrogen with differently finished surfaces. The surfaces tested were smooth, grooved and rolled, and plasma sprayed. In all cases, the highest CHF was obtained at the horizontal upward position ($\theta = 0$ deg). Their data showed a steady decrease in CHF with increasing angle for all surfaces tested.

Many boiling enhancement studies have been performed using structured surfaces, as summarized by Thome (1990). While many of the enhanced surfaces tested have demonstrated the ability to reduce wall superheat and increase CHF, their feature sizes were apparently too large to trap a large number of embryonic bubbles effectively when immersed in dielectric liquids (e.g., refrigerants). Tests by You et al. (1990) have shown that both the boiling nucleation and the boiling site density can be efficiently increased by manufacturing optimum cavity sizes on a heated surface. You et al. (1991) introduced a ''particle layering'' technique, which was applied to a flat surface. Alumina (Al_2O_3) particles (0.3 to 3 μm) were sprayed to a heater surface and tested in FC-72. The deposited particles adhered to the surface by van der Waals molecular attraction forces. They reported significant reductions in incipient and nucleate boiling superheats (≈ 50 percent), and an increase in CHF (≈ 32 percent). Recently, O'Connor and You (1995) developed a boiling enhancement paint with silver flakes (3 to 10 μm). Their treated surface immersed in saturated FC-72

showed ≈80 percent reduction in nucleate boiling superheat and a ≈109 percent increase in CHF over the nonpainted surface. O'Connor et al. (1995) developed a dielectric paint, made with diamond particles (8 to 12 μm), for applications in electronic component cooling. Their dielectric paint surface showed nearly identical pool boiling enhancement with that of the silver flake paint.

In response to the trend of increased power loads from miniaturized electronic devices, direct immersion cooling has been considered as one of the most promising cooling schemes for high-heat-density devices. Proper packaging of future electronic devices will require the accurate prediction of heat transfer characteristics for nucleate boiling and CHF. Surface orientation is an important packaging parameter, which affects the boiling heat transfer performance of a heated surface. As an extension of You et al. (1991), O'Connor and You (1995), and O'Connor et al. (1995), the present research was conducted with a flush-mounted, thick metal heater immersed in saturated FC-72, a highly wetting dielectric fluid. In this research, the micro-porous enhancement technique was used to produce boiling-enhanced surfaces. Experiments were performed to understand the effects of enhanced-surface heater orientation on pool boiling heat transfer. Two different micro-porous surfaces and a plain reference surface were tested.

Experimental Apparatus and Procedure

Test Facility. The pool boiling test facility used for this research is shown in Fig. 1. The test liquid was contained within a glass vessel, 260 mm high and 160 mm in diameter, which was submerged in a Lexan water container. The water container served as an isothermal bath. Water temperature was controlled by a 1000 W immersion heater/circulator. A magnetic stirring bar was located inside the test vessel and was used to accelerate the degassing process before each test. A water-cooled condenser was used during degassing and testing to minimize loss of the test liquid. Atmospheric pressure was maintained by venting the test vessel to ambient. Two copper-constantan thermocouples were placed within the test vessel to measure bulk liquid temperature. The test heater assembly was mounted to an aluminum support bar, which enabled rotation of the heater to a desired inclination angle.

A DC power supply was connected in series with a shunt resistor and the test heater. The shunt resistor, rated at 100 mV and 10 A, was used to determine the current in the electric circuit. Direct current was supplied to the heating element by the DC power supply. A measured voltage drop across the test heater was used to estimate heat flux applied by the power supply.

Figure 2 shows the test heater assembly used during this study. Serpentine windings of a thin nichrome wire (0.144 mm diameter) were attached to a Teflon substrate (11 mm thick) using Omegabond 200 high-temperature epoxy ($k \approx 1.4$ W/mK). A 1.5-mm-thick block of copper (10 mm × 10 mm) was bonded on top of the heating element also using Omegabond 200 epoxy. Two layers of epoxy assured electrical insulation between the copper and the nichrome. To minimize the epoxy thickness, it was cured within an oven maintained at 423 K with a weight resting on top of the copper block. Electrical leads were soldered to each end of the nichrome wire. The
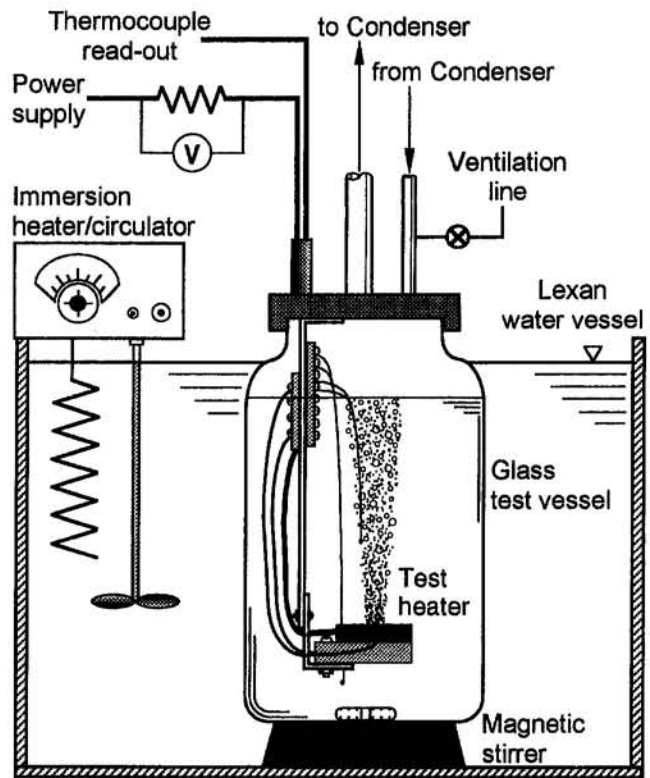

Fig. 1 Schematic of test apparatus

resulting heating element resistance was about 12 ohms. This heating element was set in a Lexan frame and surrounded by a two-part, 3M epoxy (1832L-B/A, $k \approx 0.067$ W/mK) to generate a flush-mounted heating surface. The copper block had two holes (1 mm diameter and 5 mm depth) drilled into its center from one edge. Two copper-constantan thermocouples (30 wire gage, 0.255 mm diameter) were inserted and soldered in the holes to provide surface temperature measurements. The completed test heater was attached to the aluminum support bar with a bolt.

Test Procedure. The immersion heater/circulator was turned on to heat the water bath to the saturation temperature of test liquid. Once the test liquid reached its saturation temperature, it was left at this state for two hours to remove dissolved gases. A magnetic stirrer was used during this process to accelerate dissolved gas removal. After degassing, the magnetic stirrer was turned off and data acquisition begun.

Heat flux was controlled by the voltage input of a DC power supply. After each voltage increase (heat-flux increment), a 15-second delay was imposed before initiating data acquisition. After the delay, the computer collected and averaged 125 surface-temperature data points from each thermocouple, which took about 15 seconds. This was immediately followed by the acquisition and averaging of an additional 125 data points per thermocouple. A comparison was then made between these two average temperatures for each thermocouple. This procedure

Nomenclature

CHF = critical heat flux, W/cm^2
CHF$_{max}$ = maximum critical heat flux, W/cm^2
CHF$_z$ = CHF predicted by Zuber (1959), W/cm^2
$C(\theta)$ = coefficient of Eq. (2)

h_{fg} = heat of vaporization, kJ/kg
k = thermal conductivity, W/mK
q_w = heat flux, W/cm^2
θ = surface inclination angle from horizontal upward position, deg

ρ_l = density of boiling liquid, kg/m^3
ρ_v = vapor density of boiling liquid, kg/m^3
σ = surface tension of boiling liquid, N/m

Copper block with
two thermocouple holes of
1-mm diameter & 5-mm depth

Nichrome wire insulated
with Omegabond 200

(a) Heating element

3M 1838-L B/A
epoxy filler

Flush-mounted copper heater
(10 mm x 10 mm)

Teflon substrate

Lead
wires

25 mm

Lexan frame
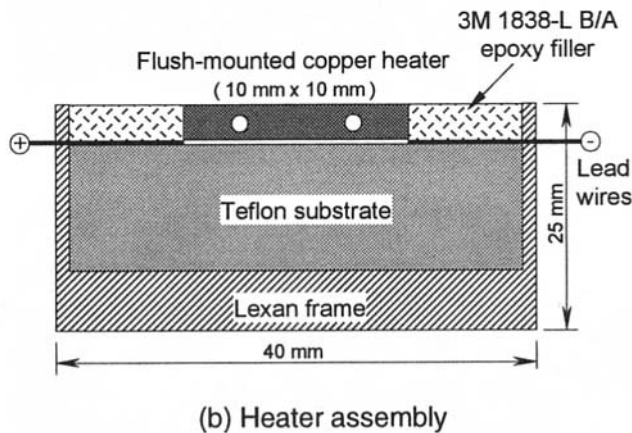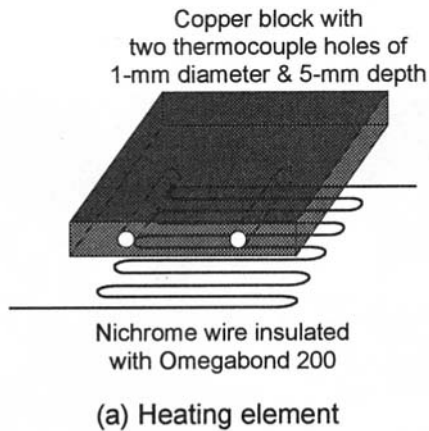
40 mm

(b) Heater assembly

Fig. 2   Test heater geometry

was repeated until the temperature differences for all thermocouples were less than 0.2 K. The test section at this point was assumed to be steady state. Usually it took about 45 seconds to reach the steady-state condition after each heat-flux increment. After reaching steady state, bulk fluid temperature was measured and heat flux was calculated.

For heat-flux values greater than ≈80 percent of CHF, instantaneous surface temperature was monitored for 45 seconds after each heat-flux increment to prevent heater burnout. Each instantaneous surface temperature measurement was compared with the average surface temperature from the previous heat flux. If a temperature difference larger than 30 K from any thermocouple was detected, the data acquisition algorithm assumed CHF and immediately shut down the power supply. The CHF value was computed as the steady-state heat-flux value just prior to power supply shutdown plus half of the increment. The heat-flux increments used near CHF were ≈0.1 W/cm² for the facing downward position ($\theta = 180$ deg) and ≈0.5 W/cm² for the other angular positions. When the data acquisition algorithm detected CHF, vapor film was observed to form over the heater surface, assuring transition to film boiling. If CHF was not detected during the 45-second delay, collecting and averaging of 125 surface temperature data points from each thermocouple was initiated and repeated until the steady-state condition was achieved. At least two consecutive runs were conducted for each surface tested. The time interval between these runs was determined by monitoring test heater surface temperature. The surface was assumed to reach thermal equilibrium if the surface temperature averaged over approximately 10 s was within ±0.1 K of the saturated bulk fluid temperature. In all cases, this time interval between runs was no less than 1 hour.

Since the thermocouples were embedded within the copper block, temperatures measured with them were averaged and

corrected by a one-dimensional heat conduction model to obtain the representative heater surface temperature at each applied heat flux. This correction was less than 0.5 K for all cases, however.

Substrate conduction losses were estimated based upon those conducted by O'Connor and You (1995) whose heater had a design similar to that of the present one. Heat losses for their heater were estimated to be between 15 and 5 percent for heat fluxes between 0.5 and 15 W/cm², respectively. Their overall uncertainty estimates in heat flux were 15.5 and 5 percent for the above-referred heat-flux conditions. The uncertainty estimates of the present heater can be estimated to be smaller than those of O'Connor and You for the larger surface area (1.0 versus 0.825 cm²) with comparable thicknesses. Also, the uncertainties associated with the CHF values of the present tests were estimated to be 7 percent for the plain surfaces and 5 percent for the enhanced surfaces.

Results and Discussion

All experiments were conducted using saturated FC-72 at 1 atm. The tested surfaces included a smooth or "plain" reference surface and two plain surfaces coated with two different microporous-enhancement coatings.

Pool Boiling Tests of Plain Surfaces.   The plain surface was tested first. Four plain-surface heaters were constructed to examine nucleate boiling heat transfer. The copper surface of the heater was polished using Brasso. After polishing, a small amount of 3M epoxy (1832L-B/A) was carefully applied around the perimeter of the heater surface to prevent undesired edge nucleation sites. Figure 3 illustrates the reproducibility of the plain surface roughness. Each boiling curve was generated from a different test heater. The natural convection and nucleate boiling data fall within scatter bands of ±0.4 K and ±2.0 K, respectively. Incipient superheat values range from 25 to 40 K. The CHF values range between 13.2 and 16.0 W/cm². Zuber's (1959) correlation predicts $CHF_z = 15.1$ W/cm² for saturated FC-72.

The saturated pool boiling curves are compared with that of O'Connor et al. (1995) in Fig. 3. The natural convection data of the current heaters showed about 30 percent lower heat transfer coefficients, which can be primarily attributed to larger surface
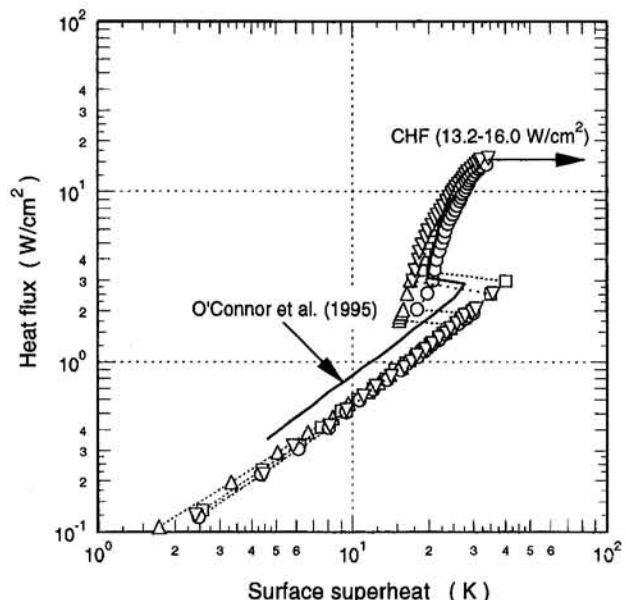

Fig. 3   Surface-to-surface variations of plain-surface pool boiling—horizontal-upward position ($\theta = 0$ deg)

area (1.0 versus 0.825 cm^2) and smaller aspect ratio (1.0 versus 3.3). Incipient superheat, nucleate boiling superheat, and CHF are in good agreement for the two types of heaters. The boiling curve with a CHF of 13.4 W/cm^2 was selected to serve as a reference for comparison with the enhanced-surface heaters.

Pool Boiling Tests of Micro-Porous-Enhanced Surfaces. Optimum cavity geometry and high nucleation site density are of great importance for boiling heat transfer enhancement. In the technique developed by O'Connor and You (1995), the enhancement paint was manufactured by combining silver flake particles with epoxy (Omegabond 101) and isopropyl alcohol. O'Connor et al. (1995) used diamond particles instead of silver flakes.

In the present study, copper particles and aluminum particles were used. Isopropyl alcohol and Omegabond 101 were replaced with M.E.K. (methyl-ethyl-ketone) and Devcon Brushable-Ceramic epoxy, respectively. Optimum paint composition studies were conducted, suggesting the following mixtures: 1.5 g of metal particles, 10 ml of M.E.K., and 0.4 ml of Devcon Brushable-Ceramic. The resulting new coatings are identified as "CBM" and "ABM," named from the initial letters of each of the three components (e.g., copper-brushable ceramic-M.E.K.). These coatings were painted on the copper reference surfaces following the application technique given by O'Connor and You (1995). M.E.K. is a highly volatile solvent that quickly evaporates. To completely cure in a reduced time, the coated heaters were baked in an oven at 423 K for about 1 hour.

Scanning electron microscope (SEM) images of the top views of the CBM and ABM coatings are shown in Fig. 4. Aluminum particle sizes in the ABM coating (1 to 20 μm) are smaller than the particle sizes in the CBM coating (1 to 50 μm). However, large copper particles within the CBM coating have numerous additional cavity structures on their surfaces with sizes on the order of microns. Both coatings are multilayered micro-porous structures having thicknesses of ≈ 100 μm for the CBM coating and ≈ 50 μm for the ABM coating.

Figure 5 illustrates representative pool boiling data for the CBM and ABM coated surfaces. The CBM and ABM surfaces show incipient superheats of ≈ 8.8 K and ≈ 6.3 K, respectively. These incipient superheats are close to the $8.5-10$ K reported by O'Connor and You (1995) for the silver flake coating and O'Connor et al. (1995) for the diamond coating. The incipient superheats for the CBM and ABM surfaces were about 80 percent lower than that of the reference surface and were repeatable. Upon incipience, both micro-porous-enhanced surfaces produced nucleate boiling over the entire surface area, generating discrete tiny bubbles less than 0.2 mm in diameter. The reference-surface natural convection regime was replaced almost entirely by the nucleate boiling regime of the coated surfaces as seen in Fig. 5. At lower heat fluxes, the uncoated surface experienced about 10 times higher wall superheats than the coated surfaces.

Throughout the nucleate boiling regime, both CBM and ABM surfaces consistently augmented heat transfer coefficients by approximately 330 percent compared to those of the reference surface. This enhancement was the result of the dramatically increased active nucleation site density caused by the surface microstructures provided by each coating. The CBM and ABM coatings provided repeatable CHF values with ≈ 100 percent enhancement over the reference surface. These enhanced CHF values (26.8 W/cm^2 for CBM and 26.3 W/cm^2 for ABM) confirmed the CHF dependence on surface microstructures, which was discussed by O'Connor and You (1995). These values pointed out that the CHF prediction by Zuber (1959) did not account for the role of surface microstructures.

Heater Orientation Effect. The effects of heater orientation on CHF and nucleate boiling heat transfer were investigated for the plain, CBM, and ABM surfaces. Five orientations ($\theta = 0, 45, 90, 135,$ and 180 deg) were considered for each surface.
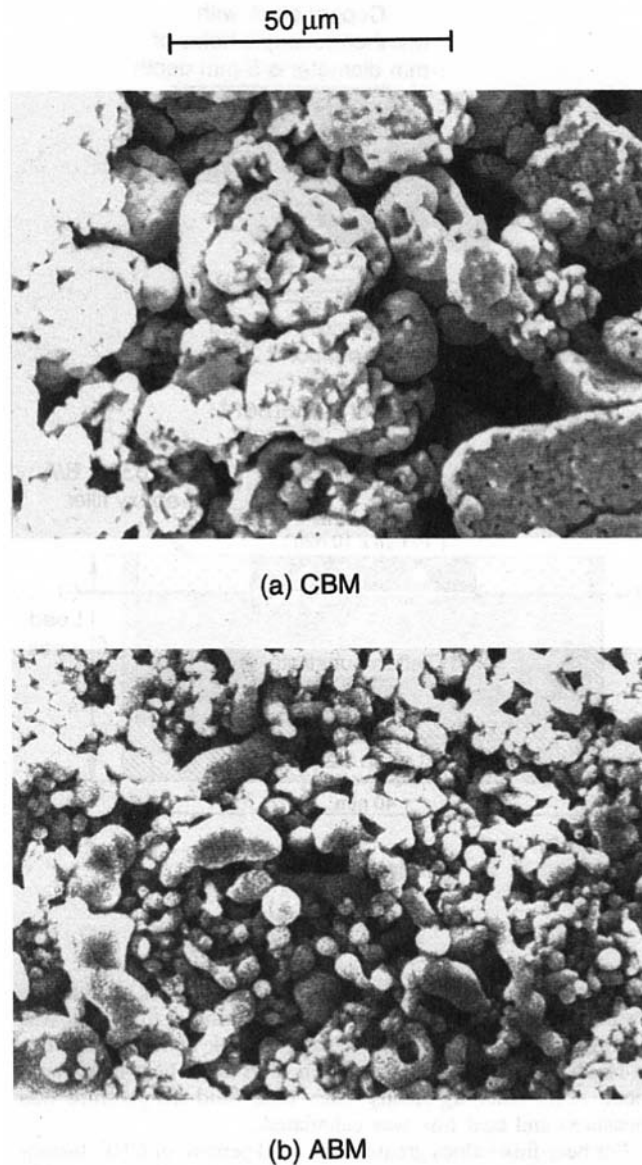

(a) CBM

(b) ABM

Fig. 4 Surface microstructure SEM images of CBM and ABM coatings

Test results for the plain surface are presented in Fig. 6. The orientation effect on single-phase natural convection is to decrease heat transfer substantially between 135 and 180 deg. In the nucleate boiling regime, higher inclination angles (between 0 and 90 deg) provided better heat transfer. This is attributed to an increased number of active nucleation sites. In the $\theta = 90$ deg case, inactive nucleation sites were activated by the rising bubbles from active sites below them on the surface. However, as heat flux was increased further, this effect disappeared. For $\theta = 90$ and 135 deg, a noticeable decrease in nucleate boiling heat transfer coefficient was observed with increasing inclination angle, which appears to be opposite to that reported by Nishikawa et al. (1984) for boiling water. Nishikawa et al. observed that the surface orientation effect was substantial in the low-heat-flux nucleate boiling region where heat transfer increased as inclination angle increased from $\theta = 0$ to 175 deg. However, in the high-heat-flux region, no marked effect was noticed. During the tests performed by Nishikawa et al., the transitional heat flux (≈ 17 W/cm^2) between those distinct heat-flux ranges was approximately 15 percent of CHF$_z$ for saturated water. An important difference between the tests of Nishikawa et al. and the present test is that Nishikawa et al. used decreasing
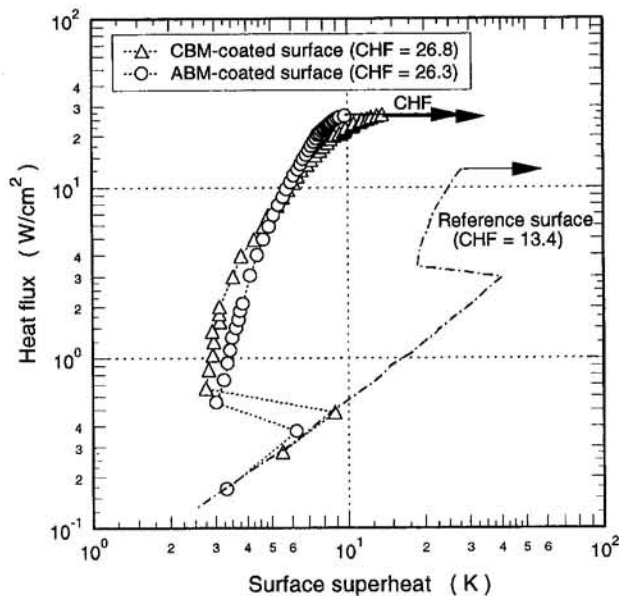
Fig. 5 Pool boiling of enhanced surfaces—horizontal-upward position ($\theta = 0$ deg)

Fig. 7 Inclination effects on pool boiling (CBM-coated surface)

heat-flux conditions, whereas the present test was conducted under increasing heat-flux conditions. Under decreasing heat-flux conditions, cessation of bubbles is retarded for downward-facing surfaces in the partially developed nucleate boiling region. Therefore, higher heat transfer coefficients might be observed with increasing inclination angle. For the present test, since a higher heat-flux value (or wall superheat value) is required to initiate nucleate boiling in FC-72 than in water, the partially developed nucleate boiling region (equivalent to that of water boiling) was replaced by single-phase natural convection. Fully developed nucleate boiling was then observed from the initiation of nucleate boiling. In the fully developed nucleate boiling regime, the decrease in the nucleate boiling heat transfer coefficient for the $\theta = 135$ deg case in Fig. 6 may be due to the increased thermal resistance from the elongated bubbles with decreased departure frequency over the inclined downward-facing heater surface. Nishikawa et al. also observed the
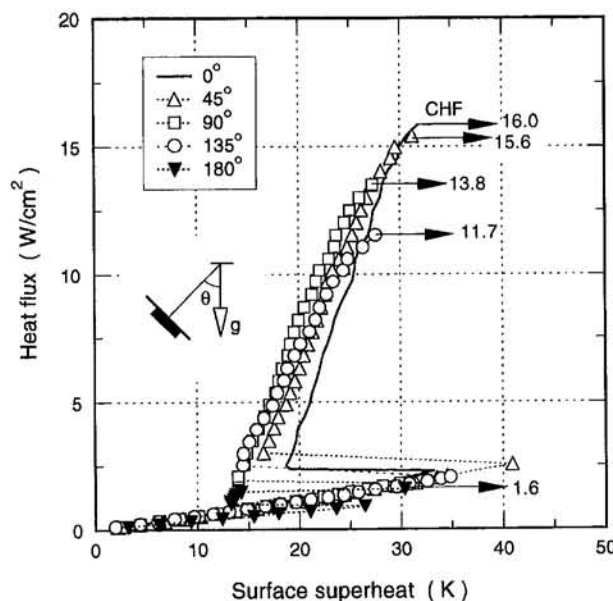
similar trend of decreasing heat transfer coefficient from the inclined downward-facing surface above the transitional heat flux, although it was slight. As described previously, You (1990) observed pool boiling curve trends that were similar to the present test.

At an inclination angle of 180 deg, a dramatic difference in the heat transfer mechanism was observed. At incipience, a large vapor bubble formed, which eventually covered the entire heated surface. This bubble was nearly stationary, moving slightly as it grew. Departure of this bubble from the heater surface was followed by the formation of a new bubble. The departing bubbles were much larger than those of the upward-facing cases, accompanied by a corresponding decrease in departure frequency. The increased thermal resistance due to the vapor bubble covering the surface produced a very low value of CHF (1.6 W/cm²) for the $\theta = 180$ deg case. The boiling crisis mechanism in this case could be described as "dry-out" rather than "hydrodynamic" CHF.

Figure 7 shows the heater orientation effect on the CBM surface. The trends observed in this figure are quite different from those in Fig. 6 with the plain surface. The nucleate boiling curves for all orientations are almost identical. This trend shows that the micro-porous structures of the CBM coating provided stable nucleation at any angle. Considering application to immersion-cooled electronic device surfaces, this stable nucleation is beneficial in producing a uniform temperature field as well as enhancing boiling over coated surfaces of different configurations. By implementing the coating technique over heat-generating device surfaces, thermal stress induced from nonuniform temperature fields can be effectively reduced, and hence failure rate is also reduced. In all CBM cases, incipient superheats were observed to be repeatable within a range of 5 to 8 K. Test results of the ABM surface (not shown) indicated similar behavior with the CBM surface. After testing at five different angular positions, the $\theta = 0$ deg pool boiling curve was reproduced for each surface tested. Identical pool boiling curves for each surface assured the consistency and repeatability of the present data.

The heater orientation effect on CHF is presented in Fig. 8 for the plain, CBM, and ABM surfaces. The CHF data were normalized by the maximum CHF. Maximum CHF was always obtained at the horizontal-upward position ($\theta = 0$ deg). As seen in Fig. 8, CHF data for each surface follow a similar trend versus angular position. The CHF value is decreased as
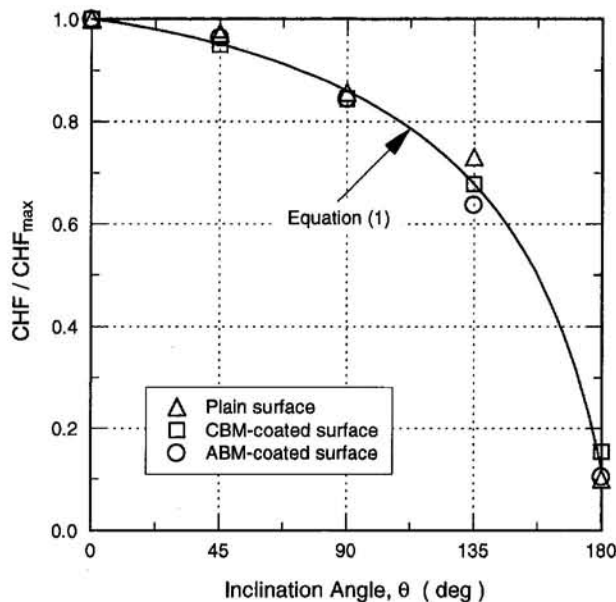

Fig. 6 Inclination effects on pool boiling (plain surface)

Fig. 8 Normalized CHF versus inclination angle

inclination angle is increased, decreasing dramatically for 135 deg $< \theta <$ 180 deg. The similarity in the normalized CHF data for each of the three different heater surfaces shows that the CHF mechanism is strongly affected by heater orientation. The normalized CHF data were correlated against inclination angle using the following empirically derived equation:

$$\frac{CHF}{CHF_{max}} = 1.0 - (0.00120)\theta \tan (0.414\theta)$$

$$- 0.122 \sin (0.318\theta) \quad (1)$$

As seen in Fig. 8, Eq. (1) is within ± 8 percent of the experimental data for $\theta <$ 135 deg, and ± 27 percent for $\theta =$ 180 deg.

For plain, untreated surfaces, El-Genk and Guo (1993) used a different equation to correlate normalized CHF data with inclination angle. They used the general form suggested by Kutateladze (1952) and Zuber (1959), except here the coefficient, $C(\theta)$, is a function of inclination angle:

$$CHF(\theta) = C(\theta)\rho_v^{1/2} h_{fg} [\sigma g (\rho_l - \rho_v)]^{1/4} \quad (2)$$

In Eq. (2), Kutateladze and Zuber used a constant value of 0.131 in place of $C(\theta)$. El-Genk and Guo derived three different $C(\theta)$ functions for three boiling liquids based upon the experimental data of Beduz et al. (1988), El-Genk and Guo (1993), and Vishnev et al. (1976). The experimental data and their fitted curves are plotted together in Fig. 9 to compare with Eq. (1). Beduz et al. (1988) tested for nitrogen, El-Genk and Guo (1993) for water, and Vishnev et al. (1976) for helium. Beduz et al. used two different heater materials, copper and aluminum. The data sets from the copper and aluminum heaters were compared with the current correlation. For 0 deg $< \theta <$ 160 deg, the normalized CHF data of Beduz et al. from the copper heater agree well with Eq. (1), whereas the data from the aluminum heater scatter below Eq. (1). As inclination angle is increased further, their copper and aluminum CHF data show larger values than the correlation and increased scatter. El-Genk and Guo produced CHF data for downward-facing positions ($\theta =$ 90 to 180 deg). The CHF_{max} of their data was not reported and was therefore assumed to match Zuber's (1959) prediction: CHF_z = 111 W/cm^2 for saturated water. Their normalized CHF data show a similar scattering trend with those of Beduz et al. around Eq. (1). The CHF data of helium from Vishnev et al. and those of FC-72 from You (1990) are located below and above Eq.

(1), respectively. Most of the other data fell between the two bounds provided by the data of Vishnev et al. and You. You (1990) used a platinum-sputtered heater (5 mm $\times$ 5 mm) in gassy subcooled FC-72. As discussed by Bar-Cohen and McNeil (1992), and Carvalho and Bergles (1992), a thin-film heater with a small heater effusivity experiences a different CHF mechanism from the conventional "thick" metal heater. Local dry patches on some portions of the thin-film heater can produce lower CHF values than those of thick heaters by the hydrodynamic CHF mechanism. Considering the different characteristics of the test heaters, both the present data and those of You exhibit similar trends.

Conclusions

Experiments were performed to understand the effects of surface orientation on the pool boiling performance of flush-mounted square heaters. Three heater surfaces (plain, copper-particle-coated, and aluminum-particle-coated) were tested in a pool of saturated FC-72 at atmospheric pressure.

1 Micro-porous-enhanced surfaces (CBM and ABM) showed about an 80 percent reduction in incipience superheat, about a 330 percent enhancement in the nucleate boiling heat transfer coefficient, and about a 100 percent enhancement in CHF over an unenhanced surface. These performance enhancements were due to the creation of micro-porous structures on the heater surface, which significantly increased the number of active nucleation sites.

2 When the plain surface was rotated from $\theta =$ 0 to 90 deg, higher inclination angles provided better heat transfer in the nucleate boiling regime. However, as the orientation angle was further increased from $\theta =$ 90 to 180 deg, nucleate boiling heat transfer noticeably decreased at higher heat fluxes. This reduction in boiling heat transfer contrasts with previous researchers' observations at the partially developed nucleate boiling region. For the present test, due to the higher heat-flux value (or wall superheat value) required to initiate nucleate boiling in FC-72, the partially developed nucleate boiling region was replaced by single-phase natural convection.

3 Nucleate boiling superheats of the micro-porous-enhanced surfaces were independent of orientation. This behavior is attributed to the presence of active nucleation sites over the entire heater surface regardless of orientation angle.
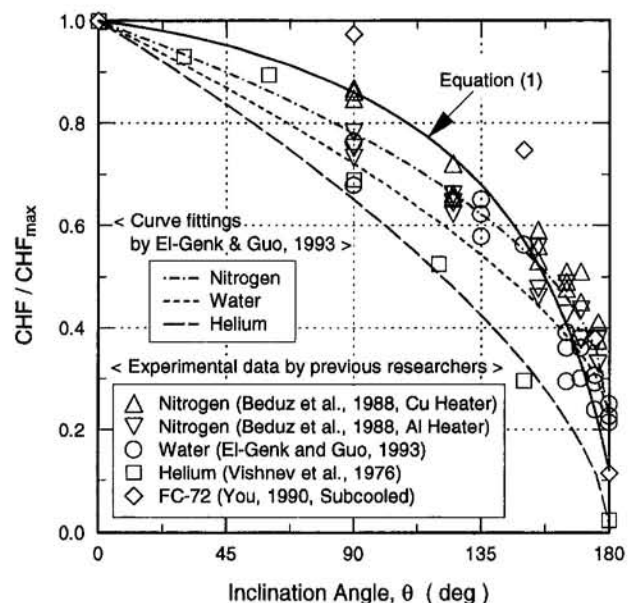

Fig. 9 CHF value comparisons with published data

4   Normalized CHF data at different orientations were correlated against inclination angle using the following empirically derived equation:

$$\frac{CHF}{CHF_{max}}$$

$$= 1.0 - (0.00120)\theta \tan (0.414\theta) - 0.122 \sin (0.318\theta)$$

The similarity in normalized CHF data for the three different heater surfaces (plain, CBM, and ABM) shows that the CHF mechanism is strongly affected by heater orientation.

Acknowledgments

References

Bar-Cohen, A., and McNeil, A., 1992, ''Parametric Effects of Pool Boiling Critical Heat Flux in Dielectric Liquids,'' *Pool and External Flow Boiling,* ASME, pp. 171–175.

Beduz, C., Scurlock, R. G., and Sousa, A. J., 1988, ''Angular Dependence of Boiling Heat Transfer Mechanisms in Liquid Nitrogen,'' *Advances in Cryogenic Eng.,* Vol. 33, pp. 363–370.

Carvalho, R. D. M., and Bergles, A. E., 1992, ''The Effects of the Heater Thermal Conductance/Capacitance on the Pool Boiling Critical Heat Flux,'' *Pool and External Flow Boiling,* ASME, pp. 203–211.

Chen, L. T., 1978, ''Heat Transfer to Pool-Boiling Freon From Inclined Heating Plate,'' *Letters in Heat and Mass Transfer,* Vol. 5, pp. 111–120.

Czikk, A. M., O'Neill, P. S., and Gotzzman, C. F., 1981, ''Nucleate Boiling From Porous Metal Film: Effect of Primary Variables,'' ASME HTD-Vol. 18, pp. 109–122.

El-Genk, M., and Guo, Z., 1993, ''Transient Boiling From Inclined and Downward-Facing Surfaces in a Saturated Pool,'' *Int. J. Refrig.,* Vol. 16, No. 6, pp. 414–422.

Fujii, M., Nishiyama, E., and Yamanaka, G., 1979, ''Nucleate Pool Boiling Heat Transfer From Micro-porous Heating Surface,'' ASME HTD-Vol. 18, pp. 45–51.

Githinji, P. M., and Sabersky, R. H., 1963, ''Some Effect of the Orientation of the Heating Surface in Nucleate Boiling,'' ASME JOURNAL OF HEAT TRANSFER, Vol. 85, No. 4, p. 379.

Ishigai, S., Inoue, K., Kiwaki, Z., and Inai, T., 1961, ''Boiling Heat Transfer From a Flat Surface Facing Downward,'' *Int. Heat Transfer Conf.,* Paper No. 26.

Jung, D. S., Venart, J. E. S., and Sousa, A. C. M., 1987, ''Effects of Enhanced Surfaces and Surface Orientation on Nucleate and Film Boiling Heat Transfer in R-11,'' *Int. J. Heat Mass Transfer,* Vol. 30, No. 12, pp. 2627–2639.

Kutateladze, S. S., 1952, ''Heat Transfer in Condensation and Boiling,'' AEC Report No. AEC-tr-3770.

Lienhard, J. H., 1985, ''On the Two Regimes of Nucleate Boiling,'' ASME JOURNAL OF HEAT TRANSFER, Vol. 107, pp. 262–264.

Marcus, B. D., and Dropkin, D., 1963, ''The Effect of Surface Configuration on Nucleate Boiling Heat Transfer,'' *Int. J. Heat Mass Transfer,* Vol. 6, pp. 863–867.

Moissis, R., and Berenson, P. J., 1963, ''On the Hydrodynamic Transition in Nucleate Boiling,'' ASME JOURNAL OF HEAT TRANSFER, Vol. 85, No. 3, pp. 221–229.

Nishikawa, K., Fujita, Y., Uchida, S., and Ohta, H., 1984, ''Effect of Surface Configuration on Nucleate Boiling Heat Transfer,'' *Int. J. Heat Mass Transfer,* Vol. 27, No. 9, pp. 1559–1571.

Nishio, S., and Chandratilleke, G. R., 1989, ''Steady-State Pool Boiling Heat Transfer to Saturated Liquid Helium at Atmospheric Pressure,'' *JSME Int. J.,* Series II, Vol. 32, No. 4, pp. 639–645.

O'Connor, J. P., and You, S. M., 1995, ''A Painting Technique to Enhance Pool Boiling Heat Transfer in Saturated FC-72,'' ASME JOURNAL OF HEAT TRANSFER, Vol. 117, pp. 387–393.

O'Connor, J. P., You, S. M., and Price, D. C., 1995, ''Thermal Management of High Power Microelectronics via Immersion Cooling,'' *IEEE Trans. CPMT,* Part A, Vol. 18, No. 3, pp. 656–663.

Thome, J. R., 1990, *Enhanced Boiling Heat Transfer,* Hemisphere Pub. Corp., New York.

Vishnev, I. P., Filatov, I. A., VinoKur, Y. G., Gorokhov, V. V., and Svalov, G. G., 1976, ''Study of Heat Transfer in Boiling of Helium on Surfaces With Various Orientations,'' *Heat Transfer—Soviet Res.,* Vol. 8, No. 4, pp. 104–108.

You, S. M., Simon, T. W., Bar-Cohen, A., and Tong, W., 1990, ''Experimental Investigation of Nucleate Boiling Incipience With a Highly Wetting Dielectric Fluid (R-113),'' *Int. J. Heat Mass Transfer,* Vol. 33, No. 1, pp. 105–116.

You, S. M., 1990, ''Pool Boiling Heat Transfer with Highly-Wetting Dielectric Fluids,'' Ph.D. Thesis, Univ. of Minnesota, Minneapolis, MN.

You, S. M., Simon, T. W., and Bar-Cohen, A., 1991, ''A Technique for Enhancing Boiling Heat Transfer With Application to Cooling of Electronic Equipment,'' *IEEE Trans. CHMT,* Vol. 15, No. 5, pp. 90–96.

Zuber, N., 1959, ''Hydrodynamic Aspects of Boiling Heat Transfer,'' AEC Report No. AECU-4439, Physics and Mathematics.

Modeling of Nonequilibrium Surface Melting and Resolidification for Pure Metals and Binary Alloys

G.-X. Wang

E. F. Matthys
email: matthys@engineering.ucsb.edu

Department of Mechanical and
Environmental Engineering,
University of California,
Santa Barbara, CA 93106

A model was developed for surface melting and resolidification of both pure metal and binary alloy substrates. Nonequilibrium kinetics are introduced in the model to account for the departure from thermodynamic equilibrium at the solid/liquid interface. The modeled problem involves a moving boundary with both heat and solute diffusion and is solved by an implicit control volume integral method with solid/liquid interface immobilization by coordinate transformation. To illustrate the model capabilities, we have analyzed laser-induced surface melting of pure metals (Al, Cu, Ni, Ti) and dilute Al–Cu alloys, and some typical results are presented. The computation results show some large solid overheating and melt undercooling effects, which result from the high heat flux and the slow kinetics. Large interface velocity variations are also seen during the process, depending on the substrate material and laser flux. Complex interface velocity variations during the earlier stages of resolidification were also predicted for the alloys, and result from interactions between the several physical mechanisms involved. Results on interface temperatures, solute concentrations, and nonequilibrium partition coefficients are also presented.

1 Introduction

Surface modification by laser processing techniques has been used increasingly in recent years. It is intended to alter the composition and microstructure of the surface layer and thereby to improve the surface properties. The beneficial effects of using a high-power laser for surface treatment are: conservation of strategic or expensive alloying elements, formation of nonequilibrium crystalline and amorphous phases, grain refinement, homogenization of microstructures, increased solid solubilities of alloying elements, and modification of segregation patterns (Molian, 1989). Many such effects of laser surface processing are attributed to the rapid heating and subsequent nonequilibrium solidification achieved. In addition, quantitative measurements of interface velocity and temperature of pulsed laser irradiation of semiconductors (Tsao et al., 1986a), as well as of aluminum (Tsao et al., 1986b) and some noble metals (MacDonald et al., 1989), have provided important information toward the understanding of the fundamental physics of nonequilibrium melting and solidification.

Experimental work on various laser surface techniques has been conducted for both fundamental studies (Gill and Kurz, 1995) and engineering applications (Molian, 1989). Numerical work has also been carried out to analyze the related solidification process, with much of the earlier work on heat transfer and melt pool formation being based on an equilibrium phase change model (e.g., Hsu et al., 1978; Sekhar et al., 1983). This equilibrium model assumes that the solid/liquid interface remains at local equilibrium during melting and solidification, i.e., that the interface temperature remains at the equilibrium melting temperature. This assumption excludes the kinetics effects of phase change and reduces the analysis of the process to a pure thermal and hydrodynamic problem. This is a good approximation for cases with low laser energy and long laser exposure time, but in order to take full advantage of the laser surface modification technique, one might want instead a high intensity and a very short exposure time. This combination would then generate very fast melting and rapid resolidification. Under such conditions, the solid/liquid interface may exhibit strong nonequilibrium effects. These nonequilibrium features may then result in the physical effects that make these surface processing techniques attractive.

The existence of nonequilibrium effects in the surface melting process makes its analysis more complicated, however, because of strong interactions between heat transfer, mass diffusion, and nonequilibrium melting and solidification kinetics. Mathematically, the boundary conditions at the moving solid/liquid interface need then to reflect the nonequilibrium phase change kinetics. These conditions are usually expressed by interface response functions (Baker and Cahn, 1971), which relate the interface velocity to the interface temperature and the composition of the liquid or solid.

The interface response functions are a mathematical description of how atoms leave from or are incorporated onto lattice sites during melting or solidification, and reflect the kinetics of the phase change process. A kinetics analysis indicates that the interface growth can be either short-range diffusion-limited or collision-limited (Turnbull, 1981; Aziz and Boettinger, 1994). In the former case, the movement of atoms across the interface from liquid to solid is similar to the diffusion in the bulk melt. In the latter case, however, crystallization events are assumed to be limited only by the impingement rate of atoms on the crystal surface. Experimental results suggest that diffusion-limited growth would occur for crystallization of oxide glasses and covalent materials, but that the collision-limited growth may be better suited to the cases of simple molecular melts (Aziz and Boettinger, 1994).

Some models of laser surface melting using various types of nonequilibrium kinetics relationships have been developed in the literature. For example, Wood and Geist (1986) include the kinetics-induced overheating and undercooling when analyzing

pulsed laser melting of amorphous silicon thin film deposed on crystalline silicon. MacDonald et al. (1989) developed a similar model but used an implicit finite difference method and an updated melting and solidification kinetics theory to analyze the laser surface melting of noble metals (copper and gold). Some simplified analyses, which include nonequilibrium effects in alloy solidification, have also been conducted for the planar alloy solidification in pulsed laser surface melting by Reitano et al. (1994). Their work, however, decouples the heat and mass diffusion problems, and the interface velocity calculated by a one-dimensional heat conduction model is used as input in a one-dimensional diffusion model with ''solute trapping'' taken into account. Kar and Mazumder (1987) also performed an analysis of the laser-cladding process with a one-dimensional heat and mass diffusion model. This model included solute trapping but did not include the variation of the interface temperature with the velocity and solute concentrations at the interface.

In the present paper, a general model of heat and mass transfer during pulsed laser surface melting is developed for both pure metals and dilute binary alloys. The collision-limited growth kinetics relationships were thought to be better suited for such materials and were thus incorporated into this model to treat both nonequilibrium melting and resolidification. Therefore, both the overheating during melting and the undercooling during resolidification at the solid/liquid interface can be calculated. For a dilute binary alloy, the solute trapping phenomena is also included by using Aziz's (1982) continuous growth solute trapping model. The resulting model is a moving boundary problem with heat and solute diffusion and strongly nonlinear coupled moving boundary conditions. The numerical treatment of this problem is based on a recently developed numerical technique (Wang and Matthys, 1993) used to model planar alloy solidification during the splat cooling process. This numerical method is based on an implicit finite difference method with solid/liquid interface immobilization by coordinate transformation. An efficient iteration scheme and a nonuniform grid are also used to treat the unknown interface parameters and the large solute gradient in front of the interface. For illustration of the model capabilities, laser surface melting of pure metals (Al, Cu, Ni, Ti) and dilute Al–Cu alloys is analyzed and some typical results are presented. Although we are not aware of experimental data that would enable us to verify the model predictions directly, we believe that these numerical results will contribute to a better understanding of the basic physics of this complex process.

2 Physical Model and Formulation

2.1 Assumptions. In laser surface melting, the substrate will heat up when the laser is fired at the substrate, with the melting process starting when the surface temperature reaches the melting temperature of the material. As the substrate is further irradiated, the liquid layer thickens and the surface temperature may keep increasing. After the laser is turned off, the melt superheat may result in the melting process continuing for some time until the molten layer reaches a maximum depth (when the heat flux from the melt into the solid/liquid interface is equal to the heat flux from the interface into the solid). At that point, the interface stops and the melt begins to resolidify.

In an actual situation, the process is complicated by the complex geometry of the melt pool and by complex solidification morphologies. To make this difficult problem solvable, however, we have developed a simple one-dimensional model with the following simplifying assumptions: (1) The substrate is treated as a semi-infinite solid of uniform composition extending in the positive y direction; (2) the laser beam is assumed to have a large cross section compared to the depth into the substrate over which significant temperature changes occur; (3) the laser energy is distributed evenly over the substrate and can be represented by a constant heat flux; (4) the melt pool is assumed to be shallow, so that convective effects can be neglected and only diffusion (of both heat and mass) is taken into account; (5) a stable planar solid/liquid interface exists during both melting and resolidification, which excludes bulk nucleation in the liquid region.

The first assumption is easy to justify and understand. The second and fourth assumptions can also be satisfied in practice for pulsed laser surface melting, which make the one dimensionality of the model acceptable. A uniform laser beam is not so readily achievable, however, so the third assumption is only an approximation of the real condition. In addition, the absorption and reflection of light from a material is not strictly a surface phenomenon and some penetration of the laser radiation may affect a significant fraction of the molten layer. In this model, we use a constant heat flux at the surface rather than an energy source in the substrate such as that used by Wood and Geist (1986), but considering the inevitable uncertainties in the laser reflectivity and absorption coefficients of the material, this simplification is believed to be appropriate. The first four assumptions are therefore adequate for most laser surface processes, but the fifth assumption may limit our model to some more specific situations. Indeed, a stable planar interface may readily exist in pure metals, but is present in alloy systems only when the interface velocity is either very small (i.e., less than the constitutional undercooling criterion) or larger than the absolute stability velocity (Mullins and Sekerka, 1964). For the conditions considered in this work, the calculated interface velocities are indeed much greater than this absolute velocity (e.g., about 3.0 m/s for Al-2wt%Cu alloy) except at the end of melting, when the interface stops. In addition, if bulk nucleation takes place in the liquid region (Baeri, 1994), the assumption of a planar interface will be invalid. We are also considering here

---

Nomenclature

C = local solute concentration, wt%
C_0 = initial solute concentration, wt%
D = solute diffusivity, m²/s
d_{max} = maximum melt depth, μm
ΔG = free energy difference between solid and liquid, J/mole
ΔH_m = heat of fusion, J/mole
k = partition coefficient
L = latent heat of solidification, J/kg
m = slope of liquidus or solidus, K/wt%
Q = laser heat flux, W/m²
R = universal gas constant = 8.314 J/K-mole

ΔS = entropy of crystallization, J/K-mole
T = temperature, K
T_0 = temperature at which the solid and liquid (of same solute concentration) have the same free energy, K
T_{sub} = initial substrate temperature, K
t = time, ns
Δt = duration of laser pulse, ns
u_s = speed of sound in liquid metal, m/s
V_D = interfacial characteristic diffusion velocity, m/s
V_i = interface velocity, m/s

y = spatial coordinate perpendicular to the substrate, μm
α = thermal diffusivity, m²/s
λ = thermal conductivity, W/m-K
μ_k = linear kinetics coefficient, m/s-K
ρ = density, kg/m³

Subscripts and Superscripts

e = equilibrium
i = interface
j = solid or liquid phase
L = liquid
S = solid
m = melting temperature

only cases where the time and length scales are such that the continuous media assumption and Fourier's diffusion law still hold. This would likely be the case for surface melting processes with laser pulses longer than a nanosecond or so.

2.2 Mathematical Description of the Model. Using the assumptions mentioned above, the situation can be modeled as one-dimensional heat and mass diffusion with nonequilibrium phase change. The corresponding governing equations for a binary alloy are:

$$\frac{\partial T_j}{\partial t} = \frac{\partial}{\partial y}\left(\alpha_j \frac{\partial T_j}{\partial y}\right) \tag{1}$$

and

$$\frac{\partial C_j}{\partial t} = \frac{\partial}{\partial y}\left(D_j \frac{\partial C_j}{\partial y}\right) \tag{2}$$

where T is the temperature, C is the solute concentration, t is the time, y is the coordinate into the substrate perpendicular to the surface, α is the thermal diffusivity, and D is the solute diffusivity (both assumed independent of temperature or concentration). The subscript j stands for either the solid or liquid phase. Naturally, the mass transfer equation is not necessary for the case of a single-component system.

At the solid/liquid interface, energy and mass conservation should be satisfied, which gives two interface conditions:

$$\rho_L L V_i = \lambda_s \left.\frac{\partial T_S}{\partial y}\right|_i - \lambda_L \left.\frac{\partial T_L}{\partial y}\right|_i \tag{3}$$

and

$$(C_L^i - C_S^i)V_i = D_S \left.\frac{\partial C_S}{\partial y}\right|_i - D_L \left.\frac{\partial C_L}{\partial y}\right|_i \tag{4}$$

where L is the latent heat of fusion, V_i the interface velocity, C_L^i and C_S^i the solute concentrations in the liquid and solid phases at the interface, ρ the density, and λ the thermal conductivity. The subscripts S and L represent solid and liquid, respectively. The subscript or superscript i indicate that the gradients are evaluated at the interface. It should be pointed out that these two equations are valid for both melting and resolidification if a proper sign is used for the interface velocity. In the present case, we assign to this velocity a positive value for the melting process and a negative one for resolidification.

2.3 Nonequilibrium Kinetics Conditions at the Interface. Besides the energy and mass conservation equations shown above, we need additional interface conditions to complete the problem description. These conditions arise from thermodynamic and kinetic considerations of phase change, and provide two more relationships between the interface parameters, needed because there are four unknowns at the interface: V_i, T_i, C_L^i, and C_S^i.

In a conventional melting or solidification problem with low interface velocity, it is usually acceptable to assume that the kinetics are very fast and that the solid/liquid interface is at thermodynamic equilibrium. The interface conditions can then be easily derived from thermodynamic constraints of phase change. For example, the interface will remain at the equilibrium melting temperature during melting and solidification of pure metals; whereas for a binary alloy, the interface temperature is related to the solute concentrations at the interface through the equilibrium phase diagram. Under these conditions, the phase change process is primarily controlled thermally. In laser surface melting, however, the interface velocity may be so large that the interface may not be at equilibrium and that

Table 1 Physical properties for the pure metals used in the calculations (Brandes, 1983; Iida and Guthrie, 1988)

Parameter	Units	Al	Cu	Ni[†]	Ti[‡]
T_m	K	933.6	1356	1728	1941
L	J/kg	3.97×10^5	2.0×10^5	2.92×10^5	3.0×10^5
ΔH_m	J/mole	1.05×10^4	1.3×10^4	1.7×10^4	1.5×10^4
λ_L	W/m-K	105	170	43	13
λ_S	W/m-K	210	244	74	13
C_{PL}	J/kg-K	1080	495	620	700
C_{PS}	J/kg-K	1180	473	595	680
ρ_L	kg/m³	2390	8000	7900	4110
ρ_S	kg/m³	2550	8900	8900	4500
α_L	m²/s	4.1×10^{-5}	4.3×10^{-5}	0.9×10^{-5}	0.5×10^{-5}
α_S	m²/s	7.0×10^{-5}	5.8×10^{-5}	1.4×10^{-5}	0.4×10^{-5}
$\Delta H_m/RT_m^2$	1/K	14.4×10^{-4}	8.5×10^{-4}	6.9×10^{-4}	4.7×10^{-4}
$\Delta S_m/R$	-	1.35	1.15	1.19	0.9
u_s	m/s	4688	3485	4036	5230
μ_k	m/s-K	1.74	0.94	0.85	1.0

† Data for thermal conductivity from Hsu *et al.* (1978);
‡ Data for liquid thermal conductivity was assumed to be the same as that of solid.

solidification kinetics may play an important role. Consequently, more general interface conditions are necessary.

2.3.1 Pure Metals. Collision-limited growth theory provides the following kinetics relationship for crystal growth of pure metals (Jackson, 1975; Tsao et al., 1986a; MacDonald et al., 1989):

$$V_i = u_s \exp(-\Delta S/R)[1 - \exp(-\Delta G/RT_i)] \tag{5}$$

where u_s is the speed of sound in the melt, ΔS the entropy of crystallization, R the universal gas constant, ΔG the free energy difference between the liquid and solid, and T_i the interface temperature. With the approximation $\Delta G = \Delta H_m(T_m - T_i)/T_m$, where ΔH_m is the heat of fusion and T_m is the equilibrium melting temperature, we can approximate Eq. (5) for small deviations of the interface temperature from the equilibrium melting temperature (i.e., $T_i - T_m$) as follows:

$$V_i = -\mu_k(T_m - T_i) \tag{6}$$

with μ_k (the linear kinetics coefficient) defined as

$$\mu_k = u_s \exp(-\Delta S_m/R)\Delta H_m/(RT_m^2). \tag{7}$$

A minus sign is added to the kinetics equation, Eq. (6), for consistency with the energy equation, Eq. (3), i.e., we use a positive velocity for melting and a negative one for resolidification. Equation (6) is used for both melting and resolidification. Table 1 gives the linear kinetics coefficients for four metals (Al, Cu, Ni, Ti) calculated with Eq. (7). It should be pointed out that the linear kinetics coefficient obtained from this collision-limited kinetics model is about two orders of magnitude larger than that obtained from a diffusion-limited kinetics model, which was often used in the modeling of splat cooling and melt spinning (Clyne, 1984; Wang and Matthys, 1991).

2.3.2 Binary Alloys. The addition of solute to a pure metal changes in principle the crystallization process and its kinetics mechanisms. For dilute alloys, however, it is expected that the kinetics do not differ too much from those of a pure metal and that the kinetics equation, Eq. (5), may still be valid with the free energy change between liquid and solid being re-evaluated to account for the existence of a solute element. For a dilute binary alloy with straight equilibrium liquidus and solidus of slopes m_L^e and m_S^e, respectively, the corresponding linear kinetics relationship can be written (Boettinger and Coriell, 1986; Aziz and Boettinger, 1994):

$$V_i = -\mu_k(T_m + m_L C_L^i - T_i) \tag{8}$$

with the slope of the nonequilibrium liquidus curve

$$m_L = m_L^e[1 + (k_e - k(1 - \ln k/k_e))/(1 - k_e)]. \quad (9)$$

The linear kinetics coefficient μ_k is the same as that for the solvent and is given by Eq. (7). $k = C_S^i/C_L^i$ is the nonequilibrium partition coefficient, which will be closer to unity than the equilibrium partition coefficient $k_e = m_L^e/m_S^e$. T_m is the equilibrium melting temperature of the solvent.

In the kinetics relationship (8) for dilute binary alloys, a new parameter—the nonequilibrium partition coefficient k—is implicitly introduced in m_L. Its value should be derived from the same kinetics theory of phase change. Various models have been proposed to describe this parameter, and we use here the functional form by Aziz (1982) for continuous growth of dilute alloys:

$$k(V_i) = (k_e + V_i/V_D)/(1 + V_i/V_D) \quad (10)$$

where V_D is the interface characteristic diffusion velocity.

Compared to the equilibrium interface conditions for a binary alloy, two important features are introduced by the kinetics models: the interface solid overheating or melt undercooling and the nonequilibrium partitioning or solute trapping. When an interface velocity much larger than V_D is achieved, Aziz's model (Eq. (10)) will give a nonequilibrium partition coefficient very close to one. This means complete solute "trapping" or "partitionless" solidification.

These equations are needed for the solidification part of the process, but when applying this kinetics model to melting, some simplification may be made if the interface velocity is much greater than the interface characteristic diffusion velocity. Since the solute diffusivity in the solid phase is small, there is limited solute redistribution in the solid phase during melting, and solute partitioning may be suppressed. The melt would then have the same composition as the solid. In this case, the partition coefficient k for melting has a value of one and the melting kinetics reduces to

$$V_i = -\mu_k(T_0 - T_i) \quad (11)$$

where T_0 is the temperature at which the free energy of the solid is the same as that of a liquid with the same solute concentration. For a dilute binary alloy, it can be calculated as (Boettinger and Coriell, 1986):

$$T_0 = T_M - (m_L^e C_0 \ln k_e)/(1 - k_e). \quad (12)$$

The use of T_0 as equivalent equilibrium interface temperature for the alloy during melting is an appropriate simplification for our case over most of the melting phase, with the possible exception of the very end of melting (when the planar interface assumption may also break down), a very short period. This simplification allows us to avoid having to calculate solute diffusion in the solid, which would require an inordinately fine grid in that boundary layer. Note also that we assume here that the temperature is continuous at the interface even if the solute concentration is discontinuous at that location.

With these equations, the mathematical description of the nonequilibrium conditions at the solid/liquid interface for both melting and solidification is complete for both pure metals and dilute binary systems. The other thermal boundary conditions can be easily defined. The substrate top surface is assumed to be adiabatic, except during laser heating, when a constant heat flux Q is exerted over a period Δt. Indeed, the radiative and convective heat losses from this surface are so small compared to the fluxes into the substrate that the former can be safely neglected. The substrate is also taken as a semi-infinite body with a constant and uniform temperature before heating.

3 Numerical Approach

The mathematical problem described above is a moving boundary problem with both heat and solute diffusions. The temperature and concentration fields are also strongly coupled

at the moving interface through the nonequilibrium kinetics relationships. We have solved this problem by combining an implicit control volume integral method with an immobilization of the moving interface by coordinate transformation. A detailed general description of the coordinate transformation, the nonuniform grid, the derivation of the difference equations, and the iteration scheme for the moving interface can be found elsewhere (Wang and Matthys, 1993; Wang 1995). Accordingly, we describe hereafter only their implementation for the laser surface melting problem.

At first, after the laser is turned on at time $t = 0$, there is only heat conduction in the solid substrate. An implicit method is used in this calculation. Then, as soon as the surface temperature reaches the melting temperature (i.e., the equilibrium melting temperature for pure metals or the T_0 temperature for binary alloys), the melting process should start. A solid "overheating" (i.e., the solid showing a temperature higher than these equilibrium melting temperatures) is, however, possible, and is calculated by satisfying both the kinetics relationships and the energy balance conditions through an iterative process. At each iteration within a given time step, the interface temperature is first calculated from a guessed interface velocity through the corresponding melting kinetics equations. The temperature field can then be solved with the temperature equations. A new interface velocity is then estimated from the energy conservation equation using the temperature profile just calculated. Convergence is reached when the velocity changes little over two successive iterations. The next time step is then tackled, and so on. When the laser is turned off, the corresponding surface boundary condition is changed to adiabatic.

When the calculated interface velocity finally shows a negative value, the melting kinetics relationships are replaced by the solidification kinetics relationships (these are the same for pure metals) and resolidification starts. For pure metals, no change in the solution procedure is needed because of the symmetry of the two processes. For binary alloys, however, a change in the solution sequence must be made. In this case, during each iteration, the solute concentration equations are first solved using a guessed interface velocity to determine the solute concentration field as well as the solute concentrations of the solid and liquid phases at the interface. This is done by using the mass conservation condition at the interface together with the model for the nonequilibrium partition coefficient. The interface temperature can then be estimated from the same interface velocity and the calculated interface solute concentration through the solidification kinetics relationship. After having determined the interface temperature, the temperature field is solved for, and a correction to the interface velocity can be made from the energy conservation condition. This process is repeated until convergence is reached, after which the next time step is handled in the same manner.

4 Numerical Results and Discussions

Calculations have been performed to provide some quantitative information on laser surface melting of both pure metals and binary alloys. Four metals (Al, Cu, Ni, and Ti) were chosen to represent a range of equilibrium melting temperature and thermal properties. A dilute Al–Cu alloy was also studied as a representative case of alloy solidification. Some results are presented here. In all cases, the computation domain was 50 μm, which is much thicker than the molten layer thickness. A uniform grid was used for the temperature equations in the liquid region and for the concentration equations in the solid region, but a nonuniform grid was used for the temperature equations in the solid region and for the concentration equations in the liquid region. A total of 600 nodes were used in the calculation with 300 nodes in each region. The relaxation factor chosen ranged from 0.1 to 0.5. An extensive grid study was performed and it was found that these parameters gave grid-
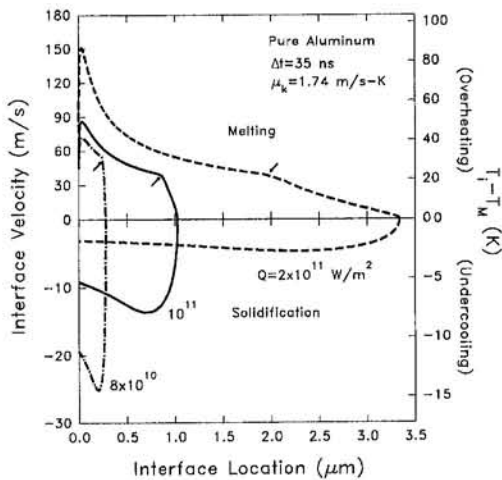
Fig. 1 Interface velocity and solid overheating or melt undercooling during laser surface melting of pure aluminum as a function of the solid/ liquid interface location for three laser fluxes: Q = 8 × 10¹⁰, 10¹¹, and 2 × 10¹¹ W/m². Note the different vertical scales for melting and solidification. The arrows indicate when the laser is turned off. [Δt = 35 ns, T_{sub} = 300 K].

independent results. An appropriate time step is also critical to maintain solute conservation during the solidification calculations. The time step used in these calculations is 0.01 ns, which ensures solute conservation within 0.1 percent. This time step also gives time step-independent results.

4.1 Pure Metals. Table 1 shows the materials properties of the four pure metals (Al, Cu, Ni, and Ti). All the materials properties correspond to elevated temperatures near the equilibrium melting point. Because the physical properties of the undercooled liquid or overheated solid were not available, the properties of the corresponding equilibrium phase were used instead. Table 1 also gives the linear kinetics coefficient, μ_k, together with its three constituting components: $\Delta H_m / RT_m^2 = \Delta S_m / RT_m$, $\Delta S_m / R$, and the speed of sound u_s (Iida and Guthrie, 1988). Because $\Delta S_m / R$ for pure metals with simple crystal structure (bcc or fcc) does not vary much (the Richard rule), the linear kinetics coefficients of pure metals depend mainly on their equilibrium melting temperature T_m (the higher the T_m, the smaller the μ_k), and the speed of sound u_s. The speed of sound in liquid metals varies with the metal but is mostly in the range of about 3000 to 5500 m/s. As we can see, the values of the linear kinetics coefficient are close to 1.0 m/s-K for the high melting point metals Cu, Ni, and Ti (i.e., for $T_m > 1250$ K). The value for aluminum is slightly larger because of its low melting temperature and was estimated to be about 1.74 m/s-K.

Typical interface velocity variations during laser surface melting of pure aluminum are shown in Fig. 1 for three heat fluxes within the range typical for this type of application (8 × 10¹⁰, 10¹¹, and 2 × 10¹¹ W/m²) taking into account nonequilibrium effects at the interface. The duration of the laser pulse used is 35 ns. In Fig. 1, the horizontal coordinate is the interface location (distance from the substrate surface). The vertical axes are (1) the interface velocity with the positive values in the upper part of the graph representing the melting phase and the negative ones in the lower part for resolidification; and (2) the corresponding level of overheating or undercooling. These quantities are proportional for the linearized case discussed here (per Eq. (6)). (Note that different scales are used for the upper and lower parts.)

Let us first look at the interface velocity during melting (the positive values). As we can see, a maximum value is reached very quickly after melting is initiated, and in all cases within a melt thickness less than 35 nm. This maximum is then followed

by a gradual decrease. As the melt layer thickens, the interface velocity slows down until the instant when the laser is turned off (indicated by arrows on the graph). The melting velocity drops then much faster, and especially so for the case of lower laser heat flux. As expected, for a given exposure time, the larger the laser heat flux, the higher the maximum velocity and the thicker the melt pool. In the present case, as the laser heat flux increases from 8 × 10¹⁰ to 2 × 10¹¹ W/m², the maximum interface velocity increases from 72 m/s to 151 m/s and the melt pool depth increases from 0.28 μm to 3.33 μm.

The occurrence of a maximum interface velocity during melting is a result of the interactions between heat transfer and melting kinetics. At the very beginning, the heat transfer into the interface is so fast that the melting is limited by the finite kinetics. As the melt layer begins to thicken, the thermal resistance of this layer reduces the high heat transfer from the surface to the interface. After the maximum is reached, the influence of kinetics quickly decreases, and the melting is dominated by heat transfer.

Melting stops when the heat flux from the melt to the solid/ liquid interface equals that from the interface to the solid. After that, the heat flux into the solid from the interface will be larger than that from the melt to the interface and the melt begins to resolidify. As we can see in Fig. 1, the absolute value of the solidification velocity first increases after the resolidification starts because of the diminishing melt superheat. (Here and hereafter, we use the absolute value of the solidification velocity when discussing relative change, even though the solidification velocity is given as negative in the graphs for clarity.) Later, the interface velocity reaches a maximum value. After that, the solidification velocity decreases because the substrate heats up. Figure 1 also shows that the maximum solidification velocity is a function of the laser flux for the same pulse duration. The larger the laser flux, the smaller the maximum solidification velocity, e.g., 4.7 m/s compared to 25.1 m/s when the input heat flux decreases from 2 × 10¹¹ to 8 × 10¹⁰ W/m². This variation of solidification velocity with laser flux can be better understood by considering the fact that the solidification velocity depends mainly on the temperature gradients in the solid and liquid near the interface. The smaller the laser flux (while still leading to surface melting), the smaller the melt thickness and the smaller the melt superheat and the solid heating, which will then result in a higher solidification rate.

Having introduced finite phase change kinetics in both melting and solidification (e.g., a linear kinetics coefficient μ_k = 1.74 m/s for pure aluminum) in the model, we can also calculate the corresponding interface overheating and undercooling as shown in the right-hand-side vertical axis in Fig. 1. (Note that solid overheating during melting is shown as positive values and melt undercooling during solidification as negative ones in Fig. 1.) As we can see, significant solid overheating and melt undercooling are calculated under these heat flux conditions. For example, a maximum solid overheating during melting of about 87 K is obtained for Q = 2 × 10¹¹ W/m², and a maximum melt undercooling of about 14 K for Q = 8 × 10¹⁰ W/m². It should be pointed out here that this model does not take into account nucleation issues for both melting and solidification. The solid overheating and melt undercooling result therefore only from the melting or crystalline growth processes: a large solid overheating or melt undercooling at the interface has to be generated in order to maintain a high melting or solidification velocity because of the finite kinetics taken into account in our model.

To illustrate better the kinetics of laser surface melting, some calculations for other pure metals have also been carried out, and some results are given in Fig. 2. This figure shows how the interface temperature departs from its equilibrium value for these metals (Al, Cu, Ni, Ti) as a function of the interface depth nondimensionalized by the maximum melt depth. (Note that the deviation of the interface temperature from its equilibrium
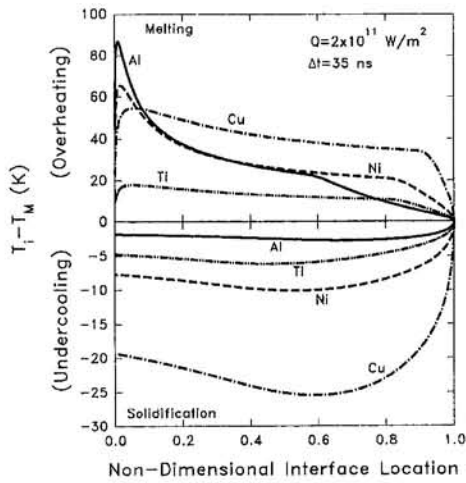
Fig. 2 Deviation of the interface temperature from its equilibrium value as a function of the solid/liquid interface location nondimensionalized by the maximum melt depth (d_{max}) during laser surface melting of four pure metals: Al (d_{max} = 3.33 μm), Cu (0.73), Ni (0.60), and Ti (0.56). Note the different vertical scales for melting and solidification. [Q = 10¹¹ W/m², Δt = 35 ns, T_{sub} = 300 K].

Table 2 Physical properties for the dilute aluminum alloys used in the calculations (Kurz and Fisher, 1989)

Parameter	Units	Al-Cu
T_m	K	933.6
C_0	wt%	2 or 5
m_L^o	K/wt%	-2.6
k_e	-	0.14
D_L	m²/s	3.0×10^{-9}
D_S	m²/s	3.0×10^{-13}
V_D	m/s	10

value is related to the interface velocity through the linear kinetics relationship (Eq. (6)).) In all cases, the input heat flux (Q = 2 × 10¹¹ W/m²) and the exposure time (Δt = 35 ns) are kept the same. As we can see, the materials properties have a strong effect on the processes. A large variation in solid overheating (and therefore in melting velocity) takes place during melting for Al, Ni, and Cu whereas smaller ones are seen for Ti, especially during the early stages of melting. For the resolidification process, however, small variations in melt undercooling are seen for Al, Ti, and Ni and larger ones for Cu. The higher thermal conductivity of copper leads to the largest melt undercooling (i.e., the largest solidification rate) and the largest solid overheating at the interface, except during the very beginning of melting when the kinetics dominate the process. For aluminum, however, the relatively large thermal conductivity is counterbalanced by a greater kinetics coefficient, resulting in the smallest undercooling. Its low melting temperature, on the other hand, affects the melting overheating. Experimental data are not available for direct comparison with these calculations, but a large solid overheating and melt undercooling has indeed been observed in experiments of laser surface melting of noble metals (MacDonald et al., 1989).

We need to point out here that for pure metals with rather large linear kinetics coefficients (e.g., around 1.0 m/s-K), the solid overheating and the melt undercooling needed under the present processing conditions are not large enough to change the thermal characteristics significantly. (The level of overheating and undercooling calculated justifies also the use of the linearized kinetics relationship (Eq. (6)).) The nonequilibrium model, however, does predict melt undercooling at the interface, which may be very important for better understanding of the phase selections and microstructure development, especially for materials with rather slow kinetics (e.g., Paul et al., 1994).

4.2 Binary Alloys. Next we examine the mass transfer effect on the laser surface melting process under nonequilibrium conditions at the interface. As discussed above, treatment of an alloy complicates the procedure on two counts: First, the solute partition at the interface resulting from the different solubilities of the solute in the solid and liquid phases leads to solute diffusion, which makes the mathematical analysis more complicated. Second, the kinetics model must include the nonequilibrium liquidus slope m_L and nonequilibrium partition coefficient k, both of which are strong functions of the interface velocity. The present model includes all these factors, and the effect of

nonequilibrium kinetics on laser surface melting of alloy is illustrated with sample calculations for dilute Al–Cu alloys (C_0 = 2 or 5 wt%). The laser flux was chosen as Q = 10¹¹ W/m² and the pulse duration Δt = 35 ns. The property values used in the calculations for the binary alloys (assumed to be the same for both) are given in Table 2 with values for pure aluminum used for the basic bulk thermal properties (Table 1).

Figure 3 shows the effect of initial Cu concentration on interface velocity variations during laser surface melting of dilute Al–Cu alloys. The effect of solute presence is also reflected by the varying melting temperature: T_m = 933.6 K for pure metal and a concentration-dependent T_0 temperature for binary alloys: T_0 = 921.7 K for C_0 = 2 wt% and T_0 = 903.9 K for C_0 = 5 wt%. As we can see in the figure, the difference in T_0 has little effect on the melting process before the laser is stopped. After that, melting continues as the superheated melt cools down, and as expected, the lower the melting temperature (i.e., for Al–5wt%Cu), the more superheated the melt is and therefore the deeper the melting process.

As the melt starts to resolidify, the solidification velocity for the alloys shows more complex variations. As shown in Fig. 3, for both alloys the resolidification velocity shows a small local maximum and then decreases very fast. The interface velocity then increases quickly again to another larger maximum and then finally decreases slowly to a quasi-steady state. We also see a strong effect of the solute concentration: the larger the solute concentration, the larger the maximum interface velocity.

The first small maximum in the interface velocity at the very beginning of resolidification likely results from our model assumptions on the transition from melting to resolidification.
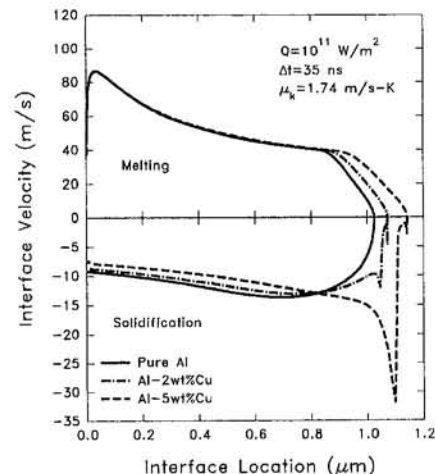

Fig. 3 Interface velocity variations during laser surface melting of dilute binary Al–Cu alloys as a function of the solid/liquid interface location for three initial solute concentrations: C_0 = 0, 2, and 5 wt%. Note the different vertical scales for melting and solidification. [Q = 10¹¹ W/m², Δt = 35 ns, T_{sub} = 300 K].
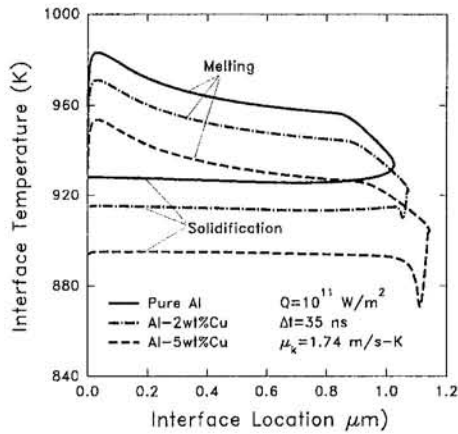
Fig. 4 Interface temperature variations during laser surface melting of dilute binary Al–Cu alloys as a function of the solid/liquid interface location for three initial solute concentrations: $C_0 = 0$, 2, and 5 wt%. [$Q = 10^{11}$ W/m^2, $\Delta t = 35$ ns, $T_{sub} = 300$ K].

Indeed, in this mode, resolidification is assumed to occur when the heat flux from the liquid to the interface is smaller than the heat flux from the interface to the solid phase. As soon as this happens, the kinetics model used is switched from its melting form (Eq. (11)) to its resolidification form (Eq. (8)). At the end of melting, the calculated interface temperature is T_0, which is, however, an undercooled state relative to the liquidus temperature. This melt undercooling will therefore result in a large solidification velocity at first per Eq. (8), followed by recalescence. During recalescence the undercooled melt near the interface will be rapidly heated up and the melt undercooling disappears quickly. This process takes place over a few tens of nanometers under the present conditions. It is this apparent undercooling that leads to the local maximum see in Fig. 3.

In an actual process, the situation may be even more complicated, in that the planar interface may become unstable and may break down to form cells when the melting velocity slows down. The transition from melting to solidification would then occur in a rather different configuration. As we see in Fig. 3, the interface velocity does increase quickly after solidification, however, and the stable planar interface assumption would be appropriate again.

The second maximum in interface velocity during resolidification results from the interactions between heat transfer, solute partitioning and diffusion, and nonequilibrium solidification kinetics. As solidification takes place, the superheat in the melt eventually dissipates away, which results in an increase in the interface velocity because latent heat can be transferred faster into the solid substrate. Meanwhile, the solute rejected by the solid phase will accumulate on the liquid side of the interface, which lowers the interface temperature. In addition, the solid substrate is continuously heating up, which decreases the temperature gradient on the solid side of the substrate and therefore reduces the solidification rate. All these phenomena acting together result in a quick increase in the interface velocity followed by a quick decrease. Figure 3 also shows that the initial solute concentration C_0 has a large effect on the interface velocity during the earlier stages of resolidification. For the case of $C_0 = 2$ wt%, after the second peak, the interface velocity decreases to a second minimum, then slowly increases again, and finally decreases slowly. For $C_0 = 5$ wt%, on the other hand, the interface velocity decreases continuously until the end of resolidification after the second maximum.

The variations in interface temperature for the three cases above are shown in Fig. 4. In all cases, we can see a large variation in the interface temperature during melting, which is of course following the same variation pattern as the interface velocity because of the linear kinetics relationship used. For

the resolidification phase, however, the variation in interface temperature takes place mainly during the early stages of the process, and is followed by a period of almost constant interface temperature. The interface temperature variation over the whole resolidification process for the pure metal is less than 8 K with an initial slow decrease. The fast increase in the interface velocity for dilute alloys after the resolidification starts as seen in Fig. 3 is reflected here by a quick decrease in the interface temperature, followed by a fast recovery back to a quasi-steady-state interface temperature.

Figure 5 gives the solute concentration in the melt at the interface for both Al–2wt%Cu and Al–5wt%Cu. In this case, the interface location is nondimensionalized by the maximum melt depths for better comparison. The horizontal curves corresponding to C_0 indicate the initial uniform melt concentration during melting. As the resolidification starts, solute is rejected from the solid because of solute partitioning. The relatively small solute diffusivity in the melt (3×10^{-9} m^2/s) will then lead to an accumulation of rejected solute in a very thin layer in front of the interface, the highest concentration being located at the interface itself. As resolidification goes on further, more solute will be rejected by the interface and more and more solute will be accumulated in the front of the interface. Meanwhile, the interface velocity keeps increasing. These two effects combine to form an overshoot of solute concentration in the melt at the interface as shown by the maximum occurring at the very beginning of resolidification. As expected, the larger the initial solute concentration, the higher the maximum solute concentration reached: 7.3 wt% for Al–2wt%Cu and 21.5 wt% for Al–5wt%Cu. After the solute concentration in the melt reaches this peak, it drops very quickly. For Al–2wt%Cu, the solute concentration stays then almost the same over the remainder of the solidification process. For Al–5wt%Cu, however, the solute concentration in the melt at the interface keeps increasing. This may result from the decrease in nonequilibrium partition coefficient due to the continuous decrease in interface velocity, because a smaller partition coefficient means greater solute rejection from the solid. The solute "trapping" phenomenon is quantified by a partition coefficient greater than the equilibrium value. This is shown in Fig. 6 for both alloys under the same processing conditions. As can be seen, the nonequilibrium partition coefficient, k, increases very rapidly after resolidification begins, as did the interface velocity. Figure 6 shows also a slightly different pattern for Al–2wt%Cu and Al–5wt%Cu. The highest k achieved for Al–2wt%Cu is about 0.6 but the maximum for Al–5wt%Cu is about 0.8. It should also be noted that
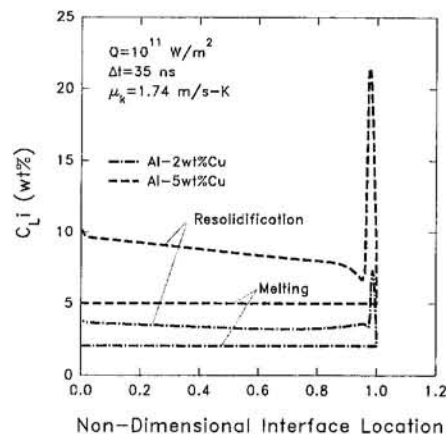

Fig. 5 The solute concentration in the melt at the interface during laser surface melting of dilute binary Al–Cu alloys, as a function of the solid/liquid interface location nondimensionalized by the maximum melt depth (d_{max}) for two initial solute concentrations: $C_0 = 2$ wt% ($d_{max} = 1.07$ μm) and 5 wt% ($d_{max} = 1.14$ μm). [$Q = 10^{11}$ W/m^2, $\Delta t = 35$ ns, $T_{sub} = 300$ K].
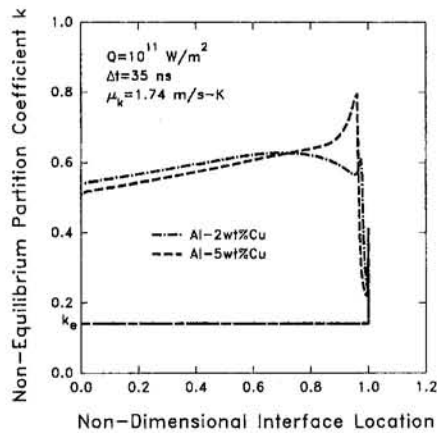
Fig. 6 Nonequilibrium partition coefficient during laser surface melting of dilute binary Al–Cu alloys as a function of the solid/liquid interface location nondimensionalized by the maximum melt depth (d_{max}) for two initial solute concentrations: C_0 = 2 wt% (d_{max} = 1.07 μm) and 5 wt% (d_{max} = 1.14 μm). [Q = 10^{11} W/m^2, Δt = 35 ns, T_{sub} = 300 K].

overall, a high partition coefficient is achieved for both initial concentration conditions (the equilibrium value is 0.14).

5 Summary and Conclusions

A heat and mass transfer model incorporating phase-change kinetics has been developed to quantify the effect of departure from thermodynamic equilibrium on laser surface melting. A collision-limited kinetics model including different features for melting and resolidification was used for both pure metals and binary alloys. The model was used to analyze pulsed laser surface melting for four pure metals (Al, Cu, Ni, and Ti) and dilute Al–Cu alloys. Some conclusions can be drawn based on our model calculations:

The achievable resolidification rate will depend strongly on the laser flux and the pulse duration. A proper combination may provide adequate control of the melt layer thickness and the solidification rate. In addition, the substrate material properties also have a strong effect on the melting and solidification processes.

A large variation in interface velocity during the earlier stages of resolidification is calculated for laser surface melting of a dilute Al–Cu alloy. This complex variation pattern for the interface velocity suggests strong interactions between heat transfer, solute partitioning and trapping, and the phase change kinetics. The initial solute concentration is also found to have a significant effect on the interface velocity variation.

Strong solute trapping, reflected by a large calculated nonequilibrium partition coefficient of about 0.6 during most of the resolidification, is predicted for these processing conditions.

Acknowledgments

References

Aziz, M. J., 1982, "Model for Solute Redistribution During Rapid Solidification," *J. Appl. Phys.*, Vol. 53, pp. 1158–1168.

Aziz, M. J., and Boettinger, W. J., 1994, "On the Transition From Short-Range Diffusion to Collision-Limited Growth in Alloy Solidification," *Acta Metall. Mater.*, Vol. 42, pp. 527–537.

Baeri, P., 1994, "Pulsed Laser Quenching of Metastable Phases," *Mater. Sci. Engng.*, Vol. A178, pp. 179–183.

Baker, J. C., and Cahn, J. H., 1971, "Thermodynamics of Solidification," *Solidification*, ASM, Metals Park, pp. 23–58.

Boettinger, W. J., and Coriell, S. R., 1986, "Microstructure Formation in Rapidly Solidified Alloys," *Science and Technology of the Undercooled Melt*, P. R. Sahm, H. Jones, and C. M. Adam, eds., Martinus Nijhoff, Dordrecht, pp. 81–109.

Brandes, E. A., 1983, *Smithells Metals Reference Book*, 6th ed., Butterworths, United Kingdom.

Clyne, T. W., 1984, "Numerical Treatment of Rapid Solidification," *Metal. Trans. B*, Vol. 15B, pp. 369–381.

Gill, S. G., and Kurz, W., 1995, "Rapid Solidified Al–Cu Alloys—II. Calculation of the Microstructure Selection Map," *Acta. Metall. Mater.*, Vol. 43, pp. 139–151.

Hsu, S. C., Chakravorty, S., and Mehrabian, R., 1978, "Rapid Melting and Solidification of a Surface Layer," *Metall. Trans. B*, Vol. 9B, 221–229.

Iida, T., and Guthrie, R. I. L., 1988, *The Physical Properties of Liquid Metals*, Clarendon Press, Oxford, pp. 10–108.

Jackson, K. A., 1975, "Theory of Melt Growth," *Crystal Growth and Characterization*, R. Ueda and J. B. Mullin, eds., North-Holland Pub., Amsterdam, pp. 21–32.

Kar, A., and Mazumder, J., 1987, "One-Dimensional Diffusion Model for Extended Solid Solution in Laser Cladding," *J. Appl. Phys.*, Vol. 61, pp. 2645–2655.

Kurz, W., and Fisher, D. J., 1989, *Fundamentals of Solidification*, Trans. Tech. Pub., Switzerland, pp. 293–294.

MacDonald, C. A., Malvexxi, A. M., and Spaepen, F., 1989, "Picosecond Time-Resolved Measurements of Crystallization in Noble Metals," *J. Appl. Phys.*, Vol. 65, pp. 129–136.

Molian, P. A., 1989, "Surface Alloying Using Lasers," *Surface Modification Technologies*, T. S. Sudarshan, ed., Marcel Dekker, New York, pp. 421–492.

Mullins, W. W., and Sekerka, R. K., 1964, "Stability of a Planar Interface During Solidification of a Dilute Binary Alloy," *J. Appl. Phys.*, Vol. 35, pp. 444–451.

Paul, A. J., Levi, C. G., and Mehrabian, R., 1994, "Phase Selection During Surface Melting of Titanium Aluminides," private communication.

Reitano, R., Smith, P. M., and Aziz, M. J., 1994, "Solute Trapping of Group III, IV, and V Elements in Silicon by an Aperiodic Stepwise Growth Mechanism," *J. Appl. Phys.*, Vol. 76, pp. 1518–1529.

Sekhar, J. A., Kou, S., and Mehrabian, R., 1983, "Heat Flow Model for Surface Melting and Solidification of an Alloy," *Metall. Trans. A*, Vol. 14A, pp. 1169–1177.

Tsao, J. Y., Aziz, M. J., Thompson, M. O., and Peercy, P. S., 1986a, "Asymmetric Melting and Freezing Kinetics in Silicon," *Phys. Rev. Lett.*, Vol. 56, pp. 2712–2715.

Tsao, J. Y., Picraux, S. T., Peercy, P. S., and Thompson, M. O., 1986b, "Direct Measurement of Liquid/Solid Interface Kinetics During Pulsed-Laser-Induced Melting of Aluminum," *Appl. Phys. Lett.*, Vol. 48, pp. 278–280.

Turnbull, D., 1981, "Metastable Structures in Metallurgy," *Met. Trans. B*, Vol. 12B, pp. 217–230.

Wang, G.-X., 1995, "Experimental and Numerical Study of Heat Transfer and Solidification for Molten Metal in Contact With a Cold Substrate," Ph.D. Thesis, University of California, Santa Barbara, CA.

Wang, G.-X., and Matthys, E. F., 1991, "Modeling of Heat Transfer and Solidification During Splat Cooling: Effect of Splat Thickness and Splat/Substrate Thermal Contact," *Int. J. Rapid Solidification*, Vol. 6, pp. 141–174.

Wang, G.-X., and Matthys, E. F., 1993, "Modeling of Rapid Planar Solidification of a Binary Alloy," *Heat and Mass Transfer in Materials Processing and Manufacturing*, ASME HTD-Vol. 261, pp. 35–44.

Wood, R. F., and Geist, G. A., 1986, "Modeling of Non-equilibrium Melting and Solidification in Laser-Irradiated Materials," *Phys. Rev. B*, Vol. 34, pp. 2606–2620.

A Unified Correlation for the Prediction of Heat Transfer Coefficients in Liquid/Solid Fluidized Bed Systems

Mohammad Jamialahmadi
Dean of Postgraduate Studies and Prof. of
Chemical Engrg.,
The University of Petroleum Industry,
Ahwaz, IRAN

Mohammad Reza Malayeri
Ph.D. Student of Chemical Engineering

Hans Müller-Steinhagen
Prof. and Head of Dept. of Chemical and
Process Engrg.

The University of Surrey,
Surrey GU2 5XH,
Guildford, England

In recent years, there has been considerable interest in the development of solid-liquid fluidized bed heat exchangers for efficient utilization of energy and for the control of heat transfer surface fouling. However, the design for optimum heat transfer remains uncertain and essentially empirical. In this study, a data bank containing a large number of measured heat transfer coefficients over a wide range of operational parameters (solid and liquid phase physical properties and heat transfer surface configurations) are compared with the prediction of almost all available correlations in the literature. A unified model for the prediction of heat transfer coefficients for wall-to-bed and immersed heater-to-bed systems is presented which predicts the published experimental data with good accuracy.

Introduction

The most important advantage of liquid/solid-fluidized bed systems over single phase flow is that the rate of heat transfer is greatly enhanced. The solid particles stir the thermal boundary layer and increase the heat transfer coefficient up to 8 times (Richardson et al., 1976). The role of various operating parameters, and the mechanisms of heat transfer in liquid-fluidized beds, have been the subject of extensive investigations (Baker et al., 1978; Grewal and Zimmerman, 1988; Khan et al., 1983). Although these investigations could not produce a definite answer as to the mechanism of heat transfer, they have nevertheless been successful in identifying the main influence variables. The conclusions of these investigations can be summarized as follows:

1 In liquid fluidization, the bed expands in particulate mode when the liquid velocity increases above that required for incipient fluidization. Exceptions to this behavior have also been reported by some investigators (Harrison et al., 1961; Jackson, 1963; Wilhelm and Kwauk, 1948).
2 The principal resistance to heat transfer is a liquid film at the heat transfer surface which is reduced by the scouring action of the moving fluidized particles. Heat transfer via the solid phase is unimportant for small values of $\rho_s c_{p,s} \lambda_s$, e.g., for glass particles. For solids such as copper particles, the product of $\rho_s c_{p,s} \lambda_s$ is large and heat transfer by particle conduction should be taken into consideration.
3 For given particle size and material, and liquid, the heat transfer coefficient increases as the bed voidage increases. A maximum value of the heat transfer coefficient appears at a bed voidage between 0.7–0.75 which corresponds to the point of maximum aggregation of solid particles in the bed (Brea and Hamilton, 1971; Chiu and Ziegler, 1985; Wasmund and Smith, 1967).

A considerable number of correlations have been suggested in the literature for the prediction of heat transfer coefficients of liquid-fluidized bed systems. All correlations can be presented in the following form:

$$Nu_p = Z Pr^{Z1} Re_p^{Z2} \left[\frac{d_p}{D} \right]^{Z3} \epsilon^{Z4} (1 - \epsilon)^{Z5}. \tag{1}$$

The coefficient and exponents suggested by the various authors, and the range of applicability of the correlations, are summarized in Table 1. Typical results of the comparison between the measured and calculated heat transfer coefficients for wall-to-bed and immersed heater-to-bed systems are shown in Figs. 1 and 2. Even though individual investigators have been reasonably successful in correlating their own results, the variation between the prediction of the various correlations is considerable. The reasons for this discrepancy are the complex nature of fluidization and the effect of a number of interdependent parameters on the heat transfer coefficient. Additionally, the use of dissimilar heat transfer surface geometries gives rise to different hydrodynamic characteristics of the fluidized bed.

The ultimate objective of any fundamental approach to the problem of heat transfer in liquid-fluidized bed systems is to be able to predict the heat transfer coefficient for a given condition through the knowledge and understanding of the processes involved. In this investigation, published heat transfer coefficients for liquid/solid fluidized bed systems are collected and classified into two groups, namely, wall-to-bed and immersed heater-to-bed heat transfer. Predictions of various published correlations are compared with these experimental data. A unified theoretical model for the prediction of heat transfer coefficients for wall-to-bed and immersed heater-to-bed systems is presented to correlate all the available published experimental data.

Hydrodynamics of Liquid Fluidized Bed Systems

The hydrodynamic behavior of solid-liquid fluidization depends on system geometry, bed voidage, and physical properties of solid and liquid phases. It controls the collision frequency of the solid phase with the heat transfer surface and the state of aggregation of the solid phase within the bed and at the heat transfer surface. The operating conditions can produce several modes of fluidization, namely, particulate fluidization, aggregative fluidization, and transition from particulate to aggregative fluidization. Particulate and aggregative fluidization represent

---

Table 1 The coefficients of Eq. (1) suggested by various authors

References	Configuration of heater	Z	Z1	Z2	Z3	Z4	Z5	Additional characteristic numbers	Range investigated by the author
Allen et al. (1977)	HIH	1.85	0.33	0.52	0.2	-0.04	0.52	0	$0.76 \le \epsilon$
		1.823	0.33	0.52	0.2	0	0.48	0	$0.4 < \epsilon < 0.76$
Baker et al. (1978)	VIH	1323	0	0	0	0	0	$U^{0.158} d_p^{1.168} (\frac{1}{\lambda_l})$	$1 < Re_p < 1500$
									$Pr \approx 6.9$
Brea and Hamilton (1971)	WTB	0.943	0.52	0.55	0.15	0	0.45	0	$10.4 < Re_p < 370$
Chiu and Zeigler (1985)	WTB	0.762	0.638	0.646	0	-1	1	$(\frac{U_{mf}}{U_t})^{0.266} \phi^{-1}$	$48 < Re_p < 619$
									$6.9 < Pr < 7.9$
Coulson and Richardson (1985)	PIH	*	0.37	*	0	0	0.725	$*0.0325 Re_p$ $+1.88 Re_p^{0.43}$	
Grewal and Zimmerman (1988)	HIH	33.54	0.14	0.365	0.694	0	0.635	0	$6.65 < Re_p < 1621$
									$Pr \approx 9$
Hamilton (1970)	WTB	3.38	0.33	0.565	0.57	0	0.435	0	$1.7 < Re_p < 2500$
									$Pr \approx 6.1$
Kang et al. (1991)	VIH	0.191	0.33	0.69	0	-1	0.31	0	$68 < Re_p < 480$
									$Pr \approx 5.6$
Kato et al. (1981)	WTB	0.044	0.78	0.78	0	-1	0.22	0	$1.4 < Re_p < 351$
									$6.2 < Pr < 60$

the two extremes of a continuous spectrum of possible behavior patterns for fluidized bed systems.

In particulate fluidization the solid bed expands homogeneously as the liquid velocity increases above that required for incipient fluidization. Heat is transferred to the fluid phase by normal convection and by stirring of the thermal sublayer which is the major resistance to heat transfer. In this mode of fluidization, the heat transfer rate and the bed voidage are strongly

---

Nomenclature

$a–d$ = coefficient and exponents in equation (22)
A = heat transfer surface area, m^2
c_i = constant
C_p = specific heat capacity, J/kg.K
d_p = particle diameter, m
D = bed diameter, m
D_h = hydraulic diameter of bed, m
D_i = heater diameter, m
f = collision frequency, s^{-1}
f_i = friction factor
F_U = defined by equation (2)
g = acceleration due to gravity, m/s^2
L = heater height, m
L_l = heater length in horizontal direction, m
K = constant
m = coefficient in eq. (19)
$m1$ = exponent in eq. (19)
n = Richardson and Zaki exponent
n_p = number of particles in closed contact with the heat transfer surface
N = total number of particles present in the system
$\dot{q}$ = heat flux, W/m^2
R = parameter in eq. (22), see Table 3
T = temperature, K
U = superficial fluid velocity, m/s
U_e = dynamic wave velocity, m/s

U_{mf} = minimum fluidization velocity, m/s
U_t = particle terminal velocity corrected for wall effect, m/s
U_c = continuity wave velocity, m/s
V = volume, m^3
$Z–Z5$ = coefficient and exponents in equation (1)
x = length in flow direction, m

Greek Letters

α = heat transfer coefficient, $W/m^2.K$
ϵ = bed voidage
λ = thermal conductivity, W/m.K
μ = dynamic viscosity, kg/m.s
ν = kinematic viscosity, m^2/s
ρ = density, kg/m^3
ϕ = shape factor

Subscripts-Superscripts

c = forced convection
i = immersed
l = liquid
max = point at witch the aggregation state reaches to its maximum
p = particle
pk = packed bed
RZ = Richardson-Zaki

s = solid
T = total
w = wall

Dimensionless Groups

Ar = $(g d_p^3 (\rho_s - \rho_l))/(\rho_l \nu^2)$, Archimedes number
Nu = $D\alpha/\lambda_l$, Nusselt number
Nu_p = $d_p \alpha/\lambda_l$, Nusselt number based on particle diameter
Pr = $\mu C_{p,l}/\lambda_l$, Prandtl number
Re = UD/ν, Reynolds number based on bed diameter
Re_x = Ux/ν, Reynolds number
Re_p = $U d_p/\nu$, particle Reynolds number
Re_h^+ = $(U d_p/\epsilon \nu) \cdot (2\pi^2 \epsilon^2/(9(1 - \epsilon))^2)^{1/3}$, modified Reynolds number defined by Wehrmann and Mersmann (1981)
Re_t = $U_t d_p/\nu$, particle terminal Reynolds number, corrected for wall effect

Abbreviations

HIH = horizontal immersed heater
M.E = mean relative error
PIH = plate immersed heater
VIH = vertical immersed heater
WTB = wall-to-bed

Table 1 (Continued)

Khan et al. (1983)	PIH	*	0.37	*	0	0	0.725	$+0.0325Re_p$ $+1.19Re_p^{0.43}$	$0.1<Re_p<1000$ $20<Pr<14000$
Khan et al. (1978)	PIH	11.8	0.14	0.48	0.38	0	0.56	0	$0.1<Re_p<1000$ $20<Pr<14000$
Kim et al. (1986)	VIH	0.0722	0.5	0.25	0	-0.25	0.25	$Ar^{0.25}$	$0.4<Re_p<960$ $1.6<Pr<1161.4$
Kollbach (1987)	WTB	0.118	0.5	0.7	0	-1	0.2	$Re_h^*>30$	$0.5<Re_h^*<40000$
		0.231	0.5	0.7	0	-1	0.33	$Re_h^*<30$	$1.7<Pr<14000$
Midoux et al. (1986)	WTB	0.177	0.41	0.71	0	0	0.145	$(\frac{16}{5+11\epsilon})^{-0.71}$	
Muroyama et al. (1986)	WTB	0.137	0.33	0.729	0	-1	0.271	0	$11<Re_p<2621$
Richardson et al. (1976)	PIH	0.67	0.33	0.62	0	-1	0.38	0	$13.2<Re_p<380$ $Pr=135.5$
Richardson and Mitson (1958)	WTB	119	0.4	-0.075	1.075	0	0	$Re_t^M(\frac{C_{p,s}}{C_{p,l}})^{0.28}(\frac{\lambda_s}{\lambda_l})^{-0.02}$ $M=0.02(\frac{\rho_s}{\rho_l}+3.45)$	$35<Re_p<1610$ $6.8<Pr<29.6$
Ruckenstein and Shorr (1959)	WTB	0.067	0.33	-0.237	0	0	0	$Ar^{0.522}$	$Re_pAr^{-0.58}>0.09$
		0.326	0.33	0.423	0	0	0	$Ar^{0.14}$	$Re_pAr^{-0.58}<0.09$
Schimanski et al. (1973)	WTB	0.23	0	0.25	0	0	0	$Ar^{0.26}$	$3<Re_p<300$
Schütt (1982)	WTB	0.4114	0.5	0.629	0	0	0.375	0	$120<Re_p<3300$ $2<Pr<7.8$
Tripathi and Pandey (1970)	WTB	0.0173	0.31	0.73	-0.19	-1.6	0	$(\frac{\rho_s-\rho_l}{\rho_l})^{-0.19}$	$40<Re_p<1000$ $1<Pr<10$
Tusin et al. (1979)	WTB	0.11	0.56	0.72	0.28	0	0	$(\frac{Pr}{Pr_w})^{0.25}$	$80<Re_p<5000$ $3<Pr<10$
Varma et al. (1972)	WTB	c_i	0.33	1.21	-0.58	0	0	$(\frac{1-\epsilon_{pk}}{1-\epsilon})^{-1.1}$ $c_l=0.00285$ for Glass particles $c_l=0.0032$ for Aluminium particles	$185<Re_p<3360$ $3.45<Pr<5$
Wehrmann and Mersmann (1981)	WTB	0.148	0.5	0.70	0	-1	0.20	$Re_h^*>30$	$1<Re_h^*<10000$
		0.2895	0.5	0.50	0	-1	0.33	$Re_h^*<30$	$7<Pr<1150$

dependent on particle size and particle density (Richardson and Mitson, 1958; Schütt, 1982; Wasmund and Smith, 1967, Wehrmann and Mersmann, 1981).

In aggregative fluidization, small groups of particles are imagined to move as individual units through the system as the solid phase is fluidized. Because of the intense circulation of the liquid phase, the extent of mixing and, therefore, the rate of heat transfer, is high. Heat transfer rate and bed voidage in aggregative fluidization are almost independent of particle size and particle density (Jamialahmadi et al., 1995; Muroyama et al., 1986; Richardson and Mitson, 1958; Wehrmann and Mersmann, 1981). Several attempts have been made to establish a theoretical hydrodynamic criterion for the transition from particulate to aggregative fluidization. Wallis (1969) has shown that the stability of a fluidized bed system depends entirely on the relative magnitude of dynamic and continuity wave velocities in the bed. Gibilaro et al. (1986, 1988) quantified Wallis' stability criterion using the following dimensionless function:

$$F_U = \frac{U_e - U_\epsilon}{U_e}. \tag{2}$$

The values of U_e and U_ϵ can be obtained from the following equations given by Foscolo and Gibilaro (1984) and Slis et al. (1959), respectively:

$$U_e = \left(\frac{3.2gd_p(1-\epsilon)(\rho_s-\rho_l)}{\rho_s}\right)^{0.5} \tag{3}$$

$$U_\epsilon = U_t n(1-\epsilon)\epsilon^{n-1}. \tag{4}$$

Positive and negative values of F_U represent particulate and aggregative behavior of the bed respectively. The zero value of this function pinpoints the voidage at which transition from particulate to aggregative fluidization is predicted to occur. The F_U function displays a quadratic relationship with a minimum which always occurs within the operating voidage range. This minimum which is the point of maximum aggregation of the solid phase corresponds to the point of maximum heat transfer rate. It can be obtained by differentiating F_U with respect to ϵ:

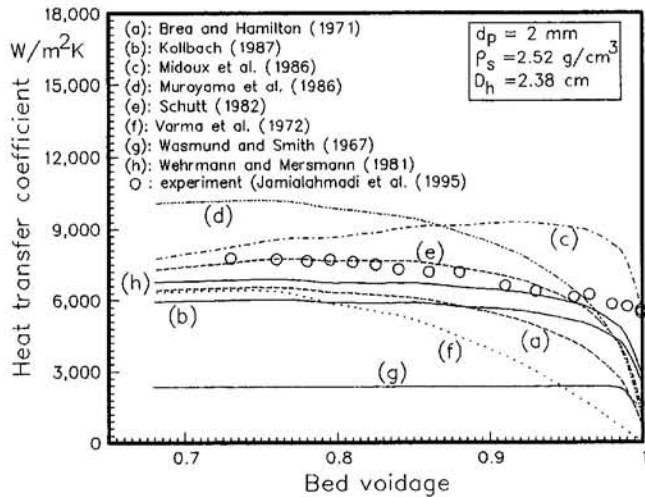$$\epsilon_{max} = \frac{n-1}{n-0.5}. \tag{5}$$

Fig. 1 Comparison of measured and predicted heat transfer coefficients from the wall to a fluidized bed of glass particles in water
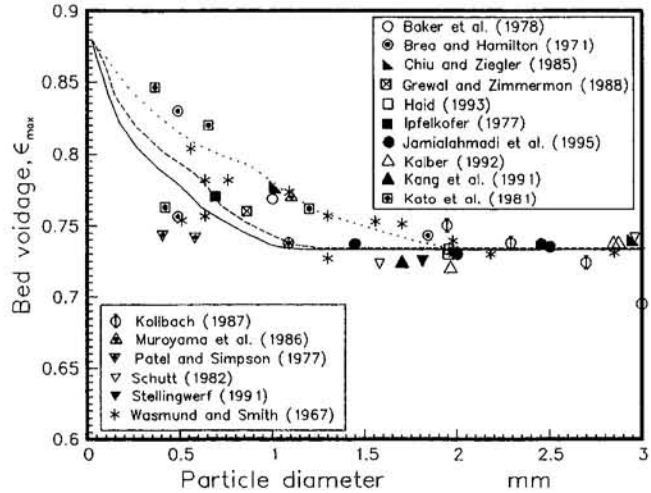

Fig. 3 Measured and predicted maximum bed voidage for water and various particle types and sizes ($\cdots \rho_s = 2.5$ g/cm³, $---\rho_s = 7.9$ g/cm³, $——\rho_s = 11.3$ g/cm³)

The Richardson and Zaki exponent, n, can be obtained from the equation given by Rowe (1987):

$$n = \frac{2.35(2 + 0.175 Re_t^{0.75})}{(1 + 0.175 Re_t^{0.75})}. \qquad (6)$$

For a given particle type and size Eq. (5) can be used to predict the bed voidage at which the heat transfer rate reaches its maximum. The experimental results reported by various investigators for three different particle types and sizes are compared with the prediction of Eq. (5) in Fig. 3. The results show that for particles greater than 2 mm the maximum heat transfer rate should occur at a bed voidage of 0.73. This prediction is in an excellent agreement with the reported experimental results.

Prediction of Bed Voidage

Accurate prediction of bed voidage is essential for the prediction of the state of aggregation of the solid phase and for the calculation of heat transfer coefficients from various correlations. The bed voidage can be predicted with very good accuracy if the original Hirata and Bulos (1990) correlation is modified to apply for particulate and aggregative fluidization, respectively, as described by Jamialahmadi et al. (1996).

$$\epsilon = \epsilon_{pk} + (1 - \epsilon_{pk})\epsilon_{RZ}^{(2.168n + 1.576(d_p/D))}$$
$$\times \exp(2.634n(1 - \epsilon_{RZ})) \quad (7)$$

$$\epsilon = \epsilon_{pk} + (1 - \epsilon_{pk})\epsilon_{RZ}^{(2.41n - 2.36(d_p/D))}$$
$$\times \exp(2.258n(1 - \epsilon_{RZ})) \quad (8)$$

The Reynolds number at the terminal settling velocity should be obtained from the Hartman et al. (1989) correlation.

Effect of the State of Aggregation of the Solid Phase

Over the past three decades substantial experimental results on heat transfer in liquid-fluidized bed systems have been accumulated in the literature. One of the more systematic investigations in plain tubes was that of Wasmund and Smith (1967). These authors used glass and aluminum particles, which places their experiments into the particulate and the transition zone of fluidization. Data by Wasmund and Smith (1967) are plotted as a function of F_U in Fig. 4. The results demonstrate that in a semi-logarithmic plot a linear relationship exists between the heat transfer coefficient and F_U. The heat transfer coefficient increases significantly if the degree of aggregation of the particles in the bed is increased. Interesting results emerge when the
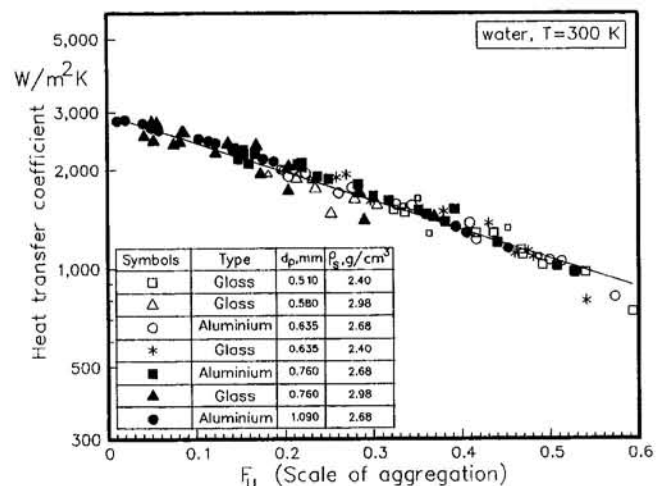

Fig. 2 Comparison of measured and predicted heat transfer coefficients for an immersed heater in fluidized bed

Fig. 4 Variation of heat transfer coefficients as a function of F_u for particulate fluidization. Data from Wasmund and Smith (1967).
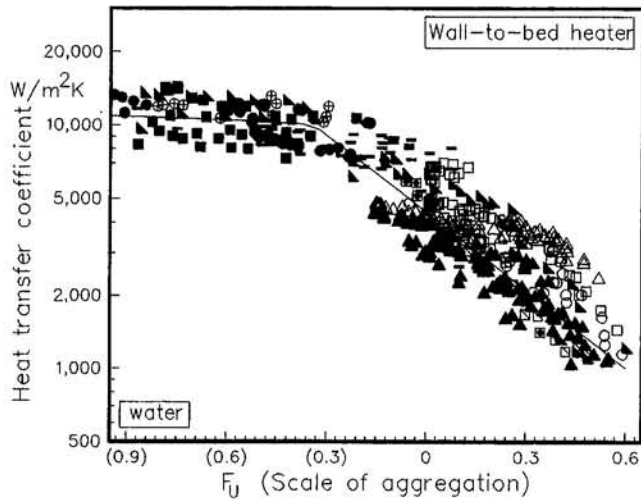
Fig. 5 Heat transfer coefficient as a function of F_u. Data from: △ Brea & Hamilton (1971), Φ Ipfelkofer (1977), ■ Jamialahmadi et al. (1995), ● Kälber (1992), ○ Kato et al. (1981), – Kolbach (1987), □ Muroyama et al. (1986), ▣ Schütt (1982), ⊕ Stellingwerf (1991), ◁ Varma et al. (1972), ▲ Wasmund & Smith (1967), ◤ Wehrmann & Mersmann (1981), ◪ Wesser & Mardus (1957).

experimental results of several investigators are plotted as a function of F_U in Fig. 5. The three distinctive zones of particulate, transition, and aggregative fluidization can easily be distinguished in this figure. The sharp rise in heat transfer rate in the particulate zone indicates that fluid convection is the main mechanism of heat transfer in beds with particulate behavior. In aggregative fluidization the heat transfer coefficient is almost independent of F_U which implies that heat transfer by particle conduction is important and should be taken into consideration when developing a heat transfer model.

Effect of Heat Transfer Surface Geometry

The previously published heat transfer data in liquid-fluidized beds can be classified into two groups, namely, wall-to-bed heat transfer and immersed heater-to-bed heat transfer. The immersed heat transfer surface can be installed vertically or horizontally. The effect of surface geometry on the heat transfer rate is illustrated in Fig. 6, where heat transfer data, reported by Brea and Hamilton (1971) for wall-to-bed and by Baker et al. (1978) and Kang et al. (1991) for vertical immersed heaters,
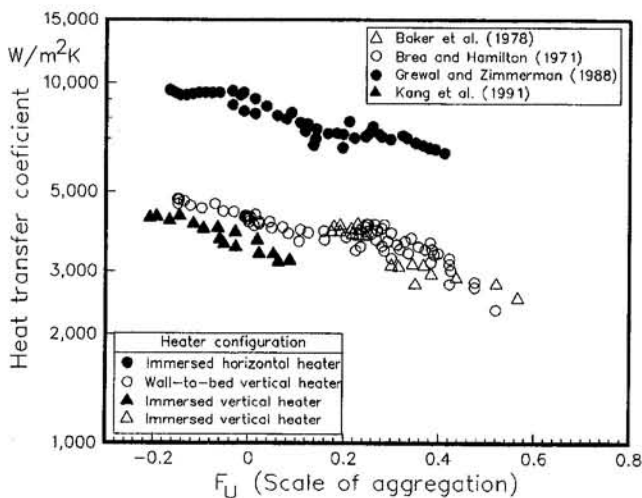
Fig. 6 Effect of heat transfer surface configuration on the heat transfer rate for glass particles in water
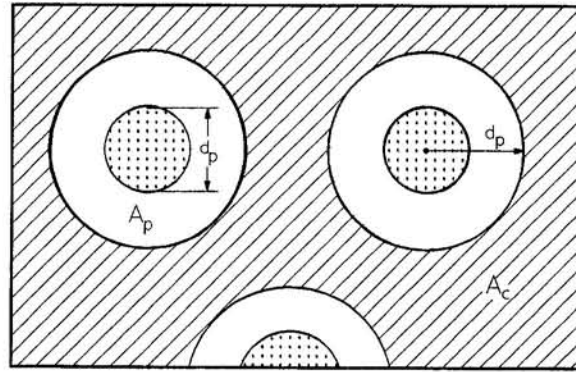
Fig. 7 Area of the heat transfer surface affected by particles and forced convection

are compared with experimental data for a horizontal immersed surface reported by Grewal and Zimmerman (1988). The results show that for identical scale of aggregation, F_u, the heat transfer coefficients for horizontal heaters are more than 50 percent higher than those for vertical heaters.

General Heat Transfer Model

Regardless of its configuration, the heat transfer surface can be divided into two zones: the area affected by particles, A_p, and the remaining area, A_c, where transfer of heat occurs by forced convection. Both mechanisms occur in parallel in separate zones of the heat transfer surface area as shown in Fig. 7. The total heat flux transferred over both separate areas is therefore equal to:

$$\dot{q}A = \dot{q}_c A_c + \dot{q}_p A_p \qquad (9)$$

where

$$\dot{q} = \alpha \Delta T$$
$$\dot{q}_p = \alpha_p \Delta T$$
$$\dot{q}_c = \alpha_c \Delta T \qquad (10)$$

and

$$A = A_p + A_c. \qquad (11)$$

From the combination of the above equations the fluidized bed heat transfer coefficient, α, can be obtained:

$$\alpha = \alpha_c + \frac{A_p}{A}(\alpha_p - \alpha_c). \qquad (12)$$

In the area affected by the particles, heat is transferred into the fluid by transient heat conduction from the heat transfer surface to the adjacent liquid layer. When particles depart from the heat transfer surface the hot liquid layer is transported in their wake into the liquid bulk and replaced by cooler liquid. The area from which the hot liquid layer is pumped away by a particle leaving the heat transfer surface is πd_p^2 (Han and Griffith, 1965). Some heat is also transferred by conduction to the particles while they are in contact with the heat transfer surface. Therefore,

$$\frac{A_p}{A} = \frac{n_p \pi d_p^2}{A}. \qquad (13)$$

From the definition of the bed voidage we also write,

$$\epsilon = 1 - \frac{V_p}{V_T} = 1 - \frac{N\pi d_p^3}{6V_T} \qquad (14)$$

Transactions of the ASME

Table 2 Constants for use with Eq. (19), Knudsen and Katz (1958)

Re	m	m1
0.4-4	0.898	0.33
4-40	0.911	0.385
40-4000	0.683	0.466
4000-40,000	0.193	0.618
40,000-400,000	0.0266	0.805

Combining Eq. (14) with Eqs. (12) and (13) yields:

$$\alpha = \alpha_c + \frac{6(1 - \epsilon)}{d_p} \cdot \frac{V_T}{A} \cdot \frac{n_p}{N} \cdot (\alpha_p - \alpha_c) \quad (15)$$

where

$$\frac{V_T}{A} = \frac{D_h^2}{4D_i} \quad \text{for a vertically immersed cylindrical heater,}$$

$$\frac{V_T}{A} = \frac{\pi D^2}{4L} \quad \text{for a thin, vertically immersed plate,}$$

$$\frac{V_T}{A} = \frac{D^2}{4L_1} \quad \text{for a horizontally immersed cylindrical heater and,}$$

$$\frac{V_T}{A} = \frac{D}{4} \quad \text{for wall to bed heat transfer surfaces.}$$

Prediction of α_c and α_p

The local forced convective heat transfer coefficient, α_c, for wall-to-bed and vertical immersed surfaces can be calculated from the Gnielinski (1986) correlation:

$$Nu = \frac{\frac{f_i}{8}(Re - 1000)Pr}{1 + 12.7\sqrt{\frac{f_i}{8}}(Pr^{2/3} - 1)} \left[1 + \frac{1}{3}\left(\frac{D_h}{L}\right)^{1/3} \right]. \quad (16)$$

The friction factor is to be calculated from (Filonenko, 1954):

$$f_i = (1.82 \log_{10}Re - 1.64)^{-2}. \quad (17)$$

For immersed plate surfaces the correlation recommended by Khan et al. (1983) is used:

$$Nu = 0.022 Re_x + 1.72 (Re_x Pr)^{0.3}. \quad (18)$$

Finally, for horizontally immersed heaters, the forced convective heat transfer coefficient is calculated from the correlation of Knudsen and Katz (1958):

$$Nu = m Re^{m1} Pr^{1/3}. \quad (19)$$

The constants m and $m1$ are tabulated in Table 2. The heat transfer coefficient for the particle controlled area can be obtained from the following equation (Jamialahmadi et al., 1995):

$$\alpha_p = \left[\frac{2}{\sqrt{\pi}} \sqrt{\lambda_l \rho_l C_{p,l}} + K\sqrt{\lambda_s \rho_s C_{p,s}} \right] \sqrt{f} \quad (20)$$

where K is a constant taking into account the relative area of contact between particles and heat transfer surface and is equal to 0.0705 for spherical particles and 0.141 for cylindrical particles (Jamialahmadi et al., 1995). The collision frequency in Eq. (20) can be predicted according to Martin (1981, 1990):

$$f = 0.3354 \sqrt{\frac{g}{d_p}\left(\frac{\rho_s - \rho_l}{\rho_s}\right)\frac{\epsilon - \epsilon_{pk}}{(1 - \epsilon_{pk})(1 - \epsilon)}}. \quad (21)$$

Prediction of n_p/N

In fluidized bed systems, particles move randomly throughout the bed and often collide with each other and with the heat transfer surface. Meijer (1984) has shown that the number of collisions of particles with the heat transfer surface is a function of bed voidage, particle size, and physical properties of the system. The number of collisions increases from zero, for the static bed, up to a maximum value and subsequently decreases to zero for the empty system. This functionality can be expressed in the following form:

$$\frac{n_p}{N} = a\left[\frac{d_p}{R} \right]^b (1 - \epsilon)^c (\epsilon - \epsilon_{pk})^d. \quad (22)$$

The value of n_p/N can be estimated from the experimental data in conjunction with Eqs. (15)–(21) for particulate and aggregative fluidization and for various configurations of the heat transfer surface.

The predicted values of n_p/N are used to estimate the parameters a, b, c, and d in Eq. (22). The calculated parameters for various heat transfer configurations are summarized in Table 3. In Figs. 8 and 9, n_p/N values calculated from the experimental data are compared with the curve-fit according to Eq. (22) for wall-to-bed and for immersed heat transfer surfaces.

Comparison With Experimental Data

The predictions of Eq. (15) for glass particles and various heat transfer surface configurations are compared with experimental data in Fig. 10. The predicted trends are in excellent agreement with the experimental results of all investigators.

Table 3 Source of data, heat transfer surface configuration and exponents of Eq. (22) for particulate and aggregative fluidization

| Source of data	Configuration of Heater	Aggregative Fluidization	Particulate Fluidization	R
Khan et al.(1983) Romani and Richardson (1974)		a=10.43 b=2.670 c=-0.23 d=1.240	a=0.650 b=2.000 c=-0.24 d=0.760	D
Grewal and Zimmerman (1988)		a=2.380 b=0.740 c=0.860 d=1.390	a=2.330 b=1.560 c=-0.06 d=-0.28	D
Baker et al.(1978) Kang et al.(1991)		a=0.530 b=1.340 c=0.050 d=0.018	a=0.380 b=1.440 c=-0.17 d=0.630	D_h
References are summarized in Fig. 11		a=5.760 b=1.360 c=0.350 d=0.080	a=0.980 b=1.260 c=0.000 d=-0.49	D
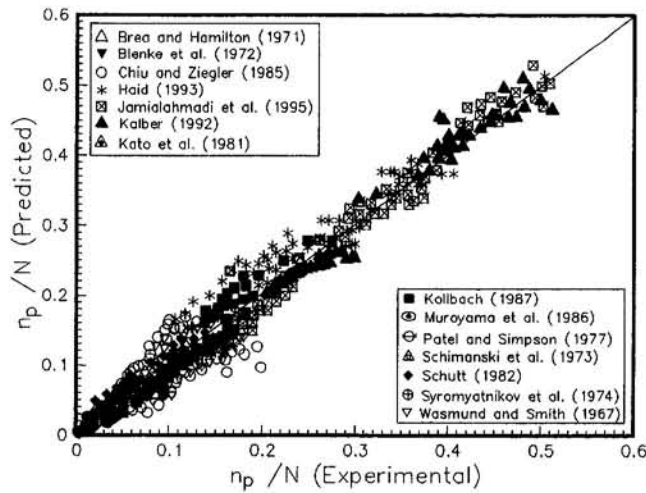
Fig. 8 Comparison of calculated and predicted n_p/N values for wall-to-bed heat transfer. Various particle sizes and densities in water.
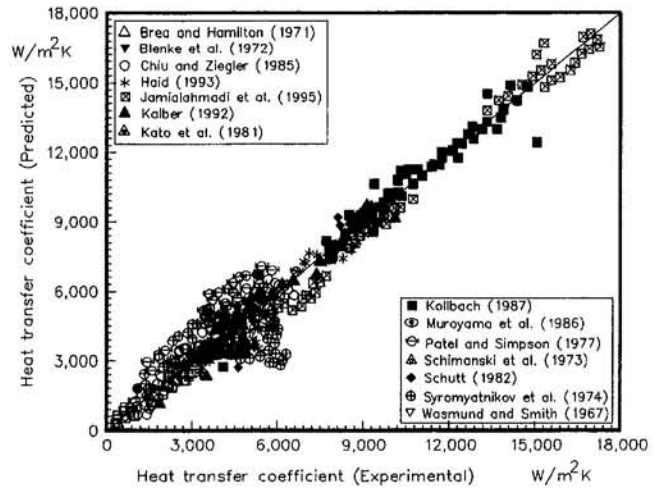

Fig. 11 Comparison of measured heat transfer coefficients with values calculated from Eq. (15) for wall-to-bed heat transfer
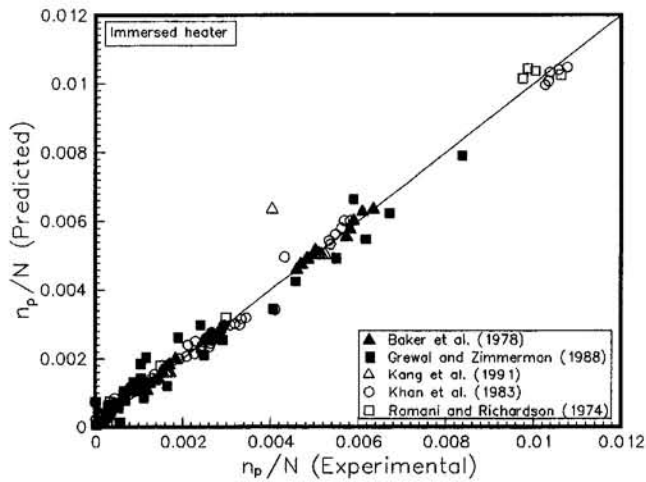

Fig. 9 Comparison of calculated and predicted n_p/N values for immersed heaters, for glass particles in water, and kerosine lubricating oil mixtures
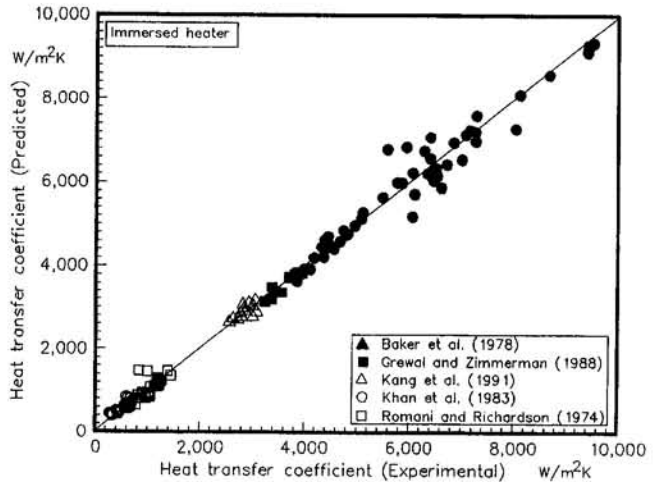

Fig. 12 Comparison of measured heat transfer coefficients with values calculated from Eq. (15) for immersed heaters

Equation (15), for wall-to-bed systems, predicts a maximum heat transfer at bed voidage of about 0.73, which is in accordance with previously reported results. The applicability of the presented model for wall-to-bed and immersed heater with different hydrodynamic characteristics is demonstrated in Figs. 11 and 12 where the experimental data of various investigators are compared with values predicted from Eq. (15). The mean relative errors between all measured data shown in Figs. 11 and 12, and the predicted values are summarized in Table 4, demonstrating that Eq. (15) predicts the published experimental data for various heat transfer surface configurations with good accuracy.
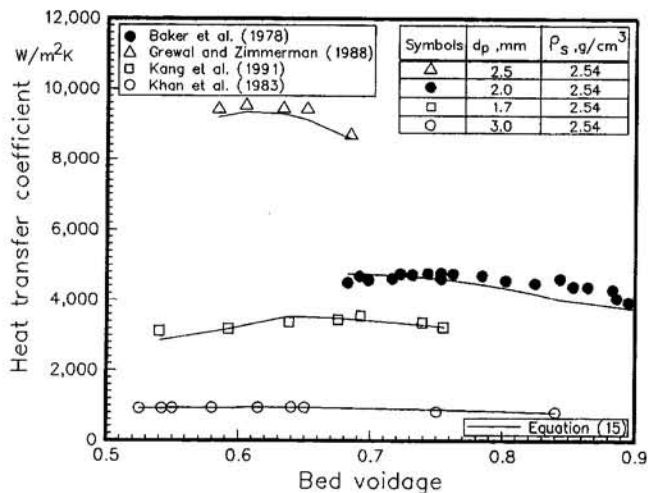

Fig. 10 Comparison of measured and predicted heat transfer coefficients for various heater configurations for glass particles in water and kerosine lubricating oil mixtures

Table 4 Mean relative error of predictions from Eq. (15), for the data depicted in Figs. 11 and 12

Configuration of heater	M.E. in aggregation zone	M.E. in particulate zone
WTB	15%	18%
VIH	2%	7.5%
HIH	2.4%	4.81%
PIH	11.5%	16.5%

958 / Vol. 118, NOVEMBER 1996

Transactions of the ASME

Conclusions

A new model was developed to predict heat transfer coefficients for wall-to-bed and immersed heater-to-bed fluidization with particulate or aggregate behavior. The model is generic and includes the effects of various operational and geometrical parameters on the heat transfer rate. The predictions of the model are in good agreement with experimental data for a variety of heat transfer surface geometries.

References

Allen, C. A., Fukuda, O., Grimmett, E. S., and McAtee, R. E., 1977, "Liquid Fluidized Bed Heat Exchangers-Horizontal Configuration Experiments and Data Correlations," *12th Intersociety Energy Conversion Engineering Conference.*, pp. 824–831.

Baker, C. G. J., Armstrong, E. R., and Bergougnou, M. A., 1978, "Heat Transfer in Three Phase Fluidized Beds," *Powder Techn.*, Vol. 21, pp. 195–204.

Blenke, H., Nenkirchen, B., and Noack, R., 1972, "Wärmeübergang quer angeströmten waagerechten Einzelrohr in einer Flüssigkeitswirbelschicht," *Verfahrenstech*, Vol. 6, pp. 80–83.

Brea, F. M., and Hamilton, W., 1971, "Heat Transfer in Liquid Fluidized Beds," *Trans. Inst. Chem. Engrs.*, Vol. 49, pp. 196–203.

Chiu, T. M., and Ziegler, E. N., 1985, "Liquid Hold-Up and Heat Transfer Coefficient in Liquid-Solid and Three-Phase Fluidized Beds," *AIChE J.*, Vol. 31, pp. 1504–1509.

Coulson, J. M., and Richardson, J. F., 1985, *Chemical Engineering*, Vol. 2, Pergamon Press, Oxford, pp. 250–255.

Filonenko, G. K., 1954, "Hydraulic Resistance in Pipes," *Teploenergetika*, Vol. 1, pp. 40–44.

Foscolo, P. U., and Gibilaro, L. G., 1984, "A Fully Predictive Criterion for the Transition Between Particulate and Aggregate Fluidization," *Chem. Eng. Sci.*, Vol. 39, pp. 1667–1675.

Gibilaro, L. G., di Felice, R., Waldram, S. P., 1988, "Fluidization Quality: A Criterion for Indeterminate Stability," *Chem. Eng. J.*, Vol. 37, pp. 25–33.

Gibilaro, L. G., Hossian, I., and Foscolo, P. U., 1986, "Aggregate Behaviour of Liquid Fluidized Beds," *Can. J. Chem. Eng.*, Vol. 64, pp. 931–938.

Gnielinski, V., 1986, *Wärmeübertragung in Rohren*, VDI-Wärmeatlas, 5th ed., VDI-Verlag, Düsseldorf.

Grewal, N. S., Zimmerman, A. T., 1988, "Heat Transfer From A Horizontal Tube Immersed in a Liquid-Solid Fluidized Bed," *Powder Techn.*, Vol. 54, pp. 137–145.

Haid, M., 1993, "Wärmeübertragung an Flüssigkeits-Feststoffwirbelschichtern," *Diplomarbeit*, Unversität Karlsruhe.

Hamilton, W., 1970, "A Correlation for Heat Transfer in Liquid Fluidized Beds," *Can. J. Chem. Eng.*, Vol. 48, pp. 52–56.

Han, C. Y., and Griffith, P., 1965, "The Mechanism of Heat Transfer in Nucleate Pool Boiling-Part I and II," *Int. J. Heat Mass Transfer*, Vol. 8, pp. 887–917.

Harrison, D., Davidson, J. F., de Kock, J. W., 1961, "On the Nature of Aggregative and Particulate Fluidisation," *Trans. Inst. Chem. Engrs.*, Vol. 39, pp. 202–211.

Hartman, M., Havlin, V., Trnka, O., and Carsky, M., 1989, "Predicting the Free-Fall Velocities of Spheres," *Chem. Eng. Sci.*, Vol. 44, pp. 1743–1745.

Hirata, A., and Bulos, F. B., 1990, "Predicting Bed Voidage in Solid-Liquid Fluidization," *J. of Chem. Eng. of Japan*, Vol. 23, pp. 599–604.

Ipfelkofer, R., 1977, "Zum Wärmeübergang an queraugeströmten waagerechten Rohr im Flüssigkeitsfließbett," Ph.D. thesis, Universität Stuttgart.

Jackson, M. A., 1963, "The Mechanics of Fluidised Beds: Part I: The Stability of the State of Uniform Fluidisation," *Trans. Inst. Chem. Engrs.*, Vol. 41, pp. 13–21.

Jamialahmadi, M., Malayeri, M. R., and Müller-Steinhagen, H., 1995, "Prediction of Heat Transfer to Liquid Fluidized Beds," *Can. J. Chem. Eng.*, Vol. 73, pp. 444–455.

Jamialahmadi, M.; Malayeri, M. R., and Müller-Steinhagen, H., 1996, "Prediction of bed voidage in particulate and aggregative liquid-solid fluidized beds," Accepted for pub. in Iranian J. Sci. Techn.

Juma, A. K. A., and Richardson, J. F., 1985, "Heat Transfer to Cylinder From Segregating Liquid-Solid Fluidized Beds," *Chem. Eng. Sci.*, Vol. 40, pp. 687–691.

Kälber, S., 1992, "Untersuchungen zum Betriebsverhalten von Wärmeübertragern im Bayer-Prozeß," *Diplomarbeit*, Universität Karlsruhe.

Kang, Y., Fan, L. T., and Kim, S. D., 1991, "Immersed Heater-Type Bed Heat Transfer in Liquid-Solid Fluidized Beds," *AIChE J.*, Vol. 37, pp. 1101–1106.

Kato, Y., Kago, T., Uchida, K., and Morroka, S., 1981, "Liquid Hold-Up and Heat Transfer Coefficient Between Bed and Wall in Liquid-Solid and Gas-Liquid-Solid Fluidized Beds," *Powder Techn.*, Vol. 28, pp. 173–179.

Khan, A. R., Juma, A. K. A., and Richardson, F., 1983, "Heat Transfer From a Plane Surface to Liquids and Liquid-Solid Fluidized Beds," *Chem. Eng. Sci.*, Vol. 38, pp. 2053–2066.

Khan, A. R., Richardson, J. F., and Shakiri, K. J., 1978, "Heat Transfer Between a Fluidized Bed and a Small Immersed Surface," *Fluidization*, Davidson, J. F. and Keairn, D. L., eds., Cambridge University Press, pp. 351–356.

Kim, S. D., Kang, Y., and Kwon, H. K., 1986, "Heat Transfer Characteristics in Two- and Three-phase Slurry-Fluidized Beds," *AIChE J.*, Vol. 32, pp. 1397–1400.

Knudsen, J. D., and Katz, D. L., 1958, *Fluid Dynamics and Heat Transfer*, McGraw-Hill Book Company, New York.

Kollbach, J. S., 1987, "Entwicklung eines Verdampfungsverfahrens mit Wirbelschicht-wärmeaustauscher zum Eindampfen krustenbildender Abwässer," Ph.D. thesis, RWTH Aachen.

Martin, H., 1981, "Fluid Bed Heat Exchangers—A New Model for Particle Convective Energy Transfer," *Chem. Eng. Comm.*, Vol. 13, pp. 1–16.

Martin, H., 1990, "Fluidized Beds," *Heat Exchanger Design Handbook*, Hemisphere Publishing Corporation, Washington, DC, pp. 2.8.4.1–2.8.4.14.

Meijer, J. A. M., 1984, "Inhibition of Calcium Sulphate Scale by a Fluidized Bed," Ph.D. thesis, Delft University of Technology.

Midoux, N., Wild, G., Purwasamita, M., Chapentier, J. C., and Martin, H., 1986, "Zum Flüssigkeitsinhalt und zum Wärmeübergang in Rieselbettreaktoren bei hoher Wechselwirkung des Gases und der Flüssigkeit," *Chem. Ing. Techn.*, Vol. 58, No. 2, pp. 142–143.

Muroyama, K., Fukuma, M., and Yasunishi, A., 1986, "Wall-to-Bed Heat Transfer in Liquid-Solid and Gas-Liquid-Solid Fluidized Beds," *Can. J. Chem. Eng.*, Vol. 64, pp. 399–408.

Patel, R. D., and Simpson, J. M., 1977, "Heat Transfer in Aggregative and Particulate Liquid Fluidized Beds," *Chem. Eng. Sci.*, Vol. 32, pp. 67–77.

Richardson, J. F., and Mitson, A. E., 1958, "Sedimentation and Fluidization. Part II—Heat Transfer From a Tube Wall to a Liquid-Fluidized System," *Trans. Inst. Chem. Engrs.*, Vol. 36, pp. 270–282.

Richardson, J. F., and Smith, J. W., 1962, "Heat Transfer to Liquid-Fluidized Systems and to Suspensions of Coarse Particles in Vertical Transport," *Trans. Inst. Chem. Engrs.*, Vol. 40, pp. 13–22.

Richardson, J. F., Romani, M. N., and Shakiri, K. J., 1976, "Heat Transfer From Immersed Surfaces in Liquid Fluidized Beds," *Chem. Eng. Sci.*, Vol. 31, pp. 619–624.

Romani, M. N., and Richardson, J. F., 1974, "Heat Transfer From Immersed Surface to Liquid Fluidized Beds," *Letter Heat Mass Transfer*, Vol. 1, pp. 55–62.

Rowe, P. N., 1987, "A Convenient Empirical Equation for Estimation of the Richardson-Zaki Exponent," *Chem. Eng. Sci.*, Vol. 42, pp. 2795–2796.

Ruckenstein, E., and Shorr, V., 1959, "Despre transferul de caldura dintre un strat fluidizat culichid si peretelevasului care-I contine," *Studii cercetari fiz. Akad. rep. populare Romine.*, Vol. 10, pp. 235–246.

Schimanski, G. N., Jancuk, E. N., and Nikitin, P. G., 1973, "Untersuchung der Wärmeübertragung zwischen einem waagerechten Rohrbündel und einer Wirbelschicht," *Archiv Energiewirtschaft*, Vol. 27, No. 1, pp. 25–29.

Schütt, U., 1982, "Wärmeübertragung in der Flüssigkeitswirbelschicht mit senkrechten Rohren," *Wiss. Zeitung der Techn. Hochschule Magdeburg.*, Vol. 26, pp. 71–74.

Slis, P. L., Willemse, TH.W., and Kramers, H., 1959, "The Response of The Level of a Liquid Fluidized Bed to a Sudden Change in the Fluidizing Velocity," *Appl. Sci. Res.*, A8, pp. 209–215.

Stellingwerf, B., 1991, "Wärmeübergang an eine Flüssigkeits-Feststoffwirbelschicht im Ringspalt," *Diplomarbeit*, Universität Karlsruhe.

Syromyatnikov, N. I., Vasanora, L. K., and Karpenko, A. I., 1974, "Heat Transfer in Liquid Fluidized Bed," *Heat Transfer Sov. Res.*, Vol. 6, pp. 135–139.

Tripathi, G., and Pandey, G. N., 1970, "Heat Transfer in Liquid Fluidized Beds," *Indian J. of Techn.*, Vol. 8, pp. 285–289.

Tusin, A. M., Vasanova, L. K., Syromyatnikov, N. J., 1979, "Heat Transfer From a Transverse Steamlined Cylinder During Surface Boiling in a Liquid Fluidized Bed," *J. Eng. Physics*, Vol. 32, pp. 263–266.

Varma, R. L., Pandey, C. N., Tripathi, G., 1972, "Heat Transfer in Semifluidized Beds," *Indian J. Techn.*, Vol. 10, pp. 11–15.

Wallis, G. B., 1969, *One-Dimensional Two-Phase Flow*, McGraw-Hill, New York.

Wasmund, B. W., and Smith, J. W., 1967, "Wall to Fluid Heat Transfer in Liquid Fluidized Beds," *Can. J. of Chem. Eng.*, Vol. 45, pp. 156–165.

Wehrmann, M., and Mersmann, A., 1981, "Wärmeübertragung in flüssigkeits-durch-strömten Fest- und Fließbetten", *Chem. Ing. Techn.*, Vol. 53, pp. 804–805.

Wesser, G., Mardus, G., 1957, "Zum Wärmeübergang in Wirbelschichten," *Chem. Ing. Techn.*, Vol. 29, pp. 332–335.

Wilhelm, R. H., Kwauk, M., 1948, "Fluidization of Solid Particles," *Chem. Eng. Prog.*, Vol. 44, pp. 201–218.

P. S. Wei
Professor.
email: piehp@mail.nsysu.edu.tw
Mem. ASME

C. Y. Chang
Graduate Student.

C. T. Chen
Graduate Student.

Institute of Mechanical Engineering,
National Sun Yat-Sen University,
Kaohsiung, Taiwan

Surface Ripple in Electron-Beam Welding Solidification

The occurrence of ripples on the workpiece surface after solidification in electron-beam welding or melting is experimentally and analytically investigated. The maximum accelerating voltage and welding current of the electron-beam welder are 60 kV and 50 mA, respectively, while the workpieces are Al 1100 and SS 304. The average pitches and amplitudes of surface ripples are measured for different beam powers and welding speeds. Using a scale analysis to account for heat transfer and fluid flow induced by a negative temperature-dependent surface tension gradient in the molten pool the variations of ripples with dimensionless beam power, Marangoni, Peclet, Prandtl, Stefan, and Biot numbers are found for the first time. The predicted results show good agreement with experimental data.

Introduction

A significant difference between poor and good welding is that significant rippling or roughening may result on the solidified workpiece surface (e.g., O'Brien, 1991). Ripples are generally associated with segregation, porosity, and other microstructural defects. Even though surface ripples commonly occur in metals processing, theoretical or experimental investigations of rippling phenomena are limited. Several propositions for possible causes of ripples are presented as follows:

1 Thermocapillary Force. Anthony and Cline (1977) proposed a simplified model to study rippling resulting from the laser melting of stainless steel 304. Rippling was attributed to thermocapillary or Marangoni force, which is proportional to the tangential component of temperature-dependent surface tension gradient along the liquid–vapor interface. The outward fluid flow caused the liquid at the back of the pool to climb and produce a raised section upon solidification. Mills and Keene (1990) pointed out that surface agitation and coarse frozen ripples superimposed on a background of fine ripples would be associated with low surface tension and a positive temperature gradient. A quiescent fluid surface coupled with fine ripples was characterized by high surface tension and a negative temperature coefficient.

2 Periodic Oscillations During Solidification. D'annessa (1970) proposed that the rippling phenomenon resulted from the interaction of solidification growth rate fluctuations and surface tension effects. The peaks and valleys of ripples were associated with increasing and decreasing growth rate intervals, respectively. The changes in the height and pitch of ripples were explained by variations in thermal conditions.

3 Power Source Ripples. Garland and Davies (1970) concluded that the ripples were not due to growth rate fluctuations, but were related to the cyclic current supply. Using a pulsed arc source Ecer et al. (1982) observed up and down oscillations of the weld pool that exhibited a constant period. These oscillations cyclically provided liquid metal above the weld surface into which solid can grow and ripples were formed.

4 Periodic Swellings of Liquid Metal. Arata et al. (1973) observed the dynamic behavior (Tong and Giedt, 1969) of the weld pool by using a high-speed camera. The weld pool periodically swelled as a result of the alternatively narrowed and expanded cavity produced by a high-intensity electron beam. Ripples were closely related to the periodic swelling of molten liquid.

Thermocapillary convection and unsteady deformation of the free surface near the solidification front appear to be responsible for the formation of rippling. A fundamental and important investigation on thermocapillary flows interacting with free surfaces in a shallow rectangular cavity was provided by Sen and Davis (1982). They considered vertical walls at distinct temperatures and the bottom wall being adiabatic. A perturbation approach associated with a numerical computation was used to study float-zone processing, where small Reynolds ($\equiv -(d\gamma/dT)A\Delta Td/\mu\nu$) and Marangoni numbers ($\equiv$ PrRe) of an order of the perturbation parameter A and capillary number ($\equiv -(d\gamma/dT)A\Delta T/\gamma_m$) the order of A^4 were assumed. A free surface layer driven by thermocapillary force was found to flow from hot to cold, and recirculating below. Deformation of the interface was enhanced by increasing the capillary number. Strani et al. (1983) considered the same problem with milder restrictions on Reynolds and Marangoni numbers.

Imposing the same boundary conditions as Sen and Davis (1982), Zebib et al. (1985) provided a scale analysis of steady fluid flow in the free surface layer, corner, wall, and core regions of an open square cavity for high Marangoni numbers. The characteristic velocity of the free surface flow induced by thermocapillary force was of the magnitude of $\mathrm{Re}^{-1/3}$ (Ostrach, 1982) where Reynolds number is defined as $-(d\gamma/dT)\Delta Td/\mu\nu$. The free surface layer decreased in velocity and turned downward as the corner region was approached. The vertical extent and horizontal velocity in the corner region was equal to that in the free surface layer while the width was of the magnitude of $\mathrm{Re}^{-2/3}$ and the vertical components of velocity an order of unity. Pressure in the entire region was determined from an invicid Bernoulli's equation and equal to the dynamic pressure in the free surface layer. Rivas and Ostrach (1992) pointed out that this pressure can be overestimated.

Rivas and Ostrach (1992) presented a scale analysis to stationary and steady welding processes for Prandtl number Pr ≪ 1. In order to avoid the effects of the complexity of the phenomena in the corner region, the analysis was only applied to the core region. The characteristic surface velocities obtained from balances between thermocapillary force, viscous stress, and inertia force (Ostrach, 1982) for small Reynolds number, high Reynolds and Marangoni numbers agreed with experimental data and computed maximum surface velocities in the literature. Interrelationships between the incident energy and shape of the molten region, and deformation of the free surface were not accounted for. Rivas (1991) simulated flow patterns numeri-
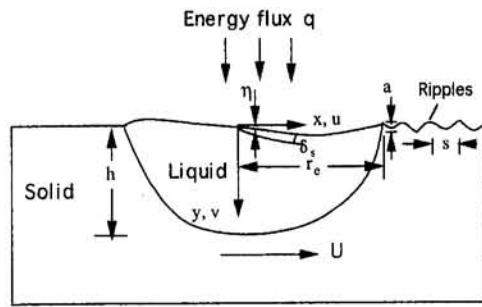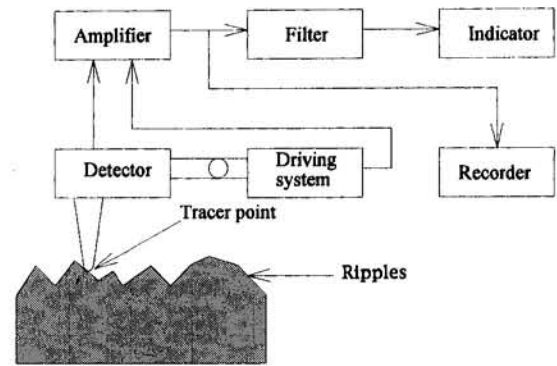
Fig. 1 Physical model

Fig. 2 Experimental setup to measure roughness of ripples

cally in a shallow rectangular pool. It was found that as inertia effects became important the wall vortex induced a depression of the free surface near the wall. This behavior was opposite to that for small Reynolds numbers (Sen and Davis, 1982).

Thermocapillary flows in open containers become oscillatory under certain conditions but its cause is not yet completely understood. Ostrach et al. (1985) suggested the oscillations result from the deformation of the free surface. Conversely, Schwabe and Scharmann (1979) and Xu and Davis (1984) concluded that oscillations were due to instability that occurs for Marangoni number above a critical value. Recently, Kamotani et al. (1995) experimentally verified the former theory. More detailed analysis is required.

In this study, roughness affected by different working parameters is experimentally and analytically determined. The flow pattern in the weld pool, which involves unsteady deformations of solid–liquid and liquid–vapor interfaces and interactions between the free surface layer, corner and core regions, and boundary layer with phase transition on the solid–liquid interface, is quite complex and uncertain. A scale analysis (Bejan, 1984) of rippling therefore is provided for an exploratory study. From a practical point of view, this work presents an understanding on how to adjust working conditions to reduce ripples. From a theoretical viewpoint, an interpretation for the occurrence of ripples is provided. An electron-beam welder whose energy source is steady and stable and surroundings clean in a vacuum chamber is used.

Experimental Setup and Procedure

Electron-beam welding was accomplished in a vacuum chamber. The electron-beam emitted from an electrode impinges steadily and continuously on the surface of a workpiece moving at a constant speed U. The workpiece surface thus experiences melting, solidification and rippling, as illustrated in Fig. 1. The pitches and amplitudes of the ripples were measured with a Kosaka surfcoder SE 3300 surface roughness instrument, as shown in Fig. 2. The roughness instrument consists of a detector, electric driving system, amplifier, filter, indicator, and recorder. A tracer point moved by a electric driving system is mounted at the tip of the instrument. Its movement delineates the surface of the ripples. The amplifier is used to enhance the spectrum of roughness transmitted from the amplifier. The spectrum includes short wavelengths from ripples and long wavelengths from curvatures of the workpiece surface. After eliminating components of long wavelength from the treble filter the outputs of the recorder are the pitches and amplitudes of ripples.

Experimental Procedure. The procedure is described as follows:

1 Specimen. Workpieces chosen were an aluminum alloy Al 1100, and stainless steels SS 304. Each specimen having a thickness of 0.008 m was finished by 800 grit emery paper and

———— Nomenclature ————

a = average ripple amplitude
A = d/l
Bi = Biot number = $h_c h/k$
c = proportional constant
c_a = empirical constant
Ca = capillary number = $-(d\gamma/dT)A\Delta T/\gamma_m$
c_p = specific heat
d = depth of rectangular cavity
f, F, g = functions or gravitational acceleration
h = fusion zone depth
h_c = heat transfer coefficient
h_{sl} = latent heat for solidification
K = loss coefficient
k, k_s = liquid and solid conductivity
l = length of rectangular cavity
Ma = Marangoni number = $-(d\gamma/dT)(T_m - T_\infty)h/\mu\alpha$
p = pressure
Pr = Prandtl number = ν/α

Pe = Peclet number = Uh/α
Q = dimensional beam power
Q^* = dimensionless beam power = $Q/[kh(T_m - T_\infty)]$
q = incident flux
q_c = incident flux = Q/r_e^2
R = correlation coefficient
r_e = rear length of molten pool, as illustrated in Fig. 1
s = average pitch between ripples
Ste = Stefan number = $h_{sl}/[c_p(T_m - T_\infty)]$
t = time
T = temperature
U = welding speed
$u, \mathbf{u}$ = horizontal velocity and velocity vector, $\mathbf{u} = u\mathbf{i} + v\mathbf{j}$
v = vertical velocity
x, y = coordinate, as illustrated in Fig. 1
z = coordinate

α = liquid diffusivity = $k/\rho c_p$
γ, γ_m = surface tension at T and melting point T_m, $\gamma = \gamma_m + (d\gamma/dT)(T - T_m)$, where $d\gamma/dT$ is negative constant
δ_s = thickness of free surface layer
Δh_{loss} = head loss
ΔT = temperature difference between vertical walls
$\Delta T_c = T_m - T_\infty$
η = deflection of free surface
μ, ν = viscosity
ρ = density

Subscripts

e = solidification front on workpiece surface
l = liquid
m = melting
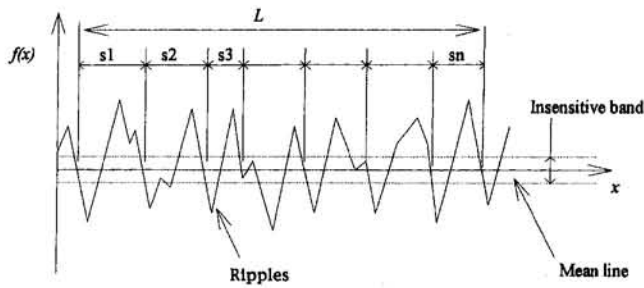s = free surface boundary layer or solid
∞ = ambient

Fig. 3 Specification of ripples

cleaned with acetone to remove oxide layers and debris, and produce a smooth surface prior to welding.

2 Electron-Beam Welding. A bead-on-plate weld on the workpiece surface was made with an electron-beam welder having a maximum accelerating voltage of 60 kV and welding current of 50 mA. In this study, an accelerating voltage of 50 kV was used while welding currents and speeds ranged from 15–45 mA, and 20–90 mm/s, respectively. A constant accelerating voltage is crucial because the spot size is more sensitive to the accelerating voltage than the welding current (Burgardt, 1986; Hicken et al., 1991; Giedt and Tallerico, 1988). The focal spot was located at the workpiece surface because of its strong influence on the depth of penetration (Wei and Chow, 1992). A vacuum less than 10^{-5} torr ($\sim 10^{-3}$ Pa) was used.

3 Observation of Fusion Zone. After welding the specimen was cut and polished with 1200 grit emery paper. Minor contaminants were removed in an ultrasonic wave cleaner filled with acetone. A chemical solution to etch the specimen was also required. The chemical etchant used for Al 1100 was 1 ml HF (48 percent) and 200 ml H_2O, while that for SS 304 was 4 g $CuSO_4$, 20 ml HCl, and 20 ml H_2O.

4 Observation of Ripples. Specimens were cleaned with acetone in the ultrasonic wave cleaner before observation and measurement. Ripples were observed and photographed with an optical microscope at magnifications of 25–50×.

5 Roughness Measurement. Surface ripples consist of various wavelengths. A Fourier series was used to analyze the surface topography. An appropriate cut-off wavelength was selected to eliminate long wavelengths attributed to curvature of the workpiece surface. From the regulation of DIN (Deutscher Industrial Normungl) the cut-off wavelength was chosen to be 2.5×10^{-3} m which was one-fifth of the total length for measuring.

The roughness is defined by an average pitch and amplitude of ripples along the weld centerline. As illustrated in Fig. 3, a mean line is defined as a line ($y = 0$) below and above which curves of the rough surface have the same area. The ordinate $y = f(x)$ represents the surface of ripples, where the x axis is in the welding direction. Selecting a total length, L, for measuring, the average amplitude is determined from

$$a \equiv \frac{1}{L} \int_0^L |f(x)| \, dx \approx \frac{1}{n} \sum_{i=1}^{n} |f(x_i)| \qquad (1)$$

where the number of points $n = 7990$. The average pitch between adjacent ripples is defined as

$$s \equiv \frac{1}{n} \sum_{i=1}^{n} |s_i| \qquad (2)$$

Average values were obtained from different sections, alternative directions along the weld centerline, and different tests, where ripples exhibited regular patterns. The regularity appeared for a long welding length and time.

Statistical Analysis. The standard deviation and coefficient of determination for the results were estimated. The calculated coefficient of determination are shown in the following figures. The system errors of the roughness instrument were checked with a standard sample, whose amplitude is 3.9×10^{-6} m and maximum height between the peak and valley of the surface ripples 9.5×10^{-6} m, by bias errors of -0.02×10^{-6} m and $+0.125 \times 10^{-6}$ m, respectively.

Scale Analysis

Conservation equations of mass, momentum, and energy in the molten region are, respectively,

$$\nabla \cdot \mathbf{u} = 0 \qquad (3)$$

$$\frac{\partial \mathbf{u}}{\partial t} + (\mathbf{u} \cdot \nabla)\mathbf{u} = -\frac{1}{\rho} \nabla p + \nu \nabla^2 \mathbf{u} \qquad (4)$$

$$\frac{\partial T}{\partial t} + (\mathbf{u} \cdot \nabla)T = \alpha \nabla^2 T \qquad (5)$$

Since the capillary number $Ca \approx 0.2$ and 0.3 for aluminum and SS 304, respectively, small deformation of the free surface (i.e., $\eta/h \ll 1$) can be assumed. The balance of thermocapillary force and viscous stress on the liquid–vapor interface therefore reduces to (e.g., Sen and Davis, 1982)

$$\mu \frac{\partial u}{\partial y} = -\frac{d\gamma}{dT} \frac{\partial T}{\partial x} \qquad (6)$$

A balance between liquid pressure and pressure due to surface tension on the free surface yields

$$p - p_\infty = \gamma \frac{\partial^2 \eta}{\partial x^2} \qquad (7)$$

The incident flux equals conduction into liquid on the free surface. That is,

$$q = -k \frac{\partial T}{\partial y} \qquad (8)$$

The Stefan boundary condition on the solidification front is

$$-k \frac{\partial T}{\partial x} + \rho U h_{sl} = -k_s \frac{\partial T_s}{\partial x} \qquad (9)$$
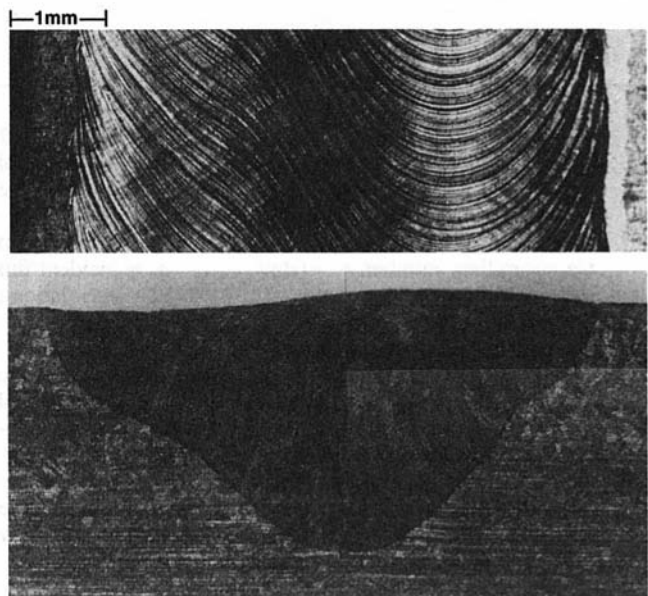

Fig. 4 (a) Top view of surface ripples, and (b) transverse cross section of fusion zone in SS 304 irradiated by an overfocused beam with an accelerating voltage of 50 kV, welding current 30 mA, and a welding speed of 0.02 m/s
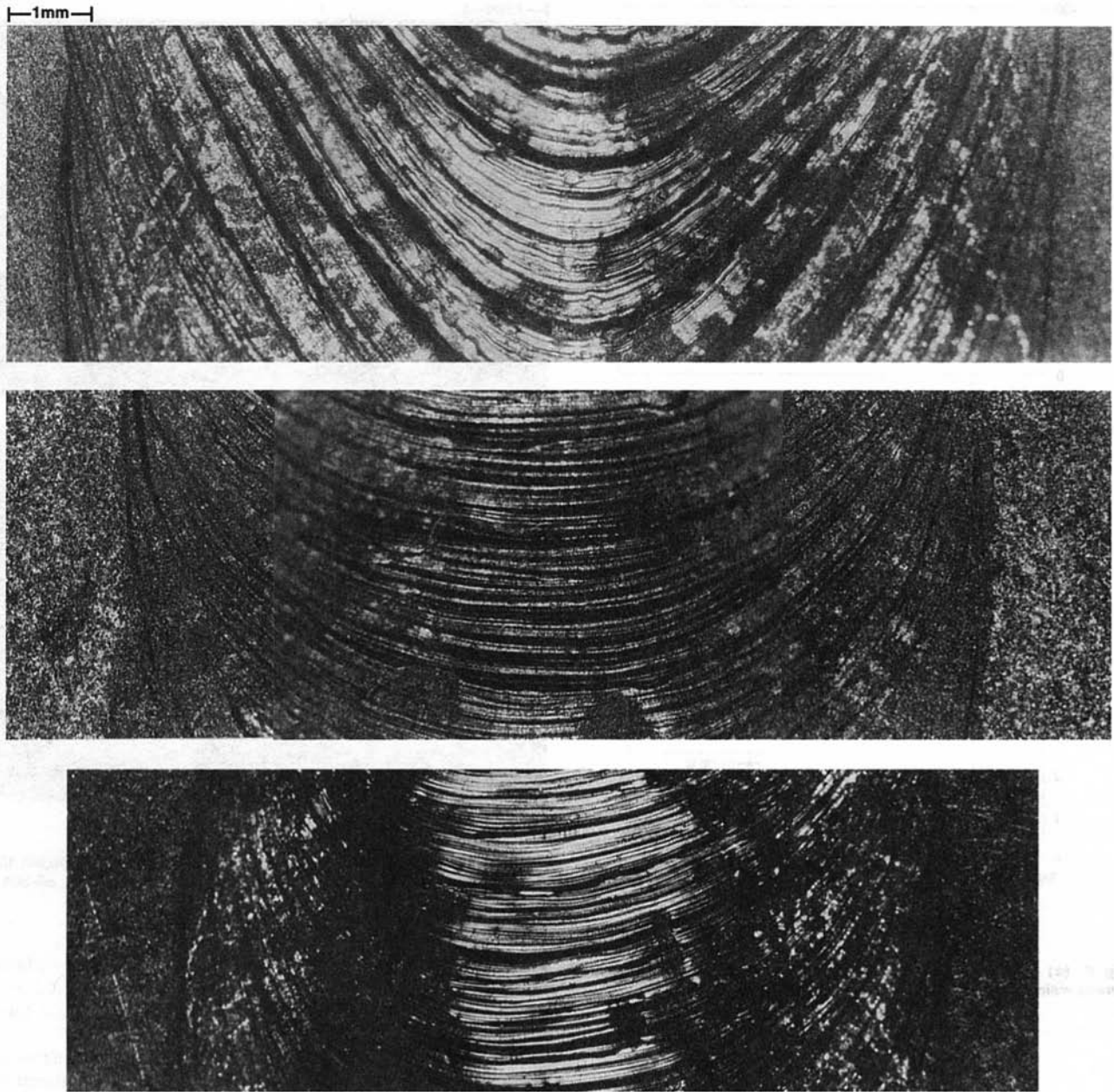
Fig. 5 Top views of surface ripples on Al 1100 irradiated by a surface-focused beam with accelerating voltage of 50 kV and (a) 30 mA, 0.02 m/s, (b) 20 mA, 0.02 m/s, and (c) 30 mA, 0.04 m/s

where the second term on the left-hand side is latent heat due to solidification. The kinematic boundary condition is also required for a free surface:

$$v = \frac{\partial \eta}{\partial t} + u \frac{\partial \eta}{\partial x} \qquad (10)$$

The characteristic velocities of the free surface layer having a high Reynolds number and small Prandtl number as derived by Ostrach (1982) and Rivas and Ostrach (1992) are

$$u_s = \left[\left(\frac{d\gamma}{dT} \frac{q_c h}{k\mu} \right)^2 \frac{\nu}{r_e} \right]^{1/3} \qquad (11)$$

$$v_s = \left(\left| \frac{d\gamma}{dT} \right| \frac{q_c h}{k\mu} \frac{\nu^2}{r_e^2} \right)^{1/3} \qquad (12)$$

which can be derived from the horizontal component of momentum Eq. (4), and Eqs. (6), (3), and (8). That is,

$$\frac{u_s^2}{r_e} \sim \nu \frac{u_s}{\delta_s^2}, \quad \mu \frac{u_s}{\delta_s} \sim \left| \frac{d\gamma}{dT} \right| \frac{\Delta T_c}{r_e},$$

$$\frac{u_s}{r_e} \sim \frac{v_s}{\delta_s}, \quad q_c \sim k \frac{\Delta T_c}{h} \qquad (13)$$

where the first relation represents a force balance between inertia and viscous force, the second relation is an interfacial momentum balance between tangential viscous stress and thermocapillary force, the third relation conservation of mass, the last an energy balance between incident flux and conduction. For liquid metals Prandtl numbers Pr ≪ 1 indicates that the thickness of the free surface viscous layer is much smaller than the fusion zone depth. The Marangoni and Reynolds numbers are greater
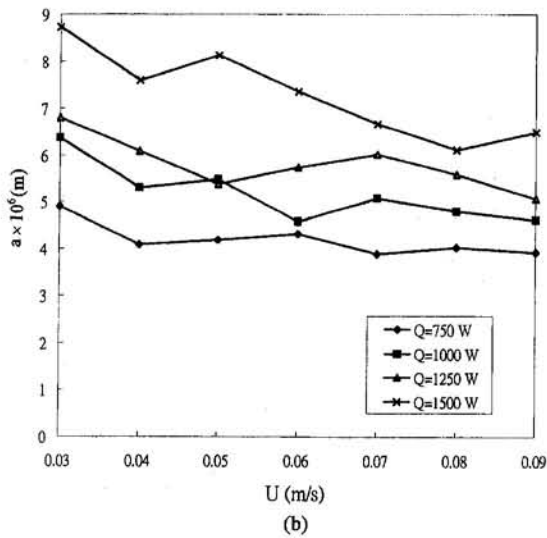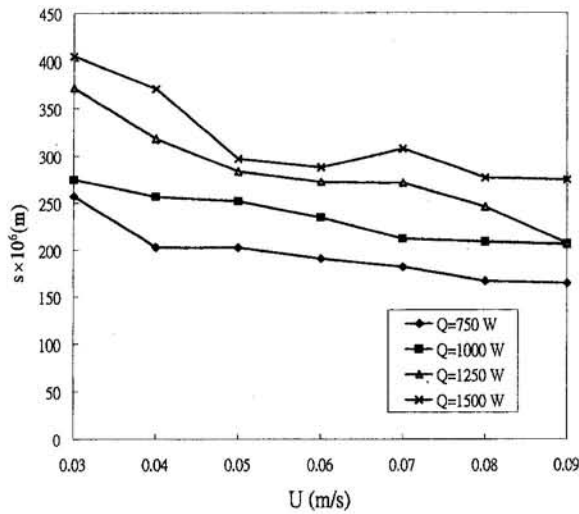
Fig. 6 (a) Average pitch, and (b) average amplitude of surface ripples versus welding speed for different beam powers in Al 1100
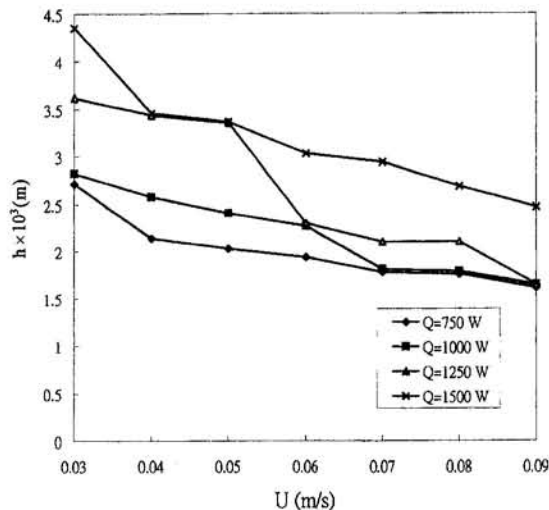

Fig. 7 Variation of fusion zone depth with beam power and welding speed for Al 1100
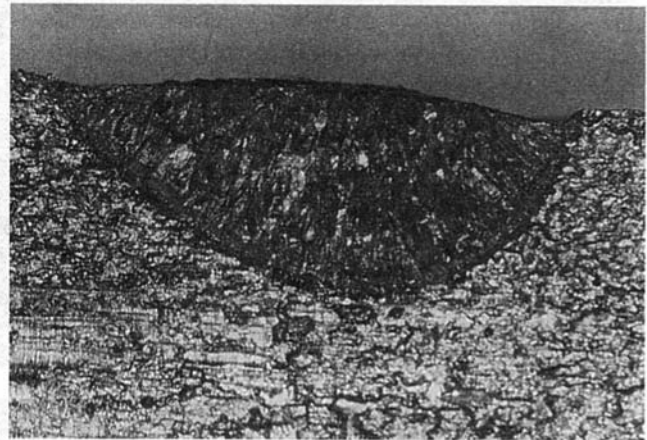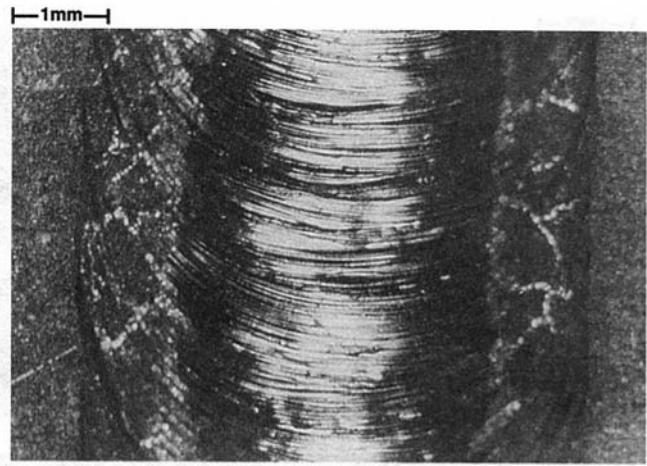
Fig. 8(a)

Fig. 8 Surface roughness and fusion zone shape, (a) Al 1100, 50 kV, 15 mA, 0.09 m/s, and (b) Al 1100, 50 kV, 30 mA, 0.08 m/s, and (c) SS 304, 50 kV, 30 mA, 0.02 m/s

than thousands, which confirm a strong flow in the free surface boundary layer governed by the first, second, and third relations of Eq. (13). Outside the surface boundary layer incident flux is balanced by conduction.

Considering an incident flux of 10^8 W/m^2 or a temperature difference of 1000 K and a fusion zone depth of aluminum $h = 10^{-3}$ m the characteristic velocities in the free surface layer are $u_s \approx 3$ m/s and $v_s \approx 0.01$ m/s, as calculated from Eqs. (11) and (12).

Amplitude of Ripples. Oscillations of the free surface at the rear edge of the molten pool determine the roughness of the solidified surface. Applying Eq. (7) at locations where the maximum velocity occurs and solidification front of the molten pool yields, respectively:

$$p_s - p_\infty = \gamma \frac{\partial^2 \eta_s}{\partial x^2} \tag{14}$$

$$p_e - p_\infty = \gamma \frac{\partial^2 \eta_e}{\partial x^2} \tag{15}$$

Subtracting Eq. (14) from Eq. (15) leads to

$$p_e - p_s = \gamma \frac{\partial^2 a}{\partial x^2} \tag{16}$$

where the average amplitude of ripples $a = \eta_e - \eta_s \approx \eta_e$. This is because the location where the maximum velocity occurs is far from the corner region and the free surface is nearly flat by
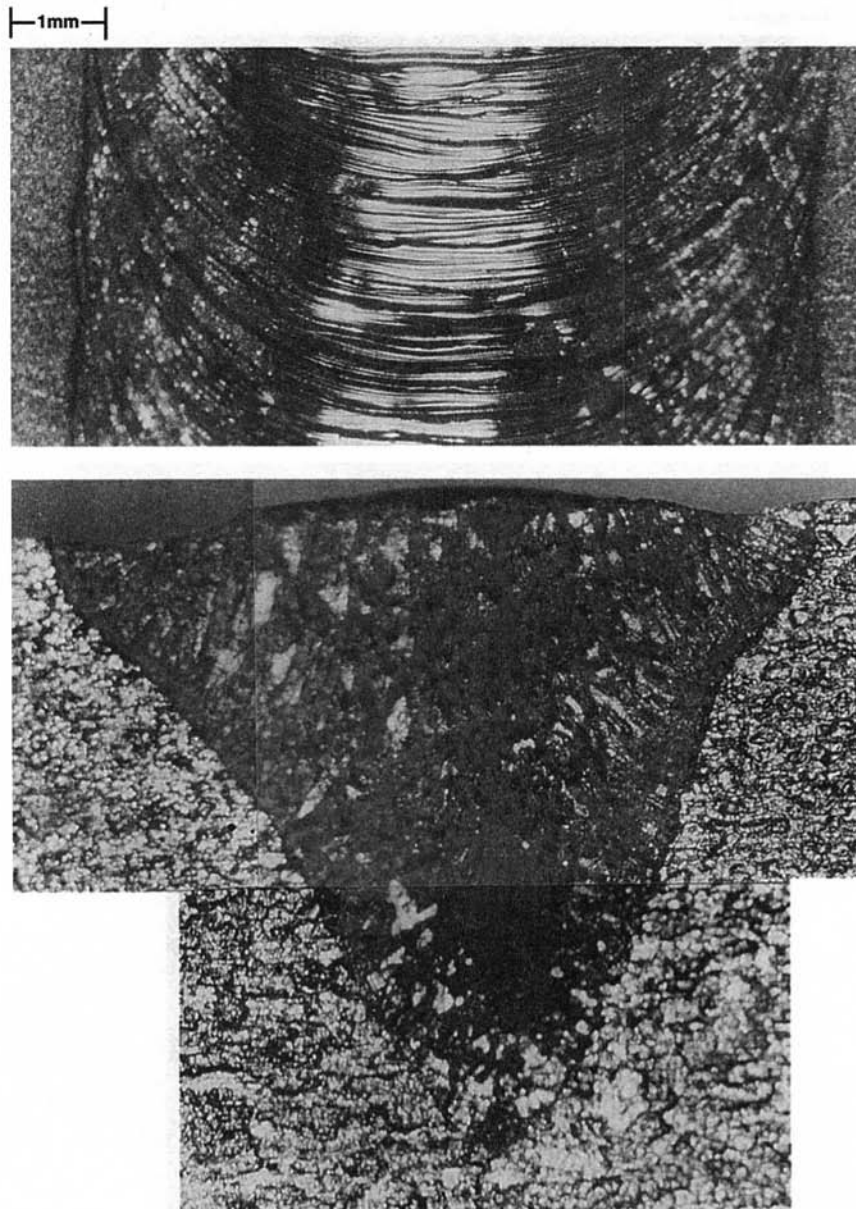
|—1mm—|

Fig. 8(b)

comparison with that near the solidification front (Rivas, 1991). Velocities of the free surface layer drop from 3 m/s to 10^{-2} m/s (i.e., the welding speed) within one tenth or hundredth of a millimeter in the corner region (Zebib et al., 1985). In view of strong viscous stress and rapid increase in the thickness of the surface layer, using the Bernoulli's equation without head losses to evaluate the pressure difference is invalid. A relevant and simple way to calculate pressure difference between two locations is

$$\frac{p_s}{\rho} + \frac{u_s^2}{2} = \frac{p_e}{\rho} + \frac{U^2}{2} + g\,\Delta h_{\text{loss}} \qquad (17)$$

where the welding speed $U \ll u_s$. It should be noted that Eq. (17) is similar to the analysis of piping systems (e.g., White, 1979). The head losses due to viscous dissipation and sudden expansion in the corner region can be determined by

$$\Delta h_{\text{loss}} = K\frac{u_s^2}{2g} \qquad (18)$$

where the loss coefficient K approaches unity for a strong sudden expansion. Substituting Eq. (18) into Eq. (17) and using Eq. (16) give

$$p_e - p_s = (1 - K)\rho u_s^2 \sim \gamma_m \frac{a}{r_e^2} \qquad (19)$$

which indicates that the maximum difference in pressure along the free surface cannot be as large as the dynamic pressure. Substituting Eq. (11) into Eq. (19) gives

$$a = (1 - K)\frac{\rho}{\gamma_m}\left[\nu\left(\frac{d\gamma}{dT}\frac{q_c hr_e}{k\mu}\right)^2\right]^{2/3} \qquad (20)$$

where the amplitude is found to increase with incident flux and surface tension gradient. It is noted that incident flux q_c in Eq. (20) has a lower bound of an critical flux in order to melt the workpiece. The rear length of the molten region and incident flux in Eq. (20) should be interrelated. Although more complete models were presented by Eagar and Tsai (1983) and Wei and
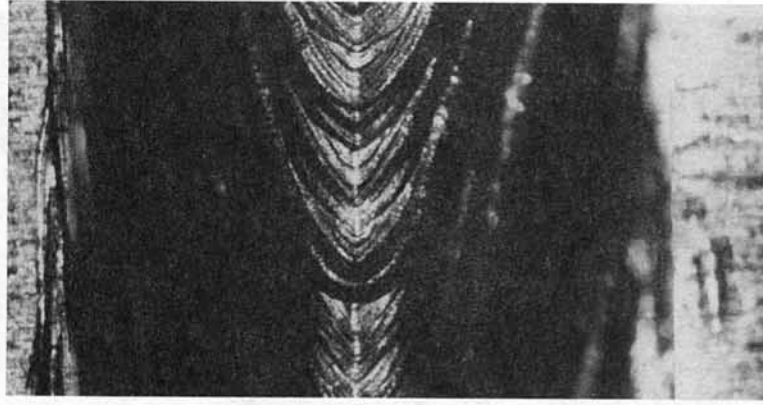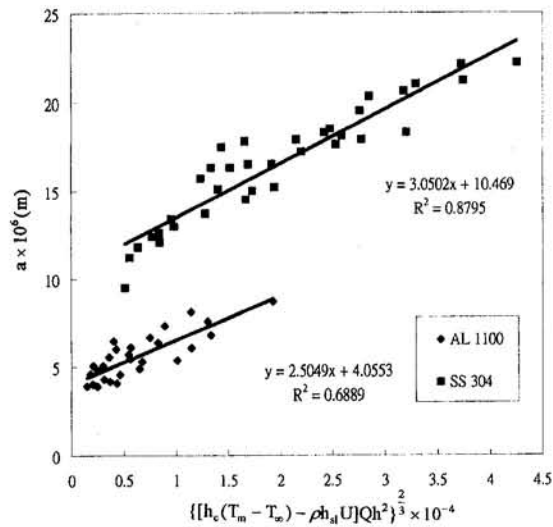
|—1mm—|

Fig. 8(c)

Fig. 9 Dimensional average amplitude versus product of working variables for Al 1100 and SS 304
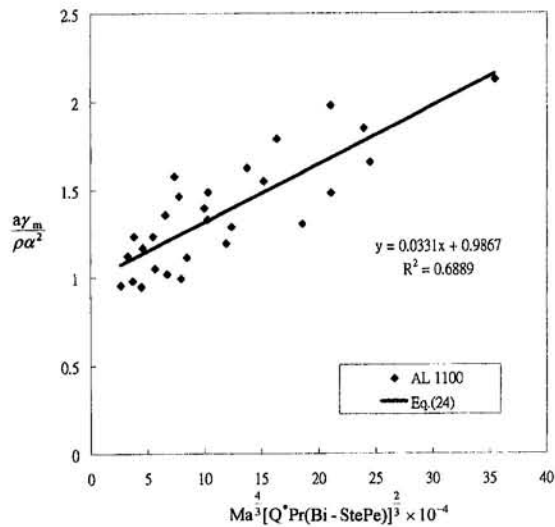

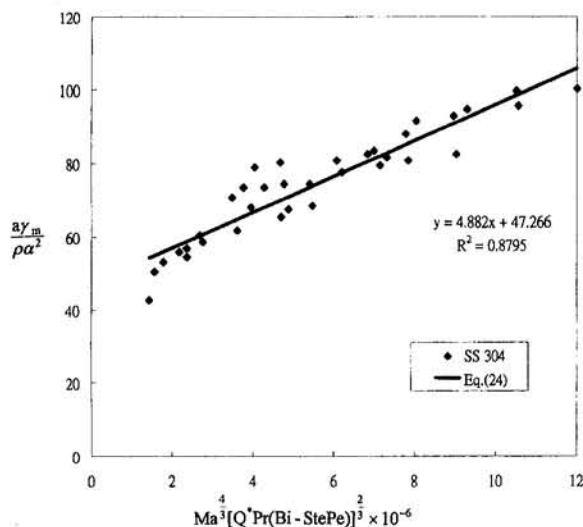Fig. 10 Dimensionless average amplitude versus product of dimensionless parameters for Al 1100

Fig. 11 Dimensionless average amplitude versus product of dimensionless parameters for SS 304
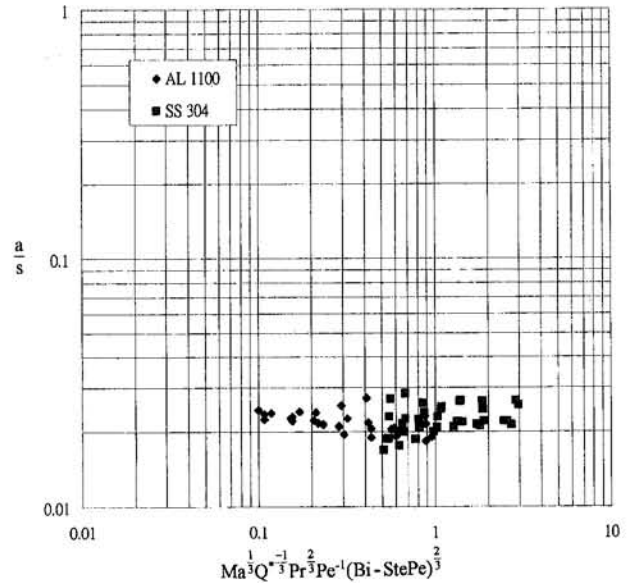

Fig. 12 Amplitude-to-pitch ratio versus product of dimensionless parameters for Al 1100 and SS 304

Shian (1993), a simple and successful evaluation of the shape of the molten region as provided by Christensen et al. (1965) can be used. The temperature distribution was determined from Rosenthal's point source solution (Rosenthal, 1941), which was obtained from Eq. (5) by neglecting convection for a low Peclet number in a quasi-steady state

$$\frac{T - T_\infty}{T_m - T_\infty} = \frac{Q}{2\pi k(T_m - T_\infty)\sqrt{x^2 + y^2 + z^2}}$$

$$\times \exp\left[-\frac{U}{2\alpha}(\sqrt{x^2 + y^2 + z^2} - x)\right] \quad (21)$$

which gives the temperature gradient at the solidification front on the workpiece surface:

$$-k\frac{\partial T}{\partial x} = \frac{Q}{2\pi r_e^2} \quad (22)$$

Equation (22) is relevant by considering that beam power is removed by conduction at a hemispheric surface of a radius r_e. Substituting Eq. (22) into Eq. (9) and introducing a heat transfer coefficient to evaluate conduction into the solid leads to

$$\frac{Q}{2\pi r_e^2} + \rho h_{sl}U = h_c(T_m - T_\infty) \quad (23)$$

where the heat transfer coefficient is an empirical quantity, i.e., introducing incident flux $q_c = Q/r_e^2$ and substituting Eq. (23) into Eq. (20) to replace length r_e give a dimensionless relationship between the average amplitude of ripples and working parameters:

$$\frac{a\gamma_m}{\rho\alpha^2} = c_a(1 - K) \text{ Ma}^{4/3}[PrQ*(Bi - Ste\ Pe)]^{2/3} \quad (24)$$

where the factor c_a can be determined from experiments. In deriving Eq. (24), lengths are nondimensionalized by the fusion zone depth, which is a function of beam power, welding speed, and thermal properties. Although fusion zone depths can be determined from Eq. (21), which is only valid for a low-power density beam, measured depths are chosen as a length scale for reality.

Pitch of Ripples. The average pitch of the ripples can be estimated from

$$s = Ut = U \frac{a}{v_e} \qquad (25)$$

where the time scale is obtained by equating the term on the left-hand side and the first term on the right-hand side of Eq. (10). In Eq. (25) the vertical velocity component in the corner region is estimated to be $v_e = 10^{-4}$ m/s for a welding speed of 10^{-2} m/s, an amplitude of 10^{-6} and pitch of 10^{-4} m, as can be seen later. Unlike the horizontal velocity component, which is identical to the welding speed, an estimation of the vertical velocity component near the corner region is difficult. It is proposed that

$$v_e = F(Q, U, 1 - K, \ldots)v_s \qquad (26)$$

where the function F includes complicated variables. Its value, however, can be estimated to be of an order of 0.01. This is because vertical velocity components in the free surface layer and corner region are, respectively, 10^{-2} m/s and 10^{-4} m/s, as discussed previously. Substituting Eqs. (12), (20), and (26) into Eq. (25) leads to

$$s = \frac{1 - K}{F(Q, U, 1 - K, \ldots)} \frac{\rho U}{\gamma_m} \left| \frac{d\gamma}{dT} \right| \frac{q_c h r_e^2}{k\mu} \qquad (27)$$

A dimensionless form of Eq. (27) therefore yields

$$\frac{s\gamma_m}{\rho\alpha^2} = \frac{1 - K}{F(Q, U, 1 - K, \ldots)} \text{Pe Ma}Q^* \qquad (28)$$

A reliable determination of average pitches from Eq. (28) is difficult unless the function F is known. Fortunately, experimental measurements from this work reveal that the ratios of the amplitude to pitch are relatively constant for Al 1100 and SS 304. That is,

$$a = cs \qquad (29)$$

where the proportional constant $c = 0.015 - 0.03$. A reliable predication of surface ripples therefore is obtained from Eqs. (24) and (29).

Results and Discussion

In this study, roughness characterized by an average pitch and amplitude of surface ripples on the workpiece as a function of beam power, welding speed, and properties of workpieces is investigated. Using a constant accelerating voltage, for example, 50 kV in the present work, to maintain the focal spot on the workpiece surface is crucial. Otherwise, as shown in Fig. 4, asymmetric ripples on the top surface and a corresponding fusion zone on a transverse cross section in a workpiece of SS 304 take place. In this case, the focal spot was above the workpiece surface. Unfortunately, an interpretation of the observation is impossible at the present time.

Figure 5(a) shows that the surface of the specimen of Al 1100 exhibits coarse ripples superimposed on fine ripples. Both types of ripple occur periodically. The pitches between fine and coarse ripples are around 5×10^{-6} and $0.5-3 \times 10^{-4}$ m, respectively. Slopes of faces in front and rear of each ripple are observed to be different. An extensive investigation on the oscillations of the free surface near the corner region between the molten pool and solid is required. In Figs. 5(b) and 5(c) it is seen that pitches of coarse ripples decrease with reduced welding current and increased welding speed, respectively. A decrease in welding current or beam power reduces the free surface temperature gradient (see Eq. (22)), which decreases thermocapillary flow of the free surface layer or difference in liquid pressure (see Eq. (19)). Roughness therefore decreases.

On the other hand, increasing the welding speed increases the rear length of the molten pool (see Eq. (23)) in order to reduce heat conduction to the solidification front. As a result, a decrease of temperature gradient reduces thermocapillary flow and roughness.

Quantitative results for average pitches and amplitudes of ripples as a function of beam power and welding speed for welding Al 1100 are shown in Figs. 6(a) and 6(b) respectively. It is noted that after a comparison between outputs of the roughness instrument and observations from an optical microscope, the pitches measured from the roughness instrument were due to coarse ripples. Pitches and amplitudes are of magnitudes of 10^{-4} m and 10^{-6} m, respectively. It is required to present the variations of fusion zone depth with the beam power and welding speed. As shown in Fig. 7, an increase in beam power and decrease in welding speed increase the depth of the fusion zone.

Surface ripples associated with fusion zone depths of Al 1100 by changing beam power or welding speed are shown in Figs. 8(a) and 8(b), where the upper and lower photographs represent top and transverse views of the fusion zone, respectively. It can be seen that an increase in the beam power from 750 to 1500 W and a decrease in the welding speed from 0.09 to 0.08 m/s increase the depth of the fusion zone and enhances roughness of the surface. A decrease in welding speed increases the fusion zone depth of SS 304 and produces coarser ripples, as shown in Fig. 8(c).

A relationship between the dimensional amplitude and a product of working variables for workpieces of Al 1100 and SS 304 is shown in Fig. 9. The abscissa represents a combination of working variables of Eq. (20). As a result, for a given material use of Eq. (20) leads to a linear relationship in the figure. It can be seen that experimental data are best fitted by straight lines for both materials. Agreement between the scale analysis and experimental results in this work therefore is achieved. Aside from the effects of beam power and welding speed on roughness, as discussed previously, an increase in the heat transfer coefficient or decrease in latent heat for solidification increase roughness. This is because the rear length of the molten pool is decreased by increasing the heat transfer coefficient and reducing latent heat (see Eq. (23)). As a consequence, incident flux near the solidification front at the workpiece surface increases.

The dimensionless amplitude versus a product of dimensionless parameters (see Eq. (24)) for workpieces of Al 1100 is shown in Fig. 10. It can be seen that increases of the dimensionless beam power, Marangoni, Prandtl, and Biot numbers enhance roughness in contrast to Stefan and Peclet numbers. Similar results for SS 304 are also shown in Fig. 11.

A prediction of the average pitch of surface ripples is more difficult than that of the average amplitude, as mentioned previously. Fortunately, in Fig. 12 it can be seen that the average amplitude is nearly proportional to the average pitch over a wide range of working conditions for Al 1100 and SS 304. The proportional constant is between 0.015 and 0.03. Use of Eq. (29) instead of Eq. (28) therefore is more reliable. In order to obtain general results for the average pitch of surface ripples, a further investigation of Eq. (28) is required.

Conclusions

The following conclusions are drawn:

1 In this study, it is found that dimensionless average amplitude and pitch governed by Eqs. (24) and (29), respectively, increase with increasing dimensionless beam power, Marangoni, Prandtl, Biot numbers and decreasing Stefan and Peclet numbers. A physical mechanism of rippling resulting from a Marangoni flow driven by a negative temperature-dependent surface tension gradient in a molten pool is discovered.

2 Coarse ripples were observed to be superimposed on fine ripples. The pitches between fine and coarse ripples are around 5×10^{-6} and 10^{-4} m, respectively, while the amplitude is of the order of 10^{-6} m. The ratios between the amplitude and pitch are relatively constant between 0.015 to 0.03 for Al 1100 and SS 304.

Acknowledgments

References

Anthony, T. R., and Cline, H. E., 1977, "Surface Rippling Induced by Surface-Tension Gradients During Laser Surface Melting and Alloying," *Journal of Applied Physics*, Vol. 48, pp. 3888–3894.

Arata, Y., Matsuda, F., and Murakami, T., 1973, "Some Dynamic Aspects of Weld Molten Metal in Electron Beam Welding," *Transactions of Japan Welding Research Institute*, Vol. 2, pp. 23–32 (152–161).

Bejan, A., 1984, *Convective Heat Transfer*, Wiley, New York, Chap. 2.

Burgardt, P., 1986, "Electron Beam Beam Size Calibration," *Summary of Calibration of Welding Systems Meeting*, L. N. Tallerico, ed., Sandia National Lab., Livermore, CA, Feb., pp. 258–266.

Christensen, N., Davies, V. de L., and Gjermundsen, K., 1965, "Distribution of Temperatures in Arc Welding," *British Welding Journal*, Vol. 12, pp. 54–75.

D'annessa, A. T., 1970, "Sources and Effects of Growth Rate Fluctuations During Weld Metal Solidification," *Welding Journal*, Vol. 49, pp. 41-s-45-s.

Eagar, T. W., and Tsai, N.-S., 1983, "Temperature Fields Produced by Traveling Distributed Heat Sources," *Welding Journal*, Vol. 62, pp. 346-s to 355-s.

Ecer, G. M., Tzavaras, A., Gokhale, A., and Brody, H. D., 1982, "Weld Pool Fluid Motion and Ripple Formation in Pulsed-Current GTAW," in: *Trends in Welding Research in the United States*, S. A. David, ed., Proceedings of a conference sponsored by the Joining Division of American Society for Metals, New Orleans, Nov. 16–18, 1981, pp. 419–442.

Garland, J. G., and Davies, G. J., 1970, "Surface Rippling and Growth Perturbations During Weld Pool Solidification," *Metal Construction and British Welding Journal*, Vol. 2, pp. 171–175.

Giedt, W. H., and Tallerico, L. N., 1988, "Prediction of Electron Beam Depth of Penetration," *Welding Journal*, Vol. 67, pp. 299-s to 305-s.

Hicken, G. K., Giedt, W. H., and Bentley, A. E., 1991, "Correlation of Joint Penetration With Electron Beam Current Distribution," *Welding Journal*, Vol. 70, pp. 69-s–75-s.

Kamotani, Y., Ostrach, S., and Pline, A., 1995, "A Thermocapillary Convection Experiment in Microgravity," ASME JOURNAL OF HEAT TRANSFER, Vol. 117, pp. 611–618.

Mills, K. C., and Keene, B. J., 1990, "Factors Affecting Variable Weld Penetration," *International Materials Reviews*, Vol. 35, pp. 185–216.

O'Brien, R. L., ed., 1991, *Welding Handbook, Welding Processes*, Vol. 2, 8th ed., American Welding Society, Miami, p. 64.

Ostrach, S., 1982, "Low-Gravity Fluid Flows," *Annual Reviews of Fluid Mechanics*, Vol. 14, pp. 313–345.

Ostrach, S., Kamotani, Y., and Lai, C. L., 1985, "Oscillatory Thermocapillary Flows," *PCH PhysicoChemical Hydrodynamics*, Vol. 6, pp. 585–599.

Rivas, D., and Ostrach, S., 1992, "Scaling of Low-Prandtl-number Thermocapillary Flows," *International Journal of Heat and Mass Transfer*, Vol. 35, pp. 1469–1479.

Rivas, D., 1991, "High-Reynolds-Number Thermocapillary Flows in Shallow Enclosures," *Physics of Fluids A*, Vol. 3, pp. 280–291.

Rosenthal, D., 1941, "Mathematical Theory of Heat Distribution During Welding and Cutting," *Welding Journal*, Vol. 20, pp. 220-s to 234-s.

Schwabe, D., and Scharmann, A., 1979, "Some Evidence for the Existence and Magnitude of a Critical Marangoni Number for the Onset of Oscillatory Flow in Crystal Growth Melts," *Journal of Crystal Growth*, Vol. 46, pp. 125–131.

Sen, A. K., and Davis, S. H., 1982, "Steady Thermocapillary Flows in Two-Dimensional Slots," *Journal of Fluid Mechanics*, Vol. 121, pp. 163–186.

Strani, M., Piva, R., and Graziani, G., 1983, "Thermocapillary Convection in a Rectangular Cavity: Asymptotic Theory and Numerical Simulation," *Journal of Fluid Mechanics*, Vol. 130, pp. 347–376.

Tong, H., and Giedt, W. H., 1969, "Radiographs of the Electron Beam Welding Cavity," *The Review of Scientific Instruments*, Vol. 40, pp. 1283–1285.

Wei, P. S., and Chow, Y. T., 1992, "Beam Focusing Characteristics and Alloying Element Effects on High-Intensity Electron Beam Welding," *Metallurgical Transactions B*, Vol. 23B, pp. 81–90.

Wei, P. S., and Shian, M. D., 1993, "Three-Dimensional Analytical Temperature Field Around the Welding Cavity Produced by a Moving Distributed High-Intensity Beam," ASME JOURNAL OF HEAT TRANSFER, Vol. 115, pp. 848–856.

White, F. M., 1979, *Fluid Mechanics*, McGraw-Hill, New York, pp. 353–360.

Xu, J-J., and Davis, S. H., 1984, "Convective Thermocapillary Instabilities in Liquid Bridges," *Physics of Fluids*, Vol. 27, pp. 1102–1107.

Zebib, A., Homsy, G. M., and Meiburg, E., 1985, "High Marangoni Number Convection in a Square Cavity," *Physics of Fluids*, Vol. 28, pp. 3467–3476.

Journal of Heat Transfer

Technical Notes

This section contains shorter technical papers. These shorter papers will be subjected to the same review process as that for full papers.

Closed-Form Solutions for Transcendental Equations of Heat Transfer

R. A. Leathers[1,2] and N. J. McCormick[1,3]

1 Introduction

In an era with modern computers and well-established root-finding algorithms, the numerical solution of transcendental equations is relatively straightforward. It may be of interest to heat transfer researchers and students, however, that it is also possible to state explicit solutions for transcendental equations arising in a variety of heat transfer problems. Explicit solutions to many transcendental equations have been developed for a variety of non-heat-transfer applications, such as celestial mechanics [the solution of Kepler's equation for elliptic and hyperbolic orbits (Siewert and Burniston, 1972)], ferromagnetism [the molecular field equation (Siewert and Essig, 1973)], nuclear reactor theory [the "critical condition" for a bare reactor (Siewert, 1973)], and applied mechanics [the eigenvalues of a clamped plate (Siewert and Phelps, 1978)]. The general theory for solving these problems is based on the methods of Muskhelishvili (1953) and has been developed by Burniston and Siewert (1973).

The procedure for solving transcendental equations for roots $\pm z_m$, $m = 0, 1, \ldots$, depends on formulating an appropriate Riemann problem of complex variable theory and then expressing the solution(s) of that transcendental equation in terms of a canonical solution of that problem. For the Riemann problem a function $\Omega_m(z)$ that is analytic in the complex plane except for the branch cut $[-1, 1]$ is separated into a product of functions,

$$\Omega_m(z) = \Lambda_m(z)\Lambda_m(-z), \qquad (1)$$

(i.e., the so-called Wiener–Hopf factorization), where $\Lambda_m(z)$ is analytic in the complex plane except for the branch cut $[0, 1]$. The Riemann problem is defined by the boundary condition

$$\Phi_m^+(x) = \Theta_m(x)\Phi_m^-(x), \quad x \in (0, 1), \qquad (2)$$

where the superscripts $+$ and $-$ denote the approach of z to the real axis $x \in (0, 1)$ from above and below, and

$$\Theta_m(x) = \frac{\Omega_m^+(x)}{\Omega_m^-(x)} = \exp[2i \arg \Omega_m^+(x)]. \qquad (3)$$

Here and elsewhere, $\arg \Omega_m^+(x) = \tan^{-1}[\operatorname{Im} \Omega_m^+(x)/\operatorname{Re}\Omega_m^+(x)]$. The objective is to find a function $\Phi_m(z)$ that is analytic in the plane cut from 0 to 1 along the real axis and nonvanishing in the finite plane so that $\Theta_m(x)$ will be continuous and nonvanishing for $x \in (0, 1)$. Then the canonical solution for $\Phi_m(z)$ can be written as (Burniston and Siewert, 1973)

$$\Phi_m(z) = (1 - z)^{-\kappa_m} \exp\left[\frac{1}{\pi}\int_0^1 \arg \Omega_m^+(x) \frac{dx}{x - z}\right], \qquad (4)$$

with $\arg \Omega_m^+(0) = 0$. The index κ_m is such that $2\pi\kappa_m$ is the change in the argument of $\Theta_m(x)$ as x varies from 0 to 1.

Our objective here is to bring together in one place some existing closed-form solutions of transcendental equations, available in mathematics literature, and show they are applicable to heat transfer. In the process we illustrate that the transcendental equation for the convectively cooled thin fin problem is a special case of a transcendental equation arising in a radiative heat transfer problem. A secondary objective is to check the closed-form solutions numerically.

We illustrate in Sec. 2 the general procedure for solving such problems with the solution of the transcendental equation arising in the convective heat loss from a thin fin. In Sec. 3 we provide the closed-form solutions for two one-dimensional heat conduction problems in rectangular geometry. Then in Sec. 4 the solutions of the Wien displacement law and the asymptotic eigenvalue of the radiative transfer equation are given. Section 5 contains a few comments about the numerical evaluation of the closed-form equations.

2 Convectively Cooled Thin Fin Problem

The fin we consider is thin enough that there is only one dimension in which the temperature $T(x)$ varies along $0 \le x \le L$ due to a convective heat loss along the perimeter $\mathcal{P}$. The temperature at the base of the fin is a given value $T(x) = T_0$ and the environment is at an external temperature T_e. The fin cross-sectional area is A, its thermal conductivity is k, and the constant convective heat transfer coefficient is h_c. The governing partial differential equation is

$$\frac{d^2\theta(x)}{d^2x} - \beta^2\theta(x) = 0, \qquad (5)$$

where $\theta(x) = [T(x) - T_e]/[T_0 - T_e]$ and where $\beta^2 = h_c\mathcal{P}/kA$.

We shall assume the fin has an insulated tip so that $dT(x)/dx|_{x=L} = 0$. The equation for the fin efficiency η, $0 \le \eta \le 1$, is given in introductory heat transfer textbooks as (Holman, 1990; Incropera and DeWitt, 1996; Mills, 1993)

$$\eta = \frac{\dot{Q}}{h_c{}^p L(T_0 - T_e)} = \frac{1}{\chi} \tanh(\chi), \qquad (6)$$

for $\chi = \beta L$, and where the overall heat transfer from the fin is $\dot{Q}$. This is a transcendental equation if we seek L for a specified η. The equation can be rearranged so that we seek the zeros of the function

$$\Lambda(z) = 1 - \eta z \tanh^{-1}(1/z),$$
$$= 1 - \frac{\eta z}{2} \int_{-1}^{1} \frac{d\mu}{z - \mu}, \qquad (7)$$

where $z = 1/\eta\chi$.

Because the roots of Eq. (7) are the two eigenvalues $\pm\nu_0$ of the radiative transfer equation for isotropic scattering (Case and Zweifel, 1967), the function $\Lambda(z)$ has been extensively investigated and the eigenvalues were tabulated many years ago (Case et al., 1953). We can obtain closed-form solutions for $\chi = (\eta\nu_0)^{-1}$ after taking over from Siewert (1980) the previously developed solutions for ν_0, which will now be briefly summarized.

$\Lambda(z)$ is analytic in the complex plane cut from -1 to 1 along the real axis, and satisfies the equations $\Lambda(0) = 1$, $\Lambda(\infty) = 1 - \eta$, and, for $|z| > 1$, $\Lambda(z) = \Lambda(\infty) - \eta(z^{-2}/3 + z^{-4}/5 + \ldots)$. The boundary values as the function approaches the cut from above/below are given by

$$\Lambda^{\pm}(\nu) = \lim_{\epsilon \to 0^+} \Lambda(\nu \pm i\epsilon)$$
$$= \lambda(\nu) \pm \pi i \eta \nu/2, \quad \nu \in (-1, 1), \qquad (8)$$

where

$$\lambda(\nu) = 1 - \eta\nu \tanh^{-1} \nu, \quad \nu \in (-1, 1). \qquad (9)$$

Since $\Lambda(z)$ vanishes at $\pm\nu_0$, the function $\Lambda_0(z) = [\Lambda(\infty)]^{1/2} \times \Phi_0(z)(\nu_0 - z)$ is chosen to satisfy Eq. (1). Then the function $\Phi_0(z)$ is continuous and nonvanishing for $x \in (0, 1)$ and satisfies Eq. (2) with index $\kappa_1 = 1$ since 2π is the change in the argument of $\Theta_0(x)$ as x varies from 0 to 1. Thus from Eqs. (4) and (8),

$$\Phi_0(z) = (1 - z)^{-1} \exp\left[\frac{1}{\pi} \int_0^1 \tan^{-1}\left(\frac{\pi\eta\nu/2}{\lambda(\nu)} \right) \frac{d\nu}{\nu - z} \right]. \qquad (10)$$

Because

$$\Omega(z) = \Lambda(\infty)\Phi_0(z)\Phi_0(-z)(\nu_0^2 - z^2), \qquad (11)$$

it follows that the desired root we seek satisfies the equation

$$\nu_0^2 = z^2 + \Lambda(z)[\Lambda(\infty)\Phi_0(z)\Phi_0(-z)]^{-1}. \qquad (12)$$

From this equation Siewert (1980) obtained two particularly concise equations for ν_0^2 by setting $z = 0$ and by letting $z \to \infty$, respectively:

$$\nu_0^2 = \frac{1}{\Lambda(\infty)} \exp\left[-\frac{2}{\pi} \int_0^1 \tan^{-1}\left(\frac{\pi\eta\nu/2}{\lambda(\nu)} \right) \frac{d\nu}{\nu} \right], \qquad (13a)$$

$$\nu_0^2 = 1 + \frac{\eta}{3\Lambda(\infty)} - \frac{2}{\pi} \int_0^1 \tan^{-1}\left(\frac{\pi\eta\nu/2}{\lambda(\nu)} \right) \nu \, d\nu. \qquad (13b)$$

From either of these equations the value of ν_0 can be computed, which can be used to determine $\chi = \beta L = (\eta\nu_0)^{-1}$.

3 Heat Conduction Problems

We turn now to the consideration of transcendental equations that arise in the solutions of one-dimensional heat conduction problems using the separation of variables technique. We consider the solutions of the problems (Özışık, 1989, 1993)

$$\frac{d^2 T(x)}{dx^2} + \beta^2 T(x) = 0, \quad 0 < x < L, \qquad (14)$$

$$-\alpha_1 \frac{dT(x)}{dx} + H_1 T(x) = 0, \quad \text{for} \quad x = 0, \qquad (15)$$

$$\alpha_2 \frac{dT(x)}{dx} + H_2 T(x) = 0, \quad \text{for} \quad x = L, \qquad (16)$$

where $\alpha_j = 0$ or 1 and $H_j = 0$, 1, or h_{cj}/k, where h_{cj} is the convective heat transfer coefficient at surface $j = 1$ or 2 and k_j is the corresponding thermal conductivity. We seek the eigenvalues β_m that are the roots of different transcendental equations depending on the values of the coefficients α_j and H_j.

One Insulated Surface. We consider the case where $\alpha_1 = \alpha_2 = 1$ and either $H_1 = H$ or $H_2 = H$. Then the equation for the eigenvalues $\pm\beta_m$ is (Özışık, 1989, 1993)

$$\beta_m L \tan \beta_m L = \omega, \qquad (17)$$

which is a transcendental equation when $\omega = HL > 0$ is known. Numerical values are given in Table 4.20 of Abramowitz and Stegun (1964) and in Appendix II of Özışık (1993). This equation was solved by Burniston and Siewert (1973) where it was transformed with the substitution $\beta_m L = i\omega z$ to one where the roots are to be determined for the equation

$$z - \frac{1}{2\omega}\left[\ln\left(\frac{z - 1}{z + 1} \right) \pm 2m\pi i \right] = 0, \qquad (18)$$

where the symbol "ln" denotes the principal branch of the natural logarithm function in the plane cut from -1 to 1 along the real axis. For

$$\Lambda_0(z) = z\left[z - \frac{1}{2\omega} \ln\left(\frac{z - 1}{z + 1} \right) \right], \qquad (19a)$$

$$z\Lambda_m(z) = \Lambda_0(z) - im\pi z/\omega, \qquad (19b)$$

the results for the positive roots are (Burniston and Siewert, 1973)

$$\beta_0 L = \left(\frac{\pi\omega}{2} \right)^{1/2} \exp\left\{ -\frac{1}{\pi} \int_0^1 \left[\arg \Lambda_0^+(\nu) \right. \right.$$
$$\left. \left. + \frac{\pi}{2} \right] \frac{d\nu}{\nu} \right\}, \qquad (20a)$$

and

$$\beta_m L = \frac{\pi}{2}(4m^2 - 1)^{1/2} \exp\left[-\frac{1}{\pi} \int_0^1 \arg \Omega_m^+(\nu) \frac{d\nu}{\nu} \right],$$
$$m = 1, 2, \ldots, \qquad (20b)$$

where

$$\Lambda_0^+(\nu) = \nu\left[\nu - \frac{1}{2\omega} \ln\left(\frac{1 - \nu}{1 + \nu} \right) \right] - \pi i \nu/2\omega, \qquad (21a)$$

$$\nu^2 \Omega_m^+(\nu) = [\Lambda_0^+(\nu)]^2 + m^2\pi^2\nu^2/\omega^2. \qquad (21b)$$

Fixed Surface Temperature. We next consider the case where one surface is at temperature T_B and shift the temperature variable so that the surface temperature is 0. Then from Eqs. (15)–(17) we set $\alpha_1 = 1$, $H_1 = H$, $\alpha_2 = 0$ or $H_2 = 1$ (or, alternatively, $\alpha_1 = 0$, $H_1 = 1$, $\alpha_2 = 1$ or $H_2 = H$). The equation for the eigenvalues $\pm\beta_m$ is (Özışık, 1989, 1993)

$$\beta_m L \cot \beta_m L = -HL. \tag{22}$$

Numerical values are given in Table 4.19 of Abramowitz and Stegun (1964) and in Appendix II of Özışık (1993). Burniston and Siewert (1973) showed that the roots of Eq. (22) are

$$\beta_m L = m\pi \, \exp\left[\frac{1}{\pi}\int_0^1 \arg \Omega_m^+(\nu)\,\frac{d\nu}{\nu}\right], \quad m = 1, 2, \ldots, \tag{23}$$

where, for known values of $\omega = -1/HL < 0$,

$$\Omega_m^+(\nu) = [\Lambda_0^+(\nu)]^2 + m^2\pi^2\omega^2\nu^2, \tag{24a}$$

and

$$\Lambda_0^+(\nu) = 1 + \frac{\omega\nu}{2}\ln\left(\frac{1-\nu}{1+\nu}\right) + \pi i\omega\nu/2. \tag{24b}$$

4 Radiative Transfer Problems

The Wien Displacement Law. The equation for the black-body emissive power $E_{b\lambda}$ as a function of wavelength λ and absolute temperature T is

$$E_{b\lambda} = \frac{C_1\lambda^{-5}}{\exp(C_2/\lambda T) - 1}, \tag{25}$$

where $C_1 = 3.742 \times 10^8$ W μm^4/m^2 and $C_2 = 1.4389 \times 10^4$ μm K. From $dE_{b\lambda}/d\lambda = 0$ it follows that the wavelength λ_m for the maximum power is the solution of the transcendental equation

$$(5 - x)\exp(x) = 5, \tag{26}$$

where $x = C_2/\lambda_m T$. The solution has been given as (Siewert, 1981)

$$x = 4 \exp\left\{-\frac{1}{\pi}\int_0^\infty\left[\tan^{-1}\left(\frac{\pi}{\ln 5 - 5 - t - \ln t}\right) - \pi\right]\right.$$

$$\left. \times \frac{dt}{t+5}\right\}, \tag{27}$$

which gives a value of $x = 4.96511\ldots$.

The Eigenvalues of the Radiative Transfer Equation. Siewert (1980) developed closed-form solutions for computing the largest three eigenvalues ν_j, $j = 0$, 1, and 2, for the radiative transfer equation

$$\mu\frac{\partial}{\partial\tau}I(\tau,\mu) + I(\tau,\mu)$$

$$= \frac{\eta}{2}\sum_{l=0}^{L}(2l+1)f_l P_l(\mu)\int_{-1}^{1}P_l(\mu')I(\tau,\mu')d\mu', \tag{28}$$

that arise after the substitution

$$I_\nu(\tau,\mu) = \phi(\nu,\mu)\exp(-\tau/\nu). \tag{29}$$

(The eigenvalues ν_1 and ν_2 can occur when the scattering is more than linearly anisotropic.) The eigenvalues can be computed as roots of the equation

$$\Lambda(z) = 1 - \frac{\eta z}{2}\int_{-1}^{1}\frac{g(\mu,\mu)d\mu}{z-\mu}, \tag{30}$$

where

$$g(z,z) = \sum_{l=0}^{L}(2l+1)f_l g_l(z)P_l(z) \tag{31}$$

and $g_l(z)$ are the Chandrasekhar (1960) polynomials

$$(l+1)g_{l+1}(z) - zh_l g_l(z) + lg_{l-1}(z) = 0 \tag{32}$$

with $h_l = (2l+1)(1-\eta f_l)$ and $g_0(z) = 1$ and $g_{-1}(z) = 0$. Note Eq. (7) is a special case of Eq. (30) for the case of isotropic scattering with $g(\mu,\mu) = 1$. The generalizations of Eqs. (13) for the closed-form equations for ν_0^2, the square of the largest eigenvalue, are

$$\nu_0^2 = \frac{1}{\Lambda(\infty)}\exp\left[-\frac{2}{\pi}\int_0^1\tan^{-1}\left(\frac{\pi\eta\nu g(\nu,\nu)/2}{\lambda(\nu)}\right)\frac{d\nu}{\nu}\right], \tag{33a}$$

$$\nu_0^2 = 1 - \frac{2}{\pi}\int_0^1\tan^{-1}\left(\frac{\pi\eta\nu g(\nu,\nu)/2}{\lambda(\nu)}\right)\nu d\nu$$

$$+ \frac{\eta}{\Lambda(\infty)}\sum_{l=0}^{L}f_l B_l \tag{33b}$$

and the generalizations of the $\Lambda(\infty)$ and $\lambda(\nu)$ in Eq. (9) are given by

$$\Lambda(\infty) = \prod_{l=0}^{L}(1-\eta f_l), \tag{34a}$$

$$\lambda(\nu) = 1 + \frac{\eta\nu}{2}g(\nu,\nu)\ln\left(\frac{1-\nu}{1+\nu}\right)$$

$$+ \eta\nu\sum_{l=1}^{L}(2l+1)f_l g_l(\nu)\Gamma_l(\nu). \tag{34b}$$

Siewert (1980) has given equations for computing the B_l and $\Gamma_l(\nu)$.

5 Numerical Tests

All the explicit solutions were numerically verified by comparing their values to those obtained by iterative solution of the corresponding implicit equations for a variety of values of the independent variables. Roots of the implicit equations were found to a precision of 10^{-15} using a combination of the Newton–Raphson and bisection methods.

Integrals for the explicit solutions other than the radiative transfer eigenvalues were evaluated using Simpson's rule and were evaluated with sufficient precision to obtain roots that agreed to within 10^{-6} of the implicit solutions. For the thin fin problem, the integral was divided into two integrals of the ranges $0 \leq \nu \leq 0.95$ and $0.95 \leq \nu \leq 1.0$, and equally spaced points along the abscissa were concentrated in the second integral. Agreement of the roots of the implicit solutions over the full range of the parameter η required between 10^3 and 7×10^4 points, depending on the value of η. For the conduction problems, agreement in the solutions was verified over a large range of the parameter and for different eigenvalue indices m. Agreement in the roots for the fixed surface temperature problem for $m = 1$ and $-5 \leq \omega \leq 0$ required 6.5×10^4 integration points. Agreement in the roots for the insulated surface problem for $m = 1$ and $0 \leq \omega \leq 10$ required between 3.2×10^4 and 1.3×10^5 points, depending on the value of ω. Finally, verifica-

tion of the solution to the Wien equation required 1.6×10^4 points.

For the radiative transfer eigenvalue problem, integration in the explicit solution was performed using the Clenshaw–Curtis quadrature procedure of MAPLE V (Char et al., 1992). Agreement in the eigenvalue was obtained to at least nine significant digits using both Eq. (33a) and Eq. (33b) for a fourth-order binomial model of the coefficients f_l. It was observed it was much easier to obtain good numerical accuracy with Eq. (33b) than with Eq. (33a).

6 Summary

We have shown there is a rich literature of closed-form solutions of transcendental equations that can be taken over to five classical conduction, convection, and radiation heat transfer problems. All solutions evolve from the same canonical form given by Eq. (4) but are so complicated they reveal little physical insight. While it can hardly be recommended that these complicated integrals are easier to implement than a straightforward iteration routine, the solutions of the associated transcendental equations contribute an interesting perspective to the folklore surrounding the solution of such problems.

Acknowledgments

We appreciate the help and encouragement of C. E. Siewert.

References

Abramowitz, M., and Stegun, I. A., eds., 1964, *Handbook of Mathematical Functions*, National Bureau of Standards, Washington, DC, pp. 224–225.

Burniston, E. E., and Siewert, C. E., 1973, "The Use of Riemann Problems in Solving a Class of Transcendental Equations," *Proc. Cambridge Philosophical Society*, Vol. 73, pp. 111–118.

Case, K. M., de Hoffmann, F., and Placzek, G., 1953, *Introduction to the Theory of Neutron Diffusion*, Vol. I, Los Alamos Scientific Laboratory, Los Alamos, NM.

Case, K. M., and Zweifel, P. F., 1967, *Linear Transport Theory*, Addison-Wesley, Reading, MA.

Chandrasekhar, S., 1960, *Radiative Transfer*, Dover, New York, pp. 151–154.

Char, B. W., Geddes, K. O., Gonnet, G. H., Leong, B. L., Monagan, M. B., and Watt, S. M., 1992, *First Leaves: A Tutorial Introduction to Maple V*, Springer-Verlag, New York.

Holman, J. P., 1990, *Heat Transfer*, 7th ed., McGraw-Hill, New York, p. 46.

Incropera, F. P., and Dewitt, D. P., 1996, *Introduction to Heat Transfer*, 3rd ed., Wiley, New York, p. 122.

Mills, A. F., 1992, *Heat Transfer*, Irwin, Homewood, IL, p. 85.

Muskhelishvili, N. I., 1953, *Singular Integral Equations*, Noordhoff, Groningen.

Özışık, M. N., 1989, *Boundary Value Problems in Heat Conduction*, Dover, New York, pp. 43–59.

Özışık, M. N., 1993, *Heat Conduction*, 2nd ed., Wiley, New York, pp. 44–50.

Siewert, C. E., and Burniston, E. E., 1972, "An Exact Analytical Solution of Kepler's Equation," *Celestial Mechanics*, Vol. 6, pp. 294–304.

Siewert, C. E., 1973, "An Exact Analytical Solution of an Elementary Critical Condition," *Nuclear Science and Engineering*, Vol. 51, p. 78.

Siewert, C. E., and Essig, C. J., 1973, "An Exact Solution of a Molecular Field Equation in the Theory of Ferromagnetism," *Zeitschrift für Angewandte Mathematik und Physik*, Vol. 24, pp. 281–285.

Siewert, C. E., and Phelps, J. S., 1978, "On Solutions of a Transcendental Equation Basic to the Theory of Vibrating Plates," *Journal of Computational and Applied Mathematics*, Vol. 4, pp. 37–39.

Siewert, C. E., 1980, "On Computing Eigenvalues in Radiative Transfer," *Journal of Mathematical Physics*, Vol. 21, pp. 2468–2470.

Siewert, C. E., 1981, "An Exact Expression for the Wien Displacement Constant," *Journal of Quantitative Spectroscopy and Radiative Transfer*, Vol. 26, p. 467.

Viscous Dissipation Effect on Pressure Gradient for Laminar Flow of a Non-Newtonian Liquid Through a Duct of Subfreezing Wall Temperature

W. C. Luelf[1,2] and L. C. Burmeister[1,3]

Nomenclature

d = dimensionless differential operator
e = dimensionless natural number = 2.71828...
f = dimensionless friction factor, Eq. (20)
g_c = constant, 1 kg m/N s^2
k = thermal conductivity, W/m K
n = dimensionless power-law exponent, Eq. (2)
P = pressure, N/m^2
P' = pressure gradient = dP/dz
Q = volumetric flow rate, m^3/s
q = heat flux, W/m^2
R = tube radius, m
Re_M = dimensionless Reynolds number based on reference viscosity, Eq. (18)
r = radial distance, m
T = temperature, K
T_o = temperature, K

u = velocity in z direction, m/s
z = axial distance, m
β = dimensionless parameter, Eq. (30)
δ = unfrozen tube radius, m
λ = dimensionless shear rate parameter, Eq. (18)
μ = Newtonian viscosity, N s/m^2
μ_o = power-law viscosity coefficient, N s^n/m^2
μ^+ = reference viscosity, N s/m^2, Eq. (19)
ξ_∞ = dimensionless parameter, Eq. (31)
π = dimensionless natural number = 3.14159...
τ = shear stress, N/m^2

Superscripts

$*$ = dimensionless quantity

Subscripts

avg = average value
m = melting value
o = high shear rate value
r = in r direction, on r face
s = value for the solid
w = wall value
z = in z direction

[1] Department of Mechanical Engineering, University of Kansas, Lawrence, KS 66044-2234.

[2] Graduate Student.

[3] Professor; Mem. ASME.

Introduction

The solidification of flowing liquids occurs in the molding of plastics, casting of metals, energy storage, and so forth. In such applications the wall of the duct through which flow occurs is maintained below the freezing temperature of the liquid, resulting in the formation of a layer of frozen material on the duct wall, as surveyed by Fukusako and Yamada (1994). Except for Yang et al. (1992), who treated unsteady solidification of a power-law liquid in the inlet region, the effects of viscous dissipation have been neglected in most analyses. Viscous dissipation at specified volumetric flow rate enables the thickness of the frozen layer always to be less than the duct radius as energy

tion of the solution to the Wien equation required 1.6×10^4 points.

For the radiative transfer eigenvalue problem, integration in the explicit solution was performed using the Clenshaw–Curtis quadrature procedure of MAPLE V (Char et al., 1992). Agreement in the eigenvalue was obtained to at least nine significant digits using both Eq. (33a) and Eq. (33b) for a fourth-order binomial model of the coefficients f_l. It was observed it was much easier to obtain good numerical accuracy with Eq. (33b) than with Eq. (33a).

6 Summary

We have shown there is a rich literature of closed-form solutions of transcendental equations that can be taken over to five classical conduction, convection, and radiation heat transfer problems. All solutions evolve from the same canonical form given by Eq. (4) but are so complicated they reveal little physical insight. While it can hardly be recommended that these complicated integrals are easier to implement than a straightforward iteration routine, the solutions of the associated transcendental equations contribute an interesting perspective to the folklore surrounding the solution of such problems.

Acknowledgments

We appreciate the help and encouragement of C. E. Siewert.

References

Abramowitz, M., and Stegun, I. A., eds., 1964, *Handbook of Mathematical Functions*, National Bureau of Standards, Washington, DC, pp. 224–225.

Burniston, E. E., and Siewert, C. E., 1973, "The Use of Riemann Problems in Solving a Class of Transcendental Equations," *Proc. Cambridge Philosophical Society*, Vol. 73, pp. 111–118.

Case, K. M., de Hoffmann, F., and Placzek, G., 1953, *Introduction to the Theory of Neutron Diffusion*, Vol. I, Los Alamos Scientific Laboratory, Los Alamos, NM.

Case, K. M., and Zweifel, P. F., 1967, *Linear Transport Theory*, Addison-Wesley, Reading, MA.

Chandrasekhar, S., 1960, *Radiative Transfer*, Dover, New York, pp. 151–154.

Char, B. W., Geddes, K. O., Gonnet, G. H., Leong, B. L., Monagan, M. B., and Watt, S. M., 1992, *First Leaves: A Tutorial Introduction to Maple V*, Springer-Verlag, New York.

Holman, J. P., 1990, *Heat Transfer*, 7th ed., McGraw-Hill, New York, p. 46.

Incropera, F. P., and Dewitt, D. P., 1996, *Introduction to Heat Transfer*, 3rd ed., Wiley, New York, p. 122.

Mills, A. F., 1992, *Heat Transfer*, Irwin, Homewood, IL, p. 85.

Muskhelishvili, N. I., 1953, *Singular Integral Equations*, Noordhoff, Groningen.

Özışık, M. N., 1989, *Boundary Value Problems in Heat Conduction*, Dover, New York, pp. 43–59.

Özışık, M. N., 1993, *Heat Conduction*, 2nd ed., Wiley, New York, pp. 44–50.

Siewert, C. E., and Burniston, E. E., 1972, "An Exact Analytical Solution of Kepler's Equation," *Celestial Mechanics*, Vol. 6, pp. 294–304.

Siewert, C. E., 1973, "An Exact Analytical Solution of an Elementary Critical Condition," *Nuclear Science and Engineering*, Vol. 51, p. 78.

Siewert, C. E., and Essig, C. J., 1973, "An Exact Solution of a Molecular Field Equation in the Theory of Ferromagnetism," *Zeitschrift für Angewandte Mathematik und Physik*, Vol. 24, pp. 281–285.

Siewert, C. E., and Phelps, J. S., 1978, "On Solutions of a Transcendental Equation Basic to the Theory of Vibrating Plates," *Journal of Computational and Applied Mathematics*, Vol. 4, pp. 37–39.

Siewert, C. E., 1980, "On Computing Eigenvalues in Radiative Transfer," *Journal of Mathematical Physics*, Vol. 21, pp. 2468–2470.

Siewert, C. E., 1981, "An Exact Expression for the Wien Displacement Constant," *Journal of Quantitative Spectroscopy and Radiative Transfer*, Vol. 26, p. 467.

Viscous Dissipation Effect on Pressure Gradient for Laminar Flow of a Non-Newtonian Liquid Through a Duct of Subfreezing Wall Temperature

W. C. Luelf[1,2] and L. C. Burmeister[1,3]

Nomenclature

d = dimensionless differential operator
e = dimensionless natural number = 2.71828...
f = dimensionless friction factor, Eq. (20)
g_c = constant, 1 kg m/N s^2
k = thermal conductivity, W/m K
n = dimensionless power-law exponent, Eq. (2)
P = pressure, N/m^2
P' = pressure gradient = dP/dz
Q = volumetric flow rate, m^3/s
q = heat flux, W/m^2
R = tube radius, m
Re_M = dimensionless Reynolds number based on reference viscosity, Eq. (18)
r = radial distance, m
T = temperature, K
T_o = temperature, K

u = velocity in z direction, m/s
z = axial distance, m
β = dimensionless parameter, Eq. (30)
δ = unfrozen tube radius, m
λ = dimensionless shear rate parameter, Eq. (18)
μ = Newtonian viscosity, N s/m^2
μ_o = power-law viscosity coefficient, N s^n/m^2
μ^+ = reference viscosity, N s/m^2, Eq. (19)
ξ_∞ = dimensionless parameter, Eq. (31)
π = dimensionless natural number = 3.14159...
τ = shear stress, N/m^2

Superscripts

$*$ = dimensionless quantity

Subscripts

avg = average value
m = melting value
o = high shear rate value
r = in r direction, on r face
s = value for the solid
w = wall value
z = in z direction

[1] Department of Mechanical Engineering, University of Kansas, Lawrence, KS 66044-2234.

[2] Graduate Student.

[3] Professor; Mem. ASME.

Introduction

The solidification of flowing liquids occurs in the molding of plastics, casting of metals, energy storage, and so forth. In such applications the wall of the duct through which flow occurs is maintained below the freezing temperature of the liquid, resulting in the formation of a layer of frozen material on the duct wall, as surveyed by Fukusako and Yamada (1994). Except for Yang et al. (1992), who treated unsteady solidification of a power-law liquid in the inlet region, the effects of viscous dissipation have been neglected in most analyses. Viscous dissipation at specified volumetric flow rate enables the thickness of the frozen layer always to be less than the duct radius as energy
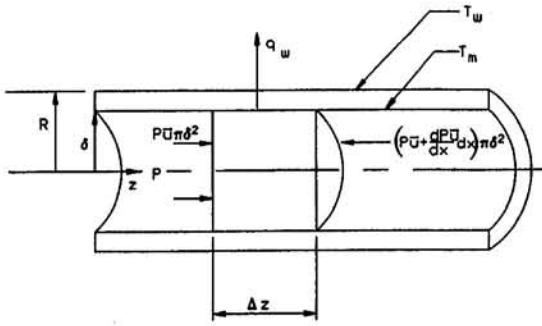
Fig. 1 Laminar flow in a tube with a layer frozen onto the wall of sub-freezing temperature

continuously converted from mechanical into thermal form in the flowing liquid is conducted across the frozen layer to the chilled wall.

The main features of the dependence of the pressure gradient and thickness of the frozen layer on the tube wall upon viscous dissipation were laid out by Ahmadian and Burmeister (1990a, b) for Newtonian and power-law liquids in laminar flow through ducts of subfreezing wall temperatures. The solutions for the power-law case suffer in accuracy because the power-law formulation results in the shear stress becoming small near the centerline from a higher value than is the case for a real liquid. The solutions for the Newtonian case neglect the shear thinning or thickening that can occur in the high shear rate region near the wall.

Representation of the gradual change in the shear stress-versus-shear rate relationship from a linear one at low shear rate to a power-law one at a high shear rate is provided by Dunleavy and Middleman (1966), as previously used by Brewster and Irvine (1987) for laminar flow without consideration of either freezing or viscous dissipation. In the following, this relationship is used to provide results that bridge the region between the two extremes of a Newtonian and a power-law liquid.

Analysis

The equation of motion for a specified volumetric flow rate Q of a constant property liquid in fully developed laminar flow through a circular duct of radius R and unfrozen radius δ illustrated in Fig. 1 is

$$-\frac{dP}{dz} + \frac{1}{r}\frac{d(r\tau_{rz})}{dr} = 0 \qquad (1)$$

The gradient of pressure P is constant for fully developed flow. The shear stress τ_{rz} is related to the shear rate du/dr and the axial velocity $u(r)$ by

$$\tau_{rz} = \frac{\mu(du/dr)}{1 + (\mu/\mu_o)|du/dr|^{1-n}} \qquad (2)$$

as discussed by Brewster and Irvine (1987). Here, μ is the viscosity for a Newtonian liquid, μ_o is the viscosity coefficient for a power-law liquid, and n is the power-law exponent. Inspection of Eq. (2) reveals a linear Newtonian relationship at low shear rate and a power-law relationship at high shear rate. Newtonian behavior with an effective viscosity of $\mu/(1 + \mu/\mu_o)$ is always obtained for $n = 1$; when $\mu \ll \mu_o$, it is obtained for all but extremely large flow rates.

It is assumed that there is no slip at the liquid–solid interface so that

$$u(\delta) = 0 \qquad (3)$$

that the velocity near the centerline is finite or, restated, of zero gradient so that

$$u(r \to 0) \text{ finite} \qquad (4a)$$

or

$$du(r = 0)/dr = 0 \qquad (4b)$$

The volumetric flow rate Q is specified so that

$$Q = \int_0^\delta u 2\pi r \, dr \qquad (5)$$

Use of Eq. (2) in Eq. (1) gives, after integration and account of the boundary condition of Eq. (4b),

$$\frac{du}{dr} = \frac{r}{2\mu}\frac{dP}{dz} + \frac{r}{2\mu_o}\frac{dP}{dz}\left(-\frac{du}{dr}\right)^{1-n} \qquad (6)$$

The temperature T distribution in the flowing liquid is obtained from the energy equation

$$k\frac{d(rdT/dr)}{dr} + \frac{d(ur\tau_{rz})}{dr} - ru\frac{dP}{dz} = 0$$

Use of Eq. (1), including its integrated form, in the energy equation puts it into the form

$$k\frac{d(rdT/dr)}{dr} + \frac{r^2}{2}\frac{dP}{dz}\frac{du}{dr} = 0 \qquad (7)$$

The boundary conditions imposed on the temperature distribution are that the temperature at the centerline is either finite or, restated, of zero gradient as

$$T(r = 0) \text{ finite} \qquad (8a)$$

or

$$dT(r = 0)/dr = 0 \qquad (8b)$$

and the temperature at the liquid–solid interface is the melting temperature T_m so that

$$T(r = \delta) = T_m \qquad (9)$$

At the liquid–solid interface, the rate of heat flow by conduction from the liquid equals that by conduction through the frozen shell so that

$$-k\frac{dT(r = \delta)}{dr} = \frac{k_s(T_m - T_w)}{\delta \ln\left(\dfrac{\delta}{R}\right)} \qquad (10)$$

A dimensionless form of these equations convenient for numerical computations is obtained by letting $r^* = r/\delta$, $T^* = (T - T_m)/(T_o - T_m)$ where T_o is the initially unknown centerline temperature, and $u^* = \pi\delta^2 u/Q$. Then Eqs. (3) and (5)–(10) to be solved become

$$u^*(r^* = 1) = 0 \qquad (11)$$

$$1 = \int_0^1 2u^* r^* dr^* \qquad (12)$$

$$\frac{du^*}{dr^*} = \frac{\pi\delta^4 r^*}{2\mu Q}\frac{dP}{dz} + \frac{\pi^n \delta^{1+3n} r^*}{2\mu_o Q^n}\frac{dP}{dz}\left(-\frac{du^*}{dr^*}\right)^{1-n} \qquad (13)$$

$$\frac{d(r^* dT^*/dr^*)}{dr^*} = -\frac{r^{*2}Q}{2\pi k(T_o - T_m)}\frac{dP}{dz}\frac{du^*}{dr^*} \qquad (14)$$

$$T^*(0) = 1 \qquad (15a)$$

or

$$\frac{dT^*(0)}{dr^*} = 0 \qquad (15b)$$

$$T^*(1) = 0 \qquad (16)$$

$$\ln(R^*) = \frac{k_s}{k} \frac{T_w^*}{(dT^*(1)/dr^*)} \qquad (17)$$

Equations (11)–(17) were numerically solved in an iterative manner. After the flow rate Q was specified, values of the unfrozen radius δ and pressure gradient dP/dz were first assumed. Then du^*/dr^* was determined from Eq. (13) at numerous equally spaced r^* values, after which u^* was determined from the du/dr^* versus r^* values by application of the trapezoidal rule with account taken of the no-slip requirement of Eq. (11). The average value of the dimensionless velocity u^* was then compared to the unity value required by Eq. (12). If $u_{avg}^* \neq 1$, a new value of dP/dz was assumed. This procedure was repeated until u_{avg}^* was sufficiently close to unity, at which point the velocity distribution was available for use in evaluating the temperature distribution.

To determine the temperature distribution numerically, a value of the dimensionless centerline temperature T_o was first assumed. Then a fourth-order Runge–Kutta method was employed to solve Eq. (14) for the dimensionless temperature T^* at numerous values of dimensionless radius r^*, taking into account the condition of Eq. (15a). The value of $T^*(1)$ obtained from this procedure was then compared with the zero value required by the no-temperature-jump condition of Eq. (16). The value of T_o was changed if $T^*(1) \neq 0$, and the temperature distribution was recalculated. This procedure was repeated until $T^*(1)$ was sufficiently close to zero. From this temperature distribution, the dimensionless temperature gradient $dT^*(1)/dr^*$ at the liquid–solid interface was evaluated by application of Simpson's rule. With the dimensionless temperature gradient at the liquid–solid interface available, the value of the unfrozen radius δ was determined from Eq. (17) and compared with the value first assumed. If a significant discrepancy was found, the value of δ was changed and the procedure was repeated from the beginning, continuing in such a manner until there was no meaningful change. Calculations were terminated after the third significant figure had been ascertained for all quantities. In the course of this procedure, the number of equally spaced radial solution points was increased until the results ceased to change, thereby establishing that a grid-independent solution had been achieved.

To verify the accuracy of the results obtained as described above, an approximate solution was devised. In this, advantage was taken of an approximation adduced by Brewster and Irvine (1987) without solidification but for otherwise the same conditions. They found that the friction factor f could be represented with less than 0.1 percent error as

$$f\,\mathrm{Re}_M = \frac{1 + \lambda}{\dfrac{1}{64} + \dfrac{\lambda}{2^{3n+3}\left(\dfrac{3n+1}{4n}\right)^n}} \qquad (18)$$

in which

$$\lambda = \frac{\mu}{\mu_o}\left(\frac{u_{avg}}{2\delta}\right)^{1-n}, \quad u_{avg} = \frac{Q}{\pi\delta^2},$$

$$\mathrm{Re}_M = \frac{\rho u_{avg} 2\delta}{\mu^+}, \quad \text{and} \quad \mu^+ = \frac{\mu}{1+\lambda} \qquad (19)$$

The modified Reynolds number Re_M reduces to the familiar
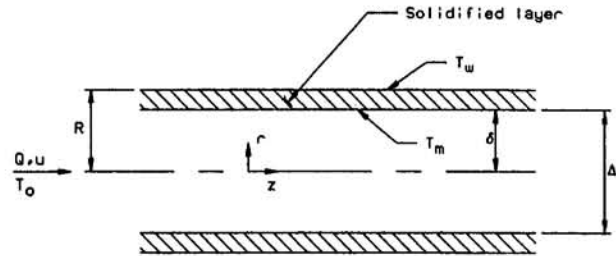

Fig. 2 Energy balance on a control volume for flow through the unfrozen portion of a tube

Reynolds number Re when the liquid is Newtonian. From these relationships the pressure gradient is given by

$$-\frac{dP}{dz} = \frac{f}{2\delta}\frac{\rho u_{avg}^2}{2g_c} \qquad (20)$$

The appropriate substitutions for the friction factor and Reynolds number from Eqs. (18) and (19) used in Eq. (20) put it into the form

$$-\frac{dP}{dz} = \frac{8}{g_c}\left[\frac{\mu\left(\dfrac{Q}{\pi\delta^4}\right)}{1 + 2^{2-2n}\left(\dfrac{4n}{3n+1}\right)^n\dfrac{\mu}{\mu_o}\left(\dfrac{Q}{\pi\delta^3}\right)^{1-n}}\right] \qquad (21)$$

Performing an energy balance on the control volume shown in Fig. 2 yields

$$-\frac{\pi\delta^2}{2}u_{avg}\frac{dP}{dz} = 2\pi\delta q_w \qquad (22)$$

in which the conductive heat flux q_w through the frozen shell on the tube wall is

$$q_w = \frac{k_s(T_m - T_w)}{\delta \ln(R/\delta)} \qquad (23)$$

Combining Eqs. (21)–(23) gives

$$\frac{4}{g_c}\left[\frac{\mu\left(\dfrac{Q^2}{\pi^2\delta^4}\right)}{1 + 2^{2-2n}\left(\dfrac{4n}{3n+1}\right)^n\dfrac{\mu}{\mu_o}\left(\dfrac{Q}{\pi\delta^3}\right)^{1-n}}\right]$$

$$= \frac{k_s(T_m - T_w)}{\ln(R/\delta)} \qquad (24)$$

Equation (24) was iteratively solved for the value of R/δ and the result was used in Eq. (21) to obtain the pressure gradient dP/dz.

Approximations for the conditions at the minimum of the pressure gradient-versus-flow rate curve were obtained by differentiation of Eqs. (21) and (24) followed by lengthy rearrangement as described by Luelf (1995). It was found that the dimensionless minimum pressure gradient

$$-P'^* = -P'\frac{R^2}{[\mu k_s(T_m - T_w)]^{1/2}} \qquad (25)$$

is related to the dimensionless flow rate

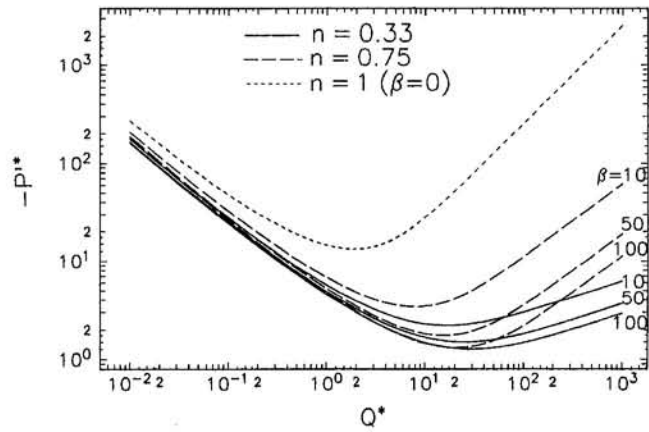$$Q^* = \frac{Q}{R^2}\left[\frac{\mu}{k_s(T_m - T_w)}\right]^{1/2} \qquad (26)$$

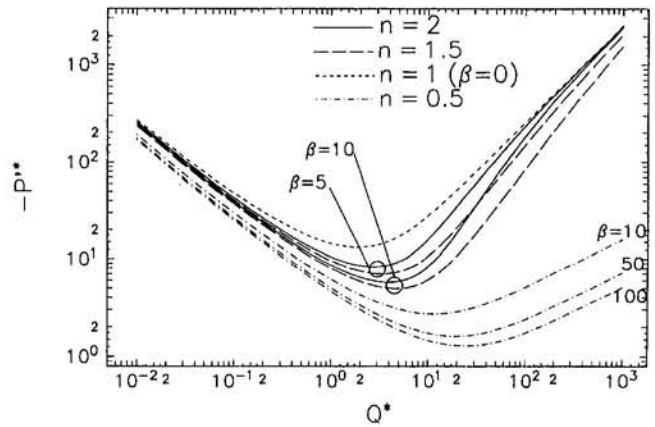Fig. 3 Dimensionless pressure gradient versus dimensionless flow rate for shear thinning fluids

Fig. 4 Dimensionless pressure gradient versus dimensionless flow rate for shear thickening fluids

as

$$-P'^*_{min} \approx \frac{8}{\pi} \frac{Q^*_{min}/\delta^{*4}}{1 + \xi_\infty} \qquad (27)$$

The dimensionless volumetric flow rate at which the minimum dimensionless pressure gradient occurs is

$$Q^*_{min} \approx \pi \left[\frac{\left(1 + \frac{1 + 3n}{4} \xi_\infty\right)(1 + \xi_\infty)}{1 + n\xi_\infty} \right]^{1/2}$$
$$\exp\left(-\frac{1}{2} \frac{1 + n\xi_\infty}{1 + \frac{1 + 3n}{4} \xi_\infty}\right) \qquad (28)$$

The dimensionless unfrozen radius δ^* at this minimum is

$$\delta^* = \frac{\delta_{min}}{R} \approx \exp\left(-\frac{1}{4} \frac{1 + n\xi_\infty}{1 + \frac{1 + 3n}{4} \xi_\infty}\right) \qquad (29)$$

In Eqs. (25)–(29),

$$\beta = \frac{4n}{3n + 1} \frac{\mu}{\mu_o} \left[\frac{\mu k_s (T_m - T_w)}{4R^2 \mu_o^2} \right]^{(1-n)/2n} \qquad (30)$$

which is a viscous dissipation index, and

$$\xi_\infty = \left(2^4 \frac{1 + 3n}{n} \right)^{(1-n)/(1+n)} \beta^{2n/(1+n)}$$
$$\times \exp\left[\frac{2n(1 - n)}{(1 + n)(1 + 3n)} \right] \qquad (31)$$

Results and Discussion

The dimensionless pressure drop versus dimensionless flow rate for a modified power-law liquid is shown in Fig. 3 for a shear-thinning liquid ($n \leq 1$) and in Fig. 4 for a shear-thickening liquid with several values of the viscous dissipation index β. The corresponding dimensionless unfrozen radius δ^* is shown in Fig. 5 for $\beta = 10$; the Newtonian liquid ($n = 1$, $\beta = 0$) has a greater δ^*, the superiority increasing as the departure of n from unity increases without regard for the direction of the departure.

The parameter β represents a major part of the effect of non-Newtonian behavior of the liquid on viscous dissipation.

Because no single dimensionless group was found that completely characterized non-Newtonian effects, both β and the power-law parameter n are needed. The results in Figs. 3–5 are more affected by the β than the n values.

At high flow rates the pressure gradient increases with increasing flow rate and the unfrozen radius closely approaches the tube radius as a consequence of the viscous dissipation rate increasing more than linearly with increasing flow rate, an increasingly large heat flux then being provided to the liquid–solid interface that can only be conducted across the already thin solidified shell. This pressure gradient versus flow rate behavior is qualitatively similar to that expected without freezing onto the wall. For both Newtonian and power-law liquids, at low flow rates the pressure gradient decreases with increasing flow rate as a consequence of the thickness of the solidified shell rapidly decreasing with increasing flow rate. A consequence of this behavior is that two different flow rates are possible if a pressure gradient exceeding the minimum is specified. Also, in a branched duct the flow might not be equally split at the branch even if the pressure gradients are equal in the branches.

The numerical results for the dimensionless pressure gradient shown in the foregoing figures are closely approximated by Eqs. (21)–(24). The difference between the two is less than 0.15 percent, and usually less than 0.03 percent.

A Newtonian fluid has $\beta = 0$ for which Eq. (31) gives $\xi_\infty = 0$; following this, Eqs. (27)–(29) give the results previously found by Ahmadian and Burmeister (1990a):

$$Q^*_{min} \approx \pi \exp(-1/2), \quad \delta^* \approx \exp(-1/4), \quad \text{and}$$
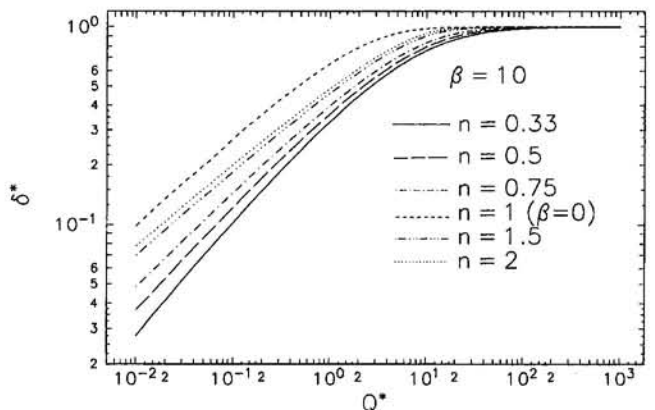$$-P'^*_{min} \approx 8 \exp(1/2) \qquad (32)$$

Fig. 5 Dimensionless unfrozen tube radius versus dimensionless flow rate

A power-law fluid has $\beta \to \infty$ for which Eqs. (27)–(29) give the results previously found by Ahmadian and Burmeister (1990b)

$$Q^*_{min} \approx \pi 8^{(1-n)/(1+n)} \left[\frac{1+3n}{4n} \right]^{1/(1+n)} \beta^{n/(1+n)} \exp\left(-\frac{n}{1+n} \right),$$

$$\delta^* \approx \exp\left(-\frac{n}{1+3n} \right) \quad \text{and}$$

$$-P'^* \approx \left[\frac{16(1+3n)e}{4n\beta} \right]^{n/(1+n)}$$

The dimensionless flow rate at which the minimum pressure gradient occurs is predicted, usually too high, by the approximate Eq. (28) with less than 7 percent, usually less than 2 percent, error; the error increases as the power-law exponent n increases. The dimensionless unfrozen radius at the minimum is predicted by the approximate Eq. (29) with less than 1 percent, usually less than 0.2 percent, error. The minimum dimensionless pressure gradient is predicted by Eq. (27) with less than 8 percent error; for $n \le 0.75$ the error is less than 0.7 percent with the prediction being low, while for $n \ge 1.50$ the prediction is high with the error increasing with increasing n.

The effect of Newtonian viscosity μ is incorporated not only in the viscous dissipation index β but also in the dimensionless flow rate and pressure gradient defined in Eqs. (25) and (26). The effect of variation in viscosity for a Newtonian liquid, for example, on the minimum flow rate and pressure gradient can be ascertained by introducing the corresponding dimensionless values from Eq. (32) into Eqs. (25) and (26) to get

$$Q_{min} = \pi \exp(-1/2)R^2 \left[\frac{k_x(T_m - T_w)}{\mu} \right]^{1/2} \quad \text{and}$$

$$-P'_{min} = 8 \exp(1/2) \frac{[\mu k_s(T_m - T_w)]^{1/2}}{R^2}$$

Further detail, including treatment of the parallel plate geometry, is available (Luelf, 1994, 1995).

References

Ahmadian, M. T., and Burmeister, L. C., 1990a, "Viscous Dissipation Effect on Solidification of a Liquid Onto a Tube Wall," *Polymer Engineering and Science*, Vol. 30, pp. 776–782.

Ahmadian, M. T., and Burmeister, L. C., 1990b, "Viscous Dissipation Effect on Solidification of a Power-Law Liquid Onto a Tube Wall," *Fundamentals of Phase Change: Freezing, Melting, and Sublimation*, ASME HTD-Vol. 143, pp. 31–37.

Brewster, R. A., and Irvine, Th. F., Jr., 1987, "Similitude Considerations in Laminar Flow of Modified Power Law Fluids in Circular Ducts," *Wärme- und Stoffübertragung*, Vol. 21, pp. 83–86.

Dunleavy, J., and Middleman, S., 1966, "Relation of Shear Behavior of Solutions of Polyisobutylene," *Trans. Soc. Rheol.*, Vol. 10, pp. 151–168.

Fukusako, S., and Yamada, M., 1994, "Solidification of Pure Liquids and Liquid Mixtures Inside Ducts and Over External Bodies," *Applied Mechanics Reviews*, Vol. 47, pp. 589–621.

Luelf, W. C., 1994, "Dissipation Effect on Pressure Gradient for Non-Newtonian Liquid Flowing Laminarly Through a Duct of Subfreezing Wall Temperature," M. S. thesis, University of Kansas, Lawrence, KS.

Luelf, W. C., 1995, "Viscous Dissipation Effects on Pressure Gradient Through a Duct With Subfreezing Wall Temperature," *General Papers in Heat and Mass Transfer (Proc. 30th National Heat Transfer Conf., V. 8)*, ASME HTD-Vol. 310, pp. 35–42.

Yang, L. C., Charmchi, M., and Chen, S. J., 1992, "Numerical Simulation of Semicrystalline Polymer Flowing in an Empty Tube With Solidification," *Polymer Engineering and Science*, Vol. 32, pp. 724–731.

On Flow Separation With Adverse Rotational Buoyancy

S. Dutta,[1] M. J. Andrews,[2] and J.-C. Han[2]

Nomenclature

D = hydraulic diameter of channel
Gr = Grashof number based on centrifugal acceleration = $\rho^2 \Omega^2 z \beta \Delta T D^3 / \mu^2$
J = Taylor number $J = \rho \Omega D^2 / 2\mu$
Nu_r/Nu_o = Nusselt number ratio of rotating channel and stationary smooth channel conditions
z = distance measured from the center of rotation along the axis of the channel
Re = Reynolds number = $\rho w_o D / \mu$
ΔT = wall to coolant temperature difference
u, v = cross-stream velocities
w, w_0 = axial velocity, mean axial velocity
β, μ = volume expansion coefficient, laminar viscosity
Ω, ρ = rotational speed, coolant (air) density

Introduction

Several experimental and numerical papers have been published recently about the flow and thermal analysis of turbine

[1] Department of Mechanical Engineering, University of South Carolina, Columbia, SC 29208.

[2] Department of Mechanical Engineering, Texas A&M University, College Station, TX 77843-3123.

rotor blade cooling. This work characterizes the mechanism of flow separation in a rotating internal coolant passage and extend it in a more general sense. Emphasis is placed on the process of flow separation due to adverse buoyancy forces. In a rotating channel, the main body force is generated by the centrifugal acceleration and not by the gravitational acceleration. The centrifugal acceleration in a turbine rotor blade coolant channel can exceed 1000g. In the experiments of Wagner et al. (1991) mixed convection (forced and natural convection) was noted for a high channel Reynolds number of 50,000. The serpentine internal coolant passages of turbine rotor blades comprise outward and inward flow directions. The centrifugal force acts radially outward, irrespective of the flow direction, so buoyancy from the centrifugal acceleration has opposite influences on the flow field for the two different flow situations.

Mathematical Considerations

Radial Outward Flow. The coordinate system is selected with the z direction as the axis of the rotating channel, and with the rotation vector aligned with the y axis. The present paper considers axial flow separation in adverse rotational buoyancy, so the axial (z direction) momentum equation for a rotating laminar flow can be given by:

$$\rho u \frac{\partial w}{\partial x} + \rho v \frac{\partial w}{\partial y} + \rho w \frac{\partial w}{\partial z} = -\frac{\partial \left(P - \frac{\rho \Omega^2 z^2}{2} \right)}{\partial z}$$

$$+ 2\rho \Omega u - \rho \Omega^2 z \beta \Delta T + \frac{\partial}{\partial x}\left(\mu \frac{\partial w}{\partial x} \right)$$

$$+ \frac{\partial}{\partial y}\left(\mu \frac{\partial w}{\partial y} \right) + \frac{\partial}{\partial z}\left(\mu \frac{\partial w}{\partial z} \right) \quad (1)$$

A power-law fluid has $\beta \rightarrow \infty$ for which Eqs. (27)–(29) give the results previously found by Ahmadian and Burmeister (1990b)

$$Q_{\min}^* \approx \pi 8^{(1-n)/(1+n)} \left[\frac{1+3n}{4n} \right]^{1/(1+n)} \beta^{n/(1+n)} \exp\left(-\frac{n}{1+n} \right),$$

$$\delta^* \approx \exp\left(-\frac{n}{1+3n} \right) \quad \text{and}$$

$$-P'^* \approx \left[\frac{16(1+3n)e}{4n\beta} \right]^{n/(1+n)}$$

The dimensionless flow rate at which the minimum pressure gradient occurs is predicted, usually too high, by the approximate Eq. (28) with less than 7 percent, usually less than 2 percent, error; the error increases as the power-law exponent n increases. The dimensionless unfrozen radius at the minimum is predicted by the approximate Eq. (29) with less than 1 percent, usually less than 0.2 percent, error. The minimum dimensionless pressure gradient is predicted by Eq. (27) with less than 8 percent error; for $n \leq 0.75$ the error is less than 0.7 percent with the prediction being low, while for $n \geq 1.50$ the prediction is high with the error increasing with increasing n.

The effect of Newtonian viscosity μ is incorporated not only in the viscous dissipation index β but also in the dimensionless flow rate and pressure gradient defined in Eqs. (25) and (26). The effect of variation in viscosity for a Newtonian liquid, for example, on the minimum flow rate and pressure gradient can be ascertained by introducing the corresponding dimensionless values from Eq. (32) into Eqs. (25) and (26) to get

$$Q_{\min} = \pi \, \exp(-1/2) R^2 \left[\frac{k_s (T_m - T_w)}{\mu} \right]^{1/2} \quad \text{and}$$

$$-P'_{\min} = 8 \, \exp(1/2) \frac{[\mu k_s (T_m - T_w)]^{1/2}}{R^2}$$

Further detail, including treatment of the parallel plate geometry, is available (Luelf, 1994, 1995).

References

Ahmadian, M. T., and Burmeister, L. C., 1990a, "Viscous Dissipation Effect on Solidification of a Liquid Onto a Tube Wall," *Polymer Engineering and Science*, Vol. 30, pp. 776–782.

Ahmadian, M. T., and Burmeister, L. C., 1990b, "Viscous Dissipation Effect on Solidification of a Power-Law Liquid Onto a Tube Wall," *Fundamentals of Phase Change: Freezing, Melting, and Sublimation*, ASME HTD-Vol. 143, pp. 31–37.

Brewster, R. A., and Irvine, Th. F., Jr., 1987, "Similitude Considerations in Laminar Flow of Modified Power Law Fluids in Circular Ducts," *Wärme- und Stoffübertragung*, Vol. 21, pp. 83–86.

Dunleavy, J., and Middleman, S., 1966, "Relation of Shear Behavior of Solutions of Polyisobutylene," *Trans. Soc. Rheol.*, Vol. 10, pp. 151–168.

Fukusako, S., and Yamada, M., 1994, "Solidification of Pure Liquids and Liquid Mixtures Inside Ducts and Over External Bodies," *Applied Mechanics Reviews*, Vol. 47, pp. 589–621.

Luelf, W. C., 1994, "Dissipation Effect on Pressure Gradient for Non-Newtonian Liquid Flowing Laminarly Through a Duct of Subfreezing Wall Temperature," M. S. thesis, University of Kansas, Lawrence, KS.

Luelf, W. C., 1995, "Viscous Dissipation Effects on Pressure Gradient Through a Duct With Subfreezing Wall Temperature," *General Papers in Heat and Mass Transfer (Proc. 30th National Heat Transfer Conf., V. 8)*, ASME HTD-Vol. 310, pp. 35–42.

Yang, L. C., Charmchi, M., and Chen, S. J., 1992, "Numerical Simulation of Semicrystalline Polymer Flowing in an Empty Tube With Solidification," *Polymer Engineering and Science*, Vol. 32, pp. 724–731.

On Flow Separation With Adverse Rotational Buoyancy

S. Dutta,[1] M. J. Andrews,[2] and J.-C. Han[2]

Nomenclature

D = hydraulic diameter of channel
Gr = Grashof number based on centrifugal acceleration = $\rho^2 \Omega^2 z \beta \Delta T D^3 / \mu^2$
J = Taylor number $J = \rho \Omega D^2 / 2\mu$
$\mathrm{Nu}_r / \mathrm{Nu}_o$ = Nusselt number ratio of rotating channel and stationary smooth channel conditions
z = distance measured from the center of rotation along the axis of the channel
Re = Reynolds number = $\rho w_o D / \mu$
ΔT = wall to coolant temperature difference
u, v = cross-stream velocities
w, w_0 = axial velocity, mean axial velocity
β, μ = volume expansion coefficient, laminar viscosity
Ω, ρ = rotational speed, coolant (air) density

Introduction

Several experimental and numerical papers have been published recently about the flow and thermal analysis of turbine

[1] Department of Mechanical Engineering, University of South Carolina, Columbia, SC 29208.
[2] Department of Mechanical Engineering, Texas A&M University, College Station, TX 77843-3123.

rotor blade cooling. This work characterizes the mechanism of flow separation in a rotating internal coolant passage and extend it in a more general sense. Emphasis is placed on the process of flow separation due to adverse buoyancy forces. In a rotating channel, the main body force is generated by the centrifugal acceleration and not by the gravitational acceleration. The centrifugal acceleration in a turbine rotor blade coolant channel can exceed 1000g. In the experiments of Wagner et al. (1991) mixed convection (forced and natural convection) was noted for a high channel Reynolds number of 50,000. The serpentine internal coolant passages of turbine rotor blades comprise outward and inward flow directions. The centrifugal force acts radially outward, irrespective of the flow direction, so buoyancy from the centrifugal acceleration has opposite influences on the flow field for the two different flow situations.

Mathematical Considerations

Radial Outward Flow. The coordinate system is selected with the z direction as the axis of the rotating channel, and with the rotation vector aligned with the y axis. The present paper considers axial flow separation in adverse rotational buoyancy, so the axial (z direction) momentum equation for a rotating laminar flow can be given by:

$$
\rho u \frac{\partial w}{\partial x} + \rho v \frac{\partial w}{\partial y} + \rho w \frac{\partial w}{\partial z} = -\frac{\partial \left(P - \frac{\rho \Omega^2 z^2}{2} \right)}{\partial z}
$$
$$
+ 2\rho \Omega u - \rho \Omega^2 z \beta \Delta T + \frac{\partial}{\partial x} \left(\mu \frac{\partial w}{\partial x} \right)
$$
$$
+ \frac{\partial}{\partial y} \left(\mu \frac{\partial w}{\partial y} \right) + \frac{\partial}{\partial z} \left(\mu \frac{\partial w}{\partial z} \right) \quad (1)
$$

The flow in the channel is assumed to be near fully developed, so cross-stream convective terms are neglected because u and v are small. Moreover, near the point of flow separation w is also small and so we neglect the term $w(\partial w/\partial z)$, and it is this step that takes us away from the usual Gr/Re^2 parameter. The resulting w-momentum equation is:

$$\frac{\partial P'}{\partial z} + \rho \Omega^2 z \beta \Delta T = \frac{\partial}{\partial x}\left(\mu \frac{\partial w}{\partial x}\right) \qquad (2)$$

where P' includes the hydrostatic and centrifugal pressure fields.

At the point of separation, the viscous effects diminish and buoyancy force balances the pressure gradient. A Pohlhausen parameter (Λ), for model flow separation in an adverse pressure driven Poiseuille flow is given (White, 1991) as:

$$\Lambda = \frac{D^2}{w_0 \mu}\left(\frac{\partial P}{\partial z}\right) \qquad (3)$$

Similarly, for an adverse buoyancy flow, the driving pressure gradient is developed by adverse buoyancy at the point of flow separation, and a buoyancy Pohlhausen parameter (Λ_b) results:

$$\Lambda_b = \frac{D^2}{w_0 \mu}(\rho \Omega^2 r \beta \Delta T) = \frac{Gr}{Re} \qquad (4)$$

Just as in the model Poiseuille flow separation problem (White, 1991), Λ_b should be of the order of 1 for laminar flow separation to occur. However, in turbulent flow the laminar boundary layer thickness is much less than the channel hydraulic diameter, D, and so we can expect $\Lambda_b \gg 1$ to characterize flow separation.

An alternative approach to derive this buoyancy Pohlhausen parameter is to balance viscous and buoyancy terms as:

$$\frac{\text{Rotational Buoyancy}}{\text{Viscous Effect}} = \frac{\rho \Omega^2 z \beta \Delta T}{\mu \partial^2 w/\partial x^2} \approx \frac{\rho \Omega^2 z \beta \Delta T D^2}{\mu w_0} \approx \frac{Gr}{Re} \qquad (5)$$

which again gives the Grashof number to Reynolds number ratio.

Radial Inward Flow. Flow separation in a radial inward flow occurs in the core flow due to the buoyancy effect. The present analysis is developed from the analytical velocity profile derived by Siegel (1985) in a rotating pipe and is limited to a low Reynolds number (Re < 50) laminar flow regime. Since flow separation for this situation occurs at the core flow, for convenience, the analysis focuses at the centerline of a circular rotating pipe. The velocity profile at the center of a pipe is given as (Siegel, 1985): $w = w_0 + Jw_1 + J^2 w_2$, where J is the Taylor number and is constant for a given flow and rotation situation; w_0, w_1, and w_2 are functions in a series expansion of the axial velocity, details are given in Siegel (1985). At the center of the pipe, $w_1 = 0$, and at the point of flow separation axial velocity, $w = 0$. Thus by expanding the terms of Siegel (1985) gives:

$$0 = -\frac{1}{4} + J^2\left(\frac{1}{4608} - \frac{119}{18432}\frac{r/Dq_w}{Re}\right) \qquad (6)$$

where q_w is the nondimensional wall heat flux, $q_w = \beta \Delta T$, and $J^2 q_w (r/D)/Re$ is:

$$\frac{J^2 q_w z/D}{Re} = \frac{\Omega^2 D^4 \rho^2}{4\mu^2}\frac{\beta \Delta T z/D}{Re} = \frac{Gr}{Re} \qquad (7)$$

Substituting Eq. (7) into Eq. (6) reveals that for a fixed Taylor number the Gr/Re parameter again characterizes flow separation in the core of the radially inward flow.

Application of Gr/Re

Figure 1 shows a compilation of local leading side heat transfer coefficient results from three different sources (Wagner et al., 1991; Han et al., 1994; Yang et al., 1992). Data from Figs. 8, 9, 10, and 11 of Wagner et al. (1991), Figs. 7, 8, 9, and 10 of Han et al. (1994), and Figs. 5 and 6 of Yang et al. (1992) are included here. These experimental data include effects of rotation number, density ratio, Reynolds number, mean rotating radius, and different operating pressures. Experimental data points are carefully selected from the leading side of the radial outward flow channel to minimize the inlet and outlet effects. Rotating channels used in those experiments were short, and therefore, data may not be entirely free from the inlet and outlet effects. The low Reynolds number (Re = 12,500) and low rotation number (Ro = 0.12) data of Wagner et al. (1991) are not included because of higher uncertainty and less effect of rotation (rotation speed is low) on these two sets of data. Wagner et al. (1991) and Han et al. (1994) tried to correlate the leading side heat transfer coefficient by rotation number (Ro = $\Omega D/w$) and buoyancy parameter (Gr/Re^2) but showed a large scatter in the data.

Figure 1 shows that the Nusselt number ratio in rotation initially decreases with an increase in the adverse buoyancy (Gr/Re). From computational work of Dutta et al. (1996) a minimum in the Nusselt number corresponds to flow stagnation near separation that causes reduced convection and hence a low Nusselt number. This flow stagnation (separation) occurs in the vicinity of Gr/Re = 2500. Figure 1 shows that best operation is obtained for Gr/Re < 1000 and for Gr/Re > 10,000, and should be avoided around 2500. For higher values of Gr/Re the separation occurs earlier along the channel providing enhanced mixing downstream and hence a higher local heat transfer coefficient. The two lines in Fig. 1 correspond to the best fit linear regression curves to the experimental data. The Nusselt number ratio for Gr/Re < 2500 can be correlated as $Nu_r/Nu_o = -0.28$ log (Gr/Re) + 1.35. The regression correlation coefficient for this linear curve fit is $r = 0.94$. The Nusselt number ratio for Gr/Re > 2500 is correlated as $Nu_r/Nu_o = 0.48$ log (Gr/Re) − 1.49 and the least-square regression correlation coefficient is $r = 0.9$.

Figure 2 shows changes in the leading side Nusselt number ratio with Gr/Re ratio for a ribbed channel, with the experimental data from Wagner et al. (1994) and Parson et al. (1994). Their experimental conditions in the ribbed channel were simi-
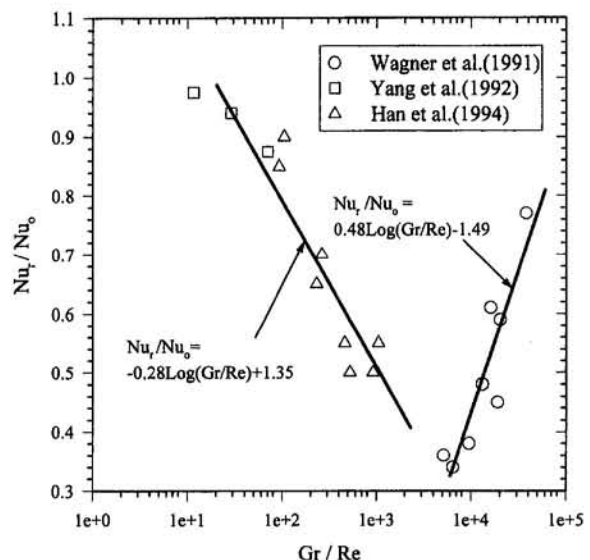

Fig. 1 Variation of leading side Nusselt number ratio with different adverse buoyancy levels in rotating smooth walled channels
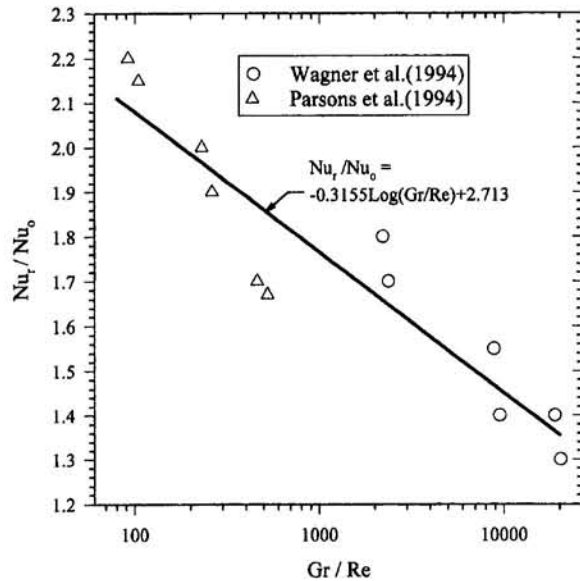
Fig. 2 Variation of leading side Nusselt number ratio with different adverse buoyancy levels in rotating ribbed channels

lar to those with the smooth-walled channels. The Nusselt number ratios are again regionally averaged taken from the published experimental data. Addition of turbulators to enhance heat transfer delays separation (other than the separation past the rib turbulators) by lowering the Reynolds number effect on the buoyancy Pohlhausen parameter due to a thinner boundary layer region. Figure 2 shows that the trend in the Nusselt number ratio is similar to that of the smooth leading surface (see Fig. 1) prior to flow separation. The correlated relationship of the Nusselt number ratio with the Gr/Re ratio can be given as $Nu_r/Nu_o = -0.3155 \log (Gr/Re) + 2.713$ with a regression correlation coefficient, $r = 0.93$. Turbulence promoters effectively increase the momentum in the boundary layer to levels that normally correspond to a higher Re in a smooth channel. This lowers the effective Gr/Re ratio and delays the flow separation and gives a higher performance. Moreover, in ribbed channels the enhanced turbulent mixing reduces the temperature gradient in the fluid and thus the buoyancy effects are further reduced.

References

Dutta, S., Andrews, M. J., and Han, J. C., 1996, "Prediction of Turbulent Heat Transfer in Rotating Smooth Square Ducts," *International Journal of Heat and Mass Transfer*, Vol. 39, No. 12, pp. 2505–2514.

Han, J. C., Zhang, Y. M., and Lee, C. P., 1994, "Influence of Surface Heating Condition on Local Heat Transfer in a Rotating Square Channel With Smooth Walls and Radial Outward Flow," ASME *Journal of Turbomachinery*, Vol. 116, pp. 149–158.

Parsons, J. A., Han, J. C., and Zhang, Y. M., 1994, "Wall Heating Effect on Local Heat Transfer in a Rotating Two-Pass Square Channel With 90° Rib Turbulators," *International Journal of Heat and Mass Transfer*, Vol. 37, No. 9, pp. 1411–1420.

Siegel, R., 1985, "Analysis of Buoyancy Effect on Fully Developed Laminar Heat Transfer in a Rotating Tube," ASME JOURNAL OF HEAT TRANSFER, Vol. 107, pp. 338–344.

Wagner, J. H., Johnson, B. V., and Kooper, F. C., 1991, "Heat Transfer in Rotating Serpentine Passages With Smooth Walls," ASME *Journal of Turbomachinery*, Vol. 113, pp. 321–330.

Wagner, J. H., Johnson, B. V., Graziani, R. A., and Yeh, F. C., 1994, "Heat Transfer in Rotating Serpentine Passages With Trips Normal to the Flow," ASME *Journal of Turbomachinery*, Vol. 116, pp. 113–123.

White, F. M., 1991, *Viscous Fluid Flow*, 2nd ed., McGraw-Hill Inc., New York, p. 268.

Yang, W. J., Zhang, N., and Chiou, J., 1992, "Local Heat Transfer in a Rotating Serpentine Flow Passage," ASME JOURNAL OF HEAT TRANSFER, Vol. 114, pp. 354–361.

The Thermal Entrance Length Problem for Slug Flow in Rectangular Ducts

M. Spiga[1] and G. L. Morini[1]

Introduction

Rectangular ducts have increasing importance in compact heat exchangers, while slug flow in the entrance region occurs in many applications of low-Prandtl-number fluids. The thermal behavior in the thermal entrance region of rectangular ducts has stimulated the interest of many authors, as proved in the exhaustive review of Shah and Bhatti (1987). According to the classification proposed by Hartnett and Kostic (1989), this paper considers the H2 condition (i.e., constant wall heat flux and constant fluid axial heat flux) with different situations for every side of the rectangle. The developing Nusselt numbers for slug flow in H2 boundary conditions are quoted in literature only for parallel plates and square duct geometry (Chandrupatla, 1977). The aim of this work is the determination of the Nusselt number in the thermal entry of rectangular ducts, with arbitrary aspect ratio for all the eight H2 versions involving different combinations of heated and adiabatic walls, symbolically specified as follows: 4 (four heated sides), 3L (three heated sides and one adiabatic short side), 3S (three heated sides and one adiabatic long side), 2L (two heated long sides and two adiabatic short sides), 2S (two heated short sides and two adiabatic long sides), 2C (one long and one short heated sides), 1L (one heated long side), 1S (one heated short side).

Analysis and Solution

Consider a steady slug flow in the thermal entry length of a rectangular duct (a and b are the long and the short side, respectively), with uniform axial heat flux. A Cartesian system of coordinates ξ, η, ζ is assumed, having its origin in the left bottom corner of the inlet rectangular cross section, with ξ along the long side a, ζ perpendicular to the cross section. The inlet fluid conditions are uniform velocity V and temperature θ_0. Assuming constant physical properties, neglecting axial conduction, natural convection, and power sources, the nondimensional energy balance equation reads:

$$\frac{\partial^2 T}{\partial x^2} + \frac{\partial^2 T}{\partial y^2} = \frac{(1 + \beta)^2}{4\beta^2} \frac{\partial T}{\partial z} \tag{1}$$

with the boundary conditions $T(x, y, z = 0) = 0$, and:

$$\left.\frac{\partial T}{\partial x}\right|_{x=0} = d_1 \frac{(1 + \beta)}{2\beta}; \quad \left.\frac{\partial T}{\partial x}\right|_{x=1} = d_2 \frac{(1 + \beta)}{2\beta};$$

$$\left.\frac{\partial T}{\partial y}\right|_{y=0} = d_3 \frac{(1 + \beta)}{2\beta}; \quad \left.\frac{\partial T}{\partial y}\right|_{y=\beta} = d_4 \frac{(1 + \beta)}{2\beta} \tag{2}$$

where β is the aspect ratio ($\beta = b/a \le 1$) and the dimensionless temperature T and coordinates are:

[1] DIENCA, Facoltà di Ingegneria, Università di Bologna, Viale Risorgimento 2, 40136 Bologna, Italy.
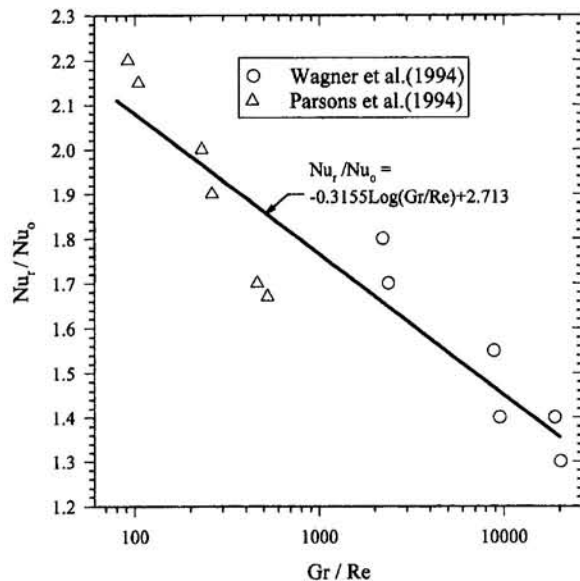
Fig. 2 Variation of leading side Nusselt number ratio with different adverse buoyancy levels in rotating ribbed channels

lar to those with the smooth-walled channels. The Nusselt number ratios are again regionally averaged taken from the published experimental data. Addition of turbulators to enhance heat transfer delays separation (other than the separation past the rib turbulators) by lowering the Reynolds number effect on the buoyancy Pohlhausen parameter due to a thinner boundary layer region. Figure 2 shows that the trend in the Nusselt number ratio is similar to that of the smooth leading surface (see Fig. 1) prior to flow separation. The correlated relationship of the Nusselt number ratio with the Gr/Re ratio can be given as $Nu_r/Nu_o = -0.3155 \log (Gr/Re) + 2.713$ with a regression correlation coefficient, $r = 0.93$. Turbulence promoters effectively increase the momentum in the boundary layer to levels that normally correspond to a higher Re in a smooth channel. This lowers the effective Gr/Re ratio and delays the flow separation and gives a higher performance. Moreover, in ribbed channels the enhanced turbulent mixing reduces the temperature gradient in the fluid and thus the buoyancy effects are further reduced.

References

Dutta, S., Andrews, M. J., and Han, J. C., 1996, "Prediction of Turbulent Heat Transfer in Rotating Smooth Square Ducts," *International Journal of Heat and Mass Transfer*, Vol. 39, No. 12, pp. 2505–2514.

Han, J. C., Zhang, Y. M., and Lee, C. P., 1994, "Influence of Surface Heating Condition on Local Heat Transfer in a Rotating Square Channel With Smooth Walls and Radial Outward Flow," ASME *Journal of Turbomachinery*, Vol. 116, pp. 149–158.

Parsons, J. A., Han, J. C., and Zhang, Y. M., 1994, "Wall Heating Effect on Local Heat Transfer in a Rotating Two-Pass Square Channel With 90° Rib Turbulators," *International Journal of Heat and Mass Transfer*, Vol. 37, No. 9, pp. 1411–1420.

Siegel, R., 1985, "Analysis of Buoyancy Effect on Fully Developed Laminar Heat Transfer in a Rotating Tube," ASME JOURNAL OF HEAT TRANSFER, Vol. 107, pp. 338–344.

Wagner, J. H., Johnson, B. V., and Kooper, F. C., 1991, "Heat Transfer in Rotating Serpentine Passages With Smooth Walls," ASME *Journal of Turbomachinery*, Vol. 113, pp. 321–330.

Wagner, J. H., Johnson, B. V., Graziani, R. A., and Yeh, F. C., 1994, "Heat Transfer in Rotating Serpentine Passages With Trips Normal to the Flow," ASME *Journal of Turbomachinery*, Vol. 116, pp. 113–123.

White, F. M., 1991, *Viscous Fluid Flow*, 2nd ed., McGraw-Hill Inc., New York, p. 268.

Yang, W. J., Zhang, N., and Chiou, J., 1992, "Local Heat Transfer in a Rotating Serpentine Flow Passage," ASME JOURNAL OF HEAT TRANSFER, Vol. 114, pp. 354–361.

The Thermal Entrance Length Problem for Slug Flow in Rectangular Ducts

M. Spiga[1] and G. L. Morini[1]

Introduction

Rectangular ducts have increasing importance in compact heat exchangers, while slug flow in the entrance region occurs in many applications of low-Prandtl-number fluids. The thermal behavior in the thermal entrance region of rectangular ducts has stimulated the interest of many authors, as proved in the exhaustive review of Shah and Bhatti (1987). According to the classification proposed by Hartnett and Kostic (1989), this paper considers the H2 condition (i.e., constant wall heat flux and constant fluid axial heat flux) with different situations for every side of the rectangle. The developing Nusselt numbers for slug flow in H2 boundary conditions are quoted in literature only for parallel plates and square duct geometry (Chandrupatla, 1977). The aim of this work is the determination of the Nusselt number in the thermal entry of rectangular ducts, with arbitrary aspect ratio for all the eight H2 versions involving different combinations of heated and adiabatic walls, symbolically specified as follows: 4 (four heated sides), 3L (three heated sides and one adiabatic short side), 3S (three heated sides and one adiabatic long side), 2L (two heated long sides and two adiabatic short sides), 2S (two heated short sides and two adiabatic long sides), 2C (one long and one short heated sides), 1L (one heated long side), 1S (one heated short side).

Analysis and Solution

Consider a steady slug flow in the thermal entry length of a rectangular duct (a and b are the long and the short side, respectively), with uniform axial heat flux. A Cartesian system of coordinates ξ, η, ζ is assumed, having its origin in the left bottom corner of the inlet rectangular cross section, with ξ along the long side a, ζ perpendicular to the cross section. The inlet fluid conditions are uniform velocity V and temperature θ_0. Assuming constant physical properties, neglecting axial conduction, natural convection, and power sources, the nondimensional energy balance equation reads:

$$\frac{\partial^2 T}{\partial x^2} + \frac{\partial^2 T}{\partial y^2} = \frac{(1+\beta)^2}{4\beta^2} \frac{\partial T}{\partial z} \tag{1}$$

with the boundary conditions $T(x, y, z = 0) = 0$, and:

$$\left.\frac{\partial T}{\partial x}\right|_{x=0} = d_1 \frac{(1+\beta)}{2\beta}; \quad \left.\frac{\partial T}{\partial x}\right|_{x=1} = d_2 \frac{(1+\beta)}{2\beta};$$

$$\left.\frac{\partial T}{\partial y}\right|_{y=0} = d_3 \frac{(1+\beta)}{2\beta}; \quad \left.\frac{\partial T}{\partial y}\right|_{y=\beta} = d_4 \frac{(1+\beta)}{2\beta} \tag{2}$$

where β is the aspect ratio ($\beta = b/a \le 1$) and the dimensionless temperature T and coordinates are:

[1] DIENCA, Facoltà di Ingegneria, Università di Bologna, Viale Risorgimento 2, 40136 Bologna, Italy.

$$x = \frac{\xi}{a} \ (0 \le x \le 1); \quad y = \frac{\eta}{a} \left(0 \le y \le \beta = \frac{b}{a} \right);$$

$$z = \frac{1}{\text{Gz}} \ge 0; \quad T = \frac{K(\theta - \theta_0)}{qD} \quad (3)$$

The dimensionless temperature T depends on the thermal conductivity K, the wall heat flux q (constant on the heated perimeter), and the hydraulic diameter D. The dimensionless longitudinal coordinate z represents the inverse of the Graetz number ($\text{Gz} = VD^2/\zeta\alpha$), with α the fluid thermal diffusivity. The coefficients d_1, d_2, d_3, d_4 depend on the combination of heated and adiabatic walls, they constitute a set of four numbers for every version; d_1 and d_2 refer to the short sides of the rectangular wetted perimeter, d_3 and d_4 refer to the long sides; they are 0 for adiabatic walls, +1 or −1 for heated walls (the sign depending on the way of the temperature gradient).

The solution to the partial differential equation is sought as a double series of orthogonal functions:

$$T(x, y, z) = \sum_{n=0}^{\infty} \sum_{m=0}^{\infty} C_{nm}(z) \cos(n\pi x) \cos\left(m\pi \frac{y}{\beta}\right) \quad (4)$$

By substituting Eq. (4) into Eq. (1), multiplying each term by $\cos(k\pi x) \cos(j\pi y/\beta)$ and integrating over x and y on their respective domains, a simple equation can be obtained that allows one to determine the unknown coefficients $C_{kj}(z)$:

$$\begin{cases} C_{kj}(z) = 0 \quad \text{if} \quad k \ne 0, j \ne 0 \\[2mm] C_{k0}(z) = [d_2(-1)^k - d_1]\dfrac{1 + \beta}{k^2\pi^2\beta} \\[2mm] \quad \times \left[1 - \exp\left(-\dfrac{4k^2\pi^2\beta^2}{(1 + \beta)^2} z \right) \right] \quad \text{if} \quad k \ne 0, j = 0 \\[4mm] C_{0j}(z) = [d_4(-1)^j - d_3]\dfrac{1 + \beta}{j^2\pi^2} \\[2mm] \quad \times \left[1 - \exp\left(-\dfrac{4j^2\pi^2}{(1 + \beta)^2} z \right) \right] \quad \text{if} \quad k = 0, j \ne 0 \\[4mm] C_{00}(z) = \dfrac{2L}{1 + \beta} z \quad \text{if} \quad k = 0, j = 0 \end{cases}$$
$$\tag{5}$$

Developing Nusselt Numbers and the Thermally Developed Flow

The local Nusselt number ($\text{Nu} = hD/K$) can be calculated starting from the fluid bulk temperature T_{bulk} and average wall temperature T_w. Resorting to the temperature solution, Eq. (4), one obtains:

$$T_{\text{bulk}}(z) = \int_0^\beta \int_0^1 T(x, y, z)dxdy = \frac{2L}{(1 + \beta)} z \quad (6)$$

where L is the dimensionless heated perimeter length. As usual the average wall temperature is defined as:

$$T_w(z) = \frac{1}{L}\left(-d_1 \int_0^\beta T(0, y, z)dy + d_2 \int_0^\beta T(1, y, z)dy \right.$$

$$\left. - d_3 \int_0^1 T(x, 0, z)dx + d_4 \int_0^1 T(x, \beta, z)dx \right) \quad (7)$$

The local developing Nusselt number is then:

$$\text{Nu}(z) = \frac{1}{T_w(z) - T_{\text{bulk}}(z)} \quad (8)$$

while the dimensionless thermal entrance length L_{th} is defined in the literature by the equation $\text{Nu}(z = L_{th}) = 1.05\, \text{Nu}_\infty$, being Nu_∞ the established Nusselt number in the fully developed region. Equation (4) can be used in order to obtain also the temperature distribution $T_\infty(x, y)$ for the thermally developed flow, in the limit $z \to \infty$. As is well known, the H2 boundary conditions permits deduction of the two-dimensional temperature profile apart from an arbitrary constant. The asymptotic values of the coefficients C_{kj}, Eqs. (5), are easily computable. Resorting to the sum of cosinusoidal series, the fully developed temperature profile, apart from the constant C_{00}, reads:

$$T_\infty(x, y) = \frac{1 + \beta}{2\beta}\left[\frac{d_2}{2}\left(x^2 - \frac{1}{3} \right) - d_1\left(\frac{1}{3} - x + \frac{x^2}{2} \right) \right.$$

$$\left. + \frac{d_4}{2}\left(\frac{y^2}{\beta} - \frac{\beta}{3} \right) - d_3\left(\frac{\beta}{3} - y + \frac{y^2}{2\beta} \right) \right] \quad (9)$$

The average wall temperature in the fully developed region becomes:

$$T_{w,\infty} = \frac{1 + \beta}{6L}(d_1^2 + d_2^2 + d_3^2 + d_4^2 + d_1 d_2 + d_3 d_4) \quad (10)$$

while the bulk temperature is 0. These results, obtained as the limiting situation of the general solution (4), coincide exactly with the expression proposed recently by Gao and Hartnett (1994) for slug flow in the thermally developed region, deduced with a quite different technique.

Results and Conclusions

Table 1 shows the thermal entry length and the fully established Nusselt number as functions of the aspect ratio, for all the H2 versions. The thermal entrance length is a decreasing function of β for the 1S, 2S, 2C, 3L, 3S, and 4 versions, and increases with β only for the 1L and 2L versions. The established Nusselt number Nu_∞ decreases with β for the 1L, 2L, 3L versions and increases for the 1S, 2S, 3S versions; it is constant (respectively 3 and 6) for the 2C and 4 versions. The numerical results offer the opportunity to put in evidence some interesting analogies for the developing Nusselt numbers for the 1L, 1S, 2L, and 2S versions of H2 boundary conditions. It is suitable to introduce the axial dimensionless coordinate $z_{th} = z/L_{th}$; in fact the Nusselt ratio $\text{Nu}(z_{th})/\text{Nu}_\infty$ presents exactly the same values and does not depend on the aspect ratio, as shown in Table 2. The developing Nusselt number for the 1L, 2L, 1S, 2S versions is given, with an agreement within 0.8 percent, by the approximate polynomial:

$$\text{Nu}(z_{th}) = \text{Nu}_\infty (3.1415 - 13.5012\, z_{th} + 40.9178 z_{th}^2$$

$$- 64.717 z_{th}^3 + 50.9097 z_{th}^4 - 15.6026 z_{th}^5) \quad (11)$$

A comparison between the numerical results obtained by Eq. (8) and the graphic data quoted in the literature can be performed only in the square duct with four heated walls (p. 293 in Hartnett and Kostic, 1989), the agreement is quite satisfactory, as shown in Fig. 1, where the Nusselt number is reported as a function of the Graetz number.

Moreover a rigorous correlation between the thermal entrance length and the aspect ratio can be simply obtained. Considering the 1L and 1S versions, the ratio between the developing and the fully established Nusselt number reads:

Table 1 Dimensionless thermal entrance length and established Nusselt number

	1L		1S		2L		2S		2C		3L		3S		4	
β	L_{th}	Nu_∞	L_{th}	Nu_∞	L_{th}	Nu_∞	L_{th}	Nu_∞	L_{th}	Nu_∞	L_{th}	Nu_∞	L_{th}	Nu_∞	L_{th}	Nu_∞
1	0.2581	3	0.2581	3	0.0645	6	0.0645	6	0.2723	3	0.2099	9/2	0.2099	9/2	0.0719	6
0.9	0.2329	60/19	0.2875	54/19	0.0582	120/19	0.0719	108/19	0.2756	3	0.2340	87/19	0.1897	84/19	0.0730	6
0.8	0.2090	10/3	0.3266	8/3	0.0523	20/3	0.0816	16/3	0.2876	3	0.2653	14/3	0.1727	39/9	0.0764	6
0.7	0.1864	60/17	0.3805	42/17	0.0466	120/17	0.0951	84/17	0.3139	3	0.3095	81/17	0.1600	72/17	0.0838	6
0.6	0.1652	15/4	0.4588	9/4	0.0413	30/4	0.1147	9/2	0.3642	3	0.3731	39/8	0.1539	33/8	0.0977	6
0.5	0.1452	4	0.5806	2	0.0363	4	0.1451	4	0.4556	3	0.4723	5	0.1575	4	0.1229	6
0.4	0.1265	30/7	0.7903	12/7	0.0316	60/7	0.1976	24/7	0.6192	3	0.6426	36/7	0.1791	27/7	0.1672	6
0.3	0.1090	60/13	1.211	18/13	0.0273	120/13	0.3028	36/13	0.9504	3	0.9853	69/13	0.2491	48/13	0.2561	6
0.2	0.0929	5	2.323	1	0.0232	10	0.5806	2	1.8238	3	1.8883	11/2	0.4721	7/2	0.4903	6
0.1	0.0781	60/11	7.806	6/11	0.0195	120/11	1.9515	12/11	6.1090	3	6.3311	63/11	1.5880	36/11	1.6463	6

$$\frac{Nu^{1L}(z_{th})}{Nu_\infty^{1L}} = \left[1 - \frac{6}{\pi^2} \sum_{j=1}^{\infty} \frac{1}{j^2} \exp\left(\frac{-4\pi^2 j^2 L_{th,1L}}{(1+\beta)^2} z_{th} \right) \right]^{-1} \quad (12)$$

$$\frac{Nu^{1S}(z_{th})}{Nu_\infty^{1S}} = \left[1 - \frac{6}{\pi^2} \sum_{j=1}^{\infty} \frac{1}{j^2} \exp\left(\frac{-4\pi^2 j^2 \beta^2 L_{th,1S}}{(1+\beta)^2} z_{th} \right) \right]^{-1} \quad (13)$$

As shown in Table 1, this ratio must be independent on the aspect ratio; consequently Eqs. (12) and (13) state that the thermal entrance lengths must be functions of β in the form:

$$L_{th,1L} = \lambda_1 (1+\beta)^2 \quad L_{th,1S} = \lambda_1 \frac{(1+\beta)^2}{\beta^2} \quad (14)$$

The constant λ_1 is the same for the 1L and 1S versions, since $L_{th,1L} = L_{th,1S}$ for $\beta = 1$. This constant has a well-defined physical meaning: it is the dimensionless thermal entry length for slug flow between infinite parallel plates ($\beta = 0$) heated on one side only.

With analogous considerations the thermal entrance lengths for the 2L and 2S versions are obtained:

$$L_{th,2L} = \lambda_2 (1+\beta)^2 \quad L_{th,2S} = \lambda_2 \frac{(1+\beta)^2}{\beta^2} \quad (15)$$

where λ_2 is the thermal entrance length for slug flow between infinite parallel plates heated on both sides.

In order to evaluate λ_1 and λ_2, the problem of infinite parallel plates must be tackled. Let us consider a slug flow in a semi-infinite slab, in a two-dimensional system of Cartesian coordinates x, z, with z being the axial coordinate in the flow direction and $z = 0$ is the fluid inlet cross section. Considering only one heated side, the dimensionless fluid temperature profile $T_{slab,1}$ is the solution to the balance equation linked to its boundary conditions:

$$\frac{\partial^2 T_{slab,1}}{\partial x^2} = \frac{1}{4} \frac{\partial T_{slab,1}}{\partial z} \quad \text{with} \quad T_{slab,1}(x, z = 0) = 0,$$

$$\left. \frac{\partial T_{slab,1}}{\partial x} \right|_{x=1} = \frac{1}{2}, \quad \left. \frac{\partial T_{slab,1}}{\partial x} \right|_{x=0} = 0 \quad (16)$$

Table 2 Ratio between the developing and the established Nusselt numbers for any aspect ratio: 1L, 1S, 2L, and 2S versions

	z_{th}=0.1	z_{th}=0.2	z_{th}=0.3	z_{th}=0.4	z_{th}=0.5	z_{th}=0.6	z_{th}=0.7	z_{th}=0.8	z_{th}=0.9	z_{th}=1
Nu/Nu_∞	2.143	1.627	1.408	1.285	1.206	1.152	1.114	1.086	1.065	1.05

If the slab has two heated sides, the temperature profile $T_{slab,2}$ must satisfy the same Eqs. (16), but the last boundary condition, in the plane $x = 0$, becomes:

$$\left. \frac{\partial T_{slab,2}}{\partial x} \right|_{x=0} = -\frac{1}{2} \quad (17)$$

According to the finite Fourier transform technique (multiplying each term of Eq. (16) by cos $(n\pi x)$ and integrating over $0 \le x \le 1$), the fluid temperatures are given by the series:

$$T_{slab,1}(x, z) = 2z + \frac{1}{\pi^2} \sum_{n=1}^{\infty} \frac{(-1)^n}{n^2} [1 - \exp(-4n^2\pi^2 z)] \cos(n\pi x) \quad (18)$$

$$T_{slab,2}(x, z) = 2z + \frac{2}{\pi^2} \sum_{n=2,even}^{\infty} \frac{1}{n^2} [1 - \exp(-4n^2\pi^2 z)] \cos(n\pi x) \quad (19)$$

The developing Nusselt numbers are determined through Eq. (8) and the fully established Nusselt numbers are calculated in the limit of $z \to \infty$; their ratio reads:

$$\frac{Nu_{slab,1}(z)}{Nu_{slab,1}^\infty} = \left[1 - \frac{6}{\pi^2} \sum_{n=1}^{\infty} \frac{\exp(-4n^2\pi^2 z)}{n^2} \right]^{-1} \quad (20)$$

$$\frac{Nu_{slab,2}(z)}{Nu_{slab,2}^\infty} = \left[1 - \frac{24}{\pi^2} \sum_{n=2,even}^{\infty} \frac{\exp(-4n^2\pi^2 z)}{n^2} \right]^{-1} \quad (21)$$
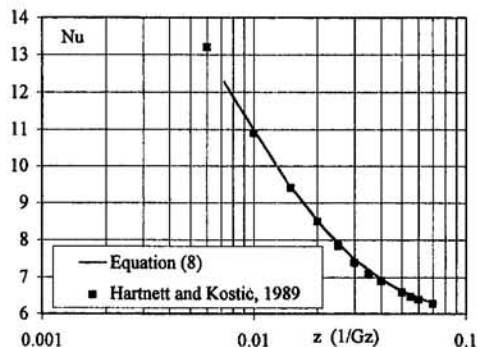

Fig. 1 Developing Nusselt number as a function of the Graetz number for a square duct (4 version)

These developing Nusselt numbers in the slab geometry show a perfect agreement with the analogous results quoted in the graph at p. 292 of Hartnett and Kostic (1989). Finally, resorting to their definition, the thermal entrance lengths are easily numerically obtained with a precision up to the fifth digit: $\lambda_1 = 0.064515$ and $\lambda_2 = \lambda_1/4 = 0.016129$. The thermal entry lengths, Eqs. (14) and (15), for rectangular ducts in H2 condition (1L, 1S, 2L, and 2S versions) are so completely specified.

Acknowledgments

References

Chandrupatla, A. R., 1977, "Analytical and Experimental Studies of Flow and Heat Transfer Characteristic of a Non-Newtonian Fluid in a Square Duct," Ph.D. thesis, Indian Institute of Technology, Madras, India.

Gao, S. X., and Hartnett, J. P., 1994, "Analytical Nusselt Number Predictions for Slug Flow in Rectangular Ducts," Int. Comm. Heat Mass Transfer, Vol. 20, pp. 751–760.

Hartnett, J. P., and Kostic, M., 1989, "Heat Transfer to Newtonian and Non-Newtonian Fluids in Rectangular Ducts," Adv. Heat Transfer, Vol. 19, Academic Press, New York, pp. 247–356.

Shah, R. K., and Bhatti, M. S., 1987, "Laminar Convective Heat Transfer in Ducts," Handbook of Single Phase Convective Heat Transfer, S. Kakaç, R. K. Shah, and W. Aung, eds., Vol. 1, Section 7-87, Wiley, New York.

Measurement of Convective Heat Transfer Using Hot Film Sensors: Correction for Sensor Overheat

J. W. Scholten[1] and D. B. Murray[1]

Nomenclature

k = fluid thermal conductivity, W/mK
q_{conv} = convective heat flux, W/m^2
q_{sensor} = heat flux from the sensor, W/m^2
q_{shear} = heat flux for shear stress conditions, W/m^2
T = temperature, K
T_{amb} = ambient temperature, K
T_{overh} = temperature difference between surface and sensor, K
T_{sensor} = sensor temperature, K
T_{surf} = surface temperature, K
T_{y^+} = air temperature at distance y^+, K
$T_{y^+,unh}$ = temperature at y^+ for shear stress conditions, K
y = coordinate perpendicular to the surface, m
y^+ = small distance above the surface, m

Introduction

The need for an improved understanding of convective heat transfer in applications involving turbulent flows has led to the use of hot film sensors for time-resolved measurements of local heat flux (Schultz and Jones, 1973; Beasley and Figliola, 1988). For cylinders in crossflow, Rosiczkowski & Hollworth (1991)

[1] Department of Mechanical Engineering, Trinity College, Dublin 2, Ireland.

used a hot film sensor maintained at a constant surface temperature to measure time varying heat flux on the surface of an oscillating cylinder in crossflow. In all cases, it is necessary to modify the measured heat flux to account for conduction between the heated metallic film and the sensor substrate, as described by Beasley and Figliola (1988). Problems with the use of hot and cold film sensors in stagnation regions, and where surface temperature discontinuities exist, have also been identified by van Heiningen et al. (1976). In addition, a recent study by Scholten & Murray (1995) of time-resolved heat transfer on the surface of a cylinder in crossflow has shown that errors arise in determining time-averaged Nusselt numbers from heat flux measurements obtained with a hot film sensor. These errors have been found to be directly linked to the degree of overheating of the hot film sensor; however, Moen and Schneider (1994) have found that low overheating leads to reduced sensor sensitivity. Thus, it is not possible to eliminate the measurement error by operating the hot film sensor with a negligible degree of overheat.

The present paper analyzes the error in time-averaged heat flux arising from sensor overheat and describes a method that can be used to correct for this problem.

Analysis of Overheat Correction

Figure 1 displays a hot film sensor mounted on a heated surface for the purpose of measuring convective heat flux. As mentioned above a certain degree of sensor overheating is needed in order to achieve high sensitivity. The error in heat flux measurement encountered by Scholten and Murray (1995), for nominally uniform wall temperature conditions, is a consequence of the surface temperature discontinuity induced by this sensor overheating.

For convective heat transfer, the heat flux from the sensor can be represented by one-dimensional conduction at the wall as:

$$q_{sensor} = -k \frac{\partial T}{\partial y}\bigg|_0 \qquad (1)$$

where T is the fluid temperature, k is the fluid thermal conductivity, and y represents the coordinate direction normal to the surface. Introducing y^+ as an arbitrary location close to the heated surface, the wall temperature gradient can be approximated as follows:

$$q_{sensor} = k \frac{T_{sensor} - T_{y^+}}{y^+} = k \frac{T_{surf} + T_{overh} - T_{y^+}}{y^+} \qquad (2)$$

Although the thermal boundary layer thickness varies with both Reynolds number and angular position on the cylinder, y^+ always constitutes a small fraction of the thermal boundary layer thickness. T_{overh} represents the temperature difference between
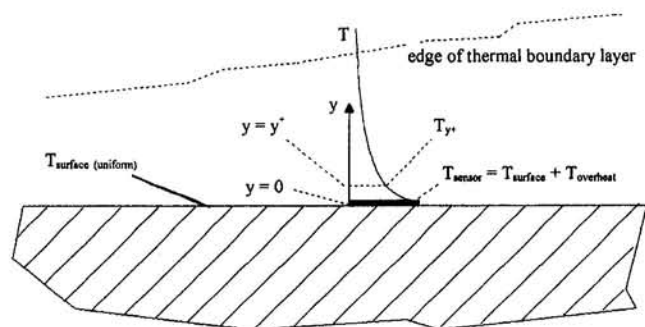

Fig. 1 Air temperature profile in the boundary layer above the hot film sensor

These developing Nusselt numbers in the slab geometry show a perfect agreement with the analogous results quoted in the graph at p. 292 of Hartnett and Kostic (1989). Finally, resorting to their definition, the thermal entrance lengths are easily numerically obtained with a precision up to the fifth digit: $\lambda_1 = 0.064515$ and $\lambda_2 = \lambda_1/4 = 0.016129$. The thermal entry lengths, Eqs. (14) and (15), for rectangular ducts in H2 condition (1L, 1S, 2L, and 2S versions) are so completely specified.

Acknowledgments

References

Chandrupatla, A. R., 1977, "Analytical and Experimental Studies of Flow and Heat Transfer Characteristic of a Non-Newtonian Fluid in a Square Duct," Ph.D. thesis, Indian Institute of Technology, Madras, India.

Gao, S. X., and Hartnett, J. P., 1994, "Analytical Nusselt Number Predictions for Slug Flow in Rectangular Ducts," *Int. Comm. Heat Mass Transfer*, Vol. 20, pp. 751–760.

Hartnett, J. P., and Kostic, M., 1989, "Heat Transfer to Newtonian and Non-Newtonian Fluids in Rectangular Ducts," *Adv. Heat Transfer*, Vol. 19, Academic Press, New York, pp. 247–356.

Shah, R. K., and Bhatti, M. S., 1987, "Laminar Convective Heat Transfer in Ducts," *Handbook of Single Phase Convective Heat Transfer*, S. Kakaç, R. K. Shah, and W. Aung, eds., Vol. 1, Section 7-87, Wiley, New York.

Measurement of Convective Heat Transfer Using Hot Film Sensors: Correction for Sensor Overheat

J. W. Scholten[1] and D. B. Murray[1]

Nomenclature

k = fluid thermal conductivity, W/mK
q_{conv} = convective heat flux, W/m^2
q_{sensor} = heat flux from the sensor, W/m^2
q_{shear} = heat flux for shear stress conditions, W/m^2
T = temperature, K
T_{amb} = ambient temperature, K
T_{overh} = temperature difference between surface and sensor, K
T_{sensor} = sensor temperature, K
T_{surf} = surface temperature, K
T_{y^+} = air temperature at distance y^+, K
$T_{y^+,unh}$ = temperature at y^+ for shear stress conditions, K
y = coordinate perpendicular to the surface, m
y^+ = small distance above the surface, m

Introduction

The need for an improved understanding of convective heat transfer in applications involving turbulent flows has led to the use of hot film sensors for time-resolved measurements of local heat flux (Schultz and Jones, 1973; Beasley and Figliola, 1988). For cylinders in crossflow, Rosiczkowski & Hollworth (1991)

used a hot film sensor maintained at a constant surface temperature to measure time varying heat flux on the surface of an oscillating cylinder in crossflow. In all cases, it is necessary to modify the measured heat flux to account for conduction between the heated metallic film and the sensor substrate, as described by Beasley and Figliola (1988). Problems with the use of hot and cold film sensors in stagnation regions, and where surface temperature discontinuities exist, have also been identified by van Heiningen et al. (1976). In addition, a recent study by Scholten & Murray (1995) of time-resolved heat transfer on the surface of a cylinder in crossflow has shown that errors arise in determining time-averaged Nusselt numbers from heat flux measurements obtained with a hot film sensor. These errors have been found to be directly linked to the degree of overheating of the hot film sensor; however, Moen and Schneider (1994) have found that low overheating leads to reduced sensor sensitivity. Thus, it is not possible to eliminate the measurement error by operating the hot film sensor with a negligible degree of overheat.

The present paper analyzes the error in time-averaged heat flux arising from sensor overheat and describes a method that can be used to correct for this problem.

Analysis of Overheat Correction

Figure 1 displays a hot film sensor mounted on a heated surface for the purpose of measuring convective heat flux. As mentioned above a certain degree of sensor overheating is needed in order to achieve high sensitivity. The error in heat flux measurement encountered by Scholten and Murray (1995), for nominally uniform wall temperature conditions, is a consequence of the surface temperature discontinuity induced by this sensor overheating.

For convective heat transfer, the heat flux from the sensor can be represented by one-dimensional conduction at the wall as:

$$q_{sensor} = -k \frac{\partial T}{\partial y}\bigg|_0 \qquad (1)$$

where T is the fluid temperature, k is the fluid thermal conductivity, and y represents the coordinate direction normal to the surface. Introducing y^+ as an arbitrary location close to the heated surface, the wall temperature gradient can be approximated as follows:

$$q_{sensor} = k \frac{T_{sensor} - T_{y^+}}{y^+} = k \frac{T_{surf} + T_{overh} - T_{y^+}}{y^+} \qquad (2)$$

Although the thermal boundary layer thickness varies with both Reynolds number and angular position on the cylinder, y^+ always constitutes a small fraction of the thermal boundary layer thickness. T_{overh} represents the temperature difference between
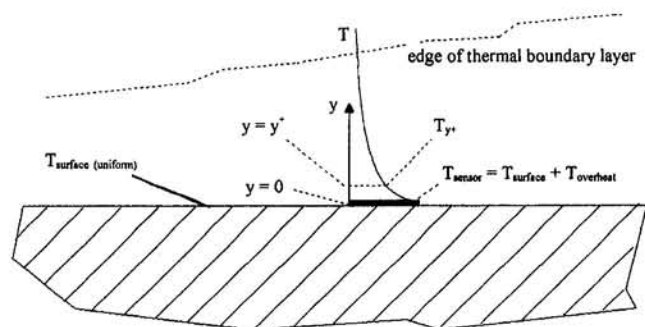

Fig. 1 Air temperature profile in the boundary layer above the hot film sensor

the hot film and the surface of the sensor substrate. This expression can be split into two parts:

$$q_{sensor} = k \frac{T_{surf} - T_{y^+}}{y^+} + k \frac{(T_{overh} + T_{y^+,unh}) - T_{y^+,unh}}{y^+} \quad (3)$$

in which $T_{y^+,unh}$ is the temperature at location y^+ when the surface is not heated. It then follows that the second term on the right-hand side of Eq. (3) represents the heat flux from the thin film sensor when it is used to measure shear stress. The first term on the right-hand side is the convective heat flux for the ideal boundary condition in which the sensor is maintained at the same temperature as the surrounding surface. It is therefore concluded that, when convective heat transfer rates are required for a constant-temperature boundary condition, the measured heat transfer rate has to be corrected for the small overheat temperature by means of subtracting the shear stress heat transfer rate:

$$q_{conv}\Big|_{T_{sensor}=T_{surface}}$$

$$= q_{sensor}\Big|_{T_{sensor}=T_{surface}+T_{overh}} - q_{shear}\Big|_{T_{sensor}=T_{overh}+T_{amb}} \quad (4)$$

Experimentation

The validity of the overheat correction technique is illustrated by examining experimental data obtained from a 25-mm-diameter internally heated copper tube, mounted horizontally in a low-turbulence wind tunnel with an upstream velocity of 15 m/s (corresponding to a Reynolds number of 24,000). Midway along the tube length, a Dantec 55R47 hot film sensor was mounted directly above an embedded type-T thermocouple junction with the hot film itself being aligned with the axis of the cylinder. This gives a spatial resolution in the circumferential direction of 0.9 deg.

The hot film was connected to a Dantec 55M10 standard bridge, which maintains the temperature of the hot film constant. The estimated uncertainty in the absolute temperature of the hot film and of the tube surface is ±0.3°C. However, the uncertainty in temperature difference between the hot film and the tube surface is ±0.1°C. The output from the bridge and the
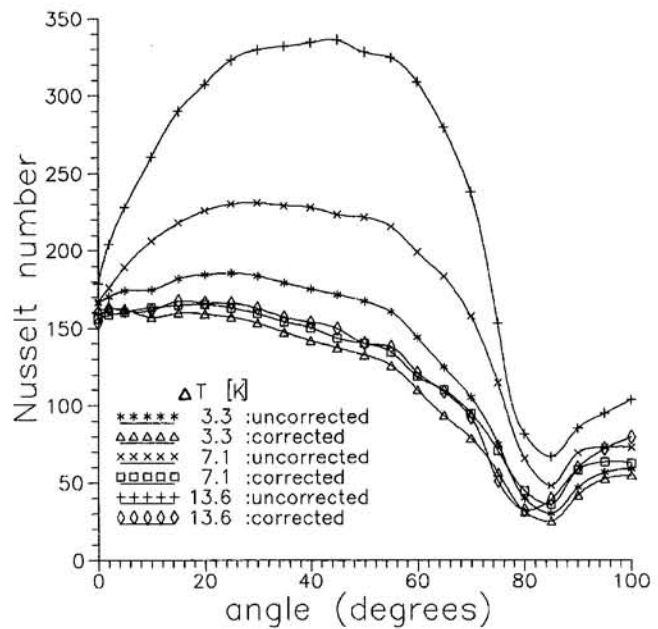
Fig. 3 Variation in Nusselt number, with and without shear stress correction for tests conducted with overheats of 3.3°C, 7.1°C, and 13.6°C

surface temperature were logged into a computer through an A–D board. The heat transfer rates were calculated by dividing the power dissipated in the hot film by its effective surface area (1.5 × actual area) where the effective area is used to quantify lateral conduction within the substrate (Beasley and Figliola, 1988). For the range of sensor overheat and convective heat transfer coefficients encountered in the present study it has been established, using the approach of Beasley and Figliola (1988), that the effective surface area is essentially constant. The contribution of radial conduction into the tube through the sensor substrate has been accounted for by use of the embedded type-T thermocouple located directly beneath the sensor. Details of the experimental setup have been given by Scholten and Murray (1995).

Results and Discussion

Figure 2 shows the measured shear stress variation around the tube circumference. The values given are the local heat transfer rates per °C temperature difference between the sensor and the air flow over the cylinder. Note that thin film sensors are unable to measure negative values and do not detect the expected zero shear stress at boundary layer separation. Thus, the correction procedure should not be applied to the results for the separated flow region.

The variation in Nusselt number with and without shear stress correction is shown in Fig. 3 for tests conducted with overheats of 3.3°C, 7.1°C, and 13.6°C, with overheat defined as for Eq. (2). It should be noted that the two larger overheat ratios are used solely to confirm the validity of the correction procedure and would not be used under normal test conditions. The actual temperature difference between the hot film and the copper tube is as small as 0.5°C in the smallest overheat case, and this approaches the limit for stable sensor operating conditions, with a reasonable sensitivity. It is clear that the uncorrected data show a heat transfer maximum at around 30–40 deg whereas the results obtained using Eq. (4) show the characteristic pattern for a single tube in crossflow of a maximum at the front stagnation point. The minimum heat transfer at 85 deg corresponds to boundary layer separation, and it can be seen that the low shear stress and heat flux levels in this region mean that the magnitude of the Nusselt number correction is very small.
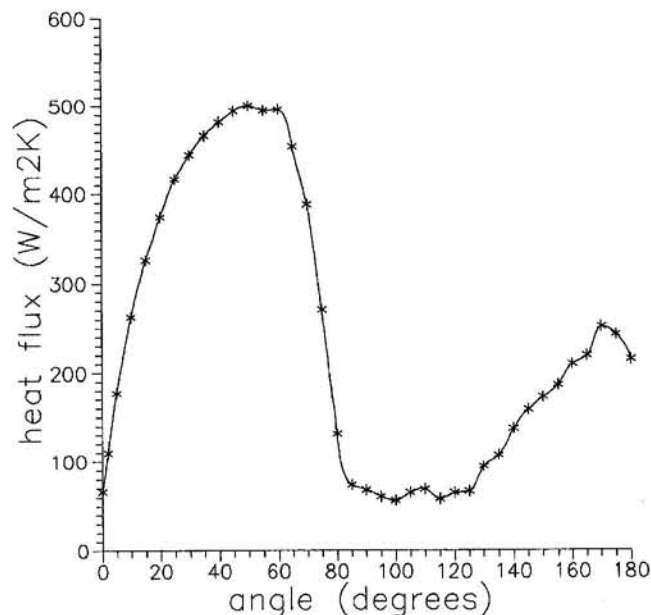
Fig. 2 Local heat transfer rates for shear stress conditions, given per degree temperature difference between the sensor and the ambient air

All tests were carried out for the same flow conditions and Reynolds number. It is clear that increasing the overheat ratio leads to an ever-increasing distortion in the measured Nusselt number pattern as compared with that expected for a single tube in crossflow. The heat transfer pattern for the highest overheat ratio is now closer in shape to the characteristic shear stress variation shown in Fig. 2. Examination of the Nusselt numbers obtained using Eq. (4), however, indicates that the expected variation in heat transfer with angular position is achieved, and the corrected variation in time-averaged Nusselt number is consistent with the findings of van Meel (1962), for a Reynolds number of 26,620.

Conclusions

Tests carried out with a single cylinder in crossflow have shown that the use of hot film sensors for measuring time-averaged local heat transfer can lead to substantial errors in local Nusselt number. The magnitude of the error is dependent on the overheat ratio, but the need for high sensitivity means that it cannot be eliminated by reducing the degree of overheat to a negligible value. Analysis of the temperature discontinuities associated with the surface-mounted sensor has led to the development of a procedure for correcting for a degree of overheat. Although it is possible to correct for large degrees of overheat, it is preferable to operate with the smallest film-to-surface tem-

perature difference consistent with the requirement for sensor sensitivity. For the present conditions, this corresponds to an overheat of 3.3°C. The results obtained using this correction have been shown to be consistent with the anticipated heat transfer variation for a single tube in crossflow. Although the overheat correction has been applied to the crossflow case only, the analysis is general and could find application in many convective heat transfer problems.

References

Beasley, D. E., and Figliola, R. S., 1988, "A Generalised Analysis of a Local Heat Flux Probe," *J. Physics E.,* Vol. 21, pp. 316–322.

Moen, M. J., and Schneider, S. P., 1994, "The Effect of Sensor Size on the Performance of Flush-Mounted Hot-Film Sensors," ASME *Journal of Fluids Engineering,* vol. 116, pp. 273–277.

Rosiczkowski, J., and Hollworth, B., 1991, "Local and Instantaneous Heat Transfer From an Isothermal Cylinder in a Cross Flow," *Fund. Exp. Meas. in Heat Transfer,* ASME HTD-Vol. 179, pp. 49–56.

Scholten, J. W., and Murray, D. B., 1995, "Time Resolved Heat Transfer Measurements for a Cylinder With Boundary Layer Transition," *Proc. 4th U.K. National Heat Transfer Conference,* Manchester, pp. 111–115.

Schultz, D. L., and Jones, T. V., 1973, "Heat Transfer Measurements in Short Duration Hypersonic Facilities," AGARDograph No. 165.

van Heiningen, A. R. P., Mujamdar, A. S., and Douglas, W. J. M., 1976, "On the Use of Hot and Cold Film Sensors for Skin Friction and Heat Transfer Measurements in Impingement Flows," *Letters in Heat and Mass Transfer,* Vol. 3, pp. 523–528.

van Meel, D. A., 1962, "A Method for Determination of Local Convective Heat Transfer From a Cylinder Placed Normal to an Airstream," *Int. J. Heat Mass Transfer,* Vol. 5, pp. 715–722.

Mixed Convective Heat Transfer Between a Series of Vertical Parallel Plates With Planar Heat Sources

J. C. Watson,[1,2] N. K. Anand,[1,3] and L. S. Fletcher[1]

Nomenclature

B = width of channel (x direction)
B_t = width of domain (wall + channel width)
c_p = specific heat
D_h = hydraulic diameter
Gr = Grashof number based on channel width = $g\beta q'' B^4/\nu^2 k$
Gr* = Grashof number defined with wall temperature = $g\beta(T_h - T_0)D_h^3/\nu^2$
g = acceleration due to gravity
K = ratio of wall or plate conductivity to fluid conductivity
k = thermal conductivity
L = length of wall (y direction)
L_e = length of extended domain (y direction)
L_t = length of entire domain (y direction)
Nu = Nusselt number, = hD_h/k_f
P = pressure
Pr = Prandtl number = $\mu c_p/k_f$
$\dot{Q}$ = source heat rate
q'' = source heat flux
Re = Reynolds number based on channel width = $v_o B/\nu$
Re_D = Reynolds number based on hydraulic diameter = $v_o D_h/\nu$
T = temperature (dimensional)
u = transverse velocity (dimensional)
V = axial velocity (nondimensional) = v/v_o
v = axial velocity (dimensional)

W = width of wall (x direction)
X = non-dimensional horizontal location = x/B_t
x = horizontal allocation (dimensional)
x' = alternate non-dimensional location (origin at the cold wall) = x/B
Y = nondimensional vertical distance = y/L
y = vertical location (dimensional)
β = thermal expansion coefficient
θ = nondimensional temperature = $(T - T_o)k_f/q''B$
μ = dynamic viscosity
ν = kinematic viscosity
ρ = density

Subscripts

0 = inlet
av = average
c = cold surface
D = properties based on hydraulic diameter
f = fluid
h = hot surface
P = pressure
w = wall

Superscript

$-$ = average

Introduction

Convective heat transfer among parallel plates has important applications in the areas of electronics packaging, heat exchanger design, and solar energy collection. In the electronics

All tests were carried out for the same flow conditions and Reynolds number. It is clear that increasing the overheat ratio leads to an ever-increasing distortion in the measured Nusselt number pattern as compared with that expected for a single tube in crossflow. The heat transfer pattern for the highest overheat ratio is now closer in shape to the characteristic shear stress variation shown in Fig. 2. Examination of the Nusselt numbers obtained using Eq. (4), however, indicates that the expected variation in heat transfer with angular position is achieved, and the corrected variation in time-averaged Nusselt number is consistent with the findings of van Meel (1962), for a Reynolds number of 26,620.

Conclusions

Tests carried out with a single cylinder in crossflow have shown that the use of hot film sensors for measuring time-averaged local heat transfer can lead to substantial errors in local Nusselt number. The magnitude of the error is dependent on the overheat ratio, but the need for high sensitivity means that it cannot be eliminated by reducing the degree of overheat to a negligible value. Analysis of the temperature discontinuities associated with the surface-mounted sensor has led to the development of a procedure for correcting for a degree of overheat. Although it is possible to correct for large degrees of overheat, it is preferable to operate with the smallest film-to-surface tem-

perature difference consistent with the requirement for sensor sensitivity. For the present conditions, this corresponds to an overheat of 3.3°C. The results obtained using this correction have been shown to be consistent with the anticipated heat transfer variation for a single tube in crossflow. Although the overheat correction has been applied to the crossflow case only, the analysis is general and could find application in many convective heat transfer problems.

References

Beasley, D. E., and Figliola, R. S., 1988, "A Generalised Analysis of a Local Heat Flux Probe," *J. Physics E.*, Vol. 21, pp. 316–322.

Moen, M. J., and Schneider, S. P., 1994, "The Effect of Sensor Size on the Performance of Flush-Mounted Hot-Film Sensors," ASME *Journal of Fluids Engineering*, vol. 116, pp. 273–277.

Rosiczkowski, J., and Hollworth, B., 1991, "Local and Instantaneous Heat Transfer From an Isothermal Cylinder in a Cross Flow," *Fund. Exp. Meas. in Heat Transfer*, ASME HTD-Vol. 179, pp. 49–56.

Scholten, J. W., and Murray, D. B., 1995, "Time Resolved Heat Transfer Measurements for a Cylinder With Boundary Layer Transition," *Proc. 4th U.K. National Heat Transfer Conference*, Manchester, pp. 111–115.

Schultz, D. L., and Jones, T. V., 1973, "Heat Transfer Measurements in Short Duration Hypersonic Facilities," AGARDograph No. 165.

van Heiningen, A. R. P., Mujamdar, A. S., and Douglas, W. J. M., 1976, "On the Use of Hot and Cold Film Sensors for Skin Friction and Heat Transfer Measurements in Impingement Flows," *Letters in Heat and Mass Transfer*, Vol. 3, pp. 523–528.

van Meel, D. A., 1962, "A Method for Determination of Local Convective Heat Transfer From a Cylinder Placed Normal to an Airstream," *Int. J. Heat Mass Transfer*, Vol. 5, pp. 715–722.

Mixed Convective Heat Transfer Between a Series of Vertical Parallel Plates With Planar Heat Sources

J. C. Watson,[1,2] N. K. Anand,[1,3] and L. S. Fletcher[1]

Nomenclature

B = width of channel (x direction)
B_t = width of domain (wall + channel width)
c_p = specific heat
D_h = hydraulic diameter
Gr = Grashof number based on channel width = $g\beta q''B^4/\nu^2 k$
Gr* = Grashof number defined with wall temperature = $g\beta(T_h - T_0)D_h^3/\nu^2$
g = acceleration due to gravity
K = ratio of wall or plate conductivity to fluid conductivity
k = thermal conductivity
L = length of wall (y direction)
L_e = length of extended domain (y direction)
L_t = length of entire domain (y direction)
Nu = Nusselt number, = hD_h/k_f
P = pressure
Pr = Prandtl number = $\mu c_p/k_f$
$\dot{Q}$ = source heat rate
q'' = source heat flux
Re = Reynolds number based on channel width = $v_o B/\nu$
Re_D = Reynolds number based on hydraulic diameter = $v_o D_h/\nu$
T = temperature (dimensional)
u = transverse velocity (dimensional)
V = axial velocity (nondimensional) = v/v_o
v = axial velocity (dimensional)
W = width of wall (x direction)
X = non-dimensional horizontal location = x/B_t
x = horizontal allocation (dimensional)
x' = alternate non-dimensional location (origin at the cold wall) = x/B
Y = nondimensional vertical distance = y/L
y = vertical location (dimensional)
β = thermal expansion coefficient
θ = nondimensional temperature = $(T - T_o)k_f/q''B$
μ = dynamic viscosity
ν = kinematic viscosity
ρ = density

Subscripts

0 = inlet
av = average
c = cold surface
D = properties based on hydraulic diameter
f = fluid
h = hot surface
P = pressure
w = wall

Superscript

$-$ = average

Introduction

Convective heat transfer among parallel plates has important applications in the areas of electronics packaging, heat exchanger design, and solar energy collection. In the electronics

[1] Texas A&M University, Department of Mechanical Engineering, College Station, TX 77843-3123.
[2] Currently with Adapco, Melville, NY.
[3] To whom all correspondence should be addressed.

industry, for instance, parallel plates with heat sources can simulate the cooling passages of a series of printed circuit boards (PCB) with heat-generating components. As power demands for these electronic components continue to rise, as they have for the past few decades, heat dissipation issues become increasingly important. Standard methods of cooling the channels formed by an array of PCBs include free and forced convection, as well as substrate conduction. Much of the research in this area has focused on either free convection, where buoyancy forces cause fluid motion, or forced convection, where an external mechanism drives the fluid. Mixed or combined convection refers to a flow regime where both free and forced convection effects are comparable. The focus of the present work is steady laminar mixed convection between a series of vertical parallel plates. A detailed review of the literature on this topic has been previously reported (Watson, 1995; Watson et al., 1995).

Most of the research in mixed convection has concentrated on single-channel geometries. However, many important applications exist where multiple plates are aligned in an array, creating a series of channels. In these geometries, the heat generated on the surface of the plates will not only be removed by convection but will also be conducted through the walls to the adjacent channels. Thus, it is important to capture both heat transfer mechanisms. The research conducted by Kim et al. (1991) modeled these effects, but was limited to the free convection regime. There has been no research conducted to date to model cases of mixed convection with conjugate wall conduction in a series of vertical channels. The intent of this research was numerically to model laminar steady-state buoyancy-aided mixed convection between a series of vertical parallel plates, including wall conduction. Each plate had a planar or sheet heat source on one surface, which manifested itself as a line source when the problem was reduced to two dimensions. Cases involving buoyancy-aided flow were considered.

Model Development

Figure 1(a) illustrates the geometry considered in this study. A series of plates, each of the same material and thickness, are aligned in parallel at a constant spacing, B. The plates are sufficiently long in the z direction so that the problem can be reduced to two dimensions. This series of plates in turn creates a series of channels through which a fluid can flow. A uniform, upward-flowing velocity profile is introduced by an external means at each channel inlet, as seen in Fig. 1(a). If the inlet velocity profile of each channel, as well as the heat input on each plate surface, is identical, then the resulting flow and thermal fields will also be identical. This is a repeated or cyclic condition, which conveniently allows the problem domain to be isolated in a single wall and channel, as seen in Fig. 1(b). This approach is limited to the interior channels, as the channels on either extreme of the series are exposed to different boundary conditions.

It is important to note that the computational domain presented in Fig. 1(b) includes a region that extends well beyond the top of the plates. The inclusion of this region is necessary for the following reasons. First, it enables the capture of heat transfer to the fluid out of the top of the plate. Second, if the governing parameters are such that flow recirculation in the channel might be present, then the extended region is critical to model this phenomenon accurately.

Also, the extended region allows for the study of how the wake behind each plate is affected by the heating parameter. In previous studies, which predominantly considered flow in a single vertical channel, the assumption was made that the flow field was parabolic at the channel exit and natural boundary conditions were imposed. Thus, the "end effects" mentioned above have not been studied by previous investigators.

Consideration is given to steady-state laminar buoyancy-aided mixed convection flow of air in a channel, as shown in
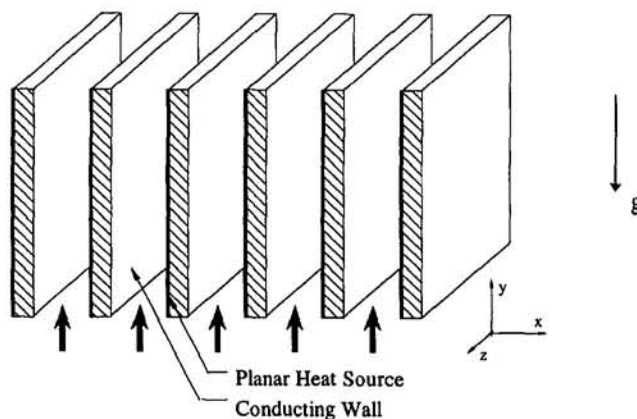

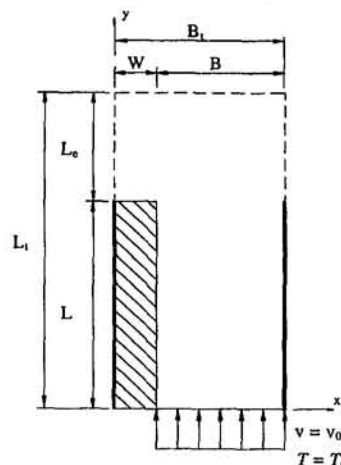Fig. 1(a) Geometric configuration

Fig. 1(b) Computational model

Fig. 1 Model

Fig. 1(b). Thermophysical properties of air and solid are assumed to remain constant. However, the Boussinesq approximation was invoked to confine the density variation of air to the axial momentum equation. Based on these simplifying assumptions, the governing equations can be:

Continuity:

$$\frac{\partial u}{\partial x} + \frac{\partial v}{\partial y} = 0 \tag{1}$$

Transverse Momentum:

$$\rho\left(u\frac{\partial u}{\partial x} + v\frac{\partial u}{\partial y}\right) = -\frac{\partial P}{\partial x} + \frac{\partial}{\partial x}\left(\mu\frac{\partial u}{\partial x}\right) + \frac{\partial}{\partial y}\left(\mu\frac{\partial u}{\partial y}\right) \tag{2}$$

Axial Momentum:

$$\rho\left(u\frac{\partial v}{\partial x} + v\frac{\partial v}{\partial y}\right) = -\frac{\partial P}{\partial y} + \frac{\partial}{\partial x}\left(\mu\frac{\partial v}{\partial x}\right)$$

$$+ \frac{\partial}{\partial y}\left(\mu\frac{\partial v}{\partial y}\right) + g\beta(T - T_0) \tag{3}$$

Energy:

$$\rho c_p\left(u\frac{\partial T}{\partial x} + v\frac{\partial T}{\partial y}\right) = \frac{\partial}{\partial x}\left(k\frac{\partial T}{\partial x}\right) + \frac{\partial}{\partial y}\left(k\frac{\partial T}{\partial y}\right) \tag{4}$$

Note that the energy equation, Eq. (4), is valid for a fluid

where heat can be transported by convection and diffusion or a solid where only diffusion is present. In the latter case the u and v velocities are zero, reducing Eq. (4) to the heat diffusion equation. Thus Eqs. (1)–(4) form a set of coupled, nonlinear partial differential equations with u, v, P, and T as unknowns. The nonlinear nature of these equations precludes the possibility of obtaining a closed-form solution and thus a numerical procedure is pursued.

Boundary Conditions. Figure 1(b) shows the computational domain. In solving for the velocity field, the solid plate is not included in the computational domain. At the solid–fluid interface, no-slip conditions are imposed for the velocities. In the extended domain region, the repeated condition $u(0, y) = u(B_t, y)$ and $v(0, y) = v(B_t, y)$ were imposed. The fluid was assumed to enter the channel with a uniform velocity V_o. At the outlet, the natural conditions were imposed. For the temperature field in the transverse direction, repeated conditions $T(0, y) = T(B_t, y)$ and "heat flux continuity" were imposed. The fluid entered the channel with a uniform temperature T_0. The bottom surface of the plate was in thermodynamic equilibrium with the fluid. Accordingly, the temperature along the bottom surface of the plate was fixed at T_0. An alternative boundary condition is to treat the bottom surface of the plate as adiabatic. A constant-temperature condition along the bottom surface will act as a heat sink and will significantly impact the temperature field in the solid and fluid regions. Appropriate thermal conductivities were used in the solid and fluid. At the solid–fluid interface, the thermal conductivity is represented as the weighted harmonic mean of the solid and fluid conductivities. At the outlet boundary the natural condition was used. The energy equation requires one additional boundary condition. This condition is obtained by applying heat flux continuity at the hot surface as follows:

$$q'' = -k_w \left.\frac{\partial T}{\partial y}\right|_{(0^+, y)} + k_f \left.\frac{\partial T}{\partial y}\right|_{(0^-, y)} \qquad (5)$$

Equation (5) states that the heat supplied by the planar source is diffused away at the interface by conduction through the wall and the fluid. The reason that the heat transfer mechanism for the fluid is only diffusion is that, at the wall, the fluid's velocity is zero due to the no-slip condition.

Solution Technique. The set of governing equations with associated boundary conditions was solved by using a finite volume technique. Velocity and pressure fields were stored at staggered locations. The convection and diffusion terms were linked by the Power Law. The pressure and velocity equations were linked by the SIMPLER algorithm (Patankar, 1980). A set of discretization equations was solved by the line-by-line procedure, which is a combination of the tridiagonal matrix algorithm (TDMA) and the Gauss–Seidel technique. However, due to the repeated conditions in the transverse direction, the cyclic tridiagonal matrix algorithm (CTDMA) was used to sweep in the streamwise direction. Strong underrelaxation factors (0.3–0.4) were required to ensure convergence, especially for cases with higher heat fluxes. Convergence for the velocity field was declared when the total mass residue was less than 1×10^{-6}. The temperature field converged when the temperature difference between iterations for all nodes was less than 1×10^{-5} for thermal conductivity ratios (K) of 0.1 to 10. For cases involving $K = 100$, a convergence criterion of 1×10^{-6} ensured an overall energy balance within 0.25 percent. This is the reason for using different convergence criteria for $K = 0.1 - 10$ and $K = 100$. Details can be found elsewhere (Watson, 1995).

Validation and Grid Independence

When conducting a numerical study, it is desirable to compare computational results with experimental data as a means
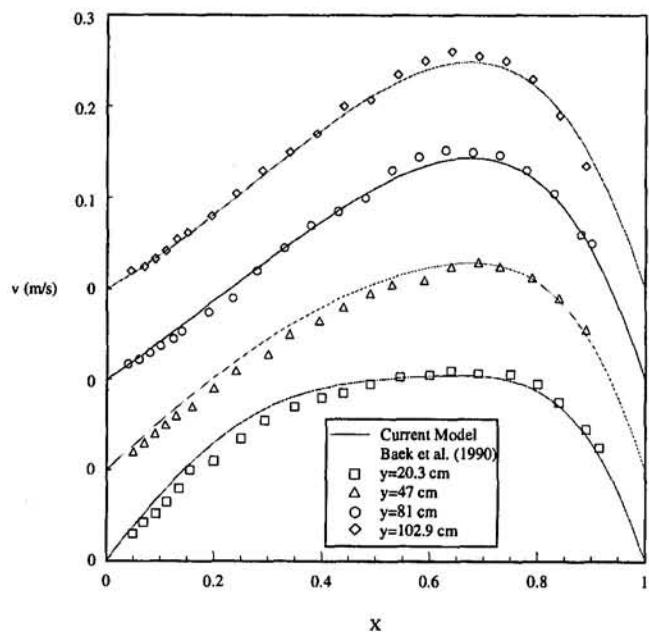

Fig. 2(a) Comparison of experimental and numerical velocity distributions
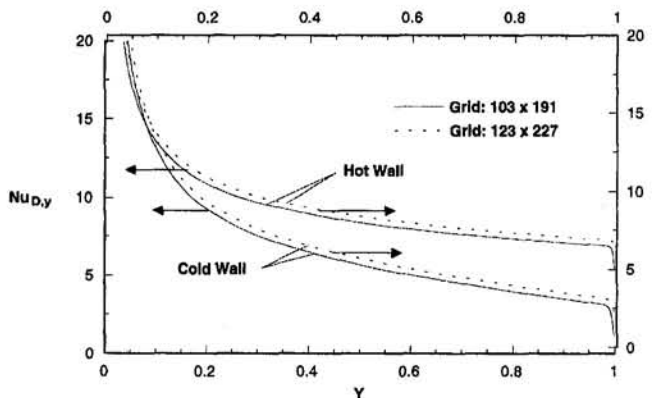

Fig. 2(b) Local Nusselt number distribution on hot and cold walls

Fig. 2 Validation

of validating the accuracy of the code. Baek et al. (1990) conducted experimental tests for mixed convection in a single vertical channel with uniform but asymmetric wall temperatures. Figure 2(a) shows velocity profiles at four streamwise locations for Re = 305 and Gr* = 22,500. The experimental results show that the flow is progressively accelerated near the hot wall and the numerical results from this study are in good agreement with the experimental data. Another means of validation was to examine the limiting case of fully developed forced convection (Gr/Re = 0) between parallel plates, since theoretical solutions are available. The cases of symmetric UHF heating and asymmetric UHF heating, where one wall was at UHF and the other was adiabatic, were considered. For both cases the numerical results for the fully developed Nu_D converged to the theoretical solutions, which are 8.235 for the symmetric UHF case and 5.385 for the asymmetric UHF case (Kays and Crawford, 1993). One further validation effort was to compare the numerical results from the mixed convection work of Aung and Worku (1987) with numerical results from this study. Such a comparison showed an excellent agreement (Watson, 1995).

Another important consideration in a numerical study is ensuring that the results obtained are independent of the computational grid. In this investigation a grid independence study was conducted to establish the proper grid size. Results are presented

for the case of Gr/Re = 1500, $K = 0.1$, and $W/B = 0.2$, since this had the largest velocity and temperature gradients and thus was the most stringent test of grid independence. The number of grid points in the computational domain was increased from a coarse grid of 11×22 until the results for the local Nusselt number and friction factor remained unchanged. Figure 2(b) shows local Nusselt number distributions along the hot and cold surfaces for grid sizes of 103×191 and 123×227. The two sets of results are virtually identical, but to differentiate the results the right axis scale is shifted slightly upward; thus the grid employed in this study was 103×191.

Results and Discussion

In this section the governing independent parameters are identified and representative velocity and temperature profiles are presented. The maximum interface temperature and heat flux distributions are discussed. A more detailed discussion of results can be found in Watson (1995) and Watson et al. (1995).

Independent Parameters. After defining the model equations and boundary conditions, it is necessary to identify the independent parameters that need to be varied to conduct a complete study of the specified problem. These parameters are the ratio of Grashof number to Reynolds number (Gr/Re), the ratio of plate thermal conductivity to fluid thermal conductivity (K), the ratio of plate thickness to channel width (W/B), the channel length to channel width ratio (L/B), and the fluid Prandtl number (Pr). For this study, two of the independent parameters, Pr and L/B, remained constant. The Prandtl number was chosen to be approximately that of air at moderate temperatures (Pr = 0.71). To begin with, the L/B ratio was fixed at 16, which provided a channel long enough to extend beyond the initial inertially dominated inlet region of the flow. However, the L/B ratio was varied from 4 to 16 to examine its effect on fluid friction factor and average Nusselt number. A parametric study was conducted by varying the other three independent parameters. The buoyancy parameter, Gr/Re, ranged from 0 to 1500. Note that the present analysis is valid for steady two-dimensional laminar flows. Gau et al. (1991) noticed unsteady turbulent flow downstream of a recirculation pocket in a buoyancy-assisted flow in a single channel for Gr/Re = 8250. The Gr/Re values considered in this study are well below 8250 and no recirculation pockets were noticed for the entire parametric range considered. Therefore, the assumption of two-dimensional steady laminar flow for the range of parameters considered in this study seems valid. A range of thermal conductivity ratios was chosen that was representative of common substrates used in electronics packaging. While substrates composed of a combination of epoxy-glass, copper, and ceramic laminates have a value of K on the order of 0.1, the effective conductivities can actually reach much higher values due to the varying amounts of materials such as copper alloys, silicon, and beryllia (Kim, 1993; Sathe and Joshi, 1990; Incropera, 1988). Thus, calculations were made for K of 0.1, 1, 10, and 100. Generally, the wall thickness for cooling passages is substantially less than the width of the channels, so W/B was chosen to be 0.1 and 0.2.

Velocity Profiles. At the channel inlet the velocity profile is constant ($V = 1$) across the width of the channel. In the case of pure forced convection (Gr/Re = 0), the velocity profile symmetrically develops to a parabolic profile, with a centerline value of $V = 1.5$, at a sufficiently large distance downstream. However, in the case of mixed convection, the development of the velocity profile is dependent on the heating conditions, with the hotter regions of the fluid tending to have larger upward velocities than the cooler portions.

Figure 3(a) shows transverse velocity profiles at 20 and 80 percent of the channel length. At the upstream position ($Y = $

0.2), the deviation between the profiles starts to become apparent. For $K = 0.1$ the plate is relatively nonconductive as compared to the fluid, which leads to a substantial temperature difference between the hot and cold surfaces. The effect of this asymmetric heating in turn affects the velocity profiles. As the Gr/Re increases, the profiles skew to the hotter wall where the fluid is flowing at a higher velocity. This effect is more pronounced at the downstream position ($Y = 0.8$). Note that higher values of Gr/Re lead to peak velocities greater than $V = 1.5$, with this peak in the profile occurring progressively closer to the hot wall. The reason for this increased "skewness" in the velocity profile is due to the manner in which the temperature distribution on each wall develops. Since the heating condition is that of a uniform heat flux, the wall temperature starts at a low value toward the inlet and increases in the downstream direction. This is due to the boundary layer being thin near the inlet and growing as the flow progresses downstream. A thin boundary layer implies that the velocity gradient at the wall is large, allowing a substantial amount of heat to be convected away and in turn keeping the wall temperature low. As the boundary layer thickens, the wall temperature must increase to maintain the same level of heat flux. This increase in fluid temperature near the hot wall drives the flow velocity higher and in turn increases the skewness of the profile. The skewness in the profile occurs since the channel flow rate is constant, and an increase in velocity in one part of the velocity profile will have an accompanying decrease in velocity somewhere else, namely near the cold wall. As K is increased, the asymmetry in the wall temperatures is lessened as the heat is conducted through the plate. The effect of increasing wall thickness ratio (W/B) is to increase the thermal resistance of the plate. The influence of wall conduction effects (K and W/B) on transverse velocity and axial temperature distributions is discussed in detail elsewhere (Watson, 1995; Watson et al., 1995).

Temperature Profiles. Although the governing equations were presented using primitive variables, including T, the following results are presented in terms of a nondimensional temperature, θ, which is defined as

$$\theta = \frac{(T - T_0)k_f}{q''B} \tag{6}$$

The temperature at the channel inlet for the hot and cold surfaces is $\theta = 0$, which is also the boundary condition for the bottom surface of the plate. This Dirichlet boundary condition becomes important, acting as a sink, as the plate conductivity and thickness increase. In general, the axial temperature distributions for the hot wall, θ_h, and the cold wall, θ_c, start at zero and increase in the downstream direction as the boundary layer thickens. Note that T_h could increase while θ_h is decreasing because temperature is nondimensionalized with respect to the heat flux that appears in Gr. However, once θ_h is known, one can very easily calculate T_h by using Eq. (6).

Figure 3(b) shows the effect of the buoyancy parameter, Gr/Re, on the axial temperature distribution. It can be seen that the effect of Gr/Re on the hot surface temperature is to decrease θ_h as Gr/Re increases. This is because the flow skews increasingly toward the hot wall at higher heating values, as previously observed in Fig. 3(a). Since the velocity gradient at the hot wall increases with Gr/Re, more heat is convected away by the fluid, which results in decreasing θ_h values.

Interestingly, higher values of Gr/Re also decrease the cold surface θ distribution, though to a lesser degree. However, this is due to the plate conduction, not to a change in the convective forces at the cold wall. Indeed, Fig. 3(a) shows that the velocity gradient at the cold wall is essentially unchanged for $K = 0.1$, even though the flow skews toward the hot wall at higher Gr/Re values. Thus the amount of heat that can be convected away from the cold wall remains essentially constant. The decrease
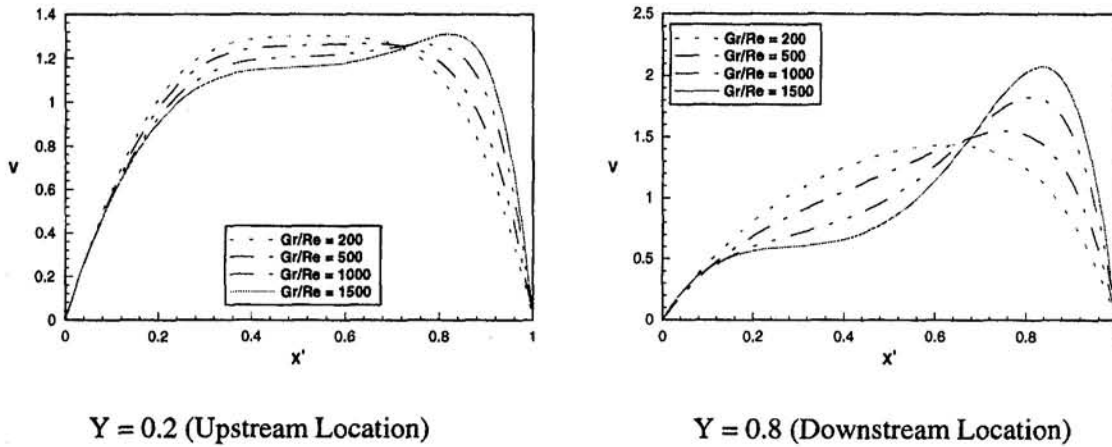
Y = 0.2 (Upstream Location)   Y = 0.8 (Downstream Location)

Fig. 3(a) Velocity profile

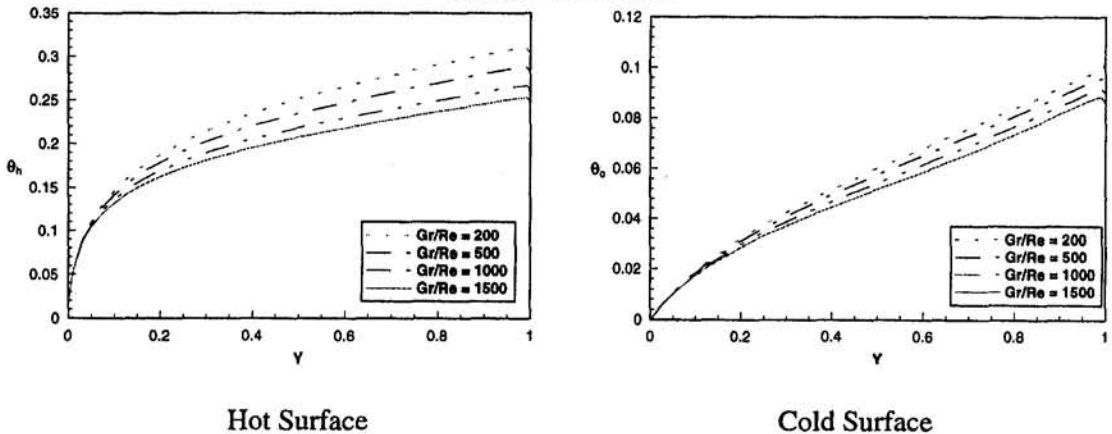Hot Surface   Cold Surface

Fig. 3(b) Temperature profile

Fig. 3 Effect of Gr/Re on velocity and temperature distribution (W/B = 0.1; K = 0.1)

in θ_c, at higher Gr/Re values is a result of the decrease in θ_h. Since more heat is convected away by the faster moving fluid near the hot wall, less heat is conducted to the cold wall, leading to lower values for both θ_h and θ_c.

Note that the end of the plate has an effect on the local temperature distributions. For nearly all combinations of the independent parameters, θ_h and θ_c decrease near the end of the plate. For low values of K ($K = 0.1$), the decrease is rather abrupt and close to the end of the plate. This is because the low conductivity suppresses axial conduction within the plate, so the effect of the exposed plate top is only felt at the very end of the plate. For high values of K ($K = 100$), the decrease in the θ distribution is more gradual as the end effects are sensed further upstream, especially for $W/B = 0.2$ (Watson et al., 1995). The combination of high conductivity and a thicker wall promote axial conduction, which flattens out the temperature distribution near the end of the plate. The exception to these trends occurs in the θ_c distribution for $K = 0.1$ and Gr/Re = 200. For this combination of parameters a small recirculation zone occurs at the top of the plate near the cold wall (Fig. 5(a)) in which heat transfer is into the plate, causing a slight increase for θ_c at the end of the plate.

An important design parameter for the electronics industry is the maximum temperature attained by a heat-generating component. It is the maximum temperature, as well as thermal cycling, that aid in determining the useful life of an electronic component. Thus, this section presents the maximum interface temperatures on the hot plate surface.

The effect of the different independent parameters on temperature can be summarized by examining Fig. 4, which shows

the maximum hot surface temperature. The effect of increasing the buoyancy parameter is to decrease $\theta_{h,\max}$, with this effect being more pronounced at lower values of K and Gr/Re. This is due to the flow skewing toward the hotter surface at higher Gr/Re values, which allows more heat to be convected from the hot surface and in turn decreases $\theta_{h,\max}$. The effect of increasing K is to decrease $\theta_{h,\max}$ monotonically, which is due to the increasing amount of heat that can be conducted away from the hot surface at higher values of K. The effect of W/B on $\theta_{h,\max}$ is dependent on K. For $K < 10$, the effect of increasing the wall thickness is to increase $\theta_{h,\max}$ because of the increased
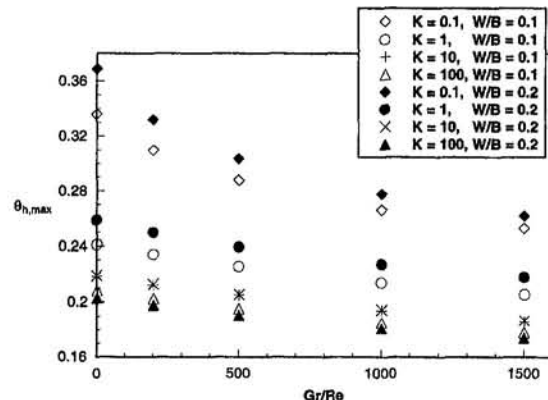

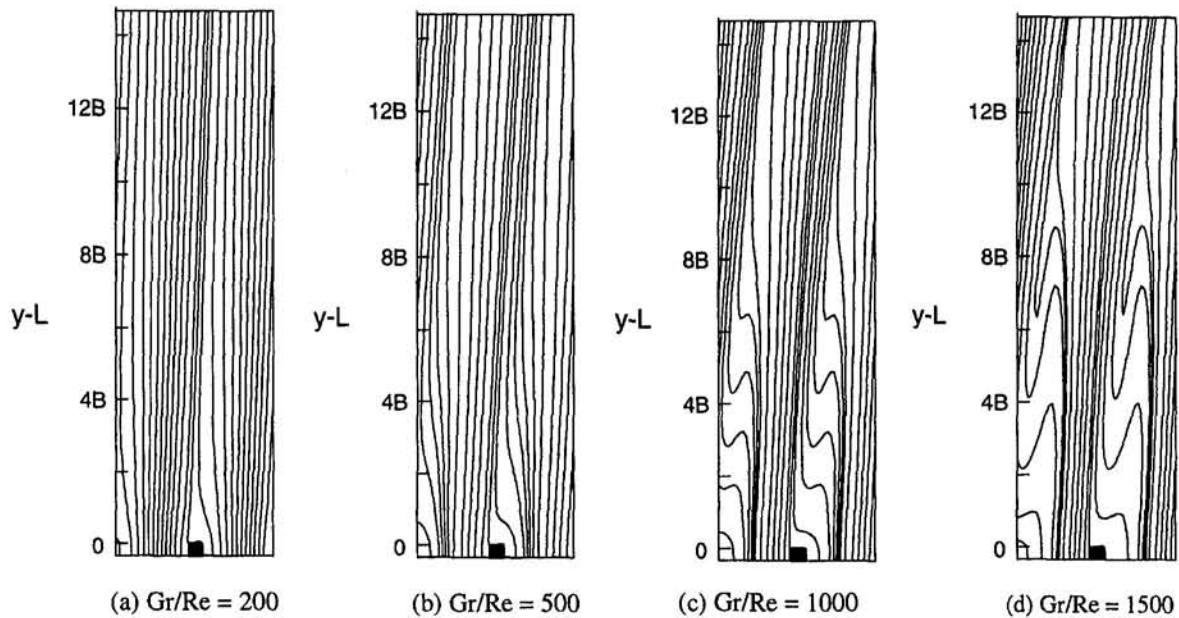Fig. 4 Maximum hot surface temperature

Fig. 5 Flow structure in extended region (W/B = 0.2; K = 0.1)

thermal resistance of the wall, which results in less heat being conducted through the wall. This effect is diminished as Gr/Re increases because of the increase in convection on the hot surface at higher values of Gr/Re. For $K > 10$, the effect of increasing W/B is actually to decrease $\theta_{h,\max}$ because of the increased axial conduction and heat loss to the lower wall.

The maximum interface temperature on a hot surface is of interest to design engineers in the field of electronic packaging. Therefore, a correlation based on least-squares method was developed as:

$$\theta_{h,\max} = 2.91 \left(1 - \frac{\mathrm{Gr}}{5000\,\mathrm{Re}}\right)^{0.5356} K^{-0.06198} \left(\frac{w}{B}\right)^{0.0525} \quad (7)$$

The coefficient of determination (COD) for this correlation was 0.898. After examining several different correlations, the correlation given above was chosen to maximize the value of COD. This correlation is only valid for the range of parameters considered in this study and Re $\neq$ 0.

Flow Structure Downstream of Plates. Figure 5 displays the entire extended domain, which was set at 15 channel widths long (15B) for this study. It was necessary to have the domain extended far enough downstream of the plate that flow could be considered locally parabolic and the outflow boundary conditions could be applied. Of particular importance was the need to ensure that the domain exit was placed downstream of any regions in which flow reversals would occur. However, the appropriate extension length was not known a priori. It is apparent from Fig. 5 that this distance is dependent on the buoyancy parameter and plate conductivity. Figure 5(a) shows that for a low value of Gr/Re (Gr/Re = 200), the streamlines are relatively straight and parallel after a short distance from the plate tip. However, as the buoyancy parameter increases, a wake region forms that includes substantial amounts of flow reversal. Figure 5 shows the extended region for progressively higher values of Gr/Re, ranging from 200 to 1500. Figure 5(d) shows that for Gr/Re = 1500, the wake region extends approximately 10 to 12 channel widths from the exit. This implies that placement of the domain exit at a location appropriate for cases involving low values of Gr/Re might become unsuitable as Gr/Re is increased. This effect is diminished as K is increased since the asymmetry in the wall temperatures is reduced, which

in turn reduces the asymmetry of the velocity profile. It should be noted that no flow reversals within the channel region were observed for the range of parameters used in this study.

Summary

A numerical study was performed for laminar mixed convection between a series of vertically aligned parallel plates with planar heat sources. Conjugate conduction effects were included that thermally coupled the adjacent channels. An extended region above the plates was included in the computational domain to capture any elliptic effects that might be present. The velocity profiles within the channel are skewed substantially to the hot wall as Gr/Re increases and K decreases. The effect of increasing Gr/Re on the interface temperature distribution is to decrease θ_h and θ_c, though the latter is affected to a much smaller degree. The effect of the exposed top of the plate is to reduce the temperature of the channel walls near the exit of the channel, with this effect being felt further upstream as the wall conductivity increases. For high values of Gr/Re (Gr/Re = 1500) and low values of K ($K = 0.1$), an extended wake develops behind the plate that includes flow reversals that are present as far as 10 to 12 channel widths from the exit.

References

Aung, W., and Worku, G., 1987, "Mixed Convection in Ducts With Asymmetric Wall Heat Fluxes," ASME JOURNAL OF HEAT TRANSFER, Vol. 109, pp. 947–951.

Baek, B. J., Palaski, D. A., and Armaly, B. F., Chen, T. S., 1990, "Mixed Convection in an Asymmetrically Heated Vertical Parallel-Plate Duct Flow," *Proc. Ninth International Heat Transfer Conference*, Jerusalem, Israel, Vol. 2, pp. 369–374.

Gau, C., Yih, K. A., and Aung, W., 1991, "Observed Flow Reversals and Heat Transfer Measurements for Buoyancy-Assisted Convection in a Heated Vertical Channel," AIAA Paper No. 91-1309.

Incropera, F. P., 1988, "Convection Heat Transfer in Electronic Equipment Cooling," ASME JOURNAL OF HEAT TRANSFER, Vol. 110, pp. 1097–1110.

Kays, W. M., and Crawford, M. E., 1993, *Convective Heat and Mass Transfer*, McGraw-Hill, New York.

Kim, S. H., Anand, N. K., and Fletcher, L. S., 1991, "Free Convection Between Series of Vertical Parallel Plates With Embedded Line Heat Sources," ASME JOURNAL OF HEAT TRANSFER, Vol. 113, pp. 108–115.

Kim, S. H., 1993, "A Numerical Analysis of Convective Heat Transfer in Channels Simulating Electronic Components," Ph.D. Dissertation, Texas A&M University, College Station, TX.

Patankar, S. V., 1980, *Numerical Heat Transfer and Fluid Flow*, Hemisphere, New York.

Sathe, S., and Joshi, Y., 1990, "Natural Convection Liquid Cooling of a Substrate-Mounted Protrusion in a Square Enclosure: Effect of Thermophysical Properties, Geometric Dimensions and Boundary Conditions," Thermal Modeling and Design of Electronic Systems and Devices, ASME HTD-Vol. 153, pp. 73–80.

Watson, J. C., 1995, "Numerical Model of Mixed Convective Heat Transfer Between a Series of Vertical Parallel Plates With Planar Heat Sources," M. S. Thesis, Texas A&M University.

Watson, J. C., Anand, N. K., and Fletcher, L. S., "Mixed Convection Heat Transfer Between a Series of Vertical Parallel Plates With Planar Heat Sources," ASME HTD-Vol. 317-1, pp. 401–412, 1995.

Re-examination of Natural Convection in a Horizontal Layered Porous Annulus

C. P. Pan[1] and F. C. Lai[2]

Nomenclature

D = gap width = $r_2 - r_1$, m
K = permeability, m^2
k = effective thermal conductivity of porous medium, W/m·K
Nu = average Nusselt number = hD/k
p = pressure, Pa
q = constant heat flux, W/m^2
R = dimensionless radial distance = r/D
r = radial distance, m
Ra$_i$ = sublayer Rayleigh number = $K_i g\beta qD^2/k_1\alpha_1\nu$, $i = 1, 2$
Ra$_1$ = Rayleigh number based on the inner layer properties = $K_1 g\beta qD^2/k\alpha_1\nu$
T = temperature, K
T_{1m} = average surface temperature of the inner cylinder, K
U_i = dimensionless velocity in the r direction = $(1/R)(\partial\psi_i/\partial\theta)$
u_i = Darcy velocity in the r direction = $\alpha_1 U_i/D$, m/s
V_i = dimensionless velocity in the θ direction = $-\partial\psi_i/\partial R$
v_i = Darcy velocity in the θ direction = $\alpha_1 V_i/D$, m/s
α = thermal diffusivity of porous medium = $k/(\rho c_p)_f$, m^2/s
β = thermal expansion coefficient = $(-1/\rho)(\partial\rho/\partial T)_p$, K^{-1}
$\odot$ = dimensionless temperature = $(T - T_o)/(qD/k_1)$
θ = angular coordinate
ν = kinematic viscosity, m^2/s
ψ = dimensionless stream function

Introduction

Numerical and experimental results are available for a uniform porous annulus in vertical and horizontal positions (Cal-

[1] Graduate student, School of Aerospace and Mechanical Engineering, University of Oklahoma, Norman, OK 73019.

[2] Assistant Professor, School of Aerospace and Mechanical Engineering, University of Oklahoma, Norman, OK 73019; Mem. ASME; email: lai@leo.ecn.uoknor.edu.

tagirone, 1976; Burns and Tien, 1979; Prasad and Kulacki, 1984). On the other hand, a layered porous annulus, although encountered frequently in engineering applications, has received very little attention. The results were reported only by Muralidhar et al. (1986). However, their results show little dependence on the permeability contrast that characterizes the system. In addition, the agreement between their numerical prediction and experimental data was inconsistent. The purpose of this study is to re-examine the problem and to resolve the discrepancy found in the previous study. To this end, a detailed numerical analysis is performed over a wide range of parameters (i.e., $10 \le \text{Ra} \le 10^4$, $10^{-2} \le K_1/K_2 \le 10^2$, and $0.5 \le k_1/k_2 \le 2$). Particular attention is focused on the interfacial conditions. It is believed that the reported discrepancy may be due to the improper implementation of interfacial conditions.

Analysis

The geometry considered is a horizontal porous annulus comprising two sublayers (Fig. 1). Each sublayer is assumed to be fully saturated and has a different permeability and thermal conductivity. The inner cylinder is heated by a constant heat flux, q, while the outer cylinder is maintained at a uniform temperature T_o. The dimensionless governing equations based on the Darcy's law and Boussinesq approximation are given by (Lai, 1993)

$$\frac{\partial V_i}{\partial R} + \frac{V_i}{R} - \frac{1}{R}\frac{\partial U_i}{\partial\theta} = \text{Ra}_i\left(\cos\theta\frac{\partial\odot_i}{\partial R} - \frac{\sin\theta}{R}\frac{\partial\odot_i}{\partial\theta}\right), \quad (1)$$

$$U_i\frac{\partial\odot_i}{\partial R} + \frac{V_i}{R}\frac{\partial\odot_i}{\partial\theta} = \frac{\alpha_i}{\alpha_1}\left[\frac{1}{R}\frac{\partial}{\partial R}\left(R\frac{\partial\odot_i}{\partial R}\right) + \frac{1}{R^2}\frac{\partial^2\odot_i}{\partial\theta^2}\right], \quad (2)$$

To solve the simultaneous equations defined above, a coordinate transformation (Eq. (3)) has been used to facilitate calculations. Although other methods are available, this approach is favored because it has been successfully used in other problems dealing with a similar geometry (Lai, 1993; Pan and Lai, 1995).

$$x = \frac{\ln R - \ln R_1}{\ln R_2 - \ln R_1} - \frac{1}{2}, \quad y = \frac{\theta}{2\pi} - \frac{1}{2}. \quad (3)$$

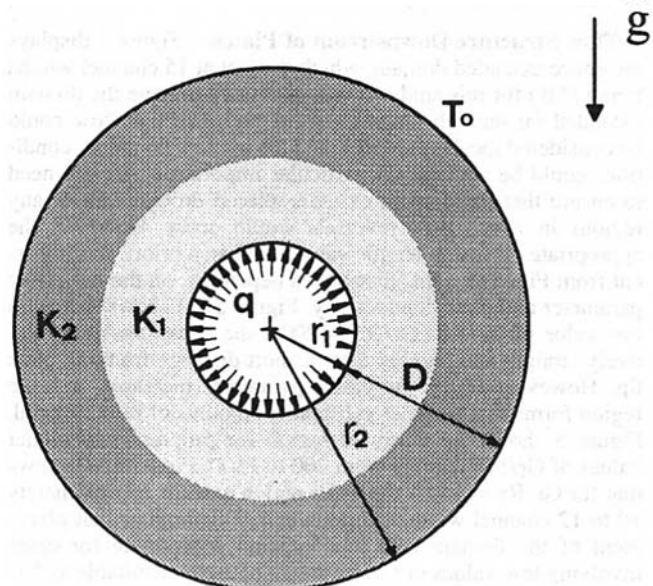Thus, the governing equations in terms of stream function are transformed to

Fig. 1 A horizontal layered porous annulus

Kays, W. M., and Crawford, M. E., 1993, *Convective Heat and Mass Transfer,* McGraw-Hill, New York.

Kim, S. H., Anand, N. K., and Fletcher, L. S., 1991, "Free Convection Between Series of Vertical Parallel Plates With Embedded Line Heat Sources," ASME JOURNAL OF HEAT TRANSFER, Vol. 113, pp. 108–115.

Kim, S. H., 1993, "A Numerical Analysis of Convective Heat Transfer in Channels Simulating Electronic Components," Ph.D. Dissertation, Texas A&M University, College Station, TX.

Patankar, S. V., 1980, *Numerical Heat Transfer and Fluid Flow,* Hemisphere, New York.

Sathe, S., and Joshi, Y., 1990, "Natural Convection Liquid Cooling of a Substrate-Mounted Protrusion in a Square Enclosure: Effect of Thermophysical Properties, Geometric Dimensions and Boundary Conditions," Thermal Modeling and Design of Electronic Systems and Devices, ASME HTD-Vol. 153, pp. 73–80.

Watson, J. C., 1995, "Numerical Model of Mixed Convective Heat Transfer Between a Series of Vertical Parallel Plates With Planar Heat Sources," M. S. Thesis, Texas A&M University.

Watson, J. C., Anand, N. K., and Fletcher, L. S., "Mixed Convection Heat Transfer Between a Series of Vertical Parallel Plates With Planar Heat Sources," ASME HTD-Vol. 317-1, pp. 401–412, 1995.

Re-examination of Natural Convection in a Horizontal Layered Porous Annulus

C. P. Pan[1] and F. C. Lai[2]

Nomenclature

D = gap width = $r_2 - r_1$, m
K = permeability, m^2
k = effective thermal conductivity of porous medium, W/m·K
Nu = average Nusselt number = hD/k
p = pressure, Pa
q = constant heat flux, W/m^2
R = dimensionless radial distance = r/D
r = radial distance, m
Ra_i = sublayer Rayleigh number = $K_i g\beta qD^2/k_1\alpha_1\nu$, $i = 1, 2$
Ra_1 = Rayleigh number based on the inner layer properties = $K_1 g\beta qD^2/k\alpha_1\nu$
T = temperature, K
T_{1m} = average surface temperature of the inner cylinder, K
U_i = dimensionless velocity in the r direction = $(1/R)(\partial\psi_i/\partial\theta)$
u_i = Darcy velocity in the r direction = $\alpha_1 U_i/D$, m/s
V_i = dimensionless velocity in the θ direction = $-\partial\psi_i/\partial R$
v_i = Darcy velocity in the θ direction = $\alpha_1 V_i/D$, m/s
α = thermal diffusivity of porous medium = $k/(\rho c_p)_f$, m^2/s
β = thermal expansion coefficient = $(-1/\rho)(\partial\rho/\partial T)_p$, K^{-1}
$\odot$ = dimensionless temperature = $(T - T_o)/(qD/k_1)$
θ = angular coordinate
ν = kinematic viscosity, m^2/s
ψ = dimensionless stream function

Introduction

Numerical and experimental results are available for a uniform porous annulus in vertical and horizontal positions (Cal-

[1] Graduate student, School of Aerospace and Mechanical Engineering, University of Oklahoma, Norman, OK 73019.

[2] Assistant Professor, School of Aerospace and Mechanical Engineering, University of Oklahoma, Norman, OK 73019; Mem. ASME; email: lai@leo.ecn.uoknor.edu.

tagirone, 1976; Burns and Tien, 1979; Prasad and Kulacki, 1984). On the other hand, a layered porous annulus, although encountered frequently in engineering applications, has received very little attention. The results were reported only by Muralidhar et al. (1986). However, their results show little dependence on the permeability contrast that characterizes the system. In addition, the agreement between their numerical prediction and experimental data was inconsistent. The purpose of this study is to re-examine the problem and to resolve the discrepancy found in the previous study. To this end, a detailed numerical analysis is performed over a wide range of parameters (i.e., $10 \leq Ra \leq 10^4$, $10^{-2} \leq K_1/K_2 \leq 10^2$, and $0.5 \leq k_1/k_2 \leq 2$). Particular attention is focused on the interfacial conditions. It is believed that the reported discrepancy may be due to the improper implementation of interfacial conditions.

Analysis

The geometry considered is a horizontal porous annulus comprising two sublayers (Fig. 1). Each sublayer is assumed to be fully saturated and has a different permeability and thermal conductivity. The inner cylinder is heated by a constant heat flux, q, while the outer cylinder is maintained at a uniform temperature T_o. The dimensionless governing equations based on the Darcy's law and Boussinesq approximation are given by (Lai, 1993)

$$\frac{\partial V_i}{\partial R} + \frac{V_i}{R} - \frac{1}{R}\frac{\partial U_i}{\partial\theta} = Ra_i\left(\cos\theta\frac{\partial\odot_i}{\partial R} - \frac{\sin\theta}{R}\frac{\partial\odot_i}{\partial\theta}\right), \quad (1)$$

$$U_i\frac{\partial\odot_i}{\partial R} + \frac{V_i}{R}\frac{\partial\odot_i}{\partial\theta} = \frac{\alpha_i}{\alpha_1}\left[\frac{1}{R}\frac{\partial}{\partial R}\left(R\frac{\partial\odot_i}{\partial R}\right) + \frac{1}{R^2}\frac{\partial^2\odot_i}{\partial\theta^2}\right], \quad (2)$$

To solve the simultaneous equations defined above, a coordinate transformation (Eq. (3)) has been used to facilitate calculations. Although other methods are available, this approach is favored because it has been successfully used in other problems dealing with a similar geometry (Lai, 1993; Pan and Lai, 1995).

$$x = \frac{\ln R - \ln R_1}{\ln R_2 - \ln R_1} - \frac{1}{2}, \quad y = \frac{\theta}{2\pi} - \frac{1}{2}. \quad (3)$$

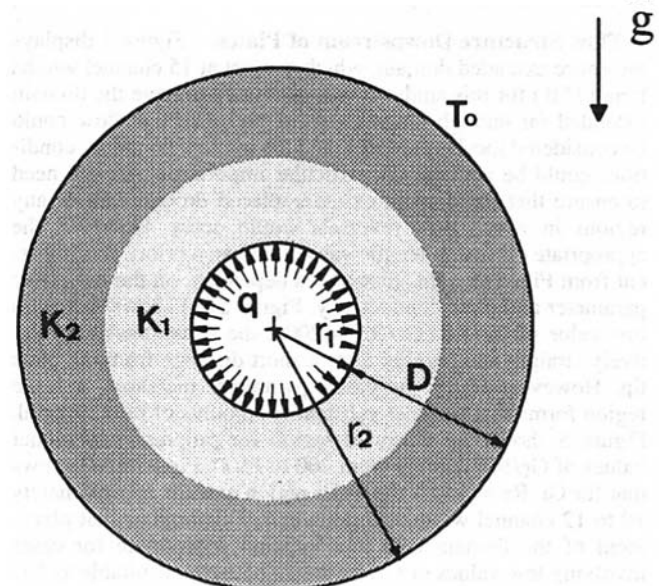Thus, the governing equations in terms of stream function are transformed to

Fig. 1 A horizontal layered porous annulus

$$x_0^2 \frac{\partial^2 \psi_i}{\partial x^2} + y_0^2 \frac{\partial^2 \psi_i}{\partial y^2} = -\mathrm{Ra}_i (R_1 R_2)^{1/2} \left(\frac{R_2}{R_1} \right)^x$$

$$\times \left[x_0 \frac{\partial \odot_i}{\partial x} \cos \left(\frac{y}{y_0} + \theta_m \right) - y_0 \frac{\partial \odot_i}{\partial y} \sin \left(\frac{y}{y_0} + \theta_m \right) \right], \quad (4)$$

$$x_0 y_0 \left(\frac{\partial \psi_i}{\partial y} \frac{\partial \odot_i}{\partial x} - \frac{\partial \psi_i}{\partial x} \frac{\partial \odot_i}{\partial y} \right) = \frac{\alpha_i}{\alpha_1} \left[x_0^2 \frac{\partial^2 \odot_i}{\partial x^2} + y_0^2 \frac{\partial^2 \odot_i}{\partial y^2} \right],$$

$$(5)$$

where $x_0 = 1/\ln (R_2/R_1)$, $y_0 = \frac{1}{2}\pi$, and $\theta_m = \pi$.

The boundary conditions are given by

$$\frac{\partial \odot_1}{\partial x} = -\frac{(R_2/R_1)^x}{x_0} (R_1 R_2)^{1/2},$$

$$\psi_1 = 0, \quad \text{on the inner wall} \qquad (6a)$$

$$\odot_2 = 0, \quad \psi_2 = 0, \quad \text{on the outer wall} \qquad (6b)$$

whereas the interface conditions are expressed as

$$\frac{\partial \psi_1}{\partial x} = \frac{K_1}{K_2} \frac{\partial \psi_2}{\partial x}, \qquad (7a)$$

$$\odot_1 = \odot_2, \qquad (7b)$$

$$\psi_1 = \psi_2, \qquad (7c)$$

$$\frac{\partial \odot_1}{\partial x} = \frac{\alpha_2}{\alpha_1} \frac{\partial \odot_2}{\partial x}, \qquad (7d)$$

which are found from the continuity requirements for pressure, temperature, radial mass flow, and radial heat flux. The justification of these boundary conditions is given by Rana et al. (1979) as well as McKibbin and O'Sullivan (1981). Since both sublayers are saturated with the same fluid, it is important to note that $\alpha_1/\alpha_2 = k_1/k_2$.

The transformed governing equations and boundary conditions are solved using a finite difference method which has been successfully employed by the authors (Lai, 1993; Pan and Lai, 1995). The conditions at the interface are implemented using imaginary nodal points as suggested by Rana et al. (1979). In the previous study (Muralidhar et al., 1986), the interface conditions (Eqs. $7(a)$–$7(d)$) were not specifically implemented; they were accounted for only in the "average" sense since an average property value was used at the interface nodes. Uniform grids, 51×121, in the transformed domain are used for the present study. It should be noted that further grid refinement does not produce any significant improvement in the calculated Nusselt numbers. As an additional check on the accuracy of the computational results, an overall energy balance has been performed after each calculation. For the present study, the energy balance for most calculations is satisfied within 1 percent (only a few cases are 3 percent). To validate the numerical code, the solutions thus obtained have been compared with those reported in the literature for the case of a homogeneous annulus by setting K_1/K_2 and k_1/k_2 ($= \alpha_1/\alpha_2$) to unity. The agreement is very good as reported in an earlier work by the authors (Pan and Lai, 1995).

To examine the general trend of heat transfer across a layered porous annulus, the geometry is fixed in the beginning of the study and has a dimension of $R_1 = r_1/D = \frac{1}{2}$ and $R_2 = r_2/D = \frac{3}{2}$. In addition, the layer interface has been fixed at $r = (r_1 + r_2)/2$.

Results and Discussion

When heated at a moderate Rayleigh number, natural convection in a homogeneous porous annulus is established in the form
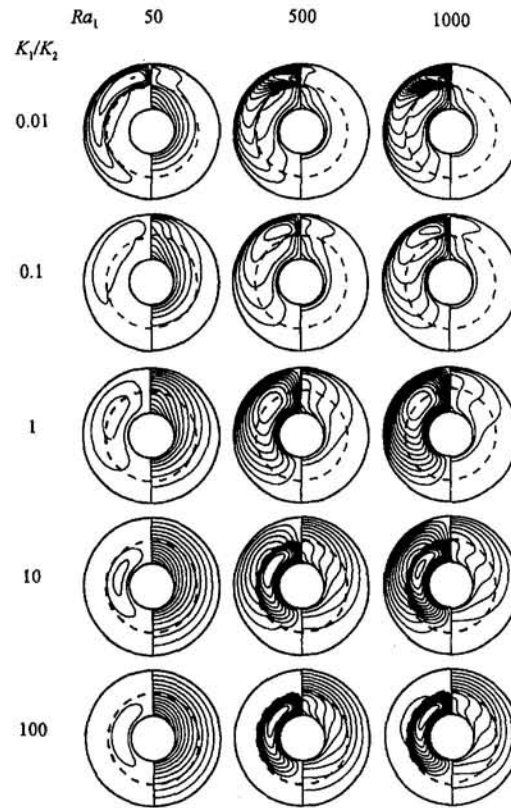

Fig. 2 Effects of permeability contrast on the flow and temperature fields of a layered barrier system ($k_1/k_2 = 1$, $\triangle \odot = 0.05$, $\triangle \psi = 3$ for $K_1/K_2 = 0.01$ and 0.1, $\triangle \psi = 1$ for $K_1/K_2 = 1$, $\triangle \psi = 0.5$ for $K_1/K_2 = 10$ and 100)

of two primary cells. Heated fluid rises to the top along the inner cylinder and, when cooled, returns to the bottom along the outer cylinder. For a layered porous annulus, the flow and temperature profiles are very different from those of a homogeneous one due to the step change in permeabilities (Fig. 2). The effect of permeability contrast can be examined by holding the permeability of the inner layer constant while changing the permeability of the outer layer. When the outer layer is more permeable (i.e., $K_1/K_2 < 1$), the convective cell becomes notably stronger when compared with that of a uniform case. Since less flow resistance is encountered in the outer layer, the buoyancy-induced flow is initiated at a smaller Rayleigh number. The outer sublayer thus acts like a convection promoter. If the outer layer is less permeable (i.e., $K_1/K_2 > 1$), the added flow resistance in the outer layer inhibits the penetration of the convective flow such that the recirculating cell is primarily confined to the inner layer. The outer sublayer in this case acts like a convection suppressor. Due to the difference in the role played by the inner sublayer, the heat transfer modes in these two cases are also distinctive. For a layered annulus with $K_1/K_2 > 1$, heat transfer is mainly by conduction at a small Rayleigh number, which is evident from the corresponding isotherms shown in Fig. 2. As the Rayleigh number increases, it changes gradually from conduction to weak convection. On the other hand, heat transfer is always by convection for a layered annulus with $K_1/K_2 < 1$.

When a system is inhomogeneous in permeability, its thermophysical properties are usually nonuniform. This is especially true when the two sublayers are composed of materials with distinct thermal properties. The nonuniformity in thermal conductivity can further complicate the flow and temperature fields. When the inner layer is less conductive (i.e., $k_1/k_2 < 1$), the thermal resistance across the inner layer is greater than that of the outer layer. Thus, a larger temperature gradient is experi-

enced in the inner region. As a result, the buoyancy-induced flow becomes stronger in the inner region. As the conductivity ratio increases ($k_1/k_2 > 1$), the thermal resistance across the inner layer decreases while it is increased for the outer layer. Consequently, the strength of the convective flow in the inner region is reduced and it is increased for the flow in the outer region. With the combined effects of nonuniform permeability and thermal conductivity, it is observed that the temperature gradient (and therefore the strength of the convective flow) in the inner region is the largest when $k_1/k_2 = 0.5$ and $K_1/K_2 = 0.01$ while it is the smallest when $k_1/k_2 = 2$ and $K_1/K_2 = 100$.

For the present study, the average surface temperature of the inner cylinder is given in terms of the Nusselt number,

$$\text{Nu} = \frac{hD}{k_1} = \frac{qD}{k_1(T_{1m} - T_o)} = \frac{1}{\odot_{1m}} \quad (8)$$

It is observed that the Nusselt number for a layered annulus of $K_1/K_2 < 1$ is always greater than that of a homogeneous one, while it is constantly less for a system with $K_1/K_2 > 1$. When taking into account the effect of nonuniform thermal conductivity, it is found that the Nusselt number decreases as the conductivity ratio k_1/k_2 increases for a given Rayleigh number. Since the average surface temperature of the inner cylinder is the reciprocal of the Nusselt number, this implies that the average surface temperature is actually increased.

For problems involving a layered system, it is a common practice to use a lumped system approach (i.e., assume an effective permeability) in the analysis. It has been shown (Muralidhar et al., 1986; Pan and Lai, 1995) that a harmonic mean permeability, $K_H = 2K_1K_2/(K_1 + K_2)$, usually provides a satisfactory result. While this approach has greatly simplified the problem, there is clearly one major drawback of this approach, that is, it completely ignores the differences in the layer structure. For example, one would obtain the same effective permeability for two layered annuli in which the sublayers are interchanged. As a consequence, the heat transfer results of these two annuli would be the same if the lumped system approach described above were employed. This is exactly what has been shown in the previous study (Muralidhar et al., 1986): The heat transfer results are insensitive to the layer structure of the system. This, of course, is contradicted by the results obtained here.

Experimental data on the heat transfer across a layered porous annulus have been reported for two cases (Muralidhar et al., 1986): $K_1/K_2 = 0.22$ and 4.5. In their study, experiments were conducted using glass beads of 3 mm and 6 mm diameter to comprise the two sublayers. The dimensions of the annulus were $r_1 = 200$ mm and $r_2 = 303.2$ mm, which gave a radius ratio of $R_2/R_1 = 1.516$. It is interesting to note that a good agreement between the numerical and experiment results has been reported only for the case of $K_1/K_2 = 0.22$. The discrepancy found in the case of $K_1/K_2 = 4.5$ was attributed to the non-Darcy effects (for example, viscous and channeling effects). While non-Darcy effects may have some contributions to the discrepancy found, it is felt that a proper treatment of the interface conditions may also be a critical factor in resolving the problem. To verify this point, numerical calculations using the present approach have been repeated for the same problem and the heat transfer result is presented in Fig. 3 for comparison. Although some deviations still exist, the agreement between the numerical and experimental results is much improved. At this
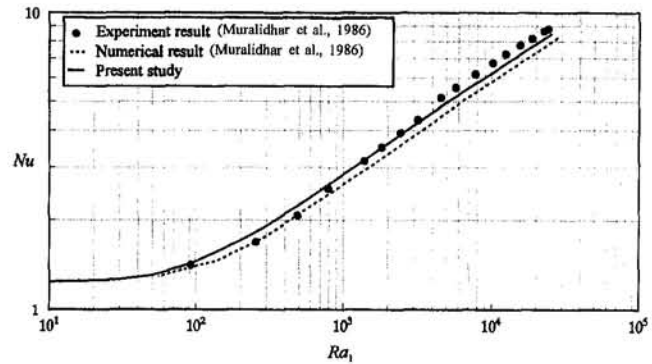

Fig. 3 Comparison of heat transfer results

point, one can conclude that further discrepancy may be due to the non-Darcy effects. Among several possible mechanisms such as flow inertia and wall effects, dispersion resulting from layer interface may also be an important factor (Moranville et al., 1977).

Conclusions

Heat transfer across a layered porous annulus has been examined numerically. It is found that the interface conditions need to be implemented exactly to produce a better agreement with experimental data. While the present study has explored a fundamental heat transfer problem in a layered porous annulus, the results obtained are useful for engineers in the design of a barrier system for a nuclear waste canister. From the present results, it is found that an ideal barrier system can be realized by requiring that the material used for the outer sublayer be less permeable and more conductive than that for the inner layer (i.e., $K_1/K_2 > 1$ and $k_1/k_2 < 1$). The former requirement can result in a better confinement for radionuclide and the latter can reduce the maximum temperature on the canister surface so that corrosion processes can be effectively controlled.

References

Burns, P. J., and Tien, C. L., 1979, "Natural Convection in Porous Media Bounded by Concentric Spheres and Horizontal Cylinders," *International Journal of Heat and Mass Transfer*, Vol. 22, pp. 929–939.

Caltagirone, J. P., 1976, "Thermoconvective Instabilities in a Porous Medium Bounded by Two Concentric Horizontal Cylinders," *Journal of Fluid Mechanics*, Vol. 76, pp. 337–362.

Lai, F. C., 1993, "Improving Effectiveness of Pipe Insulation by Using Radial Baffles to Suppress Natural Convection," *International Journal of Heat and Mass Transfer*, Vol. 36, pp. 899–906.

McKibbin, R., and O'Sullivan, M. J., 1981, "Heat Transfer in a Layered Porous Medium Heated From Below," *Journal of Fluid Mechanics*, Vol. 111, pp. 141–173.

Moranville, M. B., Kessler, D. P., and Greenkorn, R. A., 1977, "Dispersion in Layered Porous Media," *AIChE Journal*, Vol. 23, pp. 786–794.

Muralidhar, K., Baunchalk, R. A., and Kulacki, F. A., 1986, "Natural Convection in a Horizontal Porous Annulus With a Step Distribution in Permeability," ASME JOURNAL OF HEAT TRANSFER, Vol. 108, pp. 889–893.

Pan, C. P., and Lai, F. C., 1995, "Natural Convection in Horizontal Layered Porous Annuli," *Journal of Thermophysics and Heat Transfer*, Vol. 9, pp. 792–795.

Prasad, V., and Kulacki, F. A., 1984, "Natural Convection in a Vertical Porous Annulus," *International Journal of Heat and Mass Transfer*, Vol. 27, pp. 207–219.

Rana, R., Horne, R. N., and Cheng, P., 1979, "Natural Convection in a Multi-Layered Geothermal Reservoir," ASME JOURNAL OF HEAT TRANSFER, Vol. 101, pp. 411–416.

Heat Transfer by Natural Convection Across a Vertical Air Cavity of Large Aspect Ratio

E. Shewen,[1] K. G. T. Hollands,[2]
and G. D. Raithby[2]

Nomenclature

A = aspect ratio = H/b
b = cavity width, m, Fig. 1
H = cavity height, m, Fig. 1
k = thermal conductivity, W/m^2
g = gravitational acceleration, m/s^2
Nu = Nusselt number = $q''b/k(T_h - T_c)$
q'' = average heat flow from hot plate onto cold plate, W/m^2
Ra = Rayleigh number = $g\beta(T_h - T_c)b^3/\nu\alpha$
T_h, T_c = hot and cold plate temperatures, respectively, K
α = thermal diffusivity, m^2/s
β = expansion coefficient, K^{-1}
ν = kinematic viscosity, m^2/s
$\rho_h, \rho_c, \rho_{\mathrm{avg}}$ = air densities at T_h, T_c, and $(T_h + T_c)/2$, respectively, kg/m^3

1 Introduction

Heat transfer by natural convection across vertical air layers is of practical interest, most especially in the estimation of heat transfer through windows. This paper provides new experimental data, which validate and extend the range of previous data for such high aspect ratio cavities. A simple new correlation is also provided that closely fits the data of this and a previous study.

The problem is defined in Fig. 1 (inset). The cavity is bounded by vertical parallel walls with spacing b, and by horizontal walls of spacing H. The other vertical walls, parallel to the plane of Fig. 1, are assumed to have an asymptotically large spacing. The problems of interest have large aspect ratio, $A = H/b$. The vertical walls are isothermal, the horizontal walls have a linear profile from T_h to T_c, and the cavity is filled with air. The linear endwall temperatures are appropriate if the ratio of conductivity of the enclosure wall to the air is large, a requirement met by all solid materials (ElSherbiny et al., 1982b). Assuming the temperature difference $T_h - T_c$ is relatively modest, dimensional analysis on such a problem shows that the Nusselt number has the functional dependence Nu = $f(\mathrm{Ra}, A)$.

The study of this problem was begun by DeGraff and Van der Held (1953) and Batchelor (1954). Theoretical and numerical studies include those of Bergholz (1978), Raithby and Wong (1981), deVahl Davis and Jones (1984), Lee and Korpela (1983), Chenoweth and Paollucci (1985), Ramanan and Korpela (1989), Chait and Korpela (1989), Wright and Sullivan (1994) and Suslov and Paollucci (1995). In an experimental study ElSherbiny et al. (1982a, b) resolved the separate effect of Rayleigh number, Ra, and aspect ratio, A, and correlations based on these data are widely used for window design.

The data reported in this note were measured by a technique that is different from that used by ElSherbiny et al., and therefore they provide important independent corroboration of the previous data. In addition, the maximum Rayleigh number is extended by about a factor of five. At high Rayleigh numbers the new correlation provided in this paper is significantly more accurate than the previous correlation of ElSherbiny et al.

Apparatus and Method

The vertical plates had height H = 750 mm, were 850 mm wide and 25 mm thick, and were made of aluminum. The outside edges of the cavity formed between the plates were closed by 0.038-mm-thick aluminum foil, thermally bonded to the plates and covered on the outside by 25 mm of glass fiber insulation; this foil thickness was chosen to ensure a linear temperature profile between the plates. Three plate spacings, b, were used: 18.97, 12.48, and 6.81 mm. The aspect ratios studied were therefore A = 39.5, 60.1, and 110.1, which values may be safely rounded to 40, 60, and 110, respectively. Based on the flatness tolerance of the plates (± 0.013 mm) and the standard deviation of 12 different measurements, the experimental uncertainty of b was 0.07 mm.

The temperature of each plate was set, and held uniform to within 0.1 K, by circulating water through a grid of copper tubes on 30 mm centers that were thermally connected to the back of each plate. Plate temperatures were measured using thermocouples embedded in each plate, whose individual readings for one plate never varied by more than 0.07 K.

The experiments were conducted with T_h = 310 K and T_c = 296 K, which meant that fluid property variation should be small, the ratio $(\rho_c - \rho_h)/\rho_{\mathrm{ave}}$ being kept at 0.056. The Rayleigh number was varied by changing the air density, in turn varied through the pressure. This was accomplished by locating the entire apparatus in a pressure vessel with an inside diameter of 1.525 m. By varying the pressure from a very low value up to 1.04 MPa, the Rayleigh number based on H could be varied from very small to about 6.5×10^{10}. The pressure was carefully measured using a transducer, as described by Moore and Hollands (1992).

ElSherbiny et al. measured the heat loss from the hot plate through the use of separate electrically heated plates recessed into the hot plate. In the present study, a different method was used that permitted independent measurements of both the heat loss from the hot plate and the heat gain by the cold plate. Along the vertical centerline of each plate, five 140 × 140 mm Peltier Heat Flux Meters (or PHFMs) were recessed into the aluminum plates such that the surface remained flat. There was a spacing of 10 mm between adjacent PHFMs, and 5 mm between the outside boundary and the edge of the PHFM nearest the boundary, so that a total of 700 mm of the total height of
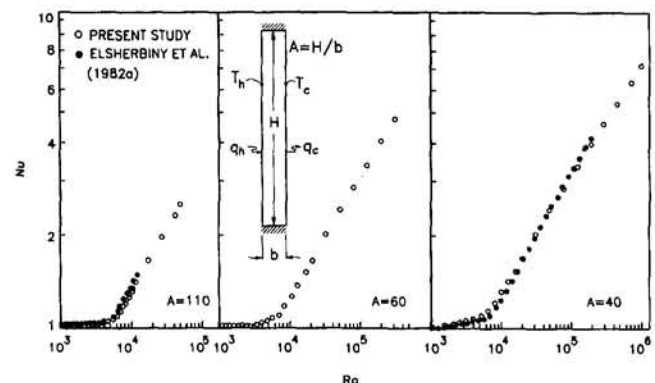

Fig. 1 Schematic of geometry (inset), and experimental data of present study for A = 40, 60, and 110

---

[1] ITX Technologies, Cambridge, ON, Canada, N1R 6R1; Mem. ASME.
[2] Professor, Dept. Mech. Eng., University of Waterloo, Waterloo, ON, Canada, N2L 3G1, Fellow ASME.

$H = 750$ mm was covered. The measured heat transfer from the five PHFMs were averaged to obtain the average plate heat flux q_h'' and q_c'' on each plate. These two fluxes were averaged to find the average heat flux q'' used in the Nusselt number Nu (see Nomenclature). The details of the construction and calibration of these PHFMs are provided by Shewen (1986) and Shewen et al. (1989).

The procedure and the method of data reduction (including the property value equations for air and the method of correcting for the radiative transfer) were essentially the same as those used by ElSherbiny et al. (1982a). After adjusting the pressure, sufficient time (at least 15 minutes) was allowed for steady state to be established, and the measurement period itself lasted 30 minutes, with readings being taken every 10 seconds or so over this period, and then averaged. An error analysis (Shewen, 1986) indicated that the expected error in Nusselt number, Nu, was 1.7 percent, and the expected error in Rayleigh number was 3.3 percent. The expected error in aspect ratio A was less than 1 percent. In converting the data to Nu and Ra, property values were evaluated at the mean temperature, $(T_h + T_c)/2$.

Several tests were performed to check the integrity of the experiment. As described by Shewen et al. (1989), the integrity of the heat flux measurement (as well as the measurement of b) was validated in certain preliminary experiments. One of these experiments demonstrated the equality of the two heat fluxes q_h and q_c, to within experimental error, or ± 1 percent, over a range of plate temperatures. In the second validation test, the thermal conductivity of dry air at 303 K was measured by measuring the average heat flux at various values of b, under stagnant air conditions (the plates were rotated through 90 deg with heating from above). The resulting value of the thermal conductivity agreed with the accepted literature value to within 0.5 percent. As a validation of the Rayleigh number measurement, the apparatus was used to measure the critical Rayleigh number Ra_c of an extensive horizontal fluid layer heated form below, which is known to be $Ra_c = 1708$. To do this the plates were rotated through 90 deg, and the method of Hollands and Konicek (1973) was used. The results were as follows: at $b = 19.0$ mm, $Ra_c = 1737 \pm 34$; at $b = 12.5$ mm, $Ra_c = 1709 \pm 24$.

Results

Figure 1 plots the present results on a separate graph of Nu versus Ra for each aspect ratio. Also plotted on the figure are the data of ElSherbiny et al. (1982a) for $A = 40$ and $A = 110$. The two sets of data agree within 1 percent over much of the Ra range, although there are ranges where the differences are
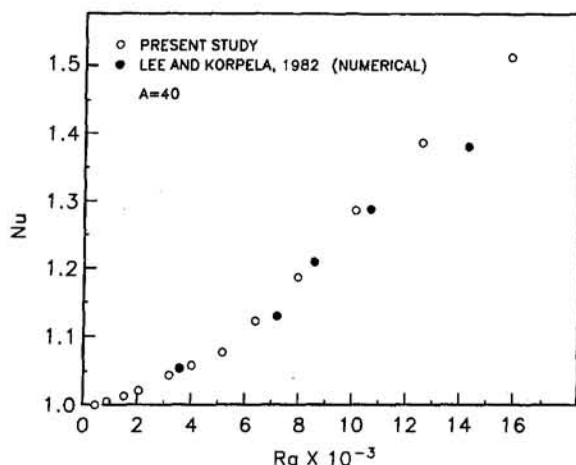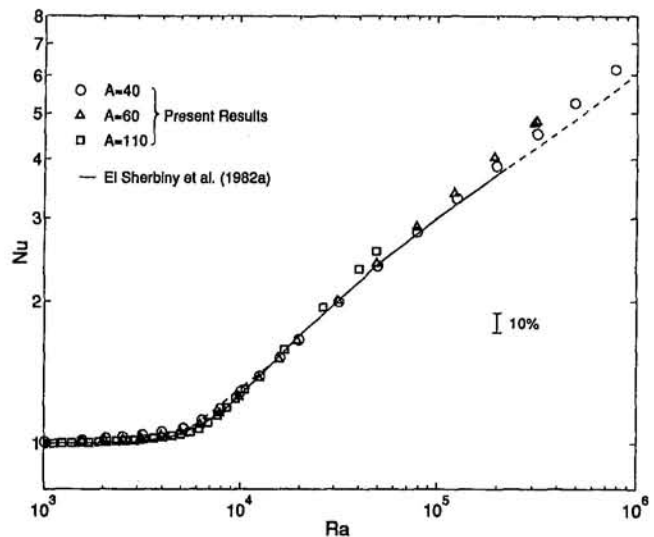
Fig. 3 Correlation of ElSherbiny et al. (solid line) compared to present data. Dashed line for Ra > 2 × 10⁵ extrapolates the correlation beyond its stated range of validity. The dashed line between Ra = 5.5 × 10³ and 1.5 × 10⁴ indicates an unintended clipping that occurred in the correlation equation.

larger. The differences rarely exceed 3 percent, which is roughly the sum of the experimental errors from the two experiments.

Figure 2 compares the results at $A = 40$ with the numerical predictions of Lee and Korpela (1983), which were based on the Boussinesq approximation. The agreement is seen to be excellent and well within the uncertainty in the experimental data, except for the numerically obtained point at the highest values of Ra, i.e., at Ra = 14,000. It is opined that the low predicted heat transfer at this high Ra resulted from the failure of the computations to resolve the finest structures of the flow.

Figure 3 plots the present results for the various aspect ratios merged onto a common graph. The data appear to be nearly independent of aspect ratio. ElSherbiny et al. made a similar observation for $A \geq 20$. A closer examination of Fig. 3 does reveal that there is a slight increase of Nu with A, the effect becoming more pronounced at high values of Ra.

The correlation equation of ElSherbiny et al. (1982a), which was intended to fit the main features of the Nu dependence on Ra and A, is plotted in Fig. 3. For $A \geq 30$, there was no dependence on A. When the correlation is extrapolated beyond the range of the experimental data on which it was based (see the dashed portion in Fig. 3 for Ra > 2 × 10⁵), it lies below the present data. Also, as pointed out by Wright (1994), the correlation of ElSherbiny et al. (inadvertently) clipped the intended curve in the small region 5.5 × 10³ < Ra < 1.5 × 10⁴, thereby giving the dotted curve shown, instead of the intended solid curve.

The following correlation equation was found to fit very closely the combined data of ElSherbiny et al. and the present data:

$$ \mathrm{Nu} = \left[1 + \left(\frac{0.0665 \, \mathrm{Ra}^{1/3}}{1 + (9000/\mathrm{Ra})^{1.4}} \right)^2 \right]^{1/2} \quad (1) $$

The equation is plotted in Fig. 4 along with the present data and the data of ElSherbiny et al. for $A \geq 40$. The equation fits the combined data sets within an rms deviation of 1.7 percent, and a maximum deviation of 5.2 percent, and it is intended for $A \geq 40$, $Pr \approx 0.7$ (gases) and Ra < 10⁶.

Conclusions

Previous experiments reporting Nu–Ra data for natural convection heat transfer across a high aspect ratio ($40 \leq A \leq 110$)

Fig. 2 Comparison of the calculations of Lee and Korpela (1982) with the present data for $A = 40$
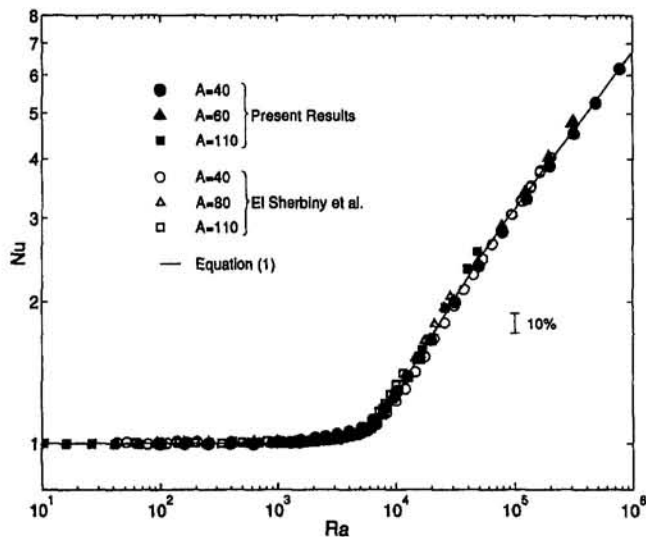
Fig. 4 Comparison of Eq. (1) with present data and those of ElSherbiny et al. (1982a)

gas layer have been successfully corroborated and extended to higher Ra, raising the maximum Ra studied by a factor of about five. The new data at $A = 40$ are in excellent agreement with numerically obtained results for $Ra \le 11{,}000$. The data show a very modest effect of aspect ratio A. A new correlation equation for cavities having aspect ratio greater or equal to 40 fits the data with a tolerance that is consistent with the expected experimental error, of about ± 1.7 percent. It is recommended that Eq. (1) be used in place of the earlier equation of ElSherbiny et al. for the heat transfer across high aspect ratio cavities.

Acknowledgments

References

Batchelor, G. K., 1954, "Heat Transfer by Free Convection Across a Closed Cavity Between Vertical Boundaries at Different Temperatures," *Quarterly J. of Applied Mathematics,* Vol. 12, pp. 209–233.

Bergholz, R. F., 1978, "Instability of Steady Natural Convection in a Vertical Fluid Layer," *Journal of Fluid Mechanics,* Vol. 84, pp. 743–768.

Chait, A., and Korpela, S. A., 1989, "The Secondary Flow and Its Stability for Natural Convection in a Tall Vertical Enclosure," *Journal of Fluid Mechanics,* Vol. 200, pp. 189–216.

Chenoweth, D. R., and Paollucci, S., 1985, "Gas Flow in Vertical Slots With Large Horizontal Temperature Differences," *Phys. Fluids,* Vol. 28, No. 8, pp. 2365–2374.

DeGraaf, J. G. A., and Van der Held, E. F. M., 1953, "The Relation Between the Heat Transfer and Convection Phenomena in Enclosed Plane Air Layers," *Applied Science Research,* Vol. 3, pp. 393–409.

de Vahl Davis, G., and Jones, I. P., 1984, "The Effect of Vertical Temperature Gradients on Multi-cellular Flows in High Aspect Ratio Cavities," *Proc. Conference on Liquid Metal Technology in Energy Production,* Oxford, United Kingdom, pp. 9–13.

ElSherbiny, S. M., Raithby, G. D., and Hollands, K. G. T., 1982a, "Heat Transfer by Natural Convection Across Vertical and Inclined Air Layers," ASME JOURNAL OF HEAT TRANSFER, Vol. 104, pp. 96–102.

ElSherbiny, S. M., Hollands, K. G. T., and Raithby, G. D., 1982b, "Effect of Thermal Boundary Conditions on Natural Convection in Vertical and Inclined Air Layers," ASME JOURNAL OF HEAT TRANSFER, Vol. 104, pp. 515–520.

Hollands, K. G. T., and Konicek, L., 1973, "Experimental Study of the Stability of Differentially Heated Inclined Air Layers," *International Journal of Heat and Mass Transfer,* Vol. 16, pp. 1467–1476.

Lee, Y., and Korpela, S. A., 1983, "Multicellular Natural Convection in a Vertical Slot," *Journal of Fluid Mechanics,* Vol. 126, pp. 91–121.

Moore, G. A., and Hollands, K. G. T., 1992, "Natural Convection Heat Transfer From a Plate in a Semi-circular Enclosure," ASME JOURNAL OF HEAT TRANSFER, Vol. 114, pp. 121–126.

Raithby, G. D., and Wong, H. H., 1981, "Heat Transfer by Natural Convection Across Vertical Air Layers," *Numerical Heat Transfer,* Vol. 4, pp. 447–457.

Ramanan, N., and Korpela, S. A., 1989, "Multigrid Solution of Natural Convection in a Vertical Slot," *Numerical Heat Transfer,* Vol. 15, pp. 323–339.

Shewen, E. C., 1986, "A Peltier-Effect Technique for Natural Convection Heat Flux Measurement Applied to the Rectangular Open Cavity," Ph.D. thesis, Department of Mechanical Engineering, University of Waterloo, Waterloo, Ontario, Canada.

Shewen, E. C., Hollands, K. G. T., and Raithby, G. D., 1989, "The Measurement of Surface Heat Flux Using the Peltier Effect," ASME JOURNAL OF HEAT TRANSFER, Vol. 113, pp. 708–803.

Suslov, S. A., and Paollucci, S., 1995, "Stability of Natural Convection Flow in a Tall Vertical Enclosure Under Non-Boussinesq Conditions," *International Journal of Heat and Mass Transfer,* Vol. 38, No. 12, pp. 2143–2157.

Wright, J. L., and Sullivan, H. F., 1994, "A 2D Numerical Model for Natural Convection in a Vertical, Rectangular Window Cavity," *ASHRAE Transactions,* Vol. 100, pp. 1193–1206.

Wright, J. L., 1994, personal communication.

The Effect of Turbulence on Solidification of a Binary Metal Alloy With Electromagnetic Stirring[1]

J. L. Lage.[2] I have read with interest the subject research work published recently by the ASME JOURNAL OF HEAT TRANSFER. In it, two fundamental aspects caught my attention: (1) the inclusion of a Darcy-like term in the momentum equation to model the viscous drag effect imposed by the solid dendrites to the fluid flow within the mushy zone; (2) the use of a $\kappa-\epsilon$ turbulence model to evaluate the eddy viscosity.

My initial comments relate to item (1) above. The momentum Eqs. (7) and (8) of are written in terms of mixture velocity (Bennon and Incropera, 1987). The drag effect of the solid phase is modeled via a Darcy-like term, that is, they treat the mushy zone as a porous medium and assume an isotropic model for the drag effect of the dendrites. Visualization of dendrite growth shows the mushy zone to be highly anisotropic. One would expect this morphologic aspect to play an important role in the flow within this region. My question then is: To what degree is the anisotropic aspect of dendrite growth responsible for the nonaxisymmetric character of the macrosegregation pattern observed experimentally but not revealed by the numerical results of the laminar model assuming symmetric permeability (Prescott et al., 1994)?

My most important comment, item (2) above, concerns the $\kappa-\epsilon$ model used by the authors. Their initiative in taking turbulence effects into consideration is commendable. Their analysis, though, seems to be questionable in one fundamental aspect: The $\kappa-\epsilon$ equations are not built from a physical law as are the momentum equations (Newton's second law of motion). Rather, they are derived from the momentum equations via suitable algebraic manipulations. Therefore, the final form of any $\kappa-\epsilon$ equations is rigidly tied to the form of the momentum equation from which they are derived (e.g., the Jones and Launder, 1972, model equations are consistent only with the momentum equations from which they were derived, namely those used by Jones and Launder). With that in mind, one should immediately identify the absence, for instance, of any buoyancy effect on the κ equation, Eq. (14), of the subject paper. In modeling phase change with strong convective effect, this term, written using Prescott and Incropera's nomenclature as $\rho_l g \beta_T$ $(\nabla T \cdot e_z)$, should be extremely important (note that e_z is introduced here as the unit vector in the z direction) as indicated by their numerical results in which the temperature gradient within the mushy zone seems very high. It is noteworthy that Prescott

and Incropera modified the original κ equation, Eq. (14) into their Eq. (17), including the effect of the Darcy-like term of the momentum equation. They, however, did not recognize that an extra term should also be included in the ϵ equation. Afterall the Darcy-like momentum term should affect both the κ and the ϵ equations. This extra term of the ϵ equation has the interesting general property of being a depletion term for the turbulence dissipation rate equation (Antohe and Lage, 1996), and this term can counterbalance the depletion term brought about by the Darcy-like term into the turbulence kinetic energy equation. The important conclusion is that turbulence can be important within the mushy zone depending upon the relation of these two terms.

The subject work indicates the importance of developing a consistent turbulence model of flow through permeable media, in which the effects of the extra drag terms (viscous and form) present in the momentum equations are taken into consideration. A step toward this objective has been recently taken by Antohe and Lage (1996).

References

Antohe, B. V., and Lage, J. L., 1996, "A General Two-Equation Turbulence Model for Incompressible Flow Through a Porous Medium," *Transport in Porous Media*, in review.

Bennon, W. D., and Incropera, F. P., 1987, "A Continuum Model for Momentum, Heat and Species Transport in Binary Solid–Liquid Phase Change Systems—1. Model Formulation," *International Journal of Heat and Mass Transfer*, Vol. 30, pp. 2161–2170.

Jones, W. P., and Launder, B. E., 1972, "The Calculation of Low-Reynolds-Number Phenomena With a Two-Equation Model of Turbulence," *International Journal of Heat and Mass Transfer*, Vol. 16, pp. 1119–1130.

Prescott, P. J., Incropera, F. P., and Gaskell, D. R., 1994, "Convective Transport Phenomena and Macrosegregation During Solidification of a Binary Metal Alloy: II—Experiments and Comparisons With Numerical Predictions," ASME JOURNAL OF HEAT TRANSFER, Vol. 116, pp. 742–749.

Authors' Closure

Professor Lage correctly points out that the permeability of a columnar dendritic structure is better characterized as anisotropic than isotropic. However, it is generally accepted that an agglomeration of equiaxed dendrites should be modeled with an isotropic permeability. Yoo and Viskanta (1992) examined the effects of anisotropic permeability on numerical predictions of double diffusive convection. It is our opinion that the advantages of using such an anisotropic model can only be reaped if there is access to a reliable directional permeability data base. Unfortunately, such data are, at best, sparse. Three-dimensional simulations, similar to those performed by Neilson and Incropera (1993) (with an isotropic permeability model) would have to be performed to test Professor Lage's hypothesis that anisotropic permeability contributes to the formation of three-dimensional macrosegregation patterns.

The main thrust of Professor Lage's comments was directed at our use of a $k-\epsilon$ model to account for turbulence. Our objective was to determine how turbulence might affect the solidifi-